UNIVERSIDAD COMPLUTENSE DE MADRID

FACULTAD DE CIENCIAS GEOLÓGICAS

TESIS DOCTORAL

The monogenetic volcanism of the Michoacán-Guanajuato volcanic field (México): petrogenesis and geodynamics implications

El volcanismo monogenético del campo volcánico de Michoacán-Guanajue¡ato (México): petrogénesis e implicaciones geodinámicas

MEMORIA PARA OPTAR AL GRADO DE DOCTOR

PRESENTADA POR

Emma Losantos Guillén

Directores

José María Cebriá
Dante Jaime Morán-Zenteno

Madrid, 2017

PhD Thesis

The monogenetic volcanism of the Michoacán - Guanajuato Volcanic Field (Mexico): petrogenesis and geodynamic implications

El volcanismo monogenético del Campo Volcánico de Michoacán - Guanajuato (México): petrogénesis e implicaciones geodinámicas

Emma Losantos Guillén

IGEO
INSTITUTO DE GEOCIENCIAS

Facultad de Ciencias Geológicas

Madrid, 2017

UNIVERSIDAD COMPLUTENSE DE MADRID
FACULTAD DE CIENCIAS GEOLÓGICAS
INSTITUTO DE GEOCIENCIAS
DEPARTAMENTO DE DINÁMICA TERRESTRE
Y OBSERVACIÓN DE LA TIERRA

Tesis Doctoral

The monogenetic volcanism of the Michoacán - Guanajuato Volcanic Field (México): petrogenesis and geodynamic implications

El volcanismo monogenético del Campo Volcánico de Michoacán - Guanajuato (México): petrogénesis e implicaciones geodinámicas

Memoria presentada para optar al grado de Doctor en Ciencias Geológicas

Emma Losantos Guillén

Madrid, 2017

Directores:

José-María Cebriá
Dante Jaime Morán-Zenteno

UNIVERSIDAD COMPLUTENSE DE MADRID
FACULTAD DE CIENCIAS GEOLÓGICAS
INSTITUTO DE GEOCIENCIAS
DEPARTAMENTO DE DINÁMICA TERRESTRE
Y OBSERVACIÓN DE LA TIERRA

Tesis Doctoral

The monogenetic volcanism of the Michoacán - Guanajuato Volcanic Field (México): petrogenesis and geodynamic implications

El volcanismo monogenético del Campo Volcánico de Michoacán - Guanajuato (México): petrogénesis e implicaciones geodinámicas

Memoria presentada para optar al grado de Doctor en Ciencias Geológicas

Emma Losantos Guillén

Madrid, 2017

Tesis Doctoral realizada en el Instituto de Geociencias (UCM-CSIC) con ayuda de una beca de Formación de Personal Investigador (BES-2012-052390) del Ministerio de Economía y Competitividad, e integrada en el proyecto de investigación CGL2011 - 23422 (Origen, evolución y distribución del volcanismo adakítico y asociado en el Campo Volcánico de Michoacán-Guanajuato, México) del Ministerio de Economía y Competitividad.

Vº Bº de los directores de la tesis:

Dr. José María Cebriá

Dr. Dante Jaime Morán-Zenteno

Agradecimientos

La elaboración de un trabajo tan largo y complejo como una tesis doctoral nunca es producto exclusivo del esfuerzo individual, por eso a continuación me gustaría hacer una mención a todas las personas que a lo largo de estos años han contribuido a que este proyecto llegara a buen puerto.

En primer lugar quiero dar las gracias a mi director, el Dr. José María Cebriá, por su inestimable ayuda e interés que han hecho posible el buen desarrollo de esta investigación y también por los buenos ratos tanto de oficina como de campo. Sus enseñanzas y consejos que me han aportado una visión de conjunto sin la cual todavía seguiría sin ver el bosque entre tanto árbol.

A mi codirector el Dr. Dante Jaime Morán Zenteno le agradezco también su interés, las interesantes discusiones sobre la geología de México y su hospitalidad durante mi estancia en la Universidad Autónoma de México. Asimismo agradezco a la Dra. Barbara Martiny su hospitalidad y la ayuda prestada tanto académica como personal durante dicha estancia.

A David Orejana, mi tutor, le agradezco las largas charlas que me ayudaron a asentar conceptos así como su ayuda logística con temas prácticos del doctorado. También le estoy muy gradecida al Dr. José López Ruiz, ha sido una suerte poder haber aprendido directamente de el.

Agradezco también la importante labor desarrollada y la ayuda recibida por parte del personal de los distintos laboratorios donde se llevaron a cabo las distintas técnicas analíticas: a Mario Alfredo Ramos Arias por su asistencia en las labores de campo, a Alfredo Fernández Larios por sus explicaciones y consejos sobre el uso de la Microsonda Electrónica; a Gabriela Solís y Peter Schaaf por la formación recibida sobre preparación de muestras en el laboratorio de química ultrapura y manejo del espectrómetro de masas; a Rufino Lozano por la formación recibida en la técnica de fluorescencia de rayos X y a Santiago Avilés por su ayuda con la misma y con la preparación de mues-

tras; a Arturo Gómez-Tuena, Elena Lounejeva y Ofelia Pérez Arvizu por su labor en la obtención de datos de elementos traza; a Luca Ferrari por cedernos su extensa base de datos de geoquímica de roca total de México; a Pilar Montero por su labor en la obtención de isótopos de Sr y Nd; a Laura Luna por facilitarnos la cartografía de la zona y por su ayuda en el campo; a Terry Donnelly, Alison McDonald and Adrian Boyce por la formación recibida en la técnica de fluorinización para análisis de isótopos de oxígeno en roca total y a Rob Ellam por facilitar mi estancia en el SUERC y por su ayuda durante la misma; a Manuel Castillejo por su trabajo con la elaboración de las láminas delgadas y por sus consejos sobre la preparación y el machaqueo de muestras; y por último al Museo Nacional de Ciencias Naturales de España por poner a mi disposición los talleres para la preparación y el machaqueo de muestras, el laboratorio de microscopía óptica y un espacio donde trabajar.

También en relación al Museo de Ciencias quiero agradecer a mis "Crazy becarias" Alba, Cristina, Elena, Jenny, Miriam y Raquel por los buenos ratos, las risas y sobre todo por el apoyo durante el tiempo que compartimos despacho, ¡se os echa de menos!

Muy importante ha sido también toda la gente que de una manera u otra me ha apoyado y ha ejercido una influencia positiva en mí, por ello quiero dar las gracias a mis amigas/os y especialmente a Alberto, Emillio, Fede, Michael, Nicky y Oscar por los buenos ratos y las charlas reconfortantes, ¡muy necesarias para recargar fuerzas!

También por supuesto a mi familia que siempre ha sido un acicate para mí, y especialmente a mi tía Consu quien me enseño el pensamiento científico cuando era pequeña.

Finalmente quiero agradecer a mis padres todo su cariño y confianza en mí desde siempre y a Alan, que hace que todo sea más fácil y bonito, a ellos les dedico esta tesis.

Table of contents

Abstract

The present study focuses on the petrogenesis of Plio-Quaternary to Holocene monogenic volcanism of the Michoacán-Guanajuato Volcanic Field (MGVF) in Mexico, one of the largest volcanic fields of the Trans Mexican Volcanic Belt (TMVB). In this volcanic field, an association of alkaline and calcalkaline magmas coexists in its northern sector that has not yet been fully studied. Alkaline and subalkaline magmatism are traditionally attributed to different geodynamic environments (intraplate volcanism vs. volcanism related to subduction) and their coexistence is still a matter of debate both in a general sense and in the context of the TMVB.

The main goal of this project was to accurately characterise the petrogenesis of the MGVF monogenetic volcanism, especially in regard to the alkaline - calcalkaline magmatic association present in the northern sector, and its relationship with the calcalkaline volcanism that predominates in the rest of the volcanic field. The obtained petrogenetic information and its integration with geological and tectonic observations has in turn allowed essential inferences to be made about the geodynamic environment in which the different petrologic types could have been generated and thus establishing a general tectono-magmatic model to explain its origin.

The methodology used was based on a complete petrographic and geochemical study of an exhaustive sampling of the extruded lavas in monogenetic volcanic edifices, mostly from small cones and maars, although two major volcanoes have also been considered (Parícutin and El Metate). The collected samples were studied from a petrographic and geochemical point of view, both in whole rock (major and trace elements and Sr-Nd-Pb-O isotopes) and in mineral phases (major elements). The geochemical data have been the basis of a thermobarometric study and, after the identification of the dominant genetic processes (from petrographic and geochemical observations),

and a quantitative petrogenetic modelling has been carried out in order to reproduce the behaviour of the major and trace elements as well as the Sr-Nd-Pb-O isotopes during the identified differentiation processes.

The main results, some already published and others under revision, suggest that most of the rocks studied represent differentiated magmas produced mostly by Assimilation and Fractional Crystallization (AFC) processes. Alkaline volcanism is represented by two different differentiation trends, one of OIB-type signature and the other with intermediate characteristics between the first one and the calcalkaline magmatism. The petrogenetic modelling of these trends indicates that each of them evolved from different initial magmas, through similar differentiation processes and with no interaction between them, nor with the calcalkaline magmas whose differentiation occurs under parameters similar to those identified for the alkaline suite.

According to thermobarometry data, alkaline magmas have the highest temperatures and pressures of crystallization (up to T ~ 1260 °C and P ~ 16 kbar) with respect to calcalkalines (T ~ 1230 °C and P ~ 11 kbar). In both cases the data suggest polybaric differentiation, although the calcalkaline magmas show abundant evidence of intracortical stagnation, practically absent in the case of the alkaline volcanism.

The quantitative petrogenetic modelization supports in all cases that the AFC processes are the prevalent mechanism of evolution in this volcanic field. The calculated data suggest crystallization percentages of about 30 % of different proportions of olivine, plagioclase, pyroxenes, apatite and oxides, and the assimilation of a compositionally heterogeneous granitic component, similar to the sampled in basement upper crustal rocks of this sector of the CVM, discarding the possible assimilation of other lithologies (e.g granulites). The high assimilation rates obtained (r ~ 0.3 and even higher in some cases such as Paricutin) suggest that the assimilation of the granitic components occurred from partially melted sectors of the crust.

As the spatial-temporal association of alkaline magmas is difficult to reconcile in a single geodynamic environment, the results of the geochemical modelling were subsequently integrated with the available geological and geophysical data for the TMVB to propose a tectonomagmatic model. With this approach it was concluded that the approximate N–S distribution of the alkaline volcanism coincides with a major geody-

namic limit, both at the cortical level and in the configuration of the Cocos plate in that zone. The geophysical information supports the existence of a possible disruption of the subducted plate, that would facilitate the access to the mantle wedge of enriched sublithospheric melts that would act as metasomatizing agents in that region of the mantle as well as precursors of the OIB type alkaline volcanism, which would result mostly from direct ascent of the sublithospheric magmas through the mantle wedge. On the other hand, variations in the melting rate of the metasomatized mantle wedge would explain the coexistence of the alkaline volcanism with some calcalkaline characteristics and the dominant calcalkaline volcanism in the northern sector of the MGVF. Alkaline melts would be produced by very low melting degrees that would selectively tap sectors of the mantle wedge enriched by sublithospheric melts , whereas higher percentages of F would encompass larger portions of the mantle wedge mainly enriched by fluids derived from the subducted oceanic plate thus obliterating the OIB signature and producing calcalkaline magmas. The southern sector calcalkaline magmas, where contemporaneous alkaline magmatism is nearly absent, would be generated either by the same mechanism or from regions of the mantle wedge unaffected by sublithospheric melts.

Resumen

El presente trabajo de investigación aborda la petrogénesis del volcanismo monogenético Plio-Cuaternario a Holoceno del Campo Volcánico de Michoacán-Guanajuato (CVMG) en México, uno de los mayores campos volcánicos del Cinturón Volcánico Mexicano (CVM). En dicho campo volcánico coexiste una asociación de magmas alcalinos y calcoalcalinos no estudiado en detalle hasta la fecha. El magmatismo alcalino y subalcalino tradicionalmente se atribuyen a distintos ambientes geodinámicos (volcanismo de intraplaca vs volcanismo relacionado con subducción) por lo que su coexistencia sigue siendo objeto de debate tanto a nivel general como en el CVM.

El objetivo principal de este proyecto ha sido por tanto caracterizar de forma precisa la petrogénesis de dicho volcanismo, en especial por lo que respecta a la asociación de magmatismo alcalino y calcoalcalino presente en el sector norte, y su relación con el volcanismo casi exclusivamente calcoalcalino que predomina en el resto del CVMG. La información petrogenética y su integración con observaciones geológicas y tectónicas, permite a su vez obtener inferencias esenciales acerca del ambiente geodinámico en el que se pudieron generar los distintos tipos petrológicos y así establecer un modelo tectonomagmático general que permita explicar su origen y distribución.

La metodología empleada se ha basado en un completo estudio petrológico y geoquímico a partir de un exhaustivo muestreo de lavas extruidas en edificios volcánicos monogenéticos, la mayoría pertenecientes a pequeños conos y maares aunque también se han considerado dos volcanes de mayor entidad (Parícutin y El Metate). Las muestras recolectadas se estudiaron desde un punto de vista petrográfico y geoquímico, tanto en roca total (elementos mayores, traza e isótopos de Sr-Nd-Pb-O) como en fases minerales (elementos mayores). Los datos geoquímicos han sido la base de un estudio termobarométrico y tras una identificación de los procesos genéticos dominantes (a partir de las observaciones petrográficas y las variaciones geoquímicas), se ha

realizado una modelización petrogenética cuantitativa con objeto de reproducir el comportamiento de los elementos mayores, traza e isótopos de Sr-Nd-Pb-O durante los procesos de diferenciación identificados.

Los resultados principales, algunos ya publicados en artículos y conferencias o en proceso de revisión, sugieren que la mayor parte de las rocas estudiadas representan magmas diferenciados producidos en su mayoría por procesos de Asimilación y Cristalización Fraccionada (AFC). El volcanismo alcalino está representado por dos trends de diferenciación diferentes, uno de tipo OIB y otro con características intermedias entre el primero y el magmatismo calcoalcalino. La modelización petrogenética de dichos trends indica que cada uno de ellos evolucionó a partir de magmas iniciales distintos, mediante procesos de diferenciación similares y que no existió interacción entre ellos ni con los magmas de afinidad calcoalcalina, cuya diferenciación se produce bajo parámetros similares a los identificados para la suite alcalina.

De acuerdo con los datos de termobarometría, los magmas alcalinos presentan las temperaturas y presiones de cristalización más elevados (hasta T ~1260 °C y P ~16 kbar) respecto a los calcoalcalinos (T ~1230 °C y P ~11 kbar). En ambos casos los datos sugieren diferenciación polibárica si bien los magmas calcoalcalinos muestran abundantes evidencias de estancamiento intracortical, prácticamente ausentes en el caso del volcanismo alcalino.

La modelización petrogenética cuantitativa apoya en todos los casos que los procesos AFC han sido el mecanismo de evolución prevalente en este campo volcánico. Los datos calculados sugieren porcentajes de cristalización de alrededor del 30 % de proporciones minerales de olivino, plagioclasa, piroxenos, apatito y óxidos diferentes para cada suite, y la asimilación de un componente granítico composicionalmente heterogéneo, similar al muestreado en rocas de la corteza superior en este sector del CVM, descartándose la posible asimilación de otras litologías (p.ej. granulitas). Las altas tasas de asimilación obtenidas (en general r ~0.3, aunque en algún caso alcanzarían valores de 0.5) sugieren que la asimilación de los componentes graníticos se produjo a partir de sectores parcialmente fundidos de la corteza.

Puesto que la asociación espaciotemporal de magmas alcalinos y calcoalcalinos es difícil de conciliar en un ambiente geodinámico común, los resultados de la modeli-

zación geoquímica han sido posteriormente integrados junto a datos geológicos y geofísicos disponibles para el CVM en general y el CVMG en particular y así proponer un modelo tectonomagmático. Tras dicha aproximación se concluyó que la distribución aproximadamente N–S del volcanismo alcalino coincide con un límite geodinámico principal, tanto a nivel cortical como en la configuración de la placa de Cocos en esa zona. La información geofísica apoya la existencia de una posible disrupción de la placa que subduce, a través de la cual se facilitaría el acceso a la cuña del manto de fundidos sublitosféricos enriquecidos que actuarían como agentes metasomatizantes en esa región del manto así como de precursores del volcanismo alcalino de tipo OIB, que resultaría en su mayor parte por ascenso directo de los magmas sublitosféricos a través de la cuña del manto. Por otro lado, variaciones en las tasas de fusión de la cuña del manto así metasomatizada explicaría la coexistencia del volcanismo alcalino más próximo al calcoalcalino (porcentajes muy bajos de F que afectarían casi exclusivamente a porciones enriquecidas por fundidos sublitosféricos) y el volcanismo calcoalcalino dominante en el sector norte del CVMG, producido por mayores porcentajes de F que afectarían a sectores más extensos de la cuña del manto dominada por el metasomatismo producido por fluidos derivados de la placa oceánica que subduce. Los magmas calcoalcalinos del sector sur del campo, donde apenas existe magmatismo alcalino coetáneo, se generarían bien por el mecanismo anterior o bien a partir de regiones de la cuña del manto no afectadas por fundidos sublitosféricos.

1. Introduction

The Michoacán-Guanajuato Volcanic Field is one of the biggest monogenetic Pliocene to present volcanic fields in the Trans Mexican Volcanic Belt (TMVB), together with the Chichinautzin Volcanic Field, and one of the most prominent monogenetic volcanic regions in the world in terms of size and diversity of volcanic styles (see Ferrari et al., 2012 and Hasenaka & Carmichael, 1985). It has been the subject of several geochemical studies, starting from the extensive analysis of the age, volume, distribution and magma discharge rate of the cinder cones in the field performed by Hasenaka & Carmichael (1985), but those studies were mainly devoted to describing the general characteristics of magmatism (see Hasenaka & Carmichael, 1987; Luhr et al., 1989; Verma, 2015; Verma & Hasenaka, 2004) or to specific volcanoes (see for example Luhr & Carmichael, 1985; McBirney et al., 1987; Corona-Chávez et al., 2006; Cebriá et al., 2011; Chevrel et al., 2015; Losantos et al., 2014, 2015; Rasoazanamparany et al., 2016). In all cases little attention was paid to the less abundant alkaline volcanism and its possible relationship and interactions with the prominent calcalkaline magmatism. The alkaline outcrops are essentially restricted to the northern sector of the MGVF (between the Cuitzeo Lake and Salamanca, Fig. 3.4), within the so-called "Region Volcánica de las Siete Luminarias" Natural Monument in the Valle de Santiago area.

The presence of coeval OIB-like alkaline and andesitic arc-related calcalkaline magmatism in areas where magmatism is assumed to be controlled by subduction is still a matter of debate. In the Trans-Mexican Volcanic Belt (TMVB) such associations, present both in volcanic fields and also within single volcanoes, have been explained through different hypotheses, including the participation of mantle plumes, the existence of slab windows allowing the ascent of enriched asthenospheric material, selective sampling of an heterogeneously metasomatized mantle wedge by variable melting degrees, or even rejecting the influence of subduction (see among others, Díaz-Bravo et al., 2014; Ferrari et al., 2012, 1999; Gómez-Tuena et al., 2007; Márquez et al., 1999;

Verma, 2015). In this context, counting on complete information for such magmatic associations is essential to establish possible constraints on their origin and possible relationships within the framework of monogenetic volcanism.

The importance of monogenetic volcanism from a physical, geodynamic and petrologic point of view has been revised in several recent works (Németh, 2015; McGee, 2016) highlighting a greater complexity than previously assumed for this kind of volcanic activity.

Monogenetic volcanic fields are the superficial expression of small scale basaltic magmatic systems, the Earth's most common form of volcanism (Cañón-Tapia & Walker, 2004; Németh, 2015) and the smallest in terms of magma volume (McGee, 2016), with characteristic magma fluxes of 10^{-1} to 10^{-3} Km^3/ky (Connor & Conway 2000; Guilbaud et al. 2011; Le Corvec et al. 2013a, b). They are typically composed by a number of monogenetic cones (see below) distributed through a region (volcanic field) and can be found in different tectonic settings including intraplate, extensional and subduction related environments (Cañón-Tapia, 2016) and in variable sizes and rates of magmatism (see Valentine & Gregg, 2008), from smaller fields like those of Garrotxa in Olot (NE Spain; 150 km^2 and ~40 volcanic vents) or the Aukland Volcanic Field in New Zealand (300 km^2 and ~50 vents) to larger ones like the MGVF (40000 km^2 and ~1000 vents).

A monogenetic volcano has been defined as a volcanic edifice with a small cumulative volume (≤1 km^3) that was developed in a short time (≤10 years) by either continuous or discontinuous small eruptions with no sign of long time breaks between the individual eruptive phases (Németh & Kereszturi, 2015 and, McGee, 2016). They are typically fed from one or multiple magma batches that rise as a discrete body through a relatively simple, closely spaced feeder dyke system with no well-developed magma chambers associated (Németh & Kereszturi, 2015) and can have a wide range of eruptive styles and morphologies depending on the magma/water ratio. However, not all monogenetic volcanoes fit the traditional view of a volcano that erupts only once during a short time (Takada, 1994; Walker, 2000). Németh et al 2015 have also proposed two types of so-called "transitional volcanoes", including volcanoes with more than an eruptive phase during several years to ky, associated with closely spaced individual

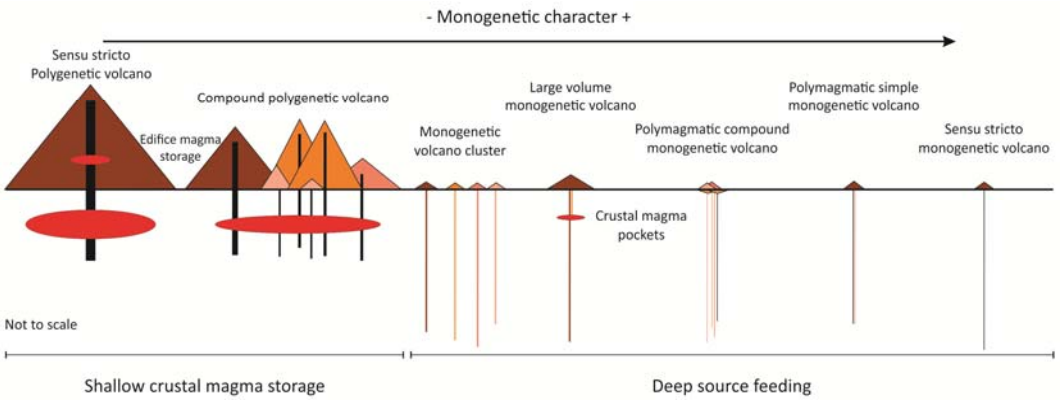

Fig. 1.1 Diagram showing the theoretical link between monogenetic and polygenetic volcanoes (after Nemeth, 2015). The so-called transitional monogenetic volcano would be akin to the El Metate and Parícutin volcanoes within the MGVF.

conduits and an edifice ≥1 km^3, and volcanoes with a single well-defined eruption that produces large volumes of eruptive products through a single conduit. In both cases the result is a larger volcanic edifice akin to a typical polygenetic edifice. Examples of these transitional types would be represented in the MGVF by volcanoes like Paricutin, Jorullo or El Metate.

Despite these exceptions, a monogenetic volcanic field is distinct from polygenetic volcanism in its disperse nature and lack of steadiness of the magmatic feeding conduits, which wander due to the solidification of the lava in the conduit between magma batches therefore preventing the next batch from using the same path to the surface (Connor et al. 1997). As a consequence, over long time periods this feeding style will produce a scattered pattern of vents that may either cluster or align depending on the particular geodynamics of the area, building a volcanic field. In contrast, a more constant feeder source and therefore a more static conduit would build a more complex and larger edifice, typical of polygenetic volcanoes (Fig. 1.1) (Németh & Kereszturi, 2015).

From a geochemical point of view, most studies confirm that lava compositions for these volcanoes are typically basaltic, alkalic and enriched in light rare earth elements and large ion lithophile elements, although they can cover a spectrum from highly enriched nephelinites to subalkalic and tholeiitic basalts. In fact, the MGVF is typically characterized by the presence of calcalkaline lavas.

As basaltic magmas originate by small scale melting of mantle sources and their compositional variety depends on the depth at which the melting processes occur, the range of melting proportions, the heterogeneity of the source and subsequent fractionation, magma mixing and assimilation that could take place within the plumbing system (McGee et al. 2016), the systematic chemical variations in monogenetic volcanoes provide an insight into the physicochemical state of the source zone, melt formation and deep fractionation/melt rising processes (Brenna et al. 2010, 2011; Genareau et al. 2010; McGee et al. 2011, 2013; Jankovics et al. 2012; Valentine 2012).

All these basic concepts on monogenetic volcanism have important implications for petrogenetic modelling. In many of the smaller monogenetic fields it has been shown that most erupted lavas may be related through common magmatic processes. This is the case for example of the primitive lavas of small monogenetic fields like Garrotxa (NE Spain) or Calatrava (Central Spain) which in general terms can be explained through variable different melting degrees from a common mantle source (Cebriá et al., 2000; Cebriá & López-Ruiz, 1996). However, in larger volcanic fields like the MGVF located in a geodynamically complex setting where subduction-related processes have an important role, such a relatively simple scenario may be inaccurate. Furthermore, if the erupting lavas are not primitive but show variable degrees of evolution through different differentiation processes, careful modelling approaches must be undertaken. For example, differences must be present when both small monogenetic and transitional vents coexist, since the former evolve in discrete and independent ascent conduits whereas the latter probably differentiate during longer periods of time in magma chambers.

The research work presented in this memory aims to provide additional data and a new perspective on the petrogenesis and distribution on this monogenetic volcanic field as well as on its geodynamical implications, especially concerning the less studied association of alkaline and calcalkaline suites. The approach followed was not constrained to the description of the evolution of individual volcanoes (also considered in some cases), but rather aims to reach a global understanding of the entire system based on a petrogenetic approach, mainly based on geochemical data gathered from the smaller and recent monogenetic volcanic vents.

To achieve this, this work encompasses a comprehensive geochemical and mineral chemistry study of the different lithologies encountered in the field, which formsthe basis for a thermobarometric study based on the chemistry of the main mineral phases, which is then applied as a starting point for a quantitative petrogenetic modelling based on major, trace elements and Sr-Nd-Pb-O ratios. These results introduce valuable constraints on the origin and conditions under which the resulting magmas evolved and also on the nature of their mantle sources, which are confronted with different models and interpretations published for other areas of the TMVB where alkaline-calcalkaline associations are also present. Finally, the distribution of volcanism in this extensive field and the geologic and tectonic characteristics of the region were considered for a contextualization within a general geodynamic framework including a working hypothesis on the origin and distribution of alkaline volcanism.

2. Geologic and geodynamic background

The Trans-Mexican Volcanic Belt (TMVB) (Fig. 2.1) was defined by Demant (1978) as a continental magmatic arc which comprises nearly 8000 volcanic structures and a few intrusive bodies. It is considered the biggest Neogene volcanic arc in north America (Ferrari et al., 2012), extending about 160000 km^2 across Mexico from the Pacific to the Atlantic ocean with *c.* 1000 km in length and an irregular width of 80 to 230 km between the latitudes 18°30' N to 21°30' N. The arc follows a generic E - W orientation, except in its western sector where it has a WNW - ESE direction, forming a ~16° angle with the Middle America Trench. It is usually divided into three main sectors (Gómez-Tuena, 2007): the West Sector, located between the Pacific Coast and the triple junction formed by the intersection of the Zacoalco, Chapala, and Colima rifts (Allan, 1986); the Central Sector, placed between this triple junction and the Taxco-San Miguel de Allende fault system (Alaniz-Álvarez et al., 2002); and the East Sector, located between these faults and the Gulf of Mexico.

The Michoacán-Guanajuato Volcanic Field (MGVF) is located in the western-central area of the TMVB and is recognized as one of the two biggest monogenetic volcanic fields, together with the Chichinautzin volcanic field (Hasenaka, 1994; Hasenaka & Carmichael, 1985 a, b; Ferrari et al., 2012).

Geodynamic framework

The volcanic arc represented by the TMVB sits on the southern edge of the North American Plate (Fig. 2.1), hence the volcanic and tectonic activity is mainly controlled by the interactions between the North American continental plate and the Cocos, Rivera, and Pacific oceanic plates that together constitute a subduction complex

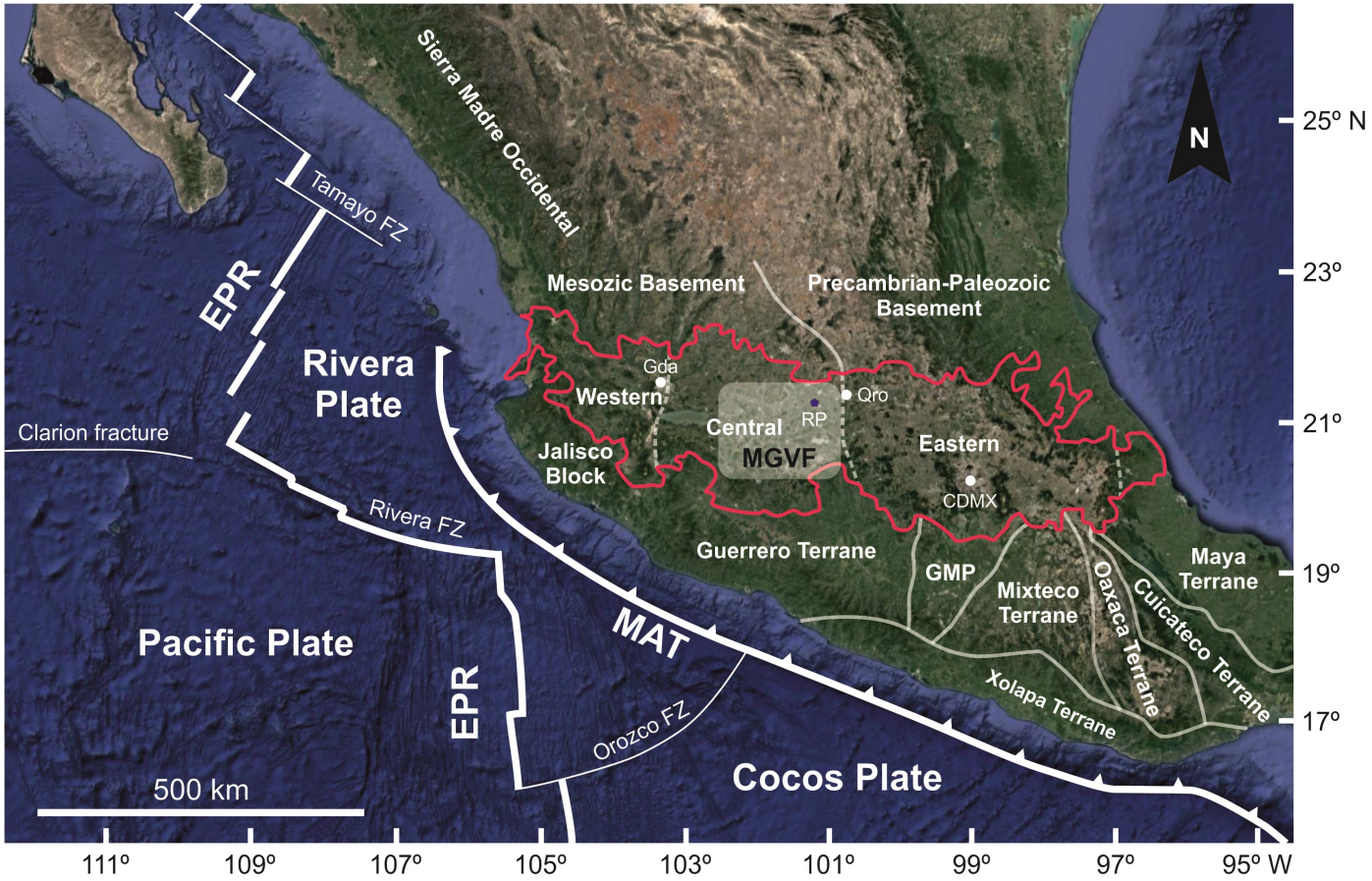

Fig. 2.1 Tectonic map of the Mexican subduction complex and continental crust structure as outlined by Ferrari et al. (2012) and Gómez-Tuena et al. (2017) over a Landsat 8 derived image provided by Earthstart Geographics SIO and processed by HERE 2017. White lines on the oceanic plate depict plate boundaries and main fractures. White faded lines on the continental plate depict main continental crust units. Red line outlines the Trans-Mexican Volcanic Belt divided in the three sectors described in the text (dashed white lines); and white faded square delimitates the approximate location of the Michoacán Guanajuato Volcanic Field. CDMX: México City; Gda: Guadalajara; Qro: Querétaro. RP: Rincón de Parangueo.

that shapes one of the most complex convergent margins of the planet (see Luhr, 1997; Gómez-Tuena et al, 2007; Ferrari et al., 2012; Gómez-Tuena et al., 2017).

Characteristics of the subduction complex

The geological complexity of this area is a consequence of several concurrent factors. The most critical are the characteristics of both the oceanic and continental plates (including the basement terranes differences) and the particular geometry of the subducting plates. In the following sections the main features of this subduction complex are described, which are essential to understand the geodynamics and evolution of the TMVB.

Continental crust

Ferrari et al. (2012) compiled a comprehensive isopach map for the TMVB that help to visualize the overall geometry of the subducting plate and the thickness of the upper plate. Such map was produced from several sources, including: 1) thickness data from several geophysical studies carried out between 2006 and 2010; 2) the MARS seismic experiments (Yang et al., 2009) (Mapping the Rivera Subduction Zone), performed by the University of Texas in collaboration with the UNAM and the University of New Mexico; 3) the MASE (Middle America Subduction Experiment) and VEOX (Veracruz-Oaxaca seismic line) projects (Melgar & Pérez-Campos, 2010; Pérez-Campos et al., 2008) , performed by the California Institute of Technology with the collaboration of the University of California and the UNAM); and 4) gravimetric data after Urrutia-Fucugauchi & Flores-Ruiz (1996) for the areas where seismic information was not available. According to this map, the thickness variations of the continental crust underneath the TMVB were inferred as rather simple, with an overall increase from the coasts to the continental interior. It also highlights an approximate N - S contrasting change in crustal thickness just to the east of 101° W, between the thicker (> 40 km) eastern and the thinner (< 40 km) western sectors (Fig. 2.2).

Basement Terranes

In addition to the variations in thickness, another important factor for the geodynamics of the Mexican continental crust is its configuration in a series of tectonostratigraphic blocks or "terranes" (Fig 1). The Mexican continental basement was first described by Campa & Coney (1983) as an assemblage of several crustal blocks accreted to the North American plate at different tectonic episodes. Later tectonic reconstructions and correlations of those tectonostratigraphic terranes by Sedlock et al. (1993) and Ortega-Gutiérrez et al. (1994) and the recognition of a Grenvillian continental segment underlying most of eastern and central Mexico, Oaxaquia (Ruiz et al., 1988; Keppie & Ortega-Gutiérrez, 1995; Ortega-Gutiérrez et al., 1995), led to the actual division of the cortical basement underneath the TMVB into three distinct tectonostratigraphic terranes: Guerrero, Mixteco, and Oaxaca.

The Guerrero Terrane is located in central-western Mexico and is the largest terrane of the North American Cordillera, measuring circa 700,000 km^2, mainly constituted by volcanic and volcanoclastic rocks of continental and oceanic affinity and marine sedimentary rocks (Campa & Coney, 1983 and Sedlock et al., 1993). Traditionally this terrane has been considered an intra-oceanic island arc or multiple arc-system constructed upon a deep marine environment relatively close to the continent (Centeno-García et al., 1993) accreted to the Mexican continental interior during Cretaceous time. However, other studies cast doubts on its aloctonous nature and propose that it originated through a volcanic and sedimentary assemblage, deposited upon a thinned North American crust, deformed by the Laramide orogeny (Cabral-Cano et al., 2000a, 2000b). This hypothesis is supported by other studies (Schaaf et al., 1995; Elías-Herrera & Ortega-Gutiérrez, 1997, 1998; Elías-Herrera et al., 1998; and Aguirre-Diaz et al., 2002) that suggest the presence of an older silicic continental basement underneath the Guerrero Terrane, which would represent its continental crystalline basement dating back to the Precambrian. Recent reconstructions (see Martini & Ortega-Gutierrez, 2017) favour a scenario in which the subduction-related volcanic rocks are emplaced in an intracontinental rift setting related to the break-up of Pangea, and the igneous and metaigneous assemblages composing the Guerrero terrane would represent a North-

American arc progressively rifted during the Early Cretaceous by back-arc spreading and then accreted back to the Mexican continental interior.

The Mixteco Terrane is located in central-south Mexico, bounded to the West by the Guerrero Terrane, to the East by the Oaxaquia microcontinent along the Caltepec fault zone (a poly-deformed tectonic boundary according to Elías-Herrera et al. (2005), and to the South by the Chatino Terrane. The northern boundary of this terrane is covered by the Trans-Mexican Volcanic Belt. The Mixteco Terrane is constituted by a Paleozoic basement (the so-called Acatlán Complex) (Yañez et al., 1991; Sedlock et al., 1993; Ortega-Gutiérrez et al., 1994; Talavera-Mendoza et al., 2005; Nance et al., 2006; Vega-Granillo et al., 2009) and the materials overlying it. On the basis of its different ages, deformation styles and metamorphic facies, the Acatlán Complex is in turn subdivided into the Acateco and Petlalcingo subgroups, the Tecomate Formation, the Totoltepec stock and the San Miguel pluton. As Gómez-Tuena et al. (2007) summarized it: "*this complex is essentially made of metasedimentary and meta-igneous rocks, with both oceanic and continental affinity, that were metamorphosed under amphibolite, eclogite, and greenschists facies and later intruded by granites and affected by migmatization*". Finally, the materials overlying the Paleozoic sequence are classified into three age groups: Triassic to Middle Jurassic volcanic and intrusive rocks (Rosario Formation and San Miguel plutons), Jurassic to Late Cretaceous marine sedimentary rocks, and Tertiary continental and volcanic sedimentary rocks, silicic ignimbrites, volcanoclastic rocks, andesitic lavas, and lacustrine deposits (Morán-Zenteno et al., 1999).

The Oaxaca Terrane is the easternmost crustal block in Mexico, with an extension of circa 1.000.000 km^2 and was defined by Ortega-Gutiérrez et al. (1995) as a grouping of different terranes according to the similarity in their Middle Proterozoic (Grenvillian) basement rocks, building the so-called microcontinent of Oaxaquia. The terranes that make up this microcontinent are Oaxaca, Juárez, Sierra Madre, Maya and part of the Coahuila terrane (Campa & Coney, 1983), also known as Zapoteco, Guachichil, Tepehuano, Maya, and part of the Cuahuiltecano Terrane, in the terminology of Sedlock et al. (1993).

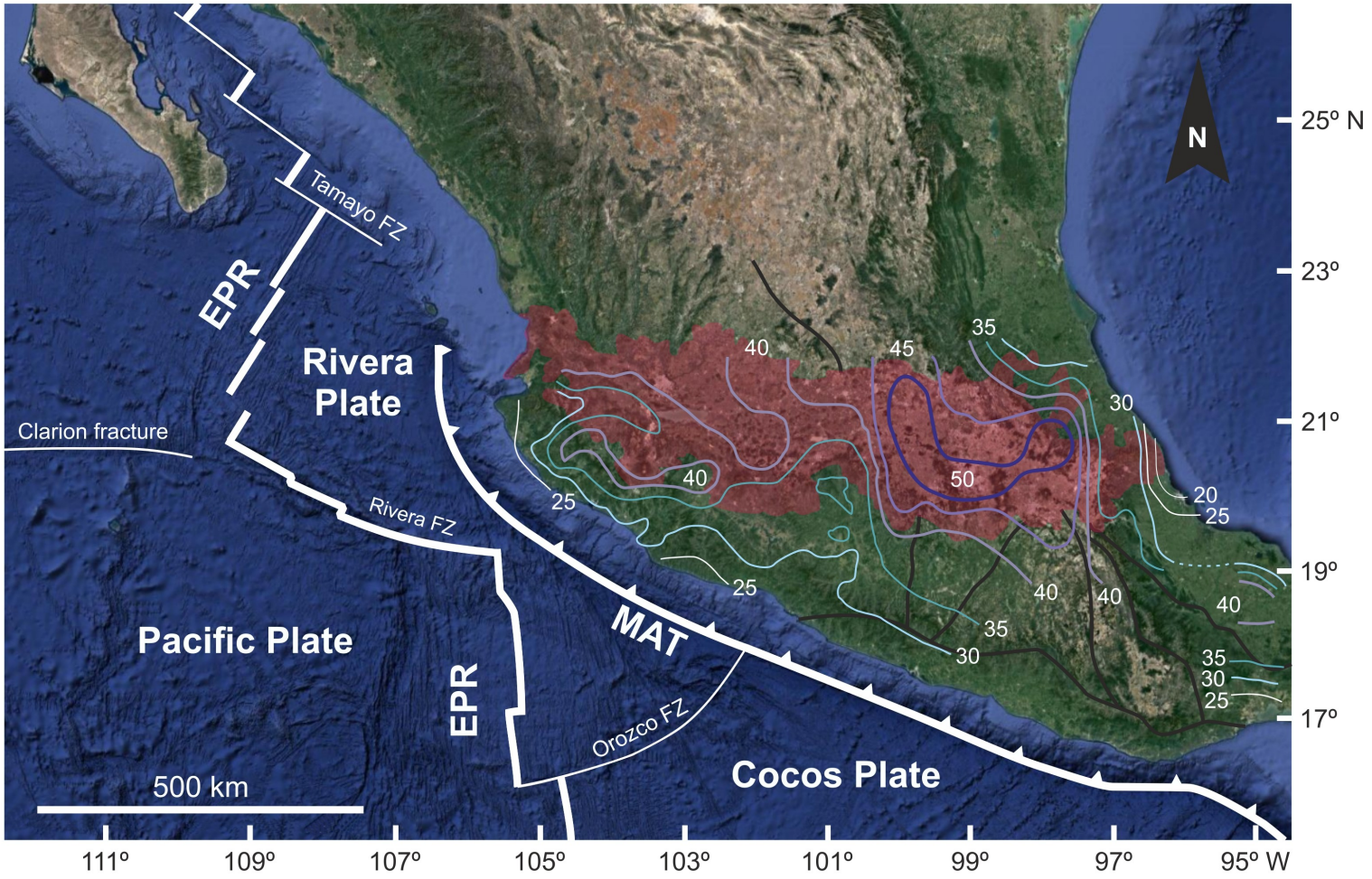

Fig. 2.2 Tectonic map of the Mexican subduction complex and thickness of the continental crust (km) as outlined by Ferrari et al. (2012) and Gómez-Tuena et al. (2017) over a Landsat 8 derived image provided by Earthstart Geographics SIO and processed by HERE 2017. Regional crustal thickness of southern Mexico from Ferrari (2012).

Oceanic plates

The North American continental plate is subducted by the Rivera Plate in its western sector and by the Cocos Plate in the central and eastern sectors (Gómez-Tuena et al., 2007). Global reconstructions by Atwater & Stock (1998) and Londsdale (2005) show that the Farallon plate fragmented into the Cocos and Nazca plates around 23 Ma ago and the Rivera plate branched off the Cocos plate at *c*. 10 Ma (DeMets & Traylen, 2000). Hence, the Rivera plate is relatively younger, between ~9 - 13 Ma at the trench off Puerto Vallarta and Manzanillo respectively (Gómez-Tuena et al., 2007). It subducts to the Northeast beneath western Mexico at a convergence rate with the North American plate that varies from 0.6 cm/yr in the North near the Tres Marias Islands, to 2.0 cm/yr in the South near Manzanillo (DeMets et al., 1990). Subsequent works have recalculated the convergence rate to be between 1.7 and 2.2 cm/yr (DeMets et al., 1994) or between 4 and 4.9 cm/yr (Kostoglodov & Bandy, 1995), depending on the model used. The Cocos plate on the other hand is older, at estimated ages between 12.7 and 16 Ma (Gómez-Tuena et al., 2007) along the trench, getting older to the East. It subducts north-eastward into the Middle America Trench (Fisher, 1961) beneath the Pacific coasts of Mexico and Central America (Molnar & Sykes 1969; Nixon, 1982) at a convergence velocity that increases from ~5 cm/yr in the West to ~8 cm/yr in the East (Minster & Jordan, 1978; McNally & Minster, 1981; DeMets et al., 1990), or from ~4.7 to ~6.7 cm/yr according to Pardo & Suárez (1995).

Geometry of the subducting plates

Based on the assumed subduction rates for the Rivera (~2 cm/yr) and Cocos plates (~5 cm/yr), Nixon (1982) and Eissler & McNally (1984) hypothesized that the boundary between these two oceanic plates was a zone of left-lateral strike slip with a ~3 cm/yr convergent rate in the ~N 45"8 direction. Later on, the aforementioned geophysical studies MARS, MASE and VEOX helped to define the geometry and position of the subducting plates first defined by Pardo & Suárez (1995). Ferrari et al. (2012) combined those data to obtain a general view of the subduction geometry as a map of isobaths (Fig. 2.3) that allows visualizing a contrasted change in the oceanic plate depths. Ac-

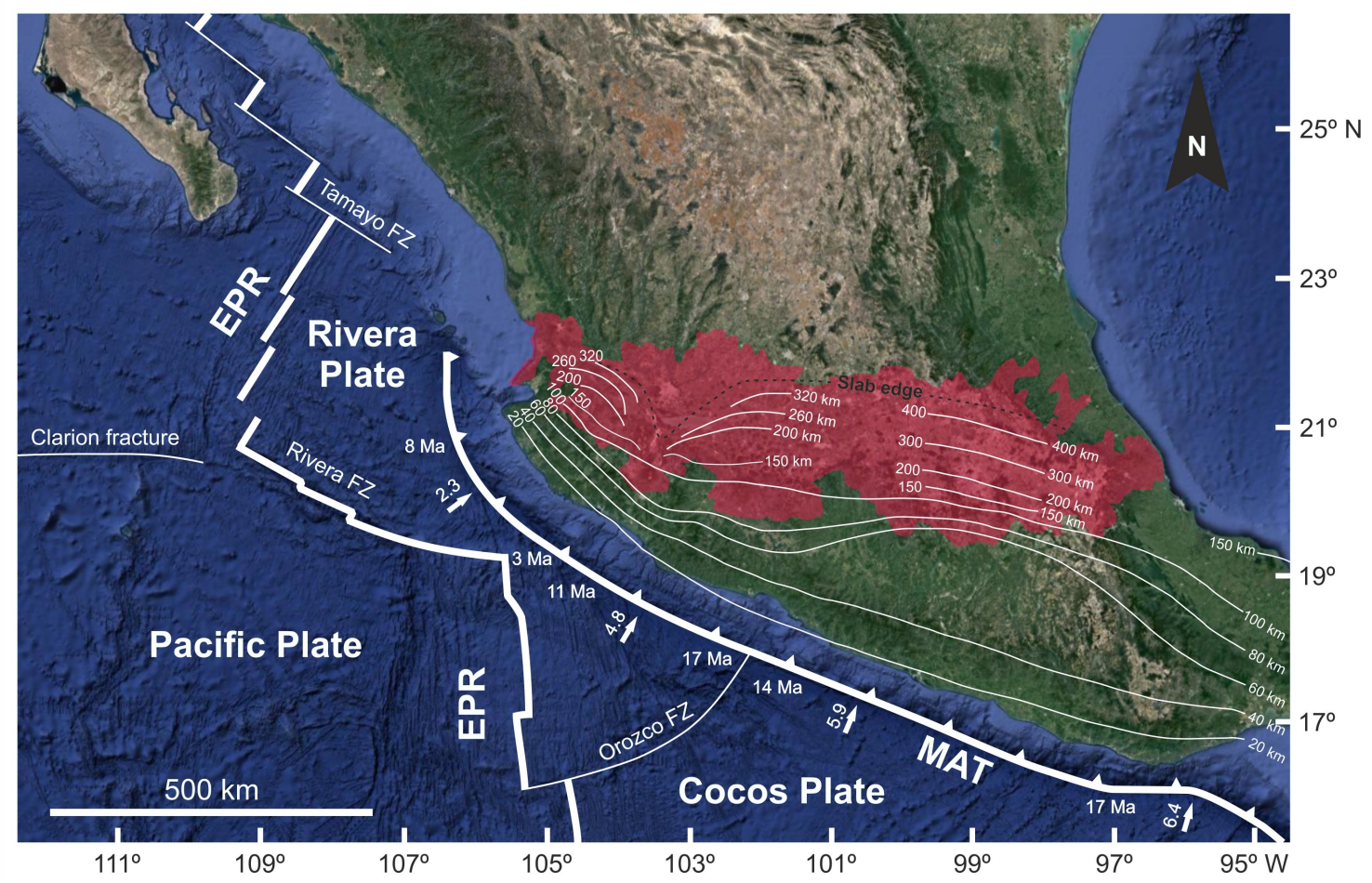

Fig. 2.3 Tectonic map of the Mexican subduction complex and depth of the subducted slab beneath central Mexico as outlined by Ferrari et al. (2012) over a Landsat 8 derived image provided by Earthstart Geographics SIO and processed by HERE 2017. Slab ages (Ma) and convergence rates (cm/year) as portrayed by Gómez-Tuena et al. (2017).

cording to such data, the Rivera Plate beneath the forearc dips at a ~40° angle and then increases up to 70° beneath the TMVB. Meanwhile the dip of the Cocos plate is lower and more variable, decreasing progressively from its boundary with the Rivera plate until approximately the 101° W longitude, coinciding with the edge of the Guerrero Terrane. East of 101° W the dip angle becomes almost horizontal, initially dipping 15° until 80 km inland and then flattening at 50 km depth (Kim et al., 2010; Pérez-Campos et al., 2008) to increase again to 45 - 50° East of the Pico de Orizaba volcano (97°16' 5" W), beneath the Tehuantepec isthmus, the Chiapas massif, and the Central American arc (Pardo & Suárez, 1995). Bandy et al. (1995) associated these differences with the development of the southern Colima Rift that according to Ferrari et al. (2012) would represent the separation of the two oceanic plates in a trench-orthogonal tear that broadens to the North. Gómez-Tuena et al. (2007) remarked as well that such geometry is consistent with the obliquity of the arc, farther away from the trench where the plate is at its shallowest dip angle. From south to north, the end of the flat segment (east of 101° W) corresponds roughly with the southernmost limit of the TMVB but, from there on the dip angle of the plate increases with a different value on each side of the 101° W meridian (see Ferrari et al., 2012 and Fig. 2.3). As will be shown in later chapters, this feature has important implications concerning the petrogenesis of the volcanism in the MGVF.

Volcanism in Mexico

The Cenozoic distribution of volcanism in Mexico is usually divided into four main volcanic areas: the California Province, the Sierra Madre Occidental, the Eastern Alkaline Province, and the Trans-Mexican Volcanic Belt.

The *California Province* is located in the westernmost side of Mexico and includes all the Plio-quaternary basaltic manifestations associated with the Gulf of California-Saint Andreas system (see Lonsdale, 1989; Ferrari et al., 2013; Duque-Trujillo et al., 2014). Those include the igneous rocks of Baja California and the basaltic alkaline emissions at Pinacate-Magdalena (Sonora) and Mazatlán-Choix (Sinaloa). This province can be subdivided in two sectors, north and south, separated by the Santa

Rosalía fault. The volcanic activity started in the northern sector in the Cretaceous (calcalkaline Alisitos Formation; Allison,1974), and did not start in the southern sector until Miocene times (Comundú Formation). The alkaline volcanism associated with the rifting process of the Gulf of California-San Andreas System started during Plio-Quaternary times and formed mainly plateaus.

The *Sierra Madre Occidental Province* represents the largest continuous ignimbritic province in the world at more than 2000 km in length along the Gulf of California (see Demant & Robin, 1975 and Ferrari et al., 2005b). The magmatic activity started in Cretaceous times with a calcalkaline phase in the shape of diorite and gabbro batholiths, but it was in the Miocene (29 to 22 Ma, McDowell & Ciabaugh, 1972) when the ignimbritic emissions started along the occidental coast. During the Pliocene and Quaternary those ignimbrites got covered by alkaline basalts in mainly in Durango, Zacatecas and Sonora.

The *Eastern Alkaline Province* has a NNW-SSE orientation on the easternmost side of Mexico with the alkaline character of the various lithological types and their shared tectonic context being its unifying characteristic (see Ferrari et al., 2005a and references therein). It consists of a series of volcanic intrusions and lavas in the coastal planes between Veracruz and Tamaulipas and some acid fissural events that cover the Mesozoic and Cenozoic folded sediments of the Sierra Madre Oriental. The volcanic activity in this area started during the Oligocene in Sierra de Tamaulipas with the extrusion of alkaline volcanism (rhyolites, syenites and phonolites) and followed during the Miocene in the Tampico, Veracruz and Hidalgo areas with basanites in the plains and intermediate basalts and ignimbrites on the plateau, some even showing interference with the Trans-Mexican Volcanic Belt volcanism. In Plio-quaternary times more alkaline intermediate basalts were emplaced on the plateau as well as basalts and phonolites in the plains.

The *Trans-Mexican Volcanic Belt* (see Ferrari et al., 2012 and references therein for an updated review of this area) is named after its geometry, transversally distributed relative to most of the NNW-SSE trending Mexican Basement terranes (Ortega-Gutiérrez et al., 1992). It is fragmented along its axis by an N-S to NW-SE graben system that caused depressions where alluvial and lacustrine deposits accumulated. Some of

the most important ones from East to West are the grabens of Valle de México, Santiago de Querétaro, Celaya, Penjamillo, Colima and Puerto Vallarta. The composition of the magmatic products is mostly of calcalkaline affinity, particularly those erupted from stratovolcanoes like Nevado de Toluca and middle size monogenetic volcanoes like Paricutin. Minor but significant outcrops of alkaline lavas are also found in the Tepic graben to the west, in the centre (e.g. Chichinautzin and Michoacán-Guanajuato volcanic fields), and in the Palma Sola - Jalapa region to the east. Volcanism started here in the late Oligocene with some dacites and andesites, especially on the eastern side. Later in the Miocene the activity expanded to all the TMVB with predominance of dacites and continued to Plio-Quaternary times coexisting with basic terms (basalts and andesite basalts).

Geodynamic evolution of Central Mexico during the Cenozoic

The above described magmatic provinces and the main identified periods of activity (Cretaceous, Eocene-Oligocene, Miocene and Plio-Quaternary) were considered along their regional tectonic framework by the early work of Demant & Robin (1975) to synthesize the geodynamic evolution of Mexican volcanism.

During Cretaceous times the eastern side of Mexico was an epicontinental transgressive sea that originated at the end of middle Jurassic times with the opening of the Gulf of Mexico (De Cserna, 1960; De Antuñano et al., 2000). The western side began to emerge at the beginning of late Cretaceous as a prolongation to the south of the Californian batholitic granites and the calcalkaline volcanic arc series of Sonora and Sinaloa, both related to the subduction of the Farallon plate (Atwater, 1970; Demant & Robin, 1975 and De Antuñano et al. 2000).

Compressive movements induced the uplifting of the central zone during Albi-Cenomanian times. Andesitic volcanism started to develop afterwards during the Oligocene along the Pacific coast and plutonic intrusions developed the basement of the later Sierra Madre Occidental ignimbrites. At the end of the Oligocene andesitic volcanism started to develop as well in the Trans-Mexican Volcanic Belt in places like Valle de México (Gunn & Mooser, 1970) and Pachuca (Geyne et al., 1963), indicating a change

in strain directions, and the first ignimbritic emissions started to appear in Sierra Madre Occidental.

The Miocene is characterized by an intense activity with andesitic volcanism in the Californian province getting younger to the south as the Farallon plate disappears (Atwater, 1970) and a large ignimbritic phase started covering the pre-existent topography in the Sierra Madre Occidental, where up to 1000 m thick deposits have been interpreted as rift-like activity in an andesitic back-arc (Demant & Robin, 1975).

In Plio-quaternary times a segment from the Pacific ridge collided with the Farallon – North American trench causing the Farallon plate to fragment into the Guadalupe and Juan de Fuca plates to the north and south of the collided segment. Later, the Guadalupe plate would in turn fragment into the Rivera and Cocos plates.

In this new configuration the Baja California zone started to couple with the Pacific plate getting displaced to the NW (Larson, 1972), ultimately leading to the birth of a rift in the Gulf of California-Saint Andreas System and the basin and range-style structure in Sonora, California and Arizona (see Lonsdale, 1989; Henry & Aranda-Gómez, 1992; Ferrari et al., 2012, 2013) . The extensional tectonics regime also implied the appearance of the alkaline volcanism of Sonora in Baja California and Sinaloa (Choix-Mazatlán). In the trans-Mexican Volcanic Belt the calcalkaline volcanism associated with subduction continued but with an increase in the basic terms. It is now clear that it does not maintain the parallelism with the trench like in the Central America sector (McBirney & Weill, 1966).

In summary, until Miocene times volcanism was associated with the W-E movement of the Farallon plate that generated a continental margin type volcanism in the front and an ignimbrite region in the back arc extensional zone. Afterwards, the subduction direction changed progressively from W-E to almost S-N establishing the present distribution of volcanism in the TMVB. Finally, from Pliocene times the coupling of the Baja California with the Pacific plate originated the distensive Quaternary phase that originated the modern configuration of that region.

The Trans-Mexican Volcanic Belt

The individualization of the Trans-Mexican Volcanic Belt as an independent province started in the Middle to Late Miocene. It is characterized by its E-W orientation resulting from the progressive counterclockwise rotation of the magmatic arc of the Sierra Madre Occidental, and its change in compositional and eruptive style from silicic and explosive to intermediate and effusive (Ferrari et al., 1999; Ferrari et al., 2012; Gómez-Tuena et al., 2007).

The geological evolution of the TMVB has been divided into four episodes attending to the time of emplacement, while also having implications concerning its spatial distribution and compositional features (see Gómez-Tuena et al., 2007 and Ferrari et al., 2012).

Episode 1: Early to Late Miocene

The earliest accounts of magmatism in the TMVB are dated as Early Miocene (~22–16.5 Ma; Albarrán, 1985; García-Palomo et al., 2000; Lenhardt et al., 2010; Pasquaré et al., 1991; Ferrari et al., 2012). This activity was interpreted as resulting from an E-W oriented arc that began to take shape between the 101°30' W longitude and the Gulf of Mexico. During this first stage, volcanism was mainly effusive and of subalkaline affinity, with predominant andesite to dacite compositions. According to Orozco-Esquivel et al. (2010) the geochemical features of these lithologies also indicate a progressive decrease in the influence of subduction components (mainly fluids) as the distance to the trench increases (i.e. towards the N and NE).

Between ~16.5 Ma and ~8.9 Ma magmatism expanded to the North, farther from the trench, and to the Gulf of Mexico, widening the arc as evidenced by stratovolcanoes and lava cones emplaced to the north of the TMVB (see Carrasco-Núñez et al., 1989; Pérez-Venzor et al., 1996; Suter et al., 1997; Gómez- Tuena & Carrasco-Núñez, 2000; Verma & Carrasco-Núñez, 2003; Mori et al., 2007; Vassallo et al., 2008; Ferrari et al., 2012). The predominant andesitic signature was then replaced with the appearance of adakite-like lavas (Gómez-Tuena et al., 2003; Ferrari et al., 2012) such as the ones in

the eastern end at the Palma Sola area in form of gabbroic to dioritic plutonic and sub-volcanic bodies emplaced during ~16-9 Ma (Cantagrel & Robin, 1979; Ferrari et al., 2005; López-Infanzón, 1991; Negendank et al., 1985). This late adakitic magmatism of the Episode 1 was interpreted by Gómez- Tuena et al. (2003) and Mori et al. (2007) as the result of partial melting of the subducted slab promoted by a prolonged flat sub-duction. This hypothesis is consistent with the gradual migration of the arc away from the trench since the Middle Miocene and its broadening and the decrease to the north of the slab-derived fluids (Gómez-Tuena et al., 2007 and Ferrari et al., 2012). Since these magmas are found only at the greatest distance from the trench, Ferrari et al. (2012) interpreted them as marking the end of the arc migration to the North.

Episode 2: Late Miocene

The beginning of the second episode is defined by a sudden change in the style and composition of volcanism (Gómez-Tuena et al., 2007 and Ferrari et al., 2012). Along the arc between Nayarit and Veracruz States but to the north of the previous episode, large volumes of mafic lavas were emplaced (Ferrari, 2004; Ferrari et al., 1994, 2000, 2005b). Volcanic outcrops are mainly represented by fissural basaltic lava flows, often forming basaltic plateaus, small shield volcanoes and lava cones. Available age data indicate a clear eastward migration pattern starting in the west-central sector at ages between 11.5-8.4 Ma (Alva-Valdivia et al., 2000; Ferrari et al., 2000; Moore et al., 1994; Nieto-Obregón et al., 1981; Rosas-Elguera et al., 1997, 2003; Rossotti et al., 2002; Verma et al., 1985), continuing at 9-7.5 Ma between longitudes 101° W and 99° W (Aguirre-Díaz & López-Martínez, 2001; Pasquaré et al., 1991; Suter et al., 1995a,b), and reaching the eastern sector between 7.5-6.5 Ma in the Pachuca area and between 7-3 Ma in the Palma Sola area (Cantagrel & Robin, 1979; Ferrari et al., 2005b; López-Infanzón, 1991).

Episode 3: Latest Miocene to Early Pliocene

In the transition from the Miocene to Pliocene, magmatism changed again in compositional style to more evolved dacitic and rhyolitic compositions and started to migrate towards the trench (Gómez-Tuena et al., 2007 and Ferrari et al., 2012). On the East side of the TMVB (i.e. East of 101° W longitude) magmatism was emplaced just south of the previous episode in the form of ignimbrites erupted from regional large calderas, dome complexes and lava flows (Ferrari et al., 1991; Herrera & Milán, 1981; Nichols, 1970; Ferrari et al., 2012). To the west of the 103° W longitude dome complexes predominated over ignimbrites and were emplaced on the same area where the previous episode developed (Ferrari et al., 2000; Rossotti et al., 2002) between ~8.5 and 6.0 Ma (Castillo & Romero, 1991; Gilbert et al., 1985; Rossotti et al., 2002). Silicic volcanism is absent between these longitudes during the whole TMVB history (Gómez-Tuena et al., 2007).

Since the end of the Miocene (~6 Ma) magmatism became bimodal, represented by low-volumes of slightly alkaline basaltic lava flows interstratified with subalkaline silicic rocks or mingled with some ignimbrites (Allan, 1986; Ferrari et al., 2000; Frey et al., 2004; Gilbert et al., 1985; Moore et al., 1994; Delgado-Granados et al., 1995; Righter & Rosas-Elguera, 2001). Both subalkaline silicic and bimodal (subalkaline silicic + alkaline) volcanism have been present from the Miocene up to the present as well as the migration towards the trench, but more pronounced in the eastern sector (200 Km) than in the west (100 Km), where it was mostly confined to the Tepic-Zacoalco graben (Ferrari, 2012).

Episode 4: Late Pliocene to Holocene

This last episode started with a diversification in the compositional characteristics of the volcanism. Silicic and bimodal volcanism was replaced by dominant calcalkaline lavas coexisting in some areas with smaller volumes of intraplate-like alkaline lavas, lamprophyres and potassium rich rocks as well as rhyolitic peralkaline volcanic centres (Ferrari et al., 2012). In the western sector there is an additional pulse of alka-

line volcanism starting at ~3.6 Ma, as well as lavas with typical subduction signatures to the north-eastern part of the arc (Righter et al., 1995; Ferrari et al., 2000). During this period, the volcanic front continued its migration towards the trench acquiring its present-day configuration by late Pleistocene (Ferrari et al., 2012).

A characteristic feature of this episode is the development of stratovolcanoes during the last 1 Ma, with the Colima volcanic complex representing the largest edifice in the TMVB with circa 700 km^3 of erupted material (Robin et al., 1987). The Colima volcano is located at the volcanic front of the western sector and at the southern end of the homonymous graben. The Colima graben is thought to represent, together with the Tepic-Zacoalco rift, the surface manifestation of the Jalisco block (the western part of Guerrero Terrane) continental boundaries, which were reactivated during Plio-Quaternary times as a consequence of the interaction between the Rivera, Cocos and North American plates (Rosas-Elguera et al., 1996 and Ferrari & Rosas-Elguera, 2000). Recent studies (Manea et al 2013, 2017) have argued that such a reactivation forming a graben structure would have been caused by the extensional efforts resulting from a toroidal mantle flow flowing through a gap between the Rivera and Cocos slabs, which in turn would be caused by the different rollback rates presented by the two subduction segments (León-Soto et al., 2009).

Other stratovolcanoes in the western sector (Tequila, Ceboruco, Tepetiltic, Sangangüey, Las Navajas, and San Juan) have volumes of less than 100 km^3 and are located ~100 km behind the volcanic front, aligned along a regional fault system with a WNW-ESE orientation that defines the northern boundary of the Jalisco block (Gómez-Tuena et al., 2007). On the other hand, all stratovolcanoes in the East are located at the volcanic front and several belong to N-S alignments that get younger to the south like Tláloc-Iztaccíhuatl-Popocatépetl (Nixon, 1989) and Pico de Orizaba-Cofre de Perote, that display mafic volcanism younger than 1 Ma (Siebert & Carrasco-Núñez, 2002). In the central sector the only stratovolcano is Tancítaro (Maciel Peña et al., 2009).

However, in the context of this work perhaps the most relevant characteristic of this last magmatic episode is the development of monogenetic volcanic fields. In the western Trans-Mexican Volcanic Belt they have dominated the volcanic front since the Late Pliocene with the San Sebastián, Mascota (Lange & Carmichael, 1990, 1991), Los

Volcanes (Wallace & Carmichael, 1989), Ayutla and Tapalpa (Righter & Rosas-Elguera, 2001) monogenetic volcanic fields. The products in these fields tend to have lamprophyric associations with younger ages reported towards the west. The oldest are Tapalpa with 4.69 Ma (Allan, 1986) and Ayutla with 4.5 Ma (Righter & Rosas-Elguera, 2001), followed by Los Volcanes with 3.3 Ma (Wallace & Carmichael, 1989), Mascota with 2.35 Ma (Ownby et al., 2008) and San Sebastián with 1.52 Ma (Lange & Carmichael, 1991). The Michoacán Guanajuato Volcanic Field (MGVF), the most prominent monogenetic field of the TMVB in terms of size, is located in the central sector. Towards the central-eastern and eastern sectors, the main monogenetic fields are Zitácuaro-Valle de Bravo (Blatter & Carmichael, 1998), Tenango-Chichinautzin (Bloomfield, 1973, 1975), Apan-Tezontepec (García-Palomo et al., 2000), and Xalapa (Rodríguez et al., 2010). In all cases mafic products prevail (Martin-Del Pozzo, 1982; Márquez et al., 1999; Siebe et al., 2004).

Ferrari et al. (2012) proposed a geochemical framework for this episode suggesting that the most primitive and subduction influenced magmas are found at the volcanic front and in the western sector, becoming more evolved and less influenced by subduction components towards the east and the back arc, feature that evidences their increasing distance to the trench. This is mainly deduced from variations in the Mg# value, the Nb and TiO_2 contents and the Ba/Nb and TiO_2/K_2O ratios. The rocks with low Ba/Nb ratios were also found to have high-Nb and high TiO_2 compositions in many cases and were described as intraplate-type OIB-like rocks and interpreted by Luhr (1997), Petrone et al. (2003) and Wallace & Carmichael (1999) amongst others, as partial melts of enriched asthenospheric mantle sources with little or no influence from subduction components. These intraplate-type rocks are found in the west sector in the Tepic-Zacoalco graben (e.g., Petrone et al., 2003; Verma & Nelson, 1989), the Atenguillo graben (Righter & Carmichael, 1992), and the Amatlán de Cañas graben (Righter et al., 1995). In the eastern sector they are found in the volcanic fields of Michoacán-Guanajuato and Chichinautzin. The low TiO_2/K_2O ratios, on the other hand, indicate a higher contribution of K-rich components contributed from the subducting slab and are found mostly at the volcanic front, the Colima volcanic complex, and the Zitácuaro-Valle de Bravo volcanic field. This entire scenario has been reinterpreted in

the recent work by Gómez-Tuena et al. (2017), suggesting that all the compositional diversity present in the TMVB is the result of melting from a highly heterogeneous mantle wedge, enriched before subduction and later on overprinted by slab-derived fluxes.

The Michoacán-Guanajuato Volcanic Field

The Michoacán-Guanajuato Volcanic Field (Figs. 2.1, 2.4 and 2.5) is one of the two biggest monogenetic volcanic fields of the TMVB (see Hasenaka, 1994; Hasenaka & Carmichael, 1985a,b; Ferrari et al., 2012) and the biggest monogenetic field of the Late Pliocene to Holocene magmatic episode described above. It is located in the central part of the belt at an approximate distance of between 200 and 130 km from the trench and covers a > 40.000 km^2 area between the latitudes 19°00" N to 20°75" N and the longitudes 101°33" W to 102°66" W (Hasenaka, 1994; Hasenaka & Carmichael, 1985b, 1987). This volcanic field represents one of the largest concentrations of monogenetic vents on Earth (Gómez-Tuena et al., 2007) with more than 1000 volcanic outcrops, including 901 cinder cones, 43 lava domes, 22 maars or tuff rings, 13 small shield volcanoes with summit cones and 61 lava flows not associated with cones (Hasenaka & Carmichael, 1987), nearly 400 middle size polygenetic volcanoes, most of which (~377) are small shield andesitic vents (Hasenaka, 1994), and a few stratovolcanoes like Tancítaro and Patamban. The lifespan of the eruptive centres is assumed to be of less than 15 years and they rarely reactivate after becoming dormant thus suggesting that they do not contain long-lived magma chambers due to a low magma supply rate (Hasenaka & Carmichael, 1985a).

The volcanic activity started in the northern sector of the field by the Late Pliocene (2.78 Ma; Hasenaka & Carmichael, 1985a) and has continued up to present times, with the most recent historic eruptions of El Jorullo volcano (1759-1774; Luhr & Carmichael, 1985) and Parícutin (1943-1952; Wilcox 1954). The active volcanic front has shown a southwest trenchward migration during the last 2 Ma (Ban et al. 1992) that agrees with general observations in the TMVB that also confirm a trenchward migra-

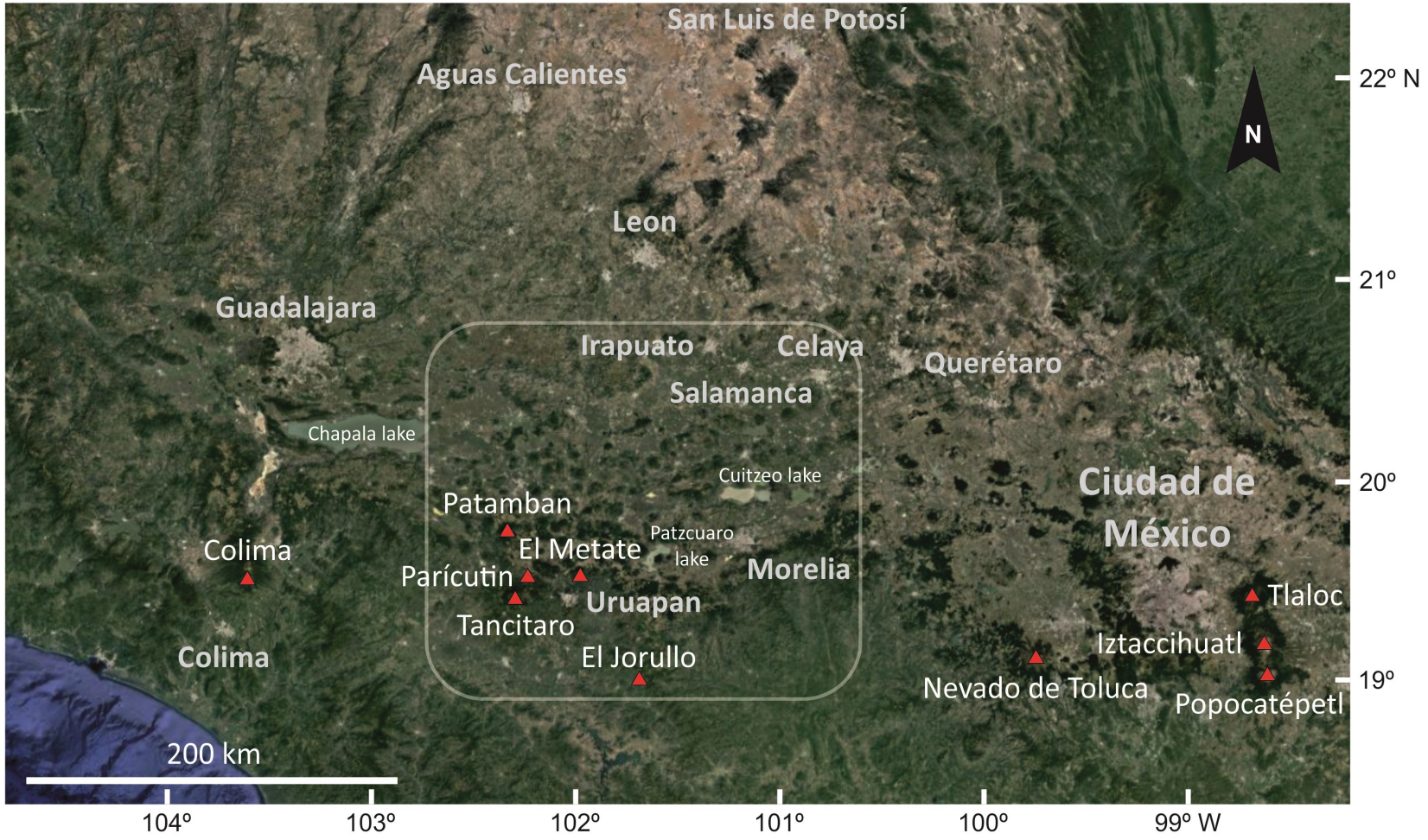

Fig. 2.4 Landsat 8 derived image provided by Earthstart Geographics SIO and processed by HERE (2017) of the Trans Mexican Volcanic Field western and central sectors. Outlined in white is the Michoacán Guanajuato Volcanic Field area. Names of the main towns are in grey bold letters and red triangles represent the main volcanos.

tion during the Quaternary (Cantagrel & Robin 1979, Luhr & Carmichael 1980, Nixon et al. 1987, Delgado-Granados et al. 1995).

Petrology and Geochemistry

Following the extensive fieldwork of Hasenaka (1986), Hasenaka & Carmichael (1987) described the analyzed lavas from cinder cones as olivine basalts and olivine andesites. They also reported that the most common mineral assemblages in those basalts and in the low-Si andesites contain plagioclase and olivine (with Cr-rich spinel inclusions) as the most widespread phenocrysts. Augite, orthopyroxene and hornblende phenocrysts were more frequently found in high-Si andesites and dacites.

From their geochemical data, these authors recognized three different petrologic groups in the MGVF based on their alkali content, with silica compositions ranging from 50 to 70 %: calcalkaline, alkaline and transitional. Furthermore, they subdivided the alkaline ones into low-Mg and high-Mg subgroups. The high-Mg rocks were described as having high concentrations of Mg, K_2O, Cr and Ni along with Sr, whereas the low-Mg ones reported high total iron (> 10 % FeOt) and TiO_2 (> 2 %), features that are in accordance with their greater abundance of Fe-Ti oxides. Both subgroups were found to be rich in P_2O_5 and REEs as well. The predominant petrologic group is represented by the calcalkaline rocks (Williams, 1950, Ferrari et al., 1990), while the other groups are very scarce.

This classification also aided in describing in general terms the compositional variations along the MGVF. Following Hasenaka & Carmichael (1987), calcalkaline and transitional terms occur throughout the entire MGVF, unlike alkaline rocks that show a more restricted distribution. High-Mg alkaline samples on one hand were found exclusively in the southern sector, between 200 and 270 km from the trench, whereas low-Mg alkaline samples were in the northern part between 350 and 400 km from the trench. Calcalkaline samples showed a similar distribution were high-Mg (> 9 %) basalts and low-Si andesites were only found between 200 and 270 km from the trench.

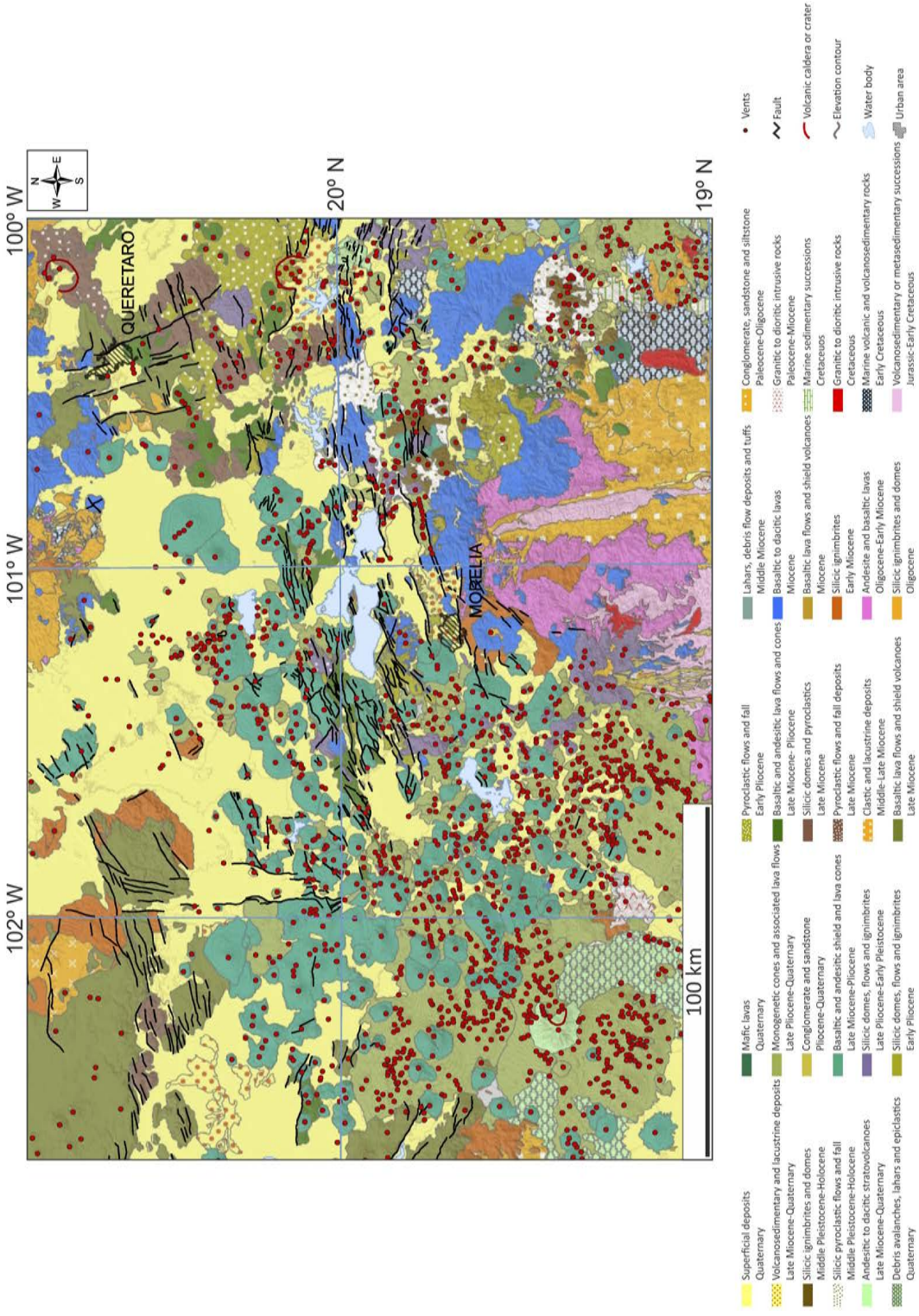

Fig. 2.5 Geological map of the Michoacán-Guanajuato Volcanic Field area after Ferrari et al. (2012).

Age distribution

The estimated ages for the volcanic vents, based on a geomorphologic assessment based on their shape characteristics calibrated against some limited ^{14}C dating (Hasenaka & Carmichael, 1985a), suggested that the distribution of the above described lithologies is related to the distance from the Middle America Trench. In the southern sector (at a distance between 200 and 300 km from the trench) only the younger (< 40000 yr) calcalkaline volcanic centres appear, in addition to the high-Mg alkaline distributed in NE-directed alignments which are nearly parallel to the relative motion of the Cocos and North American plates. In the northern sector (between 350 and 400 km from the trench), low-Mg alkaline vents predominate as well as older low-SiO_2 calcalkaline vents (Hasenaka & Carmichael, 1987; Gómez-Tuena et al., 2007) distributed in alignments subparallel to east-west normal faults (Hasenaka & Carmichael, 1987). The alkaline compositions in contrast, were found in morphologically older cones according to these authors. The exception was a coeval association of alkaline and calcalkaline volcanism reported to be close to the Middle America Trench during the late Quaternary. Such coexistence is not unique to the TMVB and it has also been reported at the Colima Rift Zone (Luhr & Carmichael, 1981; Allan & Carmichael, 1984) and near Volcán Sanganguey (Nelson & Carmichael, 1984), both related to graben structures.

Petrogenetic hypotheses

As we have seen, the petrologic and mineralogical evidence and the relatively short periods of volcanic activity typical of monogenetic fields led Hasenaka & Carmichael (1985a) to conclude that volcanism developed in the absence of long lived shallow magma reservoirs, consistent with the observed small magma supply rate in the MGVF.

In their detailed study of the historical eruption in Volcán Jorullo (1759-1774) and its associated cinder cones, Luhr & Carmichael (1985) found two different magma types, alkaline and subalkaline, and emphasized that they must represent two different

mantle partial melting events given that, although they appear closely related in space and time, no simple mechanism is able to relate them to one another. In a later study, Hasenaka & Carmichael (1987) hypothesize that the compositional variations found in the MGVF could not be the result of a single line of descent from a common primitive magma as it is not possible to derive the observed compositional variations by any scheme of fractional crystallization involving the phenocrysts observed in those lavas. According to these authors (Hasenaka & Carmichael 1984; Hasenaka & Carmichael 1987) the distribution of petrologic groups and the geochemical variations of compatible elements such as Mg, Ni and Cr, for a given SiO_2 content, tend to show a general decrease with the distance to the trench. Direct correlations between K_2O (or Rb, Ba and Zr) with increasing distances from the trench are distinct for evolved lavas only when high-Mg alkaline basalts (present in the southern area) are excluded. This distribution does not follow the traditional ideas about magma genesis in convergent margins proposed by Dickinson & Hatherton (1967) that suggested that K_2O (and other incompatible elements) contents tend to increase systematically with the distance to the trench (i.e., with slab depth).

More recently, Verma & Hasenaka (2004) also discarded a simple differentiation process to explain the petrologic diversity. These authors adopted and modified the hypothesis of Sheth et al. (2000) who suggested that the mantle wedge below México is compositionally heterogeneous and probably contains enriched metasomatic veins. To explain the origin of these veins they invoked a complex metasomatic process occurring under an ancient crustal suture beneath the proto-Trans-Mexican Volcanic Belt. This hypothesis is in part inspired by the pioneering ideas of Humboldt (1811) who already suggested that the Trans-Mexican Volcanic Belt is emplaced and governed by a first-order crustal discontinuity.

In order to elucidate the magma genesis process in the MGVF some authors have considered the Re-Os isotopic system (Lassiter & Luhr, 2001; Chesley et al., 2002) as it allows to differentiate between crustal and mantle contributions to arc volcanics (Shirey & Walker, 1998). They found that assimilation of continental crust seems to have played an important role in some of the evolved rocks which agrees with the positive correlations between K_2O and distance from the trench observed in evolved mag-

ma compositions. They also demonstrated that many of the rocks with strong subduction signals (i.e., with high LILE/HFSE ratios) are also characterized by the low $^{187}Os/^{188}Os$ ratios that are typical of mantle sources. This suggests that at least small volumes of undifferentiated magma could be transported quickly to the surface without being stored at shallow depths (Gómez-Tuena et al., 2007) therefore keeping their mantle-derived and subduction-related geochemical signature. In fact, very recently Gómez-Tuena et al. (2017) have suggested that all intermediate volcanism (from andesite to dacite and even some rhyolite) actually represents primitive melts derived from hybrid slab and mantle sources, rejecting any intra-crustal differentiation and contamination processes.

Additionally, the observed decrease of Mg, Ni and Cr and increase of TiO_2 with increasing distance from the trench aforementioned was interpreted as a clear trend of decreasing pressure for the Ol-Aug-Pl crystallization (Hasenaka & Carmichael, 1987) indicating that magmas in the southern section of the field were emplaced more rapidly and efficiently, with little fractionation at higher pressures than magmas in the northern sector which appear to stall at shallower crustal levels for longer periods of time and therefore underwent greater fractionation of mafic phases (Hasenaka & Carmichael, 1987; Gómez-Tuena et al., 2007).

To summarize, the different studies carried out so far in this volcanic field agree that the compositional variations observed here cannot be the result of partial melting from a common homogeneous source nor the consequence of simple differentiation processes. Instead, the proposed hypotheses point more at the possible involvement of a range of initial melts derived from heterogeneous mantle sources that, for most authors, could evolve through mineral differentiation, including assimilation processes at crustal levels.

3. Methodology

The workflow followed during the research work presented in this thesis was structured in the following stages:

- Review of previous research works developed in the area
- Fieldwork and Sampling
- Samples preparation
- Petrographic study
- Mineral chemistry
- Whole rock chemistry
- Study of the data and petrogenetic modelling
- Discussion

In this section the methods and techniques followed for each of these stages are described.

Fig. 3.1 General view of a typical monogenetic cinder cone from the MGVF.

Fig. 3.2 Rincón de Parangueo Maar and its stromatolite deposits.

Review of previous research

This research work was integrated within the framework of ongoing studies developed by the UNAM-CSIC research team, focused on the distribution and petrogenesis of the monogenetic volcanism in the Michoacán-Guanajuato Volcanic Field. Among the main goals put forward were to identify and characterize the less studied alkaline-calcalkaline volcanism association and to develop quantitative petrogenetic models that could be incorporated into a geodynamic framework for the region. Emphasis was put on the most recent small vents, but some of the middle-size volcanoes (Paricutin and El Metate) that were the subject of ongoing research by the team were also considered. Therefore, it was essential to carry out an initial work to digest the available information on the subject that allowed the identification of sampling areas and organization of the following analytical work.

The pioneering work of (Wilcox, 1954) on the Paricutin eruption made the MGVF known worldwide and this volcano was later on considered a classic example of AFC processes (McBirney et al., 1987). About this time Hasenaka & Carmichael (1985, 1987) published the first comprehensive studies on both volcanology and petrology-geochemistry of the Michoacán-Guanajuato Volcanic Field and therefore they have been the basis for any subsequent petrological works in the region. Although many articles were published before and after, they were focused on specific issues and just a few (e.g. Verma & Hasenaka, 2004) have been devoted to the MGVF as a whole, with the exception of studies that included observations on this extensive field as part of larger-scale reviews, such as the Trans-Mexican Volcanic Belt (see for example Aranda-Gómez et al., 2005; Díaz-Bravo et al., 2014; Ferrari, 2000; Ferrari et al., 2012). All these works and the references included were the basis for compiling the available information on the petrology and geochemistry of the MGVF and its context within the TMVB. Special acknowledgment has to be made of the extensive database compiled in Ferrari et al. (2007) which was kindly provided by the author, including information from the above-mentioned works and also additional original data.

In order to locate the volcanic field within its geological framework, other works on the geology of the Transmexican Volcanic Belt have also been studied such as those

from Ferrari et al. (2000, 2012), Gómez Tuena et al. (2003, 2007, 2014, 2016) as well as other more general works concerning the geology of Mexico and the subduction complex such as the essential works by Demant & Robin (1975), Moran-Zenteno (1986, 1994), Luhr (1997), Alaniz-Alvarez et al. (2002), Manea et al. (2013) and Straub et al (2015) which were used for a first approximation of the geodynamic and petrologic framework of the region.

Fieldwork and sampling

Fieldwork was planned to complete the developing petrologic and geochemical database on the monogenetic volcanism of the area, which was originally focused on the central/south sectors. That previous sampling demonstrated that mafic volcanism was very scarce and in all cases represented by calcalkaline lavas and some minor ada-

Fig.3.3 Fieldwork pictures. The top two photographs are outcrop examples inside maar structures portraying basaltic bombs within the tuff ring. Down left picture shows juvenile basaltic fragments within the tuff. Downright picture is a block from a plagioclase rich basaltic flow (M95 sample).

kite-like outcrops. Therefore a main objective of the new fieldwork campaigns was to identify possible alkaline monogenetic outcrops, reported to be present in the volcanic field but never studied in detail (see Hasenaka & Carmichael, 1987; Luhr et al., 1989). This was again based on the information gathered in the previous workstage, based on existing geological, geochemical and cartographical information and previous work undertaken by our research team.

As a result of the above-described approach, fieldwork and sampling was focused on the central-northern sector of the MGVF and it was split into three campaigns due to the large distances as well as some occasional security instabilities in the region that prevented us from reaching some areas at the time.

In general, just a single sample per volcano was collected, which seems appropriate in the case of the smaller vents (Fig. 1), characterized by single lava outpourings. Nevertheless, since the purpose of this work is to count on a general view of the vol-

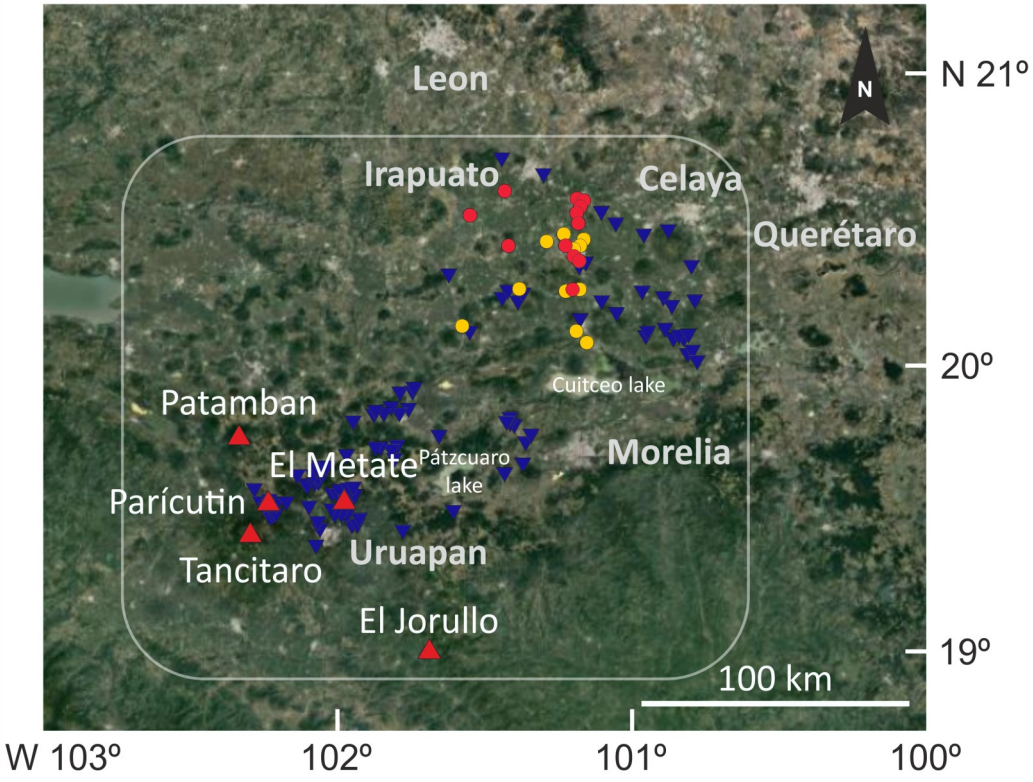

Fig. 3.4 Distribution of the samples (red circles: T1 alkaline trend, yellow circles: T2 alkaline trend, and blue triangles: calcalkaline suite). Base photograph: Landsat 8 derived image provided by Earthstart Geographics SIO and processed by HERE 2017. Names of the main cities are in white bold font, names of the main lakes in small white font. Red triangles: main volcanoes in the field.

canism in the MGVF, some larger volcanoes were also considered on a single-sample basis, but in the case of other complex volcanoes like El Metate and Parícutin more detailed sampling was carried out.

In the case of cinder cones (Fig. 3.1) or maars (Fig. 3.2) with scarce or even absent lava flows, special care was taken in distinguishing juvenile material from others that could have been dragged or ripped off from the basaltic wallrock. Since all samples were collected with the aim of performing a complete geochemical study, only the freshest portions of the rock were selected, stripping away the most external and potentially weathered layers. In general, small chips were preferred that could be easily examined under the magnifying glass for possible weathering effects.

A total of 139 samples were finally gathered throughout the volcanic field by our research group, 66 of which were collected during the last three campaigns devoted to this thesis work (Fig. 3.4).

Sample preparation

Samples were processed in different ways for the different techniques to be applied in the petrologic and geochemical study. These included the following:

Thin sections

Thin sections of every sample were prepared at the facilities of the Museo Nacional de Ciencias Naturales (CSIC. Madrid, Spain) and the Instituto de Geología of the Universidad Nacional Autónoma de México (UNAM) using similar procedures. Rock samples were first cut with a diamond saw to get a block of the appropriate size (4.5 x 2.5 cm), then polished on one side and glued with Microtec epoxy resin to a glass sample holder (28 x 48mm) and left to dry in a furnace at 60^{o}C for 1.5 hours. The exposed side was then cut and polished down to 30 µm in thickness using progressively smaller grain silicon carborundum polish (320, 400, 600, and 800).

Sample crushing and grinding

This process started during sample extraction in the field, selecting the freshest sections of the lava outcrop and reducing them to smaller pieces. These were further crushed in the lab by mechanical means (hammer and hydraulic press) into ~1-2 cm chips. The obtained chips were then examined to discard any portion that had evidence of weathering (e.g. oxidation or vacuoles with secondary mineralizations). The selected chips were then washed out with distilled water in an ultrasound bath during 1 hour at 20 minutes intervals replacing the water in between. Clean chips were finally dried in an oven at 40 degrees to remove any moisture.

The rock chips were then grinded and reduced to powder (typically under 500 microns) using two methods depending on the geochemical technique to be applied afterwards. An aliquot was pulverized with an aluminium ceramic mortar to obtain approximately 11 gr of rock powder destined to isotope analysis. Another aliquot was also pulverized in an agate mortar for major and trace element analysis. This difference in preparation was advised by the different laboratories.

In all cases cross contamination was avoided by careful cleaning of the tools used between samples. Powdered samples were stored in laboratory-grade glass vials, and the different aliquots for each laboratory were provided in individual Eppendorf microtubes.

Petrographic study

All 139 samples collected in the MGVF were studied and described by petrographic optical microscopy. Two available microscopes were used: an Optika B□353POL trinocular microscope with 4x, 10x, 20x and 50x magnification objectives, and a Nikon ECLIPSE R600 POL with 2x, 5x, 10x, 20x 40x magnification objectives. During the petrographic study, points for electron microprobe analysis of mineral phases were also identified. This was performed from microphotographs using an Optikam B9 camera attached to the Optika microscope and a Nikon camera (DIGITAL SIGHT DS-L1) attached to the Nikon microscope.

The complete description of each sample, including its location, an image of the whole thin section (obtained with a desk scanner), a basic petrographic description and the analysis performed with the electron microprobe, is presented in Appendix 1.

Mineral chemistry

Major element analyses of the mineral phases identified in the petrographic study were carried out at the Centro Nacional de Microscopía Electrónica (Universidad Complutense de Madrid, Spain) with a JEOL® "Superprobe JXA 8900 M" electron microprobe with four wavelength-dispersive spectrometers. The analyses were obtained on polished thin sections metalized with graphite, using an accelerating voltage of 15 kV and an electron beam current of 20 nA, with a beam diameter of 5 µm. The elements were counted for 10 s on the peak and 5 s on each background position. The standards used were sillimanite, albite, almandine, kaersutite, microcline, ilmenite, fluorapatite, scapolite, Ni alloy, chromite, gahnite, bentonite and strontianite; from the Smithsonian Institute (Washington DC, EEUU) and Harvard University (Boston, EEUU) (Jarosewich et al., 1980; Jarosewich & Sampson, 1987; McGuire et al., 1992).

Micro-punctual analyses were performed on olivine, plagioclase, clinopyroxene, orthopyroxene, amphibole, apatite and oxide crystals, covering the range of present mineral sizes (phenocrystals, microphenocrystals and matrix-size crystals). The elements analyzed were Si, Ti, Al, Fe, Mn, Mg, Ca, Na, K and P, expressed as weight percentage of the oxide, with iron determined in its oxidized form as total ferric iron (Fe_2O_3t). Detection limits are of 0.5 - 6 wt % for oxides with concentrations >1.5 wt % and under 10 % for oxides with concentrations <1.5 wt %.

Whole rock chemistry

Major elements

All samples were analysed for major elements in whole rock. The elements considered (SiO_2, TiO_2, Al_2O_3, Fe_2O_3t, MnO, Mg, CaO, Na_2O, K_2O and P_2O_5) were deter-

mined by X-Ray Fluorescence (XRF) using standard methods (see Lozano-Santa Cruz & Bernal, 2005) during a stay at the "Laboratorio de Fluorescencia de Rayos X" of the Instituto de Geología (UNAM).

Samples were prepared using 0.8 gr of pulverized rock mixed with 7.2 gr of lithium tetraborate per sample. This mixture was then deposited in a platinum fuse vessel with two drops of a solution of 25 % of LiBr and melted until a homogeneous fusion was achieved (Fig. 3.5). The melts were poured into a tray for cooling and the resulting fused beads were extracted and labelled.

Major elements were measured with the Controlm.qan software using a Rigaku ZSX Primus II spectrometer with Rh radiation at a 60 Kv and 50 mA for Ti, Fe, Mn, Ca, K and 40 Kv and 80 mA for Na, Mg, Sr, Al and P following the procedures described in Lozano-Santa Cruz & Bernal (2005).

In addition to the XRF determinations, major element analyses were completed with the determination of its Loss on Ignition (LOI). This was obtained by the difference in weight of a 1 gr aliquot of a sample relative to its weight after drying at 950 °C for an hour. The results are expressed as weight percentage.

Fig. 3.5 Oven melting three pulverized rock samples on the left and six other samples on their platinum fuse vessels already mixed with 25% LiBr solution (small black bottle) on the right.

Trace elements

Trace-element data were acquired by Inductively Coupled Plasma Mass Spectrometry (ICP-MS) with a Thermo Series XII spectrometer in the Centro de Geociencias (CGEO) of the UNAM, following the sample preparation and measurement procedures described in Mori et al. (2007). The reproducibility of the trace-element data at CGEO is given by the average concentrations and standard deviations of multiple digestions of the U.S. Geological Survey rock standards AGV-2, BHVO-2, BCR-2, and the Geological Survey of Japan JB-2 (see Gómez-Tuena et al., 2011; Mori et al., 2009, 2007).

Pb isotopic ratios

Lead isotopic ratios ($^{206}Pb/^{204}Pb$, $^{207}Pb/^{204}Pb$ and $^{208}Pb/^{204}Pb$) were determined during a stay at the Laboratorio Universitario de Geoquímica Isotópica (LUGIS), Instituto de Geofísica (UNAM).

Sample powders were prepared using ultraclean reagents following a three-step procedure: 1) Ambient Lead cleaning, 2) Sample digestion, and 3) Lead separation.

Ambient lead cleaning

Rock sample powder (100-150 mg) was poured into a PTFE® beaker and leached with 5 ml of 6N HCl at 90 °C for an hour to remove possible ambient Pb. Then the sample was submerged in MQ water for half an hour, rinsed (this process is repeated twice) and dried in a furnace.

Sample digestion

Once the sample was clean, it was digested to disaggregate the elements of the rock. The procedure followed involved the following stages: 1) the sample was first dissolved in a Teflon beaker with 1 ml of HNO_3 16N to remove organic matter and 3 ml of HF (8.7 pg/ml) solution to disaggregate the silicates for 48 hours at ~80 °C, 2) The acid

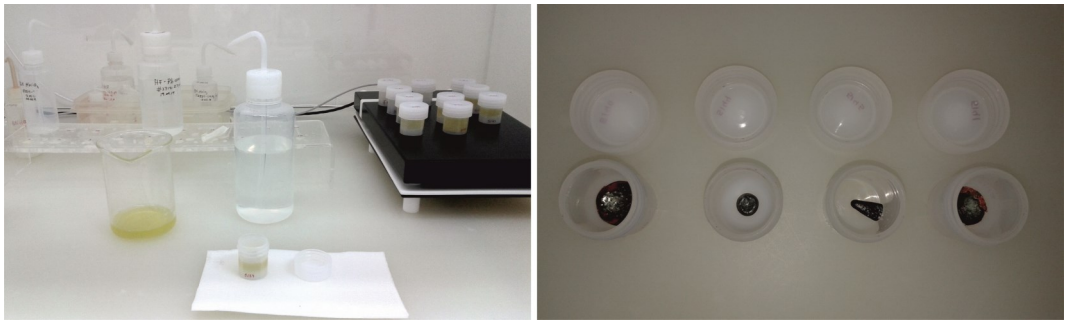

Fig. 3.6 Left picture, samples digestion on Teflon beakers under a laminar flow hood in an ultra-clean laboratory. Right picture, aspect of the samples after digestion.

was then evaporated in a furnace and 3ml of HBr 1N was added to the sample and left overnight., and 3) The acid was again evaporated and the beaker is closed (Fig. 3.6).

Lead separation

Pb was separated from the obtained dry residue in 3 cm length ionic exchange Pb was separated from the obtained dry residue in 3 cm length ionic exchange columns with anionic resin (BidRad) (Fig. 3.7). To prepare the exchange columns, Teflon (PFA®) columns were first cleaned with HNO_3 8N and rinsed with MQ water. Then the columns were placed in their holders with a beaker below them. MQ water was added to ensure drainage, followed by 235 ml of DOWEX 1x8, 100-200 mesh anion exchange resin using a pipette designed exclusively for this task. Each of the columns were then filled with 1 column volume (CV) of MQ water to rinse and settle the resin and then the resin was cleaned by adding the following acids (always letting the entire effluent pass before starting with the next one): ½ CV of HNO_3 8N, 1CV of MQ, ½ CV of HCl 6N and 1 CV of MQ. Finally, the resin was conditioned by adding ½ CV of HBr 1N. While collecting Pb, the same beakers can be kept for the waste effluent; in the case of Sr-Nd collection, new ones would be needed.

After the columns were ready, the digested sample was dissolved with 1 ml of warm HBr 1N, stirred and left to chill. Using a new unused pipette, 1 ml of the dissolved sample was loaded into the column. The unwanted elements were eluted with the following sequence of acids (always letting the entire effluent pass before starting the

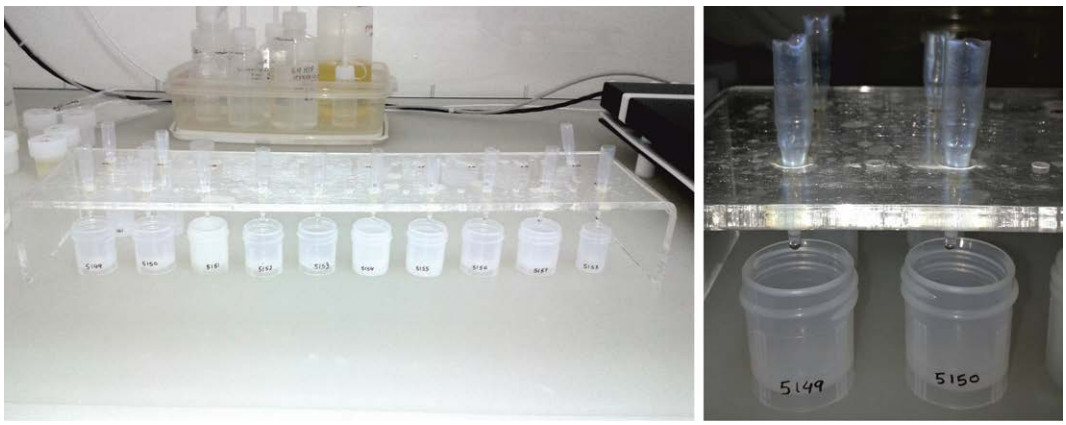

Fig. 3.7 Lead separation columns over the vials for lead collection.

next one): 300 µl of HBr 1N, 600 µl of HBr 1N, 1 ml of HBr 1N and 10 drops (~ 300 µl) of HCl 2N.

The vials for Lead collection (previously washed with HCl 6N or HNO_3 8N, heated in the grill for about 20-30 min and rinsed with MQ water) were placed under the columns. Then Pb is collected by adding 1.5 ml of HCl 6N. Finally, the vials were heated for ~ 2h to evaporate the acids of the collected Lead sample. The whole process was repeated again; except that instead of adding 1 ml of HBr 1 N now 600 µl were added. Also, in order to concentrate the lead during evaporation one drop of H_3PO_4 0.1N had to be added.

Lead isotopes determination

The samples thus prepared were loaded onto Re voltmeter filaments. For that, the filaments were first set on the voltmeter with a 100 µl drop of H_3PO_4 0.5M deposited on top of each of them. To load the samples we added 150 µl of silica gel on each one and extracted the mix with a pipette. Then the sample was placed onto the filament over the H_3PO_4 acid. Finally, in order to fix the sample to the filament, we heated them with the voltmeter until the H_3PO_4 evaporated (white smoke was released). At this stage, the filaments were ready to be set in the mass spectrometer cartridge which was to be placed in the mass spectrometer vacuum chamber (Fig. 3.8).

Fig. 3.8 From top left to bottom right photographs: Finnigan MAT262 Thermal Ionization Mass Spectrometer (TIMS) used to analyse the lead samples; cartridge to insert the samples in the source chamber of the mass spectrometer; voltmeter to load the samples on the filaments; and Re filaments with the samples loaded.

Pb isotope ratios were determined with a Finnigan MAT262 Thermal Ionization Mass Spectrometer (TIMS) equipped with 8 Faraday collectors. Isotopic measurements were made in static collection mode. Pb ratios were corrected for 0.12% fractionation per mass unit by comparing them with the mean value of 36 measurements of NIST-NBS981 (Pb) ($^{206}Pb/^{204}Pb$ = 16.89 ± 0.08%, $^{207}Pb/^{204}Pb$ = 15.44 ± 0.12%, $^{208}Pb/^{204}Pb$ = 36.54 ± 0.16%). Blanks varied between 200 and 300 pg. Sample preparation and measurement procedures for isotopic analyses are also described in Schaaf et al. (2005).

Sr and Nd isotopic analysis

Selected samples were analyzed for Sr and Nd isotope ratios at the "Servicio de Datación Radiométrica y Geología Isotópica" of the Universidad de Granada (Spain). The digestion routine was similar to the one for lead isotopes, using ultraclean reagents in a mixture of HNO_3+HF with 0.1000 g of sample powder in a Teflon-lined vessel at ~180 °C and ~200 psi for 30 min, following evaporation for dryness, and subsequent dissolution in 100 ml of 4 vol % HNO_3. Then, Sr and Nd were individually collected on

ionic exchange columns by chromatographic separation with ion-exchange resins specific for each element. The isolated elements were analyzed in multi-dynamic mode for their respective isotope ratios by TIMS in a Finnigan Mat 262 RPQ. Normalization values were $^{86}Sr/^{88}Sr = 0.1194$ and $^{146}Nd/^{144}Nd = 0.7219$. Blanks were 0.6 and 0.09 ng for Sr and Nd respectively. The external precision (2σ), estimated by analysing 10 replicates of the standard WS-E (Govindaraju et al., 1994), was better than ± 0.003 % for $^{87}Sr/^{86}Sr$ and ± 0.0015 % for $^{143}Nd/^{144}Nd$.

Oxygen isotopic analysis

Selected samples were analysed for isotopic oxygen ratios during a stay at the "Scottish Universities Environmental Research Centre (SUERC)" in Glasgow (UK). This method analyses the isotopic composition of the structural oxygen in the silicates of rock and therefore breaking the covalent bonds between oxygen and silicon is mandatory. With that purpose in mind, the samples were prepared following the laser fluorination technique defined by Kusakabe et al. (2004).

The procedure started introducing about 1.5 - 3 mg of sample or standard into each of the 12 positions of the samples holder which was placed in the reaction chamber, closed with a KBr crystal window that is transparent to infrared and visible light and prevents the gasses from escaping. The first stage in the fluorination procedure is the prefluorination of the samples and standards with ClF_3 gas overnight to remove any moisture or contaminants from inside the chamber. The next morning the reactant was removed and, after performing security measures to avoid ClF_3 escaping from the system, a small dose of ClF_3 was added by opening the valve for 5 sec. The next step was combusting the sample by shooting a CO_2 laser until the flare was exhausted. The silicates of the sample react with the ClF_3 atmosphere in the chamber and decompose into different compounds releasing the oxygen atoms in the shape of molecular oxygen (O_2). The resulting O_2 was recovered using a mercury Toepler pump and converted into CO_2 by reaction with a hot carbon (graphite) rod as the gas flows through the carbon rod container. The final CO_2 gas had to be frozen first in a cold finger at liquid nitrogen

temperatures for quality control and thereafter heated up again to allow the transport of the gas though the pipes to the mass spectrometer sample tube.

Oxygen isotope measurements were then carried out on a triple collector SIRA VG Isotech dual inlet mass spectrometer. All of the samples were calibrated against in-house olivine, garnet and quartz standards (SCXO, GP147 and TOR1), which were themselves calibrated against international and reference standards (NBS 28, UWG2). Data are reported in the conventional delta notation ($\delta^{18}O$, expressed as $^{18}O/^{16}O$ ‰) relative to the Vienna Standard Mean Ocean Water (V-SMOW). The delta notation is the oxygen isotopic composition of a sample expressed as per mil differences relative to SMOW (Faure, 1986), and is calculated as follows:

$$\delta\,^{18}O = \left[\frac{\left(^{18}O/^{16}O\right)_{spl} - \left(^{18}O/^{16}O\right)_{SMOW}}{\left(^{18}O/^{16}O\right)_{SMOW}}\right] \times 10^{3}$$

Fig. 3.8 Up left: general view of the fluorination line; Up right: Laser cage and reaction chamber; Bottom left: Pipes to conduct the molecular oxygen from the reaction chamber to the carbon rod in order to transform it into CO2; Bottom right: cold finger and sample tube for the mass spectrometer.

4. Petrography

A petrographical study is the first basic approach to the nature of any rock or suite of rocks and is an essential tool that allows the selection of the best samples for subsequent geochemical works. The petrological types identified in the study area are all very similar from a petrographic point of view and can only be clearly distinguished

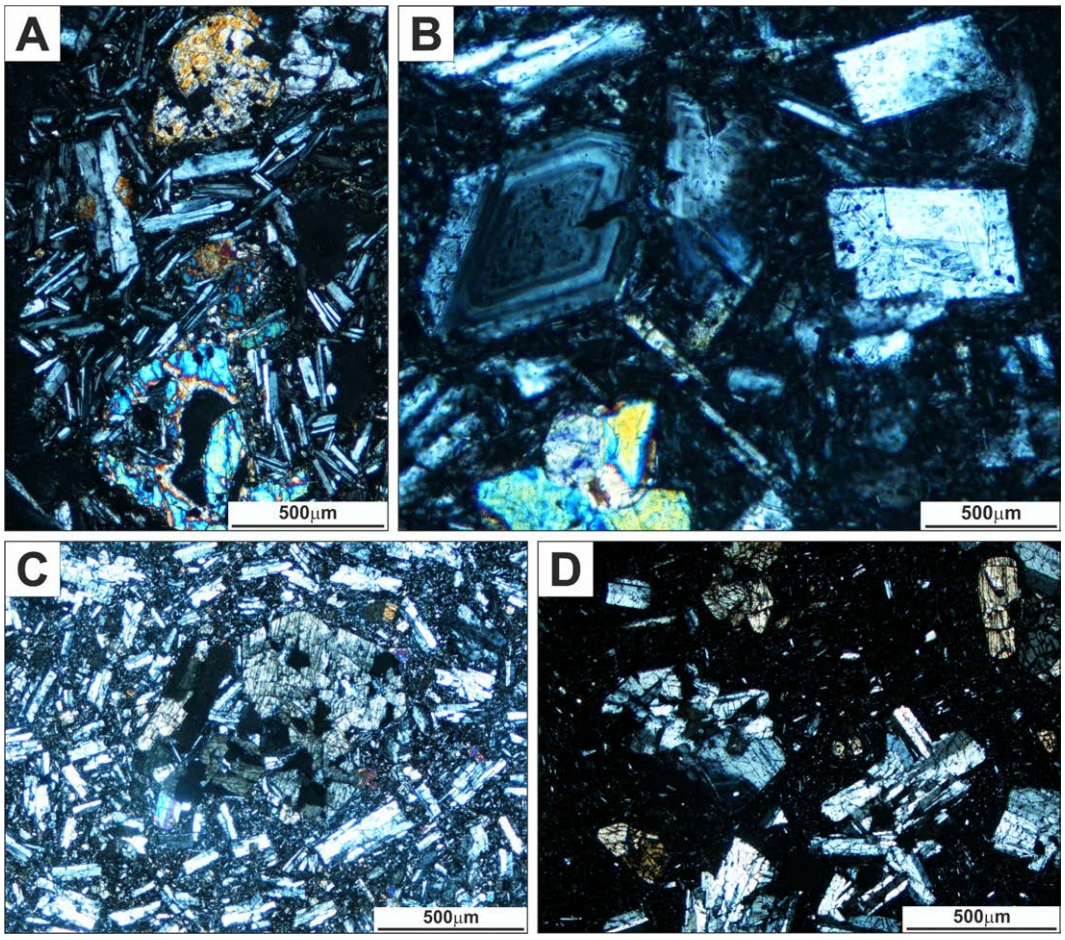

Fig. 4.1 Microphotographs of calcalkaline textures. A: M57 sample displaying a holocrystalline inequigranular seriated texture of olivine and plagioclase. B: M64 sample displaying a holocrystalline inequigranular texture of plagioclase and clinopyroxene. On the left side of the image a type 2 plagioclase phenocrystal can be appreciated and on the right the plagioclase crystal presents a regrown rim with multiple apatite inclusions. C: M91 sample displaying a holocrystalline inequigranular seriated (or porphyritic seriated) texture of plagioclases mainly and a clinopyroxene phenocryst in the middle. M53 sample portraying a holocrystalline inequigranular glomeroporphyritic texture with plagioclase and clinopyroxene aggregates.

on a geochemical basis. For this reason the descriptions in this chapter follow the groups based on the geochemical classification (Fig: 6.1 and 6.2). Even though the mineral phases encountered in each group and their characteristic are similar to one another, there are some differences that have important implications on the petrogenesis on the different rock suites and therefore they will be remarked here.

Calcalkaline Rocks

The texture of calcalkaline rocks is, as a whole, holocrystalline or hipocrystalline, depending of the sample, inequigranular seriated, porphyritic or glomeroporphyritic and often trachytic (Fig. 4.1).

The groundmass is usually microcrystalline, and occasionally cryptocrystalline, with interstitial glass that in some samples represents up to 50% of the matrix. The mineral paragenesis is relatively simple and the phases composing the matrix, except for the accessories, also appear as pheno and microphenocrystals, with plagioclase, olivine and pyroxene as the most common phases in varying proportions. Accessory minerals are mainly represented by oxides and apatite, which is found mostly in the matrix and as inclusions in larger crystals, especially of Plg.

Pheno and Microphenocrysts

Plagioclase and olivine are the most abundant phenocrystals in all samples (55% and 30% respectively as average), followed by clinopyroxene (9%), scarce orthopyroxene (2%) and amphibole (up to 4% in the samples that present it).

Plagioclase

On the rocks of this suite up to three types of plagioclase crystals can be identified attending to their petrographic characteristics:

Type 1: These plagioclase crystals are idio and sub-idiomorphic in shape with Carlsbad or polysynthetic twinning and occasionally some phenocrystals show undula-

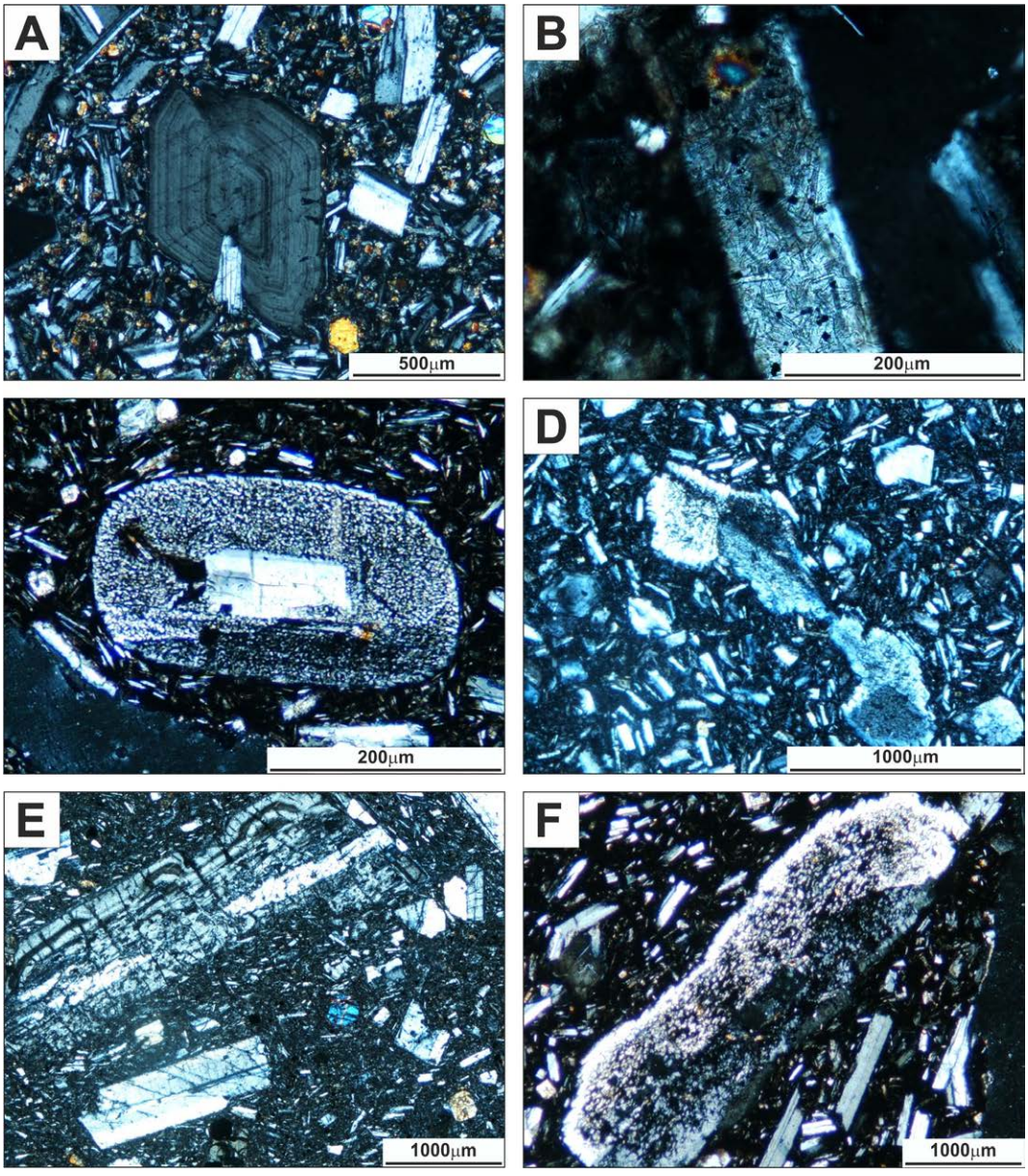

Fig. 4.2 Microphotographs of plagioclase in calcalkaline rocks. A: M6 sample displaying a Type 2 plagioclase in the centre and Type 1 as matrix and microphenocrystals. B: M21 sample displaying a matrix plagioclase with multiple apatite and oxide inclusions. C, D, E and F: examples of Type 3 plagioclase displaying different styles and degree of resorption textures. C: M28 sample with a spongy cellular resorption texture rim surrounding an unaltered nucleus. D: M64 sample portraying a Type 3 plagioclase with pervasive resorption texture affecting the whole crystal. E: M108 sample showing Type 1 and 3 plagioclase. F: M39 sample with a plagioclase showing a pervasive resorption texture affecting the whole crystal.

tory extinction or an altered nucleus. This type can be found as pheno and microphenocrystals but also as matrix size (Fig: 4.1 and 4.2). This is the most common and abundant type and their lack of destabilization textures suggest crystallization in equilibrium with their host magma, at least at the last stage.

Type 2: They are pheno and microphenocrystals with marked oscillatory zoning, and sometimes with undulatory extinction superimposed, that may show corroded and regrown borders and/or altered cores with inclusions that are not recognizable under the optical microscope. In these plagioclase type a large amount of apatite microcrystals are frequently found included in the regrown zones (Fig: 4.1B and 4.2A). Their morphology, zonation and alteration style are typical of longer times of residence and growing in a magma chamber (Ginibre et al., 2002).

Type 3: This type of plagioclase does not appear in every sample and represents crystals with obvious signs of alteration. Typically they are completely altered, with

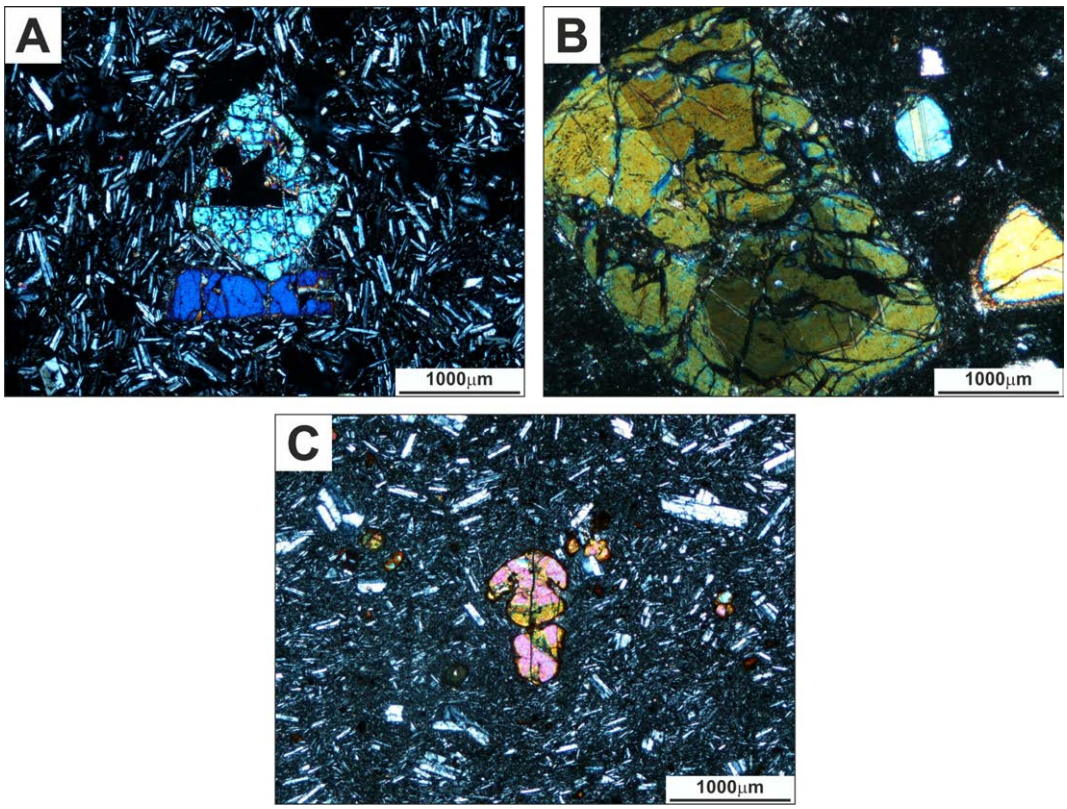

Fig. 4.3 Microphotographs of olivine in calcalkaline rocks. A: M57 sample displaying two olivine phenocrystals with broken edges on a holocrystalline plagioclase matrix. B: M54 sample displaying olivine phenocrystal with zonation. C: M94 sample olivine with corrosion gulfs and an iddingsite rim.

corroded borders, and show a generalised resorption texture called “spongy cellular, sieved” (see Streck, 2008) (Fig: 4.2C, D, E, F).

Olivine

Olivine are present as sub-idiomorphic crystals with broken edges or corrosion gulfs. Depending of the sample they may also show zonation, reaction rims or idding-site alteration (Fig: 4.3).

Pyroxene

Clinopyroxene phenocrystals (Fig. 4.4) are mostly sub-idiomorphic and usually have a thin regrown rim. The majority of microphenocrystals have inclusions of oxides

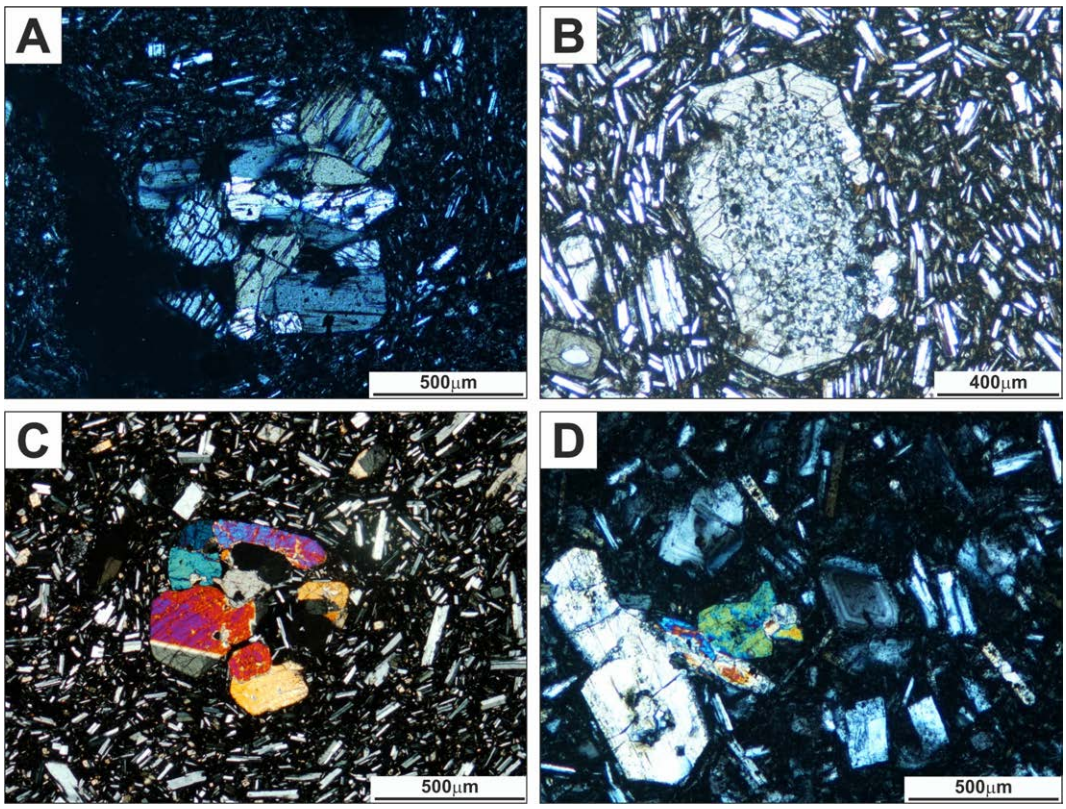

Fig. 4.4 Microphotographs of pyroxenes in calcalkaline rocks. A: M53 sample displaying a clinopyroxene glomeroporphiric texture. B: M14 sample showing a clinopyroxene phenocrystal with a pervasive resorption texture affecting the nucleus. C: M39 sample displaying a clinopyroxene glomeroporphiric texture. D: M64 sample showing an orthopyroxene phenocrystal in the down left side and a clinopyroxene microphenocrystal in the centre (green color).

or show an isotropic squared zone in the core. Some clinopyroxene crystals exhibit particular characteristics such as being in optic continuity with orthopyroxene, forming a patchy zoning pattern, or displaying a glomeroporphyritic texture where the crystals have concentric zonation with an orthopyroxene core.

Orthopyroxenes are rarely found as phenocrystals and are more common as microphenocrystals, as the centre of clinopyroxenes or forming patchy zoning textures with clinopyroxene.

Amphibole

In the samples from the El Metate volcano, amphiboles are also present as both pheno and microphenocrystals (Fig: 4.5). In other volcanoes, amphiboles could not be identified with certainty.

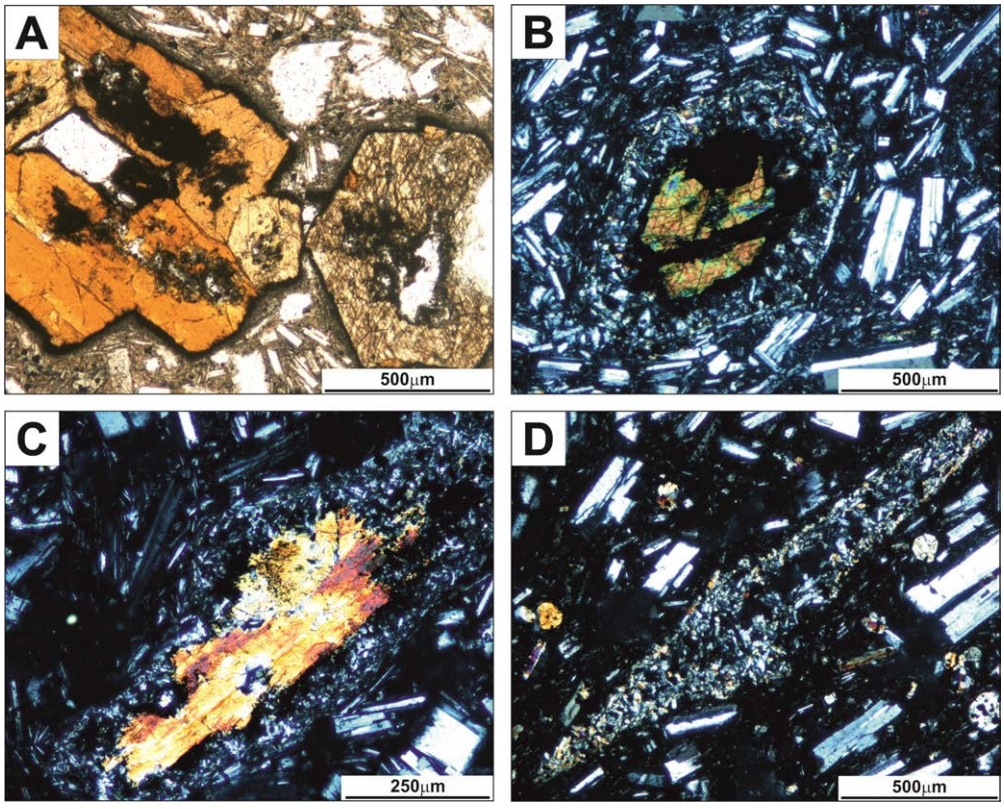

Fig. 4.5 Microphotographs of amphibole crystals found in calcalkaline rocks. A: M20 sample showing two euhedral amphibole phenocrysts with a symplectitic opacite rim B: M61 sample showing a euhedral amphibole showing a symplectitic opacite rim and an external granular opacite rim. C: M20 sample displaying a partially replaced amphibole whit a granular opacite rims. D: M60 sample showing an amphibole completely replaced by pyroxenes, plagioclases and oxides.

The best preserved ones are euhedral but often the shape is lost due to a complex alteration pattern that includes two types of opacitization (*sensu* Plechov *et al.*, 2008): in opacite coronas and in volumetric decomposition domains. All the samples containing amphiboles include both opacitizationtypes being the first one the most abundant.

Opacitization in coronas is usually divided in turn into two textural types: an internal granular rim directly developed in contact with the amphibole crystal (granular opacite) and composed by Pl, Opx, Pigeonite and oxides with sizes varying between 3 and 10 µm; and an external one called symplectitic opacite (that occasionally is the only one appearing) composed by a fine (< 1 µm) isotropic aggregate of minerals whose composition cannot be determined (Fig. 4.5A).

The volumetric decomposition domains are zones of replacement within the crystal that have developed through planes of weakness and are composed only by Ca-rich pyroxene that inherits the structural orientation of the replaced amphibole.

Attending to the opacite type we can distinguish two kinds of amphiboles. One kind presents nearly euhedral pheno and microphenocrystals with symplectitic opacite coronas that do not ussually contain volumetric decomposition domains (Fig. 4.4 A and Fig. 5.9). The other kind presents well developed Pl+Cpx+oxides granular opacite coronas (Fig. 4.4 B and C; and Fig. 5.9) that occasionally replace the whole crystal leaving pseudomorphs (Fig. 4.4 D). These crystals do not present symplectitic opacite and are usually smaller than the others.

Alkaline rocks

The texture of the alkaline rocks is, as a whole, holocrystalline inequigranular porphyritic or seriated and, in some cases, trachytic. In some samples we can also identify areas with vitreous porphyritic matrix.

The matrix is usually microcrystalline, eventually with interstitial glass, and less frequently the thin section presents sectors with microcrystalline matrix and/or sectors with vitreous matrix (Fig. 4.6 A, B and Fig. 4.7 A). The main minerals are plagioclase, oxides, olivine and/or pyroxene. As accessory minerals, some contain acicular apatite.

Pheno and Microphenocrysts

The most common phases to all samples are plagioclase and olivine, followed by oxides, Cpx, Opx and Ap, not necessarily present in all the samples. The most abundant phenocrystals is plagioclases (up to 83% of the phenocrystals in some samples), followed by Ol (17%). The other minerals only appear in minor amounts.

Plagioclase

Plagioclases can be classified considering the same three types identified in the calc-alkaline rocks (Figs. 4.6 and 4.7), but in this case Type 2 plagioclases (Fig. 4.6 C) are less common and the concentric zonation seems to be restricted to regrown borders in the larger phenocrystals.

Olivine

Olivine in alkaline rocks are texturally very similar to the olivines in calcalkaline rocks, the main difference resides in the greater abundance of this mineral and the more frequent presence of phenocrystals in this suite compared to the calcalkaline lavas (Figs. 4.6 and 4.7).

Pyroxene

Clinopyroxene is less common as phenocrystals and are usually idio- or subidiomorphic; they seem to be in equilibrium without appreciable zonations, reaction coronae or regrown borders. Orthopyroxene was not found on this suite as expected in alkaline lithologies (Figs. 4.6 and 4.7).

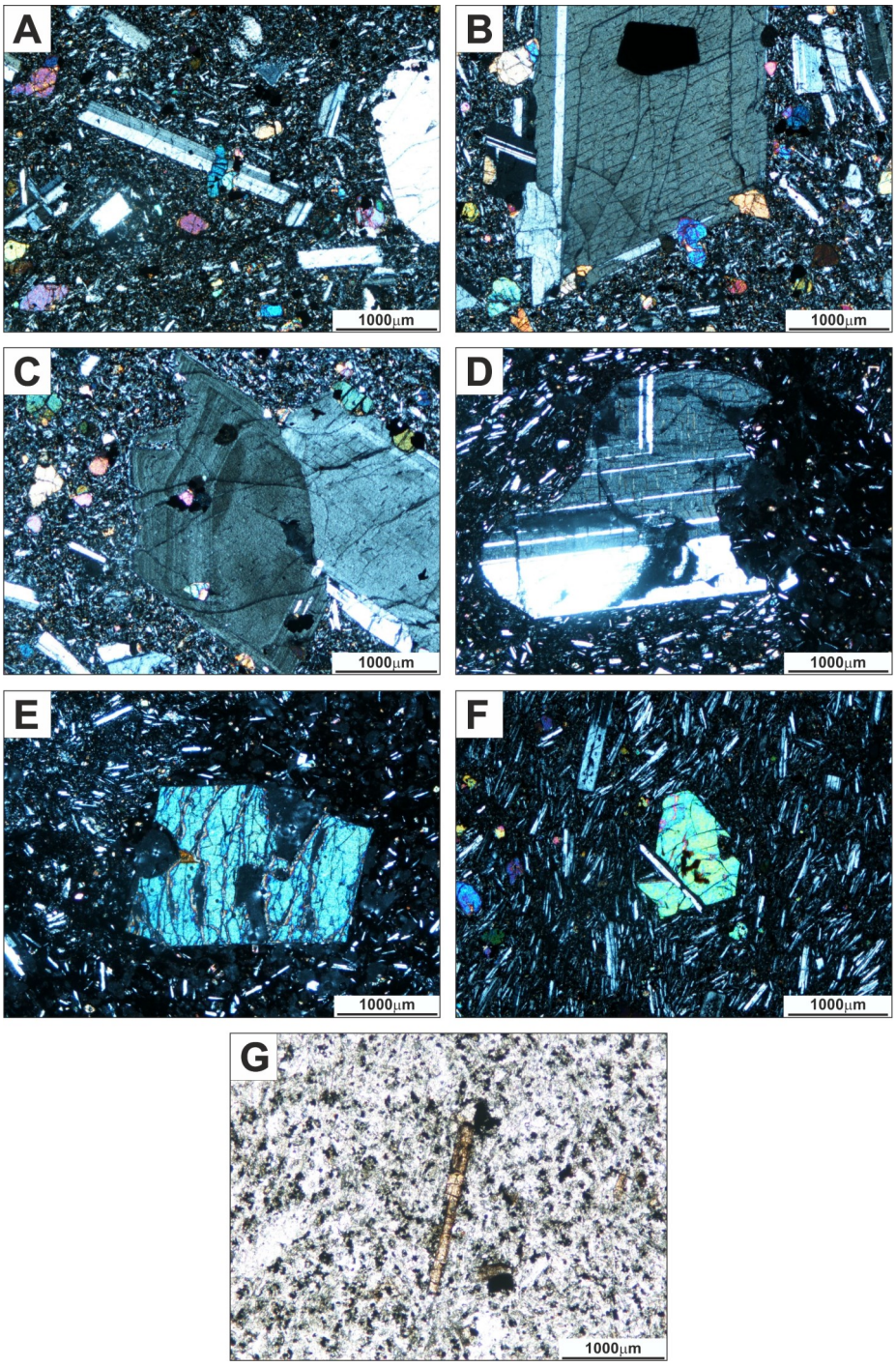

Fig. 4.6 Microphotographs of thin sections from alkaline T1 samples. A and B: M95 sample portraying a holocrystalline inequigranular seriated texture composed by plagioclase, olivine and oxides, on "B" is also noticeable a big oxide inclusion in the plagioclase phenocryst. C: plagioclase phenocrystal from M95 sample with oscillatory zonation on its corroded rim (Type 2). D: plagioclase phenocrystal with corroded and broken edges from M110 sample. E: olivine phenocrystal from M110 sample and two types of matrix: microcrystalline to the left upper side and very vacuolar and vitreous in the rest. F: olivine phenocrystal from M86 sample on a plagioclase trachytic matrix. G: apatite microphenocrystal from sample M105, one of the few examples of apatite with a measurable size.

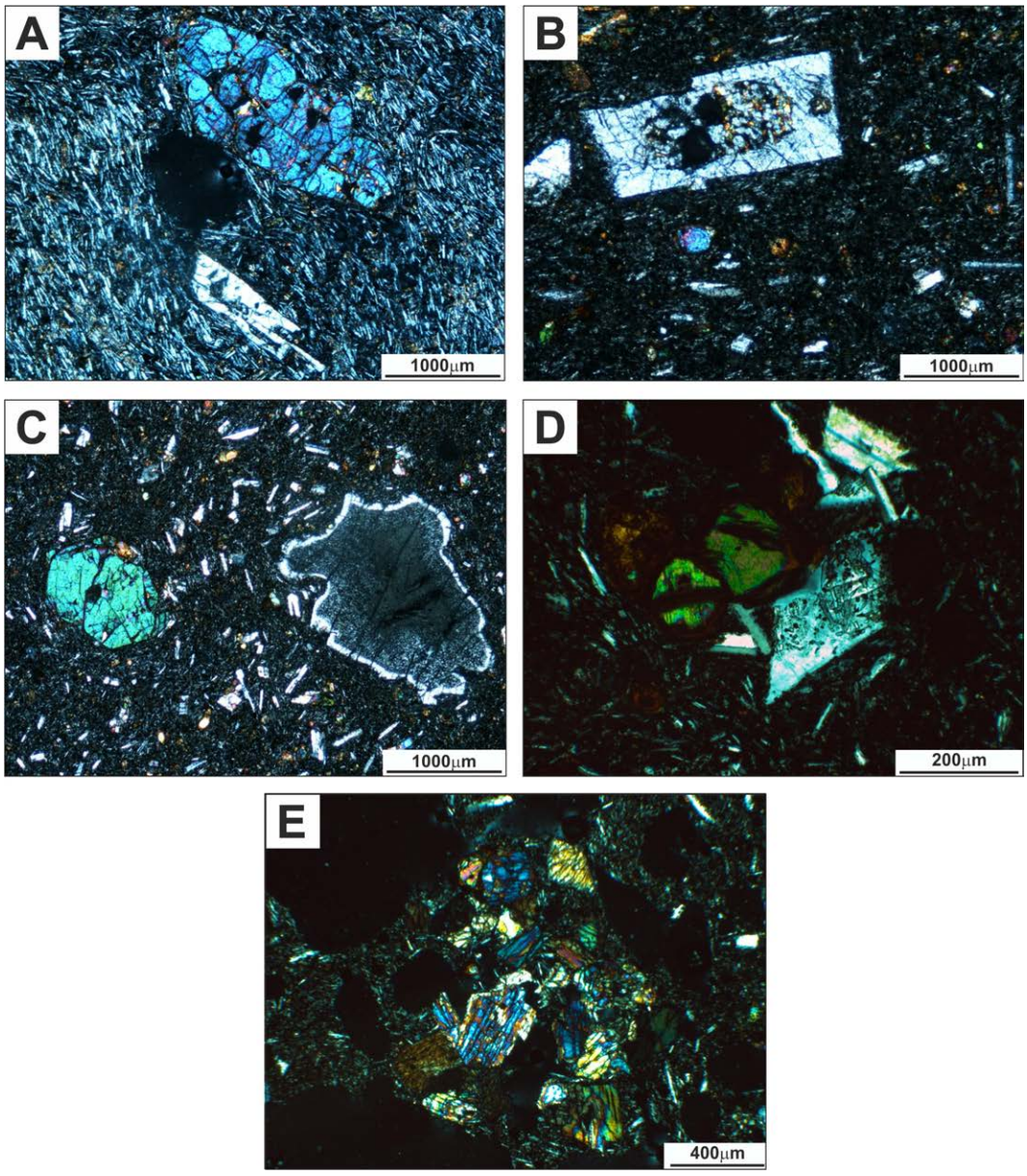

Fig. 4.7 Microphotographs of thin sections from alkaline T2 samples. A: M95 sample portraying a holocrystalline inequigranular porphyritic texture composed by plagioclase, olivine and oxides in the matrix and olivine and plagioclase phenocrystals. B: plagioclase phenocryst from M109 sample presenting multiple inclusions in the nucleus in a microcrystalline matrix. C: M109 sample displaying a spongy cellular texture plagioclase with rounded and corroded borders and a regrown rim (type 3). D: Detail of olivine and plagioclase microphenocrystals from sample M135, olivine shows an iddingsite rim and plagioclase multiple apatite inclusions. E: clinopyroxene aggregate from sample M131.

5. Mineral composition and geothermobarometry

The following sections describe the major element composition of the mineral phases identified in the petrographic study and the results of a thermobarometry study based on such data.

Mineral compositions include the main phases appearing both as phenocrystals or microphenocrystals as well as microcrystals forming the groundmass (olivine, plagioclase, clinopyroxene, orthopyroxene and amphibole) and other minor phases that appear basically as microcrystals (oxides and apatite). Results are summarized in Tables 1 to 7 and displayed in Figures 1 to 7. For clarity, data in the diagrams are grouped in two categories: 1) analyses at centres of pheno- and microphenocrystals, and 2) rims of pheno and microphenocrystals as well as crystals in matrix and coronas. In all cases, only high-quality determinations were considered, discarding data that showed some analytical uncertainty.

The obtained compositional data on mineral phases are then considered together with whole rock analyses for thermobarometric calculations in order to obtain some constraints on the physical conditions under which the mineral assemblage crystallized.

Mineral composition

Olivine

As we have seen in chapter 4, olivine can be found both as pheno- and microphenocrystals as well as microcrystals in the matrix and as inclusions in plagioclase or clinopyroxenes They are usually well preserved but occasionally they appear iddingsitized, with corrosion gulfs and sporadically surrounded by orthopyroxene coronas (Fig: 4.3, 4.6 and 4.7).

The calcalkaline pheno- and microphenocrystal centres have the narrowest and most forsteritic compositional span (Fo_{86} - Fo_{67}), while the range in the T1 alkaline lavas is slightly wider and less forsteritic (Fo_{79} - Fo_{52}) and the T2 rocks show intermediate values (Fo_{85} - Fo_{54}) (Table 1). Border and matrix analyses from T1 lavas show the narrowest and most fayalitic compositional range (Fo_{71} - Fo_{45}), whereas the T2 and CA rocks display again more forsteritic compositions, with the T2 olivines showing a slightly narrower range than those found in the CA (Fo_{84} - Fo_{53} and Fo_{79} - Fo_{44} respectively).

As it can be seen in Fig. 5.1, the centre to border variations follow a typical evolution sequence with the composition of the centres in general more forsteritic than the borders and the matrix for every rock suite. Although differences are small, the olivines present in the alkaline T2 and calcalkaline rocks are slightly more forsteritic than those found in the alkaline T1 lavas. This is also observed in the olivines that appear as inclusions within other phases, where forsterite values in CA rocks are higher (Fo_{79} - Fo_{76}) than those of T1 (Fo_{71}) and T2 shows a relatively wide span (Fo_{77} - Fo_{55}). An interesting feature of the analysed olivines is the wide compositional span for every suite

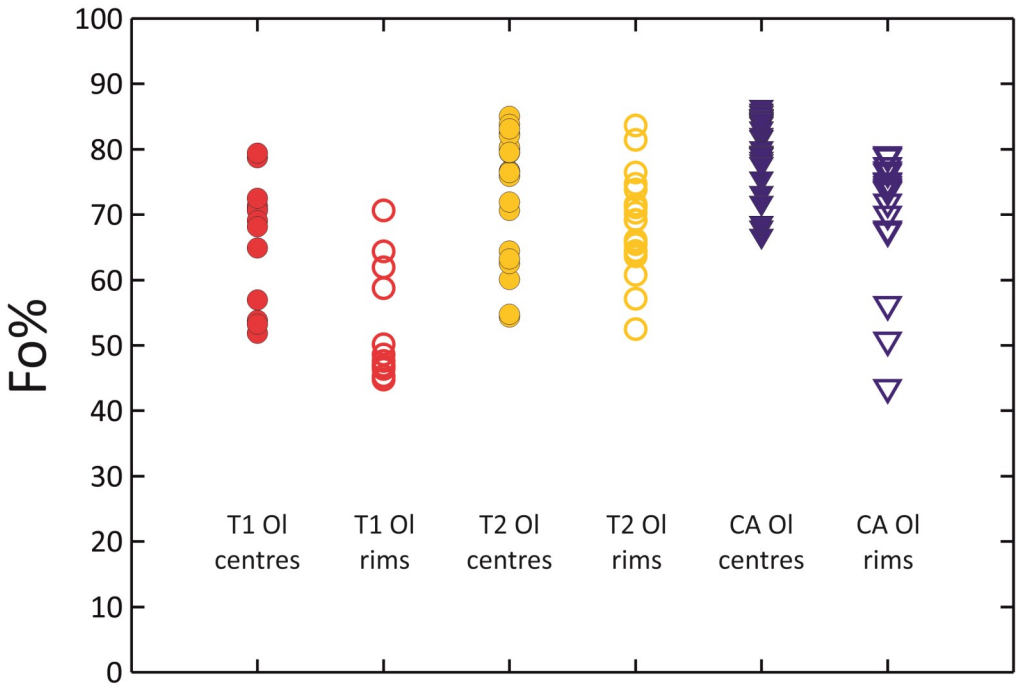

Fig. 5.1 Olivine compositions as forsterite molecule percentage (Fo %). Red circles: T1 lavas; Yellow circles: T2 lavas, and Blue triangles: CA lavas. Filled symbols represent analysis in the centres and empty symbols rims and matrix analyses.

with specimens reaching compositions as low as Fo_{52} for an olivine centre that attest the evolved signature of these rocks.

Plagioclase

In general terms, the compositional range for plagioclase in each suite is quite wide and similar to each other (Fig. 5.2 and Table 2). Plagioclase in T1 alkaline rocks yield the lowest anorthite content (An_{62} - An_{28} for the centres and An_{63} - An_{12} for the borders); In the T2 alkaline rocks, they yield values of An_{81} - An_{28} for the centres and An_{73} - An_{34} for the borders; and calcalkaline samples yield values of An_{83} - An_{52} for the centres and An_{78} - An_{20} for the borders.

Like in the case of olivine, the most anorthitic plagioclases are found in the T2 and CA rocks whereas the broadest compositional range is observed in the borders of

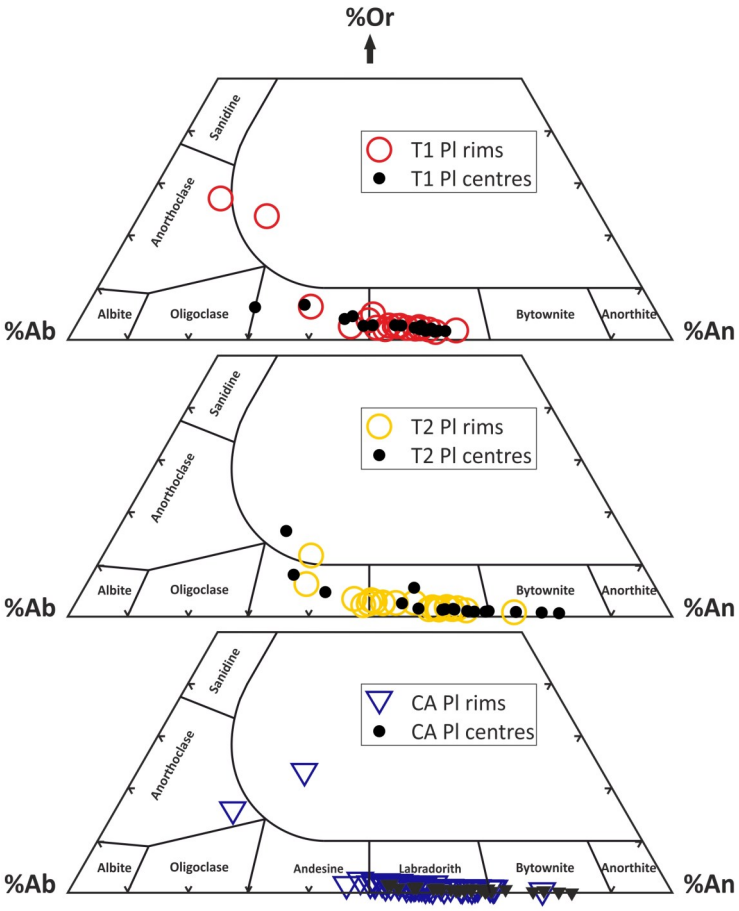

Fig. 5.2 Plagioclase classification diagrams after Deer et al. (1992). Ab: albite; An: Anorthite; Or: orthose. Red circles T1 plagioclases, Yellow circles T2 plagioclases and blue triangles CA plagioclases. Filled symbols represent analysis in centres and empty ones in rims.

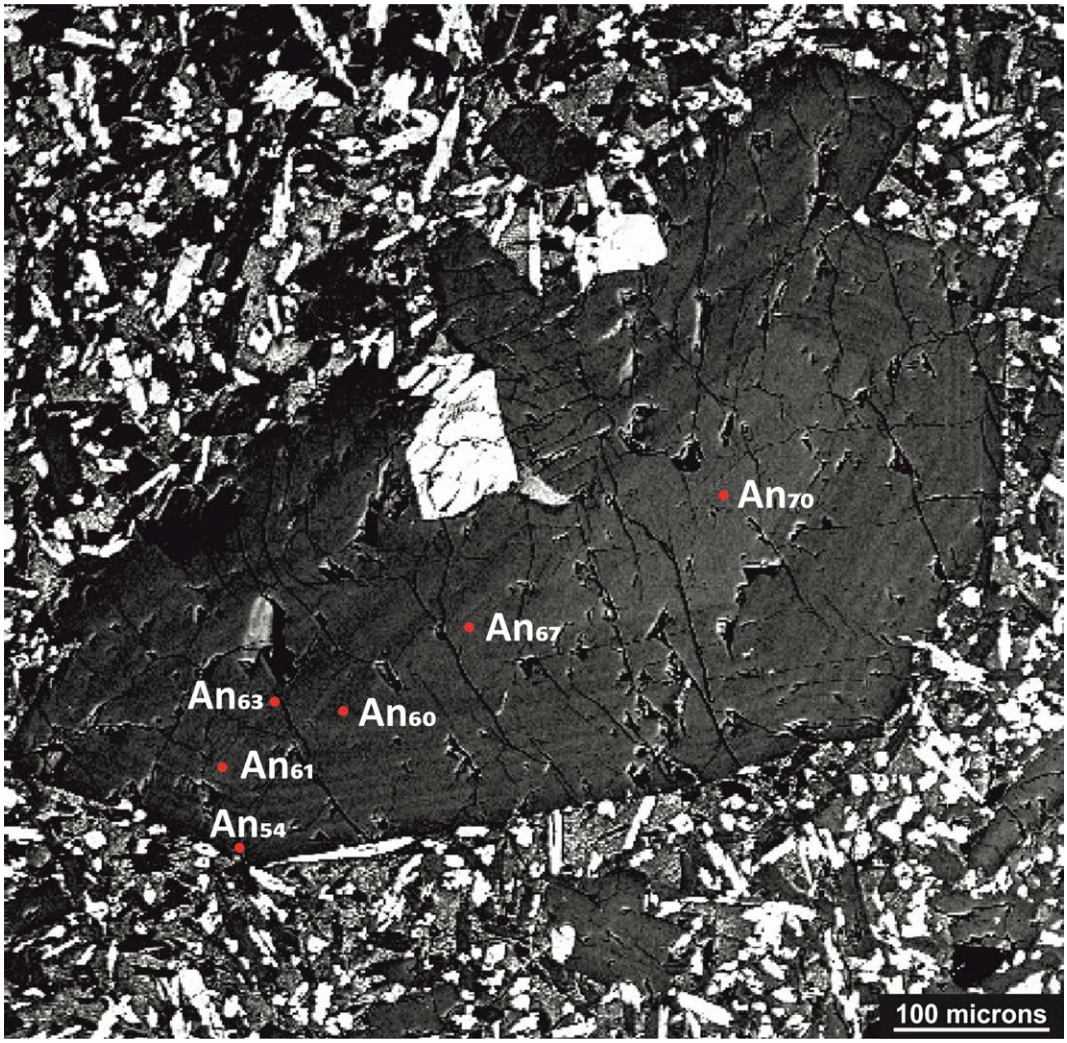

Fig. 5.3 Backscattered electron microprobe image of a Type 2 plagioclase from sample M3 (CA). Red dots represent micropuntual analysis sites and their anorthite content.

plagioclases of the T1 and CA lavas, and in the centres of the T2 plagioclases. If considered as a whole, the obtained data would suggest that, contrary to what should be expected in a standard fractional crystallization variation (i.e. progressively lower An values from centres to borders)

no significant differences are found between centres and borders within the same suite. This can be understood if we consider the complexity of the plagioclase population in these rocks. As explained in the petrography section, plagioclases appear in a wide typological variety encompassed by tree types of pheno- and microphenocrysts,

matrix crystals, and plagioclases belonging to amphibole coronas and as inclusions in clinopyroxene.

The three different types of phenocrysts are idio and sub-idiomorphic crystals of all sizes with Carlsbad or polysynthetic twinning (Type 1); pheno- and microphenocrystals with marked oscillatory zoning (Type 2); and very altered crystals showing a generalised resorption texture called “spongy cellular (sieved)” (see Streck, 2008) (Type 3). Every suite contains the three types of plagioclases, with the Type 1 being the most abundant in all cases. Regarding the other types, CA rocks are the ones showing the greatest abundance of both Type 2 and Type 3 crystals, whereas T2 alkaline rocks contains Type 3 more often than Type 2 and T1, although very diploid, hosts more of the Type 2 than the Type 3 crystals, which are barely found. The Type 1 crystals may be attributed to a typical simple fractional crystallization process where the phenocrystal borders and matrix tend to be more albitic than the centres and show no alteration textures thus suggesting equilibrium within the host rock. Type 2 plagioclases present an oscillatory zoning but still keeping a tendency to be relatively more albitic towards the borders. This zonation pattern is usually attributed to fast growth, probably in a convective environment where local variations in Ca and Na availability may produce a greater variability in the compositional zoning inside the general pattern (Ginibre et al., 2002) (Fig: 5.3). These crystals therefore are more likely to crystallize in magmatic chambers where they may acquire concentric zonations, whereas Type 1 plagioclases do not require staying in a magmatic chamber as their characteristics can be developed during magma ascent.

The Type 3 plagioclases were difficult to analyse due to their high degree of alteration. Nevertheless some of them appear as subidiomorphic phenocrysts and preserve a more or less unaltered measurable nucleus surrounded by a much altered zone with many inclusions and a regrown border. According to the results obtained, the most albitic centres on every suite belong to the centres of Type 3 crystals while their regrown borders plot amongst the most anortitic compositions only found in the borders of other Type 1 and 2 phenocrystals and matrix crystals (Fig: 5.4). These spongy cellular (sieved) textures were described by Pearce & Kolisnik (1990) and Pearce (1994) as evidence of resorption processes. Resorption is the result of a chemical disequilibri-

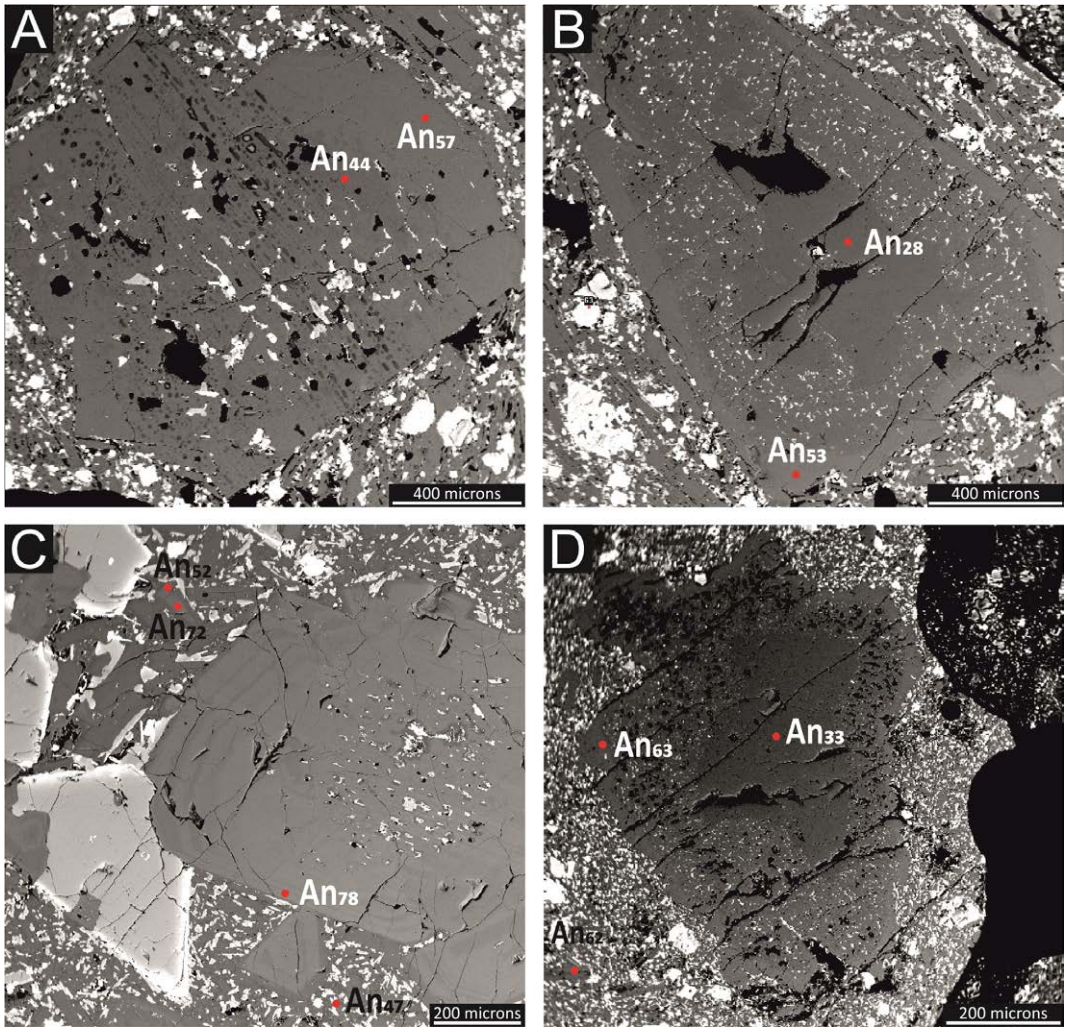

Fig. 5.4 Backscattered electron microprobe image of Type 3 plagioclases. Red dots represent micropunctual analysis sites (anorthite content indicated). A: M86 (T1) sample showing a more anortitic rim than the centre with multiple clinopyroxene and olivine inclusions in the nucleus. B: M86 (T1) sample showing a high-albitic nucleus and a rim akin to other non-Type 3 Plg rims (e. g. Fig: 3). C: M93 (CA) sample showing an altered nucleus with inclusions and a regrown border as well as the compositions of matrix and microphenocrystal plagioclases. D: M109 (T1) sample showing a high-albitic nucleus and a rim compositionally akin to other non-Type 3 plagioclases and the matrix microcrystal on the left down side of the image.

um between the mineral and the surrounding liquid and thus can be caused by magma mixing, magma recharge, contamination and decompression of water saturated magmas (Vance, 1965; Nelson & Montana, 1992). In the second case plagioclase would crystallize as volatiles are exsolved and resorption would take place during ascent prior to water saturation (Blundy & Cashman, 2001). These characteristics suggest a xenolithic origin for Type 3 plagioclases, most likely assimilated from a more evolved lithology. Such xenocrystals would not be in equilibrium with the new hosting melt thus gen-

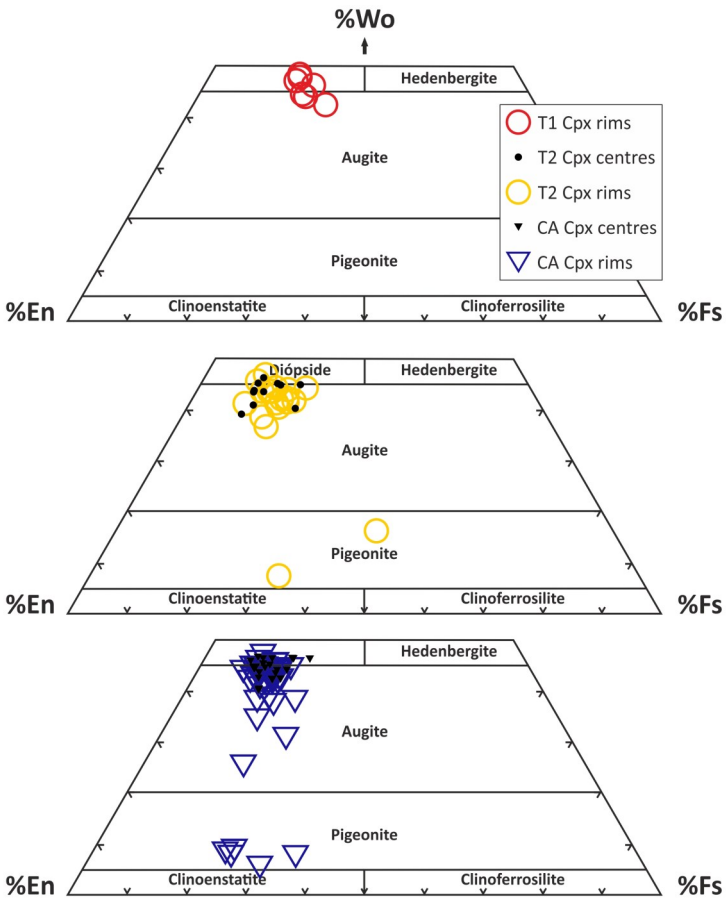

Fig. 5.5 Clinoppyroxene classification diagrams after Morimoto et al. (1988). Wo: wollastonite; En: Enstatite; Fs: ferrosilite. Red circles T1 clinopyroxenes, Yellow circles T2 clinopyroxenes and blue triangles CA clinopyroxenes. Filled symbols represent analysis in centres and empty ones in rims.

erating the spongy cellular texture and acquiring the mineral inclusions in the process. The anortitic border would presumably grow from the assimilating melt and in equilibrium with it.

Clinopyroxene

As we have seen, clinopyroxenes can be found as pheno- and microphenocrystals, as well as microcrystals in the matrix, hosted as inclusions in plagioclases, forming coronas around olivine and amphibole and as amphibole replacements. Occasionally they also appear as pseudomorphs of a previous mineral not preserved.

Following the IMA classification (Morimoto, 1998) all T1 and T2 rock clinopyroxenes and most of the CA ones plot in the Quad (Ca-Mg-Fe) field of the diagram and are therefore classified using the Wo-En-Fs triangle (Fig. 5.5 and Table 3). This classification

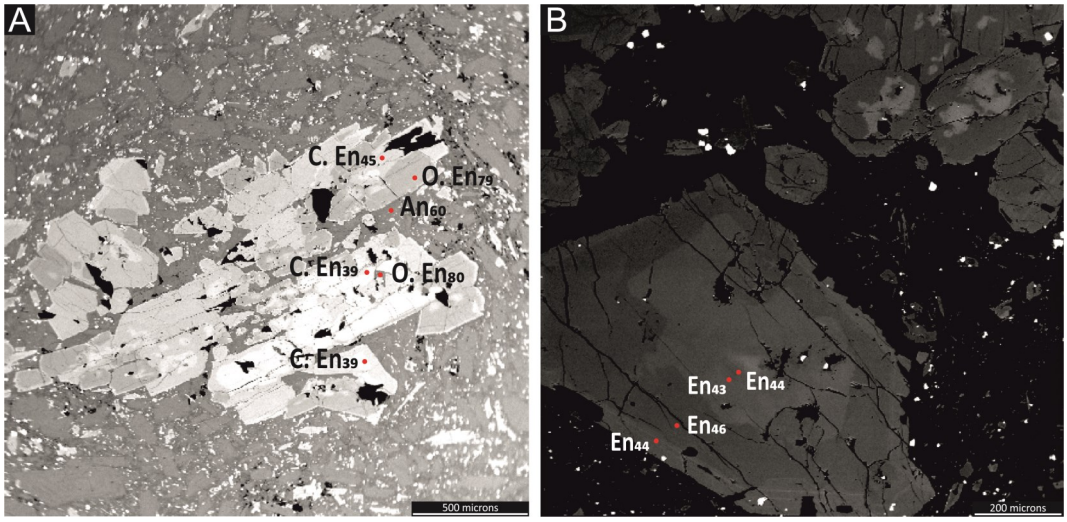

Fig. 5.6 Backscattered electron microprobe images of pyroxenes. Red dots represent micropuntual analysis sites (enstatite content shown next to each point). A: Patchy zonation of Cpx (C on the image) with Opx (O. In the image) cores in sample M64 (CA). B: coarse oscillatory zonation in a Cpx from sample M74 (CA).

reveals that the T1 clinopyroxenes are the most Ca enriched, plotting in the diopside field or in the most Ca-rich sector of the augites, while T2 clinopyroxenes plot in general in the augite field with only three corresponding to diopsides and one to pigeonite. Clinopyroxenes in CA rocks on the other hand show more heterogeneous compositions, ranging between diopside and augitic terms with also the presence of more pigeonitic ones. These latter correspond in most cases to matrix crystals and one of them belongs to an olivine corona. Another distinctive feature of clinopyroxenes from these rocks is that the borders and matrix analyses present the entire observed compositional range while centres are always represented by high-Ca augites or diopsides, while the Ca-poor augites and pigeonites are restricted to the matrix, amphibole coronas and occasionally phenocrystal borders.

Similarly to plagioclase, some clinopyroxenes also display zonation patterns which are indicative of open system processes (see Streck, 2008) such as concentric reverse zonation and step-like patchy zonation (Fig. 5.6A and 4.4 B). Concentric reverse zonation of clinopyroxenes from sub-alkaline magmas were interpreted by Anderson (1974) and Pe-Piper (1984) as evidences of magma mixing processes as well as step-like patchy zoning was interpreted as consequence of either magma mixing or contamination with solid crystal debris either by diffusional re-equilibration or by infilling of an

overgrowth on a spongy cellular crystal (Stewart & Pearce, 2004). Resorption of pyroxene in the form of spongy cellular texture is also considered a clear indication of open system behaviour (Streck, 2008). Coarse oscillatory zoning (Fig. 5.6B) in turn is indicative of convection of phenocrysts in a differentially cooling magma chamber Elardo & Shearer (2013).

Orthopyroxene

Orthopyroxenes apear only in the T2 alkaline trend and in the CA suite. As shown on the IMA classification diagrams (Morimoto, 1988) (Fig. 5.7 and Table 4), all orthopyroxenes from T2 alkaline and CA rocks are all classified as enstatites.

In the T2 trend, the only two specimens found included in Ol and Plg plot towards Mg-richer compositions than the ones forming coronas (En_{78} - En_{77} and En_{68} - En_{60} respectively). The CA orthopyroxenes, on the other hand, present a much wider compositional range which is very similar for both centres and borders (En_{85} - En_{65} and En_{79} - En_{59} respectively).

The CA orthopyroxenes, on the other hand, present a much wider compositional range which is very similar for both centres and borders (En_{85} - En_{65} and En_{79} - En_{59} respectively).

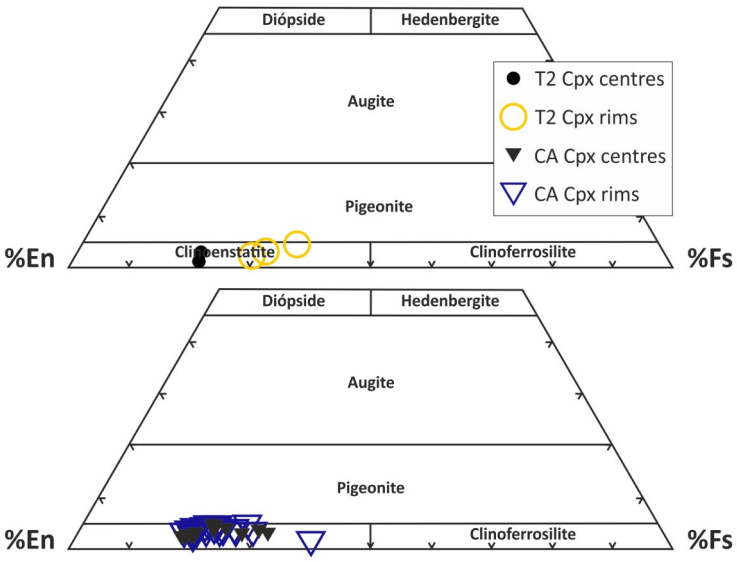

Fig. 5.7 Orthopyroxene classification diagrams after Morimoto et al. (1988). Wo: wollastonite; En: Enstatite; Fs: ferrosilite. Circles are T2 clinopyroxenes and triangles CA clinopyroxenes. Filled symbols represent analysis in centres or Opx inclusions and empty ones in rims or coronas.

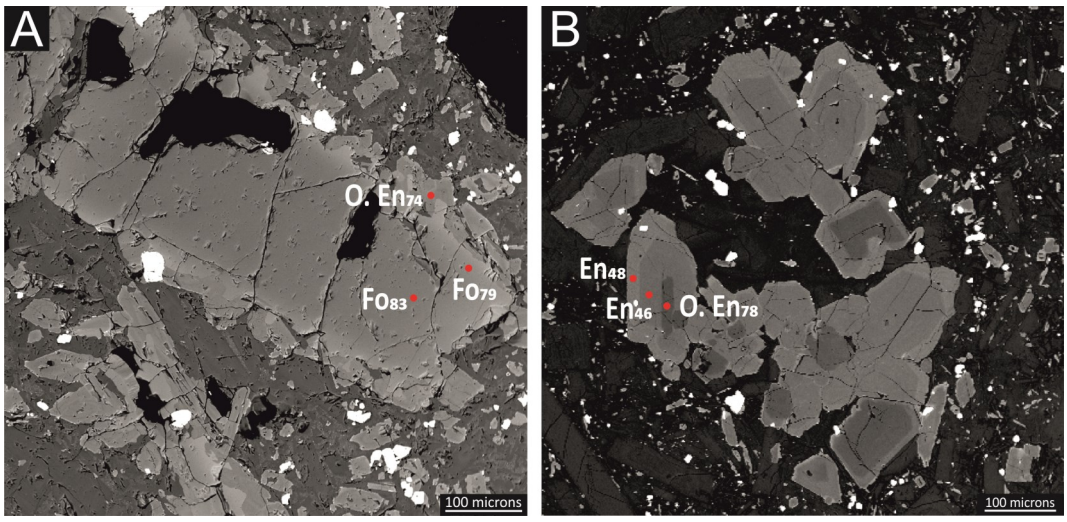

Fig. 5.8 Backscattered electron microprobe images of olivine and orthopyroxene crystals with red dots representing micropuntual analysis sites and their forsterite and enstatite content. A: Ol phenocrystal with orthopyroxene corona from sample M70 (CA). B: pyroxene phenocrystals with orthopyroxene nucleus and surrounding clinopyroxene overgrowths from sample M64 (CA).

This is a consequence of the large range of compositions related to the typological variability, including enstatitic terms that belong to orthopyroxenes from amphibole coronas, reaction zones, pseudomorphs and Opx - Cpx phenocrysts (Fig. 5.8). The orthopyroxene from olivine coronas fit however the compositional span observed in the microcrystals forming the groundmass and in phenocrystal borders.

Amphibole

This phase was only found in calcalkaline samples from El Metate volcano both as pheno- and microphenocrystals. The composition of amphiboles as well as the calculated T, P, H_2O, log fO_2 physical-chemical conditions (see section on Thermobarometry) is summarized in Table 5.

The analysed amphiboles correspond to magnesiohastingsite (14) and tschermakitic pargasite (6). All tschermakitic pargasites belong to phenocrystal centres while magnesiohastingsites can be found both in the centres and in the rims of these crystals.

As explained in the petrography section, amphibole phenocrysts present a complex alteration history that includes two opacitization types: in coronas and in volumet-

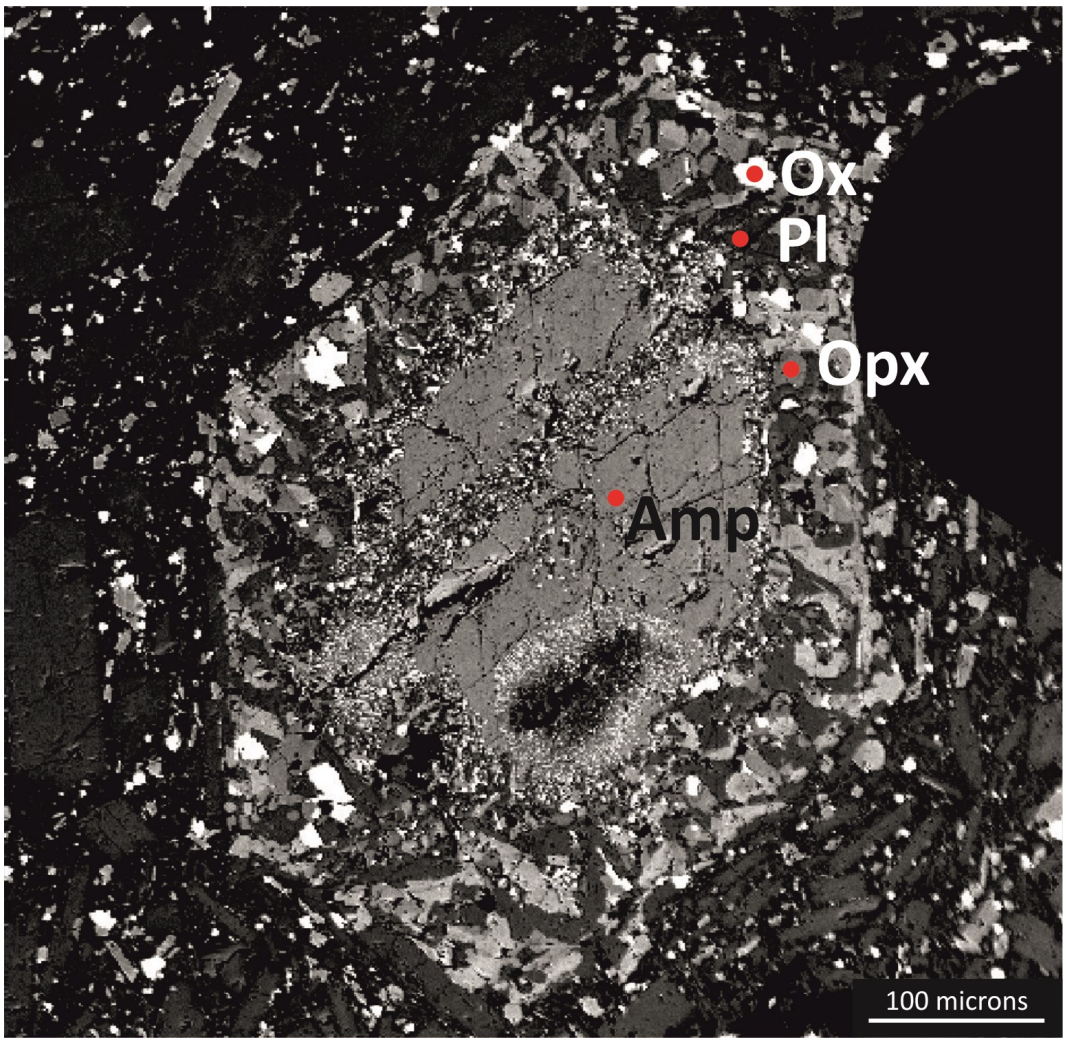

Fig. 5.9 Backscattered electron microprobe image of an amphibole phenocrystal from sample M61 (CA) displaying a well-developed granular opacite rim and volumetric decomposition domains, probably associated to fractures in the crystal. Red dots represent micropunctual analysis sites.

ric decomposition domains (sensu Plechov *et al.*, 2008). All the amphibole-bearing samples include both typologies, sometimes even within the same crystal as in Fig 5.9, being the first type the most abundant. This breakdown features are very common to amphiboles and difficult to distinguish from those caused by destabilization of the amphibole during decompression and ascent from subvolcanic reservoirs (e.g., Rutherford & Hill, 1993; Rutherford, 2008). Following these authors breakdown reactions near the rims tend to be decompression induced while more pervasive amphibole breakdown is due to open system processes. The juxtaposition of unaltered amphiboles and altered ones (or pseudomorphs) would imply magma mixing for them, asseveration supported

by Plechov (2008) whom concludes that the main reason for hornblende instability is the heating of the magmatic chamber due to an injection of new hot magma.

Oxides

Oxides (Table 6) are observed in nearly all the samples, present in the matrix or as inclusions and/or less frequently as pheno and microphenocrystals. Compositionally they are represented by spinels and ilmenites.

Suitable analyses were used to classify the spinel group oxides based on the most abundant trivalent ion in the structure into three series: spinel s.s. (Al), magnetite -ulvöspinel (Fe^{+3} and Fe^{+3} + Ti) and chromite (Cr); and further divided into varieties regarding to the most abundant divalent cation (Deer et al. 1992).

Oxides in the CA samples contain chromites, present as inclusions in Ol and also as one matrix crystal, and pheno- and microphenocrystal ilmenites in similar proportions as well as one matrix crystal of ulvöspinel. T1 rocks oxides are mostly ulvöspinel phenocrysts except for two inclusions in plagioclase of ulvöspinel and spinel s.s. Finally, T2 oxide specimens were exclusively represented by ulvöspinels as inclusion in olivine and clinopyroxene.

Apatite

Most analysed apatites (Table 7) belong to the T1 alkaline series and are present as inclusions in ulvöspinel, plagioclase, and olivine or rarely as matrix crystals. Only two microcrystals found in T2 alkaline rocks could be analysed and are represented by inclusions in clinopyroxene and magnetite.

Thermobarometry

To quantitatively describe the evolution of a melt from its source until its extrusion, it is first necessary to determine the temperature and the pressure at which the different intervening phases were formed. One of the most frequent approaches is to

estimate these parameters from the composition of the mineral phases through geothermobarometers based on mineral-mineral and mineral-liquid chemical equilibria. The application of this methodology to basaltic melts is nowadays facilitated by a complete set of calibrations available for the most common phases in igneous systems adapted to a wide range of pressure, temperature and composition conditions (see Putirka, 2008). Indeed, recent studies on geothermobarometry in basaltic magmas (e.g. Costa et al., 2013, Dahren et al., 2012; Keiding & Sigmarsson, 2012) have confirmed that this type of calculations allow obtaining detailed information on the functioning and evolution of a magmatic system during differentiation, including those taking place in open systems with magma assimilation or magma mixing, making them essential for any attempt at petrogenetic modelling. In fact, as demonstrated in other studies, having information on the mineral paragenesis evolution allows a more precise quantification of the differentiation processes (see for example Cebriá et al., 2011b).

Theoretical background

The chemical variations observed in any mineral phase are a consequence of the composition of the hosting magma and the physical conditions that prevailed during its crystallization. Many studies on mineral chemistry equilibrium over the years have been devoted to provide formulations of geothermometers and geobarometers that relate both sets of parameters (geochemistry and physical conditions) and are the basis for any thermodynamic approach to describe the crystallization of mineral phases from a wide variety of magma compositions (see Green 1994, Putirka 2008 and references therein).

Amongst the different geothermobarometers available in the literature (see Putirka, 2008) the ones selected here were those calibrations that best match the compositional range of the studied rocks as well as the main mineral assemblage, represented by plagioclase, clinopyroxene, orthopyroxene, olivine and amphibole. In all cases calculations were carried out considering the most recent calibrations after (Putirka, 2008).

The majority of this thermobarometers estimate P-T conditions from mineral-mineral or liquid-mineral chemical equilibrium. Therefore a strict application of those formulations relies on analyses that are obtained from phases in equilibrium (e.g. a mineral border in contact with a glassy matrix that would represent the composition of the liquid from which that crystal rim crystallized). However, in most cases this is not possible and for practical reasons some assumptions and simplifications have to be accepted. For example, the presence of a microcrystalline matrix (such as the one prevailing in the studied rocks) hinders the possibility of obtaining a direct analysis of the possible liquid in contact with mineral borders. In this situation it is often assumed that the whole rock may represent the composition of the magma in equilibrium with the phases contained within. However, this is a simplification that may lead to incorrect results (e.g. in the case of rocks hosting a relatively high proportion of xenocrysts or cumulate crystals). Therefore, to minimize such problems the calculations are limited to minerals that had no petrographic evidences of instability and that were in equilibrium with the hosting whole rock composition according to K_D tests. This was the procedure followed for Ol, Cpx, Opx and Pl. The amphibole thermobarometer and hygrometer, on the other hand, calculates the P-T-H_2O parameters from mineral compositions alone and therefore is applicable both to centres and borders independently of the existence of equilibrium (or lack of it) with the host rock.

Olivine

In the case of olivine, it was adopted the olivine-liquid equilibrium as calibrated in the expression 22 of Putirka (2008):

$$\mathrm{T(^{\circ}C)} = \{15294.6 + 1318.8\mathrm{P(GPa)} + 2.4834[\mathrm{P(GPa)}]^2\} / \left\{8.048 + 2.8352\ \ln \mathrm{D_{Mg}^{Ol/liq}} + 2.097 \ln\left[1.5\left(\mathrm{C_{NM}^{L}}\right)\right] + 2.575\ \ln\left[3\left(\mathrm{C_{SiO2}^{liq}}\right)\right] - 1.41\mathrm{NF} + 0.222\mathrm{H_2O^{liq}} + 0.5\mathrm{P(GPa)}\right\}$$

Where:

$$\mathrm{D_{Mg}^{Ol/liq}} = \mathrm{X_{Mg}^{Ol}} / \mathrm{X_{Mg}^{liq}}$$

$$\mathrm{C_{NM}^{L}} = \mathrm{X_{FeO}^{liq}} + \mathrm{X_{MnO}^{liq}} + \mathrm{X_{MgO}^{liq}} + \mathrm{X_{CaO}^{liq}} + \mathrm{X_{CoO}^{liq}} + \mathrm{X_{NiO}^{liq}}$$

$$C^{liq}_{SiO_2} = X^{liq}_{SiO_2}$$

$$NF = \frac{7}{2}\ln\left(1 - X^{liq}_{AlO_{1.5}}\right) + 7\ln\left(1 - X^{liq}_{TiO_2}\right)$$

This calibration is modified from the traditional model by Beattie (1993), based on the distribution of Mg between olivine and liquid rectified for temperature overestimations in hydrated conditions and the systematic error at very high temperatures and pressures as noted by Herzberg & O'Hara (2002), yielding an error of ± 29 °C. Since that expression requires an initial pressure input and considering the usual early crystallization of olivine in Bowen series, for these samples we have assumed and initial P = 16 kbar, corresponding to the highest P value (15.7 kbar) obtained from other minerals in the paragenesis.

To test the equilibrium between olivine and liquid, it is used the Fe-Mg distribution coefficient (K_D):

$$MgO^{Ol} + FeO^{liq} = MgO^{liq} + FeO^{Ol}$$

Whose expression is:

$$K_D\,(Fe - Mg)^{Ol-liq} = (X^{Ol}_{Fe} * X^{liq}_{Mg})/(X^{Ol}_{Mg} * X^{liq}_{Fe})$$

Its value varies very little with T or composition and has a nearly constant value of (0.30 ± 0.03) for basaltic systems at P < 2-3 GPa (Roeder & Emslie, 1970). Temperatures and K_D values calculated for olivines are included in Table 1. Only good-quality analyses and compositions in equilibrium with the host rock were taken into consideration for the diagrams and the following description and discussions.

As mentioned earlier, for crystal-liquid thermobarometrical calculations, crystal centres should be paired with whole rock compositions whereas mineral rims should be in equilibrium with matrix compositions (Putirka, 2008). In these samples, the lack of a vitreous matrix implies that the second situation cannot be met. As a consequence, according to their K_D values only a few of the analyses performed on crystal rims or in matrix-size minerals show equilibrium with whole rock analyses (if taken as a proxy of liquid compositions).

The results obtained from pairs with equilibrium K_D suggest that the olivine centres belonging to the T2 alkaline series crystallized at the highest temperatures (1240 -

1198 °C). The rims showed a slightly higher range (1242 - 1206 °C) but this observation has to be considered with caution since it is represented only by rim analysis in two of the samples and therefore this may not be generalized to the whole field. The olivine centres of the calcalkaline and the T1 alkaline suites result in somewhat lower ranges (1227 - 1183 °C and 1224 - 1168 °C, respectively).

Plagioclase

Plagioclase stability is very sensitive to water contents in the magma (see for example Goldsmith, 1982 or Almeev et al., 2012). Therefore, if we consider that calcalkaline rocks usually have significant water contents (typically between 1% and 4% in the MGVF volcanoes; Johnson *et al.*, 2010), equation 24a from Putirka (2008), calibrated to account for variable water contents, seems the most adequate in our case. In addition to consider the possible presence of water in the liquid, this formulation reduces the error (SEE = ± 36 °C) relative to previous calibrations (e.g. Ghiorso *et al.*, 2002; Mathez, 1973; Putirka, 2005):

$$\frac{10^4}{\mathrm{T(K)}} = 6.4706 + 0.3128\ln\left\{\frac{\mathrm{X_{An}^{Pl}}}{\mathrm{X_{CaO}^{liq}}(\mathrm{X_{AlO_{1.5}}^{liq}})^2(\mathrm{X_{SiO_2}^{liq}})^2}\right\} - 8.103\left(\mathrm{X_{SiO_2}^{liq}}\right) + 4.872\left(\mathrm{X_{KO_{0.5}}^{liq}}\right) + 1.5346\left(\mathrm{X_{Ab}^{Pl}}\right)^2 + 8.661\left(\mathrm{X_{SiO_2}^{liq}}\right)^2 - 3.341 * 10^{-2}\left(\mathrm{P(kbar)}\right) + 0.18047(\mathrm{H_2O^{liq}})$$

For pressure calculations the expression 25a from Putirka (2008) was chosen for coherence with the thermometer (SEE = ± 1.8 kbar):

$$\begin{aligned}\mathrm{P(kbar)} = {} & -42.2 + 4.94 \times 10^{-2}\mathrm{T(K)} + 1.16 \\ & \times 10^{-2}\mathrm{T(K)}\ln\left(\frac{\mathrm{X_{Ab}^{Pl}X_{AlO_{1.5}}^{liq}X_{CaO}^{liq}}}{\mathrm{X_{An}^{Pl}X_{NaO_{0.5}}^{liq}X_{SiO_2}^{liq}}}\right) - 382.3\left(\mathrm{X_{SiO_2}^{liq}}\right)^2 + 514.2\left(\mathrm{X_{SiO_2}^{liq}}\right)^3 \\ & - 19.6\ln\left(\mathrm{X_{Ab}^{Pl}}\right) - 139.8\left(\mathrm{X_{CaO}^{liq}}\right) + 287.2\left(\mathrm{X_{NaO_{0.5}}^{liq}}\right) + 163.9\left(\mathrm{X_{KO_{0.5}}^{liq}}\right)\end{aligned}$$

Equation 25b (Putirka, 2008) was also considered, given that the Plg-liq equilibrium is considered as a good hygrometer when T is known (± 1 wt% error in H_2O content):

$$H_2O(\mathrm{Wt\%}) = 25.95 - 0.0032\mathrm{T}(^{\circ}\mathrm{C})\ln\left\{\frac{X_{An}^{Pl}}{X_{CaO}^{liq}\left(X_{AlO_{1.5}}^{liq}\right)^2\left(X_{SiO_2}^{liq}\right)^2}\right\} - 18.9\left(X_{KO_{0.5}}^{liq}\right) + 14.5\left(X_{MgO}^{liq}\right) - 40.3\left(X_{CaO}^{liq}\right) + 5.7\left(X_{An}^{pl}\right)^2 + 0.108P(Kbar)$$

As a check for equilibrium of the Plg-liq pair the K_D $(An\text{-}Ab)^{Pl\text{-}liq}$ was adopted. Even though this parameter varies with P, T and H_2O, when divided into two intervals of T, the distribution coefficient yields relatively constant values of K_D $(An\text{-}Ab)^{Pl\text{-}liq}$ = 0,10 ± 0,05 for T < 1050 °C and K_D $(An\text{-}Ab)^{Pl\text{-}liq}$ = 0,27 ± 0,11 for T > 1050 °C.

Following Putirka (2008), calculations of the above described expressions were solved in an iterative way, with each expression being calculated as a function of the others until convergence is reached.

The results of these calculations are presented in Table 2 together with their corresponding plagioclase compositions. In this case the highest temperatures and pressures on plagioclases are obtained from the T1 alkaline series, showing a very similar range for centres and rims (1256 -1182 °C, 15.7 - 9.6 kbar and 0.47 - 0 H_2O wt%; and 1257 - 1194 °C, 15.7 - 11.4 kbar and 0.59 H_2O wt% respectively), followed by the T2 alkaline lavas (1249 - 1177 °C, 12.7 - 7.1 and 0.4 H_2O wt% for centres and 1246 - 1174 °C, 13.9 - 7 kbar and 0.8 H_2O wt% for rims). The calcalkaline suite on the other hand, presents a larger range of pressures and temperatures at lower values and with significantly higher water contents than the other two suites (1226 - 1148 °C, 10.7 - 3.4 kbar and 1.92 - 0.42 for cores and 1227 - 1148 °C, 10.8 - 3.4 kbar and 2.34 - 0.42 for the rims and matrix crystals).

These values for pressure and temperature are likely a consequence of the wide variety of plagioclase typology (see petrographic description). Unfortunately, the lack of equilibrium in many cases makes it unfeasible to obtain reliable P-T estimations and therefore is not possible to track with precision the differences in crystallization conditions between the different plagioclases types.

Clinopyroxene

Clinopyroxene barometers are based in the $NaO_{0.5}^{liq}$ + $AlO_{1.5}^{liq}$ + $2SiO_2^{liq}$ = $NaAlSi_2O_6^{cpx}$ reaction, with the most recent models considering H_2O^{liq} (in weight %) as a

variable to better calibrate hydrous samples (Grove & Juster, 1989; Kinzler & Grove, 1992; Patiño Douce, 2005; Putirka *et al.*, 1996; Putirka, 2008; Scaillet & MacDonald, 2003; Sisson & Grove, 1993a; Sisson & Grove, 1993b; Walter & Presnall, 1994). Among them, the expression 32c from Putirka (2008), based on the partitioning of Al between clinopyroxene and liquid, was chosen for its good fit to experimental values (± 1.5 kbar):

$$\mathrm{P(kbar)} = -57.9 + 0.0475\mathrm{T(K)} - 40.6\left(\mathrm{X}_{\mathrm{FeO}}^{\mathrm{liq}}\right) - 47.7\left(\mathrm{X}_{\mathrm{CaTs}}^{\mathrm{Cpx}}\right) + 0.676\left(\mathrm{H_2O}^{\mathrm{liq}}\right) - 153\left(\mathrm{X}_{\mathrm{CaO_{0.5}}}^{\mathrm{liq}}\mathrm{X}_{\mathrm{SiO_2}}^{\mathrm{liq}}\right) + 6.89\left[\frac{\mathrm{X}_{\mathrm{Al}}^{\mathrm{Cpx}}}{\mathrm{X}_{\mathrm{AlO_{1.5}}}^{\mathrm{liq}}}\right]$$

Similarly, equation 33 of Putirka 2008) is adopted for temperature calculations, which is reported as suitable for both hydrous and anhydrous conditions, with an estimated overall error of ± 45 °C:

$$\frac{10^4}{\mathrm{T(K)}} = 7.53 - 0.14\ln\left(\frac{\mathrm{X}_{\mathrm{Jd}}^{\mathrm{Cpx}}\mathrm{X}_{\mathrm{CaO}}^{\mathrm{liq}}\mathrm{X}_{\mathrm{Fm}}^{\mathrm{liq}}}{\mathrm{X}_{\mathrm{DiHd}}^{\mathrm{Cpx}}\mathrm{X}_{\mathrm{Na}}^{\mathrm{liq}}\mathrm{X}_{\mathrm{Al}}^{\mathrm{liq}}}\right) + 0.07\left(\mathrm{H_2O}^{\mathrm{liq}}\right) - 14.9\left(\mathrm{X}_{\mathrm{CaO}}^{\mathrm{liq}}\mathrm{X}_{\mathrm{SiO_2}}^{\mathrm{liq}}\right) - 0.08\ln\left(\mathrm{X}_{\mathrm{TiO_2}}^{\mathrm{liq}}\right) - 3.62\left(\mathrm{X}_{\mathrm{NaO_{0.5}}}^{\mathrm{liq}} + \mathrm{X}_{\mathrm{KO_{0.5}}}^{\mathrm{liq}}\right) - 1.1\left(\mathrm{Mg\#}^{\mathrm{liq}}\right) - 0.18\ln\left(\mathrm{X}_{\mathrm{EnFs}}^{\mathrm{Cpx}}\right) - 0.027\mathrm{P(kbar)}$$

To test the equilibrium of the Cpx-liquid pair, the K_D $(Fe\text{-}Mg)^{Cpx\text{-}liq}$ value was used, which should have a value of 0,28 ± 0,08 (0,38 - 0,18), showing little variation with temperature (Putirka, 2008).

The clinopyroxene temperature and pressure data are presented in Table 3 along their corresponding compositions, mineral formulas and classification parameters.

The results obtained indicate that the highest temperature clinopyroxenes crystallized from CA magmas (1233 - 1020°C) within a range of pressures of 10.3 - 4.9kbar for the centres and 1272 - 969 °C and 11.2 - 0.5 kbar for the rims and matrix), followed by the T2 series (1196 - 1033 °C and 13.2 - 4.1 kbar for the centres and 1190 - 939 °C and 11.4 - 0.8 kbar for the rims and matrix). T1 crystals instead, show the lowest crystallization temperatures and pressures (1075 - 974 °C and 7.93 - 0.26 kbar for the borders) with no centres appearing to be in equilibrium with their host rocks. Clinopyroxenes without zonation in general yield lower calculated temperatures and pressures

and matrix microcrystals provide the lowest values (in most cases) together with crystals found in amphibole coronas.

Orthopyroxene

To estimate crystallization temperatures of orthopyroxenes, the expression 28a from Putirka (2008) was adopted. This calibration is based on a previous formulation (Beattie, 1993) but rectifies some of the T overestimation problems for hydrous compositions and low-T in anhydrous compositions. This new calibration is relevant for a wide range of pressures and temperatures between 750 - 1600 °C, SiO_2 = 33 - 77 % and H_2O = 0 - 14.2 %, with an error of ± 39 °C:

$$\frac{10^4}{\mathrm{T(°C)}} = 4.07 - 0.329[\mathrm{P(GPa)}] + 0.12\left[\mathrm{H_2O^{liq}}\right] + 0.567\ln\left[\frac{\mathrm{X^{Opx}_{Fm_2Si_2O_6}}}{\left(\mathrm{X^{liq}_{SiO_2}}\right)^2\left(\mathrm{X^{liq}_{FeO}}+\mathrm{X^{liq}_{MnO}}+\mathrm{X^{liq}_{MgO}}\right)^2}\right] - 3.06\left[\mathrm{X^{liq}_{MgO}}\right] - 6.17\left[\mathrm{X^{liq}_{KO_{0.5}}}\right] + 1.89\left[\mathrm{Mg\#^{liq}}\right] + 2.57\left[\mathrm{X^{Opx}_{Fe}}\right]$$

Where Fm = Fe+Mn+Mg

Pressure values where obtained after equation 29a of Putirka (2008). This barometer is based in the positive correlation of the $FmAl_2SiO_6$ molecule with P (between 0.001 and 0.05 bar) yielding an error of ± 2.6 kbar.

$$\mathrm{P(kbar)} = -13.97 + 0.0129\mathrm{T(°C)} + 0.001416\mathrm{T(°C)}\ln\left[\frac{\mathrm{X^{Opx}_{NaAlSi_2O_6}}}{\mathrm{X^{liq}_{NaO_{0.5}}X^{liq}_{AlO_{1.5}}}\left(\mathrm{X^{liq}_{SiO_2}}\right)^2}\right] - 19.64\left(\mathrm{X^{liq}_{SiO_2}}\right) + 47.49\left(\mathrm{X^{liq}_{MgO}}\right) + 6.99\left(\mathrm{X^{Opx}_{Fe}}\right) + 37.37\left(\mathrm{X^{Opx}_{FmAl_2SiO_6}}\right) + 0.748\left(\mathrm{H_2O^{liq}}\right) + 79.67\left(\mathrm{X^{liq}_{NaO_{0.5}}} + \mathrm{X^{liq}_{KO_{0.5}}}\right)$$

Equilibrium tests for the Opx-liq pair were performed after the Rhodes diagram (Rhodes *et al.*, 1979) and the value of the distribution coefficient K_D $(Fe\text{-}Mg)^{Opx\text{-}liq}$ which should have a value of 0.29 ± 0.06. This value is independent of P and T but diminishes slightly as silica contents increase so that K_D $(Fe\text{-}Mg)^{Opx\text{-}liq}$ = 0,4805 - 0,3733 * X_{Si}^{liq}.

The results for orthopyroxene thermobarometry calculations are compiled in Table 4 along the corresponding compositional data, mineral formulas and classification parameters. The highest temperature and pressure values are obtained for the crystal centres of the T2 alkaline trend (1125 - 1105 °C and 3.9 - 2.1 kbar), with no bor-

ders found to be in equilibrium. Orthopyroxenes in the calcalkaline suite yield slightly lower values (1079 - 1051 °C and 1.6 - 0.2 kbar for the centres and 1094 - 1048 °C and 3.2 - 0.3 kbar for the rims, matrix and coronas.

Amphibole

As previously indicated, the P and T crystallization values for amphiboles were calculated after a recent thermobarometer calibrated by Ridolfi et al. (2010) which is based solely on the composition of the mineral and reported to provide reliable results in the ranges of 1064-766°C, 73-1000 MPa, -0.3 < ΔNNO < 2.5, H_2Omelt 3.4-10.6 wt %. This equation represents so far the only available model to assess the crystallization conditions of calcic amphiboles of volcanic calc-alkaline rocks and has the additional advantage of allowing to calculate the H_2O content of the magma from which the analysed amphibole should have crystallized. This calibration is expressed as:

$$T = -151.487Si^{*} + 2{,}041$$

Where:

$$\mathrm{Si}^{*} = \mathrm{Si} + \frac{^{[4]}\mathrm{Al}}{15} - 2\,^{[4]}\mathrm{Ti} - \frac{^{[6]}\mathrm{Al}}{2} - \frac{^{[6]}\mathrm{Ti}}{1.8} + \frac{\mathrm{Fe}^{3+}}{9} + \frac{\mathrm{Fe}^{2+}}{3.3} + \frac{\mathrm{Mg}}{26} + \frac{^{\mathrm{B}}\mathrm{Ca}}{5} + \frac{^{\mathrm{B}}\mathrm{Na}}{1.3} - \frac{^{\mathrm{A}}\mathrm{Na}}{15} + \frac{^{\mathrm{A}}[\ \ ]}{2.3}$$

Yielding an estimated error of ± 22 and ± 57 °C. And pressure is calculated after:

$$P = 19.209e^{(1.438Al_T)}$$

Where Al_T is total aluminium, and the estimated error can be as high as ±33 % at 1 kbar but only ±8% at the physical-chemical stability boundaries. And:

$$\mathrm{H_2O_{melt}} = 5.215\,^{[6]}\mathrm{Al}^{*} + 12.28$$

Where:

$$^{[6]}\mathrm{Al}^{*} = {}^{[6]}\mathrm{Al} + \frac{^{[4]}\mathrm{Al}}{13.9} - \frac{\mathrm{Si} + {}^{[6]}\mathrm{Ti}}{5} - \frac{^{\mathrm{C}}\mathrm{Fe}^{2+}}{3} - \frac{\mathrm{Mg}}{1.7} + \frac{^{\mathrm{B}}\mathrm{Ca} + {}^{\mathrm{A}}[\ \ ]}{1.2} + \frac{^{\mathrm{A}}}{2.7} - 1.56\mathrm{K} - \frac{\mathrm{Fe\#}}{1.6}$$

Yielding a standard error of estimate of ±0.41 wt%.

The range of temperatures, pressures and water contents obtained for this mineral is very narrow (Table 5). The crystallization conditions obtained from the centres

range from 995 to 922 °C, from 4.5 to 2.7 kbar and 7.36 to 5.21 wt% H_2O. The rims yield equivalent values, from 990 to 946 °C, from 4.0 to 3.0 kbar and from 5.55 to 5.31 wt% H_2O.

Crystallization sequence and discussion

As introduced earlier and as it will be explained in detail in the modelling and discussion chapters, the approach followed for modelling is to consider specific portions of the monogenetic field as part of a petrogenetic unit. This assumption is essential to consider samples collected from individual monogenetic vents as having some genetic link. While this can be accepted in general terms for partial melting, it introduces higher uncertainties in other cases such as differentiation, which can develop under more variable conditions for each volcanic vent (e.g. different depths of crystallization, ascent rates or participation of assimilated materials). Therefore, it is important to understand that even if care has been taken to consider monogenetic vents that are likely to be geodynamically related, heterogeneities in the development of the differentiation processes may occur and therefore the identified differentiation tendencies must be taken as a general approach rather than as a genuine evolution trend as those established from a typical polygenetic volcano (i.e. a line of descent produced by the evolution of a single homogeneous initial magma).

Another significant feature to take into account in this volcanic field is the presence of three different rock suites. In an *a priori* approach, it cannot be assumed that they are genetically related, hence the importance of considering them separately. With this in mind a generic estimation of the pressure, temperature and water conditions to which the mineral phases crystallized is mandatory as a first approximation to the conditions of the plumbing system that will later be modelled.

Regarding petrographic observations, the crystallization sequence for the T1 alkaline suite (Fig. 5.10) seems to start with the crystallization of apatite and ulvöspinel. This is inferred after the apatite appearance both as inclusions in olivine, plagioclase and ulvöspinel and also as intergrowths in ulvöspinel (Fig. 5.11). The first main mineral to appear as a phenocryst is plagioclase, at estimated maximum pressures of 16 kbar

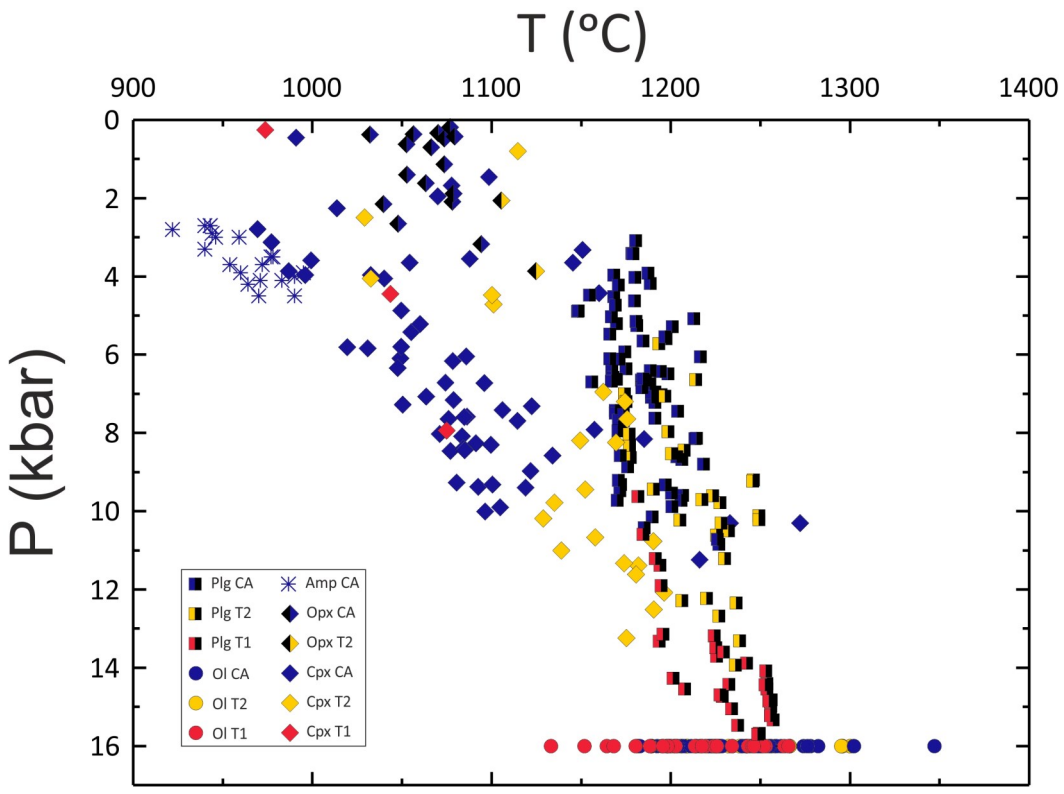

Fig. 5.10 P/T crystallization values calculated as specified in the text for olivines, plagioclases, pyroxenes and amphiboles from the different suites and trends. Olivine crystallization pressure assumed to be 16 kbar for that is the highest pressure found in other minerals and olivine is assumed to have started its crystallization first.

and 1250 °C, corresponding to depths close to the inferred thickness of the crust for central Mexico under the Guerrero Terrane (~40 km, Ferrari et al., 2012). The similarity between the temperatures and pressures obtained in plagioclase centres and rims suggests that the process likely started and ended at depth and that it was finished before reaching shallower levels. As attested by its presence as inclusions in plagioclase, olivine appears simultaneously and continues crystallizing afterwards according to the calculated temperature values (1224 - 1168 °C). The last phase to appear is clinopyroxene at much shallower levels (1075 - 974 °C and 7.93 - 0.26 kbar) although the lack of analyses for clinopyroxene centres of the T1 series avoids at this time determining the real moment of appearance for this phase. Alkaline T1 suite therefore seems to have started its crystallization at the greatest depths of all suites and does not show apparent evidences of prolonged magma storage or large scale contamination given the scarcity of oscillatory zonations or resorption textures in the minerals.

For the T2 alkaline suite the sequence is similar, with apatite and ulvöspinel appearing first (they are found as inclusions in olivine and clinopyroxene). Similarly to T1, plagioclase is the first main mineral appearing from 13.9 ? 7.1 kbar and 1249 - 1177 °C for the centres, slightly lower values than those obtained for T1 but still around the inferred average crustal thickness in central Mexico, and again with a similar range for centres and rims. Olivines crystallize again simultaneously or immediately after at slightly lower temperatures than plagioclases and closely followed by clinopyroxenes which show a wide range in pressures including very shallow ones (13.2 - 4.1 kbar for centres and 11.4 - 0.8 kbar for rims). Orthopyroxene yields the lowest temperatures

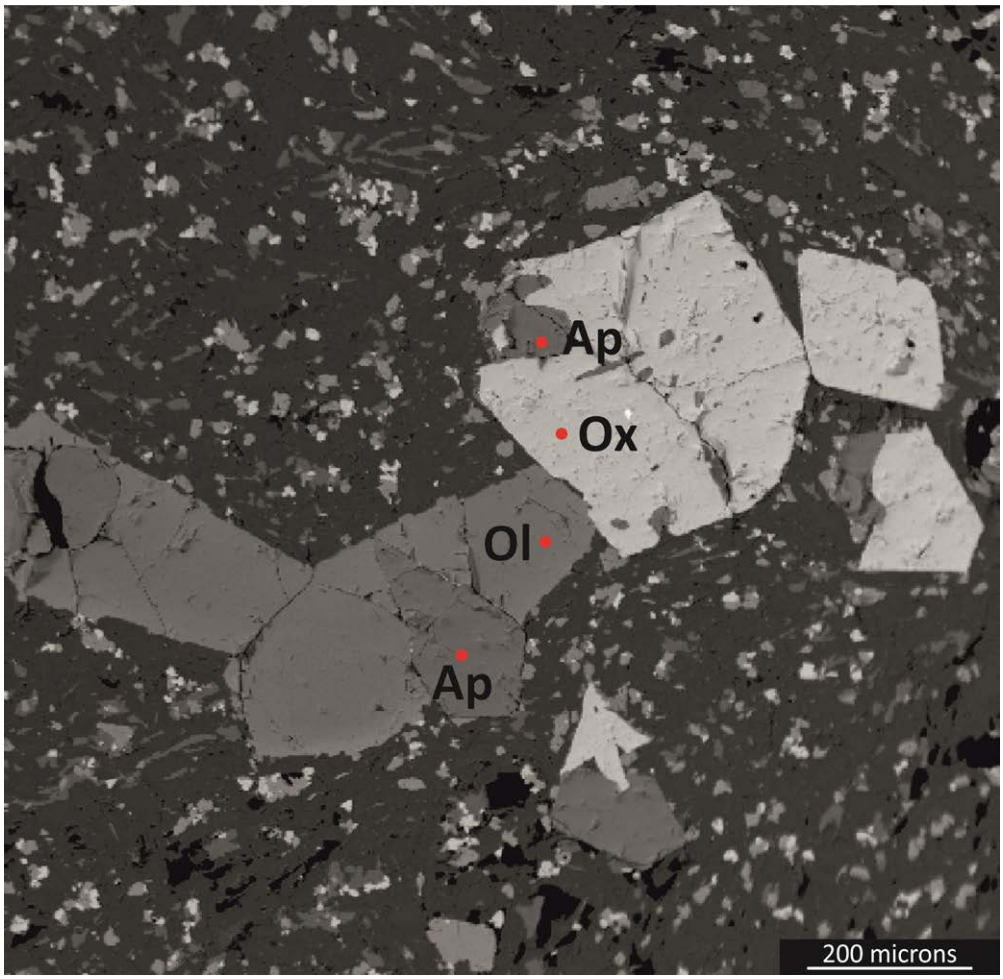

Fig. 5.11 Back scattered electrons electron microprobe image of sample M105 displaying apatite inclusions in oxide and olivine phenocrysts. The apatite phenocryst appears as an intergrowth with olivine suggesting a simultaneous crystallization, whereas apatite seems to have crystallized filling in gaps on the oxide.

and pressures agreeing with its scarce appearance within altered and embayed olivine or plagioclase crystals. The orthopyroxenes that form coronas around olivine do not show equilibrium with the whole rock but we may safely assume that these represent a late-stage product produced by destabilization reactions of the magmatic phases (Fig. 5.8).

In this trend some local variations are observed too: one example is the most anortitic plagioclase border analyzed (Fig: 5.12). This crystal displays a concentric zonation with reverse zoning in discrete compositional steps (step zoning) were the rim has higher An content but lower calculated temperatures than the centre. This particular crystal shows a rim that is more anortitic than other crystal borders, matrix crystals and even centres from the same sample (An_{73} on the rim and An_{69} on the centre). Reverse zoning could be a sign of open system behaviour inasmuch it may indicate that the rim grew from a more calcic melt, but it could also be induced by an increase in temperature or by an increase in pressure in water-saturated conditions (Blundy & Cashman, 2001). Since in this case the increase in An contents correlates with a slight decrease in temperature (or no significant variation, given the error of the thermometer), magma mixing seems to be a more likely scenario, especially as the increase in An does correlate with an increase in Fe within the crystal as well, characteristic suggested to be a sign of magma mixing with more calcic melts (Ruprecht & Wörne, 2007). Nevertheless, this possibility needs to be contrasted with stronger evidences, such as changes in $^{87}Sr/^{86}Sr$ isotopes that are not affected by changes in temperature, as increases in the Fe concentration may also be a sign of increased D_{Fe} due to higher oxygen fugacity (Wilke & Behrens, 1999) or dissolution of ferromagnesian phases. In this particular case, as this behaviour is not widely extended to all the crystals in the sample we may think that it may represent a xenocrystal that joined the evolution of this rock at a certain point. Although not analyzed, it is possible to distinguish a darker outer rim surrounding the highly An one that could be of the same composition as the rims of the rest of the plagioclase crystals.

The calcalkaline suite provides inferred maximum depths of 10.7 kbar in Plg, with clinopyroxene yielding the highest crystallization temperatures. However, the highest temperatures and pressures displayed by this phase correspond to crystals showing

step oscillatory zoning (e.g. Fig. 5.6) or inverse zoning (Fig. 5.13) whose compositional fluctuations, and hence temperature and pressure variations, are indicative of crystals originated in a convecting magmatic chamber by repositioning of the crystal within it, and latter incorporated to the magma, and/or injections of new magma batches. This phase also shows the usual presence of crystals with patchy zoning, also indicative of open system processes (Streck, 2008) and therefore the obtained P values (between 5 and 8 kbar) must be taken with caution. Therefore, the crystallization sequence in CA rocks starts with chromite that appears as inclusions in olivine. Olivine, plagioclase and clinopyroxene appear more or less at the same time, given the error of the thermome-

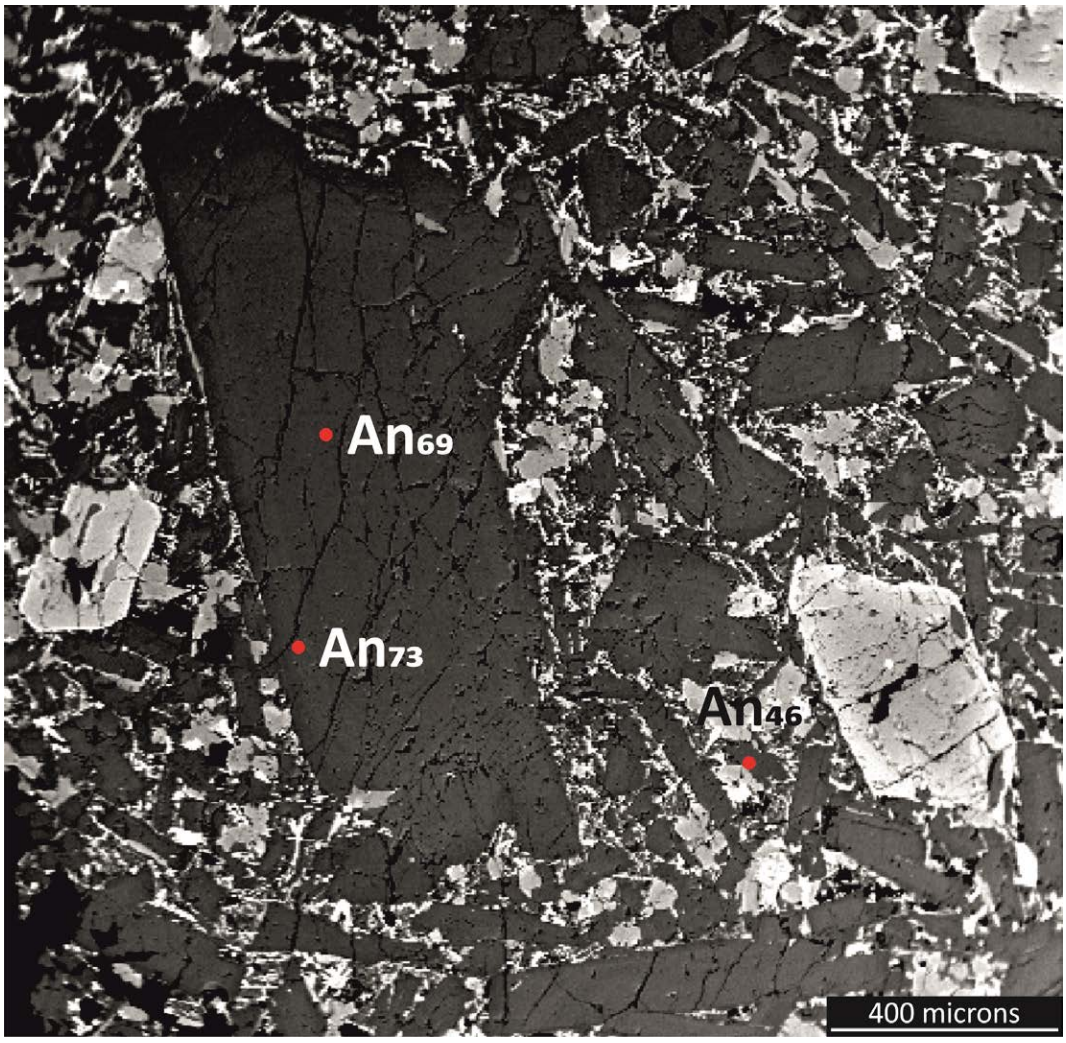

Fig. 5.12 Back scattered electrons electron microprobe image of sample M11 (T2). Red dots represent micropuntual analysis sites and their anorthite content on a reverse zoning in a plagioclase and a plagioclase from the matrix for comparison.

ter, (~1230 °C). Orthopyroxene seems to be the last phase to appear already at superficial levels (1.6 - 0.2 kbar and 1079 - 1051 °C for the centres) or as replacements or coronas in olivines. Opx also appear forming the core of some clinopyroxene crystals displaying similar temperatures (1081 °C) but at around 1 kbar.

Chromite, ulvöspinel and ilmenite kept crystallizing until the last stages of the process since they appear in significant amounts in the matrix. Apatite on the other hand seems to crystallize only at later stages as this phase only appears in the matrix or as inclusions in the borders of larger crystals. The evolution of the CA suite presents then more complexities than the alkaline, it has a greater amount and wider range of probable xenocrystal types (Type 3 Plg (Fig. 5.4), oscillatory (Fig. 5.3) and reverse zoning of Plg and Cpx and it additionally contains amphibole as a main phase in certain lavas, feature unique to this suite.

To summarize, in all cases crystallization seems to have developed in a polybaric sequence from depths near the base of the crust up to surface levels. The T1 alkaline trend appears to represent the deepest crystallization sequence starting at the highest temperatures, followed by T2 and CA having similar P-T crystallization conditions. Both petrographic and thermobarometric observations suggest that all the suites have experienced some sort of open system processes as evidenced by the reverse and patchy zonations or the spongy-cellular “sieved” textures (Type 3 plagioclases, present in most samples), reemplacements and corroded minerals. In fact, Type 3 Plg have a more albitic centre than any other plagioclases, symptomatic of a probable xenolithic origin and suggesting that there was at some stage assimilation of a component more evolved than the assimilant. These Type 3 plagioclases can be found in the three suites but more abundantly in T2 and especially in CA. Furthermore, the crystals with oscillatory zonation suggesting the presence of deep magmatic storage areas for some samples of T2 and CA rocks which would facilitate such assimilation. Other differences between suites are the presence of chromite and ilmenite (and one ulvöspinel) appearing in CA rocks only, while T1 and T2 alkaline rocks contain ulvöspinel (and minor spinel in T1), and the early crystallization of apatite in T1 and T2 while in CA it only appears at the end of the process.

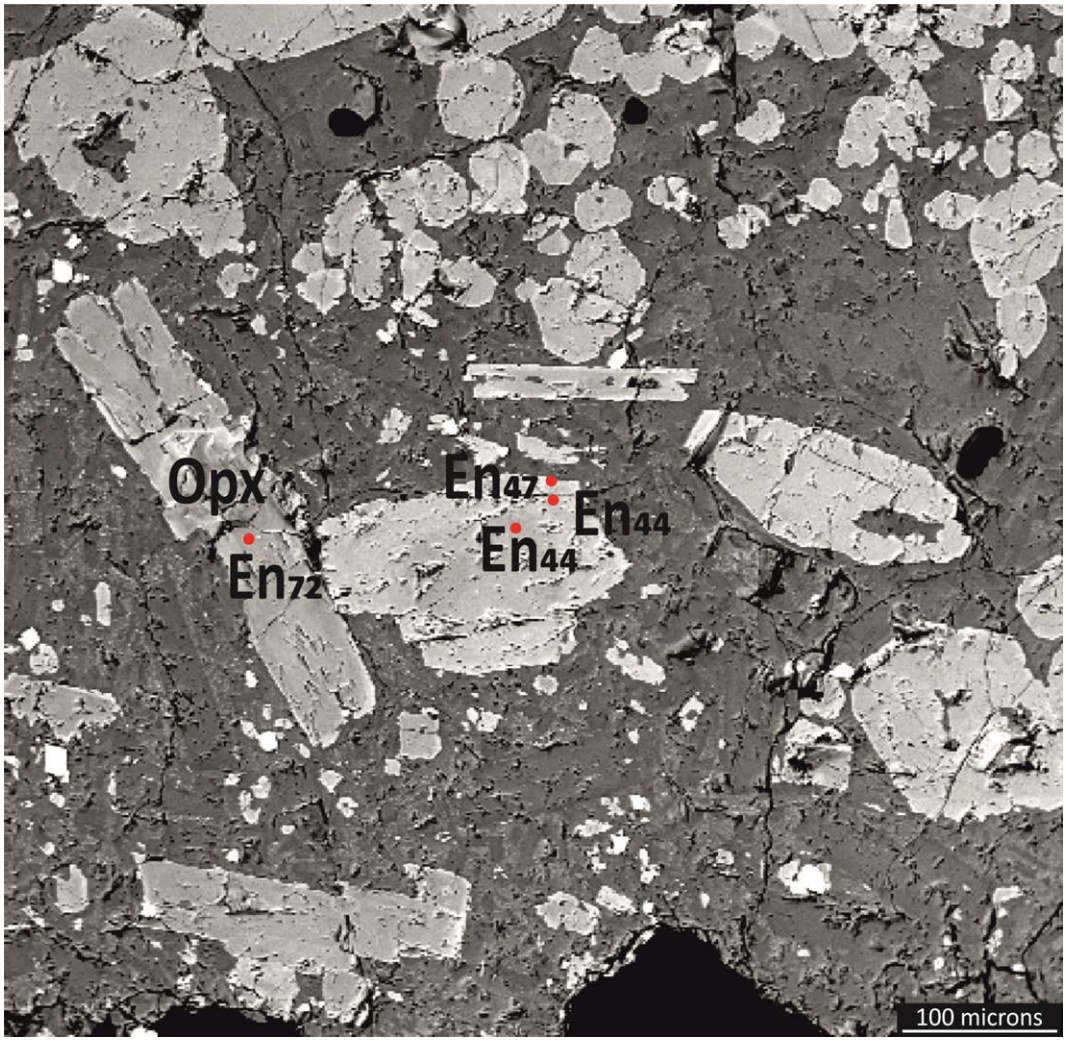

Fig. 5.13 Backscattered electrons electron microprobe micrographie of sample M70 (CA). Red dots represent micropuntual analysis sites and their enstatite content. Reverse zoning in a clinopyroxene (rounded crystal in the centre) and orthopyroxene composition (phenocrystal on the left).

6. Whole rock geochemistry

Geochemical data obtained on whole rock for the sampled lavas is included in Table 8 (see Appendix 2).

Silica-alkalis contents range from 47 % to 64 % SiO_2 and from 3.9 to 7.8 % $Na_2O + K_2O$ (see TAS diagram of Fig. 6.1, after Le Bas et al., 1986). Those values are in general encompassed within the compositional range previously reported for the MGVF (47.2 - 78.2 % SiO_2 and 2.8 - 9.0 % $Na_2O + K_2O$, after data in Ferrari et al., 2007; Gómez-Tuena et al., 2007; Verma, 2015) but restricted to the more mafic terms and showing some more alkali-rich samples.

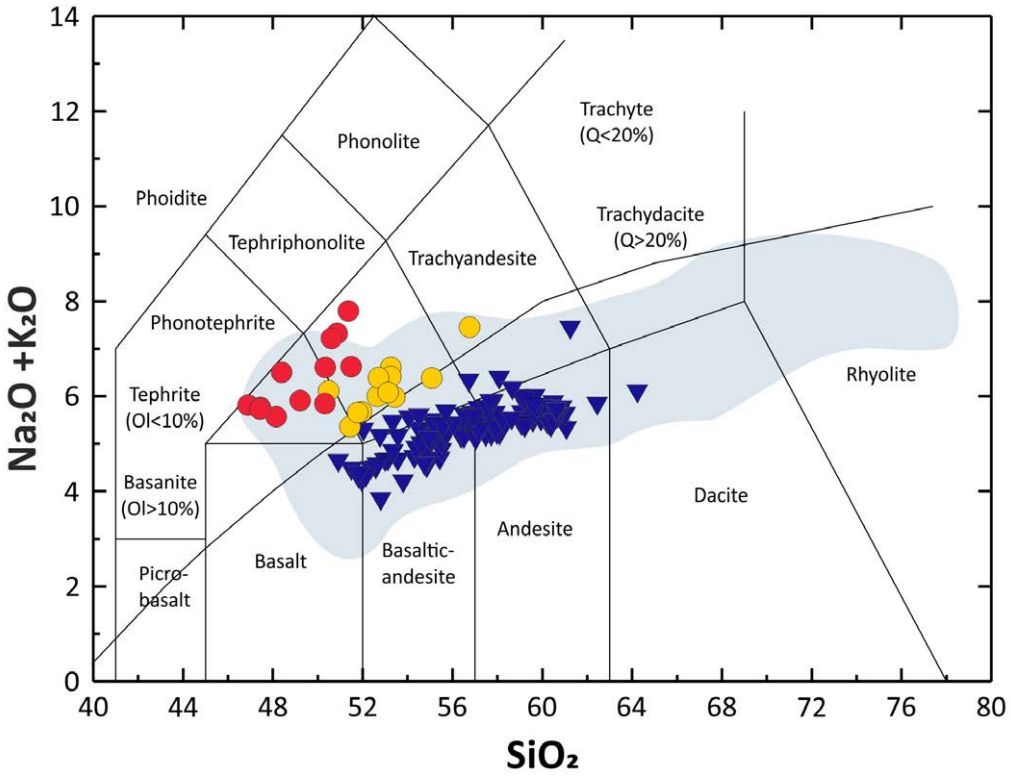

Fig. 6.1 Total alkali silica diagram after Le Bas et al. (1986). Red circles represent the T1 alkaline trend, yellow circles the T2 alkaline trend and blue triangles the calcalkaline suite. The grey shaded area encompasses the data on the MGVF from Ferrari (2007).

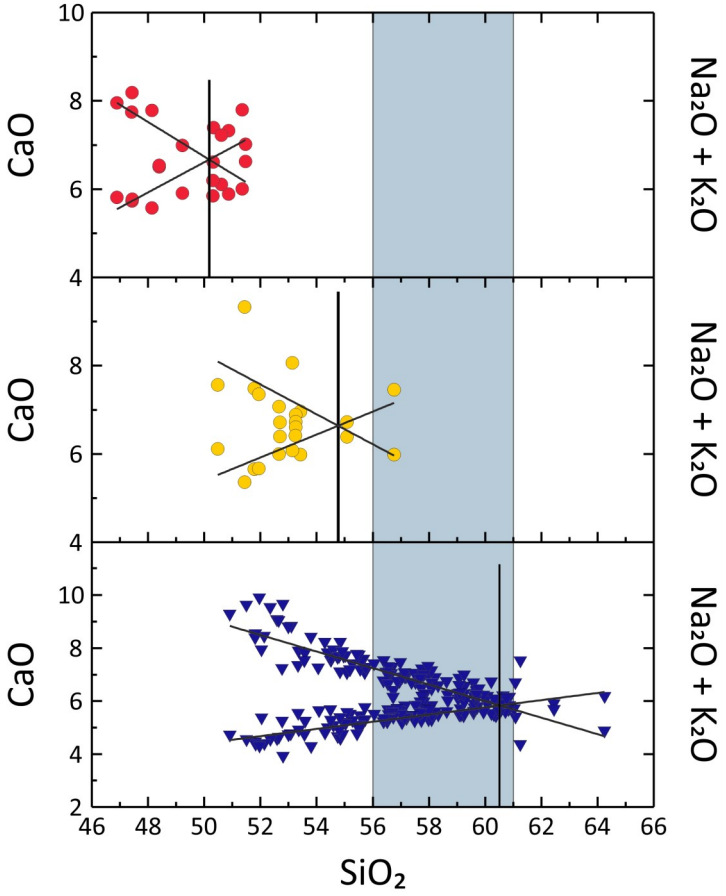

Fig. 6.1 Total alkali silica diagram after Le Bas et al. (1986). Red circles represent the T1 alkaline trend, yellow circles the T2 alkaline trend and blue triangles the calcalkaline suite. The grey shaded area encompasses the data on the MGVF from Ferrari (2007).

As presented in Chapter 4, the Irvine & Baragar (1971) dividing line reveals the existence of two main rock groups: a subalkaline one that makes up to the 83 % of the samples and an alkaline one. Some discussion has been raised concerning the use of the term "calcalkaline" (see Arculus, 2003) and therefore the subalkaline samples have been plotted following the procedure of Peacock (1931) to confirm if these samples are calcalkaline from a strict point of view. In Peacock's plot a suite of rocks is considered as calcalkaline if the best fit lines through the CaO vs. SiO_2 and $Na_2O + K_2O$ vs. SiO_2 arrays on a combined silica variation diagram intersect at a SiO_2 value between 56 and 61 wt %. In our case (Fig. 6.2), both arrays intersect at about 60.5 % SiO_2 confirming that the subalkaline suite is indeed calcalkaline. The alkaline suite in turn seems divided in two distinct trends: one characterized by higher alkali/SiO_2 ratios (T1) and another with lower ratios (T2), closer to the calcalkaline suite (CA) and separated from the T1 by a compositional gap. In detail, T1 presents a range of 46.9 - 51.5 % SiO_2 and 5.6 -

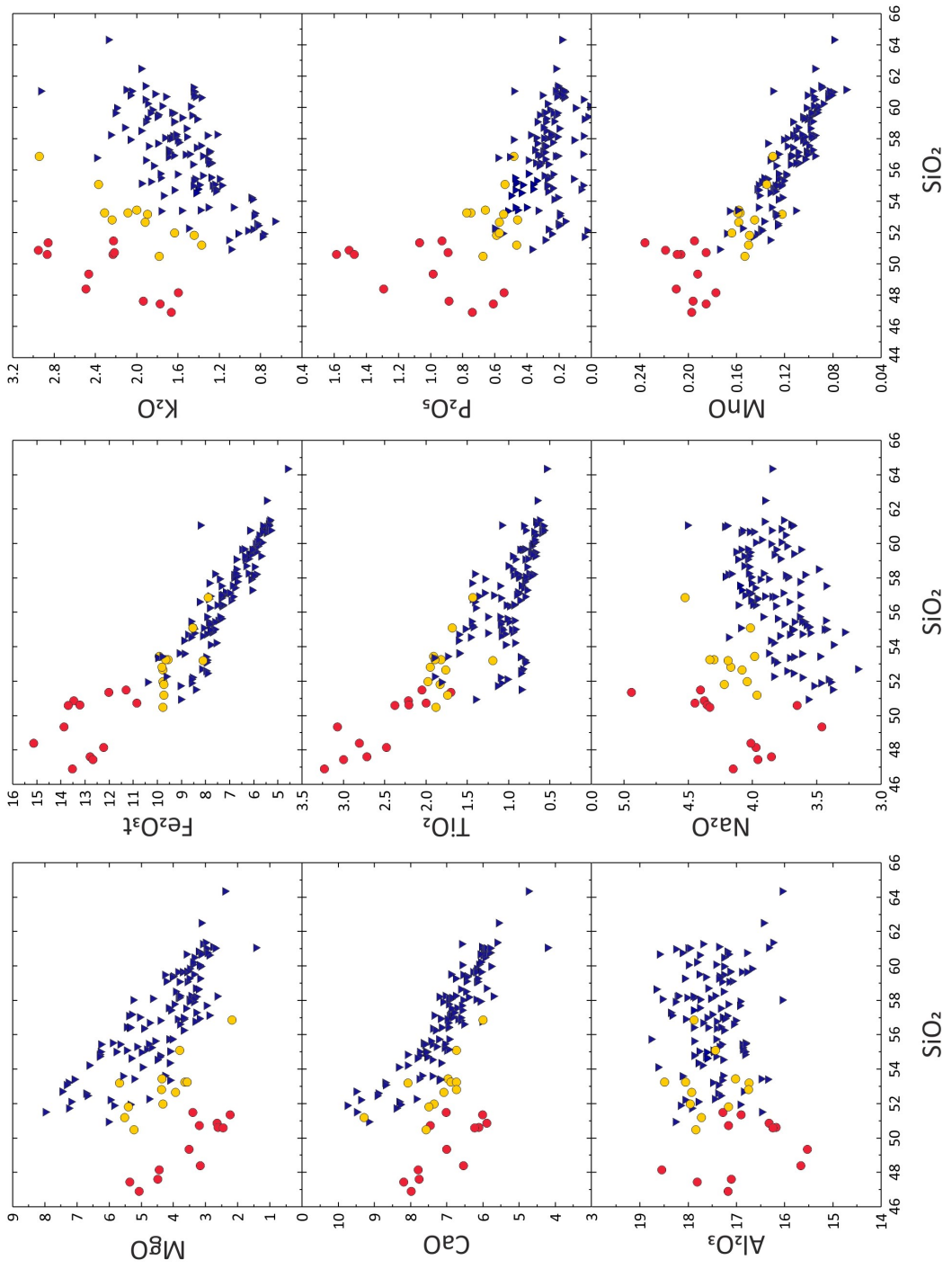

Fig. 6.3 Major element Harker variation diagrams. Red circles T1 alkaline trend, yellow circles T2 alkaline trend and blue triangles calcalkaline suite.

7.8 % $Na_2O + K_2O$, which is narrower and shifted towards the lower-SiO_2 end of the diagram relative to T2 and CA. Alkaline T2 rocks have an alkalis range similar to T1 (5.4 - 7.5 %) but higher silica abundances (50.5 - 56.8 %), closer to those displayed by the CA rocks (50.9 - 64.2 % SiO_2 and 4.7 - 6.1 % $Na_2O + K_2O$).

In the following sections the geochemical characteristics of the rocks sampled in this study are described considering the three groups established before.

To describe their geochemical characteristics (major and trace elements and Sr-Nd-Pb-O isotope ratios) several standard plots have been applied, such as normalized multielement trace element diagrams and Harker diagrams, among other binary plots.

Calcalkaline rocks

The calcalkaline suite shows in general rather homogeneous variations in Harker binary plots (Fig. 6.3) with direct correlations for Na_2O and K_2O and inverse for MgO, CaO, Total Fe_2O_3, TiO_2, P_2O_5 and MnO, with the only exception of Al_2O_3 which shows a scattered distribution.

Regarding trace element data, CA lavas are also characterized by rather homogenous patterns in normalized multielement diagrams (Fig. 6.4) with a signature similar to equivalent rocks from convergent margins, characterized by positive anomalies for most LILE (except Ti and P), Pb and Sr, and relative depletions for Nb-Ta and Ti. This pattern is also shared with other calcalkaline rocks of the TMVB (Díaz-Bravo et al., 2014; Gómez-Tuena et al., 2007). Their fractionation degree is variable (La/Lu = 3.3 - 21.7) and also show a rather wide range (1.11 to 0.70) in the Eu anomaly (calculated as $Eu/Eu^{*}=Eu_N/\sqrt{[(Sm_N)(Gd_N)]}$, after Taylor & McLennan, 1985). In general, the samples with lower SiO_2 abundances are the least fractionated and present the lowest normalized values for Th-U, Nb-Ta, K, La, Ce, Pb, Pr and Zr. On the other hand, the SiO_2-richer samples are characterized by more fractionated patterns and some of the more marked negative spikes for Ti.

Trace element binary diagrams plotted relative to Zr are presented in Figs. 6.5 to 6.9. Zr is chosen as reference element in these diagrams since it is available as good quality determinations in most analytical records and it is likely to behave as an incom-

patible element in all cases (no Zr-bearing mineral has been detected in the petrographic study and its mineral-liquid partition coefficients are very low for all present minerals and lithologies). Variations in these binary plots allow depicting a general view of the geochemical changes in trace elements produced in the different considered suites.

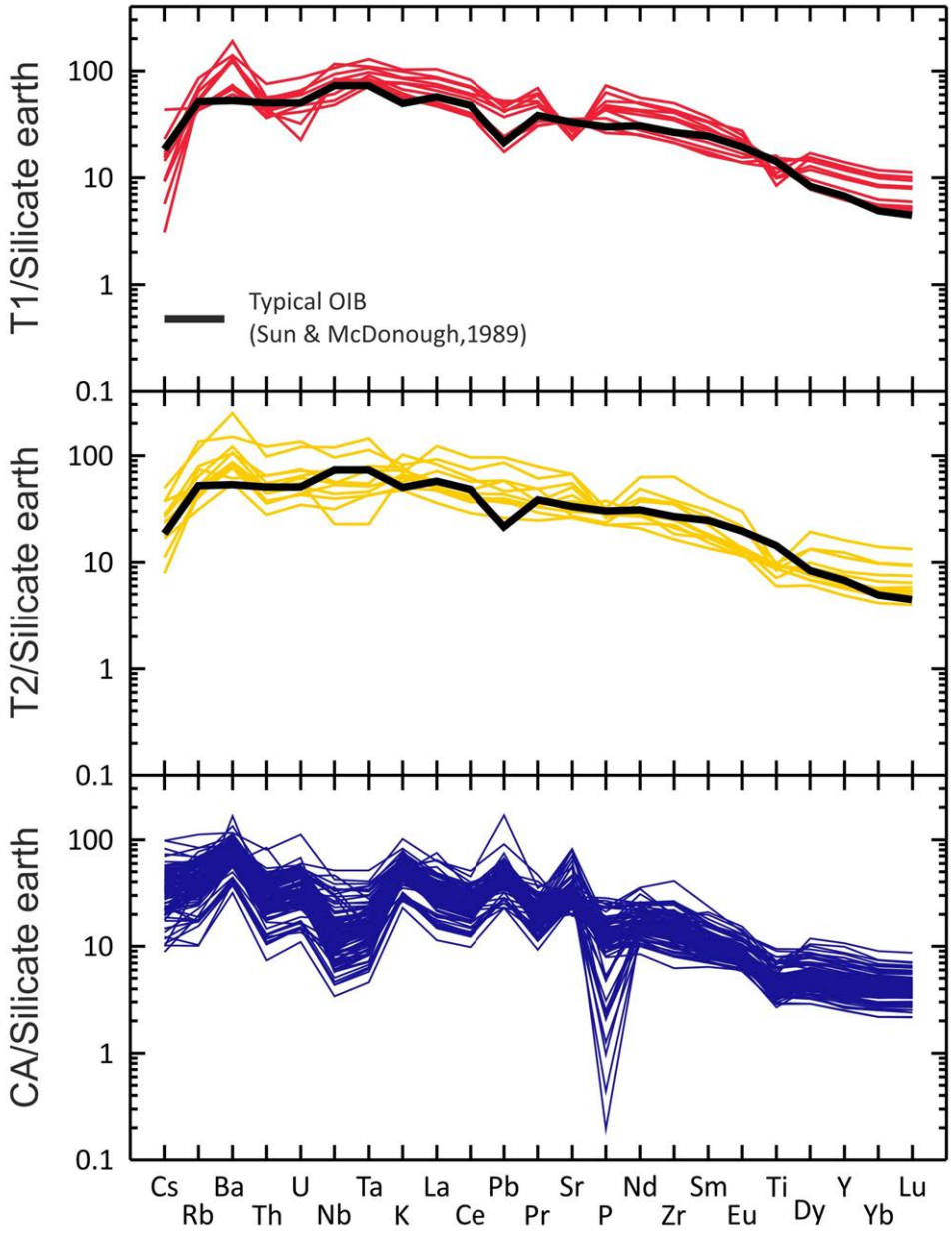

Fig. 6.4 Multielement normalized diagrams for T1, T2 and CA samples. Diagram construction after Sun & McDonough (1989) and normalization to the silicate earth values of McDonough & Sun (1995).

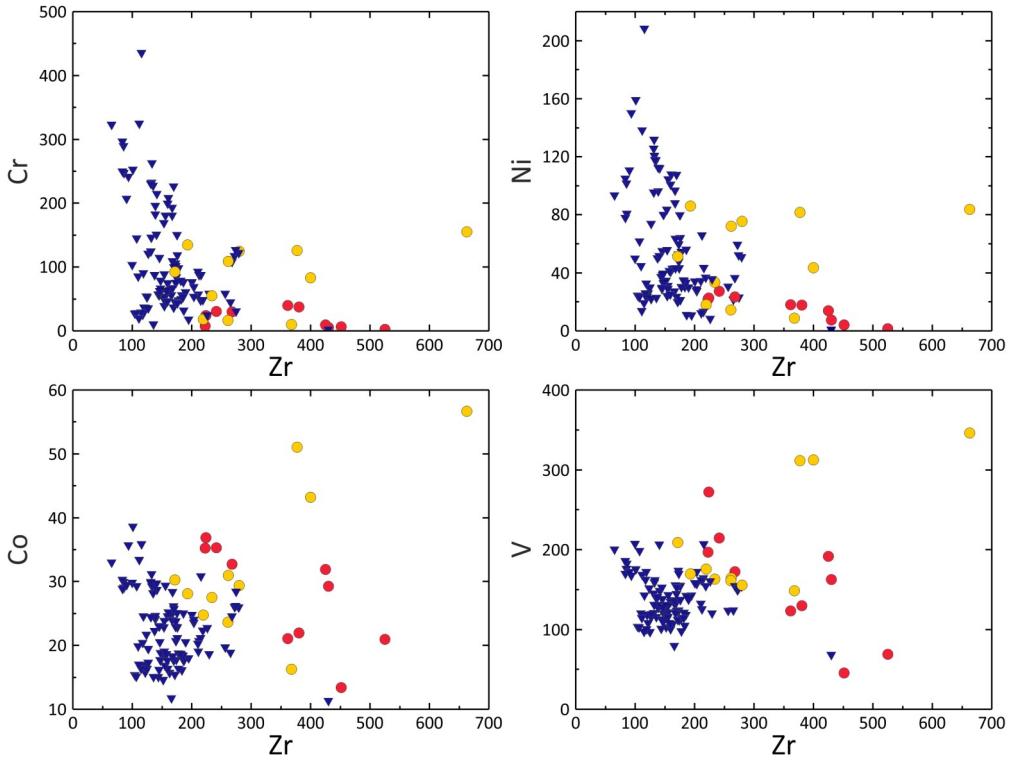

Fig. 6.5 Compatible elements binary variation diagrams vs. Zr.

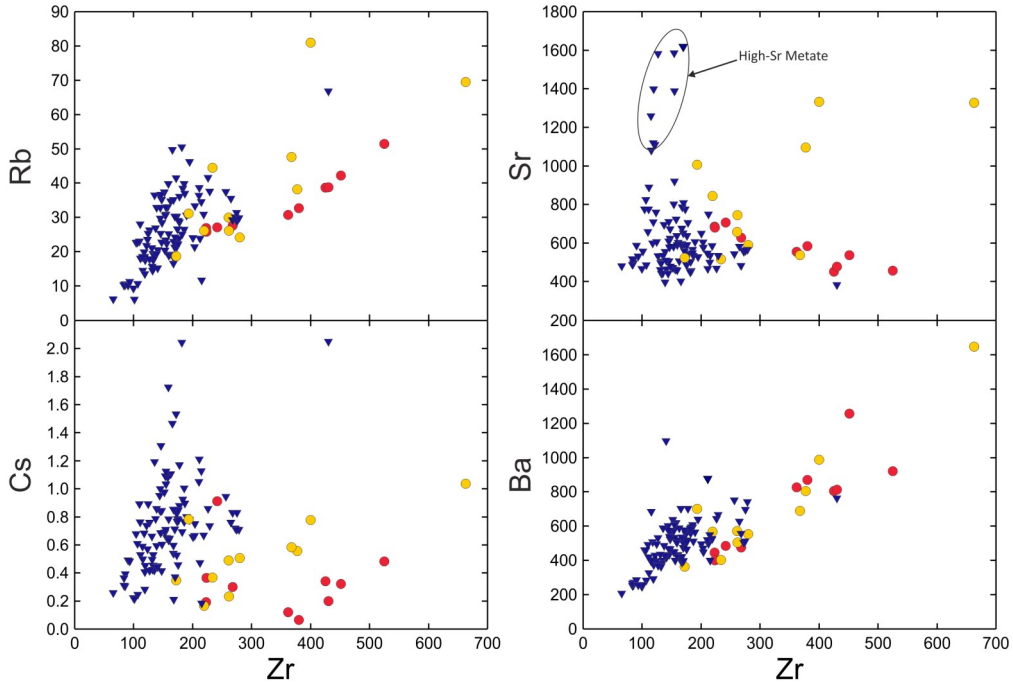

Fig. 6.6 Large ion lithophile elements (LILE) binary variation diagrams vs. Zr.

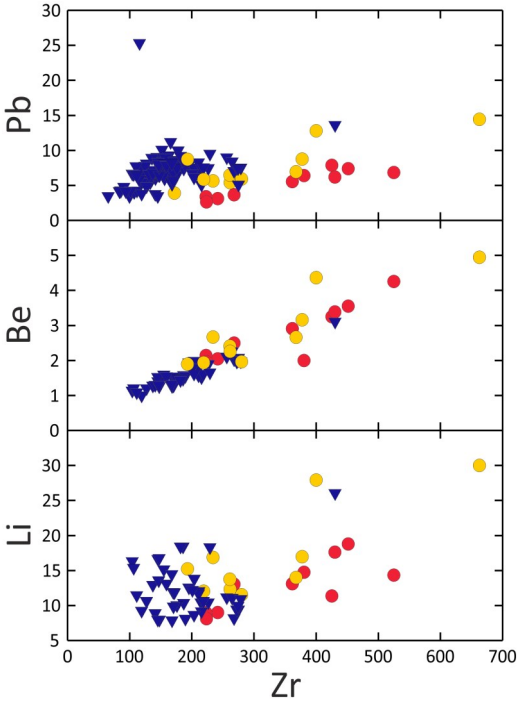

Fig. 6.7 Lead, beryllium and Lithium binary variation diagrams vs. Zr.

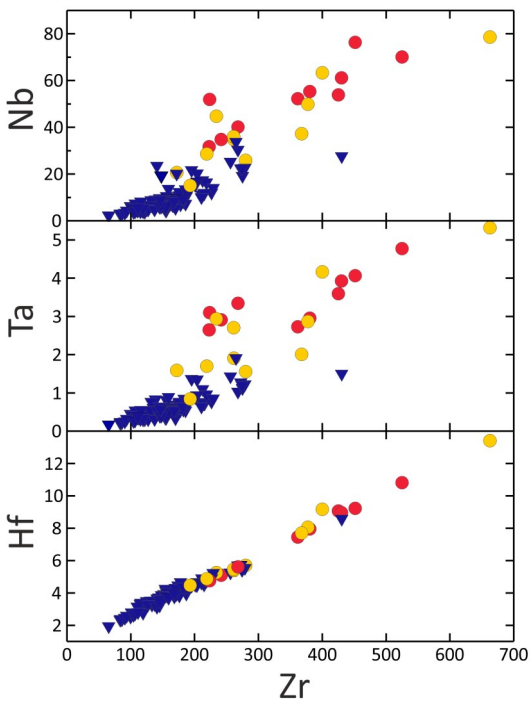

Fig. 6.8 High field strength elements binary variation diagrams vs. Zr.

In the case of the CA rocks, element-Zr diagrams show considerable scattering for most elements but with consistent direct variations for Be, P, Sc, Ti, Zn, Ga, Rb, Cs, Ba, Y, HFSE, Mo, Sn, Sb, Tl, Pb, LREE, HREE, W, Th and U. In contrast, V, Cr, Co, Ni, Cu and Sr display inverse variations. A singular feature is the high Sr concentrations of a group of rocks (see the Sr-Zr diagram), belonging to the El Metate volcano (High-Sr Metate), which probably owe their high Sr concentrations to the presence of an unusual amount of amphibole phenocrysts.

Concerning isotopic ratios, the CA rocks show an inverse $^{87}Sr/^{86}Sr$ vs. $^{143}Nd/^{144}Nd$ correlation with values ranging from 0.70307 to 0.70471 and from 0.51269 to 0.51298 respectively (Fig. 6.10), with a higher presence of ^{87}Sr-enriched samples. When plotted on a $^{87}Sr/^{86}Sr$ SiO_2 diagram (Fig. 6.11) the samples appear to have a generic increasing tendency but showing different arrays roughly characterized by different $^{87}Sr/^{86}Sr$ ratios: a) the aforementioned High-Sr Metate samples, from 0.70307 to 0.70335; b) from 0.70325 to 0.70378 that includes the Low-Sr Metate samples plus other samples spread from the northeast of this volcano up to the northern sector of the field; c) from

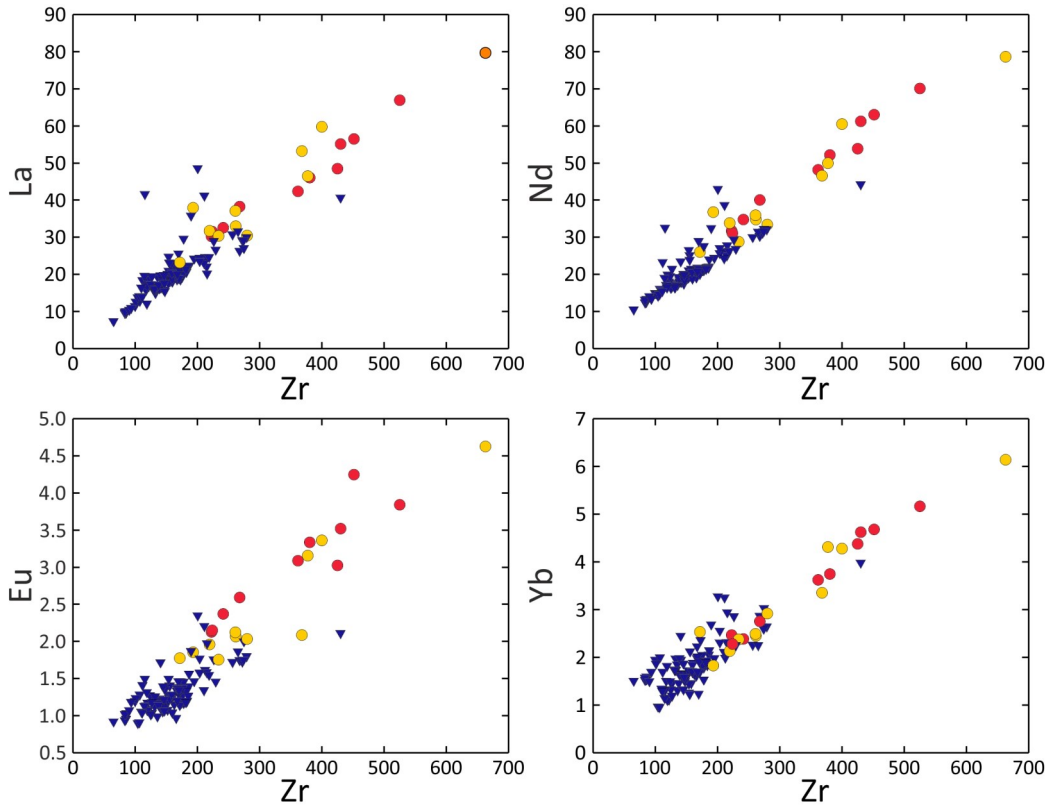

Fig. 6.9 Rare earth (REE) binary variation diagrams vs. Zr.

0.70373 to 0.70426, including samples homogeneously distributed both in the north and southern sectors (Main CA

trend); and d) from 0.70378 to 0.70471, represented by samples collected in a SW-NE alignment of monogenetic volcanoes located in the southern sector of the field, near Parícutin volcano (not included) plus two other samples in the south (Parícutin – Cherán alignment). These arrays are not clearly distinguished in a $^{143}Nd/^{144}Nd$ - SiO_2 diagram though.

Lead isotopes on the other hand, present a range of 18.537 - 18.785 for $^{206}Pb/^{204}Pb$, 15.544 - 15.630 for $^{207}Pb/^{204}Pb$ and 38.174- 38.636 for $^{208}Pb/^{204}Pb$, with direct correlations in $^{206}Pb/^{204}Pb$ - $^{207}Pb/^{204}Pb$ and $^{206}Pb/^{204}Pb$ - $^{208}Pb/^{204}Pb$ but showing a more disperse pattern in the former. When plotted against silica, lead isotopes do not show evident correlations, except in the case of the high-Sr Metate samples that show a positive tendency, especially evident on the $^{208}Pb/^{204}Pb$ - SiO_2 diagram (Fig. 6.13).

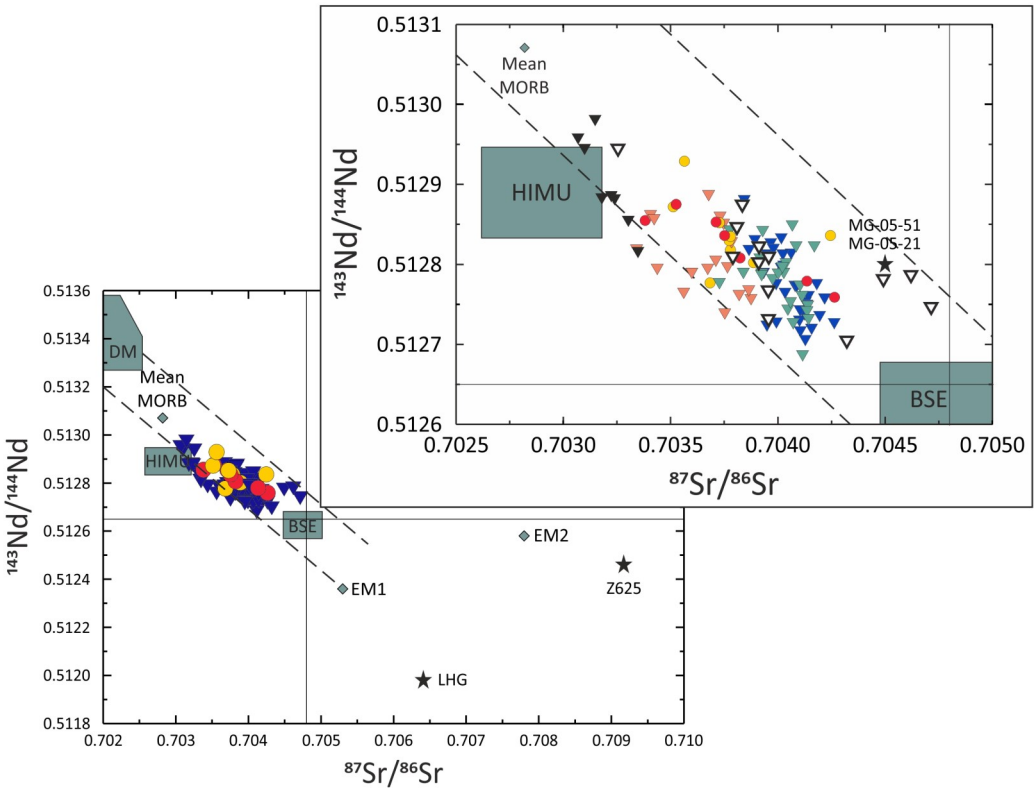

Fig. 6.10 Sr-Nd isotopic chart. Symbols in the main diagram as in previous ones. Symbols in the inset as follows: Red circles T1, yellow circles T2, purple triangles , green triangles , back triangles , black stars contaminants. Compositional filds for DM, HIMU, BSE, EMI and EMII from Zindler & Hart (1986) and Winter (2010).

Oxygen isotope ratios (see Table 8 and Fig. 6.11) in CA rocks have values on a range that comprises from +5.84 ‰ to +8.96 ‰ $\delta^{18}O$, displaying positive correlations against $^{206}Pb/^{204}Pb$, $^{207}Pb/^{204}Pb$ and $^{208}Pb/^{204}Pb$ (Fig. 6.14); positive (concave) against $^{87}Sr/^{86}Sr$ (Fig. 6.15), and negative but vey disperse against $^{143}Nd/^{144}Nd$ (Fig. 6.15), with no evident correlation against silica (Fig. 6.11).

Despite the differences observed, specially on the $^{87}Sr/^{86}Sr$ – SiO_2 diagram , it is worth to note that the obtained oxygen ranges extend towards higher $\delta^{18}O$ values relative to the most primitive values reported in olivines for the MGVF (Johnson et al., 2009), similarly to what has been observed in the Paricutin volcano (Losantos et al., 2015).

Alkaline rocks

Alkaline samples show in general inverse variations in Harker diagrams for MgO, CaO, total Fe_2O_3 and TiO_2, and direct for Al_2O_3, Na_2O and K_2O. Despite this overall similarity of major element variations with the calcalkaline suite, it can be observed that while the CA rocks display rather homogeneous variations, the alkaline lavas are distributed along the two identified trends in MgO, CaO, Na_2O and K_2O Harker diagrams, one characterized by lower silica contents (T1) and another subparallel but with higher SiO_2 contents (T2), separated by a small compositional variation gap.

A closer look at those trends reveals that the T1 lavas are characterized by higher contents in Fe_2O_3t, TiO_2, P_2O_5 and MnO relative to the T2 and the CA, whereas abundances in MgO, CaO, Al_2O_3, Na_2O and K_2O are equivalent to the T2 and CA but having lower silica contents. This group of alkaline lavas are therefore equivalent to the so-called "High-TiO_2" lavas identified in other alkaline-calcalkaline associations of the TMVB (e.g. Blatter et al., 2007; Ortega-Gutiérrez et al., 2014). The T1 rocks also present a more or less constant, even if very scattered, increase in P_2O_5 and MnO relative to SiO_2, while T2 lavas are characterized by inverse variations for P_2O_5 and MnO and lower total Fe_2O_3, TiO_2, P_2O_5, and MnO contents relative to T1. It is important to note that the T2 lavas overlap the compositional variation range of some of the more SiO_2 -poor calcalkaline rocks. Trace element data for the T1 and T2 alkaline rocks (Table 8) have been plotted in normalized multielement diagrams (Fig. 6.4) and in binary diagrams (Figs. 6.5 to 6.9).

Considered as a whole, the alkaline lavas display trace element signatures that are in general analogous to those observed in Oceanic Island Basalts (OIB), such as positive anomalies in Nb-Ta, and negative in Pb and Sr (see for example Weaver, 1991; Halliday et al., 1995). However, these patterns are relatively heterogeneous with some samples even displaying negative Nb-Ta troughs (typical of subalkaline rocks) and other elements such as Pb, Sr and Ti showing both positive and negative spikes. When compared to the calcalkaline rocks, they show significant differences of relative enrichment and fractionation. Alkaline rocks have a relatively higher enrichment in all elements,

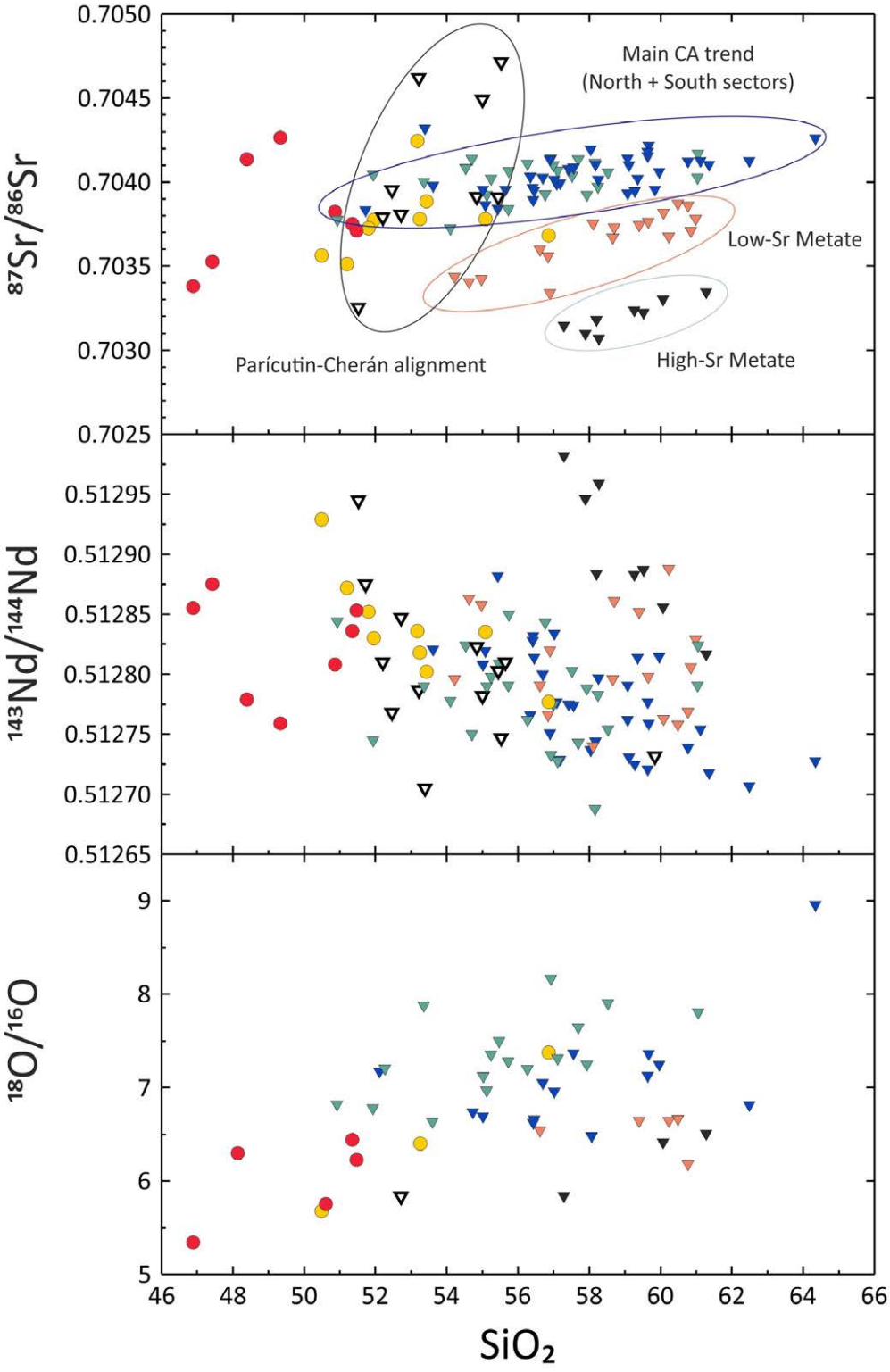

Fig. 6.11 Sr, Nd and O isotpe ratios vs. Silica diagrams. Red circles T1, yellow circles T2, blue triangles main CA trend south, green triangles main CA trend north, orange triangles low-Sr Metate trend, back triangles high-Sr Metate and white triangles Parícutin-Cherán alignment.

with equivalent Eu anomalies in both trends (1.0 - 0.8) and a smaller degree of fractionation as well as a narrower range in the La/Lu ratio (14.7 - 6.1) relative to the CA.

Some of the heterogeneity observed in the alkaline rocks can be explained if we consider the two identified trends. The signature of the T1 patterns is characterized by a narrower range of fractionation (La/Lu = 10.0 - 8.0) and is closer to typical OIB, including in all cases positive Nb-Ta, and negative U, Pb, Sr anomalies. However, the T2 lavas while having a similar signature, present some characteristics that are intermediate between the T1 and CA rocks, such as a wider range of fractionation (La/Lu = 14.7 - 6.1), positive U-Pb and Sr anomalies, and a tendency towards Nb-Ta and P depletion. This group of "mildly" alkaline rocks can be recognized as being similar to the so-called "OIB-type arc magmas" or "High-Nb arc basalts" identified in other monogenetic fields of the TMVB (see Straub et al., 2012 and references therein).

Concerning trace elements and as expected from what can be observed in the spider diagrams (see Fig 6.4 to 6.9), both trends are characterized by higher abundances for most trace elements relative to the CA suite, except for Cr, Ni, Co, Cu, Rb, Sr, Ba, Cs, Li, Pb, Sb, Sc, and Tl (i.e. for incompatible elements in general, except LILEs). Additionally, the T2 lavas have contents that usually overlap the CA and T1 suites plotting in an intermediate position, except for the same elements mentioned before (Cr, Ni, Co, Cu, Rb, Sr, Ba, Cs, Li, Pb, Sb, Sc, Tl) plus Ga, Sn, U, V, W and Ti that in some samples have variable concentrations relative to T1.

The two alkaline trends can also be recognized in the trace element-Zr variation diagrams (Fig. 6.5 to 6.9) where the T2 lavas depict variations that are similar to the calcalkaline suite (i.e. direct for Li, Be, P, Sc, Ti, Zn, Ga, Rb, Cs, Ba, Y, HFSE, Mo, Sn, Sb, Pb, LREE, HREE, W, Th and U, and inverse for Cr, Co, Ni and Cu). Only in the case of V and Tl the variations are different from the CA: direct for V and inverse for Tl. In contrast, the T1 alkaline lavas show direct variations for Li, Be, P, Zn, Ga, Rb, Cs, Ba, Y, HFSE, Mo, Sn, Sb, Tl, Pb, LREE,
HREE, W, Th and U and inverse for Sc, Ti, V, Cr, Co, Ni, Cu and Sr (i.e. T1 shows apparent opposite variations for Sc, Ti, V, Sr and Tl relative to T2).

The Sr-Nd-Pb isotopic data obtained for the alkaline lavas have narrower ranges than observed for the CA. The $^{87}Sr/^{86}Sr$ ratios range from 0.70338 to 0.70426 for T1 and

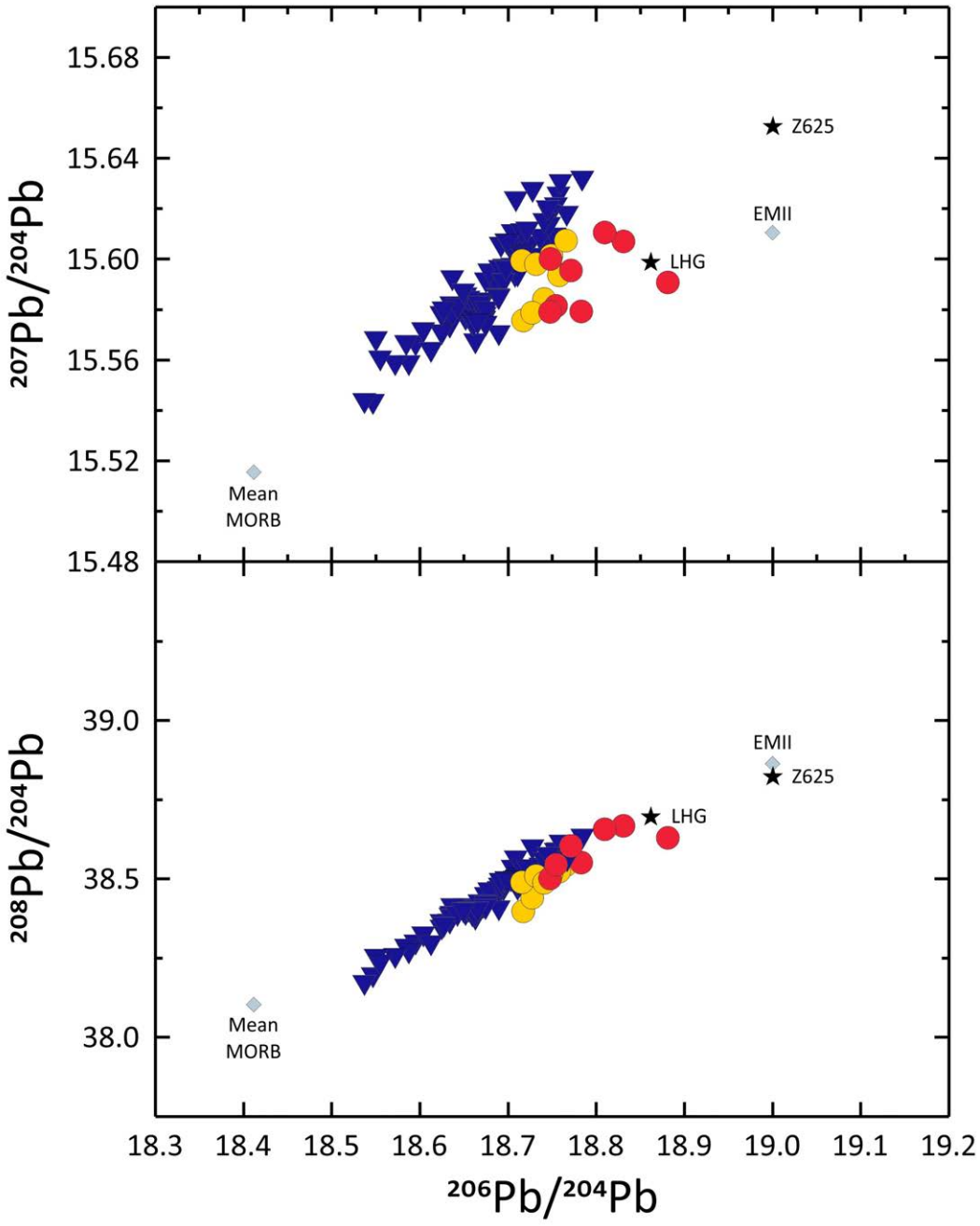

Fig. 6.12 Lead isotopes diagrams. Red circles T1, yellow circles T2, blue triangles CA. Black stars are the composition of the contaminants and grey diamonds the mantle components.

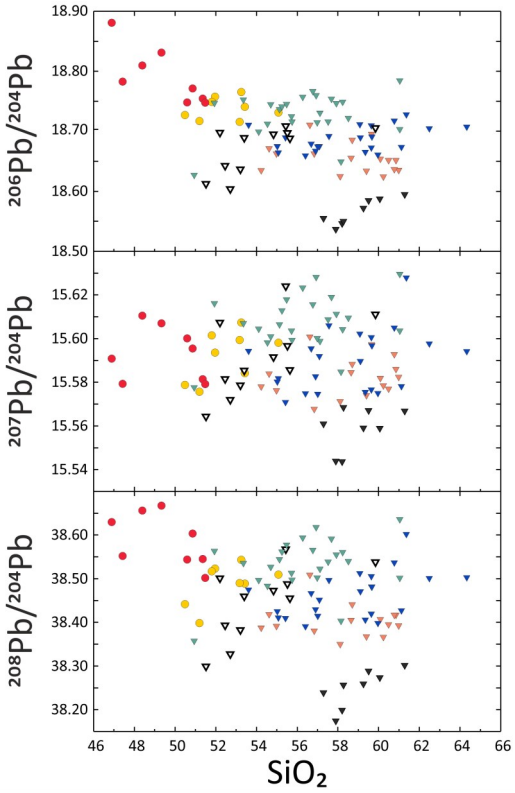

Fig. 6.13 Lead isotopes vs. silica diagrams. Red circles T1 samples; yellow circles T2; white triangles are Low ^{87}Sr Metate samples; orange triangles high ^{87}Sr Metate; purple triangles North sector Main CA trend; green triangles southern sector Main CA Trend and black triangles Parícutin-Cherán alignment.

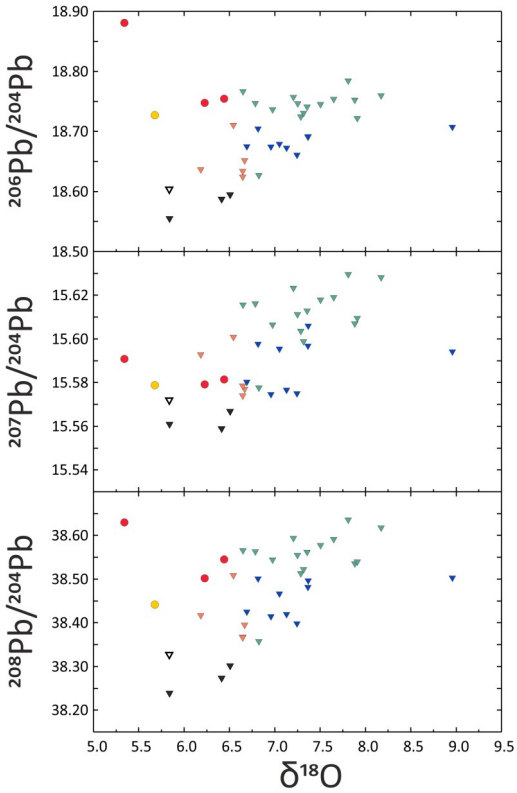

Fig. 6.14 Lead vs. Oxygen isotopes diagrams. Red circles T1 samples; yellow circles T2; white triangles are Low ^{87}Sr Metate samples; orange triangles high ^{87}Sr Metate; purple triangles North sector Main CA trend; green triangles southern sector Main CA Trend and black triangles Parícutin-Cherán alignment.

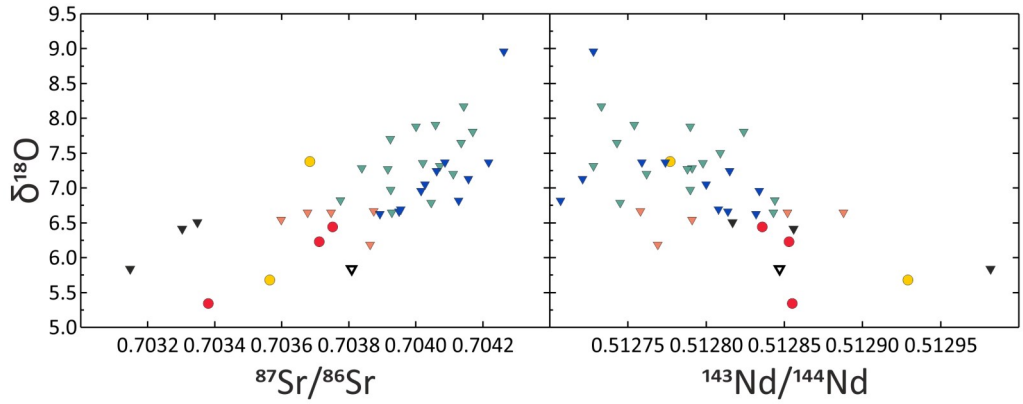

Fig. 6.15 Oxygen vs. strontium and neodymium isotope ratio diagrams. Red circles T1 samples; yellow circles T2; white triangles are Low ^{87}Sr Metate samples; orange triangles high ^{87}Sr Metate; purple triangles North sector Main CA trend; green triangles southern sector Main CA Trend and black triangles Parícutin-Cherán alignment.

from 0.70351 to 0.70425 for T2, and in the case of $^{143}Nd/^{144}Nd$ range from 0.51276 to 0.51287 for T1 and from 0.51278 to 0.51293 for T2. Concerning Pb ratios, alkaline rocks have in general higher $^{206}Pb/^{204}Pb$ ratios than the CA suite, with the T1 lavas reaching higher ratios relative to the T2 (18.881 - 18.748 and 18.766 - 18.716 respectively). The $^{207}Pb/^{204}Pb$ ratios show a similar but more constrained range than the CA (T1 from 15.579 to 15.611 and T2 from 15.576 to 15.607) with $^{208}Pb/^{204}Pb$ ratios being higher for T1 samples relative to T2 (38.502 - 38.668 and 38.398 - 38.543 respectively). It can also be observed that, unlike the Sr-Nd variation, on Pb isotopes diagrams it is possible (except for some overlapping) to identify both suites and the two alkaline trends. On a $^{87}Sr/^{86}Sr$-SiO_2 diagram is also observable that most T2 samples plot within the Main CA trend and the Parícutin-Cherán alignment arrays described for CA. Three T1 samples plot within those fields too, although most of its samples are displayed at lower SiO_2 contents.

Concerning oxygen isotopes, the alkaline rocks have in general lower $\delta^{18}O$ ratios relative to the CA and plot between typical mantle values of +5.3 ‰ (T1) to +5.7 ‰ (T2) (Bindeman, 2008) and up to +6.4 ‰ for T1 and +7.4 ‰ for T2. The $^{18}O/^{16}O$-SiO_2 diagram does not show neat correlations but just a rough direct variation.

Suite comparison and discussion

The geochemical data obtained in this work confirms the variability of petrologic types already described by previous authors for the MGVF (Hasenaka, 1994; Hasenaka & Carmichael, 1985; Gómez-Tuena, 2007; Ferrari et al., 2012) but emphasizing the relative importance of alkaline volcanism, demonstrating that this region is compositionally even more complex than previously assumed.

In general terms, the CA suite presents the geochemical features characteristic of continental arcs subduction-related magmas, whereas the alkaline suite shows in general characteristics akin to OIB-like lavas. The alkaline suit can be divided into two distinct trends: T1 with a signature closer to typical OIB, and T2 with a signature intermediate between CA and T1, equivalent to so-called “mildly” alkaline rocks identified in other monogenetic fields of the TMVB (see Straub et al., 2012 and references therein).

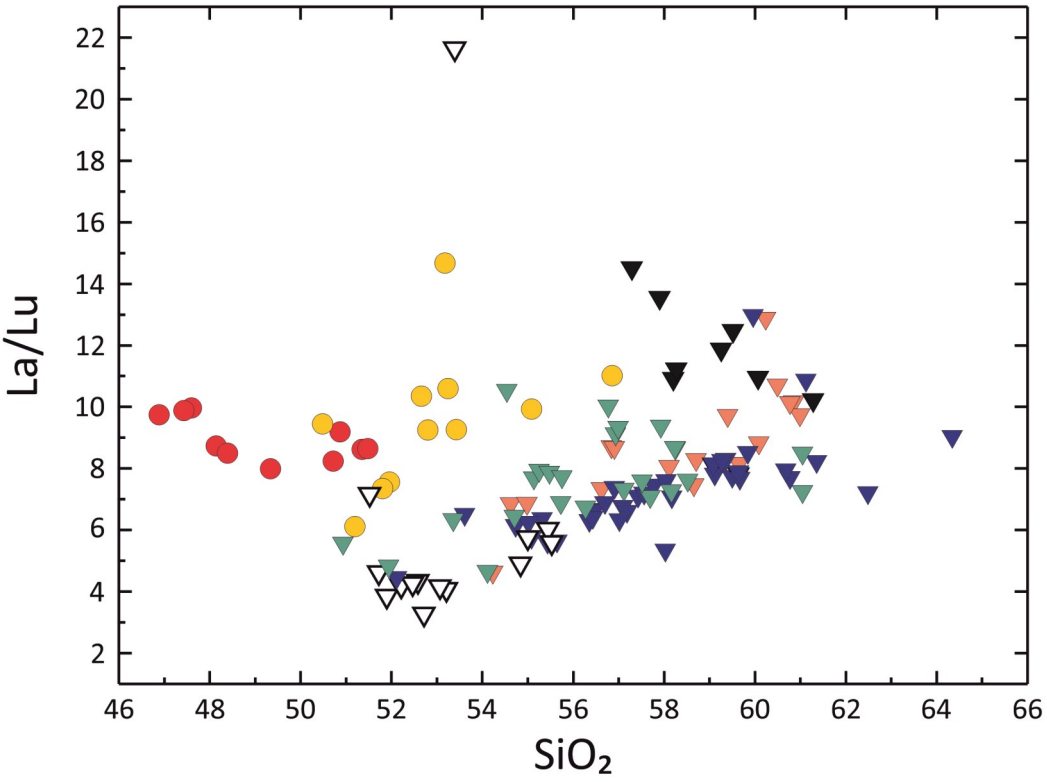

Fig. 6.16 Lanthanum – lutetium ratio vs. Silica. Red circles T1 samples; yellow circles T2; white triangles are Low ^{87}Sr Metate samples; orange triangles high ^{87}Sr Metate; purple triangles North sector Main CA trend; green triangles southern sector Main CA Trend and black triangles Parícutin-Cherán alignment.

On the other hand, although the calcalkaline suite forms a relatively heterogeneous group of rocks, their $^{87}Sr/^{86}Sr$ isotopic signature allows highlighting the apparent existence of different magmatic associations. In this case, the distinctive individual trends belong either to specific middle-size volcanoes (e.g. the high-Sr Metate and Low-Sr Metate trends), to a group of vents geographically related (e.g. Main CA trend) or to a group of vents related by a possible common geodynamical feature (e.g. Parícutin - Cherán alignment).

The observed selective enrichment of low ionic potential elements in the CA suite (K, Sr, Rb, Ba; Fig. 6.6) has been widely attributed to metasomatism of the mantle source of arc basalts by fluids released from the subducted slab (Winter, 2001) and the low abundances of elements of high ionic potential (Ta, Nb, Ce, P, Ti; Fig. 6.8) has been variably attributed to higher degrees of partial melting and to the stability of some residual mantle phases (Pearce, 1982). Furthermore, the marked inverse correlation be-

tween total iron content and SiO_2 displayed by these samples is commonly regarded as a typical calcalkaline differentiation trend due to early differentiation of magnetite (Wilson, 1989). Although these samples contain mainly chromite and ilmenite, this claim could still be valid as those minerals contain as well high quantities of Fe and Ti, what may explain the inverse TiO_2/SiO_2 correlation too. The alkaline suite, specially the T1 trend, also shows this marked negative correlation between total iron content and SiO_2 suggestive of oxides fractionation but, given the high contents in total iron and titanium at low silica concentrations, it is more likely that such fractionation would have occurred towards latter stages of evolution.

As it is apparent from the geochemical signatures of the lavas described in this chapter, none of the rocks appear to have characteristics typical of primary magmas. Even though some of the CA lavas have some of the highest Mg# values (> 66, the minimum usually assumed for primitive magmas (Winter 2001)), none of them meet other requirements such as the presence of mantle xenoliths, and values of Cr > 1000 ppm or Ni > 400 - 500 ppm (Winter, 2001). Nevertheless, it is noteworthy that all of the highest Mg#, Ni and Cr contents belong to samples located in the southern sector, as already noted by Hasenaka & Carmichael (1987) and most of them belong to the identified SW-NE alignment north of Parícutin volcano. Those samples have also the lowest contents in REE, LILE and HFSE and the highest in compatible elements such as Cr, Ni, Co, Cu and V, therefore they could be considered to be the least evolved terms in the field although still not primitive.

The geochemical variations are in agreement with the petrographic observations, suggesting that the magmatic process that all the suites share is crystal fractionation. This can be deduced by the linear variation tendencies in Harker diagrams for most major elements, feature widely accepted to indicate fractionation of ferromagnesian minerals and plagioclase from parental basalts (Wilson, 1989), and for trace elements in general against Zr. The higher FeOt, TiO_2, P_2O_5 and MnO contents found in T1 alkaline rocks (figure 6.3), followed by T2 and CA, could be a sign of a different crystal fractionation sequence between suites if those abundances were due to a greater fractionation of apatite and oxides in CA and T2 (chromite and ilmenite in the case of CA and ulvöspinel in T2) that did not occur or were scarce in the first stages of the T1 evo-

lution. At this point it cannot be concluded if these differences are a result of different crystallization conditions or a different composition of the source. This will be explored in following chapters.

The effects of fractional crystallization are also confirmed on multielement diagrams as the concentrations of incompatible trace elements in general and the fractionation ratios (e.g. La/Lu) tend to increase with a differentiation index (e.g. SiO_2) (Fig. 6.16). The CA rocks with the lowest silica contents tend to have negative spikes for Ti and P. At higher silica contents those spikes get stronger for Ti and smoother for P. The T2 rocks present a similar behaviour but to a lesser extent and both can be attributed to a constant fractionation of Ti-oxides and an early fractionation of apatite that does not continue at more advanced stages. T1 lavas on the contrary displays a relative flat pattern for Sr and a positive spike for Ti in the silica poorer rocks and a marked negative spike for both at SiO_2 richer compositions while P_2O_5 contents tend to increase with SiO_2. These features agree with low pressure plagioclase fractionation in the case of Sr (Wilson, 1989), and oxides as well as very little apatite fractionation even though it probably was crystallizing from the onset of the process.

While many major and trace element variations agree with a fractional crystallization process, these rocks present as well other characteristics which are difficult to reconcile with simple crystal fractionation. For instance, the Harker diagrams display fairly scattered arrays, aspect regarded by Cox (1980) as a natural consequence of the effects of polybaric crystal fractionation combined with either source heterogeneity, variable degrees of partial melting, crustal contamination or a mixture of the above. The CA suite shows the greatest scattering, especially on elements like Al, K, Na and P which could indicate contamination with the crust or a more heterogeneous source. This suite is also characterized by lower contents of most trace elements relative to the alkaline rocks but higher for Cr, Ni, Sr and Cs. The fact that alkaline suite, more T1 than T2, presents higher contents for most trace elements relative to the CA could be a symptom of a more enriched source for the alkaline magmas while the narrower fractionation range (as defined by normalized La/Lu ratios) of T1 could be due to smaller crystallization degrees or contamination which could suggest a faster ascent and therefore a shorter residence time in the crust.

Since radiogenic isotopic ratios do not significantly change during partial melting or fractional crystallization processes, the Sr-Nd-Pb isotopic systems are an ideal tool to assess the possible involvement of different sources and the possible influence of contamination by components with contrasting isotopic ratios.

As shown above, the CA suite exhibits a $^{143}Nd/^{144}Nd$-$^{87}Sr/^{86}Sr$ isotopic signature (Fig. 6.10) with a slightly wider range than the alkaline one, but presenting more abundance of samples towards the ^{87}Sr-enriched end of the array. In contrast, lead isotopes (Fig. 6.12) show a more clear distinction between the different series, with CA samples having a more ^{206}Pb-depleted signature than the alkaline T1 (18.785 - 18.537 and 18.881 - 18.748 respectively) and a wider range for ^{207}Pb (15.630 - 15.544) and ^{208}Pb (38.636 -38.174), whereas T2 rocks plot at intermediate compositions (^{206}Pb = 18.766 - 18.716). Therefore the Sr-Nd-Pb isotope signature for these rocks is intermediate between depleted mantle sources and the enriched components HIMU and EMII (Zindler & Hart, 1986) or continental crust components (Taylor & McLennan, 1995).

As it is well known, continental crust rocks have a more radiogenic signature than mantle-derived magmas ($^{87}Sr/^{86}Sr$ typically over 0.7040 in the former and about 0.7030 in the later; see Faure, 1986). In this volcanic field, just four alkaline samples (two T1 and two T2) and some CA plot below $^{87}Sr/^{86}Sr$=0.7035 and most of the remaining samples are much higher. Furthermore, as presented in the $^{87}Sr/^{86}Sr$ vs. SiO_2 diagram, we were able to distinguish different arrays for the CA suite, all of them characterized by variable degrees of $^{87}Sr/^{86}Sr$ enrichment directly correlated to SiO_2 variations. Oxygen isotope ratios also present significant differences between the identified trends (see Table 8 and Figs. 6.11, 6.14 and 6.15) with the lower values of each group of rocks corresponding to those typically found in primitive basalts observed in OIB (in the case of the alkaline lavas) and andesites of continental arcs (in the case of the calcalkaline lavas) (see Bindeman, 2008), extending towards higher values also related in general terms with SiO_2 variations.

As it appears from these geochemical variations, all the rocks studied seem to have undergone an evolutionary process more complex than simple crystal fractionation, most likely involving the contamination of ^{87}Sr-rich components. On the other hand, the distribution of the different arrays mainly identified in the $^{143}Nd/^{144}Nd$-

$^{87}Sr/^{86}Sr$ diagram, starting at diverse initial compositions (some of them not very evolved), seem to suggest the participation of a range of different primary magmas, which also agrees with the relatively wide range of petrologic groups. Furthermore, the different slopes displayed by each array also suggest that the possible contaminants are also likely heterogeneous. The challenge then lies in assessing whether such processes, involving melting from different mantle sources and contamination by heterogeneous crustal components are a feasible mechanism to produce the observed geochemical variability and if petrogenetic modelling can help to discern between the different possibilities and to provide additional data on the different components involved that may be applied for a general geodynamic scenario to explain the origin of the alkaline-calcalkaline association in the MGVF.

7. Petrogenetic modelling

Quantitative modelling of petrogenetic processes is an essential tool which allows discerning between petrogenetic hypotheses that are based on qualitative interpretations of petrographic and geochemical observations. It may also provide specific data on the geochemical and physical conditions that may have led to the generation of a suite of rocks.

In previous sections it has been shown that most of the sampled lavas in the MGVF have geochemical characteristics typical of differentiated magmas. Additionally, assimilation processes (involving crustal components) seem to be ubiquitous in this volcanic field (see Chesley et al., 2002; Hasenaka & Carmichael, 1987; Johnson et al., 2008; Lassiter & Luhr, 2001; Verma & Hasenaka, 2004; Schaaf et al., 2005; Corona-Chávez et al., 2006; Losantos et al., 2017). In fact, Paricutin volcano is considered as a classic world example for AFC processes (McBirney et al., 1987). Therefore, our study is mainly focussed to test from quantitative modelling of Coupled Assimilation plus Fractional Crystallization (AFC) the feasibility of the above proposed hypothesis (i.e. if AFC is able to reproduce the geochemical variations observed in the different rock suites present in the MGVF).

Methodology

Coupled Assimilation plus Fractional Crystallization in magmatic systems was quantitatively formulated by DePaolo (1981) to explain variations in trace element and isotopic ratios according to the expressions:

$$\frac{C_m}{C_m^0} = F^{-z} + \left(\frac{r}{r-1}\right)\frac{C_a}{zC_m^0}(1 - F^{-z})$$

$$\frac{\epsilon_m - \epsilon_m^0}{\epsilon_a - \epsilon_m^0} = 1 - \left(\frac{C_m^0}{C_m}\right) \cdot F^{-z}$$

Where

$$z = \frac{r + D - 1}{r - 1}$$

and *F* is the residual liquid fraction, *r* is the assimilation rate (mass of assimilated material/mass of crystals fractionated), C_m^0 is the concentration of element *m* in the uncontaminated magma, C_m is the concentration of element *m* in the contaminated magma, C_a is the concentration that element in the assimilated material, e are the corresponding isotopic ratios of element *m*, and *D* is the bulk solid/liquid partition coefficient for the element between the fractionating crystalline phases and the magma.

Such a selection of geochemical data is due to the fact that radiogenic isotopes have very distinct ratios in crustal rocks versus basaltic magmas and thus isotope variations are very sensitive to AFC processes.

Early attempts at modelling AFC processes relied on DePaolo's expressions alone and despite further formulations that consider more complex scenarios (see for example Bohrson & Spera, 2001; Spera & Bohrson, 2001), DePaolo's depiction of this process is still valid and detailed enough for modelling considering the uncertainties of natural systems. However, a more complete approach would consider the integration of the AFC expressions for isotope and trace elements into major element-based lines of descent based on phase equilibria thermodynamics (which influence the trace elements distribution coefficients). Such methodology was introduced into the MELTS software package (Ghiorso & Sack, 1995 and Asimow, 1998), also used in the PELE software package, which is an implementation for the PC-platform of the original algorithms and thermodynamic parameters introduced in MELTS showing only minor discrepancies in the results obtained by each package (see Boudreau, 1999), both demonstrating good predictive behaviour when compared to experimental work (e.g. Huang et al., 2009). Cebriá et al. (2011b) used this approach for modelling the AFC process in Paricutin (see below). However, using this kind of thermodynamic approach for differentiation processes should be restricted to rock suites that are produced from a well constrained process (e.g. a series of differentiated magmas derived by AFC developed in a common magma chamber). Although samples collected from individual vents in a monogenetic field can be considered at some extent in a similar way to lavas derived

from a polygenetic volcano, since magma differentiation has verified in different conduits or chambers, under presumably variable conditions, applying the kind of modelling used in volcanoes like Paricutin to a monogenetic field may not be realistic enough and therefore a different approach must be applied.

The use of any of the above methods implies assuming several key parameters of the process, which must be adjusted in successive calculations to replicate the observed petrologic and chemical variations. Since major element variations are mainly dependent on the fractionating assemblage, the first step to calculate a petrogenetic model that considers simultaneously the petrographic and geochemical observations is to test if a suitable set of parameters (basically temperature, pressure, and oxidation state) can reproduce the major element variations and mineralogy of the suite from an assumed initial melt. Such conditions simultaneously determine other parameters such as the bulk distribution coefficients of the trace elements, which are the basis for the calculation for the isotopic variations. In the case of assimilation, the most critical parameters to be assumed in addition to the above mentioned, are the compositions of both endmembers (i.e. the initial magma and the material assimilated) and the extent of assimilation.

Considering the above constraints we have first used the PELE package to obtain an initial approximation to a simple fractional crystallization process for major elements alone, adopting the results obtained from petrographic observations and mineral geothermobarometry as a first input for the physical conditions under which magmas could have evolved. Then these results were considered as a first input to calculate AFC models based on the expressions defined by DePaolo (1981) for trace elements and Sr-Nd-Pb isotopes, in this case with the aid of the spreadsheet programs by Ersoy & Helvacı (2010) and Ersoy (2013).

Since all sampled lavas are relatively differentiated, to avoid additional uncertainties resulting from assuming the composition of assumed or calculated primitive compositions, we have limited the calculations to starting compositions established with actual samples selected from the least evolved lavas of each series. Therefore, the obtained results do not represent the whole differentiation process but are representative of the observed variations only.

Modelling

In many small monogenetic fields it has been shown that most erupted lavas from different vents may be related through common magmatic processes. This is the case for example of the primitive lavas of Garrotxa (NE Spain) or Calatrava (Central Spain) which in general terms can be explained through variable different melting degrees from a common mantle source (see Cebriá et al., 2000; Cebriá and López-Ruiz, 1996). However, in larger volcanic fields where both small monogenetic and transitional vents coexist, it is unlikely that such a relatively simple scenario may occur, especially in the MGVF considering the geodynamic complexity of the TMVB. Additionally, as we have described earlier, while primitive magmas in monogenetic fields may derive from a common mantle source, differentiation of each individual magma batch (corresponding to different monogenetic vents) likely occurs in different conduits or chambers, under presumably variable conditions. Hence such process can only be assumed to be similar in closely and geodynamically related vents. Therefore, several assumptions have been considered here to attempt some petrogenetic modelling on the volcanism of the MGVF.

In the case of the alkaline suite, each of the identified geochemical trends might be attempted to be modelled as a unit even though the lavas belong to different vents because, besides their relatively homogeneous compositional variations, they outcrop in closely related vents distributed following an approximately linear alignment thus suggesting that they may be geodynamically related at small scale.

The CA suite however seems difficult to explain in terms of a single petrogenetic process as these lavas outcrop in vents that are spread throughout the entire volcanic field and show more compositional heterogeneities. A more appropriate approach is to consider spatially closer vents distributed as either alignments or clusters that can be considered to be geodynamically related at the scale of the specific alignment/cluster. Following such concept, the CA suite has been modelled following two different ways: 1) considering the North Sector vents to provide a comparison with the spatially-related alkaline suite, and 2) selecting an identified alignment of volcanic vents. In addition, two middle size volcanoes were studied separately, El Metate and

Parícutin, to obtain additional information for the transitional vents characteristic of this volcanic field.

Alkaline suite

As we have seen in previous sections, none of the alkaline sampled rocks display the geochemical or petrographic characteristics expected for primitive (or nearly primitive) magmas Mg# > 66, Cr > 1000 ppm or Ni > 400-500 ppm (Winter, 2001), having very low Ni (under 28 ppm for T1 and 84 ppm for T2) and Cr (under 31 ppm for T1 and 155 ppm for T2) contents, and #Mg values < 52 (T1) and < 64 (T2). In fact, the described geochemical variations in Harker and Zr-element diagrams (Figs. 6.3, 6.5, 6.6, 6.7, 6.8 and 6.9) are consistent with a differentiation process involving the fractionation of the mineral phases identified in the petrographic study. However, the significant differences observed in the mineralogy and major and trace element signature of each of the two trends suggests that their petrogenesis might be different too.

Additionally, the Sr-Nd-Pb-O isotopic variations (Figs. 6.10, 6.11, 6.12, 6.13, 6.14 and 6.15 in chapter 6) support as well contamination by a radiogenic component. Therefore, to test the possible effect of contamination by crustal components, AFC model tests have been ran to try to reproduce trace elements and isotope variations considering as potential contaminants a range of basement compositions reported in the literature for the area, including granulitic xenoliths hosted in basalts from the Valle de Santiago area (samples VS1 and VS2 of Ortega-Gutiérrez et al. (2014) and granitic samples from the Guerrero Terrane (samples MG-05-21 and MG-05-51 of Ortega-Gutiérrez et al., 2014; sample LHG of Luhr y Carmichael, 1985 and Luhr, 1997; sample Z625 of Blatter et al., 2007; and sample 96MR088 of Potra et al., 2014) (Table 9).

Alkaline trend 1

In order to reduce the number of assumptions necessary to model an AFC process, the approach followed was to obtain an initial set of physical conditions based on a simple fractional crystallization process trying to reproduce as best as possible the

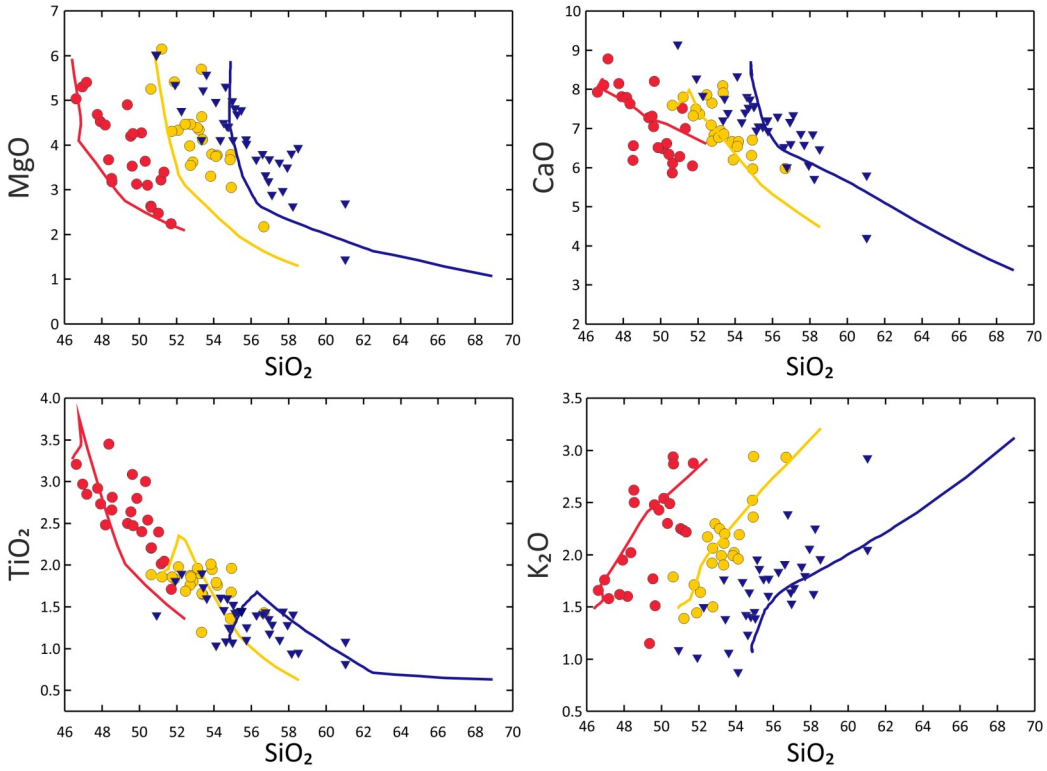

Fig. 7.1 MgO, CaO, TiO_2, and K_2O descent lines tests calculated with the PELE software for the alkaline T1 (red circles and red line), alkaline T2 (yellow circles and line) and north sector calcalkaline samples (blue triangles and line). In the examples F ranges from 0 to ~50%.

major element variations (in general, less sensitive to assimilation compared to trace elements) as well as the observed mineral assemblage.

These initial tests (Fig. 7.1) were run with the MELTS-based PELE software, which for FC processes requires as input values an initial composition, an oxygen buffer and an estimation of the initial pressure (the T for the onset of crystallization is calculated by the software, based on the provided data). The starting composition was selected from the less differentiated lavas (M85 and M110) and initial P values estimated from the highest values obtained from geothermobarometry calculations. It is important to note that the starting composition cannot be taken straight from the sample analysis and needs to be recalculated to approach a more realistic magma composition, allocating some H_2O into the composition. Since this is an unknown parameter, a range of values (from anhydrous conditions up to 4 %wt; see Anderson, 1973; Johnson et al., 2010; Luhr, 2001; Pioli et al., 2008; Plank et al., 2013) were introduced in different test calculations and its effect observed in the resulting lines of descent. Similarly different

oxygen buffers among those usual in basaltic rocks from arc settings (i.e. from QFM to QFM+2, see Kelley & Cottrell, 2009; Mullen & McCallum, 2013; Zimmer et al., 2010) were tested.

Our results show that an acceptable fit between the observed and the calculated data can be obtained for some major elements considering a starting magma composition similar to sample M85 with the addition of ~1.5 % initial water contents, crystallizing under the QFM+1 buffer during cooling (1260 °C - 1100 °C) and ascent of the magma from pressures of ~11 kbar

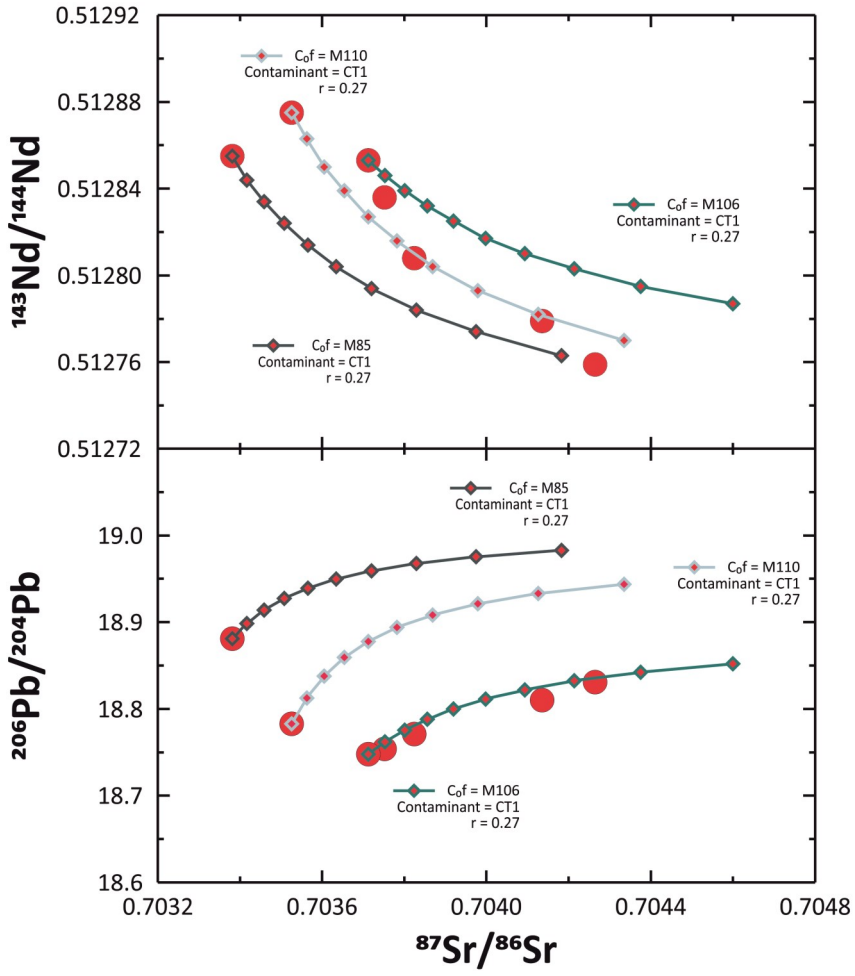

Fig. 7.2 Nd and Pb vs. Sr isotope ratios for T1 alkaline rocks. Lines with diamonds represent AFC differentiation trends calculated for initial samples M85, M110 and M106 contaminated with the CT1 contaminant (Table 9) and the parameters specified in the figure. Diamonds indicate equal F steps in the range F= 0-0.668. The calculation for three different initial compositions is necessary to cover the compositional range displayed by this samples and suggests that the lavas could not have been derived from exactly the same parental magma.

up to ~4.5 kbar. The modelled paragenetic sequence, involving Plg 63 % + Ol 25.5 % + oxides 9 % + Cpx 2 % + Ap 0.5 %, also reproduces in general terms the observed main mineral assemblage. However, oxides such as MnO, Na_2O and P_2O_5 are not adequately replicated. Actually, any calculated line of descent would likely fail to reproduce the observed data for those elements due to their relatively high degree of scattering. In addition to the fact that, as already pointed out, we are not dealing with a simple line of descent and crystallization conditions may be variable, such scattering may also suggest a variation in the conditions of the process different from that ob-

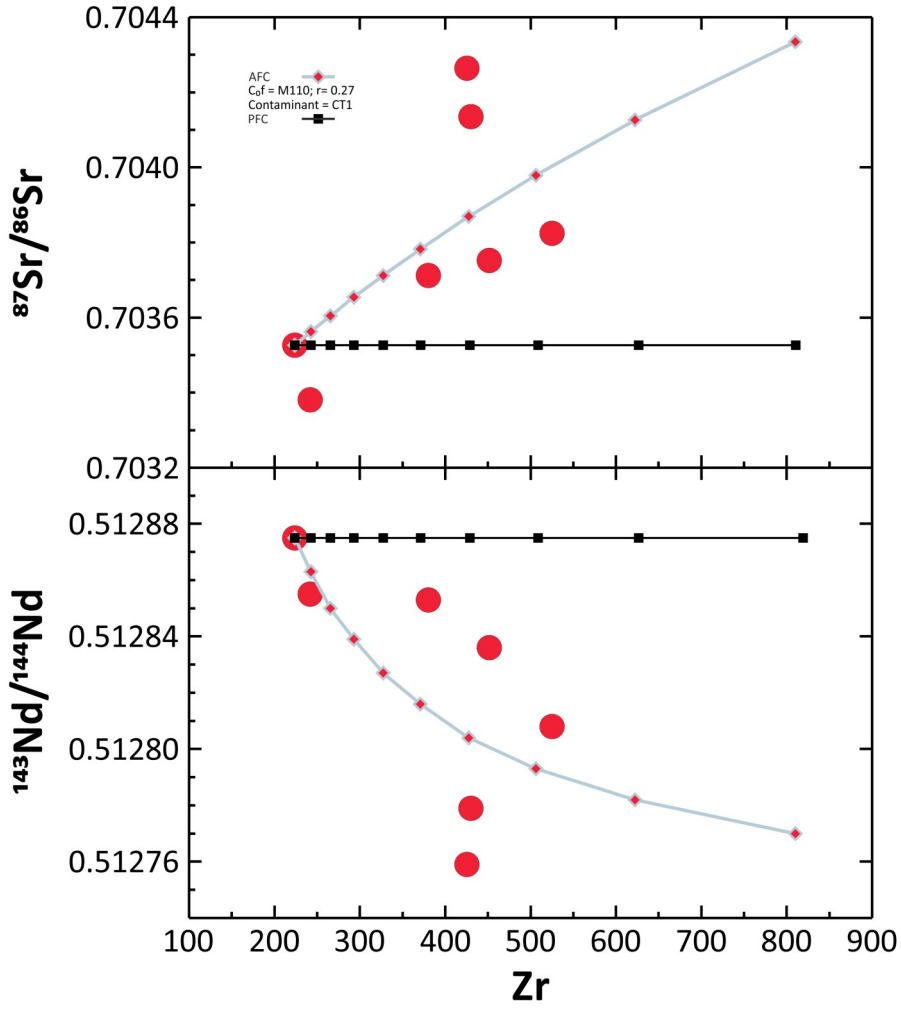

Fig. 7.3 Sr and Nd isotopic rations vs. Zr for T1 alkaline rocks. Grey line with diamonds represent AFC models calculated for initial sample M110 contaminated with the CT1 contaminant (Table 9), the parameters indicated in the figure and Kd values of Table 11. Diamonds indicate equal F steps in the range F = 0 - 0.668. For comparison the perfect fractional crystallization (PFC) is plotted in a black line with squares demonstrating that such a mechanism cannot reproduce the data.

tained from a single initial magma under an invariable set of parameters. In the case of P_2O_5, its behaviour is mainly controlled by the fractionation of apatite, which also has an effect on CaO. As we have seen, apatite is a common phase in these lavas, both as an accessory phase in the groundmass and as inclusions in other major minerals, indicating early crystallization but little or even absent fractionation (P_2O_5 in general increases with SiO_2). However, under the physical conditions of the above described model (mainly as a consequence of the assumed P_2O_5 and H_2O contents of the initial magma), apatite would fractionate in small but significant amounts thus buffering the P_2O_5 content. A possible way to inhibit the fractionation of Ap would be to consider anhydrous conditions. However, under H_2O-free conditions the calculations demonstrate that Opx would be a highly fractionating phase producing a bad fit of the calculated lines of descent for most elements and a serious discrepancy with petrographic observations, and the normative composition of alkaline rocks. Therefore it seems more reasonable to assume that during ascent degassing coupled to progressive depressurization may occur (see Annen et al., 2006; Girona et al., 2014) which would decrease the H_2O activity and minimize apatite crystallization.

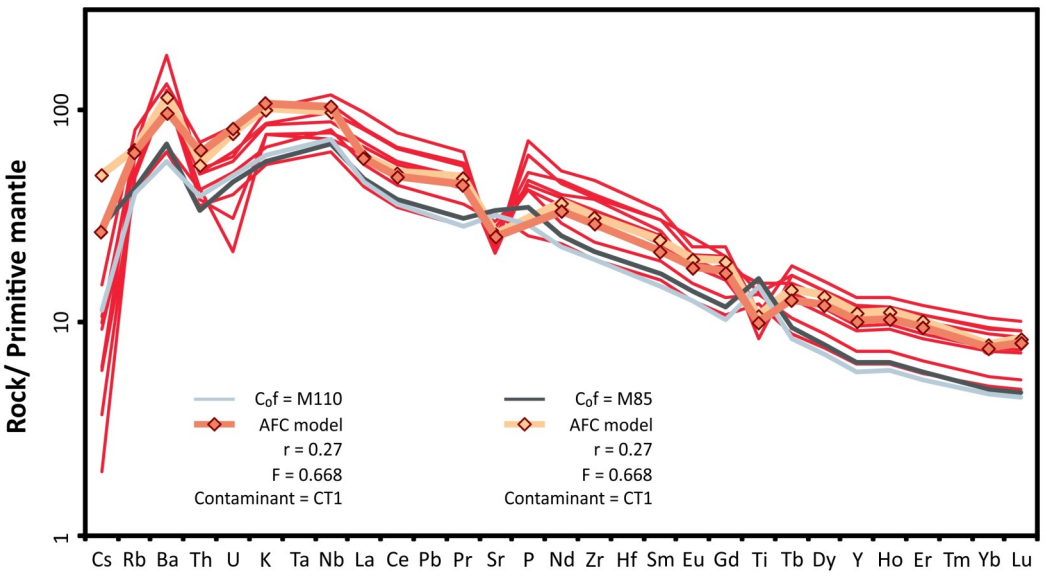

Fig. 7.4 Normalized multielement diagram for T1 alkaline rocks. Lines with diamonds represent AFC models calculated for initial samples M110 and M85 contaminated with the CT1 contaminant (Table 9), the parameters specified in the figure and Kd values of Table 11. Normalization Primitive mantle values after Palme & O'Neill (2014).

In the case of the calculated MnO and Na_2O variations, their poor fit to the observed data may be a consequence of the restricted allocation of these oxides to the mineral phases following simple solution models which do not account for Na or Mn entering Cpx or apatite, as observed in natural systems (see for example Dunn, 1987 or Miles et al., 2014).

Since the isotope variations suggest the participation of a ^{87}Sr-rich component, the above results can only be considered as a preliminary approach to the actual processes producing the T1 compositional variations. The AFC modelling for trace element

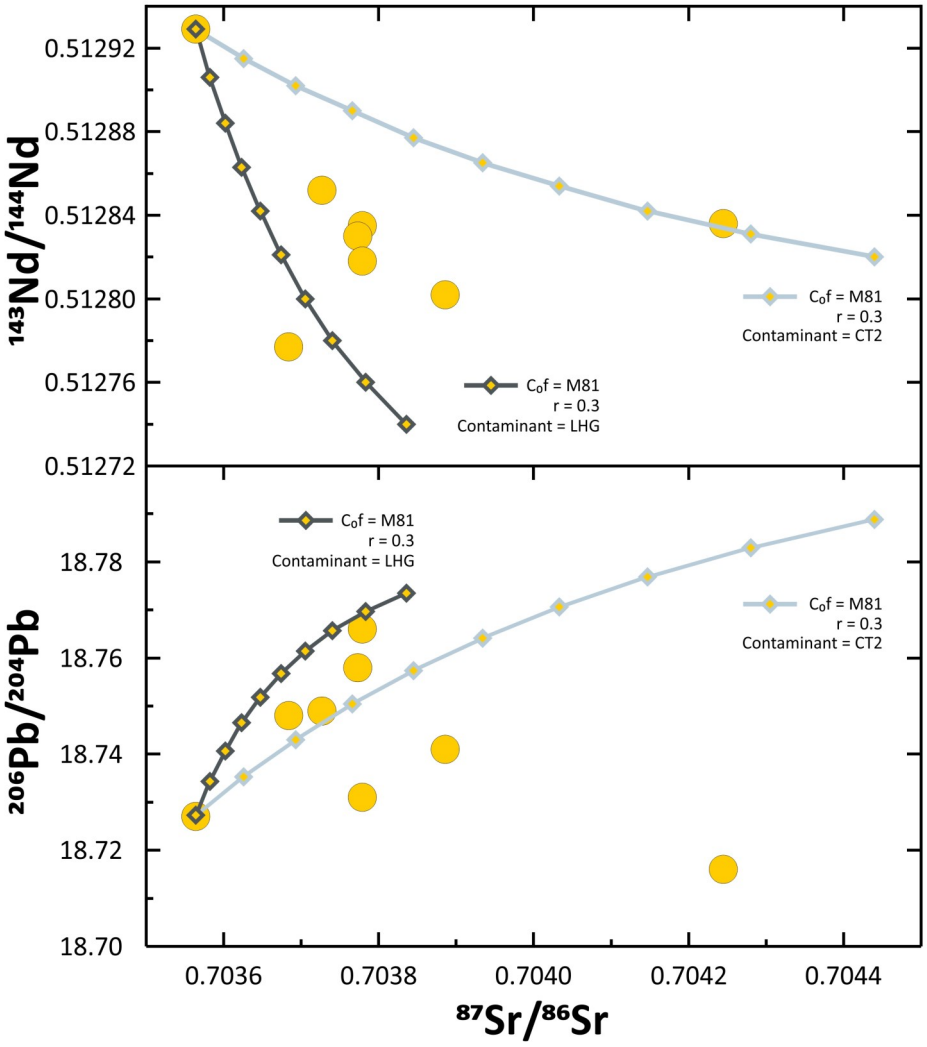

Fig. 7.5 Nd and Pb vs. Sr isotope ratios for T2 alkaline rocks. Lines with diamonds represent AFC models calculated for initial sample M81 contaminated with the CT2 contaminant (Table 9) and the parameters specified in the figure. Diamonds indicate equal F steps in the range F = 0 - 0.61.

and isotope variations in this trend was then performed considering the least evolved lavas in the series (M85, M110 and M106) as a starting material and as potential contaminants the ones mentioned before (table 9). Our tests using trace elements and Sr-Nd-Pb data (see Table 10 and Figs: 7.2, 7.3 and 7.4) confirm that the most likely scenario involves about 30 % crystallization and the addition of a granitic component as contaminant (ratio of assimilation to crystallization r ~0.3), with a trace element composition similar to the granite samples of MG-05-21 of Ortega-Gutiérrez et al. (2014), but

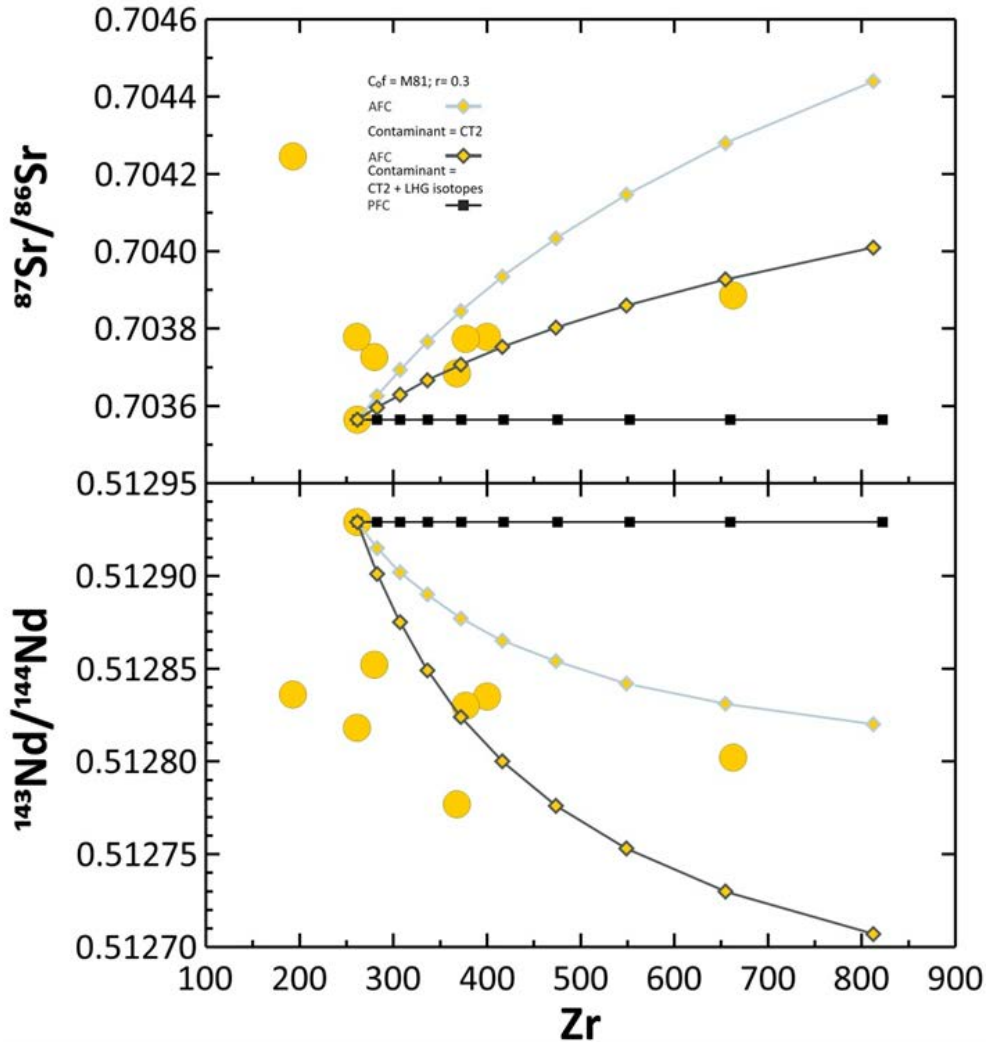

Fig. 7.6 Sr and Nd isotopic ratios vs Zr for T2 alkaline rocks. Light grey line with diamonds represent AFC models calculated for initial sample M81 contaminated with the CT2 contaminant (Table 9), the parameters specified in the figure and Kd values of Table 11. A better fit though is achieved considering the LHG isotopic composition (dark grey line with diamonds). Diamonds indicate equal F steps in the range F = 0 - 0.61. For comparison a perfect fractional crystallization (PFC) model is plotted in a black line with squares demonstrating that such a mechanism cannot reproduce the data.

with an isotopic signature closer to the Z625 sample reported by Blatter et al. (2007), similar to other Central Mexico granites (Potra et al., 2014). On the contrary, the granulitic rocks hosted by lavas in Valle de Santiago (as well as the less ^{87}Sr-enriched granitic endmember compositions) are unable to modify the starting compositions enough to reproduce the observed trace element and isotopic variations and therefore can be discarded as potential contaminants. Again, to obtain a better fit to the data, the required mineral assemblage needed to be further adjusted, but the data obtained (Plg 60 % + oxides 19 % + Ol 15 % + Cpx 6 %) agrees in general terms with the observed mineralogy and the fractionating paragenetic sequence calculated from major elements, except for a larger fractionation of magnetite, required to fit the TiO_2 variation (at the assumed mineral-liquid distribution coefficients of Table 11 compiled from the GERM Partition Coefficient Database (Nielsen, 2016).

It is important to indicate that, while the modelled trace element patterns in multielement diagrams (Fig. 7.4) can reproduce most significant characteristics of the sampled lavas (e.g. progressive Sr and Ti depletions), some features observed in individual samples do not quite fit the above model (e.g. persistent Ba spikes and small

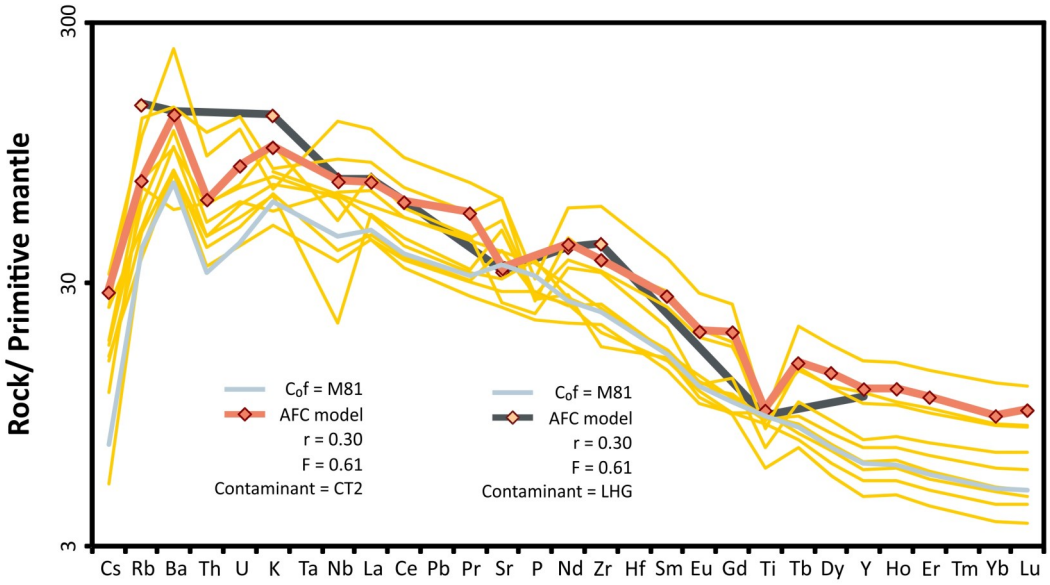

Fig. 7.7 Normalized multielement diagram for T2 alkaline rocks. Lines with diamonds represent AFC models calculated for initial sample M81 contaminated with CT2 and LHG contaminants (Table 9), the parameters specified in the figure and Kd values of Table 11. Normalization Primitive mantle values after Palme & O'Neill (2014).

negative ones in K). This is expected since we are not dealing with a single line of descent and despite overall similarities, not all lavas may have been derived from exactly the same parental magma and differentiation
took place through probably similar but still separate conduits and/or chambers thus resulting in apparent discrepancies of individual samples relative to the calculated model. For example, accumulation of fractionated or xenolithic phases in some samples, as already reported in the area (Ortega-Gutiérrez et al., 2014; Righter & Carmichael, 1993) may have geochemical effects in specific elements (e.g. high Sr concentrations are consistent with accumulation of plagioclase). Similarly, as suggested by the reported compositional range in basement rocks and the results of the model, the contaminants are likely heterogeneous and therefore, while geochemical variations are satisfactorily reproduced by the model in general terms, comparison with specific samples can be not as accurate.

Alkaline trend 2

A similar modelling approach was followed in the case of the alkaline trend T2. For this group of rocks the major element thermodynamic-based FC modelling leads to a relatively good fit to the data (Fig. 7.1) when considering sample M81 as a suitable starting composition, modified to allocate initial H_2O ~2 %, crystallizing under the QFM+1 buffer in the T range of ~1200 ^oC - 1010 ^oC from P ~8 kb up to surface levels. These conditions result in the fractionation of Plg 64 % + Ol 27 % + Oxides 5 % + Cpx 3 % + Ap 1 %. In agreement with major element observations (P_2O_5 generally decreases with SiO_2) and in contrast with alkaline T1 rocks, apatite appears to be fractionating in significant amounts.

Concerning isotope variations, the systematic variations in $^{87}Sr/^{86}Sr$ with any crystallization sensitive parameter (e.g. it increases with SiO_2) are again in favour of a contamination process involving an ^{87}Sr-rich component. Tests performed using the same potential contaminants mentioned above (see Table 9 and Fig. 7.5, 7.6 and 7.7) support contamination by a granitic component similar to the one estimated for T1, but showing more heterogeneity in $^{87}Sr/^{86}Sr$, ranging between the signatures reported

for basement granites by Luhr (1997) and Blatter et al. (2007). Other parameters are equivalent to those obtained for T1 (r = 0.3 and maximum crystallization of ~30%) but involving a different crystallization assemblage, composed of Plg 40 % + Ol 25 % + Cpx 20 % + Mt 10 % + Ap 5 %. This mineralogy agrees with the one obtained from the initial major element approach but differs in the relative amounts of fractionation, in this case suggesting lower amounts of Plg and higher of Cpx and oxides. Although any of these results can only be considered as a rough approach to the actual process, the second set of results is preferred since it also considers the effects of assimilation and

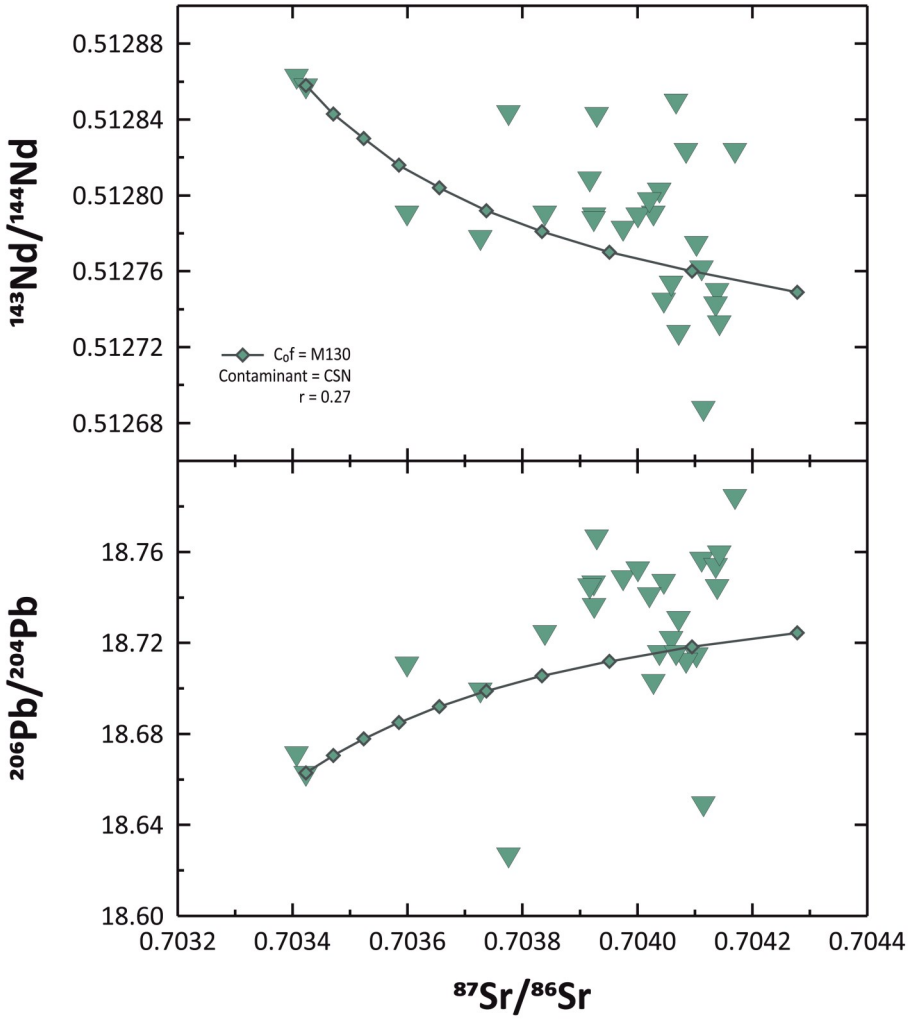

Fig. 7.8 Nd, Pb vs. Sr isotopic ratios for the calcalkaline rocks of the Northern Sector. Lines with diamonds represent AFC models calculated for initial sample M130 contaminated with the CSN contaminant (Table 9) and the parameters specified in the figure. Diamonds indicate equal F steps in the range F = 0 - 0.712.

accounts for more significant parameters, including both trace elements and isotope ratios.

It is noteworthy that some samples displaying strong Sr, Eu and Ba enrichments appear to be outliers relative to the overall variations. However, as already mentioned, these enrichments can be explained in terms of accumulation processes involving either fractionating or xenolithic phases, a feature already suggested by Righter & Carmichael (1993) in the alkaline lavas of Valle de Santiago. In this case, high Sr-Eu values may likely represent accumulation of plagioclase, whereas high-Ba anomalies may de-

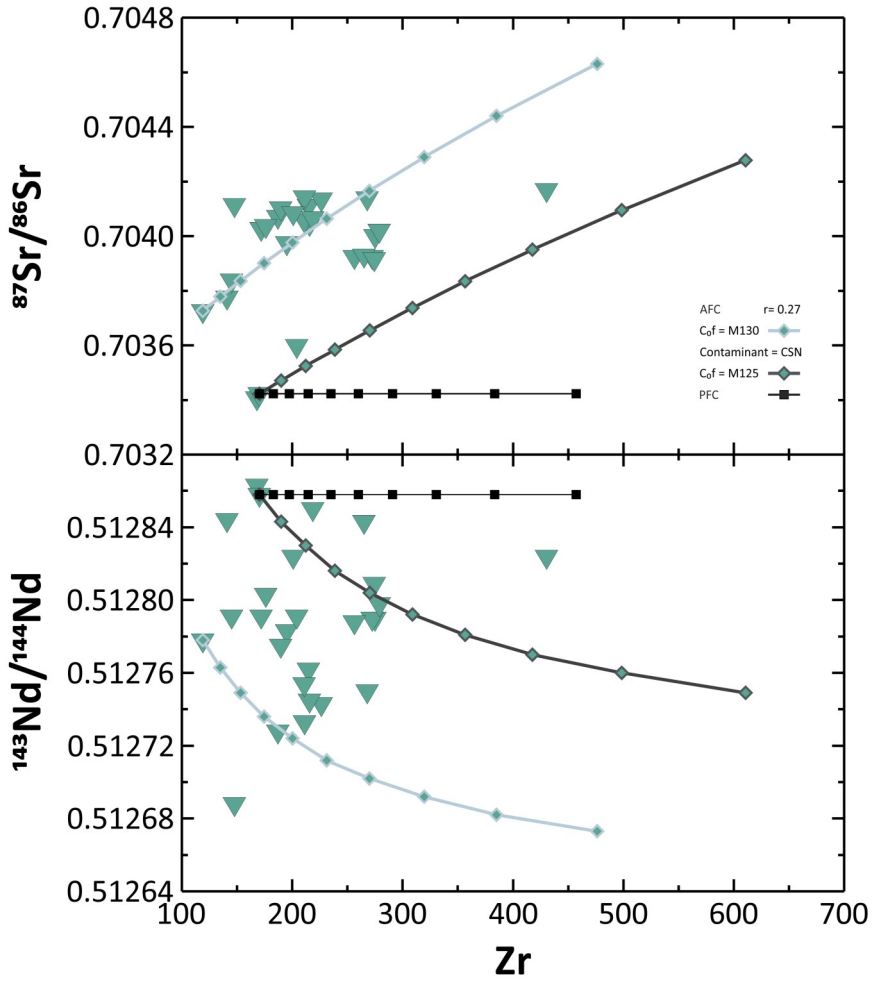

Fig. 7.9 Sr and Nd sotopic ratios vs. Zr for calcalkaline rocks of the northern sector. Dark grey lines with diamonds represent AFC models calculated for initial sample M130 contaminated with the CSN contaminant (Table 9) and the parameters specified in the figure. Also displayed the AFC model for M125 (light grey line with diamonds) to cover the observed compositional range, which suggests that the lavas are likely derived from compositionally different parental magmas. For comparison a perfect fractional crystallization model (PFC) is plotted in a black line with squares. Diamonds and squares indicate equal F steps in the range F = 0 - 0.712.

pict the presence of xenolithic feldspar as reported in the area by Righter & Carmichael (1993).

Calcalkaline suite

Similar to the alkaline suite, fractional crystallization of the mineral phases identified in the petrography study along with contamination by an ^{87}Sr-rich component is supported by the geochemical and isotopic variations observed in the calcalkaline lavas. However, there is an important difference between the north and the south sectors: Like in the case of the coeval alkaline suite, no primitive compositions are found in the northern sector (in all cases the CA #Mg<63), while in the southern sector some samples have #Mg > 64 and up to 70.

Unlike the alkaline suite that for the most part is restricted to a rather constrained sector of the field, the CA rocks are widespread in the volcanic field, including both small monogenetic vents, middle sized volcanoes and even some larger ones, showing a large range of compositional variations (see chapter 6). If we consider that

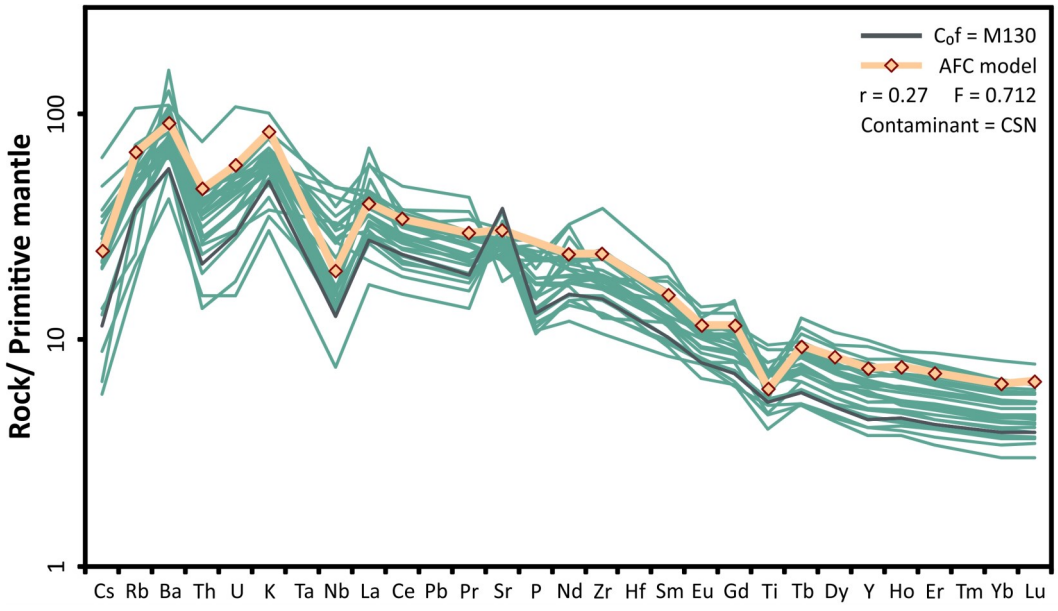

Fig. 7.10 Normalized multielement diagrams for the calcalkaline rocks of the North Sector. Lines with diamonds represent AFC models calculated for initial sample M130 contaminated with CSN contaminant and the parameters specified in the figure and Kd values of Table 11. Normalization Primitive mantle values after Palme & O'Neill (2014).

differentiation of the smaller monogenetic vents probably took place in different conduits and/or chambers (see chapter 1), any attempt to model those processes should be restricted to spatially related vents and whenever possible, sharing some geodynamic characteristics. For this reason we have undertaken two different approaches at quantitative modelling the AFC processes in CA lavas: 1) To consider the CA suite spatially associated to the alkaline lavas (i.e. the Northern sector), and 2) To consider a group of spatially related vents aligned following one of the main tectonomagmatic directions previously identified in the field from tectonic and statistic approaches

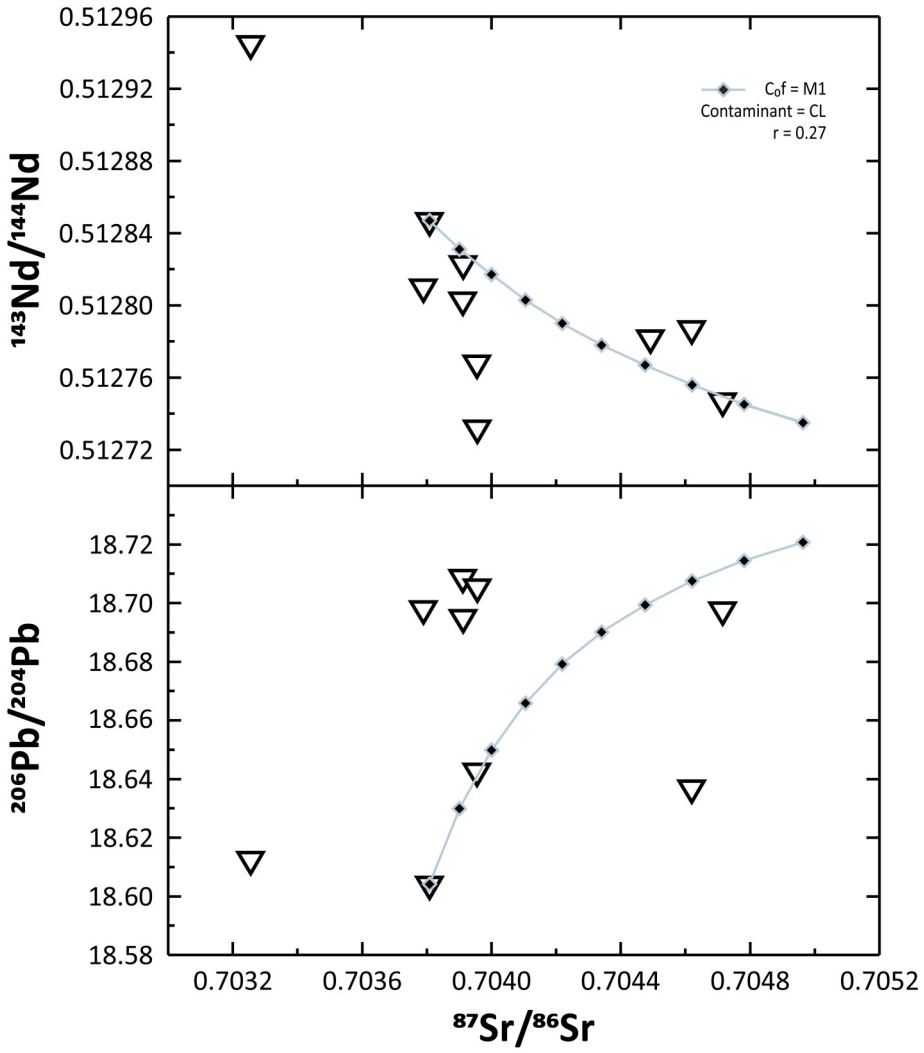

Fig. 7.11 Nd and Pb vs. Sr isotope ratios for calcalkaline rocks of the Paricutin - Cherán alignment. Lines with diamonds represent AFC models calculated for initial sample M1 contaminated with the CL contaminant (Table 9) and the parameters specified in the figure. Diamonds indicate equal F steps in the range F = 0 - 0.628.

(Connor, 1987, 1990; Wadge & Cross, 1988; Kurokawa et al., 1995; Aguirre-Díaz et al., 2006; Cebriá et al., 2011a).

The first group of vents is essential to establish any petrogenetic and geodynamic relationship with the coeval alkaline magmatism. On the other hand, selecting a specific alignment in the second case will allow testing the assumptions on the characteristics previously adopted concerning the petrogenesis in monogenetic areas (see chapter 1).

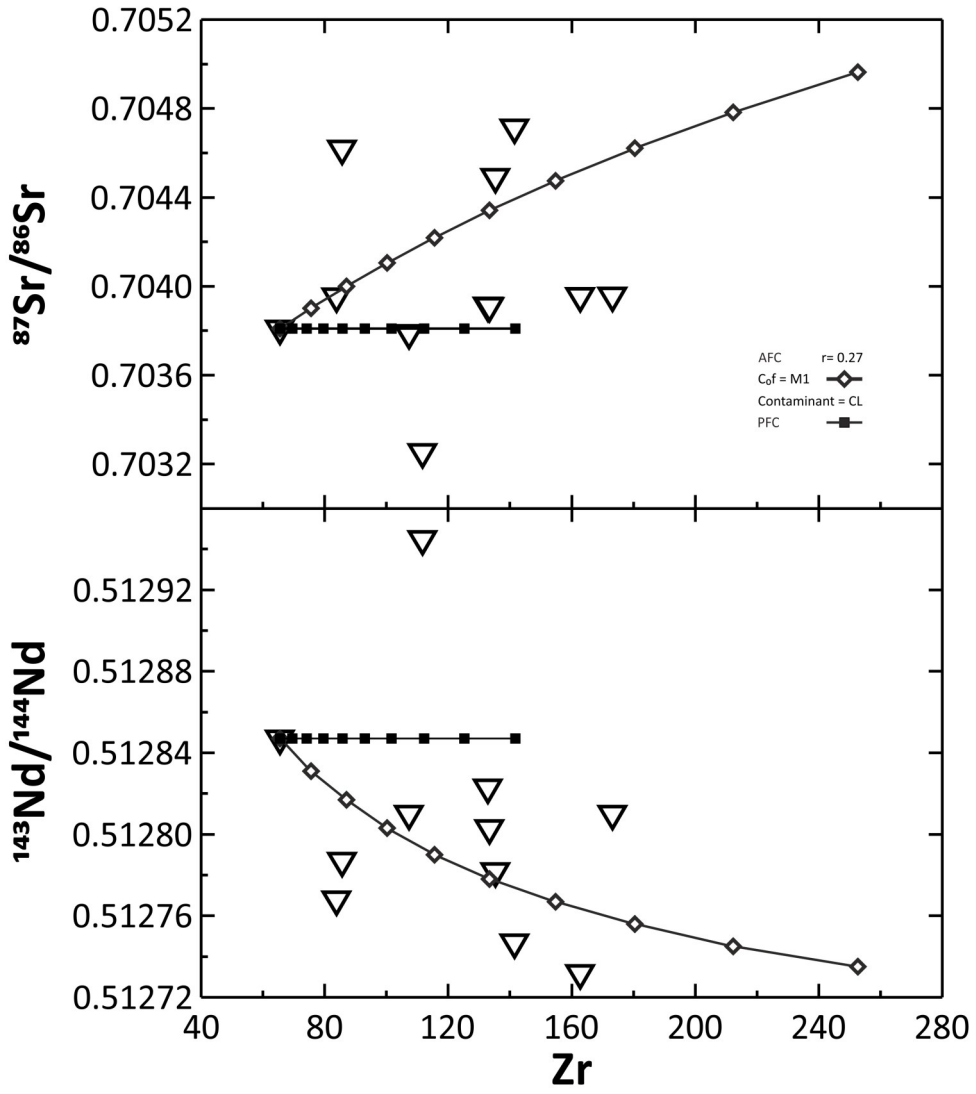

Fig. 7.12 Sr and Nd isotopic ratios vs. Zr for the calcalkaline rocks of the Parícutin-Cherán alignment. Black lines with diamonds represent AFC models calculated for initial sample M1 contaminated with the CL contaminant (Table 9) and the parameters specified in the figure. Diamonds and squares indicate equal F steps in the range F = 0 - 0.628. For comparison a perfect fractional crystallization (PFC) model is plotted in a black line with squares.

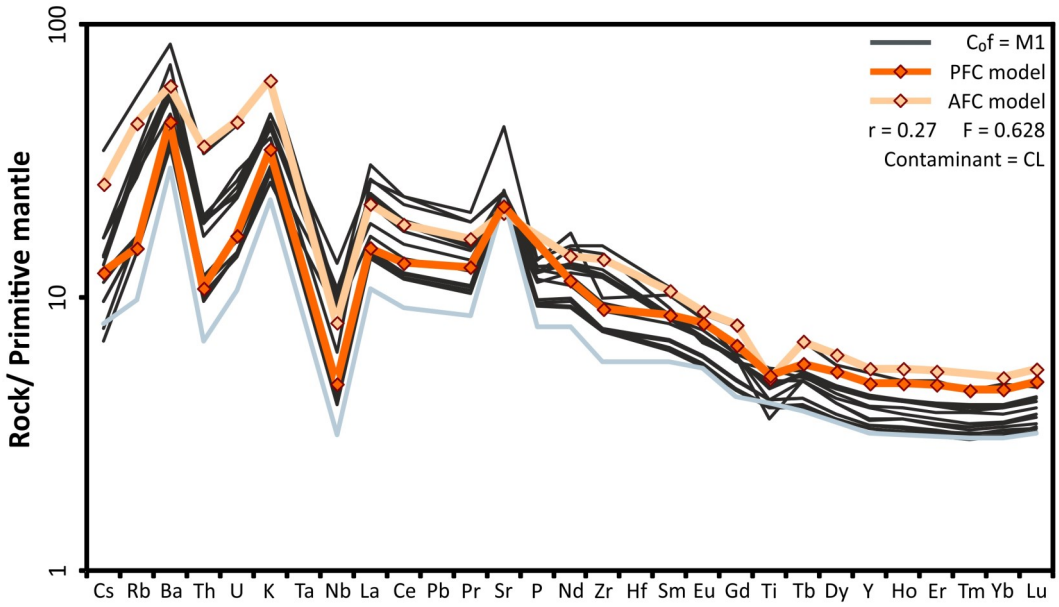

Fig. 7.13 Normalized multielement diagram for calcalkaline rocks of the Paricutin - Cherán alignment. Lines with diamonds represent FC and AFC models calculated for initial sample M130 contaminated with the CL contaminant (Table 9) and the parameters specified in the figure and Kd values of Table 11. Normalization Primitive mantle values after Palme & O'Neill (2014).

Northern sector

Following the same procedure, a first approximation to the physical conditions of the process was obtained considering major element variations and simple FC (Fig. 7.1). Acceptable results were obtained considering an initial composition similar to the less differentiated samples (e.g. M129 and M130), adjusted to allocate water contents of about 3%, crystallizing under the QFM+2 buffer from 1170 °C to 900 °C in a range of pressures from 7 kbar up to surface levels, involving the fractionation of Plg 60 % + Ol 9 % + oxides 7 % + Opx 12 % + Ap 1 % + Cpx 11 %. In this case the most prominent feature relative to the alkaline series is the presence of Opx and, according to the calculated model, larger amounts of plagioclase fractionation and smaller of olivine. These results are in agreement with the petrographic observations and what is usually expected for calcalkaline differentiation series (see for example Grove & Baker, 1984; Tatsumi & Suzuki, 2009).

The overall increase in $^{87}Sr/^{86}Sr$ ratios with any differentiation index again suggests that AFC processes are generalized in these lavas. Considering the less radiogenic

terms of the series, which coincide with the less evolved rocks mentioned above, the best fit (Table 10 and Fig. 7.8, 7.9 and 7.10) considers contamination by a granitic component similar to that estimated for the T2 alkaline series (with considerably higher Zr amounts) under similar conditions (r ~0.27 and ~35 % crystallization) and a fractionating assemblage similar to that suggested by the major element calculations, although a better adjustment to the observed variations is obtained with slightly lower amounts of Plg fractionation (at the assumed partition coefficients for this phase; see Table 11). While this model can be considered as an acceptable first estimation to the process that controls the isotope and trace element variations present in the calcalkaline rocks, it can be observed that this series is compositionally more variable than the alkaline rock trends. In fact, the increasing degree of compositional heterogeneity towards the more evolved terms favours the participation of a wider range of potential contaminants with contrasting isotopic signatures (as we have also seen for the T2 trend).

Parícutin-Cherán alignment (Southern Sector)

The Parícutin-Cherán alignment encompasses in about 40 km a series of monogenetic volcanic vents along a SW-NE direction, between the Parícutin volcano at its SW end and near the city of Cherán at its NE limit. In this context, the closely located presence of the well-studied Parícutin volcano is considered as an advantage in order to compare the petrogenesis of small monogenetic vents and middle sized volcanoes.

The lavas sampled in this alignment also show isotopic and trace element characteristics suggesting that they are the result of an AFC process. Therefore we have applied a modelling approach similar to the previous cases.

Considering sample M1 as one of the least radiogenic and evolved samples in the alignment, the best fit (Fig. 7.11, 7.12 and 7.13) is given by a fractionating assemblage made out of Plg 55 % + Cpx 11.6 % + Ol 9.5 % + Opx 12.6 % + Mt 6.3 % + Ill 1.1 % akin to the petrographic observations. In order to achieve the compositional ranges displayed though, the model requires the involvement of a granitic component as a contaminant at an r ~0.27 and F ~44.2 %. In general terms, the granite composition reported by Blatter et al. (2007) is the one that, when assimilated, best fits the geochemical varia-

tions of the alignment rocks for major elements, $^{87}Sr/^{86}Sr$ and $^{143}Nd/^{144}Nd$ isotopes and many trace elements (Ba, Pb, Y, Nb, La, Ce, Sm, Gd, Dy, Ho, Er, Yb, Lu). However, for certain elements either lower or higher contents are required to better adjust the element-element and multielement diagram tendencies. Specifically, the contaminant would need lower values of Cs, Rb, Th, U, Hf, Ta, Pr, Nd and higher of Sr, Zr, Sc, Cr, Ni, Co, V, Eu and Tb. Taking those values from other La Huacana granites reported in the area (Ortega-Gutiérrez et al., 2014, and Luhr & Carmichael, 1985) the model gets a better fit, but even with these changes some elements still show discrepancies with the model (mainly for LILE and LREE) implying that the contaminant must be more enriched than the ones selected and/or very heterogeneous.

On the multielement diagram, together with the AFC model we have plotted a perfect FC model (PFC) as comparison. The contrast between these two lines evidences the importance of the contamination with a granitic component as the FC model is not able to reproduce the enrichments shown for LILEs, HFSEs and LREEs.

Middle-size volcanoes

An important feature of this volcanic field is the presence of middle size volcanoes, characteristic in evolved monogenetic volcanic fields (McGee & Smith, 2016). In the context of this work and previous ones developed in our research team, here two examples are presented: El Metate and Parícutin.

El Metate is a shield volcano located in the southern sector of the MGVF (N 19° 32’ 19”, W 101° 59’ 27”) that has recently been recognized as the most voluminous Holocene andesitic effusive eruption in the world (Chévrel et al. 2016). It is considered monogenetic, despite being a shield volcano, because its activity took place on a single ~34 yr eruption at ~AD 1250 (^{14}C on two paleosols; Chevrel et al. 2015) outpouring 15 identified lava flows of calcalkaline composition and variable differentiation degrees that covered an area of about 103 km^2. A geochemical study of the lavas and the results from the thermobarometrical calculations were compiled in Losantos et al. (2014), and summarized here.

The mineralogy of the sampled lavas is represented by plagioclase, orthopyroxene and clinopyroxene as well as occasionally olivine and amphibole. Oxides also ap-

pear as matrix crystals. These rocks are represented almost exclusively by andesitic terms with a relatively narrow SiO_2 range (61 - 55 %) and low #Mg (66 - 58) contents that indicate they represent differentiated terms. This is supported by the variations in major element Harker diagrams where these rocks present in general a negative distribution against silica but distributed on two distinct trends that sometimes show contrasting tendencies of enrichment/depletion. For example, in the case of K_2O, Na_2O and Al_2O_3, one group of samples show a negative tendency while the other has it positive with respect to silica.

Temperatures calculated from mineral-liquid geothermobarometers for olivine, plagioclase and pyroxene, suggest that olivine was the earliest fractionating phase (1232 - 1198 °C), followed by plagioclase (1162 - 1126 °C), orthopyroxene (1147 - 1027 °C) and clinopyroxene (1147 - 1018 °C). In this sequence Ol ceases to crystallize with the appearance of Opx and the same happens with Plg phenocrysts with the appearance of Cpx. Pressure estimations indicate that crystallization started at ~8 kbar (referred to a single value from an Opx), although most of the pressures are found between ~6.5 kbar and 0.5 kbar, with a direct P/T correlation suggesting that the process took place from a depth of ~30 km and progressed up to surface levels. Water contents in the melts during crystallization of plagioclase were estimated to be ~1.6 %.

The temperatures calculated for amphiboles, provide a crystallization range between 995 and 922 °C, at an average pressure of 3.5 kbar and water contents between 5.2 % and 6.9 %. Although these values could agree with a scenario where amphibole represents a late crystallization phase belonging to a previous fractionating sequence, the systematic presence of disequilibrium textures (rounded borders, opacite rims and coronitic textures), which are also observed in other phases, and the fact that amphibole thermobarometry is based only in the mineral composition (regardless if they are in equilibrium or not with the host rock) suggest that other possibilities such as open-system crystallization cannot be discarded. In consequence, these amphiboles could also represent xenocrystals and not the last stage of crystallization.

The major elements variations suggest that El Metate lavas evolved through two contrasted differentiation trends. In every case Plg, Opx and Cpx appear as phenocrystals so it can be assumed that they have participated in the fractionation process. Oli-

vine on the other hand is only found in the least differentiated terms of the high MgO trend and amphibole, even though characteristic from the lower MgO trend is present only in the most differentiated terms of both trends. With respect to the differentiation process, the usual presence of disequilibrium textures in many of the phases suggests a relatively complex evolution (see Zellmer et al., 2016). A reasonable hypothesis would be to consider evolution within an open system that could imply both assimilation of xenolithic material and new magma inputs into the system, a not uncommon scenario in the MGVF (see Cebriá *et al.*, 2011b; Corona-Chávez *et al.*, 2006; Chesley *et al.*, 2002; Luhr & Carmichael, 1985; Urrutia-Fucugauchi & Uribe-Cifuentes, 1999).

The calculated thermobarometric conditions and the major element variations can also be explained if amphibole is considered as the last phase of crystallization. This would explain the presence of Amp in the most evolved terms of both differentiation trends producing a characteristic K_2O depletion as silica increases (consequence of amphibole fractionation). The limited pressure range (between 5 and 2.5 kbar) displayed by this phase would also explain its disequilibrium textures, consequence of magma degasification and a drastic reduction in H_2O content when the magmas reached superficial levels. Like in the case of Amp, disequilibrium evidences for other phases can be explained by their destabilization, after crystallizing in previous stages of differentiation, as physicochemical conditions vary in subsequent stages of evolution. For example, Plg destabilization can be caused by the increase of water content during crystallization. As we have seen, when Plg is crystallizing the calculated water contents are around 1.6 % at the onset of crystallization reaching up to 6.9 % when Amp crystallizes. This situation is relatively frequent in calcalkaline magmas and has been observed as well in nearby volcanoes like Parícutin (Cebriá et al., 2011b) where the disappearance of Plg as a phenocrystal, coinciding with the appearance of Opx, was interpreted as a consequence of H_2O increase due to a water input caused by assimilation of a cortical component.

Parícutin is another example of this type of intermediate volcanoes. This monogenetic cone, located in the southern sector of the MGVF (N 19°39'36" - W 102° 15'05"), represents its most recent eruptive activity (1943 - 1952) and is a world reference for calcalkaline series originated by an AFC process (McBirney et al., 1987). In the

first study of this volcano performed by Wilcox (1954), supported on petrographical observations and major element variations, this author concluded that neither crystal fractionation nor assimilation alone could have given rise to the series of lavas erupted and therefore it had to be a combination of both. He also defended that the assimilation of Phanerozoic continental crust occurred before the eruption in a compositionally zoned magmatic reservoir but could not prove if the thermal conditions were suitable for such a process. Later on, Miesch (1979) divided the evolutive process into three stages based on the three different linear trends identified for major elements. Those stages were studied via mass balance of trace elements and isotopes and explained as a first simple crystal fractionation process of Ol and Plg followed by two phases of AFC with a component enriched in radiogenic Sr and fractionation of Opx and Plg on a zoned magmatic chamber (McBirney et al., 1987). More recently, Luhr (2001) redefined the stages on the bases of their K_2O content: The first one with a flat volume/K_2O tendency, or K_2O < 1 wt %, from February to July 1943; the second one with a slightly positive volume/K_2O tendency, or K_2O ~1.2 wt %, from August 1943 to 1946; and the third

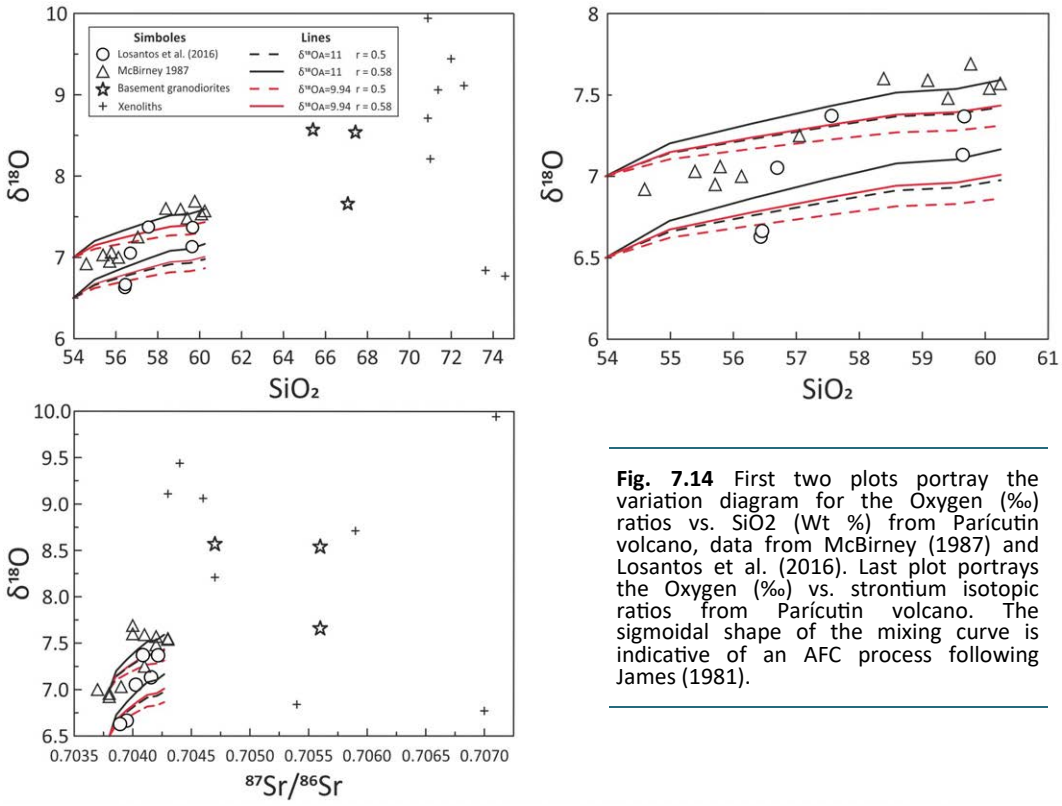

Fig. 7.14 First two plots portray the variation diagram for the Oxygen (‰) ratios vs. SiO2 (Wt %) from Parícutin volcano, data from McBirney (1987) and Losantos et al. (2016). Last plot portrays the Oxygen (‰) vs. strontium isotopic ratios from Parícutin volcano. The sigmoidal shape of the mixing curve is indicative of an AFC process following James (1981).

one with a marked volume/K_2O tendency, or K_2O from 1.2 to 1.7 wt %, from the end 1946 to 1952. He interpreted the compositional gap between the first and the second stages and the time dependent wide variation in K_2O at equal SiO_2 contents as a probe of the eruption of several magma batches before the compositional change in 1947 (interpreted by McBirney as an increase in cortical contamination). This idea was further developed by Erlund et al. (2010) who proposed an alternative model to the stratified chamber on the basis of the different composition and eruptive style between te two firsts stages. This author suggested that a magma batch, different from the one that produced the first stage, fed the second and third ones. The third stage though was explained as the extrusion of the most evolved magma stored in a dyke and sill complex. The magmas of the first stage then would have ascend from a deep reservoir and the others from a dyke and sill complex where the magma gets easily contaminated for being in close contact with the host rock. This hypothesis is sustained by their Ol crystallization depth data extracted from melt inclusions that gave 14 km depth for Ol in the first phase and much shallower for the second and third. A different approach was taken by Cebriá et al. (2011b) who explained the geochemical variations as changes in the fractionating mineralogy with a quantitative modelization using the software "PELE". In their model the AFC process would have been active from the beginning, as the calculated lines of descent (considering the fractionating assemblage proposed by Wilcox) did not support a simple crystal fractionation scenario at any point. The contaminant, given the great dispersion in the isotope-element diagrams, was interpreted as a consequence of the participation of a heterogeneous granitic component. Since from a thermodynamic point of view it was not possible to justify high rates of assimilation of a solid, they proposed that the contaminant could be represented by a granitic melt. McBirney et al. (1987) also acknowledge this, for their Ol and Plg crystallization heat calculations proved to be insufficient for assimilation, but proposed instead that new heat input to enhance assimilation could have arrived from the convecting magma that remains in the chamber. Rowe et al. (2011) on the other hand, found an abrupt compositional variation in incompatible elements that they interpreted as several small magmatic bodies with independent evolutions.

In order to complement the geochemical information and the quantitative petrogenetic AFC model for Parícutin, we analysed the oxygen isotopic values of a representative group of lavas that did not show significant signs of secondary alteration. The results of this study were presented in Losantos et al. (2015) and are part of the ongoing work on the oxygen isotope variations for the volcanic field.

The behaviour of the oxygen isotopes during an AFC process depends on the isotopic ratio of the initial liquid ($\delta^{18}O_0$), the isotopic ratio of the assimilated material ($\delta^{18}O_A$), the ratio of assimilated material versus crystallized material (r) and the percentage of residual liquid (F). For this model, we choose as starting value for the initial liquid isotopic ratio the lowest value found in the volcanic belt ($\delta^{18}O_0$ = 6.3 %; Straub et al. 2014) and an isotopic ratio calculated from a $\delta^{18}O_0$ value analysed in an Ol from Parícutin ($\delta^{18}O_0$ = 6.99 ‰; Johnson et al. 2009).

As shown in the diagrams though (Fig. 7.14), the $\delta^{18}O_0$ that best fits the data is more restricted (6.5 - 6.99 ‰) than the one we used. The isotopic ratio of the assimilated material was taken from one of the xenoliths found in the 1943 ejecta of the volcano. Specifically the 51-W-1 xenolith (McBirney et al., 1987) was chosen for showing the highest ratio of all ($\delta^{18}O_A$ = 9.94 ‰) and, even so, calculations with that or an inferior value did not allow reproducing the observed slope on the data, been necessary a value of at least $\delta^{18}O_A$ = 11 ‰, similar to the highest values observed for granitic rocks (see Bindeman, 2008). On the other hand, the initial ratio of assimilated material versus crystallized material (r = 0.5) and the percentage of residual liquid (F) were both extracted from the model in Cebriá et al., (2011b). Again, that initial value of (r = 0.5) did not reproduce the observed slope in the data and a value of r = 0.58 or lower seemed necessary to fit the curve. Therefore, the best fit to the data was performed by a model with the following parameters: $\delta^{18}O_0$ = 6.5 - 7 ‰; $\delta^{18}O_A$ = 11 ‰ and r = 0.58.

It has been found that, for the same r value, the increase of $\delta^{18}O_A$ increases slightly the slope but that the variation of r at a given $\delta^{18}O_A$ has a greater effect. As a direct consequence, we can determine that the high value of $\delta^{18}O_0 \approx 6.5$ ‰, too high for been primitive, would therefore imply a mantle source enriched by subduction fluids and that the high ($\delta^{18}O_A \geq 11$ ‰) isotopic values for the assimilated material can rule out the so far analysed xenoliths and granitic rocks in the area. The very high pro-

portion of assimilated material ($r \leq 0.58$) would as well require that contaminant to be partially molten in order to suit thermodynamic requirements. This model agrees with those established by Erlund et al. 2010 and Cebriá et al. (2011b) as long as it opts for a continuous AFC process from phase 2 onwards but requires a mechanism that allows a high rate of assimilation.

Suite comparison and discussion

The results obtained from the petrologic modelling presented above suggest that in the MGVF most geochemical variations can be explained in terms of AFC processes involving the assimilation of granitic basement components. The AFC modelling results involving similar rates of assimilation and crystallization and the variations displayed in the Harker diagrams for K_2O, CaO and most trace elements also suggest that most geochemical differences observed in the initial magmas of each series were probably preserved through differentiation. Therefore, the presence of a suite of alkaline rocks (T2) with geochemical characteristics intermediate between the alkaline T1 and CA series is very unlikely the result of derivation from T1 through differentiation and contamination.

The T1 alkaline trend seems to be produced at the deepest and highest temperatures (11 - 4.5 kbar and 1260 - 1100 ^{o}C) relative to the other groups showing as well the lowest initial water contents (1.5 %) and oxidation conditions (QFM+1), contrasting with the CA suite that appears to start crystallizing at shallower levels and lower temperatures (7 kbar - surface and 1170 - 900 ^{o}C) at more oxydizing conditions (QFM+2) which agrees with the higher water contents assumed (3 %). The T2 alkaline rocks , on the other hand, display intermediate values (P = 8 kbar - surface, T = 1200 - 1010 ^{o}C, Oxygen buffer QFM+1 and initial H_2O = 2 %).

Despite their differences in physical crystallization conditions, both alkaline trends seem to have undergone a similar petrogenetic process, through equivalent crystallization percentages (30 %) and very similar contamination parameters with analogous crustal components. Additionally, the alkaline magmas do not present petrographic evidences of stalling within the crust, which supports the inference obtained

from the relatively high assimilation rates obtained in the model that the granitic component are likely partially molten by the arrival of the basaltic magma. Finally, most of the differences between both alkaline trends cannot be explained by a difference in the composition of the contaminant, the assimilation rate or the fractionating assemblage and therefore must be a consequence of them having different mantle sources.

Concerning the CA suite as a whole and in general terms, crystallization began at shallower levels and with higher contents of magmatic water, which is a common situation in subduction related magmas. But to study these rocks it was necessary to divide them into a north and a south sector to account for their heterogeneity. The model for the north sector determines that the contamination was verified with the same or very similar crustal contaminant as the one described for the spatially-related alkaline suite but at a slightly lower assimilation to crystallization ratio (r ~0.29), thus we can conclude that the contaminant in the north sector was very similar for all the suites with perhaps only local variations.

The CA rocks of the southern sector alignment however, are characterized by a greater crystallization percentage compared to CA rocks in the north (47 % and 35 % respectively). Their ratio of assimilation vs. crystallization remains the same as in the north but the contaminant changes. Here none of the compositions described (xenoliths or basement rocks) adequately fit the model. This means that either the contaminant is represented by a basement rock (or a combination of several) that have not been sampled yet.

The intermediate volcanos, also characteristic of the south sector, are here represented by El Metate and Parícutin and display some common features. Both edifices are considered monogenetic for their products were emplaced on a single eruption that lasted several years. The composition of those magmas is calcalkaline and shows signs of contamination, most likely with a partially molten contaminant. The difference between these vents and the monogenetic cinder cones is that the former show signs of having some sort of magma storage within the crust where the magmas differentiate and contaminate. Evidences for this are the petrographic characteristics (e.g. complex zonation patterns and destabilization features) observed in some phases, the Ol crystallization depth data by Erlund et al. (2010) in Parícutin and the mineral crystallization

depth values (Losantos et al., 2014) in El Metate. Both seem to have started the crystallization at deep depths (~14 Km in the case of Ol in Parícutin), sometimes even at crust mantle boundary depths (~30 Km in El Metate) and then stalled at more superficial but variable depths (~24 km and 13 Km again in El Metate), probably in a dyke and sill complex like the one proposed by Erlund et al. (2010).

8. Summary of results and discussion

Deciphering continental arc magmatism from petrologic, geochemical, and tectonic points of view is challenging and has great significance for understanding the formation and evolution of continental crust. While it is accepted that magmatism in such environments is driven by dehydration reactions produced in the subducting slab, this is an oversimplification and magma genesis in a continental volcanic arc is not a straightforward subject since in these environments many different processes converge, such as contamination of the mantle source by fluids, melts and subducted sediments; interaction of asthenospheric derived magmas with the lithospheric mantle; contamination of the magmas with the crust; and crystal fractionation (see Ducea et al., 2015 and references therein).

In order to properly discriminate between different mantle source enrichment processes the study of primitive samples is essential. Unfortunately the samples collected for this work show geochemical and petrologic characteristics that are typical of evolved magmas and although very few might arguably represent little differentiated terms, none can actually be attributed to primitive terms. Therefore, modelling was focused on the prevailing differentiation processes. Nevertheless, the obtained results led to obtain useful inferences on the characteristics of the possible primary melts. The integration of these findings with available information on the magmatism and geodynamics in this region has allowed us to propose a comprehensive petrogenetic interpretation that may explain current observations and also represent the basis for future research.

Petrogenesis

Alkaline vs subalkaline suites identification was performed from several well-established procedures, including the TAS diagram (Le Bas et al., 1986), the dividing line of Irvine & Baragar (1971) and Peacocks' method (Peacock, 1931). Furthermore,

the geochemical variations allowed us to identify two distinct differentiation trends within the alkaline suite whereas the calcalkaline suite is composed by a rather heterogeneous group of rocks, not clearly related through a simple differentiation process.

As we discuss here, whereas the alkaline suite can be understood in terms of similar differentiation processes from primary melts generated from different (but probably genetically-related) mantle sources, the petrogenesis of the apparently heterogeneous calcalkaline suite can be examined considering subgroups in terms of shared geodynamic links.

Alkaline suite

Alkaline Trend 1

As we have seen, the first alkaline trend includes samples with typical OIB trace element signatures such as high contents for most trace elements relative to MORB (in fact, the highest relative to the other groups in the region), and Nb-Ta positive anomalies and negative in U, Pb in normalized multielemental diagrams (see for example Halliday et al., 1995 and Weaver, 1991). However, despite having the overall lowest silica contents observed in the field, these lava samples do not present primitive signatures. Instead, they show both petrologic and geochemical features that can be attributed to differentiation processes (e.g. generalized holocrystalline textures, low #Mg and linear variation arrays for most major elements and trace elements relative to differentiation indexes, see chapter 6). Additionally, the $^{87}Sr/^{86}Sr$ ratios of this group of lavas are relatively high (mostly over 0.7035) compared to typical values in primitive OIBs (~0.7030 for HIMU-like and FOZO-like endmembers; Willbold & Stracke, 2006) and more importantly, display a direct correlation with silica, which considering the evolved character of these rocks, is indicative of a differentiation-related process involving contamination with a ^{87}Sr-rich component. Such variations are in agreement with the complementary linear arrays displayed on the Nd, Pb and oxygen isotope variations relative to $^{87}Sr/^{86}Sr$ and SiO_2. Therefore, it is concluded that many of the observed geochemical

features (especially concerning some trace elements and isotope ratios) are consequence of AFC processes, by assimilation of a crustal component.

According to petrographical observations, mineral chemistry and thermobarometry calculations (see chapter 5), it was concluded that the crystallization sequence could began with small amounts of apatite and ulvöspinel as they appear included in olivine and plagioclase (Fig. 5.10), which are the minerals that yielded the higher temperatures of crystallization. However, the geochemical data (e.g. progressive enrichment in P_2O_5 and low contents of Mg, Cr and Ni) suggest that the sequence likely started with the fractionation of more forsteritic Ol (not found in the analyses performed) and that apatite, although crystallizing, did not fractionate in significant amounts. The highest temperature and pressure values obtained for a phenocrystal analysed in these rocks is plagioclase followed by olivine. The last appearing phase according to thermobarometric values would be Cpx, although an earlier crystallization cannot be dismissed as the most Ca-rich ones are found included in plagioclase phenocrystal cores (e.g. Fig. 5.4A). As mentioned before, the high Fe, Ti, P and Mn and low Sr contents further supports scarce fractionation of apatite and oxides and moderate of plagioclase towards the last stages of evolution. This also explains the relative lack of anomalies for Sr and the positive Ti spikes at silica poor contents that turn into a marked negative spike at silica richer compositions indicating plagioclase fractionation in the case of Sr (Wilson, 1989) and fractionation of Fe-Ti oxides.

This crystallization sequence can be roughly reproduced by modelling with MELTS-based software considering a fractional crystallization process from an initial sample similar to M110 with H_2O contents of about 2%. This model yielded estimated crystallization conditions of 1260 - 1100 °C from ~11 kbar to ~4.5 kbar involving an assemblage of Plg 63 % + Ol 25.5 % + oxides 9 % + Cpx 2 % +Ap 0.5 %. While these parameters agree in general terms with the phases identified on the petrographical study and with the calculated temperatures and pressures, it does not satisfactorily reproduce the variations observed of all the elements due to some limitations of the program (see chapter 7) and also to the fact that the actual process would likely involve crustal assimilation. Unfortunately, using MELTS-based approaches to refine the AFC model would introduce higher uncertainties due to the assumed complexity of the process,

the limitations of the software and the high number of unknowns involved which are required to perform the calculations. Therefore, to refine the quantitative differentiation model we have considered the classical expressions of DePaolo (1981) for AFC processes, limited to isotope ratios along their corresponding trace element variations. According to the calculated model, the crystallization degree and the fractionating assemblage were not dissimilar from the results obtained from the major elements FC approach, resulting in about 25 % crystallization of an assemblage composed of Plg 60 % + oxides 19 % + Ol 15 % + Cpx 6 %. The contamination parameters involved an assimilation/crystallization ratio (r) of ~0.3 and the assimilation of a crustal component with a trace element and isotopic signature akin to granite basement rocks such as those reported by Ortega-Gutiérrez et al. (2014) and Blatter et al. (2007).

According to the above observations and modelling results, the T1 trend represents a group of magmas related through a differentiation process from an initial OIB-like magma similar to sample M110. Crystallization started at the highest temperatures (~1260 °C) and greatest depths (~16 kbar) of all studied rocks, undergoing Ol fractionation in the early stages of evolution, followed by Cpx + Plg and oxides. Apatite crystallized but it did not fractionate in significant amounts.

The proposed model depicts the actual process in general terms but it would certainly require further refinement (e.g. obtaining some constraints on the characteristics of the primitive melts). This is evidenced by some apparent inconsistencies in some geochemical data such as the absence of a perfect correlation between SiO_2 and isotopic ratios, which can be explained if the AFC process involved relatively heterogeneous contaminants and/or not all samples were contaminated in similar amounts. Additionally, some features usually present during crustal assimilation but nearly absent in the T1 rocks can also be explained considering the characteristics of the contaminants. For example, U, Pb and Sr are usually enriched in the crust (see Taylor & McLennan, 1985; Condie, 1993) and therefore, assimilation of such components by OIB basalts should usually imply the absence of negative spikes in the normalized trace element diagrams for those elements. In the T1 lavas this is not observed although the spikes tend to be weaker towards the more enriched terms. This feature can be explained if we consider that the assumed contaminants (based on actual basement gra-

nitic compositions) are characterized by low concentrations of U, Pb and Sr relative to average upper crust values (see Taylor & McLennan, 1985 and Condie, 1993). Additionally, the tendency towards developing a negative Sr spike is further enhanced (also satisfactorily explained in the model) by the coupled fractionation of plagioclase.

Another important implication concerning the origin of this group of rocks results from the scarcity of petrographical signs of long-term storage (e.g. absence of crystals with oscillatory zonations and of resorption or disequilibrium textures in the minerals) compared to the CA and T2 lavas. This suggests that crystallization may have occurred in the absence of well-developed crustal chambers. If this is correct and taking into account the parameters obtained from the geochemical modelling that suggest relatively high assimilation rates, a classical AFC process (i.e. solid wall-rocks being progressively digested by the basaltic melt as it crystallizes in a magma chamber) does not seem probable and an alternative contamination process must be proposed.

A plausible mechanism would be to consider that the differentiation process took place during ascent, as supported by the range of pressures obtained by geothermobarometry calculations, from the base of the crust up to shallower levels (a situation that is considered in the initial FC modelling approach), and that assimilation involved incorporation of the granitic components from regions where melts were either already present in the crust or that the crust was prone to melt due to the prevailing physical conditions (e.g. high-T) at the arrival of the basaltic melts. Such scenario has already been proposed in the region (McBirney et al. 1987; Erlund et al., 2010; Cebriá et al 2011b) and attributed to magma underplating which would raise crustal temperatures and would favour the presence of melts (see Annen, 2006; Annen & Sparks, 2002). Such a mechanism is also required if we consider that the rates of assimilation obtained in the numeric modelling (r ~0.3) are relatively high for a basaltic magma digesting granitic rocks. If these inferences are correct, it seems plausible that the crystallization of the OIB melts started at depths around the base of the crust where it could have been stalled for a short time undergoing oxides, forsteritic olivine and plagioclase fractionation as mentioned before. Later on those magmas would continue ascending and differentiating, assimilating granitic melts along their way to the surface. This scenario would agree with the lack of minerals with petrographic evidences of

crystallization during long periods of time in magma chambers, the high pressures obtained in plagioclase phenocrysts and the heterogeneity of the contaminants.

Alkaline Trend 2

The T2 trend is also classified as alkaline since it plots within the alkaline field of the TAS diagram and at 54.9 SiO_2 in Peacock's diagram, but many other geochemical features are closer to the calcalkaline suite. For instance, it displays similar Fe, Ti, Mn and P contents (lower than T1) and variation patterns (inverse correlation in Fe, Ti and P vs. silica) as well as a normalized trace element signature intermediate between T1 and CA, characterized by negative Ti and P spikes, positive U, Pb and Sr spikes and a tendency towards negative Nb-Ta thoughts.

Like the T1 trend, T2 rocks cannot be considered as primitive and all show petrological and geochemical signs of some degree of differentiation as described in chapters 4 and 6. In this case, the interelemental variations are again different from the T1 rocks and in some cases more similar to those observed in the CA suite. Again, their Sr-Nd-Pb-O isotopic signature and variations are in agreement with simultaneous assimilation of a crustal component.

According to the petrographic observations and thermobarometric calculations, the crystallization sequence for T2 alkaline trend likely started with the crystallization of apatite and ulvöspinel (as they are found as inclusions in olivine and clinopyroxene). However, the lack of depletions in TiO_2 and P_2O_5 in the less differentiated samples of the trend suggests that these phases did not fractionate in significant amounts during the initial stages of crystallization and only fractionated later on. Plagioclase is the mineral with the highest crystallization temperature calculated (~1250 °C), with olivine crystallizing either simultaneously or immediately after (~1240 °C), closely followed by clinopyroxene (~1200 °C). Orthopyroxenes from coronas and reemplacements are the lowest temperature (~1070 °C) minerals analysed for this suite although they show a higher temperature than the one obtained for the CA orthopyroxenes. An earlier crystallization for this phase cannot be discarded however as Opx displaying temperatures of 1105 - 1125 °C have also been found as inclusions in Ol and Pl. The calculated pres-

sures though, lower than the ones calculated for their host minerals (3.9 and 2.1 kbar respectively), cast doubt on whether they represent early phases or xenocrysts included by Pl and Ol.

The MELTS-based simple FC modelling reproduces the sequence of minerals except for Opx (which would suggest that this phase is actually represented by xenocrystals), and yielded a fractioning assemblage formed by Plg 64 % + Ol 27 % + Oxides 5 % + Cpx 3 % + Ap 1 % with estimated crystallization conditions of ~1200 ^{o}C - 1010 ^{o}C from P ~8 kb up to surface levels. The initial water contents required to achieve those results in the model are higher than those for T1 but not as high as in CA (H_2O ~2 %). The finally adopted model parameters, based on trace element and isotope data suggests again an AFC process involved the assimilation of a compositionally heterogeneous granitic component at similar values of crystallization (~30 %) and assimilation (r ~0.3) to those obtained for T1 rocks. As the parameters of the process for both alkaline trends are very similar, their distinct geochemical features, which are maintained in the initial liquids, are therefore very likely resulting from differences in the primary magmas which therefore must be inherited from their mantle sources.

However, in contrast with T1 rocks and similarly to the CA suite, the minerals of the alkaline T2 lavas are characterized by the presence of oscillatory zonation in some Cpx and Pl phenocrystals (i. e. Type 2 Pl), typical open system textures (e.g. patchy zonation and spongy cellular textures Type 3 Pl and Cpx) and the rocks show somewhat scattered distributions of the direct variations in isotopic $^{87}Sr/^{86}Sr$ values relative to SiO_2. All these features are in favour of some sort of magma storing (magma chambers?) where contamination by an ^{87}Sr-enriched component during differentiation would more likely occur.

Calcalkaline suite

As already described (chapter 6) all the sampled subalkaline rocks show geochemical features usually attributed to subduction related magmas such as positive anomalies for most LILE (except Ti and P), Pb and Sr, negative anomalies for Nb-Ta and Ti and a marked inverse correlation between total iron content and SiO_2, usually

attributed in this suite to early magnetite differentiation (Wilson, 1989). Despite these observations, this group of lavas displays a very wide compositional range of #Mg values (~31 to ~70 %) including the highest values observed in the field. However, as we have seen in previous chapters, on the basis of both geochemical and petrographic observations, none of the samples can be considered as primitive. On the contrary, their characteristics support derivation by variable degrees of crystal fractionation. Furthermore, their isotopic signature and variations also support the participation of high-^{87}Sr components.

From the petrographic observations, mineral chemistry and thermobarometric calculations we could infer that the differentiation sequence likely started with the crystallization of chromites as they are found almost exclusively included in olivine. Compared to the alkaline suite, especially the T1 trend, the CA suite is characterized by relatively higher Mg, Ni and Cr contents which can be explained by lower fractionation percentages of olivine and their hosted chromites. This is an expected feature since alkaline magmas usually fractionate more olivine than the subalkaline ones and therefore their Mg# in differentiated terms is in general lower for a given silica content. The mineral with highest temperatures of crystallization found is clinopyroxene (~1233 °C), followed almost simultaneously by olivine and plagioclase, both at similar temperatures (~1230 °C). Clinopyroxenes are more commonly found at temperatures lower than ~1110 °C and orthopyroxene crystallizes at the lowest temperatures both as pheno- and microphenocrystals (~1080 °C) and as coronas in olivine (~1190 °C). Thermobarometric information on the oxides present in the suite (ulvöspinel and ilmenite) could not be gathered, but the inverse correlation between Fe_2O_3 and TiO_2 vs. silica suggests that they must have fractionated from an early stage and continued crystallizing up to the final stages as evidenced by the oxides encountered in thin sections both as phenocrystals and matrix crystals. Apatite only appears in the matrix or as inclusions in the borders of larger crystals and therefore it could be inferred that this phase only crystallized during late stages. However, the low contents in P_2O_5, the inverse P_2O_5 vs. SiO_2 correlation and the fact that the negative P spikes for silica poor samples tend to become deeper with differentiation suggests that apatite fractionated during the whole process.

Major element FC modelling after the MELTS-based PELE software also suggested that, to achieve a fractionating assemblage similar to the one deduced from geochemical and petrographic data (Plg 61 % + Ol 5 % + oxides 7 % + Opx 15 % + Ap 0.5 % + Cpx 1 %) crystallization likely occurred at a temperature and pressure range lower than the one for T1 alkaline magmas (1200 - 900 °C and 8 kbar to surface levels), and about 2 % initial water content. Such parameters are in agreement with the usual amounts of water assumed for subalkaline magmas in subduction related environments and especially those reported in the MGVF (see Anderson, 1973; Johnson et al., 2010; Luhr, 2001; Pioli et al., 2008; Plank et al., 2013).

As already mentioned, the MELTS-based algorithm assumes fractionation of all the crystallizing phases and this might be the cause for some of the discrepancies of its modelling results. Additionally, other uncertainties have to be considered as well. For example, the maximum pressures of crystallization may be higher than assumed if we consider that plagioclase and clinopyroxene phenocrystals with oscillatory zonation could also represent high-depth crystallizing phases that got destabilized during their ascent, instead of xenocrystals as initially assumed. In this case initial depths of crystallization would be up to ~40 km (10.8 kbar max in Plg and 11.2 kbar in Cpx). Crustal assimilation, is another factor that probably played a role in the petrogenesis of these rocks but that it was not considered in that initial approach (the number of unknown parameters makes using the MELTS-based software for such modelling rather speculative). As we have seen, most samples of this suite present distinctive open system features like the usual presence of crustal xenoliths (sometimes partly digested; e.g. Ortega et al., 2014, and Corona, 2006), replacements and corroded minerals, spongy cellular “sieved” textures and reverse and patchy zonation found in some clinopyroxenes and plagioclases (Type 3 Plg), some even with more albitic cores than their corresponding crystal rims. All these features support a xenolithic origin from a more evolved lithology than the assimilant. Some geochemical variations (e.g. scattered patterns on major elements, especially for Al, K, Na and P, and direct correlation of $^{87}Sr/^{86}Sr$ and $\delta^{18}O$ relative to SiO_2) also favour crustal contamination as the origin for most of the rocks in this suite.

While the initial simple FC approach can be thought as a rough general framework for the conditions that prevailed during differentiation, it seems unlikely that more precise AFC modelling can be performed considering a large and geodynamically diverse area as the MGVF. This is evidenced by the compositional scattering of the CA lavas when considered as a whole. While in the alkaline suite, two distinct variation trends could be identified, this is not the case for the CA rocks. It must be taken into account that the alkaline suite is represented by more homogeneous volcanic types (basically small monogenetic vents and maars) and is geographically more restricted, whereas the CA rocks cover the whole volcanic field including a wider range of volcanic vent typology. Therefore, in an attempt to constrain the modelling of AFC for the calcalkaline suite, three different subgroups of rocks were considered: 1) calcalkaline vents of the northern sector, geographically (and probably geodynamically) related to the alkaline suite; 2) a group of outcrops in the southern sector corresponding to small monogenetic vents that form a well-defined alignment between the Paricutin volcano and the city of Cherán, and 3) individual middle-sized volcanoes (Paricutin and Metate). The individualization of such groups is basically based on geodynamic grounds, trying to consider together samples belonging to similar settings and/or volcanicity style.

Such subgroup individualization already reveals some interesting patterns on the SiO_2 - $^{87}Sr/^{86}Sr$ diagram (Fig. 6.11). For example, the rocks of El Metate volcano are distributed in two parallel arrays: one of them characterized by the lowest ^{87}Sr ratios ("High-Sr Metate") found in the field and another with higher ^{87}Sr ratios ("Low-Sr Metate"), but similar to other CA samples with the lowest values in the field. These two trends were already identified in the course of this research and confirmed by later works (see Losantos et al. 2014 and Chevrel, 2016). Another group of rocks ("Main CA trend array") comprises most of the remaining sampled CA rocks from both the north and southern sectors (including the Paricutin samples) and is characterized by higher ^{87}Sr values but a subparallel distribution to those described for El Metate. Finally, the Paricutin-Cherán alignment samples form a rather different array, characterized by relatively restricted SiO_2 values but a wider range of $^{87}Sr/^{86}Sr$ ratios, including the highest values reported for the field. Only one individual vent to the southeast of that alignment is also included in that array, which nevertheless overlaps the lowest SiO_2 end of

the main CA trend. In other diagrams such as $^{143}Nd/^{144}Nd$ - $^{87}Sr/^{84}Sr$ or $^{87}Sr/^{86}Sr$ - Ce/Pb is possible to further distinguish the relative distribution of those arrays.

On the $^{143}Nd/^{144}Nd$ - $^{87}Sr/^{84}Sr$ diagram (Fig. 6.10) most of the CA samples plot in subparallel trends oblique to the mantle array with similar slopes but at different $^{87}Sr/^{86}Sr$ contents. The exception is given by the Parícutin-Cherán alignment that follows a tendency more akin to that of the alkaline trends, parallel to the mantle array. Also, within the High-^{87}Sr Metate array the samples belonging to the Metate volcano follow a clear correlation trend whereas the other samples included in this field are scattered in the SiO_2 - $^{87}Sr/^{86}Sr$ diagram towards less radiogenic Sr values forming groups related by their geographical proximity.

On a $^{87}Sr/^{86}Sr$ - Ce/Pb diagram (Fig. 8.1) those differences persist (i.e. the different arrays plot in roughly subparallel trends at different $^{87}Sr/^{86}Sr$ contents except the

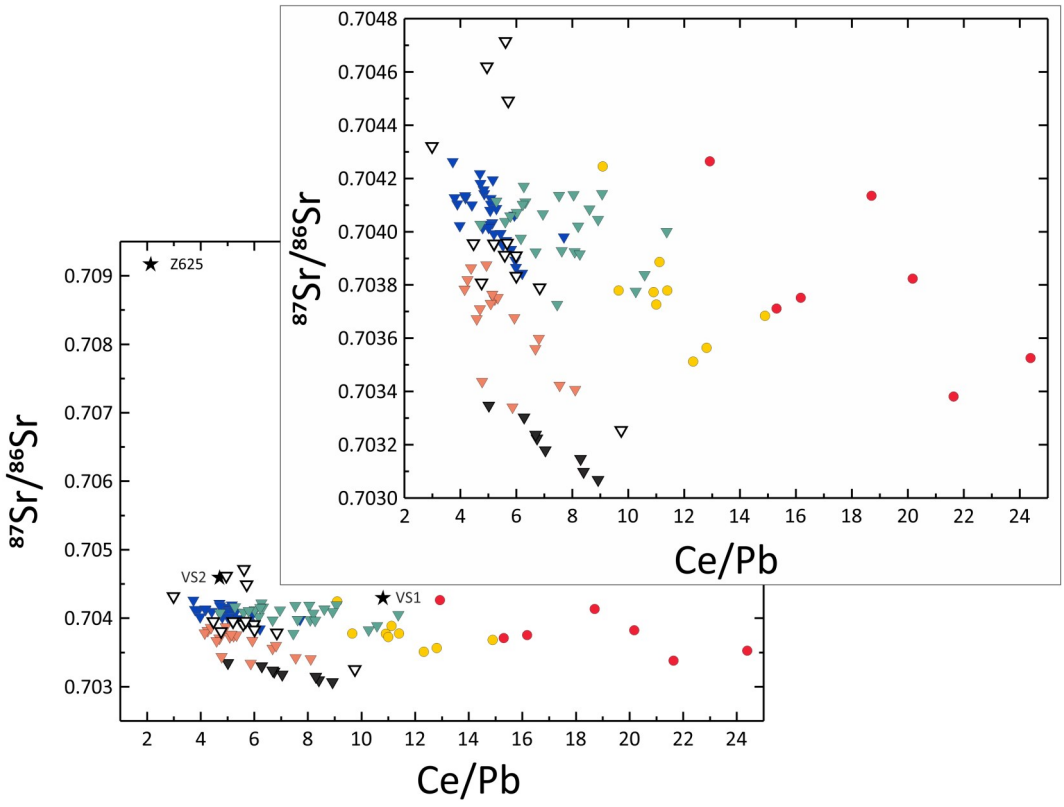

Fig. 8.1 $^{87}Sr/^{86}Sr$ vs. Ce/Pb diagram where the different trends can be clearly distinguished: Circles alkaline suite and triangles CA suite. Red dots T1 alkaline trend, yellow dots T2 alkaline trend, black triangles High-Sr Metate, orange triangles Low-Sr Metate, blues triangles southern Main CA trend, green triangles northern Main CA trend and white triangles Parícutin- Cherán alignment.

Parícutin-Cherán alignment that has a steeper slope). The average Ce/Pb mantle values are > 25 and (Chauvel & Hémond, 2000) and basaltic magmas in equilibrium with a typical depleted mantle source have Ce/Pb values > 12 (Mason et al. 1996), this is so because lead gets concentrated in the crust (Taylor & McLennan, 1985 and Condie, 1993) whereas Ce is immobile. Ce/Pb ratio can be therefore a good proxy to assess crustal contamination as a low Ce/Pb ratio would suggest contamination with the crust. In our case, the $^{87}Sr/^{86}Sr$ - Ce/Pb diagram displays the alkaline trends showing dispersed patterns at rather high Ce/Pb ratios (~10 to ~24) while all the CA arrays display negative correlations, as expected for magmas contaminated with the crust (i.e. the higher $^{87}Sr/^{86}Sr$ and the lower Ce/Pb contents, the greater crustal contamination). An interesting feature is the differences in slope within the Main CA trend, with the northern sector CA lavas diverging from the southern sector ones. While the samples from the northern and southern sectors plot together on the SiO_2 - $^{87}Sr/^{86}Sr$ and the $^{143}Nd/^{144}Nd$ - $^{87}Sr/^{84}Sr$ diagrams, here the northern calcalkaline rocks present a clear tendency towards the alkaline suite, probably due to the spatial proximity of both groups, thus supporting some geodynamic link that could have influenced the composition of their respective primary magmas. Hence the importance of considering these group of rocks independently from the southern “Main CA trend” regarding modelling. These observations confirm that, as expected, middle-sized volcanoes with well-developed lava series (i.e. resulting from evolution in a magma chamber) like Paricutin, El Metate or Jorullo must be considered independently for modelling purposes. In the case of El Metate, its distinct geochemical signature certainly deserves an individual treatment, already started in previous works and currently the subject of ongoing research. The Paricutin volcano also required its own modelling approach, but in this case it seems that its geochemical characteristics can be ascribed to the rocks of the “Main CA array” and therefore some of the petrogenetic inferences obtained for that volcano might be generalized for that group. In the case of the northern sector CA rocks, they also seem to belong to the “Main CA array” but they can be clearly distinguished from the general group on the $^{87}Sr/^{86}Sr$ - Ce/Pb diagram supporting that, as we have seen, they should be modelled separately to account for their geodynamic relationship to the alkaline suite. Finally, it also seems confirmed that specific alignments of small mono-

genetic vents such as the selected Paricutin-Cherán should also be considered independently for modelling purposes since they are probably petrogenetically related, as suggested by the likely related magma sources according to the geodynamics of monogenetic volcanism (see Németh & Kereszturi 2015; McGee, 2016, and chapter 1). This alignment includes the least differentiated (perhaps nearly primitive) composition among the CA rocks (M10), with the second lowest silica content (51.5 %), the highest #Mg value (70.4) and among the lowest Sr and highest Nd isotopic values, but it also comprises the most contaminated samples, with the highest $^{87}Sr/^{86}Sr$ and lowest $^{143}/^{144}Nd$ ratios (0.70471 and 0.5127) of the CA suite, among other features like a wide range and scatter of the Al_2O_3 and Na_2O contents for the same narrow SiO_2 range or a negative correlation in a $^{87}Sr/^{86}Sr$ vs. Ce/Pb diagram (Fig. 8.1).

In addition to the above proposed general guidelines for modelling specific groups of monogenetic vents, the above selection also implies some consequences concerning mantle sources and participating crustal components. As we have seen, the geochemical variations of the different suites studied can be explained in terms of AFC processes involving the assimilation of granitic basement components. While this does not seem to be a generalized situation in other Cenozoic volcanic fields of the TMVB (e.g. Gómez-Tuena et al., 2013), in the MGVF such processes appear to be ubiquitous, as already suggested in previous studies (Chesley et al., 2002; Hasenaka & Carmichael, 1987; Johnson et al., 2008; Lassiter & Luhr, 2001; Verma & Hasenaka, 2004). Nevertheless, the proposed petrogenetic models also imply that the initial magmas likely resulted from different mantle sources. This is further supported by the SiO_2 - $^{87}Sr/^{86}Sr$ diagram. For example, while perhaps a similar mantle source could be invoked for the main CA array in this diagram, other groups of rocks like those from El Metate and the Paricutin-Cherán alignment, require derivation from initial melts with contrasting compositions. Similarly, the different slopes of each array also suggest the participation of geochemically different crustal components.

In the northern sector the calculated model required the participation of a granitic component very similar to the ones described for the alkaline suite and with similar assimilation rates (r ~0.30) and with ~35 % crystallization. The increasing degree of compositional heterogeneity towards the more evolved terms favours the participation

of a range of potential contaminants or rather the existence of local variations with contrasting isotopic signatures. The calculated assimilation rate is again high on a thermodynamic basis, but as this suite does present abundant evidences of solid assimilation (such as frequent presence of crustal xenoliths occasionally partly digested, e.g. Corona, 2006) we can conclude that it probably assimilated both melts and rocks.

For the AFC modelling test of the southern sector alignment we considered the starting conditions obtained for the rocks of the north sector since it also reproduces in general terms (with the limitations mentioned above) the major element variations and the petrographic observations. The best fit to the compositional range is again explained by assimilation of a slightly different granitic component (CL in Table 9) at a rate of r ~0.307 and ~44.2 % crystallization. These requirements support the participation of compositionally heterogeneous granitic contaminants at similar crystallization and assimilation conditions.

The results obtained for Paricutin (Cebriá et al., 2011b and Losantos et al., 2015) as a representative of the middle-sized volcanoes, indicate similarities with the rest of the calcalkaline rocks in terms of the heterogeneity of the participating contaminants (a different granitic component was required) and the high assimilation vs. crystallization ratios ($r \leq 0.5$), again suggesting the participation of partially molten contaminants. The main difference of those larger volcanoes with the small monogenetic cinder vents lies in the presence of upper crustal magmatic chambers where the magmas may have evolved for longer periods of time.

Besides individual petrogenetic models for specific volcanoes or groups of volcanoes, an important question still remaining to be solved is if the different calcalkaline arrays are actually the consequence of evolution from different primitive melts. To test whether the range of compositions of the CA suite and the different identified arrays could be generated from the same primitive magma, some simple mixing tests were calculated for Sr-Nd trace elements and their corresponding isotopic ratios. As starting compositions we considered the only sample close to a primitive calcalkaline melt (sample M10) and also a primitive composition calculated from a melt inclusion in olivine as described in Johnson (2009) for the lavas of the Astillero volcano (closely located to Paricutin). Since the primitive melt compositions presented by Johnson (2009)

lack isotopic information a further assumption had to be made, adopting the Sr and Nd isotopic values from M10 sample (assuming lower ^{87}Sr available values do not significantly change the results).

These tests are summarized in the $^{87}Sr/^{86}Sr$ - $^{143}Nd/^{144}Nd$ diagrams of Fig. 8.2. In this kind of process the shape of the mixing curves in isotope-isotope diagrams depends on the ratio of trace element concentrations between the two mixing endmembers. Therefore the differences in the curves in our case arise from the difference between those of Astillero (Sr = 443 ppm and Nd = 9.6 ppm) and the M10 sample (Sr = 889 and Nd = 23.31) and the contaminants assumed.

This approach would then replicate the case of a limited range of primitive melts derived from a common source by different melting degrees.

The tests performed show that when plotting the mixing curves of different starting compositions (M10 and Astillero) against the same contaminant (exemplified here by the granite reported by Blatter et al., 2007 and the one assumed for the Pa-

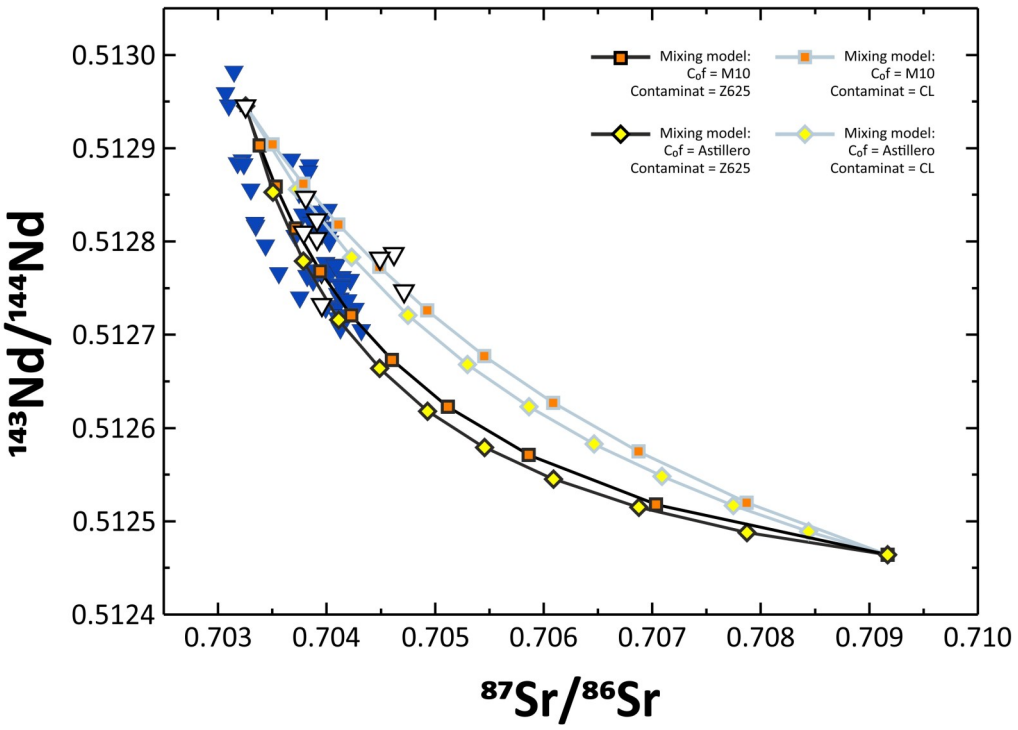

Fig. 8.2 Mixing models for M10 and Astillero starting compositions mixed with the contaminant assumed for the model of the northern CA sector and M10 and Hoya Álvarez starting compositions mixed with a contaminant compositionally equivalent to the granite reported in Blatter et al (2007).

rícutin-Cherán alignment, CL of Table 9), neither of them covers all the compositional range. As displayed in Fig. 8.2, the best fit for the Main CA array and the Metate trends is achieved by mixing the Astillero composition with the granitic composition reported by Blatter et al. (2007) while the curve that best suits the Parícutin-Cherán alignment is the M10 interacting with the contaminant assumed for the Parícutin-Cherán alignment rocks (CL in Table 9). In spite of the rather basic simplicity of this calculation, these results seem to confirm the interpretation that, since no simple model can reproduce all data, it seems more likely that a combination of more variable primitive magmas and contaminants would be required to reproduce the data thus supporting that both mantle sources and contaminants are heterogeneous at least at a regional scale.

Considering all the inferences on the petrogenesis of alkaline and calcalkaline suites presented above, and additional implication concerning mantle sources can be reached: Since the parameters obtained for the AFC processes for the coeval CA and alkaline terms are relatively similar (even if the granitic contaminants show some degree of heterogeneity), it seems likely that most geochemical differences observed in the initial magmas of northern CA, T1 and T2 were probably preserved through differentiation, as displayed in the Harker diagrams for K_2O, CaO and most trace elements. As a consequence, the presence of a suite of alkaline rocks (T2) with geochemical characteristics intermediate between the alkaline T1 and CA series is very unlikely the result of derivation from T1 through differentiation and contamination. Previous studies of alkaline-subalkaline associations in the TMVB also concluded that no geochemical interaction exists between both series (Díaz-Bravo et al., 2014; Gómez-Tuena et al., 2013; Hasenaka & Carmichael, 1987; Luhr et al., 1989; Luhr & Carmichael, 1985; Mori et al., 2007). Therefore, it is more likely that the geochemical differences observed between the less-differentiated samples of T1, T2 and CA series should be inherited from their respective primitive magmas and therefore from their mantle sources.

Geodynamic implications

The easiest way to explain the presence of the contrasting geochemical signatures of the T1 OIB-like rocks and the arc-related CA rocks is to consider the presence

of distinct mantle sources. However, given the range of intermediate compositions in the T2-CA association and the mildly alkaline nature of T2 rocks, a geodynamic scenario similar to that proposed by Díaz-Bravo et al. (2014) seems also likely. According to this model, it is possible to explain the presence of T2-type magmas by melting from a heterogeneously enriched mantle wedge where lower degrees of melting of enriched portions not fully overprinted by slab contributions would produce T2-like magmas. Increasing melting degrees would involve more extensive areas thus progressively diluting the OIB signature by tapping portions of the wedge enriched by slab-derived components that would produce calcalkaline melts. It also seems reasonable that the enriched portions of the mantle wedge may be represented by the storage of sublithospheric OIB like-melts.

The generation of OIB-like magmas from an enriched sublithospheric source that could in some cases reach crustal levels (precursors of T1 rocks) and would also contribute to an hybrid mantle wedge metasomatized by these melts as well as slab-derived fluids, as suggested above for the T2-CA association, would explain the similarity of T1 and T2 alkaline rocks and yet the compositional gap observed between both trends and it also has some geodynamic implications that may also help to account for the restricted area of appearance of the alkaline magmatism and its distribution along a rough N-S alignment in this sector of the MGVF (Fig. 8.3).

One factor that could have influenced the composition of the magmas in the region is the highly variable geometry of the Cocos oceanic plate (Ferrari et al., 2012; Manea et al., 2013). As explained in detail in chapter 2 (Fig. 2.3), the dip of this plate from west to east in the TMVB decreases progressively from its boundary with the Rivera plate until approximately the 101° W longitude, coinciding with the edge of the Guerrero Terrane. Further to the east the dip angle, that is initially of 15°, becomes almost horizontal at 80 km inland and at 50 km depth (Kim et al., 2012; Pérez-Campos et al., 2008) and increases again up to 45 - 50° east of the Pico de Orizaba volcano (97° 16’ 5” W), beneath the Isthmus of Tehuantepec, the Chiapas massif, and the Central American arc (Melgar & Pérez-Campos, 2010; Pardo & Suarez, 1995). The presence of adakitic calcalkaline magmas and the obliquity of the arc, farther away from the trench where the plate is at its shallowest dip angle, have been related to the presence

of that flat subduction segment (Gómez-Tuena et al., 2007). From south to north, the end of the flat segment (east of 101° W) corresponds roughly with the southernmost limit of the TMVB but, from there on the dip angle of the plate increases with a different value on each side of the 101° W meridian (see Fig 2.3 and Ferrari et al., 2012). The difference in the dipping angle is such that under the northern sector of the MGVF the depth of the plate on both sides of the 101° W meridian differs in about ~80 km (calculated according to available data in Ferrari et al., 2012). The nature of such a change, whether is a bend or a tear in the plate, has not been addressed yet, but it is not unreasonable to think of it as a tear given the large difference in plate depth for both sides of the 101° parallel for a given latitude.

This hypothesis, similar to the one proposed for other volcanic areas in the TMVB (Ferrari, 2004; Ferrari et al., 2001), would represent a mechanism by which an

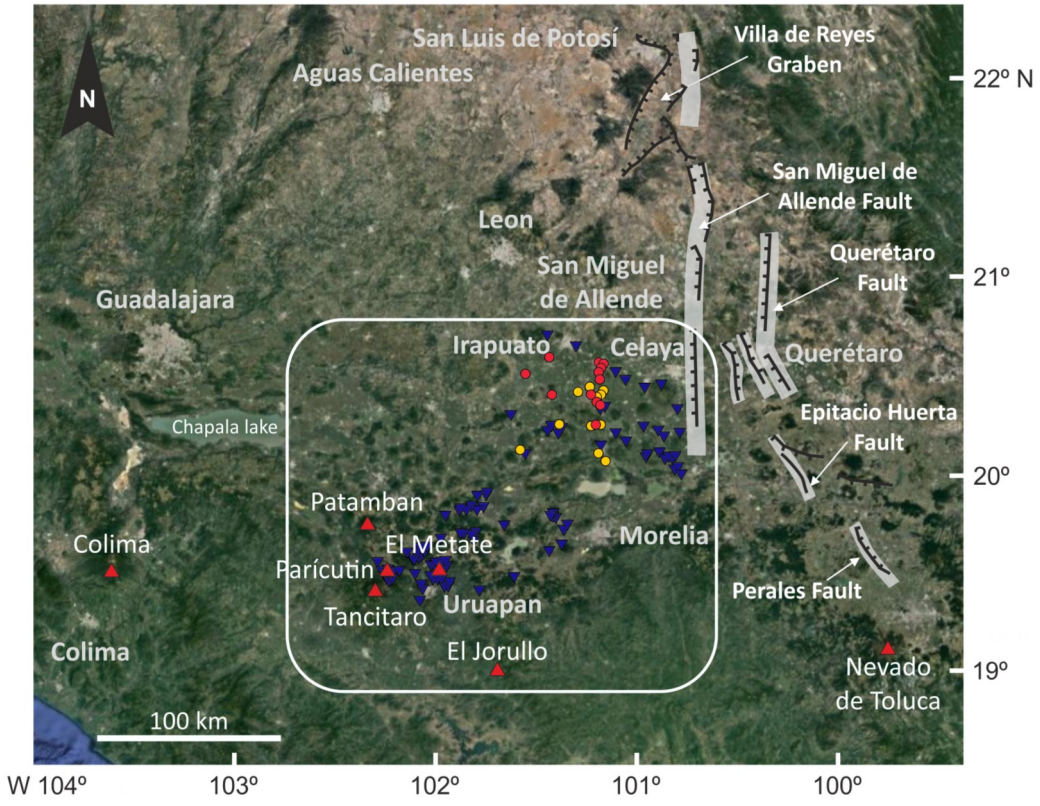

Fig. 8.3 Landsat 8 derived image provided by Earthstart Geographics SIO and processed by HERE (2017) of the Michoacán Guanajuato Volcanic Field region. Outlined in white is the Michoacán Guanajuato Volcanic Field area. Red circles represent T1 alkaline samples, yellow circles T2 alkaline samples and blue triangles calcalkaline suite samples. The names of the main towns are in grey bold letters, the red triangles are the main volcanos and the different parts of the Taxco San Miguel de Allende fault system (marked with white arrows) are outlined in grey bars with the slopes highlighted in dented black lines.

enriched asthenospheric mantle source (precursor of the alkaline T1 rocks) can ascend trough the mantle wedge and in some cases contributing as a metasomatic agent to its composition. This proposed mechanism supports a preferential N-S distribution of alkaline magmas in the northern MGVF, which nevertheless must be controlled at the shallowest levels by pre-existing crustal structures (see Valentine & Gregg, 2008).

The comprehensive isopachs and isobaths maps produced by Ferrari et al. (2012) (Figs 2.2 and 2.3) based on available gravimetric, magnetic and seismic data for the whole TMVB help to visualize the overall geometry of the subducting plate and the thickness variations of the overlying continental plate. According to those maps, in addition to an increase in continental crustal thickness from the coast to the continental interior, a striking feature is the presence of another thickening encompassed precisely within the domain of the MGVF. This discontinuity also follows an approximate N-S direction just east of the 101° W meridian, delimiting a thicker crustal domain (> 40 km) to the east and a thinner one (< 40 km) to the west. This change also coincides with a magnetic boundary between two regions of contrasting wavelength anomalies (North American Magnetic Anomaly Group, 2002) that would correspond to the westernmost known occurrence of the Palaeozoic and Precambrian basement of Oaxaquia (Ortega-Gutierrez et al., 1995) therefore representing the limit between that microcontinent to the east and an upper crust displaying high magnetic susceptibility igneous bodies to the west. This is a feature that corresponds well to the presence of the Guerrero Terrane in this area, known to be formed by a Mesozoic arc assemblage overlain by Cretaceous to Paleogene continental magmatic arcs (Ferrari et al., 2012). Hence, this N-S limit seems to represent the accretional suture between the Guerrero Terrane and the North American plate when the former overthrusted Oaxaquia during the Late Cretaceous (Centeno-García et al., 1993). Following Alaniz-Alvarez et al. (2002), the limit between Guerrero and Oaxaca was reactivated in Cenozoic times, resulting in the formation of the current Taxco-San Miguel de Allende Fault System (SMAF), that extends for more than 500 km and reaches up to 35 km in width in its thickest sector (between the cities of San Miguel de Allende and Querétaro). The deformation associated with this structure was found to be synchronic with the volcanism due to the emplacement, along the trace of the fault, of twelve stratovolcanoes and to

the different volcanic styles on both sides of the fault: monogenetic to the west and polygenetic to the east (Ferrari, 2000). Therefore, the above information suggests that the area between Salamanca and Querétaro, around the 101° W longitude, entails a drastic change in crustal thickness and composition of the North American continental plate, coinciding with the inferred crustal limit between the Guerrero Terrane, supposedly affected by arc magmatism since the early Cretaceous, and the Oaxaquia microcontinent where magmatism was scarce since Jurassic times. This crustal limit has its external expression in the SMAF (Alaniz-Alvarez et al., 2002) which was reactivated in Cenozoic times and active since then.

As we have seen alkaline lavas outcropping in the northern sector of the MGVF are mostly N-S aligned between the longitudes of 101° 18' W and 101° 10' W, just 40 km west of the SMAF. In this area no major distensive structures have been described to date but it is not unreasonable to think that the alkaline outcrops could be related to the SMAF structure or even that another N-S trending fault belonging to the same fault system could underlie the Cenozoic sediments in this area.

To summarize (Fig. 8.4), it seems reasonable that according to the above described information, the presence of alkaline intraplate magmas within a subduction context in the northern MGVF and its N-S distribution is mainly related to the possible presence of a slab window/tear within the Cocos plate in this region, further enhanced by the existence of a N-S cortical limit, represented on the surface by the extensional structures of the Taxco-San Miguel de Allende Fault System. In the case of the CA compositions, these features explain in part that the northern sector calcalkaline rocks, associated to the alkaline suite, can be considered independently, since their source (located in a metasomatized mantle wedge) should have some influence from OIB magmas in addition to slab-derived fluids.

Concluding remarks

As we have seen, in the MGVF several volcanic styles and magma compositions coexist which are related to a full range of magmatic processes, from mantle metasomatism and enrichment by both sublithospheric partial melts and slab-derived fluids,

to partial melting and differentiation both at deep levels and during ascent or in magmatic chambers, with the participation of crustal components through AFC. We propose here that the field can be divided compositionally and geographically attending to common characteristics of the erupting lavas into a northern sector where alkaline and calcalkaline lithologies coexist and a south sector dominated by subalkaline magmatism. The petrogenesis in the northern area involves similar maximum degrees of assimilation of relatively heterogeneous granitic contaminants at elevated assimilation rates that support the hypothesis that the contamination must be involving granitic melts either already present within the crust or produced shortly after the arrival of the basaltic melts, with also limited contributions from solid rock digestion in the case of CA and T2 rocks. This situation has already been proposed and would be a consequence of an anomalous heat regime of the crust in this area, very likely produced by basaltic underplating processes (see Annen et al., 2006; Annen & Sparks, 2002). The high pressure and temperature values encountered in some minerals also suggest that crystallization may have started shortly after magma segregation at depths near the base of the crust where magmas could have stalled and start their differentiation process. In fact, both scenarios are currently being proposed on the basis of crystal features for arc magmatism (see Klemetti, 2016 and Zellmer et al., 2016)

The origin of the respective primary magmas in the northern sector is here hypothesized to be related to the presence of a disruption (tear?) of the subducting Cocos plate beneath this area that allowed the ascent of enriched sublithospheric melts that could in some cases reach the surface as T1 OIB-type primitive magmas and would also act as a metasomatizing agent of small portions in the overlying mantle wedge, predominantly enriched by slab-derived fluids. Therefore, very low melting degrees could selectively produce small volumes of mildly-alkaline melts (T2 precursors) from alkaline-enriched portions of the mantle wedge. However as melting increases, the dominant slab-enriched mantle would be involved in larger amounts and the alkaline contribution would be diluted up to the point of producing typical arc-magmas alone. The ascent of OIB magmas through a roughly N - S tear would explain that the mantle region enriched by alkaline components also inherited this dominant distribution, further enhanced at surface by local N - S crustal structures, most likely related to the Tax-

co San Miguel de Allende Fault System resulting from the geodynamic evolution of this area during the development of the TMVB, reason why they crop out in an N - S alignment restricted to the north sector.

The south sector differs from the north mainly for the almost exclusive calcalkaline nature of the lavas. Otherwise, the petrogenesis in general terms is very similar to the one in the north concerning the nature of the contaminants and the amount of assimilation, but here the evidences of open system processes are frequent and imply that both melts and solids were assimilated. This is especially evident in the case of middle-sized volcanoes, typically restricted to the southern sector. A reason for that could be a longer residence period within the crust due to an additional storage of these magmas in magmatic chambers where the magmas could evolve and assimilate wall rock. That magma storage style has indeed been confirmed for volcanoes like Parícutin and is the main reason for the appearance of this kind of middle size monogenetic volcanoes.

The petrogenesis of the CA suite gets further complicated by the local differences such as different composition of the contaminants or different local stress field or composition of the crust that may influence in the distribution, the composition of the contaminant and the possibility to develop chambers that in turn influence in the kind and amount of assimilation and differentiation as exemplified with the Paricutin-Cherán alignment.

Fig. 8.4 Simplified sketch portraying the proposed hypothesis for the geodynamic origin of the alkaline - calcalkaline association in the northern sector of the MGVF. The process would be as follows:

- Enriched sublithosphere-derived melts (in pale red) would ascend through a slab gap in the Cocos plate reaching the mantle wedge.
- Some of these melts would reach the surface directly, presumably favoured by major structural pathways such as the Taxco San Miguel de Allende Fault System (SMAF).
- Other portions of the sublithospheric melts however, would act as additional metasomatizing agents of small portions in the mantle wedge (already metasomatized by slab-derived fluids).
- The metasomatized mantle wedge would produce at low fusion rates, mildly-alkaline melts (T2 precursor melts) very little influenced by slab-fluid fingerprints. At progressively higher fusion rates, the slab-enriched mantle would overprint the alkaline signature therefore producing the typical arc-magmas.
- The N – S disposition of the slab gap would imprint a similar disposition to the alkaline enriched mantle region explaining the N - S distribution of the alkaline vents, further enhanced by the SMAF structure and associated fracturing at crustal scale.

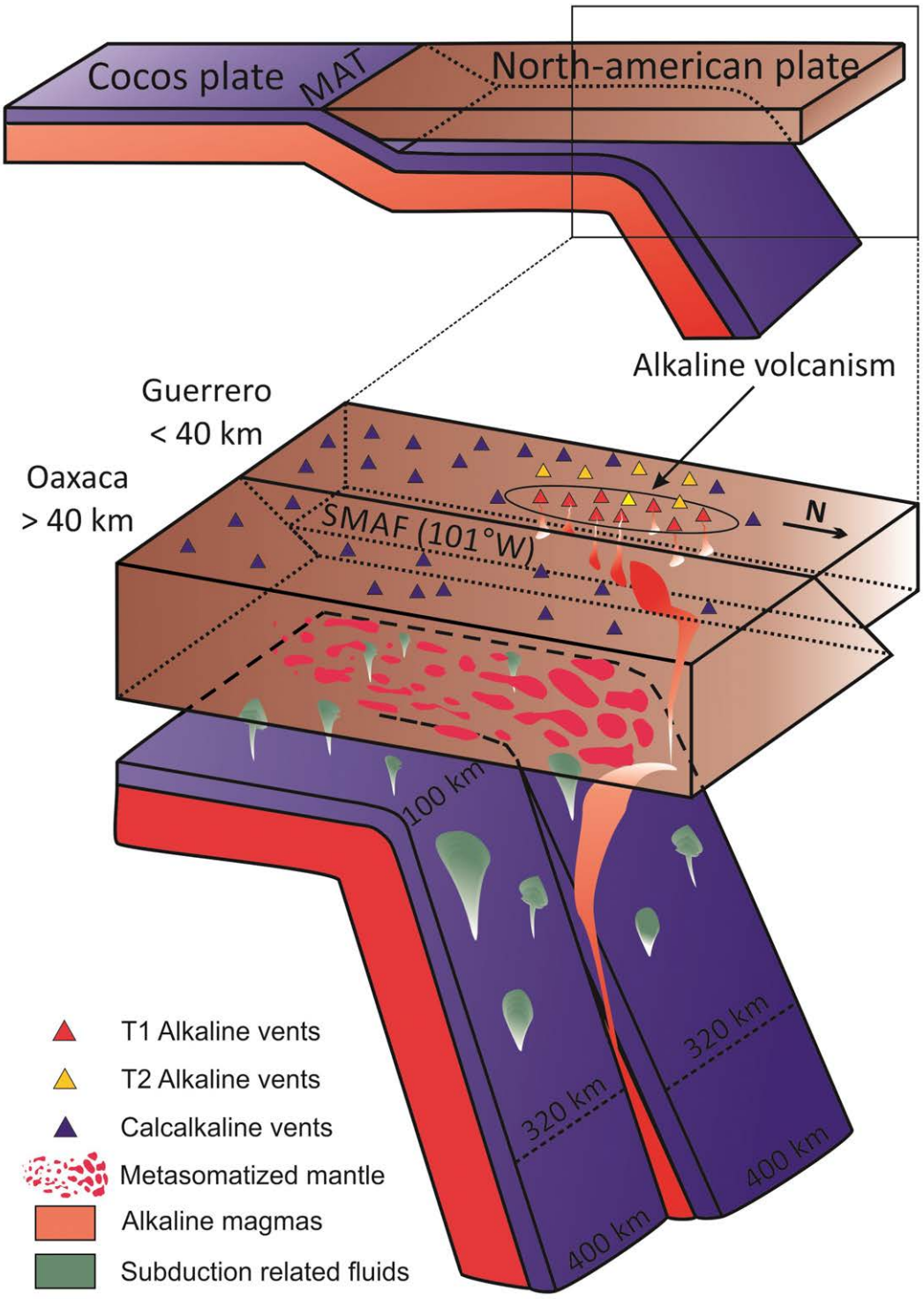
Cocos plate
MAT
North-american plate
Alkaline volcanism
Guerrero
< 40 km
Oaxaca
> 40 km
SMAF (101°W)
N
100 km
320 km
320 km
400 km
400 km
T1 Alkaline vents
T2 Alkaline vents
Calcalkaline vents
Metasomatized mantle
Alkaline magmas
Subduction related fluids

9. Conclusions

Alkaline monogenetic volcanism is mainly found in the northern sector of the MGVF, associated to predominant calcalkaline volcanism.

The alkaline suite is represented by two geochemically distinct groups: 1) an OIB -like type and 2) a transitional type, still alkaline but with a geochemical signature intermediate between the OIB-like rocks and the dominant calcalkaline suite.

Both alkaline groups define separate differentiation trends characterized by geochemical variations consistent with a differentiation process involving crystallization of the main mineral phases identified in the petrographic study and the assimilation of a crustal component.

Petrogenetic modelling calculations suggest that the OIB type trend (Alkaline Trend 1; T1) resulted by 33% polybaric crystallization of primary melts similar to the less differentiated terms in the trend with water contents of about 1.5 %, involving an assemblage composed of Plg 60 % + oxides 19 % + Ol 15 % + Cpx 6 % from temperatures ~1255 °C and pressures ~16 kbar, up to surface levels. Assimilation likely involved granitic melts (assimilation rates r ~0.27), compositionally heterogeneous and similar to those described from granite basement rocks.

Intermediate alkaline trend lavas (Alkaline Trend 2; T2) resulted from similar differentiation processes, by ~39 % polybaric crystallization of primary melts similar to the less differentiated terms with water contents of about 2 % and involving an assemblage composed of Plg 40 % + Ol 25 % + Cpx 20 % + Mt 10 % + Ap 5 %, from ~1250 ^{o}C - 1010 ^{o}C and P from ~14 kb up to surface levels. Assimilation also involved granitic melts (r ~0.30) compositionally similar to granite basement rocks.

Calcalkaline volcanism (CA) is compositionally more heterogeneous and it is widespread through the volcanic field. Groups of similar geochemical characteristics

that can be petrogenetically related within this suite have been found to be related to common geographic/geodynamic frameworks. For modelling purposes, we have considered the following groups according to their probable petrogenetic link: 1) the calcalkaline vents of the northern sector, geographically related to the alkaline suite; 2) An alignment of vents (the so-called Parícutin-Cherán alignment) in the southern sector, likely related by the extrusion of magmas along a linear tectonic structure; and 3) Individual middle size volcanoes (Parícutin and El Metate), also present in the southern sector, characterized by rock suites showing coherent evolution trends. The rest of the southern sector vents show consistent geochemical variations but it is likely that they could be further subdivided according to shared geodynamic characteristics.

Calcalkaline rocks of the northern sector, resulted by polybaric crystallization (up to 29%) from an initial melt similar to the less evolved terms of the CA suite, with higher water contents (~3%) and involving an assemblage composed of Plg 60 % + Ol 9 % + oxides 7 % + Opx 12 % + Ap 1 % + Cpx 11 %. Crystallization took place from at least ~1200 - 900 °C and 8 kbar up to surface levels, although initial depths of crystallization could be up to ~40 km (~11.2 kb) if some Plg and Cpx crystals assumed as represent xenocrystals are actually part of the crystallization sequence. AFC modelling results indicate that crystallization was coupled to the assimilation (r ~0.27) of the same heterogeneous granitic components identified for the alkaline suite.

The southern sector Parícutin-Cherán alignment CA rocks can be explained by ~37 % polybaric crystallization of an assemblage composed of Plg 55 % + Cpx 11.6 % + Ol 9.5 % + Opx 12.6 % + Mt 6.3 % + Ilm 1.1 %, assimilating a slightly different granitic component at r ~0.27 and in a P-T-H_2O regime similar to the one calculated for the northern sector CA magmas.

The middle sized volcanoes have been found to have a petrogenesis similar to the rest of the calcalkaline rocks in terms of the heterogeneity of the contaminants and the high assimilation/crystallization ratios (up to r ~0.5 for Paricutin), but present both geochemical and petrologic features that are in agreement with specific differentiation trends developed in upper crustal magmatic chambers where the magmas may have evolved. For example, in El Metate, two distinct differentiation trends can be identified

where progressive enrichment in water contents led to processes of crystallization and later destabilization of water-bearing phases (amphibole), whereas in Paricutin such a situation was not observed and in contrast water variations strongly conditioned the stability of plagioclase.

As a whole, the CA rocks of the southern sector appear to be derived from a range of primitive magmas contaminated by compositionally heterogeneous contaminants, nevertheless in all cases represented by upper crust granitic components.

According to the above results, we propose that differentiation processes started in all cases near the base of the crust where magmas could have stalled for a short time and further evolved during ascent, as supported by the obtained P-T range. Assimilation processes likely involved granitic melts already present in the crust, as suggested by the high assimilation rates calculated. Such a scenario would be in agreement with the presence of a thermally anomalous crust under the region. While T1 magmas do not show evidences of evolution in magma chambers, T2 and CA magmas seem to have undergone some sort of upper crustal storage in magma chambers where they could further evolve. In spite of this, the maximum degrees of crystallization and assimilation calculated in all suites are similar and geochemical differences arise from variations in the composition of the initial magmas, the contaminants and the different fractionating mineral assemblages.

Considering the results of the modelling tests as well as available geological and geophysical observations, the following geodynamic scenario is proposed: The existence of a disruption (probably a tear) in the subducting Cocos plate, favoured the ascent of enriched sublithospheric alkaline melts. These would act as metasomatizing agents in the overlying mantle wedge and could also ascend directly to the crust as precursors of the OIB type (T1) alkaline volcanism. On the other hand, primitive T2 alkaline magmas would be the result of very low degrees of melting that would selectively melt alkali-enriched portions of the mantle wedge. Such melts would only be very slightly influenced by portions of the ambient mantle wedge dominated by a longer history of slab-derived fluids enrichment. Progressive melting degrees would involve larger areas of the mantle wedge diluting any OIB signature and thus producing calcal-

kaline melts. This explains the dominance of CA-type melts in the southern sector of the MGVF, where the influence of the slab disruption and therefore of sublithospheric melts would be nearly absent. Additionally, the geometry of the plate disruption and the presence of a N-S oriented major crustal structure in the northern sector (likely associated to the San Miguel de Allende Fault System) would favour the ascent of the alkaline lavas following such paths and explaining the dominant N-S distribution of the alkaline volcanism.

References

Aguirre-Díaz, G. J., Dubois, M., Laureyns, J. & Schaaf, P. (2002). Nature and P-T Conditions of the Crust Beneath the Central Mexican Volcanic Belt Based on a Precambrian Crustal Xenolith. *International Geology Review* **44**, 222–242.

Aguirre-Díaz, G. J., Jaimes-Viera, M. del C. & Nieto-Obregón, J. (2006). The Valle de Bravo Volcanic Field: Geology and geomorphometric parameters of a Quaternary monogenetic field at the front of the Mexican Volcanic Belt. *Geological Society of America Special Paper* **402**, 139–154.

Aguirre-Díaz, G. J. & López-Martínez, M. (2001). The Amazcala caldera, Queretaro, Mexico. Geology and geochronology. *Journal of Volcanology and Geothermal Research* **111**, 203–218.

Agustín-Flores, J., Siebe, C. & Guilbaud, M.-N. (2011). Geology and geochemistry of Pelagatos, Cerro del Agua, and Dos Cerros monogenetic volcanoes in the Sierra Chichinautzin volcanic field, south of Mexico City. *Journal of Volcanology and Geothermal Research* **201**, 143–162.

Alaniz-Alvarez, S. A., Nieto-Samaniego, A. F., Orozco-Esquivel, M. T., Vassallo, L. F. & Xu, S. (2002). El sistema de fallas Taxco-San Miguel de Allende: implicaciones en la deformación post-eocénica del centro de México. *Boletín de la Sociedad Geológica Mexicana* **55**, 12–29.

Albarrán, J. (1985). *Estudio petrogenético de las rocas ígneas de la porción Central del Eje Neovolcánico*. México, D.F.: Instituto Mexicano del Petróleo, Subdirección de Tecnología de Exploración, 47.

Allan, J. F. (1986). Geology of the Northern Colima and Zacoalco Grabens, southwest Mexico: Late Cenozoic rifting in the Mexican Volcanic Belt. *Geological Society of America Bulletin* **97**, 473–485.

Allan, J. F. & Carmichael, I. S. E. (1984). Lamprophyric lavas in the Colima graben, SW Mexico. *Contributions to Mineralogy and Petrology* **88**, 203–216.

Allison, E. C. (1974). The Type Alisitos Formation (Cretaceous, Aptian-Albian) of Baja California and its Bivalve Fauna. *The Geology of Peninsular California*. paper presented at the AAPG 49th Annual Meeting. Los Angeles (California): AAPG, 20–59.

Almeev, R. R., Holtz, F., Koepke, J. & Parat, F. (2012). Experimental calibration of the effect of H2O on plagioclase crystallization in basaltic melt at 200 MPa. *American Mineralogist* **97**, 1234–1240.

Alvarez, E. H., Salas, M. R., Chávez, P. C., Monroy, V. H. G., Alcántara, I. I., Santacruz, R. L. & Bermea, O. M. (2006). Asimilación de xenolitos graníticos en el Campo Volcánico Michoacán-Guanajuato: el caso de Arócutin Michoacán, México. *Revista Mexicana de Ciencias Geológicas* **23**, 233–245.

Alva-Valdivia, L. M., Goguitchaichvili, A., Ferrari, L., Rosas-Elguera, J., Urrutia-Fucugauchi, J. & Zamorano-Orozco, J. J. (2000). Paleomagnetic data from the Trans-Mexican Volcanic Belt: implications for tectonics and volcanic stratigraphy. *Earth, Planets and Space* **52**, 467–478.

Anderson, A. (1973). The before-eruption water content of some high-alumina magmas. *Bulletin of Volcanology* **37**, 530–552.

Anderson, A. T. (1974a). Chlorine, sulfur, and water in Magmas and Oceans. *Bulletin of the Geological Society of America* **85**, 1485–1492.

Anderson, A. T. (1974b). Evidence for a Picritic, Volatile-rich Magma beneath Mt. Shasta, California. *Journal of Petrology* **15**, 243–267.

Annen, C., Blundy, J. D. & Sparks, R. S. J. (2006). The genesis of intermediate and silicic magmas in deep crustal hot zones. *Journal of Petrology* **47**, 505–539.

Annen, C. & Sparks, R. S. J. (2002). Effects of repetitive emplacement of basaltic intrusions on thermal evolution and melt generation in the crust. *Earth and Planetary Science Letters* **203**, 937–955.

Arculus, R. J. (2003). Use and Abuse of the Terms Calcalkaline and Calcalkalic. *Journal of Petrology* **44**, 929–935.

Asimow, P. D. (1998). Algorithmic modifications extending MELTS to calculate subsolidus phase relations. *American Mineralogist* **83**, 1127–1132.

Atwater, T. (1970). Implications of Plate Tectonics for the Cenozoic Tectonic Evolution of Western North America. *Geological Society of America Bulletin* **81**, 3513–3536.

Atwater, T. & Stock, J. (1998). Pacific-North America Plate Tectonics of the Neogene Southwestern United States: An Update. *International Geology Review* **40**, 375–402.

Ban, M., Hasenaka, T., Delgado-Granados, H. & Takaoka, N. (1992). K-Ar ages of lavas from shield volcanoes in the Michoacan-Guanajuato volcanic field, Mexico. *Geofísica Internacional* **31**, 467–473.

Bandy, W., Mortera-Gutierrez, C., Urrutia-Fucugauchi, J. & Hilde, T. W. C. (1995). The subducted Rivera-Cocos Plate Boundary: Where is it, what is it, and what is its relationship to the Colima Rift? *Geophysical Research Letters* **22**, 3075–3078.

Beattie, P. (1993). Olivine-melt and orthopyroxene-melt equilibria. *Contributions to Mineralogy and Petrology* **115**, 103–111.

Bindeman, I. (2008). Oxygen Isotopes in Mantle and Crustal Magmas as Revealed by Single Crystal Analysis. *Reviews in Mineralogy and Geochemistry* **69**, 445–478.

Blatter, D. L. & Carmichael, I. S. E. (1998). Plagioclase-free andesites from Zitácuaro (Michoacán), Mexico: petrology and experimental constraints. *Contributions to Mineralogy and Petrology* **132**, 121–138.

Blatter, D. L., Farmer, G. L. & Carmichael, I. S. E. (2007). A north-south transect across the Central Mexican Volcanic Belt at ~100°W: Spatial distribution, petrological, geochemical, and isotopic characteristics of Quaternary Volcanism. *Journal of Petrology* **48**, 901–950.

Bloomfield, K. (1973). The age and significance of the tenango basalt, central Mexico. *Bulletin Volcanologique* **37**, 586–595.

Bloomfield, K. (1975). A late-Quaternary monogenetic volcano field in central Mexico. *Geologische Rundschau* **64**, 476–497.

Blundy, J. & Cashman, K. (2001). Ascent-driven crystallisation of dacite magmas at Mount St Helens, 1980–1986. *Contributions to Mineralogy and Petrology* **140**, 631–650.

Bohrson, W. A. & Spera, F. J. (2001). Energy-constrained open-system magmatic processes II: Application of energy- constrained assimilation - Fractional crystallization (EC-AFC) model to magmatic systems. *Journal of Petrology* **42**, 1019–1041.

Boudreau, A. E. (1999). PELE—a version of the MELTS software program for the PC platform. *Computers & Geosciences* **25**, 201–203.

Brenna, M., Cronin, S. J., Németh, K., Smith, I. E. M. & Sohn, Y. K. (2011). The influence of magma plumbing complexity on monogenetic eruptions, Jeju Island, Korea. *Terra Nova* **23**, 70–75.

Brenna, M., Cronin, S. J., Smith, I. E. M., Sohn, Y. K. & Németh, K. (2010). Mechanisms driving polymagmatic activity at a monogenetic volcano, Udo, Jeju Island, South Korea. *Contributions to Mineralogy and Petrology* **160**, 931–950.

Brown, G., Hawkesworth, C. & Wilson, R. C. L. (1992). *Understanding the Earth*. Cambridge University Press.

Cabral-Cano, E., Draper, G., Lang, H. R. & Harrison, C. G. A. (2000). Constraining the Late Mesozoic and Early Tertiary Tectonic Evolution of Southern Mexico: Structure and Deformation History of the Tierra Caliente Region. *The Journal of Geology* **108**, 427–446.

Cabral-Cano, E., Lang, H. R. & Harrison, C. G. A. (2000). Stratigraphic assessment of the Arcelia–Teloloapan area, southern Mexico: implications for southern Mexico's post-Neocomian tectonic evolution. *Journal of South American Earth Sciences* **13**, 443–457.

Campa, M. F. & Coney, P. J. (1983). Tectono-stratigraphic terranes and mineral resource distributions in Mexico. *Canadian Journal of Earth Sciences* **20**, 1040–1051.

Cañón-Tapia, E. (2016). Reappraisal of the significance of volcanic fields. *Journal of Volcanology and Geothermal Research* **310**, 26–38.

Cañón-Tapia, E. & Walker, G. P. L. (2004). Global aspects of volcanism: the perspectives of "plate tectonics" and "volcanic systems." *Earth-Science Reviews* **66**, 163–182.

Cantagrel, J.-M. & Robin, C. (1979). K-Ar dating on eastern Mexican volcanic rocks — Relations between the andesitic and the alkaline provinces. *Journal of Volcanology and Geothermal Research* **5**, 99–114.

Carrasco-Nuñez, G. C., Milán, M. & Verma, S. P. (1989). Geología del volcán Zamorano, estado de Querétaro. *Revista Mexicana de Ciencias Geológicas* **8**, 194–201.

Castillo, D. & Romero, F. (1991). *Estudio geológico-regional de Los Altos, Jalisco y El Bajío*. Open file report. Comisión Federal de Electricidad, Gerencia de Proyectos Geotecnoeléctricos, 2–91.

Cebriá, J. M. & López-Ruiz, J. (1996). A refined method for trace element modelling of nonmodal batch partial melting processes: The Cenozoic continental volcanism of Calatrava, Central Spain. *Geochimica et Cosmochimica Acta* **60**, 1355–1366.

Cebriá, J. M., López-Ruiz, J., Doblas, M., Oyarzun, J., Hertogen, J. & Benito, R. (2000). Geochemistry of the Quaternary alkali basalts of Garrotxa (NE Volcanic Province, Spain): a case of double enrichment of the mantle lithosphere. *Journal of Volcanology and Geothermal Research* **102**, 217–235.

Cebriá, J. M., Martín-Escorza, C., López-Ruiz, J., Morán-Zenteno, D. J. & Martiny, B. M. (2011a). Numerical recognition of alignments in monogenetic volcanic areas: Examples from the Michoacán-Guanajuato Volcanic Field in Mexico and Calatrava in Spain. *Journal of Volcanology and Geothermal Research* **201**, 73–82.

Cebriá, J. M., Martiny, B. M., López-Ruiz, J. & Morán-Zenteno, D. J. (2011b). The Parícutin calc-alkaline lavas: New geochemical and petrogenetic modelling constraints on the crustal assimilation process. *Journal of Volcanology and Geothermal Research* **201**, 113–125.

Centeno-García, E. (2017). Mesozoic tectono-magmatic evolution of Mexico: An overview. *Ore Geology Reviews* **81**, 1035–1052.

Centeno-García, E., Ruíz, J., Coney, P. J., Patchett, P. J. & Ortega-Gutiérrez, F. (1993). Guerrero terrane of Mexico: Its role in the Southern, Cordillera from new geochemical data. *Geology* **21**, 419–422.

Chauvel, C. & Hémond, C. (2000). Melting of a complete section of recycled oceanic crust: Trace element and Pb isotopic evidence from Iceland. *Geochemistry, Geophysics, Geosystems* **1**, 1001.

Chesley, J., Ruiz, J., Righter, K., Ferrari, L. & Gomez-Tuena, A. (2002). Source contamination versus assimilation: An example from the Trans-Mexican volcanic arc. *Earth and Planetary Science Letters* **195**, 211–221.

Chevrel, M. O., Guilbaud, M.-N. & Siebe, C. (2016). The ~AD 1250 effusive eruption of El Metate shield volcano (Michoacán, Mexico): magma source, crustal storage, eruptive dynamics, and lava rheology. *Bulletin of Volcanology* **78**, 32.

Chevrel, M. O., Siebe, C., Guilbaud, M.-N. & Salinas, S. (2015). The AD 1250 El Metate shield volcano (Michoacán): Mexico's most voluminous Holocene eruption and its significance for archaeology and hazards. *The Holocene* 0959683615609757.

Condie, K. C. (1993). Chemical composition and evolution of the upper continental crust: contrasting results from surface samples and shales. *Chemical geology* **104**, 1–37.

Condie, K. C. (2001). *Mantle Plumes and their Record in Earth History*. Cambridge: Cambridge University Press.

Connor, C. B. (1987). Structure of the Michoacán-Guanajuato volcanic field, Mexico. *Journal of Volcanology and Geothermal Research* **33**, 191–200.

Connor, C. B. (1990). Cinder Cone Clustering in the TransMexican Volcanic Belt: Implications for Structural and Petrologic Models. *J. Geophys. Res.* **95**.

Connor, C. B. & Conway, M. F. (2000). Basaltic volcanic fields. In: Sigurdsson, H. (ed.) *Encyclopedia of Volcanoes*. San Diego, CA: Academic Press, 331–343.

Connor, C. B., Lichtner, P. C., Conway, F. M., Hill, B. E., Ovsyannikov, A. A., Federchenko, I., Doubik, Y., Shapar, V. N. & Taran, Y. A. (1997). Cooling of an igneous dike 20 yr after intrusion. *Geology* **25**, 711–714.

Corona-Chávez, P., Reyes-Salas, M., Garduño-Monroy, V. H., Israde-Alcántara, I., Lozano-Santa Cruz, R., Morton-Bermea, O. & Hernández-Álvarez, E. (2006). Assimilation of granitic xenoliths in the Michoacán-Guanajuato volcanic field: The case of Arócutin, Michoacán, Mexico. *Revista Mexicana de Ciencias Geológicas* **23**, 233–245.

Costa, F., Andreastuti, S., Bouvet de Maisonneuve, C. & Pallister, J. S. (2013). Petrological insights into the storage conditions, and magmatic processes that yielded the centennial 2010 Merapi explosive eruption. *Journal of Volcanology and Geothermal Research* **261**, 209–235.

Cox, K. G. (1980). A Model for Flood Basalt Vulcanism. *Journal of Petrology* **21**, 629–650.

Dahren, B., Troll, V., Andersson, U., Chadwick, J., Gardner, M., Jaxybulatov, K. & Koulakov, I. (2012). Magma plumbing beneath Anak Krakatau volcano, Indonesia: evidence for multiple magma storage regions. *Contributions to Mineralogy and Petrology* **163**, 631–651.

De Jesús Aguirre-Díaz, G. & López-Martinez, A. (1998). El volcán La Joya, estados de Querétaro y Guanajuato–un estratovolcán miocénico del cinturón volcánico mexicano. *Revista Mexicana de Ciencias Geológicas* **15**, 181–197.

De Antuñano, S. E., Aranda-Garcia, M. & Marrett, R. (2000). Tectónica de la Sierra Madre Oriental, México. *Boletin de la Sociedad Geologica Mexicana* **53**, 1–26.

De Cserna, Z. (1960). Orogenesis in time and space in Mexico. *Geologische Rundschau* **50**, 595–605.

Delgado-Granados, H., Urrutia-Fucugauchi, J., Hasenaka, T. & Ban, M. (1995). Southwestward volcanic migration in the western Trans-Mexican Volcanic Belt during the last 2 Ma. *Geofísica Internacional* **34**, 341–352.

Deer, W. A., Howie, R. A. & Zussman, J. (1992). *An introduction to the rock-forming minerals*. London: Longman.

Demant, A. (1978). Características del Eje Neovolcánico Transmexicano y sus problemas de interpretación. *Revista mexicana de ciencias geológicas* **2**, 172–187.

Demant, A. & Robin, C. (1975). Las fases del vulcanismo en Mexico: una síntesis en relación con la evolución geodinámica desde el cretácico. *Revista Mexicana de Ciencias Geológicas* **75**, 66–79.

DeMets, C., Gordon, R. G., Argus, D. F. & Stein, S. (1990). Current plate motions. *Geophysical Journal International* **101**, 425–478.

DeMets, C., Gordon, R. G., Argus, D. F. & Stein, S. (1994). Effect of recent revisions to the geomagnetic reversal time scale on estimates of current plate motions. *Geophysical Research Letters* **21**, 2191–2194.

DeMets, C. & Traylen, S. (2000). Motion of the Rivera plate since 10 Ma relative to the Pacific and North American plates and the mantle. *Tectonophysics* **318**, 119–159.

DePaolo, D. J. (1981). Trace element and isotopic effects of combined wallrock assimilation and fractional crystallization. *Earth and Planetary Science Letters* **53**, 189–202.

Díaz-Bravo, B. A., Gómez-Tuena, A., Ortega-Obregón, C. & Pérez-Arvizu, O. (2014). The origin of intraplate magmatism in the western Trans-Mexican Volcanic Belt. *Geosphere* **10**, 340–373.

Dickinson, W. R. & Hatherton, T. (1967). Andesitic volcanism and seismicity around the Pacific. *Science* **157**, 801–803.

Ducea, M. N., Saleeby, J. B. & Bergantz, G. (2015). The architecture, chemistry, and evolution of continental magmatic arcs. *Annual Review of Earth and Planetary Sciences* **43**, 299–331.

Dunn, T. (1987). Partitioning of Hf, Lu, Ti, and Mn between olivine, clinopyroxene and basaltic liquid. *Contributions to Mineralogy and Petrology* **96**, 476–484.

Duque-Trujillo, J., Ferrari, L., Orozco-Esquivel, T., López-Martínez, M., Lonsdale, P., Bryan, S. E., Kluesner, J., Piñero-Lajas, D. & Solari, L. (2014). Timing of rifting in the southern Gulf of California and its conjugate margins: Insights from the plutonic record. *Geological Society of America Bulletin* B31008-1.

Eissler, H. K. & McNally, K. C. (1984). Seismicity and tectonics of the Rivera Plate and implications for the 1932 Jalisco, Mexico, earthquake. *Journal of Geophysical Research: Solid Earth* **89**, 4520–4530.

Elardo, S. M. & Shearer, C. K. (2014). Magma chamber dynamics recorded by oscillatory zoning in pyroxene and olivine phenocrysts in basaltic lunar meteorite Northwest Africa 032. *American Mineralogist* **99**, 355–368.

Elias-Herrera, M. & Ortega-Gutiérrez, F. (1997). Petrology of high-grade metapelitic xenoliths in an Oligocene rhyodacite plug–Precambrian crust beneath the southern Guerrero terrane, Mexico. *Revista Mexicana de Ciencias Geológicas* **14**, 101–109.

Elías-Herrera, M., Ortega-Gutierrez, F. & Lozano-Santa Cruz, R. (1998). Evidence for pre -Mesozoic sialic crust in the southern Guerrero terrane: Geochemistry of the Pepechuca high grade gneiss xenoliths. *Actas INAGEQ*. 8^{o} Congreso Nacional de Geoquímica. México D.F., 169–181.

Elías-Herrera, M., Ortega-Gutierrez, F., Sánchez-Zavala, J. L., Macías-Romo, C., Ortega-Rivera, M. A. & Iriondo, A. (2005). La falla de Caltepec: raíces expuestas de una frontera tectónica de larga vida entre dos terrenos continentales del sur de México. *Boletín de la Sociedad Geológica Mexicana* **57**, 83–109.

Elías-Herrera, M. & Ortega-Gutiérrez, F. (1998). The Early Cretaceous Arperos oceanic basin (western Mexico). Geochemical evidence for an aseismic ridge formed near a spreading center — Comment. *Tectonophysics* **292**, 321–326.

Erlund, E. J., Cashman, K. V., Wallace, P. J., Pioli, L., Rosi, M., Johnson, E. & Granados, H. D. (2010). Compositional evolution of magma from Parícutin Volcano, Mexico: The tephra record. *Journal of Volcanology and Geothermal Research* **197**, 167–187.

Ersoy, E. Y. (2013). PETROMODELER (Petrological Modeler): a Microsoft® Excel© spreadsheet program for modelling melting, mixing, crystallization and assimilation processes in magmatic systems. *Turkish Journal of Earth Sciences* **22**, 115–125.

Ersoy, Y. & Helvacı, C. (2010). FC–AFC–FCA and mixing modeler: A Microsoft® Excel© spreadsheet program for modeling geochemical differentiation of magma by crystal fractionation, crustal assimilation and mixing. *Computers & Geosciences* **36**, 383–390.

Faure, G. F. (1986). *Principles of Isotope Geology 2nd edition*. John Wiley & Sons.

Ferrari, L. (2000). Avances en el conocimiento de la Faja Volcánica Transmexicana durante la última década. *Boletin de la Sociedad Geológica Mexicana* **53**, 84-92.

Ferrari, L. (2004). Slab detachment control on mafic volcanic pulse and mantle heterogeneity in central Mexico. *Geology* **32**, 77–80.

Ferrari, L., Conticelli, S., Vaggelli, G., Petrone, C. M. & Manetti, P. (2000a). Late Miocene volcanism and intra-arc tectonics during the early development of the Trans-Mexican Volcanic Belt. *Tectonophysics* **318**, 161–185.

Ferrari, L., Garduño, V. H., Innocenti, F., Manetti, P., Pasquare, G. & Vaggelli, G. (1994). A widespread mafic volcanic unit at the base of the Mexican Volcanic Belt between Guadalajara and Queretaro. *Geofísica Internacional* **33**, 107–123.

Ferrari, L., Garduño, V. H., Pasquarè, G. & Tibaldi, A. (1991). Geology of Los Azufres Caldera, Mexico, and its relationships with regional tectonics. *Journal of Volcanology and Geothermal Research* **47**, 129–148.

Ferrari, L., López-Martínez, M., Aguirre-Díaz, G. & Carrasco-Núñez, G. (1999). Space-time patterns of Cenozoic arc volcanism in central Mexico: From the Sierra Madre Occidental to the Mexican Volcanic Belt. *Geology* **27**, 303–306.

Ferrari, L., López-Martínez, M., Orozco-Esquivel, T., Bryan, S. E., Duque-Trujillo, J., Lonsdale, P. & Solari, L. (2013). Late Oligocene to Middle Miocene rifting and synextensional magmatism in the southwestern Sierra Madre Occidental, Mexico: The beginning of the Gulf of California rift. *Geosphere* **9**, 1161–1200.

Ferrari, L., Morán-Zenteno, D. J. & González, E. (2007). Actualización de Mapa Geológico de México. 1:4,000,000, Instituto de Geografía (UNAM).

Ferrari, L., Orozco-Esquivel, T., Manea, V. & Manea, M. (2012b). The dynamic history of the Trans-Mexican Volcanic Belt and the Mexico subduction zone. *Tectonophysics* **522–523**, 122–149.

Ferrari, L., Pasquare, G. & Tibaldi, A. (1990). Plio-Quaternary tectonics of the central Mexican Volcanic Belt and some constraints on its rifting mode. *Geofísica Internacional* **29**, 5–18.

Ferrari, L., Pasquaré, G., Venegas-Salgado, S. & Romero-Rios, F. (2000b). Geology of the western Mexican Volcanic Belt and adjacent Sierra Madre Occidental and Jalisco Block. In: Delgado Granados, H., Aguirre-Díaz, G. & Stock, J. M. (eds) Cenozoic Tectonics and Volcanism of Mexico. Geological Society of America, 65 –83.

Ferrari, L., Petrone, C. M. & Francalanci, L. (2001). Generation of oceanic-island basalt–type volcanism in the western Trans-Mexican volcanic belt by slab rollback, asthenosphere infiltration, and variable flux melting. *Geology* **29**, 507–510.

Ferrari, L. & Rosas-Elguera, J. (2000). Late Miocene to Quaternary extension at the northern boundary of the Jalisco block, western Mexico: The Tepic-Zacoalco rift revised. *Cenozoic Tectonics and Volcanism of Mexico* **334**, 41.

Ferrari, L., Tagami, T., Eguchi, M., Orozco-Esquivel, M. T., Petrone, C. M., Jacobo-Albarrán, J. & López-Martínez, M. (2005a). Geology, geochronology and tectonic setting of late Cenozoic volcanism along the southwestern Gulf of Mexico: The Eastern Alkaline Province revisited. *Journal of Volcanology and Geothermal Research* **146**, 284–306.

Ferrari, L., Valencia-Moreno, M. & Bryan, S. (2005b). Magmatismo y tectónica en la Sierra Madre Occidental y su relación con la evolución de la margen occidental de Norteamérica. *Boletín de la Sociedad Geológica Mexicana* **57**, 343–378.

Fisher, R. L. (1961). Middle America Trench: topography and structure. *Geological Society of America Bulletin* **72**, 703–719.

Foshag, W. P. & González, G. R. (1956). Birth and development of Paricutin volcano, Mexico. *Geological Survey Bulletin* **965**–**D**, 355–489.

Frey, H. M., Lange, R. A., Hall, C. M. & Delgado-Granados, H. (2004). Magma eruption rates constrained by 40Ar/39Ar chronology and GIS for the Ceboruco–San Pedro volcanic field, western Mexico. *Geological Society of America Bulletin* **116**, 259–276.

Gadow, H. (1930). *Jorullo: the history of the volcano of Jorullo and the reclamation of the devastated district by animals and plants*. Cambridge University Press.

García-Palomo, A., Macías, J. L. & Garduño, V. H. (2000). Miocene to Recent structural evolution of the Nevado de Toluca volcano region, Central Mexico. *Tectonophysics* **318**, 281–302.

Gastil, G., Krummenacher, D. & Jensky, W. A. (1979). Reconnaissance geology of west-central Nayarit, Mexico: Summary. *Geological Society of America Bulletin* **90**, 15 –18.

Genareau, K., Valentine, G. A., Moore, G. & Hervig, R. L. (2010). Mechanisms for transition in eruptive style at a monogenetic scoria cone revealed by microtextural analyses (Lathrop Wells volcano, Nevada, USA). *Bulletin of Volcanology* **72**, 593–607.

Geyne, A. R., Fries, C., Segerstrom, K., Black, R. F., Wilson, I. F. & Probert, A. (1963). *Geology and mineral deposits of the Pachuca-Real del Monte District, State of Hidalgo, Mexico*. Consejo de Recursos Naturales no Renovables.

Ghiorso, M. S., Hirschmann, M. M., Reiners, P. W. & Kress, V. C. (2002). The pMELTS: A revision of MELTS for improved calculation of phase relations and major element partitioning related to partial melting of the mantle to 3 GPa. *Geochemistry, Geophysics, Geosystems* **3**, 1–35.

Ghiorso, M. S. & Sack, R. O. (1995). Chemical mass transfer in magmatic processes IV. A revised and internally consistent thermodynamic model for the interpolation and extrapolation of liquid-solid equilibria in magmatic systems at elevated temperatures and pressures. *Contributions to Mineralogy and Petrology* **119**, 197–212.

Gilbert, C. M., Carmichael, I. S. E. & Mahood, G. A. (1985). Volcanic stratigraphy of the Guadalajara area, Mexico. *Geofísica Internacional* **24**, 169–191.

Ginibre, C., Kronz, A. & Wörner, G. (2002). High-resolution quantitative imaging of plagioclase composition using accumulated backscattered electron images: new constraints on oscillatory zoning. *Contributions to Mineralogy and Petrology* **142**, 436–448.

Girona, T., Costa, F., Newhall, C. & Taisne, B. (2014). On depressurization of volcanic magma reservoirs by passive degassing. *Journal of Geophysical Research: Solid Earth* **119**, 2014JB011368.

Goldsmith, J. R. (1982). Review of the behavior of plagioclase under metamorphic conditions. *American Mineralogist* **67**, 643–652.

Gómez, J. J. A., Luhr, J. F., Housh, T. B., Moreno, G. V. & Cabello, G. C. (2005). El volcanismo tipo intraplaca del Cenozoico tardío en el centro y norte de México: una revisión. *Boletín de la Sociedad Geológica Mexicana* **57**, 187–225.

Gómez-Tuena, A. & Carrasco-Núñez, G. (2000). Cerro Grande volcano: the evolution of a Miocene stratocone in the early Trans-Mexican Volcanic Belt. *Tectonophysics* **318**, 249–280.

Gómez-Tuena, A., Díaz-Bravo, B., Vázquez-Duarte, A., Pérez-Arvizu, O. & Mori, L. (2013). Andesite petrogenesis by slab-derived plume pollution of a continental rift. *Geological Society, London, Special Publications* **385**, SP385.4.

Gómez-Tuena, A., LaGatta, A. B., Langmuir, C. H., Goldstein, S. L., Ortega-Gutiérrez, F. & Carrasco-Núñez, G. (2003). Temporal control of subduction magmatism in the eastern Trans-Mexican Volcanic Belt: Mantle sources, slab contributions, and crustal contamination. *Geochemistry, Geophysics, Geosystems* **4**, 8912.

Gómez-Tuena, A., Mori, L., Goldstein, S. L. & Pérez-Arvizu, O. (2011). Magmatic diversity of western Mexico as a function of metamorphic transformations in the subducted oceanic plate. *Geochimica et Cosmochimica Acta* **75**, 213–241.

Gómez-Tuena, A., Mori, L. & Straub, S. M. (2017). Geochemical and petrological insights into the tectonic origin of the Transmexican Volcanic Belt. *Earth-Science Reviews*. In press

Gómez-Tuena, A., Orozco-Esquivel, M. T. & Ferrari, L. (2007). Igneous petrogenesis of the Trans-Mexican Volcanic Belt. *Geological Society of America Special Papers* **422**, 129–181.

Govindaraju, K., Potts, P. J., Webb, P. C. & Watson, J. S. (1994). 1994 Report on Whin Sill Dolerite WS-E from England and Pitscurrie Micrograbbro PM-S from Scotland: assessment by one hundred and four international laboratories. *Geostandards and Geoanalytical Research* **18**, 211–300.

Granados, H. D., Urrutia-Fucugauchi, J., Hasenaka, T. & Ban, M. (1995). Southwestward volcanic migration in the western Trans-Mexican Volcanic Belt during the last 2 Ma. *Geofísica Internacional* **34**, 341–352.

Green, T. H. (1994). Experimental studies of trace-element partitioning applicable to igneous petrogenesis -Sedona 16 years later. *Chemical Geology* **117**, 1–36.

Grove, T. L. & Baker, M. B. (1984). Phase equilibrium controls on the tholeiitic versus calc-alkaline differentiation trends. *Journal of Geophysical Research* **89**, 3253–3274.

Grove, T. L. & Juster, T. C. (1989). Experimental investigations of low-Ca pyroxene stability and olivine-pyroxene-liquid equilibria at 1-atm in natural basaltic and andesitic liquids. *Contributions to Mineralogy and Petrology* **103**, 287–305.

Guilbaud, M.-N., Siebe, C., Layer, P. & Salinas, S. (2012). Reconstruction of the volcanic history of the Tacámbaro-Puruarán area (Michoacán, México) reveals high frequency of Holocene monogenetic eruptions. *Bulletin of Volcanology* **74**, 1–25.

Gunn, B. M. & Mooser, F. (1970). Geochemistry of the volcanics of central Mexico. *Bulletin Volcanologique* **34**, 577–616.

Halliday, A. N., Lee, D.-C., Tommasini, S., Davies, G. R., Paslick, C. R., Godfrey Fitton, J. & James, D. E. (1995). Incompatible trace elements in OIB and MORB and source enrichment in the sub-oceanic mantle. *Earth and Planetary Science Letters* **133**, 379–395.

Hasenaka, T. (1986). The cinder cones of Michoacan-Guanajuato, Central Mexico /. PhD Thesis, Berkeley, University of California.

Hasenaka, T. (1994). Size, distribution, and magma output rate for shield volcanoes of the Michoacán-Guanajuato volcanic field, Central Mexico. *Journal of Volcanology and Geothermal Research* **63**, 13–31.

Hasenaka, T. & Carmichael, I. S. E. (1985a). The cinder cones of Michoacán-Guanajuato, central Mexico: their age, volume and distribution, and magma discharge rate. *Journal of Volcanology and Geothermal Research* **25**, 105–124.

Hasenaka, T. & Carmichael, I. S. E. (1985b). A compilation of location, size, and geomorphological parameters of volcanoes in the Michoacán-Guanajuato volcanic field, México. *Geofísica Internacional* **24**, 577–608.

Hasenaka, T. & Carmichael, I. S. E. (1987). The Cinder Cones of Michoacán-Guanajuato, Central Mexico: Petrology and Chemistry. *Journal of Petrology* **28**, 241–269.

Henry, C. D. & Aranda-Gomez, J. J. (1992). The real southern Basin and Range: Mid- to late Cenozoic extension in Mexico. *Geology* **20**, 701–704.

Herrera, F. & Milán, M. (1981). *Estudio geológico de las zonas geotérmicas de Yexthó, Pathé y Taxidó, estados de Hidalgo y Querétaro*. Informe interno. Comisión Federal de Electricidad, 13–81.

Herzberg, C. & O'Hara, M. J. (2002). Plume-associated ultramafic magmas of phanerozoic age. *Journal of Petrology* **43**, 1857–1883.

Huang, F., Lundstrom, C. C., Glessner, J., Ianno, A., Boudreau, A., Li, J., Ferré, E. C., Marshak, S. & DeFrates, J. (2009). Chemical and isotopic fractionation of wet andesite in a temperature gradient: Experiments and models suggesting a new mechanism of magma differentiation. *Geochimica et Cosmochimica Acta* **73**, 729–749.

Humboldt, A. von (1811). *Essai politique sur le royaume de la Nouvelle-Espagne*. Paris : Chez F. Schoell .

INEGI (2016). *Mapa digital de México*. http://gaia.inegi.org.mx/mdm6/. Last accessed 2016-10-26.

Irvine, T. N. & Baragar, W. R. A. (1971). A Guide to the Chemical Classification of the Common Volcanic Rocks. *Canadian Journal of Earth Sciences* **8**, 523–548.

James, D. E. (1981). The combined use of oxygen and radiogenic isotopes as indicators of crustal contamination. *Annual Review of Earth and Planetary Sciences* **9**, 311–344.

Jankovics, M. É., Harangi, S., Kiss, B. & Ntaflos, T. (2012). Open-system evolution of the Füzes-tó alkaline basaltic magma, western Pannonian Basin: Constraints from mineral textures and compositions. *Lithos* **140**–**141**, 25–37.

Jarosewich, E., Nelen, J. A. & Norberg, J. A. (1980). Reference Samples for Electron Microprobe Analysis. *Geostandards Newsletter* **4**, 43–47.

Jarosewich, E. & Sampson, J. (1987). Strontianite Reference Sample for Electron Microprobe and SEM Analyses. *Journal of Sedimentary Research* **57**.

Johnson, E. R., Wallace, P. J., Cashman, K. V. & Delgado Granados, H. (2010). Degassing of volatiles (H2O, CO2, S, Cl) during ascent, crystallization, and eruption at mafic monogenetic volcanoes in central Mexico. *Journal of Volcanology and Geothermal Research* **197**, 225–238.

Johnson, E. R., Wallace, P. J., Cashman, K. V., Granados, H. D. & Kent, A. J. R. (2008). Magmatic volatile contents and degassing-induced crystallization at Volcán Jorullo, Mexico: Implications for melt evolution and the plumbing systems of monogenetic volcanoes. *Earth and Planetary Science Letters* **269**, 478–487.

Johnson, E. R., Wallace, P. J., Delgado Granados, H., Manea, V. C., Kent, A. J. R., Bindeman, I. N. & Donegan, C. S. (2009). Subduction-related Volatile Recycling and Magma Generation beneath Central Mexico: Insights from Melt Inclusions, Oxygen Isotopes and Geodynamic Models. *Journal of Petrology* **50**, 1729–1764.

Keiding, J. K. & Sigmarsson, O. (2012). Geothermobarometry of the 2010 Eyjafjallajökull eruption: New constraints on Icelandic magma plumbing systems. *Journal of Geophysical Research: Solid Earth* **117**, B00C09.

Kelley, K. A. & Cottrell, E. (2009). Water and the Oxidation State of Subduction Zone Magmas. *Science* **325**, 605–607.

Keppie, J. D. & Ortega-Gutierrez, E. (1995). Provenance of Mexican Terranes: Isotopic Constraints. *International Geology Review* **37**, 813–824.

Kereszturi, G. (2012). Monogenetic Basaltic Volcanoes: Genetic Classification, Growth, Geomorphology and Degradation. In: Németh, K. (ed.) *Updates in Volcanology - New Advances in Understanding Volcanic Systems*. InTech.

Kim, Y., Clayton, R. W. & Jackson, J. M. (2010). Geometry and seismic properties of the subducting Cocos plate in central Mexico. *Journal of Geophysical Research: Solid Earth* **115**, B06310.

Kim, Y., Miller, M. S., Pearce, F. & Clayton, R. W. (2012). Seismic imaging of the Cocos plate subduction zone system in central Mexico. *Geochem. Geophys. Geosyst.* **13**, Q07001.

Kinzler, R. J. & Grove, T. L. (1992). Primary magmas of mid-ocean ridge basalts 1. Experiments and methods. *Journal of Geophysical Research* **97**, 6885–6906.

Klemetti, E. W. (2016). Melts, mush, and more: Evidence for the state of intermediate-to-silicic arc magmatic systems. *American Mineralogist* **101**, 2365–2366.

Kostoglodov, V. & Bandy, W. (1995). Seismotectonic constraints on the convergence rate between the Rivera and North American plates. *Journal of Geophysical Research: Solid Earth* **100**, 17977–17989.

Kurokawa, K., Otsuki, K. & Hasenaka, T. (1995). Tectonic stress field and fractal distribution of volcanoes in the Michoacan-Guanajuato region of the Mexican Volcanic Belt. *Geofísica Internacional* **34**, 309–320.

Kusakabe, M., Maruyama, S., Nakamura, T. & Yada, T. (2004). CO_2 Laser-BrF_5 Fluorination Technique for Analysis of Oxygen Three Isotopes of Rocks and Minerals. *Journal of the Mass Spectrometry Society of Japan* **52**, 205–212.

Lange, R. A. & Carmichael, I. S. E. (1990). Hydrous Basaltic Andesites Associated with Minette and Related Lavas in Western Mexico. *Journal of Petrology* **31**, 1225–1259.

Lange, R. A. & Carmichael, I. S. E. (1991). A potassic volcanic front in western Mexico: The lamprophyric and related lavas of San Sebastian. *GSA Bulletin* **103**, 928–940.

Larson, R. L. (1972). Bathymetry, Magnetic Anomalies, and Plate Tectonic History of the Mouth of the Gulf of California. *Geological Society of America Bulletin* **83**, 3345 –3360.

Lassiter, J. C. & Luhr, J. F. (2001). Osmium abundance and isotope variations in mafic Mexican volcanic rocks: Evidence for crustal contamination and constraints on the geochemical behavior of osmium during partial melting and fractional crystallization. *Geochemistry, Geophysics, Geosystems* **2**, 1027.

Le Bas, M. J., Le Maitre, R. W., Streckeisen, A. & Zanettin, B. (1986). A Chemical Classification of Volcanic Rocks Based on the Total Alkali-Silica Diagram. *Journal of Petrology* **27**, 745–750.

Le Corvec, N., Menand, T. & Lindsay, J. (2013a). Interaction of ascending magma with pre-existing crustal fractures in monogenetic basaltic volcanism: An

experimental approach. *Journal of Geophysical Research: Solid Earth* **118**, 968–984.

Le Corvec, N., Spörli, K. B., Rowland, J. & Lindsay, J. (2013b). Spatial distribution and alignments of volcanic centers: Clues to the formation of monogenetic volcanic fields. *Earth-Science Reviews* **124**, 96–114.

Lenhardt, N., Böhnel, H., Wemmer, K., Torres-Alvarado, I. S., Hornung, J. & Hinderer, M. (2010). Petrology, magnetostratigraphy and geochronology of the Miocene volcaniclastic Tepoztlán Formation: implications for the initiation of the Transmexican Volcanic Belt (Central Mexico). *Bulletin of Volcanology* **72**, 817–832.

León Soto, G., Ni, J. F., Grand, S. P., Sandvol, E., Valenzuela, R. W., Speziale, M. G., González, J. M. G. & Reyes, T. D. (2009). Mantle flow in the Rivera—Cocos subduction zone. *Geophysical Journal International* **179**, 1004–1012.

Lonsdale, P. (1989). Geology and tectonic history of the Gulf of California. *The Geology of North America: The Eastern Pacific Ocean and Hawaii*. Boulder (Colorado): The Geological Society of America, 499–521.

Lonsdale, P. (2005). Creation of the Cocos and Nazca plates by fission of the Farallon plate. *Tectonophysics* **404**, 237–264.

López-Infanzón, M. (1991). Petrologic study of the volcanic rocks in the Chiconquiaco-Palma Sola area, central Veracruz, Mexico. Master Science Thesis, New Orleans, Tulane University.

Losantos, E., Cebriá, J. M., Morán-Zenteno, D. J., Martiny, B. M. & López Ruiz, José (2015). Composición isotópica de oxígeno de las lavas del volcán Parícutin (Campo volcánico de Michoacán-Guanajuato, México). *GEOS*. Reunión Anual de la Unión Geofísica Mexicana. Puerto Vallarta, México, 98–99.

Losantos, E., Cebriá, J. M., Morán-Zenteno, D. J., Martiny, B. M. & López-Ruiz, J. (2014). Condiciones de cristalización y diferenciación de las lavas del volcán El Metate (Campo Volcánico de Michoacán-Guanajuato, México). *Estudios Geológicos* **70**, 020.

Losantos, E., Cebria, J.-M., Morán-Zenteno, D. J., Martiny, B. M., López Ruiz, J. & Solís-Pichardo, G. (2017). Petrogenesis of the alkaline and calcalkaline monogenetic volcanism in the northern sector of the Michoacán-Guanajuato Volcanic Field (Central Mexico). *Lithos* (under revision).

Lozano-Santa Cruz, R. & Bernal, J. P. (2005). Characterization of a new set of eight geochemical reference materials for XRF major and trace element analysis. *Revista Mexicana de Ciencias Geológicas* **22**, 329–344.

Luhr, J. F. (1997). Extensional tectonics and the diverse primitive volcanic rocks in the western Mexican volcanic belt. *The Canadian Mineralogist* **35**, 473–500.

Luhr, J. F. (2001). Glass inclusions and melt volatile contents at Parícutin Volcano, Mexico. *Contributions to Mineralogy and Petrology* **142**, 261–283.

Luhr, J. F., Allan, J. F., Carmichael, I. S. E., Nelson, S. A. & Hasenaka, T. (1989). Primitive calc-alkaline and alkaline rock types from the western Mexican Volcanic Belt. *Journal of Geophysical Research* **94**, 4515–4530.

Luhr, J. F. & Carmichael, I. (1985). Jorullo Volcano, Michoacán, Mexico (1759–1774): The earliest stages of fractionation in calc-alkaline magmas. *Contributions to Mineralogy and Petrology* **90**, 142–161.

Luhr, J. F. & Carmichael, I. S. E. (1980). The Colima Volcanic complex, Mexico. *Contributions to Mineralogy and Petrology* **71**, 343–372.

Luhr, J. F. & Carmichael, I. S. E. (1981). The Colima volcanic complex, Mexico: Part II. Late-quaternary cinder cones. *Contributions to Mineralogy and Petrology* **76**, 127–147.

Maciel Peña, R., Goguitchaichvili, A., Garduño Monroy, V., Ruiz Martinez, V., Aguilar Reyes, B., Morales, J., Alva-Valdivia, L., Caballero Miranda, C. & Urrutia-Fucugauchi, J. (2009). Paleomagnetic and rock-magnetic survey of Brunhes lava flows from Tancitaro volcano, Mexico. *Geofísica internacional* **48**, 375–384.

Manea, V. C., Manea, M. & Ferrari, L. (2013). A geodynamical perspective on the subduction of Cocos and Rivera plates beneath Mexico and Central America. *Tectonophysics* **609**, 56–81.

Manea, V. C., Manea, M., Ferrari, L., Orozco-Esquivel, T., Valenzuela, R. W., Husker, A. & Kostoglodov, V. (2017). A review of the geodynamic evolution of flat slab subduction in Mexico, Peru, and Chile. *Tectonophysics* **695**, 27–52.

Márquez, A., Oyarzun, R., Doblas, M. & Verma, S. P. (1999). Alkalic (ocean-island basalt type) and calc-alkalic volcanism in the Mexican volcanic belt: A case for plume-related magmatism and propagating rifting at an active margin? *Geology* **27**, 51–54.

Márquez, A., Verma, S. P., Anguita, F., Oyarzun, R. & Brandle, J. L. (1999). Tectonics and volcanism of Sierra Chichinautzin: extension at the front of the Central Trans-

Mexican Volcanic belt. *Journal of Volcanology and Geothermal Research* **93**, 125–150.

Márquez-Azúa, B., Cabral-Cano, E., Correa-Mora, F. & DeMets, C. (2004). A model for Mexican neotectonics based on nationwide GPS measurements, 1993-2001. *Geofísica Internacional* **43**, 319–330.

Martin Del Pozzo, A. L. (1982). Monogenetic vulcanism in Sierra Chichinautzin, Mexico. *Bulletin Volcanologique* **45**, 9–24.

Martini, M., Fitz, E., Solari, L., Camprubi, A., Hudleston, P. J., Lawton, T. F., Tolson, G. & Centeno-García, E. (2012). The Late Cretaceous fold-thrust belt in the Peña de Bernal–Tamazunchale area and its possible relationship to the accretion of the Guerrero Terrane. *Field Guides* **25**, 19–38.

Martini, M. & Ortega-Gutiérrez, F. (2017). Tectono-stratigraphic evolution of eastern Mexico during the break-up of Pangea: A review. *Earth-Science Reviews*.

Mason, P. R. D., Downes, H., Thirlwall, M. F., Seghedi, I., Szakács, A., Lowry, D. & Mattey, D. (1996). Crustal assimilation as a major petrogenetic process in the East Carpathian neogene and quaternary continental margin arc, Romania. *Journal of Petrology* **37**, 927–959.

Mathez, E. (1973). Refinement of the Kudo-Weill plagioclase thermometer and its application to basaltic rocks. *Contributions to Mineralogy and Petrology* **41**, 61–72.

McBirney, A. R., Taylor, H. P. & Armstrong, R. L. (1987). Paricutin re-examined: a classic example of crustal assimilation in calc-alkaline magma. *Contributions to Mineralogy and Petrology* **95**, 4–20.

McBirney, A. R. & Weill, D. F. (1966). Rhyolite magmas of central America. *Bulletin Volcanologique* **29**, 435–446.

McDonough, W. F. & Sun, S. -s. (1995). The composition of the Earth. *Chemical Geology* **120**, 223–253.

McDowell, F. W. & Ciabaugh, S. E. (1972). Edades Potasio-argón de rocas volcánicas en la Sierra Madre Occidental al Noreste de Mazatlán. II Convención de la Sociedad Geológica de México, 182–185.

McGee, L. E., Beier, C., Smith, I. E. M. & Turner, S. P. (2011). Dynamics of melting beneath a small-scale basaltic system: a U-Th–Ra study from Rangitoto volcano, Auckland volcanic field, New Zealand. *Contributions to Mineralogy and Petrology* **162**, 547–563.

McGee, L. E. & Smith, I. E. M. (2016). Interpreting chemical compositions of small scale basaltic systems: A review. *Journal of Volcanology and Geothermal Research* **325**, 45–60.

McGee, L. E., Smith, I. E. M., Millet, M.-A., Handley, H. K. & Lindsay, J. M. (2013). Asthenospheric Control of Melting Processes in a Monogenetic Basaltic System: a Case Study of the Auckland Volcanic Field, New Zealand. *Journal of Petrology* **54**, 2125–2153.

McGuire, A. V., Francis, C. A. & Dyar, M. D. (1992). Mineral standards for electron microprobe analysis of oxygen. *American Mineralogist* **77**, 1087–1091.

McNally, K. C. & Minster, J. B. (1981). Nonuniform seismic slip rates along the Middle America Trench. *Journal of Geophysical Research: Solid Earth* **86**, 4949–4959.

Melgar, D. & Pérez-Campos, X. (2010). Imaging the Moho and Subducted Oceanic Crust at the Isthmus of Tehuantepec, Mexico, from Receiver Functions. *Pure and Applied Geophysics* **168**, 1449–1460.

Miesch, A. T. (1979). Vector analysis of chemical variation in the lavas of Parícutin volcano, Mexico. *Journal of the International Association for Mathematical Geology* **11**, 345–371.

Miles, A. J., Graham, C. M., Hawkesworth, C. J., Gillespie, M. R., Hinton, R. W. & Bromiley, G. D. (2014). Apatite: A new redox proxy for silicic magmas? *Geochimica et Cosmochimica Acta* **132**, 101–119.

Minster, J. B. & Jordan, T. H. (1978). Present-day plate motions. *Journal of Geophysical Research: Solid Earth* **83**, 5331–5354.

Molnar, P. & Sykes, L. K. (1969). Tectonics of the Caribbean and dalajara region and Middle American regions from focal mechanisms and seismicity. *geological Society of America Bulletin* **80**, 1639–1684.

Moore, G., Marone, C., Carmichael, I. S. E. & Renne, P. (1994). Basaltic volcanism and extension near the intersection of the Sierra Madre volcanic province and the Mexican Volcanic Belt. *Geological Society of America Bulletin* **106**, 383–394.

Morán-Zenteno, D. (ed.) (1994). *The Geology of the Mexican Republic*. American Association of Petroleum Geologists.

Moran-Zenteno, D. J. (1986). Breve revision sobre la evolucion tectonica de Mexico. *Geofisica Internacional* **25**, 9–38.

Morán-Zenteno, D. J. *et al.* (1999). Tertiary arc-magmatism of the Sierra Madre del Sur, Mexico, and its transition to the volcanic activity of the Trans-Mexican Volcanic Belt. *Journal of South American Earth Sciences* **12**, 513–535.

Mori, L., Gómez-Tuena, A., Cai, Y. & Goldstein, S. L. (2007). Effects of prolonged flat subduction on the Miocene magmatic record of the central Trans-Mexican Volcanic Belt. *Chemical Geology* **244**, 452–473.

Mori, L., Gómez-Tuena, A., Schaaf, P., Goldstein, S. L., Pérez-Arvizu, O. & SolÍs-Pichardo, G. (2009). Lithospheric Removal as a Trigger for Flood Basalt Magmatism in the Trans-Mexican Volcanic Belt. *Journal of Petrology* **50**, 2157–2186.

Mori, L., Gomez-Tuena, A., Schaaf, P., Goldstein, S. L., Perez-Arvizu, O. & Solls-Pichardo, G. (2017). Lithospheric Removal as a Trigger for Flood Basalt Magmatism in the Trans-Mexican Volcanic Belt. *Journal of Petrology* **50**, 2157–2186.

Morimoto, N. (1988). Nomenclature of Pyroxenes. *Mineralogy and Petrology* **39**, 55–76.

Mullen, E. K. & McCallum, I. S. (2013). Origin of Basalts in a Hot Subduction Setting: Petrological and Geochemical Insights from Mt. Baker, Northern Cascade Arc. *Journal of Petrology*.

Nance, R. D., Miller, B. V., Keppie, J. D., Murphy, J. B. & Dostal, J. (2006). Acatlán Complex, southern Mexico: Record spanning the assembly and breakup of Pangea. *Geology* **34**, 857–860.

Negendank, J. F. W. (1972a). Volcanics of the Valley of Mexico. Part. I: Petrography of the Volcanics. *Neues Jahrbuch für Mineralogie, Abhandlungen* **116**, 308–320.

Negendank, J. F. W. (1972b). Volcanics of the Valley of Mexico. Part II: The Opaque Mineralogy. *Neues Jahrbuch für Mineralogie, Abhandlungen* **117**, 183–195.

Negendank, J. F. W., Emmermann, R., Krawczyk, R., Mooser, F., Tobschall, H. & Werle, D. (1985). Geological and geochemical investigations on the eastern trans mexican volcanic belt. *Geofísica Internacional* **24**, 477–575.

Nelson, S. A. & Carmichael, I. S. E. (1984). Pleistocene to recent alkalic volcanism in the region of Sanganguey volcano, Nayarit, Mexico. *Contributions to Mineralogy and Petrology* **85**, 321–335.

Nelson, S. T. & Montana, A. (1992). Sieve-textured plagioclase in volcanic rocks produced by rapid decompression. *The American Mineralogist* **77**, 1242–1249.

Németh, K. & Kereszturi, G. (2015). Monogenetic volcanism: personal views and discussion. *International Journal of Earth Sciences* **104**, 2131–2146.

Nichols, C. R. (1970). The geology and geochemistry of the Pathé geothermal zone, Hidalgo, Mexico. PhD Thesis, University of Oklahoma.

Nielsen, R. L. (2016). *GERM Partition Coefficient (Kd) Database*. https://earthref.org/KDD/. Last accessed 2016-08-10

Nieto-Obregón, J., Delgado-Argote, L. & Damon, P. (1981). Relaciones petrológicas y geocronológicas del magmatismo de la Sierra Madre Occidental y el Eje Neovolcánico en Nayarit, Jalisco y Zacatecas. *Memoria Técnica, Asociación Ingenieros Mineros, Metalúrgicos y Geólogos de México* **14**, 327–361.

Nixon, G. T. (1982). The relationship between Quaternary volcanism in central Mexico and the seismicity and structure of subducted ocean lithosphere. *Geological Society of America Bulletin* **93**, 514–523.

Nixon, G. T. (1989). The Geology of Iztaccíhuatl Volcano and Adjacent Areas of The Sierra Nevada and Valley of Mexico. *Geological Society of America Special Papers* **219**, 1–59.

Nixon, G. T., Demant, A., Armstrong, R. L. & Harakal, J. E. (1987). K-Ar and geologic data bearing on the age and evolution of the Trans-Mexican volcanic belt. *Geofisica Internacional* **26**, 109–158.

Núñez, G. C., Milán, M. & Verma, S. P. (1989). Geología del volcán Zamorano, estado de Querétaro. *Revista Mexicana de Ciencias Geológicas* **8**, 194–201.

Orozco-Esquivel, M. T., López-Martínez, M. & Ferrari, L. (2010). El volcanismo miocénico de la Faja Volcánica Transmexicana: migración del arco y variación en la contribución de componentes de subducción. *Geosphere* **30**, 160–161.

Ortega-Gutiérrez, F., Gómez-Tuena, A., Elías-Herrera, M., Solari, L. A., Reyes-Salas, M. & Macías-Romo, C. (2014). Petrology and geochemistry of the Valle de Santiago lower-crust xenoliths: Young tectonothermal processes beneath the central Trans-Mexican volcanic belt. *Lithosphere* **6**, 335–360.

Ortega-Gutierrez, F., Mitre-Salazar, L. M., Roldán-Quintana, J., Aranda-Gómez, J. J., Morán-Zenteno, D. J., Alaniz-Álvarez, S. A. & Nieto-Samaniego, A. F. (1992). Carta Geológica de la República Mexicana 5a Edición. Instituto de Geología (UNAM); Secretaría de Minas e Industria Paraestatal, Consejo de Recursos Minerales.

Ortega-Gutierrez, F., Ruiz, J. & Centeno-Garcia, E. (1995). Oaxaquia, a Proterozoic microcontinent accreted to North America during the late Paleozoic. *Geology* **23**, 1127–1130.

Ortega-Gutierrez, F., Sedlock, R. L. & Speed, R. C. (1994). Phanerozoic tectonic evolution of Mexico. In: Speed, R. C. (ed.) *Phanerozoic Evolution of North*

American Continent-Ocean Transitions. Boulder, Colorado: Geological Society of America.

Ownby, S. E., Lange, R. A. & Hall, C. M. (2008). The eruptive history of the Mascota volcanic field, western Mexico: Age and volume constraints on the origin of andesite among a diverse suite of lamprophyric and calc-alkaline lavas. *Journal of Volcanology and Geothermal Research* **177**, 1077–1091.

Palme, H. & O'Neill, H. S. C. (2014). Cosmochemical Estimates of Mantle Composition. In: Holland, H. D. & Turekian, K. K. (eds) *Treatise on Geochemistry (Second Edition)*. Oxford: Elsevier, 1–39.

Pardo, M. & Suárez, G. (1995). Shape of the subducted Rivera and Cocos plates in southern Mexico: Seismic and tectonic implications. *Journal of Geophysical Research: Solid Earth* **100**, 12357–12373.

Pasquarè, G., Ferrari, L., Garduño-Monroy, V. H. & Vezzoli, L. (1991). Geology of the central sector of Mexican Volcanic Belt, States of Guanajuato and Michoacan, Mexico. Geological Society of America. GSA Map & Chart Series.

Patiño Douce, A. E. (2005). Vapor-absent melting of tonalite at 15-32 kbar. *Journal of Petrology* **46**, 275–290.

Peacock, M. A. (1931). Classification of Igneous Rock Series. *The Journal of Geology* **39**, 54–67.

Pearce, J. A. (1982). Trace element characteristics of lavas from destructive plate boundaries. *Andesites: Orogenic Andesites and Related Rocks* **8,** 525–548.

Pearce, T. H. (1994). Recent Work on Oscillatory Zoning in Plagioclase. In: Parsons, I. (ed.) *Feldspars and their Reactions*. Dordrecht: Springer Netherlands, 313–349.

Pearce, T. H. & Kolisnik, A. M. (1990). Observations of plagioclase zoning using interference imaging. *Earth-Science Reviews* **29**, 9–26.

Pe-Piper, G. (1984). Zoned pyroxenes from shoshonite lavas of Lesbos, Greece: inferences concerning shoshonite petrogenesis. *Journal of petrology* **25**, 453–472.

Pérez-Campos, X. *et al.* (2008). Horizontal subduction and truncation of the Cocos Plate beneath central Mexico. *Geophysical Research Letters* **35**, doi:10.1029/2008GL035127.

Pérez-Venzor, J. A., Aranda-Gómez, J. J., McDowell, F. & Solorio-Munguía, J. G. (1996). Geología del Volcán Palo Huérfano, Guanajuato, México. *Revista Mexicana de Ciencias Geológicas* **13**, 174–183.

Petrone, C. M., Francalanci, L., Carlson, R. W., Ferrari, L. & Conticelli, S. (2003). Unusual coexistence of subduction-related and intraplate-type magmatism: Sr, Nd and Pb isotope and trace element data from the magmatism of the San Pedro–Ceboruco graben (Nayarit, Mexico). *Chemical Geology* **193**, 1–24.

Pioli, L., Erlund, E., Johnson, E., Cashman, K., Wallace, P., Rosi, M. & Delgado Granados, H. (2008). Explosive dynamics of violent Strombolian eruptions: The eruption of Parícutin Volcano 1943-1952 (Mexico). *Earth and Planetary Science Letters* **271**, 359–368.

Plank, T., Kelley, K. A., Zimmer, M. M., Hauri, E. H. & Wallace, P. J. (2013). Why do mafic arc magmas contain 4wt% water on average? *Earth and Planetary Science Letters* **364**, 168–179.

Plechov, P. Y., Tsai, A. E., Shcherbakov, V. D. & Dirksen, O. V. (2008). Opacitization conditions of hornblende in Bezymyannyi volcano andesites (March 30, 1956 eruption). *Petrology* **16**, 19–35.

Potra, A., Hickey-Vargas, R., Macfarlane, A. W. & Salters, V. J. M. (2014). Características isotópicas de Pb, Sr, Nd de diversas litologías del terreno compuesto Guerrero, centro-oeste de México: restricciones para su origen. *Revista Mexicana de Ciencias Geológicas* **31**, 203–220.

Pozzo, A. L. M. del (1982). Monogenetic vulcanism in sierra Chichinautzin, Mexico. *Bulletin Volcanologique* **45**, 9–24.

Putirka, K. D. (2005). Igneous thermometers and barometers based on plagioclase + liquid equilibria: Tests of some existing models and new calibrations. *American Mineralogist* **90**, 336–346.

Putirka, K. D. (2008). Thermometers and Barometers for Volcanic Systems. *Reviews in Mineralogy and Geochemistry* **69**, 61–120.

Putirka, K., Johnson, M., Kinzler, R., Longhi, J. & Walker, D. (1996). Thermobarometry of mafic igneous rocks based on clinopyroxene-liquid equilibria, 0–30 kbar. *Contributions to Mineralogy and Petrology* **123**, 92–108.

Rasoazanamparany, C., Widom, E., Siebe, C., Guilbaud, M.-N., Spicuzza, M. J., Valley, J. W., Valdez, G. & Salinas, S. (2016). Temporal and compositional evolution of Jorullo volcano, Mexico: Implications for magmatic processes associated with a monogenetic eruption. *Chemical Geology* **434**, 62–80.

Rhodes, J. M., Dungan, M. A., Blanchard, D. P. & Long, P. E. (1979). Magma mixing at mid-ocean ridges: Evidence from basalts drilled near 22°N on the mid-Atlantic Ridge. *Tectonophysics* **55**, 35–61.

Richter, K. & Carmichael, I. S. E. (1993). Mega-xenocrysts in alkali olivine basalts; fragments of disrupted mantle assemblages. *American Mineralogist* **78**, 1230–1245.

Ridolfi, F., Renzulli, A. & Puerini, M. (2010). Stability and chemical equilibrium of amphibole in calc-alkaline magmas: an overview, new thermobarometric formulations and application to subduction-related volcanoes. *Contributions to Mineralogy and Petrology* **160**, 45–66.

Righter, K. & Carmichael, I. S. E. (1992). Hawaiites and related lavas in the Atenguillo graben, western Mexican Volcanic Belt. *Geological Society of America Bulletin* **104**, 1592–1607.

Righter, K., Carmichael, I. S. E., Becker, T. A. & Renne, P. R. (1995a). Pliocene-Quaternary volcanism and faulting at the intersection of the Gulf of California and the Mexican Volcanic Belt. *Geological Society of America Bulletin* **107**, 612–626.

Righter, K., Carmichael, I. S. E., Becker, T. A. & Renne, R. P. (1995b). Pliocene to Quaternary volcanism and tectonism at the intersection of the Mexican Volcanic Belt and the Gulf of California. *Geological Society of America Bulletin* **107**, 612–626.

Righter, K. & Rosas-Elguera, J. (2001). Alkaline Lavas in the Volcanic Front of the Western Mexican Volcanic Belt: Geology and Petrology of the Ayutla and Tapalpa Volcanic Fields. *Journal of Petrology* **42**, 2333–2361.

Robin, C., Mossand, P., Camus, G., Cantagrel, J.-M., Gourgaud, A. & Vincent, P. M. (1987). Eruptive history of the Colima volcanic complex (Mexico). *Journal of Volcanology and Geothermal Research* **31**, 99–113.

Rodríguez, S. R., Morales-Barrera, W., Layer, P. & González-Mercado, E. (2010). A quaternary monogenetic volcanic field in the Xalapa region, eastern Trans-Mexican volcanic belt: Geology, distribution and morphology of the volcanic vents. *Journal of Volcanology and Geothermal Research* **197**, 149–166.

Rollinson, H. R. (1993). *Using Geochemical Data: Evaluation, Presentation, Interpretation*. Longman Scientific & Technical.

Rosas-Elguera, J., Alva-Valdivia, L. M., Goguitchaichvili, A., Urrutia-Fucugauchi, J., Ortega-Rivera, M. A., Prieto, J. C. S. & Lee, J. K. W. (2003). Counterclockwise Rotation of the Michoacan Block: Implications for the Tectonics of Western Mexico. *International Geology Review* **45**, 814–826.

Rosas-Elguera, J., Ferrari, L., Garduño-Monroy, V. H. & Urrutia-Fucugauchi, J. (1996). Continental boundaries of the Jalisco block and their influence in the Pliocene-Quaternary kinematics of western Mexico. *Geology* **24**, 921–924.

Rosas-Elguera, J., Ferrari, L., Martinez, M. L. & Urrutia-Fucugauchi, J. (1997). Stratigraphy and Tectonics of the Guadalajara Region and Triple-Junction Area, Western Mexico. *International Geology Review* **39**, 125–140.

Rossotti, A., Ferrari, L., López-Martínez, M. & Rosas-Elguera, J. (2002). Geology of the boundary between the Sierra Madre Occidental and the Trans-Mexican Volcanic Belt in the Guadalajara region, western Mexico. *Revista Mexicana de Ciencias Geológicas* **19**, 1–15.

Rowe, M. C., Peate, D. W. & Ukstins Peate, I. (2011). An Investigation into the Nature of the Magmatic Plumbing System at Paricutin Volcano, Mexico. *Journal of Petrology* **52**, 2187–2220.

Ruiz, J., Patchett, P. J. & Ortega-Gutierrez, F. (1988). Proterozoic and Phanerozoic basement terranes of Mexico from Nd isotopic studies. *Geological Society of America Bulletin* **100**, 274–281.

Ruprecht, P. & Wörner, G. (2007). Variable regimes in magma systems documented in plagioclase zoning patterns: El Misti stratovolcano and Andahua monogenetic cones. *Journal of Volcanology and Geothermal Research* **165**, 142–162.

Rutherford, M. J. (2008). Magma ascent rates. *Reviews in Mineralogy and Geochemistry* **69**, 241–271.

Rutherford, M. J. & Hill, P. M. (1993). Magma ascent rates from amphibole breakdown: an experimental study applied to the 1980–1986 Mount St. Helens eruptions. *Journal of Geophysical Research* **98**, 667–685.

Scaillet, B. & MacDonald, R. (2003). Experimental constraints on the relationships between peralkaline rhyolites of the Kenya Rift Valley. *Journal of Petrology* **44**, 1867–1894.

Schaaf, P., Morán-Zenteno, D., Hernández-Bernal, M. del S., Solís-Pichardo, G., Tolson, G. & Köhler, H. (1995). Paleogene continental margin truncation in southwestern Mexico: Geochronological evidence. *Tectonics* **14**, 1339–1350.

Schaaf, P., Stimac, J., Siebe, C. & Macías, J. L. (2005). Geochemical Evidence for Mantle Origin and Crustal Processes in Volcanic Rocks from Popocatépetl and Surrounding Monogenetic Volcanoes, Central Mexico. *Journal of Petrology* **46**, 1243–1282.

Sedlock, R. L., Ortega-Gutiérrez, F. & Speed, R. C. (1993). Tectonostratigraphic terranes and tectonic evolution of Mexico. Geological Society of America Special Paper **278**, 1–153.

Sheth, H. C., Torres-Alvarado, I. S. & Verma, S. P. (2000). Beyond subduction and plumes: A unified tectonic-petrogenetic model for the Mexican volcanic belt. *International Geology Review* **42**, 1116–1132.

Shirey, S. B. & Walker, R. J. (1998). The Re-Os isotope system in cosmochemistry and high-temperature geochemistry. *Annual Review of Earth and Planetary Sciences* **26**, 423–500.

Siebe, C., Rodríguez-Lara, V., Schaaf, P. & Abrams, M. (2004a). Radiocarbon ages of Holocene Pelado, Guespalapa, and Chichinautzin scoria cones, south of Mexico City: implications for archaeology and future hazards. *Bulletin of Volcanology* **66**, 203–225.

Siebe, C., Rodriguez-Lara, V., Schaaf, P. & Abrams, M. (2004b). Geochemistry, Sr-Nd isotope composition, and tectonic setting of Holocene Pelado, Guespalapa and Chichinautzin scoria cones, south of Mexico City. *Journal of Volcanology and Geothermal Research* **130**, 197–226.

Siebert, L. & Carrasco-Núñez, G. (2002). Late-Pleistocene to precolumbian behind-the-arc mafic volcanism in the eastern Mexican Volcanic Belt; implications for future hazards. *Journal of Volcanology and Geothermal Research* **115**, 179–205.

Sigurdsson, H. (2000). *Encyclopedia of volcanoes*. San Diego: Academic Press.

Sisson, T. W. & Grove, T. L. (1993). Experimental investigations of the role of H2O in calc-alkaline differentiation and subduction zone magmatism. *Contributions to Mineralogy and Petrology* **113**, 143–166.

Soto, G. L., Ni, J. F., Grand, S. P., Sandvol, E., Valenzuela, R. W., Speziale, M. G., González, J. M. G. & Reyes, T. D. (2009). Mantle flow in the Rivera—Cocos subduction zone. *Geophysical Journal International* **179**, 1004–1012.

Spera, F. J. & Bohrson, W. A. (2001). Energy-Constrained open-system magmatic processes I: General model and energy-constrained assimilation and fractional crystallization (EC-AFC) formulation. *Journal of Petrology* **42**, 999–1018.

Stewart, M. L. & Pearce, T. H. (2004). Sieve-textured plagioclase in dacitic magma: Interference imaging results. *American Mineralogist* **89**, 348–351.

Straub, S. M. *et al.* (2015). Crustal recycling by subduction erosion in the central Mexican Volcanic Belt. *Geochimica et Cosmochimica Acta* **166**, 29–52.

Straub, S. M., Gómez-Tuena, A., Zellmer, G. F., Espinasa-Perena, R., Stuart, F. M., Cai, Y., Langmuir, C. H., Martin-Del Pozzo, A. L. & Mesko, G. T. (2012). The Processes of Melt Differentiation in Arc Volcanic Rocks: Insights from OIB-type Arc Magmas in the Central Mexican Volcanic Belt. *Journal of Petrology*.

Straub, S. M., Zellmer, G. F., Gómez-Tuena, A., Espinasa-Pereña, R., Martin-del Pozzo, A. L., Stuart, F. M. & Langmuir, C. H. (2014). A genetic link between silicic slab components and calc-alkaline arc volcanism in central Mexico. *Geological Society, London, Special Publications* **385**, 31–64.

Streck, M. J. (2008). Mineral Textures and Zoning as Evidence for Open System Processes. *Reviews in Mineralogy and Geochemistry* **69**, 595–622.

Sumner, J. R. (1972). Tectonic Significance of Gravity and Aeromagnetic Investigations at the Head of the Gulf of California. *Geological Society of America Bulletin* **83**, 3103–3120.

Sun, S. S. & McDonough, W. F. (1989). Chemical and isotopic systematics of oceanic basalts: implications for mantle composition and processes. *Geological Society, London, Special Publications* **42**, 313–345.

Suter, M., Contreras, J. & Ochoa-Camarillo, H. (1997). Structure of the Sierra Madre Oriental fold-thrust belt in east-central Mexico (PDF Download Available). *Libro -guía de las excursiones geológicas*. II Convención sobre la Evolución Geológica de México. Pachuca, 45–63.

Suter, M., Martínez, M. C., Martínez, M. L. & Farrar, E. (1995a). The Aljibes half-graben—Active extension at the boundary between the trans-Mexican volcanic belt and the Basin and Range Province, Mexico. *Geological Society of America Bulletin* **107**, 627–641.

Suter, M., Quintero-Legorreta, O., Lopez-Martinez, M., Aguirre-Díaz, G. & Farrar, E. (1995b). The Acambay graben: active intraarc extension in the trans-Mexican Volcanic Belt, Mexico. *Tectonics* **14**, 1245–1262.

Takada, A. (1994). The influence of regional stress and magmatic input on styles of monogenetic and polygenetic volcanism. *Journal of Geophysical Research: Solid Earth* **99**, 13563–13573.

Talavera-Mendoza, O., Ruiz, J., Gehrels, G. E., Meza-Figueroa, D. M., Vega-Granillo, R. & Campa-Uranga, M. F. (2005). U–Pb geochronology of the Acatlán Complex and implications for the Paleozoic paleogeography and tectonic evolution of southern Mexico. *Earth and Planetary Science Letters* **235**, 682–699.

Tatsumi, Y. & Suzuki, T. (2009). Tholeiitic vs Calc-alkalic Differentiation and Evolution of Arc Crust: Constraints from Melting Experiments on a Basalt from the Izu–Bonin–Mariana Arc. *Journal of Petrology* **50**, 1575–1603.

Taylor, S. R. & McLennan, S. M. (1985). *The continental crust: its composition and evolution*. Palo Alto, California: Blackwell.

Taylor, S. R. & McLennan, S. M. (1995). The geochemical evolution of the continental crust. *Reviews of Geophysics* **33**, 241–265.

Urrutia-Fucugauchi, J. & Flores-Ruiz, J. H. (1996). Bouguer Gravity Anomalies and Regional Crustal Structure in Central Mexico. *International Geology Review* **38**, 176–194.

Urrutia-Fucugauchi, J. & Uribe-Cifuentes, R. M. (1999). Lower-Crustal Xenoliths from the Valle de Santiago Maar Field, Michoacan-Guanajuato Volcanic Field, Central Mexico. *International Geology Review* **41**, 1067–1081.

Valentine, G. A. (2012). Shallow plumbing systems for small-volume basaltic volcanoes, 2: Evidence from crustal xenoliths at scoria cones and maars. *Journal of Volcanology and Geothermal Research* **223**, 47–63.

Valentine, G. A. & Gregg, T. K. P. (2008). Continental basaltic volcanoes — Processes and problems. *Journal of Volcanology and Geothermal Research* **177**, 857–873.

Vance, J. A. (1965). Zoning in igneous plagioclase: patchy zoning. *The Journal of Geology* **73**, 636–651.

Vassallo, L., Solorio, J., Ortega-Rivera, M., Sousa, J. & Olalde, G. (2008). Paleogene magmatism and associated skarn-hydrothermal mineralization in the central part of Mexico: Bol-e, **4**, 1–27.

Vega-Granillo, R., Calmus, T., Meza-Figueroa, D., Ruiz, J., Talavera-Mendoza, O. & López -Martínez, M. (2009). Structural and tectonic evolution of the Acatlán Complex, southern Mexico: Its role in the collisional history of Laurentia and Gondwana. *Tectonics* **28**, TC4008.

Vega-Granillo, R., Talavera-Mendoza, O., Meza-Figueroa, D., Ruiz, J., Gehrels, G. E., López-Martínez, M. & Cruz-Vargas, J. C. de la (2007). Pressure-temperature-time evolution of Paleozoic high-pressure rocks of the Acatlán Complex (southern Mexico): Implications for the evolution of the Iapetus and Rheic Oceans. *Geological Society of America Bulletin* **119**, 1249–1264.

Verma, S. P. (2015). Present state of knowledge and new geochemical constraints on the central part of the Mexican Volcanic Belt and comparison with the Central

American Volcanic Arc in terms of near and far trench magmas. *Turkish Journal of Earth Sciences* **24**, 399–460.

Verma, S. P. & Carrasco-Núñez, G. (2003). Reappraisal of the Geology and Geochemistry of Volcán Zamorano, Central Mexico: Implications for Discriminating the Sierra Madre Occidental and Mexican Volcanic Belt Provinces. *International Geology Review* **45**, 724–752.

Verma, S. P. & Hasenaka, T. (2004). Sr, Nd, and Pb isotopic and trace element geochemical constraints for a veined-mantle source of magmas in the Michoacán-Guanajuato Volcanic Field, west-central Mexican Volcanic Belt. *Geochemical Journal* **38**, 43–65.

Verma, S. P., Lopez-Martinez, M. & Terrell, D. J. (1985). Geochemistry of Tertiary igneous rocks from Arandas-Atotonilco area, northeast Jalisco, Mexico. *Geofísica Internacional* **24**, 31–45.

Verma, S. P. & Nelson, S. A. (1989). Isotopic and trace element constraints on the origin and evolution of alkaline and calc-alkaline magmas in the Northwestern Mexican Volcanic Belt. *Journal of Geophysical Research: Solid Earth* **94**, 4531–4544.

Wadge, G. & Cross, A. (1988). Quantitative methods for detecting aligned points: An application to the volcanic vents of the Michoacan-Guanajuato volcanic field, Mexico. *Geology* **16**, 815–818.

Walker, G. P. L. (2000). Basaltic volcanoes and volcanic systems. In: Sigurdsson, H. (ed.) *Encyclopaedia of Volcanoes*. San Diego, CA: Academic Press, 283–289.

Wallace, P. & Carmichael, S. E. (1989). Minette lavas and associated leucitites from the Western Front of the Mexican Volcanic Belt: petrology, chemistry and origin. *Contributions to Mineralogy and Petrology* **103**, 470–492.

Wallace, P. J. & Carmichael, I. S. E. (1999). Quaternary volcanism near the Valley of Mexico: implications for subduction zone magmatism and the effects of crustal thickness variations on primitive magma compositions. *Contributions to Mineralogy and Petrology* **135**, 291–314.

Walter, M. J. & Presnall, D. C. (1994). Melting Behavior of Simplified Lherzolite in the System CaO-MgO-Al2O3-SiO2-Na2O from 7 to 35 kbar. *Journal of Petrology* **35**, 329–359.

Weaver, B. L. (1991). The origin of ocean island basalt end-member compositions: trace element and isotopic constraints. *Earth and Planetary Science Letters* **104**, 381–397.

Wilcox, R. E. (1954). Petrology of Paricutin volcano, Mexico. *United States Geological Survey Bulletin* **965–C**, 281–353.

Wilke, M. & Behrens, H. (1999). The dependence of the partitioning of iron and europium between plagioclase and hydrous tonalitic melt on oxygen fugacity. *Contributions to Mineralogy and Petrology* **137**, 102–114.

Willbold, M. & Stracke, A. (2006). Trace element composition of mantle end-members: Implications for recycling of oceanic and upper and lower continental crust. *Geochemistry, Geophysics, Geosystems* **7**, Q04004.

Williams, H. (1950). Volcanoes of the Paricutin region, Mexico. *Geological Survey Bulletin* **965–B**, 1–279.

Wilson, M. (1989). *Igneous Petrogenesis: A Global Tectonic Approach*. London: Springer.

Winter J. D. (2009) *An introduction to Igneous and Metamorphic Petrology, 2nd Editon*. Pearson.

Yañez, P., Ruiz, J., Patchett, P. J., Ortega-Gutierrez, F. & Gehrels, G. E. (1991). Isotopic studies of the Acatlan Complex, southern Mexico: implications for Paleozoic North American tectonics. *Geological Society of America Bulletin* **103**, 817–828.

Yang, T., Grand, S. P., Wilson, D., Guzman-Speziale, M., Gomez-Gonzalez, J. M., Dominguez-Reyes, T. & Ni, J. (2009). Seismic structure beneath the Rivera subduction zone from finite-frequency seismic tomography. *Journal of Geophysical Research: Solid Earth* **114**, B01302.

Zellmer, G. F., Pistone, M., Iizuka, Y., Andrews, B. J., Gómez-Tuena, A., Straub, S. M. & Cottrell, E. (2016). Petrogenesis of antecryst-bearing arc basalts from the Trans-Mexican Volcanic Belt: Insights into along-arc variations in magma-mush ponding depths, H2O contents, and surface heat flux. *American Mineralogist* **101**, 2405–2422.

Zimmer, M. M. *et al.* (2010). The Role of Water in Generating the Calc-alkaline Trend: New Volatile Data for Aleutian Magmas and a New Tholeiitic Index. *Journal of Petrology* **51**, 2411–2444.

Zindler, A. & Hart, S. (1986). Chemical Geodynamics. *Annual Review of Earth and Planetary Sciences* **14**, 493–571.

Appendix 1: Petrographic files

Rocas Alcalinas T1

Lámina: M85		**Fecha:** 4-03-2013
Campo: (23-01-2013) Huitzatarito, en el escarpe. Cono monogenético.		
Textura: Holocristalina, inequigranular porfídica.		
Matriz: Microcristalina de Plg, opacos y Ol.	**Micro y fenocristales:** Plg los más grandes, algunos más pequeños de Ol y Cpx.	
Otros: Cpx y vidrio incluido o exsuelto dentro de Plg.		

Lámina: M86		**Fecha:** 4-03-2013
Campo: (23-01-2013) Cerros Lobería: a) fragmento lítico, basalto; b) Matriz del maar.		
Textura: Holocristalina, inequigranular porfídica.		
Matriz: Microcristalina de Plg, opacos y Ol, con vidrio intersticial.	**Micro y fenocristales:** Plg y Ol.	
Otros: Algún cristal de Plg grande alterado en el núcleo. Cpx u Ol incluidos en Plg.		

Lámina: M89		**Fecha:** 5-03-2013
Campo: (24-01-2013) Bomba en La Loma, en la cantera inferior.		
Textura: zonas holocristalinas inequigranular porfídica y otras vítreas porfídicas.		
Matriz: Vítrea y con Plg con textura traquítica.	**Microfenocristales:** Plg y Ol muy alterados.	
Otros: abundancia de vacuolas con óxido en los bordes.		

Rocas Alcalinas T1

Lámina: M95	**Fecha:** 10-4-2013
Campo: (25-01-2013) Cerro de la Cruz. En la cima de la cantera lineal. Colada de basalto plagioclásico con Plg centimétricas y algún Ol y Px.	
Textura: holocristalina inequigranular porfídica.	
Matriz: microcristalina de Plg, opacos y Clpx..	**Fenocristales:** Plg tipo 1 y 2, Ol y Op.
Otros: Dos tamaños de fenocristales, uno de ~0.2cm y los otros de ~0.8cm. Op y Ol incluidos en Plg. Ap incluido en bordes de Plg.	

Lámina: M97	**Fecha:** 15-4-2013
Campo: (25-01-2013) Cerro de la Cal. Fragmentos lávicos con mucha Plg y con xenolitos leucocráticos corticales.	
Textura: holocristalina inequigranular porfídica.	
Matriz: microcristalina de Plg con textura traquítica, Ol y opacos.	**Microfenocristales:** Ol y Plg de tamaño poco superior al de los cristales de la matriz, y Op de mayor tamaño.
Otros: Textura traquítica de las Plg de la matriz. Plg tipo 1 y 3. Ap incluido en Plg.	

Lámina: M98	**Fecha:** 15-4-2013
Campo: (25-01-2013) Bloque resto de colada en El Cerro, cerca del pueblo de Palo Blanco.	
Textura: holocristalina inequigranular porfídica.	
Matriz: microcristalina de Plg con textura traquítica, Ol, opacos y Ap.	**Microfenocristales:** Ol, Op y alguna Plg.
Otros: Los Microfenocristales de Ol son de tamaño poco mayor que los de la matriz, los de opacos son de mayor tamaño. Plg tipo 1.	

Rocas Alcalinas T1

Lámina: M99		**Fecha:** 15-4-2013
Campo: (25-01-2013) Dentro del cráter de la Peña Colorada, fragmento lávico con grandes cristales de Plg y muy oxidado.		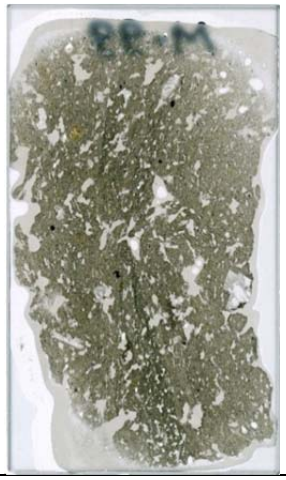
Textura: holocristalina inequigranular porfídica.		
Matriz: microcristalina de Plg con textura traquítica, Ol y Op.	**Micro y fenocristales:** Plg, Ol y Op.	
Otros: Plg tipo 1 muy rotas y algunas redondeadas con el borde muy alterado. Vacuolas de gran tamaño. Ap y Op incluidos en Ol.		

Lámina: M100		**Fecha:**
Campo: (25-01-2013) Basalto muy vacuolar y oxidado de la cantera del Cerro Guantecillos.		
Matriz: Sin lámina, muy vacuolar y alterada.		
Microfenocristales:		
Otros:		

Lámina: M101		**Fecha:** 15-4-2013
Campo: (25-01-2013) Bomba en el maar de San Nicolás.		
Textura: holocristalina inequigranular seriada.		
Matriz: microcristalina de Plg, opacos, Ol muy idingsitizado y Clpx.	**Micro y fenocristales:** Plg, Ol muy idingsitizados y Cpx.	
Otros: Zonas con rellenos de carbonato. Plg tipo 1. Ol en el centro de Cpx. Ap incluido en Plg.		

Rocas Alcalinas T1

Lámina: M105		**Fecha:** 16-4-2013
Campo: (26-01-2013) Bomba en la Hoya Pequeña, al SW de la anterior.		
Textura: holocristalina inequigranular porfídica.		
Matriz: microcristalina de Plg, Px y opacos alterada.	**Feno y microfenocristales:** Plg, Ol, Op y Ap.	
Otros: Plg tipo 1		

Lámina: M106		**Fecha:** 16-4-2013
Campo: (26-01-2013) Bomba en la Hoya de Cintora.		
Textura: holocristalina inequigranular seriada.		
Matriz: microcristalina de Plg, Ol, Clpx y opacos.	**Micro y fenocristales:** Plg y Ol idingsitizados.	
Otros: Plg tipo 1 y 2. Ap incluido en Plg de la matriz.		

Lámina: M110		**Fecha:** 17-4-2013
Campo: (27-01-2013) Fragmento lávico en San Vicente de Joyuelo, con Ol centimétricos, xenolitos volcánicos y autolitos de basalto. M-110L: Mismo afloramiento, muestra con xenolitos.		
Textura: zonas holocristalinas inequigranular seriada con vídrio intersticial y otras vítreas porfídicas.		
Matriz: vítrea alterada con microcristales de Plg y Ol en algunas zonas; en otras es microcristalina de Plg, opacos, Ol y Px con textura traquítica que se adapta a los fenocristales.	**Micro y fenocristales:** Plg y Ol.	
Otros: Plg tipo 1, 2 y 3. Ap incluido en Plg de la matriz.		

Rocas Alcalinas T2

Lámina: M-11	**Fecha:** 7-11-2012
Campo: Cicapien	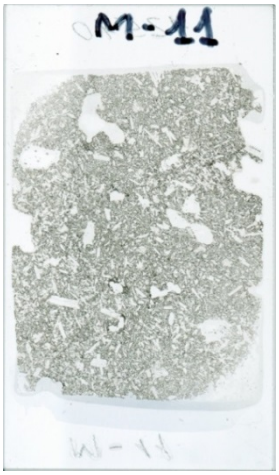
Textura: Holocristalina, inequigranular, seriada.	
Matriz: Microcristalina de Plg, Ol y Cpx	**Fenocristales:** de Plg y Ol.
Otros: Las Plg están seriadas, desde el tamaño de las de la matriz hasta los fenocristales (3 tamaños). Algunas de las grandes están partidas o corroídas o alteradas en el núcleo y con inclusiones. Vacuolas grandes.	

Lámina: M80	**Fecha:** 1-03-2013
Campo: (22-01-2013) Cerro el Melón, al borde del camino que va a las canteras. Maar en la base y cono de cínder sobre él.	
Textura: Holocristalina, inequigranular porfídica.	
Matriz: Microcristalina de Plg fundamentalmente, Cpx ofítico, Ol y Op.	**Fenocristales:** de Ol principalmente, alguno de Plg.
Otros: Muchos opacos de tamaño algo mayor que los de la matriz.	

Lámina: M81	**Fecha:** 1-03-2013
Campo: (22-01-2013) Cantera en un cerro sin nombre cerca de La Soledad (hacia el W).	
Textura: zonas holocristalinas inequigranular seriada y otras hipocristalinas inequigranular porfídica.	
Matriz: microcristalina de Plg y algún Ol y Clpx y muchos opacos.	**Fenocristales:** Ol y Plg.
Otros: Ap incluido en Plg de la matriz y bordes de Plg.	

Rocas Alcalinas T2

Lámina: M83	**Fecha:** 4-03-2013
Campo: (22-01-2013) Talud de la carretera en el Cerro Colorado, cerca de la laguna de Yuriria.	
Textura: Holocristalina, inequigranular porfídica. Zonas con mayor abundancia de vidrio.	
Matriz: microcristalina de Plg, opacos y algún Ol y Cpx, parece que con vidrio intersticial. / **Microfenocristales:** Plg y Ol idingsitizados.	
Otros: Plg xenolíticas y zonas de matriz más negra. Ap incluido en Plg de la matriz y bordes de Plg.	

Lámina: M87	**Fecha:** 4-03-2013
Campo: (23-01-2013) Colada en la cuneta cerca de Cerro Colorado.	
Textura: Holocristalina, inequigranular porfídica.	
Matriz: Microcristalina de Plg, opacos y Cpx. / **Microfenocristales:** Plg y Ol (con opacos incluidos).	
Otros: Plg de mayor tamaño en desequilibrio. Cpx incluidos en Plg.	

Lámina: M88	**Fecha:** 4-03-2013
Campo: (23-01-2013) Bomba de El Cerrito Colorado, detrás de la gasolinera.	
Textura: zonas holocristalinas inequigranular seriada y otras hipocristalinas inequigranular porfídica.	
Matriz: Microcristalina de Plg, opacos Clpx y Ol, pero está muy alterada / **Fenocristales:** Plg muy redondeados y alterados y escaso Ol y Cpx. Las zonas más negras tienen algún microfenocristal de Clpx u Ol.	
Otros: Zonas de matriz más negra y vacuolas más pequeñas (en el resto las vacuolas son grandes), podría indicar magma mixing. Fenocristal de Plg con inclusión de Ol. Ap incluido en bordes de Plg.	

Rocas Alcalinas T2

Lámina: M102		**Fecha:** 15-4-2013
Campo: (26-01-2013) Fragmentos de colada de la Hoya Rincón de Parangueo.		
Textura: holocristalina inequigranular seriada.		
Matriz: microcristalina de Plg, opacos y Cpx con vidrio intersticial.	**Micro y fenocristales:** Plg, Cpx y opacos.	
Otros: La diferencia de tamaño entre los cristales de la matriz y los fenocristales no es muy marcada. Alguna vacuola redondeada. Plg tipo 1, 2 y 3. Op y Ol como inclusiones en Cpx. Ap incluido en bordes de Plg y Plg de la matriz.		

Lámina: M103		**Fecha:** 16-4-2013
Campo: (26-01-2013) Colada de la Hoya La Alberca, en el centro de Valle de Santiago.		
Textura: holocristalina inequigranular seriada.		
Matriz: microcristalina de Plg con textura traquítica, opacos y Ol.	**Microfenocristales:** Plg, Ol y Op.	
Otros: Muy alterada, con rellenos de carbonato, Ol idingsitizado y pseudomorfos de algún mineral completamente reemplazado por opacita. Plg tipo 1. Coronas de Opx en los Ol. Ap incluido en Plg de la matriz.		

Lámina: M104		**Fecha:** 16-4-2013
Campo: (26-01-2013) Bomba de la Hoya Blanca que incluye xenolitos.		
Textura: holocristalina inequigranular seriada.		
Matriz: criptocristalina de Plg y Clpx con vidrio intersticial y opacos.	**Microfenocristales:** Plg, Ol y Clpx	
Otros: Hay algunos cristales rojizos rodeados de opacita que podrían haber sido Anf y otros muy alterados que podrían ser Clpx. Opx en coronas alrededor del Ol y como inclusiones en Plg y Ol. Crecimiento de Cpx alrededor de huecos vacíos y con Plg. Plg tipo 1 y 3. Ap incluido en el opaco.		

Rocas Alcalinas T2

Lámina: M109	**Fecha:** 17-4-2013
Campo: (27-01-2013) Bomba en el Cerro Colorado, están muy oxidadas.	
Textura: holocristalina inequigranular porfídica.	
Matriz: microcristalina de Plg, opacos y algún Ol.	**Microfenocristales:** Plg y Ol.
Otros: Plg tipo 1 y 3. Ol incluidos en Plg. Ap incluido en Plg de la matriz.	

Lámina: M131	**Fecha:** 06/02/2015
Campo: Al W de El Pilar	
Textura: holocristalinas inequigranular porfídica.	
Matriz: microcristalina de Plg, Op y Cpx con vidrio intersticial.	**Micro y fenocristales:** microfeno de Plg tipo 1 y Cpx oxidados. Fenocristales de Ol idingsitizados en los bordes y Cpx.
Otros: Abundantes vacuolas grandes y alargadas. Plg tipo 1 y 2. Ap incluido en Plg de la matriz.	

Lámina: M135	**Fecha:** 09/02/2015
Campo: Entre San Isidro de la Cuesta y Janamuato.	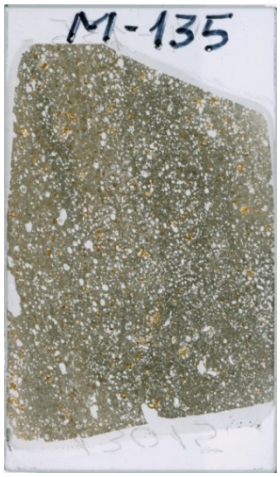
Textura: holocristalinas inequigranular porfídica.	
Matriz: Microcristalina de Plg y Ol con vidrio intersticial. También parece que hay Cpx, opacos y Ap muy pequeños.	**Micro y fenocristales:** Microfeno de Plg y fenocristales de Ol idingsitizados en los bordes.
Otros: Muy vacuolar de vacuolas pequeñas y redondas. Plg tipo 1 y 3. Ap incluido en Plg de la matriz y en bordes de Plg.	

Rocas Calcoalcalinas

Lámina: M-1	**Fecha:** 7-11-2012
Textura: Holocristalina, inequigranular seriada.	
Matriz: Microcristalina de Plg, Ol y Clpx con mucho vidrio intersticial.	**Microfenocristales:** Ol, escasos Clpx y Plg tipo 1.
Otros: Las Plg están seriadas, algunas alcanzan casi el tamaño de los microfenocristales. Muy vacuolar. Plg tipo 1, las más grandes están más rotas.	

Lámina: M-2	**Fecha:** 8-11-2012
Campo: Paracho Viejo	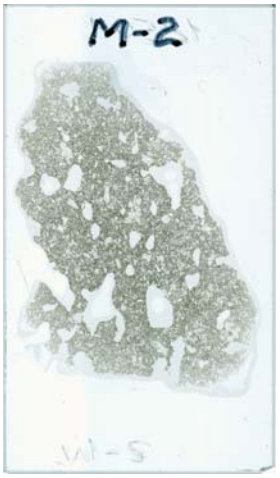
Textura: Holocristalina, inequigranular seriada.	
Matriz: Microcristalina de Plg, Px (secciones basales) y Ol, con vidrio intersticial.	**Microfenocristales:** Ol, Clpx, Pl.
Otros: Plg tipo 1 y 2 con los bordes corroídos o los núcleos alterados. Vacuolas muy grandes.	

Lámina: M-3	**Fecha:** 8-11-2012
Campo: Paracho Viejo	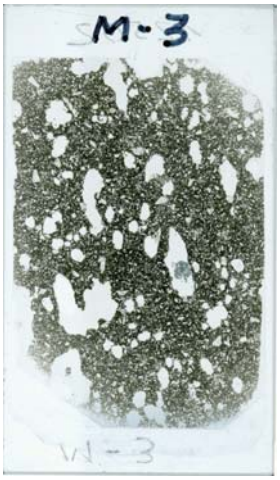
Textura: Hipocristalina, inequigranular porfídica.	
Matriz: Vítrea con cristales de Plg y Ol, zonas más criptocristalinas.	**Microfenocristales:** Plg menores que los demás microfenocristales pero mayor que las de la matriz), Ol y Clpx.
Otros: Plg tipo 1 y 2. Vacuolas muy grandes.	

Rocas Calcoalcalinas

Lámina: M-4		**Fecha:** 8-11-2012
Campo: Paracho Viejo		
Textura: Holocristalina, inequigranular porfídica.		
Matriz: Microcristalina de Plg y algún Clpx, con vidrio intersticial.	**Micro y fenocristales:** Plg (seriadas en 3 tamaños: matriz, intermedio y microfenocristal). Feno de Ol y Clpx.	
Otros: Alguna Plg con el núcleo corroído o los bordes redondeados. Vacuolas muy grandes y alargadas.		

Lámina: M-5		**Fecha:** 8-11-2012
Campo: Cumbuan		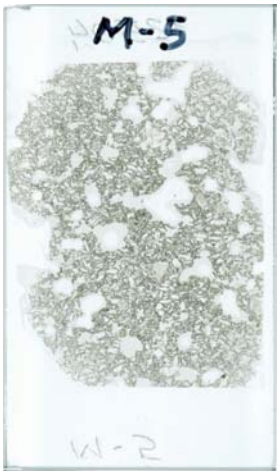
Textura: Holocristalina, inequigranular seriada.		
Matriz: Microcristalina de Plg, Px y Ol con vidrio intersticial.	**Microfenocristales:** Plg, Ol, Clpx y Opx	
Otros: Plg tipo 1 y 2. Vacuolas grandes.		

Lámina: M-6		**Fecha:** 8-11-2012
Campo: Cumbuan		
Textura: Holocristalina, inequigranular porfídica.		
Matriz: Microcristalina de Plg y Ol, Op y Cpx?	**Microfenocristales:** Plg, Clpx y/o Opx y Ol.	
Otros: Plg recrecidas.		

Rocas Calcoalcalinas

Lámina: M-7		**Fecha:** 31-10-2012
Campo: Janamo		
Textura: Holocristalina, inequigranular porfídica.		
Matriz: Microcristalina de Plg y algún Clpx. Vidrio intersticial.	**Microfenocristales:** Plg, Ol con bordes alterados y Clpx.	
Otros: Xenocristales de Plg corroídos en el centro. Textura traquítica. Bastantes vacuolas del tamaño de los microfenocristales. Hay zonas que parecen cristales totalmente reemplazados por una masa de microcristales.		

Lámina: M-8		**Fecha:** 31-10-2012
Campo: Los Amoles		
Textura: Holocristalina, inequigranular seriada.		
Matriz: Microcristalina seriada de Plg, Ol y Cpx con vidrio intersticial.	**Micro y fenocristales:** Plg, Ol y Px.	
Otros: Muy vacuolar. Los cristales están seriados desde la matriz hasta los fenocristales. Plg tipo 1.		

Lámina: M-9		**Fecha:** 31-10-2012
Campo: Los Amoles		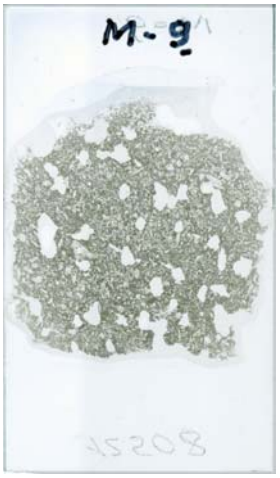
Textura: Holocristalina, inequigranular seriada.		
Matriz: Microcristalina seriada de Plg y Ol.	**Micro y fenocristales:** Plg, Ol, Cpx.	
Otros: Muy vacuolar. Los cristales están seriados desde la matriz hasta los fenocristales. Plg tipo 1.		

Rocas Calcoalcalinas

Lámina: M-10		**Fecha:** 7-11-2012
Campo: San Miguel		
Textura: Holocristalina, inequigranular seriada.		
Matriz: Microcristalina de Plg, Px y Ol con mucho vidrio intersticial.	**Microfenocristales:** Ol, Cpx y escasa Plg2.	
Otros: Algunas vacuolas inferiores en tamaño a los microfenocristales y otras más grandes y alargadas. También hay algunos cristales de Px. Plg tipo 1 y 2 muy escasas.		

Lámina: M-12		**Fecha:** 7-11-2012
Campo: Cupatacuiro		
Textura: Holocristalina, inequigranular porfídica.		
Matriz: Microcristalina de Plg alargadas, Px y algún Ol.	**Microfenocristales:** Ol y Clpx.	
Otros: Alguna Plg corroída y redondeada y una zona de acumulación de Plg tabulares. La textura general es marcadamente fluidal de zonas más plagioclásicas y otras más oscuras con mayor abundancia de Clpx, también orientados. Plg tipo 1.		

Lámina: M-13		**Fecha:** 26-10-2012
Campo: Cupatacuiro		
Textura: Holocristalina, inequigranular porfídica.		
Matriz: Microcristalina de Plg y Clpx	**Microfenocristales:** De Ol alguno de Cpx.	
Otros: Presenta algunas vacuolas y una textura traquítica muy marcada de las Plg y Clpx de la matriz que rodean y se adaptan a los fenocristales. Ol con zonación. Plg tipo 1 y 3.		

Rocas Calcoalcalinas

Lámina: M-14		**Fecha:** 26-10-2012
Campo: Paricutin		
Textura: Holocristalina, inequigranular porfídica.		
Matriz: Microcristalina, con vidrio intersticial, de Plg y Px.	**Microfenocristales:** Ol y Clpx. Plg tipo 3	
Otros: Textura fluidal. Plg tipo 1 y 3.		

Lámina: M-15		**Fecha:** 26-10-2012
Campo: Paricutin		
Textura: Holocristalina, inequigranular porfídica.		
Matriz: Microcristalina de Plg y algún Px con vidrio intersticial.	**Microfenocristales:** de Clpx en su mayoría, aunque no son muy abundantes, y alguno de Ol.	
Otros: Textura traquítica. Plg tipo 1.		

Lámina: M-16		**Fecha:** 26-10-2012
Campo: Paricutin		
Textura: Holocristalina, inequigranular porfídica.		
Matriz: Microcristalina de Plg con vidrio intersticial, Ol pequeñitos y algún Clpx.	**Microfenocristales:** Clpx y Ol, alguno de Pl.	
Otros: Textura traquítica con bastantes vacuolas grandes. Plg tipo 1.		

Rocas Calcoalcalinas

Lámina: M-17	**Fecha:** 26-10-2012
Campo: Paricutin	
Textura: Holocristalina, inequigranular porfídica.	
Matriz: Microcristalina de Plg y algún Clpx, con vidrio intersticial.	**Fenocristales:** Ol con una fina corona y Clpx.
Otros: Textura traquítica, algunas vacuolas de pequeño tamaño. Los Ol parecen tener un borde de reacción muy fino. Plg tipo 1.	

Lámina: M-18	**Fecha:** 26-10-2012
Campo: El Jabalí	
Textura: Holocristalina, inequigranular porfídica.	
Matriz: Microcristalina de Plg, Px y opacos.	**Micro y fenocristales:** Plg, Clpx y Ol.
Otros: Textura traquítica. Los fenocristales de Plg están corroídos en los bordes. Los alargados siguen la dirección del flujo y los de forma más redondeada son rodeados por las Plg de la matriz. Plg tipo 1 y 2.	

Lámina: M-19	**Fecha:** 26-10-2012
Campo: El Juanyan	
Textura: Holocristalina, inequigranular porfídica.	
Matriz: Microcristalina de Plg y algún Clpx con vidrio intersticial, zonas más vítreas y otras más microcristalinas.	**Feno y microfenocristales:** Ol y Clpx.
Otros: Bastantes vacuolas pequeñas. Plg tipo 1.	

Rocas Calcoalcalinas

Lámina: M-20		**Fecha:** 26-10-2012
Campo: Metate		
Textura: Holocristalina, inequigranular seriada.		
Matriz: Microcristalina de Plg y Clpx con vidrio intersticial.	**Fenocristales:** Anf (rodeados de opacita) y Pl.	
Otros: Pseudomorfos formados por cristales de Clpx con la forma de los Anf y en algunos casos se conserva un Anf en el centro. Plg tipo 1 y 2.		

Lámina: M-21		**Fecha:** 30-10-2012
Campo: Metate		
Textura:		
Matriz: Microcristalina de Plg, Clpx.	**Microfenocristales:** Amp rodeados de opacita, Clpx con muchas inclusiones de opacos y Pl.	
Otros: Abundante Plg tipo 3 zonada (tamaño microfenocristal) unos rotos, otros muy alterados en el núcleo y corroídos en los bordes. Bastantes vacuolas del tamaño de los microfenocristales.		

Lámina: M-27		**Fecha:** 16-10-2012
Campo: Metate		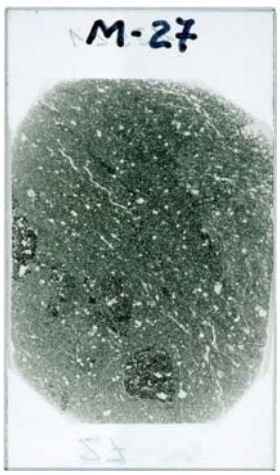
Textura: Holocristalina, inequigranular seriada.		
Matriz: Microcristalina de Plg y Ol con vidrio intersticial.	**Microfenocristales:** de Ol con inclusiones de opacos y alguno de Plg y Clpx.	
Otros: Aparecen unos aglomerados de la misma composición que el resto de la lámina pero con la matriz más vítrea, podrían ser los bordes de la cámara arrastrados por el flujo. También hay venas rellenas con minerales de alteración y Plg tipo 3.		

Rocas Calcoalcalinas

Lámina: M-28		**Fecha:** 16-10-2012
Campo: Cuate		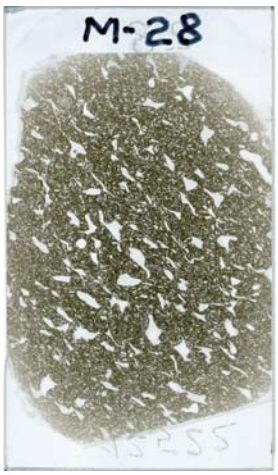
Textura: Holocristalina, inequigranular seriada.		
Matriz: Microcristalina de Plg y Clpx y mucho vidrio intersticial.	**Microfenocristales:** de Plg en su mayoría y Clpx, no mucho mayores que los de la matriz.	
Otros: Muy vacuolar (≈ 20%). Plg tipo 1 y 3. Hay un cristal que parece formado por aglomeración de pequeños cristales de Plg muy tabulares y que dentro tiene inclusiones de Ap.		

Lámina: M-29		**Fecha:** 16-10-2012
Campo: Las Cabras		
Textura: Holocristalina, inequigranular porfídica.		
Matriz: Microcristalina de Plg, Ol y Clpx con vidrio intersticial.	**Microfenocristales:** Ol, Cpx y escasas Pl.	
Otros: Textura traquítica. Plg tipo 1, 2 y 3. Algunos Ol con corona de Opx.		

Lámina: M-30		**Fecha:** 16-10-2012
Campo: Las Cabras		
Textura: Holocristalina, inequigranular porfídica.		
Matriz: Microcristalina de Plg y Op.	**Micro y fenocristales:** Ol, Clpx y escasos de Plg. Inclusiones de opacos.	
Otros: Textura de traquítica. Plg tipo 1.		

Rocas Calcoalcalinas

Lámina: M-31	**Fecha:** 16-10-2012
Campo: Las Cabras	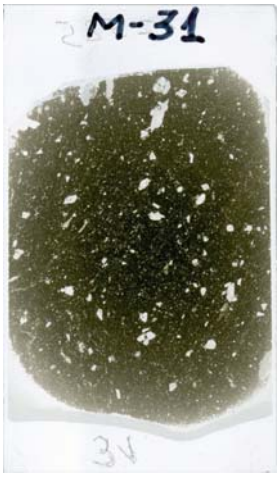
Textura: Holocristalina, inequigranular porfídica.	
Matriz: Microcristalina de Plg y Clpx? con mucho vidrio intersticial.	**Microfenocristales:** Ol con corona muy fina.
Otros: Micro dominios de Plg microcristalinas aglomeradas. Plg tipo 1 y 3.	

Lámina: M-32	**Fecha:** 16-10-2012
Textura: Holocristalina, inequigranular porfídica.	
Matriz: Microcristalina de Plg, Ol y Clpx.	**Microfenocristales:** Clpx, Ol.
Otros: Se encuentra algún pseudomorfo de Q sustituyendo a otro mineral en el hueco que dejó. Plg tipo 1, 2 y 3.	

Lámina: M-33	**Fecha:** 17-10-2012
Campo: Capaxtiro	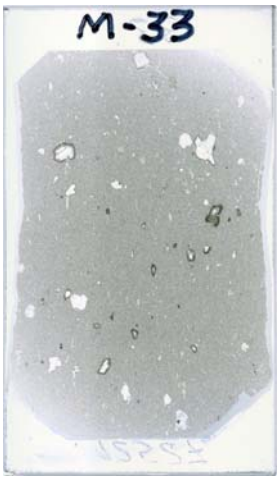
Textura: Holocristalina, inequigranular seriada.	
Matriz: Microcristalina de Plg y Clpx.	**Microfenocristales:** Clpx y Plg tipo 3.
Otros: Xenolitos de cuarcita. Textura traquítica. Plg tipo 1 y muchos de 3 algunos de los cuales están rodeados de pequeños cristales de Clpx.	

Rocas Calcoalcalinas

Lámina: M-34	**Fecha:** 17-10-2012
Campo: Capaxtiro	
Textura: Holocristalina, inequigranular seriada.	
Matriz: Microcristalina de Clpx y Plg.	**Microfenocristales:** Clpx y Plg.
Otros: Aparecen también algunos cristales de tamaño intermedio entre la matriz y los fenocristales de color marrón con fuerte pleocroísmo y relieve de forma anhedral que parecen Anf. Plg tipo 1 y 3.	

Lámina: M-35	**Fecha:** 17-10-2012
Campo: Capaxtiro	
Textura: Holocristalina, inequigranular seriada.	
Matriz: Microcristalina de Cpx, Plg, Ap, Op y escasos Ol.	**Microfenocristales:** Plg y Clpx.
Otros: Plg tipo 1 y sobretodo tipo 3. Algunas están muy corroídas y presentan una acumulación de cristalitos aciculares de Ap alrededor.	

Lámina: M-36	**Fecha:** 17-10-2012
Textura: Holocristalina, inequigranular seriada.	
Matriz: Microcristalina seriada de Plg con Ol, Clpx y Op.	**Microfenocristales:** Plg, Ol con bordes idingsitizados e inclusiones de opacos, Clpx y Opx.
Otros: Plg tipo 1 principalmente y alguna tipo 2.	

Rocas Calcoalcalinas

Lámina: M-37		**Fecha:** 17-10-2012
Campo: Cheranguarán		
Textura: Holocristalina, inequigranular seriada.		
Matriz: Microcristalina de Plg y mucho vidrio intersticial.	**Microfenocristales:** Plg, Clpx y Ol.	
Otros: Plg tipo 1. Zonas de concentración de pequeños cristales de Cpx (reemplazamiento). Hay un enclave de matriz cristalina de Plg con microfenocristales de Plg, Clpx y mayor abundancia de Ol que en el resto de la lámina. Abundancia de vesículas.		

Lámina: M-38		**Fecha:** 18-10-2012
Textura: Holocristalina, inequigranular seriada.		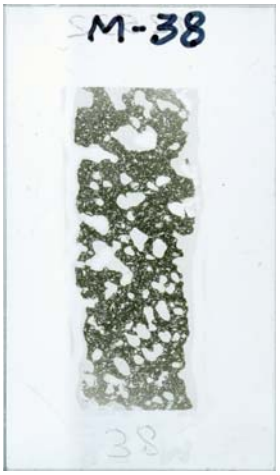
Matriz: Microcristalina de Plg con vidrio intersticial.	**Microfenocristales:** Plg, Clpx y Ol.	
Otros: Muy vacuolar. Plg tipo 1 y 2.		

Lámina: M-39		**Fecha:** 18-10-2012
Campo: Sta. Catarina		
Textura: Hipocristalina, inequigranular porfídica.		
Matriz: Microcristalina seriada de Plg y Px con mucho vidrio.	**Microfenocristales:** Px, Plg y escasos Ol.	
Otros: Plg tipos 1, 2 y 3.		

Rocas Calcoalcalinas

Lámina: M-40	**Fecha:** 18-10-2012
Campo: Metate	
Textura: Holocristalina, inequigranular porfídica.	
Matriz: Microcristalina de Plg, Op, Clpx y Ol.	**Microfenocristales:** Plg, Clpx y Amp.
Otros: Hay un pseudomorfo, probablemente de Amp, relleno de cristales de Clpx, Anf muy opacitizados y Plg tipo 1, 2 y 3.	

Lámina: M-41	**Fecha:** 18-10-2012
Campo: Paricutin	
Textura Holocristalina, inequigranular porfídica.	
Matriz: Microcristalina de Plg y escaso Clpx con vidrio intersticial.	**Microfenocristales:** Ol, Clpx y Opx.
Otros: Abundan las vacuolas pequeñas. Plg tipo 1.	

Lámina: M-42	**Fecha:** 30-11-2012
Campo: Paricutin	
Textura: Holocristalina, inequigranular porfídica.	
Matriz: Microcristalina de Plg y Clpx.	**Microfenocristales:** Ol y Px.
Otros: Muchas vacuolas pequeñas y redondeadas, y algunas grandes y alargadas.	

Rocas Calcoalcalinas

Lámina: M-43		**Fecha:** 30-11-2012
Campo: Paricutin		
Textura: Holocristalina, inequigranular porfídica.		
Matriz: Microcristalina de Plg y Clpx	**Microfeno y fenocristales:** Ol.	
Otros: Unas vacuolas pequeñas y redondeadas y otras grandes y alargadas. Plg tipo 1.		

Lámina: M-44		**Fecha:** 30-11-2012
Campo: Paricutin		
Textura: Holocristalina, inequigranular porfídica.		
Matriz: Microcristalina de Plg y Clpx con vidrio intersticial.	**Microfenocristales:** Clpx y escasos de Ol y Pl.	
Otros: Abundan las vacuolas pequeñas. Plg tipo 1.		

Lámina: M-45		**Fecha:** 30-11-2012
Campo: Paricutin		
Textura: Holocristalina, inequigranular porfídica.		
Matriz: Microcristalina de Plg y Clpx con vidrio intersticial.	**Micro y fenocristales:** Ol.	
Otros: Plg tipo 1.		

Rocas Calcoalcalinas

Lámina: M-46	**Fecha:** 30-11-2012
Campo: Paricutin	
Textura: Holocristalina, inequigranular porfídica.	
Matriz: Microcristalina de Plg, Clpx y escaso de Ol.	**Micro y fenocristales:** Ol.
Otros: Algunas vacuolas alineadas. Textura traquítica. Plg tipo 1.	

Lámina: M-47	**Fecha:** 30-11-2012
Campo: Paricutin	
Textura: Holocristalina, inequigranular porfídica.	
Matriz: Microcristalina de Plg y Cpx.	**Microfenocristales:** Microfenocristales de Ol y escasos de Px. Fenocristales de Ol.
Otros: Muchos opacos. Muy alterada. Textura traquítica. Plg tipo 1.	

Lámina: M-48	**Fecha:** 30-11-2012
Campo: Paricutin	
Textura: Holocristalina, inequigranular porfídica.	
Matriz: Microcristalina de Plg y Cpx de menor tamaño.	**Micro y fenocristales:** Ol.
Otros: Textura traquítica. Algunas vacuolas pequeñas, redondeadas y alineadas. Plg tipo 1.	

Rocas Calcoalcalinas

Lámina: M-49		**Fecha:** 30-11-2012
Textura: Holocristalina, inequigranular seriada.		
Matriz: Microcristalina de Plg y Cpx con vidrio intersticial.	**Microfenocristales:** Feno de Ol y microfeno de Pl.	
Otros: Algunas Plg parecen magmáticas, están zonadas y tienen los bordes truncados. Hay zonas de vacuolas alargadas y también una de acumulación de cristales muy pequeños. Plg tipo 1 y 2.		

Lámina: M-50		**Fecha:** 30-11-2012
Textura: Holocristalina, inequigranular porfídica.		
Matriz: Microcristalina de Plg y escasas secciones basales de Px con vidrio intersticial.	**Micro y fenocristales:** Ol y Px.	
Otros: Textura de flujo y vacuolas alargadas. Plg tipo 1.		

Lámina: M-51		**Fecha:** 30-11-2012
Textura: Holocristalina, inequigranular porfídica.		
Matriz: Microcristalina de Plg, Cpx y algún Ol rodeados de vidrio y zonas de mayor abundancia de cristales.	**Microfenocristales:** Ol y escasos de Plg. También se encuentra alguna Plg zonada.	
Otros: Vacuolas muy grandes y textura traquítica. Plg tipo 1 y 2.		

Rocas Calcoalcalinas

Lámina: M-52		**Fecha:** 30-11-2012
Textura: Holocristalina, inequigranular porfídica.		
Matriz: Microcristalina de Plg y algún Px, algún Ol disperso. Muchos opacos pequeños y homogéneamente distribuidos.	**Microfenocristales:** Plg y Clpx.	
Otros: El tamaño de los cristales está seriado desde la matriz hasta los microfenocristales. Plg tipo 1, 2 y 3.		

Lámina: M-53		**Fecha:** 29-11-2012
Textura: Holocristalina, inequigranular glomeroporfídica.		
Matriz: Microcristalina de Plg en su mayoría y algún Clpx.	**Fenocristales:** Grandes de Plg, Cpx y Opx, aparecen en agregados con forma de asterisco. Los agregados de Plg a veces incluyen alguna Plg magmática rota.	
Otros: Hay un enclave de Plg de menor tamaño que los fenocristales, cuyos cristales tienen los bordes suturados entre sí. También incluye algún Clpx y gran cantidad de opacos. Plg tipo 1 y 2.		

Lámina: M-54		**Fecha:** 30-11-2012
Textura: Holocristalina, inequigranular porfídica.		
Matriz: Criptocristalina o muy alterada, no se distinguen los minerales.	**Micro y fenocristales:** Cpx (algunos en agregados en asterisco), Ol y Plg muy alteradas.	
Otros: Lámina muy alterada. Plg tipo 1 y 2.		

Rocas Calcoalcalinas

Lámina: M-55		**Fecha:** 30-11-2012
Textura: Holocristalina, inequigranular seriada.		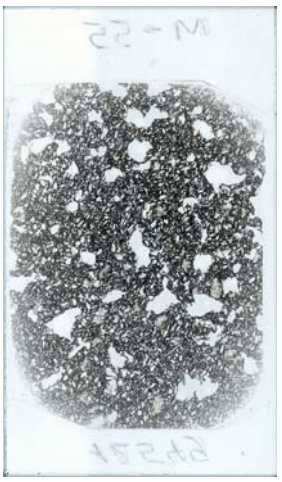
Matriz: Microcristalina de Clpx y Plg con vidrio intersticial.	**Microfenocristales:** Plg y Cpx.	
Otros: Plg magmáticas. También hay algún Ol con corona de Opx y huecos rodeados de cristalitos de Px (puede haber saltado el mineral). Ap incluidos en algunas Plg. Plg tipo 1 y 2.		

Lámina: M-56		**Fecha:** 30-11-2012
Textura: Holocristalina, inequigranular seriada.		
Matriz: Microcristalina de Plg y Clpx con algo de vidrio intersticial.	**Microfenocristales:** Plg y Clpx en menor medida.	
Otros: También hay Plg magmáticas y vacuolas grandes. Plg tipo 1 y 2.		

Lámina: M-57		**Fecha:** 20-11-2012
Campo: Metate		
Textura: Holocristalina, inequigranular seriada.		
Matriz: Microcristalina de Plg tabulares, algún Ol.	**Microfenocristales:** Ol, y Plg.	
Otros: Alguna Plg más cuadrada de bordes redondeados y con extinción ondulante y minerales. Vacuolas del tamaño de los fenocristales. Plg tipo 1.		

Rocas Calcoalcalinas

Lámina: M-58		**Fecha:** 20-11-2012
Campo: Metate		
Textura: Holocristalina, inequigranular seriada.		
Matriz: Microcristalina de Plg y Clpx con vidrio intersticial.	**Microfenocristales:** poco mayores que los de la matriz, de Plg y Clpx, y algún Ol.	
Otros: Algún cristal de Plg magmática. Muy vacuolar, de vacuolas homogéneamente distribuidas y de tamaño parecido a los microfenocristales. Plg tipo 1.		

Lámina: M-59		**Fecha:** 20-11-2012
Textura: Holocristalina, inequigranular seriada.		
Matriz: Microcristalina de Plg, Clpx y Ol.	**Microfenocristales:** Ol.	
Otros: Hay zonas donde la matriz es de grano mucho más fina. Algún xenocristal de Plg. Plg tipo 1.		

Lámina: M-60		**Fecha:** 20-11-2012
Campo: Metate		
Textura: Holocristalina, inequigranular porfídica.		
Matriz: Microcristalina Plg, Op y Ap.	**Microfenocristales:** Plg, Cpx y Amp.	
Otros: Los microfenocristales están muy bien formados, los Cpx tienen muchas inclusiones de opacos. Aparecen muchos pseudomorfos de Amp en Cpx y Amp con coronas de opacita más o menos desarrollada. Plg tipo 1 y 2.		

Rocas Calcoalcalinas

Lámina: M-61		**Fecha:** 21-11-2012
Campo: Metate		
Textura: Holocristalina, inequigranular seriada.		
Matriz: Microcristalina de Plg, Clpx y algún Ol. Muchos opacos y Ap.	**Microfenocristales:** Amp con opacita en los bordes y otros con una corona de minerales verdosos. También hay Plg y escasos Px.	
Otros: Hay una zona de Clpx con extinción ondulante y muy llenos de inclusiones de opacos que está rodeada de cristales alargados de Anf. Plg tipo 1 y 2. Algunas Plg con inclusiones de Ap en el núcleo.		

Lámina: M-62		**Fecha:** 21-11-2012
Campo: Metate		
Textura: Holocristalina, inequigranular porfídica.		
Matriz: Microcristalina de Plg, Clpx y Ap.	**Microfenocristales:** Plg y Clpx.	
Otros: Ap también incluidos en los de Plg más grandes. Plg tipo 1 y 2.		

Lámina: M-63		**Fecha:** 21-11-2012
Campo: Metate		
Textura: Holocristalina, inequigranular seriada.		
Matriz: Microcristalina de Plg, Clpx y Ap.	**Micro y fenocristales:** Plg y Clpx. Algún Ol escaso.	
Otros: Alguna Plg magmática rota. Plg tipo 1 y 2.		

Rocas Calcoalcalinas

Lámina: M-64		**Fecha:** 21-11-2012
Campo: Metate		
Textura: Holocristalina, inequigranular seriada.		
Matriz: Microcristalina de Ap, Op y Pl.	**Micro y fenocristales:** Plg con Ap en los bordes y Clpx.	
Otros: Plg tipo 1 y muy abundantes del 2.		

Lámina: M-65		**Fecha:** 26-11-2012
Campo: Metate		
Textura: Holocristalina, inequigranular seriada.		
Matriz: Microcristalina de Plg y Clpx.	**Micro y fenocristales:** Plg y Ol.	
Otros: Algunas Plg magmáticas zonadas y otras en desequilibrio con el núcleo alterado y con inclusiones. Plg tipo 1 y 2.		

Lámina: M-66		**Fecha:** 26-11-2012
Campo: Metate		
Textura: Holocristalina, inequigranular seriada.		
Matriz: Microcristalina de Plg, Ap, Op y algún Clpx.	**Micro y fenocristales:** Plg, Clpx y Amp opacitizados.	
Otros: Algunos fenocristales de Plg aparecen muy alterados en el núcleo y corroídos en los bordes. Los Clpx contienen muchas inclusiones de opacos. Plg tipo 1, 2 y 3.		

Rocas Calcoalcalinas

Lámina: M-67	**Fecha:** 26-11-2012
Textura: Holocristalina, inequigranular seriada.	
Matriz: Microcristalina de Ol alterados a idingsita en los bordes, Op y alguna Plg y Clpx con vidrio intersticial.	**Microfenocristales:** Ol y Pl.
Otros: Hay alguna Plg magmática. Plg tipo 1.	

Lámina: M-68	**Fecha:** 26-11-2012
Textura: Holocristalina, inequigranular seriada. Glomeroporfídica.	
Matriz: Microcristalina de Plg, Ap y Op. Con vidrio intersticial.	**Microfenocristales:** de dos tamaños. El tamaño mayor son Clpx, Ol, y Plg agregadas en forma de asterisco; el menor son Plg tipo 1.
Otros: Se encuentran zonas de acumulación de Plg y también Clpx rellenando los bordes de una vacuola. Acumulaciones de Clpx, Ol y opacos. Plg tipo 1 y 2.	

Lámina: M69	**Fecha:** 22-02-2013
Campo: Metate	
Textura: Holocristalina, inequigranular seriada.	
Matriz: Microcristalina de Plg y algún Px.	**Microfenocristales:** Plg, Clpx, Ol y Amp muy opacitizados.
Otros: Abundancia de opacos, sobretodo como inclusiones dentro de los Clpx. Muy alterada. Plg tipo 1 y 2.	

Rocas Calcoalcalinas

Lámina: M70		**Fecha:** 22-02-2013
Campo: Metate		
Textura: Holocristalina, inequigranular seriada.		
Matriz: Microcristalina de Plg y Clpx, con mucho vidrio intersticial.	**Micro y fenocristales:** dos tamaños separados sin seriación de Plg y Clpx, entre los más grandes también hay alguno de Ol.	
Otros: Alterada. Plg tipo 1 y 2.		

Lámina: M71		**Fecha:** 22-02-2013
Campo: Metate		
Textura: Holocristalina, inequigranular seriada.		
Matriz: Microcristalina Plg y Clpx, Op.	**Microfenocristales:** Plg, Clpx, algún Amp totalmente alterado a opacita.	
Otros: También hay cristales más grandes de Plg en desequilibrio. Plg tipo 1 y 2. Zonas de cristales de Cpx reemplazando Amp.		

Lámina: M72		**Fecha:** 22-02-2013
Campo: Metate		
Textura: Holocristalina, inequigranular seriada.		
Matriz: Microcristalina seriada de Plg, Clpx y opacos con vidrio intersticial.	**Microfenocristales:** Plg, Clpx, Amp totalmente opacitizados.	
Otros: Alguna Plg magmática zonada. Plg tipo 1 y muchas de tipo 2.		

Rocas Calcoalcalinas

Lámina: M73		**Fecha:** 26-02-2013
Campo: Metate		
Textura: Holocristalina, inequigranular seriada.		
Matriz: Vidrio desvitrificado y alterado.	**Microfenocristales:** Plg, Anf con halo de alteración de opacita, Ol, Clpx acumulados en aglomerados.	
Otros: Muchos opacos, sobretodo incluidos en los Ol. Plg xenolíticas.		

Lámina: M74		**Fecha:** 26-02-2013
Campo: Metate		
Textura: Holocristalina, inequigranular seriada.		
Matriz: Microcristalina de Plg y Cpx con vidrio intersticial.	**Microfenocristales:** Plg, Cpx (algunos zonados) y Amp con coronas de opacita.	
Otros: Opacos incluidos en los Clpx. Plg tipo 1, 2 y 3.		

Lámina: M75		**Fecha:** 26-02-2013
Campo: Metate		
Textura: Holocristalina, inequigranular seriada.		
Matriz: microcristalina de Plg, Clpx y Op con vidrio intersticial.	**Microfenocristales:** Plg, Amp con corona de opacita y Clpx.	
Otros: Plg tipo 1, 2 y 3.		

Rocas Calcoalcalinas

Lámina: M76		**Fecha:** 26-02-2013
Campo: Metate		
Textura: Holocristalina, inequigranular seriada.		
Matriz: Microcristalina de Plg, Clpx y Op con vidrio intersticial.	**Micro y fenocristales:** Fenocristales de Anf con corona de opacita. Microfenocristales de Plg y Cpx.	
Otros: Abundancia de opacos en los Clpx. Muy vacuolar. Plg tipo 1, 2 y 3.		

Lámina: M77		**Fecha:** 26-02-2013
Campo: Metate		
Textura: Holocristalina, inequigranular seriada.		
Matriz: microcristalina de Plg, Clpx y Op.	**Micro y fenocristales:** Plg, Clpx, Amp con coronas de opacita.	
Otros: Muy vacuolar. Plg tipo 1 y 2 (algunas con núcleo alterado).		

Lámina: M78		**Fecha:** 27-02-2013
Campo: Metate		
Textura: Holocristalina, inequigranular seriada.		
Matriz: Microcristalina de Plg, Clpx y opacos con vidrio intersticial.	**Microfenocristales:** Plg, Amp con coronas de opacita, y Clpx.	
Otros: Muy vacuolar. Plg tipo 1 y 3.		

Rocas Calcoalcalinas

Lámina: M79	**Fecha:** 27-02-2013
Campo: Metate	
Textura: Holocristalina, inequigranular seriada.	
Matriz: microcristalina de Plg y Cpx.	**Microfenocristales:** Amp, Plg y Cpx.
Otros: Amp muy alterados con coronas de reacción muy amplias. Alguna Plg magmática zonada.	

Lámina: M82	**Fecha:** 1-03-2013
Campo: (22-01-2013) Derrame del Cerro Prieto.	
Textura: Holocristalina, inequigranular seriada.	
Matriz: microcristalina de Plg y Opx.	**Microfenocristales:** Plg y Opx.
Otros: Muy vacuolar, de vacuolas grandes. Plg tipo 1. Ap incluido en Plg de la matriz.	

Lámina: M84	**Fecha:** 4-03-2013
Campo: (23-01-2013) Muestra de la fisura “Loma Pitahayera”, al lado izquierdo del camino.	
Textura: Holocristalina, inequigranular seriada.	
Matriz: microcristalina de Plg, opacos y Cpx con vidrio intersticial.	**Microfenocristales:** Ol y Plg de menor tamaño.
Otros: Vacuolas muy redondeadas (podrían ser cristales que han saltado), algunas con rellenos de calcita.	

Rocas Calcoalcalinas

Lámina: M90	**Fecha:** 10-4-2013
Campo: (24-01-2013) Cerro El Guilote. Parece una colada de bloques antigua que ha arrastrado bombas.	
Textura: Holocristalina, inequigranular porfídica.	
Matriz: microcristalina de Plg, Clpx y Op. / **Microfenocristales:** Plg y Ol con bordes idingsitizados e inclusiones de opacos.	
Otros: Muy alterada, vacuolas rellenas de carbonatos. Plg tipo 1 y 2.	

Lámina: M91	**Fecha:** 10-4-2013
Campo: (24-01-2013) Bomba en la cantera del maar freatomagmático. Se aprecia estratificación cruzada de los surge y fragmentos balísticos que la deforman.	
Textura: Holocristalina, inequigranular porfídica - glomeroporfídica.	
Matriz: Microcristalina muy alterada de Plg y Op. / **Microfenocristales:** Plg en su mayoría, Cpx y Ol	
Otros: Los Clpx aparecen a veces en agregados. Ap incluido en Pl.	

Lámina: M92	**Fecha:** 10-4-2013
Campo: (24-01-2013) Resto de colada parece que procedente de La Minilla, en una loma entre La Minilla y el Cerro Mandinga.	
Textura: Holocristalina, inequigranular porfídica.	
Matriz: microcristalina de Plg, Ol y Opx con vidrio intersticial. / **Microfenocristales:** Plg y Ol.	
Otros: Plg tipo 1. Olivinos con corona de Opx. Ap incluido en Pl.	

Rocas Calcoalcalinas

Lámina: M93		**Fecha:** 10-4-2013
Campo: (24-01-2013) En la ladera NW del Cerro Gordo.		
Textura: Holocristalina, inequigranular porfídica – glomeroporfídica.		
Matriz: Plg, opacos y Cpx. Muy alterada.	**Microfenocristales:** Plg, Ol y Plg xenolíticas alteradas.	
Otros: Los Ol aparecen agregados entre sí. Plg tipo 1 y 2. Ap incluido en bordes de Pl.		

Lámina: M94		**Fecha:** 10-4-2013
Campo: (24-01-2013) En la cantera, bloques caídos de la colada.		
Matriz: microcristalina de Plg y opacos muy alterada.	**Micro y fenocristales:** Ol, Plg y Cpx.	
Otros: Algunos fenocristales de Ol están corroídos con cavidades. Op incluidos en Pl.		

Lámina: M96		**Fecha:** 15-4-2013
Campo: (25-01-2013) Cerro Sotelo, fragmentos de la colada de la cara NE.		
Textura: Holocristalina, inequigranular seriada.		
Matriz: Microcristalina de Plg, Ol, Clpx y Op con vidrio intersticial, muy alterada.	**Microfenocristales:** Plg y Ol.	
Otros: Los Microfenocristales son escasos y de pequeño tamaño. Plg tipo 1 y 2. Op incluidos en Ol.		

Rocas Calcoalcalinas

Lámina: M107		**Fecha:** 17-4-2013
Campo: (26-01-2013) Bomba del cerro La Batea.		
Textura: Holocristalina, inequigranular seriada.		
Matriz: vítrea con algún cristal distinguible de Plg, Opx y Cpx.	**Microfenocristales:** Plg, Ol y Cpx de pequeño tamaño.	
Otros: Zonas de matriz más negra y vítrea. Plg tipo 1. Ap incluido en Plg de la matriz.		

Lámina: M108		**Fecha:** 17-4-2013
Campo: (26-01-2013) Bomba en la Hoya Álvarez, incluida en los depósitos piroclásticos del maar (limpiar).		
Textura: Holocristalina, inequigranular seriada.		
Matriz: microcristalina de Plg, Opx, Op y vidrio intersticial.	**Micro y fenocristales:** Plg, Opx y Cpx.	
Otros: matriz alterada. Pseudomorfos de un mineral que ha sido reemplazado por opacita, posiblementeAmp. Plg tipo 1, 2 y 3. Ap incluido en Plg de la matriz y en bordes de Pl.		

Lámina: M111		**Fecha:** 16-5-2014
Campo: (16-05-2014) Bomba vacuolar en la cantera cerca de Pantaleón		
Textura: Holocristalina, inequigranular porfídica.		
Matriz: Micro-criptocristalina de Plg con algo de vidrio.	**Micro y fenocristales:** fenocristales de Plg, Px y Op.	
Otros: Presenta un bandeado muy fino y corrugado de minerales opacos que parece haber sido formado después de la cristalización ya que los minerales incluidos en las bandas se adaptan a ellas pero sin deformarse internamente. Las Plg están muy redondeadas y alteradas con acumulación de Op en el borde de recristalización. Plg tipo 1.		

Rocas Calcoalcalinas

Lámina: M112		**Fecha:** 16-5-2014
Campo: (16-05-2014) Bomba al SW de los Cerros de las Tetillas		
Textura: Holocristalina, inequigranular seriada.		
Matriz: microcristalina de Plg, Ol y algún Op con vidrio.	**Micro y fenocristales:** microfenocristales de Plg, Ol y Px. Fenocristales de Pl.	
Otros: Los feno de Plg se presentan con distintos grados de alteración: cristales anhedrales totalmente alterados en el centro con los bordes recrecidos; cristales anhedrales con golfos de corrosión y sin recrecimiento; cristales euhedrales con zonación concéntrica; y cristales subeuhedrales parcialmente alterados. Zona de acumulación de Plg muy alteradas. Plg tipo 1, 2 y 3.		

Lámina: M113		**Fecha:** 16-5-2014
Campo: (16-05-2014) Bomba al NE de los Cerros de las Tetillas		
Textura: Holocristalina, inequigranular porfídica.		
Matriz: microcristalina de Plg, Ol y Op con mucho vidrio intersticial. Presenta zonas de matriz mucho más clara con menos vidrio intersticial.	**Micro y fenocristales:** microfenocristales de Plg y Ol idingsitizados y corroídos. Fenocristales de Pl.	
Otros: Los feno de Plg se presentan con distintos grados de alteración: cristales anhedrales totalmente alterados en el centro con los bordes recrecidos; cristales anhedrales con golfos de corrosión y sin recrecimiento; cristales euhedrales con zonación concéntrica; y cristales subeuhedrales parcialmente alterados. Plg tipo 1, 2 y 3.		

Rocas Calcoalcalinas

Lámina: M114		**Fecha:** 16-5-2014
Campo: (16-05-2014) Bomba en el banco de materiales al W de Inchamácuaro.		
Textura: Holocristalina, inequigranular porfídica.		
Matriz: microcristalina de Plg, Px y opacos con mucho vidrio intersticial.	**Micro y fenocristales:** microfenocristales de Plg y Ol y fenocristales de Plg y Ol.	
Otros: Plg tipo 1 y 3.		

Lámina: M115		**Fecha:** 16-5-2014
Campo: (16-05-2014) Colada en el cerro al S de Obrajuelo y W de Inchamácuaro.		
Textura: Holocristalina, inequigranular porfídica.		
Matriz: microcristalina de Plg, Px y Op.	**Micro y fenocristales:** microfenocristales de Plg y Ol y fenocristales de Plg, Ol y Cpx?	
Otros: Los feno de Plg se presentan con distintos grados de alteración: cristales subeuhedrales totalmente alterados en el centro con los bordes recrecidos; cristales euhedrales con zonación concéntrica; y cristales subeuhedrales parcialmente alterados. Textura traquítica. Muy alterada. Plg tipo 1, 2 y 3.		

Lámina: M116		**Fecha:** 16-5-2014
Campo: (16-05-2014) Bomba en el cerro al S de Estancia del Carmen y W de Inchamácuaro.		
Textura: Holocristalina, inequigranular porfídica.		
Matriz: microcristalina de Plg, Cpx y Op con vidrio intersticial.	**Micro y fenocristales:** microfenocristales de Plg, Cpx y Ol y fenocristales de Pl.	
Otros: Los feno de Plg se presentan con distintos grados de alteración: cristales anhedrales totalmente alterados; y cristales subeuhedrales parcialmente alterados. Muy alterada. Plg tipo 1 y 2.		

Rocas Calcoalcalinas

Lámina: M117		**Fecha:** 16-5-2014
Campo: (16-05-2014) Bomba en el cerro al S de Estancia del Carmen y W de Inchamácuaro.		
Textura: Holocristalina, inequigranular porfídica.		
Matriz: microcristalina de Plg, Op y Px escaso.	**Micro y fenocristales:** Fenocristales de Plg y Cpx.	
Otros: Muy alterada. Plg tipo 1 y 3.		

Lámina: M118		**Fecha:** 17-5-2014
Campo: (17-05-2014) Bomba en el banco de materiales al S de Salvatierra.		
Textura: Holocristalina, inequigranular porfídica.		
Matriz: Microcristalina de Plg, Op y Ol y Cpx escaso con vidrio intersticial.	**Micro y fenocristales:** Fenocristales de Ol y alguno de Pl.	
Otros: vacuolar. Muy alterada. Zonas de matriz más vítrea. Plg tipo 1.		

Lámina: M119		**Fecha:** 17-5-2014
Campo: (17-05-2014) Fragmento lávico en el cerro al SW de Estancia del Cármen.		
Textura: Holocristalina, inequigranular porfídica.		
Matriz: Microcristalina de Plg y Ol escaso con mucho vidrio intersticial.	**Fenocristales:** Ol idingsitizados.	
Otros: Vacuolar. Muy alterada. Plg tipo 1.		

Rocas Calcoalcalinas

Lámina: M120		**Fecha:** 17-5-2014
Campo: (17-05-2014) Bomba en el banco de material del Cerro Las Cruces al S de Las Cruces.		
Textura: Holocristalina, inequigranular porfídica.		
Matriz: Microcristalina de Plg, opacos.	**Fenocristales:** Ol con inclusiones de Op.	
Otros: Vacuolar. Plg tipo 1.		

Lámina: M121		**Fecha:** 17-5-2014
Campo: (17-05-2014) Bomba en el Cerro Ascañas al SW de Las Cruces.		
Textura: Holocristalina, inequigranular porfídica.		
Matriz: Microcristalina de Plg, Px, Ol a partes iguales y Op.	**Micro y fenocristales:** Microfenocristales de Px y fenocristales de Plg y Ol.	
Otros: Vacuolar. Plg tipo 1.		

Lámina: M122		**Fecha:** 17-5-2014
Campo: (17-05-2014) Bomba en el escarpe S del Maar de Yuriria.		
Textura: Holocristalina, inequigranular seriada.		
Matriz: Microcristalina de Plg y Px con vidrio intersticial.	**Microfenocristales:** Plg, Cpx y Ol escaso.	
Otros: Hay un relleno de color marrón amarillento en varias zonas, posiblemente oxidación. Plg tipo 1 y 3.		

Rocas Calcoalcalinas

Lámina: M123		**Fecha:** 17-5-2014
Campo: (17-05-2014) Fragmento lávico en el banco de materiales del Cerro Poruyo.		
Textura: Holocristalina, inequigranular seriada.		
Matriz: Microcristalina de Plg, algún Op y mucho vidrio intersticial.	**Fenocristales:** Plg y Ol.	
Otros: Vacuolar. Plg tipo 1.		

Lámina: M124		**Fecha:** 17-5-2014
Campo: (17-05-2014) Fragmento lávico en el banco de materiales al E de Cupareo.		
Textura: Holocristalina, inequigranular porfídica.		
Matriz: Microcristalina de Plg, Op y Px.	**Micro y fenocristales:** Fenocristales de Plg y Ol algunos muy idingsitizados.	
Otros: Plg tipo 1.		

Lámina: M125		**Fecha:** 18-5-2014
Campo: (18-05-2014) Fragmento lávico en el banco de materiales al N de Panales Jamaica.		
Textura: Holocristalina, inequigranular porfídica.		
Matriz: Microcristalina de Plg, Op y lo que parecen Ol idingsitizados.	**Fenocristales:** Plg y Ol.	
Otros: Plg tipo 1 y 3.		

Rocas Calcoalcalinas

Lámina: M126		**Fecha:** 18-5-2014
Campo: (18-05-2014) Fragmento lávico en el cerro SE de Las Tetillas al SW de Salvatierra.		
Textura: Holocristalina, inequigranular porfídica.		
Matriz: Microcristalina de Plg, Ol y vidrio intersticial.	**Micro y fenocristales:** Fenocristales de Ol.	
Otros: Textura Traquítica. Plg tipo 1.		

Lámina: M127		**Fecha:** 18-5-2014
Campo: (18-05-2014) Fragmento lávico en el Cerro Tetillas al S de Santo Tomás Huátzindeo.		
Textura: Holocristalina, inequigranular porfídica.		
Matriz: Microcristalina de Plg, Op, Ol o Px.	**Micro y fenocristales:** Fenocristales de Ol.	
Otros: Plg tipo 1.		

Lámina: M128		**Fecha:** 18-5-2014
Campo: (18-05-2014) Fragmento lávico en la torrentera al SW del cerro y al SE de Uriréo.		
Textura: Holocristalina, inequigranular seriada.		
Matriz: Microcristalina de Plg, opacos y Cpx con vidrio intersticial.	**Micro y fenocristales:** Fenocristales de Plg, Cpx y Opx.	
Otros: cristales de Cpx unidos en forma de estrella. Plg tipo 1 y 3.		

Rocas Calcoalcalinas

Lámina: M129		**Fecha:** 06/02/2015
Campo: S de Chamacuero		
Textura: Holocristalina, inequigranular porfídica.		
Matriz: Microcristalina de Plg, Op y Px.	**Micro y fenocristales:** Microfeno de Plg y Ol. Feno de Plg, Clpx y Ol.	
Otros: Algunos feno de Plg están alterados en el centro y recrecidos. Se encuentran Opx en contacto con Cpx. Plg tipo 1 y 2. Ap incluido en bordes de Pl.		

Lámina: M130		**Fecha:** 06/02/2015
Campo: N de Chamacuero		
Textura: Holocristalina, inequigranular porfídica.		
Matriz: zonas muy vítreas (con partes desvitrificadas) con alguna Plg. Otras zonas microcristalinas de Plg con algún Ol y Px y vidrio intersticial.	**Micro y fenocristales:** Microfeno de Plg, Cpx y Ol. Fenocristales de Plg, Cpx, Opx y Ol.	
Otros: Algún fenocristal de Plg con una zonación muy desarrollada fina y el núcleo con inclusiones. Plg tipo 1 y 2. Ap incluido en Plg de la matriz.		

Lámina: M132		**Fecha:** 06/02/2015
Campo: SW de Las Letras		
Textura: Holocristalina, inequigranular porfídica.		
Matriz: microcristalina de Plg, Cpx y opacos con vidrio intersticial.	**Micro y fenocristales:** microfeno de Plg, Ol y Cpx. Fenocristales de Plg bastante alteradas con inclusiones que probablemente sean de Ap, y Op.	
Otros: Plg tipo 1, 2 y 3.		

Rocas Calcoalcalinas

Lámina: M133		**Fecha:** 09/02/2015
Campo: NO de Las Ranas		
Textura: Holocristalina, inequigranular porfídica.		
Matriz: microcristalina de Plg fundamentalmente y algún Cpx, Ol algo de vidrio intersticial y Op.	**Micro y fenocristales:** Fenocristales de Ol con bordes idingsitizados. Alguno de Plg y Cpx.	
Otros: Plg tipo 1 y 2.		

Lámina: M134		**Fecha:** 09/02/2015
Campo: E de Janamuato		
Textura: Holocristalina, inequigranular glomeroporfídica.		
Matriz: vítrea con Plg y escasos ferromagnesianos.	**Micro y fenocristales:** Fenocristales de Plg, Ol y Cpx en agregados, también los hay sueltos.	
Otros: Zonas de mayor presencia de vidrio. Plg tipo 1 y 2.		

Lámina: M136		**Fecha:** 09/02/2015
Campo: Alberca de Los Espinos, al NE de Los Espinos.		
Textura: Hipocristalina, inequigranular.		
Matriz: Microcristalina de Plg y escaso Cpx con algo de vidrio intersticial.	**Micro y fenocristales:** Fenocristales de Plg, Cpx y Ol.	
Otros: Textura traquítica.		

Rocas Calcoalcalinas

Lámina: M137		**Fecha:** 09/02/2015
Campo: Colada al S de Caurio.		
Textura: Holocristalina, inequigranular.		
Matriz: Microcristalina de Plg, opacos y Cpx con vidrio intersticial oxidado.	**Micro y fenocristales:** Microfeno de Plg y Cpx.	
Otros: Crecimientos de Cpx radiales alrededor de fenocristales de Plg alteradas.		

Lámina: M138		**Fecha:** 26/02/2015
Campo: Maar de La Alberca de Guadalupe al W de La Alberca.		
Textura: Holocristalina, inequigranular, porfídica.		
Matriz: Microcristalina de Plg, opacos y vidrio intersticial.	**Micro y fenocristales:** Fenocristales de Plg y Cpx.	
Otros: Algunas Plg con zonado concéntrico, parece que han sido disueltas y recristalizadas en los bordes atrapando cristales de Ap.		

Lámina: M139		**Fecha:** 26/02/2015
Campo: En la carretera al S de La Alberca.		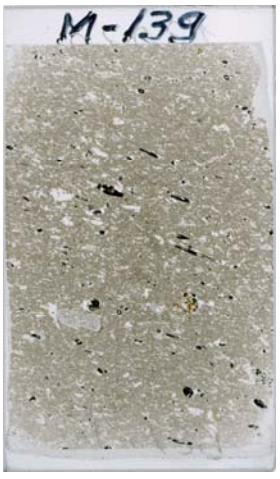
Textura: Holocristalina, inequigranular, porfídica.		
Matriz: Microcristalina de Plg opacos y Cpx.	**Micro y fenocristales:** Microfeno de Plg, Ol y Px. Fenocristales de Plg, Cpx y Amp muy opacitizado.	
Otros: Textura traquítica. Algunos feno de Plg, disueltos y recristalizados, incluso muy anhedrales, conservan el núcleo antiguo con inclusiones. Tienen zonación concéntrica. Con inclusiones de Ap.		

Rocas Calcoalcalinas

Lámina: M140		**Fecha:** 26/02/2015
Campo: Tzintzimacato Chico.		
Textura: Holocristalina, inequigranular.		
Matriz: Microcristalina de Plg y Cpx.	**Micro y fenocristales:** Microfenocristales de Cpx y Plg. Feno de Plg, algunas muy alteradas, redondeadas, con inclusiones en el núcleo. Inclusiones de Ap en los bordes.	
Otros: Textura traquítica.		

Lámina: M141		**Fecha:** 26/02/2015
Campo: N de San Bernabé.		
Textura: Hipocristalina, inequigranular.		
Matriz: Microcristalina de Plg y Px con vidrio intersticial.	**Micro y fenocristales:** Microfeno de Plg con abundantes inclusiones de Ap y Cpx. Feno de Cpx y Plg.	
Otros: Hay cristales completamente reemplazados por otros más pequeños de Pl.		

Lámina: M142		**Fecha:** 26/02/2015
Campo: Entre Las Trojes y Tiristarán.		
Textura: Holocristalina, inequigranular, porfídica.		
Matriz: Microcristalina de Plg y Px.	**Micro y fenocristales:** Fenocristales Ol muy idingsitizados y Pl.	
Otros: Carbonatos cristalizados en las vacuolas.		

Rocas Calcoalcalinas

Lámina: M143		**Fecha:** 26/02/2015
Campo: Al SE de La Noria.		
Textura: Hipocristalina, inequigranular.		
Matriz: Microcristalina de Plg con vidrio intersticial.	**Micro y fenocristales:** Un fenocristal de Ol.	
Otros: Textura Traquítica. Algunas vacuolas pequeñas.		

Lámina: M144		**Fecha:** 26/02/2015
Campo: En la carretera entre Iratzio y Capula.		
Textura: Hipocristalina, inequigranular.		
Matriz: Vítrea	**Micro y fenocristales:** Plg y Cpx. Algunas de las Plg con zonación concéntrica.	
Otros: Vacuolas grandes y redondeadas.		

Appendix 2: Tables

Table 1: Olivine major element composition (as wt%), structural formulas * and calculated temperatures [a].

Suite	T1	T1	T1	T1	T1	T1	T1	T1	T1	T1	T1	T1	T1	T1	T1
Analysis	140527 85_81	140527 85_84	140527 85_85	140527 85_90	150416 86_57	150416 86_60	150416 86_63	150416 89_87	150416 89_89	131016 95_16	131016 95_23	131016 95_26	131016 97_42	131016 97_46	150416 98_91
Type	*micropheno.*	*pheno. centre*	*iddingsite rim*	*pheno. centre*	*included in Pl*	*centre*	*micropheno. centre*	*centre*	*micropheno.*	*embedded*	*included in Pl*		*centre*	*matrix*	*centre*
SiO_2	37,22	39,17	37,07	38,18	33,49	36,96	36,80	35,64	35,98	38,34	37,89	37,20	34,66	33,58	34,47
Al_2O_3	0,03	0,01	0,37	0,02	0,16	0,01	0,10	0,04	0,08	0,04	0,00	0,03	0,01	0,02	0,05
FeO	26,07	23,15	28,42	24,71	37,03	26,32	28,39	31,02	32,70	23,73	25,93	26,82	40,16	43,63	38,39
MnO	0,65	0,38	0,44	0,48	0,96	0,43	0,54	0,46	0,45	0,30	0,36	0,33	0,85	1,07	0,95
MgO	35,25	38,96	27,32	37,70	25,42	35,74	34,62	32,15	29,87	38,71	36,25	36,26	24,24	20,28	25,09
CaO	0,27	0,18	0,52	0,20	0,52	0,25	0,38	0,26	0,35	0,17	0,29	0,28	0,37	0,35	0,32
Na_2O	0,00	0,02	0,03	0,02	0,04	0,03	0,07	0,00	0,01	0,00	0,00	0,01	0,04	0,01	0,01
K_2O	0,00	0,00	0,02	0,00	0,00	0,00	0,00	0,01	0,02	0,00	0,00	0,00	0,00	0,01	0,00
TiO_2	0,03	0,01	0,06	0,00	0,76	0,05	0,18	0,07	0,08	0,02	0,06	0,04	0,04	0,09	0,04
NiO	0,05	0,02	0,09	0,00	0,00	0,00	0,08	0,01	0,05	0,04	0,04	0,04	0,00	0,01	0,00
Cr_2O_3	0,00	0,01	0,00	0,03	0,04	0,00	0,01	0,00	0,00	0,00	0,00	0,01	0,00	0,02	0,03
P_2O_5	0,06	0,05	0,41	0,05	0,28	0,09	0,35	0,14	0,16	0,00	0,02	0,06	0,25	0,25	0,13
F	0,00	0,01	0,01	0,00	0,00	0,00	0,00	0,00	0,00	0,00	0,00	0,00	0,04	0,00	0,00
Cl	0,00	0,00	0,00	0,00	0,00	0,00	0,00	0,00	0,01	0,01	0,00	0,00	0,00	0,01	0,00
Total	99,63	101,98	94,75	101,39	98,69	99,88	101,51	99,79	99,75	101,36	100,83	101,07	100,66	99,31	99,48
Si	0,99	1,00	1,05	0,99	0,96	0,98	0,97	0,97	0,99	0,99	1,00	0,98	0,98	0,99	0,98
Al	0,00	0,00	0,01	0,00	0,01	0,00	0,00	0,00	0,00	0,00	0,00	0,00	0,00	0,00	0,00
Fe	0,58	0,49	0,67	0,54	0,89	0,59	0,63	0,71	0,75	0,51	0,57	0,59	0,95	1,07	0,92
Mn	0,01	0,01	0,01	0,01	0,02	0,01	0,01	0,01	0,01	0,01	0,01	0,01	0,02	0,03	0,02
Mg	1,40	1,48	1,15	1,46	1,09	1,42	1,37	1,31	1,23	1,49	1,42	1,42	1,03	0,89	1,07
Ca	0,01	0,00	0,02	0,01	0,02	0,01	0,01	0,01	0,01	0,00	0,01	0,01	0,01	0,01	0,01
Na	0,00	0,00	0,00	0,00	0,00	0,00	0,00	0,00	0,00	0,00	0,00	0,00	0,00	0,00	0,00
K	0,00	0,00	0,00	0,00	0,00	0,00	0,00	0,00	0,00	0,00	0,00	0,00	0,00	0,00	0,00
Ti	0,00	0,00	0,00	0,00	0,02	0,00	0,00	0,00	0,00	0,00	0,00	0,00	0,00	0,00	0,00
Ni	0,00	0,00	0,00	0,00	0,00	0,00	0,00	0,00	0,00	0,00	0,00	0,00	0,00	0,00	0,00
Cr	0,00	0,00	0,00	0,00	0,00	0,00	0,00	0,00	0,00	0,00	0,00	0,00	0,00	0,00	0,00
P	0,00	0,00	0,01	0,00	0,01	0,00	0,01	0,00	0,00	0,00	0,00	0,00	0,01	0,01	0,00
F	0,00	0,00	0,00	0,00	0,00	0,00	0,00	0,00	0,00	0,00	0,00	0,00	0,00	0,00	0,00
Cl	0,00	0,00	0,00	0,00	0,00	0,00	0,00	0,00	0,00	0,00	0,00	0,00	0,00	0,00	0,00
Fo	71	75	63	73	55	71	68	65	62	74	71	71	52	45	54
[a] T °C	1243	1228	1287	1234	1286	1219	1228	1189	1203	1202	1213	1214	1200	1234	1188
$K_{D\ (Fe\text{-}Mg)}$	0,39	0,31	0,55	0,35	0,72	0,36	0,41	0,34	0,39	0,31	0,37	0,38	0,46	0,60	0,43

* Structural formulas calculated to 4 oxygens per formula unit. Fo: forsterite content in % calculated on the basis of the forsterite (Mg_2SiO_4) and fayalite ($(Fe^{2+})_2SiO_4$) endmembers as defined by Deer et al. (1992).

[a] Temperatures calculated following the equation 22 of Putirka 2008. K_D: Fe - Mg Ol/liquid distribution coefficient (0.3 ± 0.03)

Table 1: Continued

Suite	T1	T1	T1	T1	T1	T1	T1	T1	T1	T1	T1	T1	T1	T1	T1
Analysis	150416 98_94	150416 98_99	150420 99_01	150420 99_05	150420 99_08	150420 101_11	150420 101_13	150420 101_16	150420 101_17	131016 105_36	131016 105_39	131016 105_40	150420 106_101	150420 106_102	150420 106_103
Type	*matrix*	*matrix*	*centre*	*microphenо.*	*microphenо.*	*matrix*	*iddingsite*	*microphenо.*	*microphenо.*	*centre*	*centre*	*rim*	*centre*	*centre*	*centre*
SiO_2	33,61	32,60	38,90	34,70	34,65	34,98	15,33	30,67	34,75	34,16	35,32	34,22	32,64	37,47	34,76
Al_2O_3	0,04	0,10	0,03	0,03	0,04	0,01	1,10	0,42	0,02	0,01	0,04	0,04	0,50	0,12	0,30
FeO	42,85	39,30	19,51	42,06	41,91	42,44	52,19	40,46	40,51	39,37	36,38	42,75	29,86	27,30	29,84
MnO	1,11	0,96	0,23	0,67	0,55	0,69	0,32	0,26	0,64	0,87	0,84	1,15	0,65	0,38	0,56
MgO	20,81	17,86	40,45	22,29	21,38	21,07	5,19	16,31	22,90	25,19	27,01	21,12	26,35	34,26	26,33
CaO	0,56	4,18	0,15	0,42	0,36	0,52	0,81	0,75	0,50	0,33	0,24	0,41	0,62	0,33	0,56
Na_2O	0,02	0,06	0,03	0,03	0,01	0,01	0,00	0,00	0,02	0,01	0,00	0,02	0,02	0,01	0,01
K_2O	0,03	0,02	0,01	0,01	0,00	0,02	0,00	0,01	0,02	0,00	0,00	0,00	0,02	0,00	0,03
TiO_2	0,02	0,18	0,07	0,04	0,07	0,12	0,05	0,17	0,10	0,00	0,06	0,04	0,02	0,05	0,03
NiO	0,03	0,00	0,19	0,03	0,00	0,00	0,12	0,08	0,00	0,00	0,04	0,00	0,15	0,06	0,01
Cr_2O_3	0,00	0,00	0,00	0,00	0,02	0,00	0,00	0,00	0,00	0,03	0,00	0,00	0,01	0,00	0,03
P_2O_5	0,42	3,54	0,05	0,05	0,06	0,08	0,20	0,19	0,36	0,10	0,09	0,10	0,31	0,15	0,29
F	0,00	0,22	0,00	0,00	0,02	0,01	0,00	0,01	0,03	0,01	0,00	0,02	0,02	0,03	0,02
Cl	0,00	0,03	0,01	0,00	0,00	0,02	0,01	0,01	0,01	0,02	0,00	0,01	0,00	0,02	0,01
Total	99,51	99,06	99,62	100,31	99,07	99,97	75,33	89,35	99,85	100,10	100,01	99,87	91,15	100,19	92,77
Si	0,98	0,94	1,00	1,00	1,01	1,01	–	1,01	1,00	0,97	0,99	1,00	0,99	1,00	1,02
Al	0,00	0,00	0,00	0,00	0,00	0,00	–	0,02	0,00	0,00	0,00	0,00	0,02	0,00	0,01
Fe	1,05	0,95	0,42	1,01	1,02	1,03	–	1,11	0,97	0,94	0,85	1,04	0,75	0,61	0,73
Mn	0,03	0,02	0,01	0,02	0,01	0,02	–	0,01	0,02	0,02	0,02	0,03	0,02	0,01	0,01
Mg	0,91	0,77	1,55	0,96	0,93	0,91	–	0,80	0,98	1,07	1,13	0,92	1,19	1,36	1,15
Ca	0,02	0,13	0,00	0,01	0,01	0,02	–	0,03	0,02	0,01	0,01	0,01	0,02	0,01	0,02
Na	0,00	0,00	0,00	0,00	0,00	0,00	–	0,00	0,00	0,00	0,00	0,00	0,00	0,00	0,00
K	0,00	0,00	0,00	0,00	0,00	0,00	–	0,00	0,00	0,00	0,00	0,00	0,00	0,00	0,00
Ti	0,00	0,00	0,00	0,00	0,00	0,00	–	0,00	0,00	0,00	0,00	0,00	0,00	0,00	0,00
Ni	0,00	0,00	0,00	0,00	0,00	0,00	–	0,00	0,00	0,00	0,00	0,00	0,00	0,00	0,00
Cr	0,00	0,00	0,00	0,00	0,00	0,00	–	0,00	0,00	0,00	0,00	0,00	0,00	0,00	0,00
P	0,01	0,09	0,00	0,00	0,00	0,00	–	0,01	0,01	0,00	0,00	0,00	0,01	0,00	0,01
F	0,00	0,02	0,00	0,00	0,00	0,00	–	0,00	0,00	0,00	0,00	0,00	0,00	0,00	0,00
Cl	0,00	0,00	0,00	0,00	0,00	0,00	–	0,00	0,00	0,00	0,00	0,00	0,00	0,00	0,00
Fo	46	45	79	49	48	47	–	42	50	53	57	47	61	69	61
[a] T °C	1226	1253	1133	1246	1252	1266	1595	1299	1246	1164	1152	1198	1212	1180	1216
$K_{D\ (Fe\text{-}Mg)}$	0,57	0,61	0,14	0,56	0,58	0,84	4,18	1,03	0,73	0,41	0,35	0,53	0,48	0,34	0,48

Table 1: Continued

Suite	T1	T1	T1	T1	T1	T1	T2	T2	T2	T2	T2	T2	T2	T2	T2
Analysis	150420 106_105	150420 106_106	150420 106_107	150420 106_109	131016 110_28	131016 110_32	150416 11_28	150416 11_29	150416 11_32	150416 11_33	150416 11_41	150416 11_44	150416 11_45	150416 80_02	150416 80_03
Type	*matrix*	*centre*	*rim*	*matrix*	*pheno.*		*centre*	*rim*	*centre*	*rim*	*matrix centre*	*matrix centre*	*matrix regrown*	*centre*	*centre*
SiO_2	35,34	37,87	34,33	36,56	38,46	37,04	38,66	37,80	37,91	37,56	37,39	36,82	35,28	37,10	37,35
Al_2O_3	0,05	0,07	0,37	0,06	0,04	0,06	0,06	0,02	0,02	0,06	0,02	0,10	0,04	0,00	0,01
FeO	35,00	24,98	31,14	31,22	18,96	28,27	18,82	23,41	15,82	23,06	25,76	27,32	33,48	22,45	23,38
MnO	0,73	0,39	0,33	0,65	0,31	0,64	0,40	0,54	0,21	0,47	0,47	0,59	0,68	0,24	0,39
MgO	28,00	36,91	26,49	31,67	40,95	33,95	42,13	37,12	44,27	38,25	35,79	34,31	29,15	39,80	40,03
CaO	0,30	0,21	0,51	0,25	0,20	0,31	0,22	0,32	0,20	0,28	0,45	0,47	0,41	0,15	0,14
Na_2O	0,00	0,01	0,06	0,01	0,00	0,01	0,00	0,01	0,02	0,00	0,03	0,02	0,02	0,02	0,01
K_2O	0,00	0,00	0,02	0,01	0,02	0,02	0,00	0,02	0,01	0,00	0,00	0,00	0,01	0,00	0,00
TiO_2	0,12	0,03	0,04	0,05	0,02	0,09	0,03	0,00	0,03	0,00	0,06	0,12	0,10	0,04	0,04
NiO	0,02	0,10	0,00	0,00	0,05	0,02	0,12	0,03	0,17	0,10	0,02	0,02	0,11	0,08	0,07
Cr_2O_3	0,00	0,00	0,00	0,02	0,04	0,01	0,00	0,03	0,00	0,04	0,00	0,00	0,00	0,02	0,00
P_2O_5	0,07	0,11	0,24	0,11	0,02	0,17	0,04	0,01	0,02	0,01	0,11	0,23	0,13	0,08	0,09
F	0,00	0,00	0,00	0,00	0,00	0,02	0,00	0,00	0,00	0,00	0,02	0,03	0,00	0,00	0,00
Cl	0,01	0,01	0,00	0,01	0,00	0,00	0,00	0,00	0,00	0,00	0,00	0,01	0,00	0,01	0,01
Total	99,64	100,71	93,52	100,60	99,05	100,60	100,49	99,31	98,67	99,81	100,11	100,06	99,42	99,98	101,51
Si	0,99	0,99	1,01	0,99	1,00	0,99	0,99	1,00	0,97	0,99	0,99	0,98	0,98	0,97	0,97
Al	0,00	0,00	0,01	0,00	0,00	0,00	0,00	0,00	0,00	0,00	0,00	0,00	0,00	0,00	0,00
Fe	0,82	0,55	0,76	0,71	0,41	0,63	0,40	0,52	0,34	0,51	0,57	0,61	0,78	0,49	0,51
Mn	0,02	0,01	0,01	0,01	0,01	0,01	0,01	0,01	0,00	0,01	0,01	0,01	0,02	0,01	0,01
Mg	1,17	1,44	1,16	1,28	1,58	1,35	1,60	1,46	1,70	1,50	1,41	1,37	1,21	1,55	1,54
Ca	0,01	0,01	0,02	0,01	0,01	0,01	0,01	0,01	0,01	0,01	0,01	0,01	0,01	0,00	0,00
Na	0,00	0,00	0,00	0,00	0,00	0,00	0,00	0,00	0,00	0,00	0,00	0,00	0,00	0,00	0,00
K	0,00	0,00	0,00	0,00	0,00	0,00	0,00	0,00	0,00	0,00	0,00	0,00	0,00	0,00	0,00
Ti	0,00	0,00	0,00	0,00	0,00	0,00	0,00	0,00	0,00	0,00	0,00	0,00	0,00	0,00	0,00
Ni	0,00	0,00	0,00	0,00	0,00	0,00	0,00	0,00	0,00	0,00	0,00	0,00	0,00	0,00	0,00
Cr	0,00	0,00	0,00	0,00	0,00	0,00	0,00	0,00	0,00	0,00	0,00	0,00	0,00	0,00	0,00
P	0,00	0,00	0,01	0,00	0,00	0,00	0,00	0,00	0,00	0,00	0,00	0,01	0,00	0,00	0,00
F	0,00	0,00	0,00	0,00	0,00	0,00	0,00	0,00	0,00	0,00	0,00	0,00	0,00	0,00	0,00
Cl	0,00	0,00	0,00	0,00	0,00	0,00	0,00	0,00	0,00	0,00	0,00	0,00	0,00	0,00	0,00
Fo	59	72	60	64	79	68	80	74	83	75	71	69	61	76	75
[a] T °C	1217	1168	1217	1196	1224	1263	1227	1250	1215	1244	1258	1266	1300	1202	1204
$K_{D\ (Fe\text{-}Mg)}$	0,53	0,29	0,50	0,42	0,28	0,50	0,36	0,50	0,29	0,48	0,58	0,64	0,92	0,35	0,36

Table 1: Continued

Suite	T2	T2	T2	T2	T2	T2	T2	T2	T2	T2	T2	T2	T2	T2	T2
Analysis	150416 80_04	150416 80_07	150416 80_09	150416 80_10	150416 80_12	150416 81_14	150416 81_16	150416 81_17	150416 81_18	150416 81_19	150416 81_20	150416 81_23	150416 81_24	150416 81_25	150416 83_46
Type	*rim*	*matrix*	*centre*	*rim*	*centre*	*centre*	*centre*	*rim*	*centre*	*matrix*	*matrix*	*centre*	*microphenо.*	*matrix*	*centre*
SiO_2	36,73	34,37	37,80	35,83	35,27	38,61	37,68	38,36	37,83	37,29	38,24	39,41	37,64	36,24	37,84
Al_2O_3	0,04	0,01	0,00	0,01	0,01	0,00	0,02	0,00	0,02	0,22	0,02	0,07	0,06	0,43	0,06
FeO	26,08	39,22	22,69	28,29	23,07	18,79	16,98	20,35	18,69	30,54	22,98	17,03	25,99	30,87	21,42
MnO	0,29	0,68	0,24	0,47	0,26	0,30	0,18	0,25	0,23	0,75	0,50	0,20	0,52	0,82	0,27
MgO	36,82	24,32	40,07	35,68	39,65	43,25	44,67	42,27	42,83	31,90	36,36	43,87	34,54	30,33	39,58
CaO	0,18	0,31	0,16	0,24	0,18	0,18	0,18	0,18	0,15	0,33	0,21	0,18	0,28	0,41	0,14
Na_2O	0,02	0,03	0,00	0,00	0,02	0,01	0,01	0,04	0,05	0,09	0,01	0,00	0,01	0,16	0,01
K_2O	0,00	0,04	0,00	0,01	0,00	0,00	0,00	0,00	0,00	0,03	0,01	0,00	0,00	0,09	0,00
TiO_2	0,00	0,10	0,00	0,05	0,00	0,00	0,00	0,01	0,02	0,12	0,10	0,00	0,06	0,13	0,00
NiO	0,05	0,06	0,16	0,00	0,00	0,18	0,18	0,12	0,21	0,01	0,04	0,25	0,01	0,03	0,07
Cr_2O_3	0,00	0,00	0,03	0,02	0,00	0,01	0,00	0,04	0,00	0,00	0,00	0,02	0,01	0,00	0,02
P_2O_5	0,02	0,22	0,05	0,02	0,01	0,05	0,11	0,03	0,09	0,31	0,12	0,09	0,19	0,32	0,00
F	0,00	0,00	0,01	0,00	0,00	0,02	0,00	0,00	0,04	0,00	0,02	0,00	0,00	0,00	0,00
Cl	0,00	0,00	0,01	0,00	0,01	0,00	0,00	0,00	0,01	0,00	0,00	0,00	0,01	0,01	0,00
Total	100,23	99,34	101,21	100,63	98,47	101,39	100,02	101,65	100,17	101,57	98,60	101,10	99,32	99,83	99,41
Si	0,97	0,99	0,98	0,96	0,94	0,98	0,96	0,97	0,97	0,99	1,01	0,99	1,00	0,99	0,99
Al	0,00	0,00	0,00	0,00	0,00	0,00	0,00	0,00	0,00	0,01	0,00	0,00	0,00	0,01	0,00
Fe	0,58	0,94	0,49	0,63	0,52	0,40	0,36	0,43	0,40	0,68	0,51	0,36	0,58	0,70	0,47
Mn	0,01	0,02	0,01	0,01	0,01	0,01	0,00	0,01	0,00	0,02	0,01	0,00	0,01	0,02	0,01
Mg	1,46	1,04	1,54	1,42	1,58	1,63	1,70	1,60	1,64	1,27	1,44	1,64	1,37	1,23	1,54
Ca	0,01	0,01	0,00	0,01	0,01	0,00	0,00	0,00	0,00	0,01	0,01	0,00	0,01	0,01	0,00
Na	0,00	0,00	0,00	0,00	0,00	0,00	0,00	0,00	0,00	0,00	0,00	0,00	0,00	0,01	0,00
K	0,00	0,00	0,00	0,00	0,00	0,00	0,00	0,00	0,00	0,00	0,00	0,00	0,00	0,00	0,00
Ti	0,00	0,00	0,00	0,00	0,00	0,00	0,00	0,00	0,00	0,00	0,00	0,00	0,00	0,00	0,00
Ni	0,00	0,00	0,00	0,00	0,00	0,00	0,00	0,00	0,00	0,00	0,00	0,00	0,00	0,00	0,00
Cr	0,00	0,00	0,00	0,00	0,00	0,00	0,00	0,00	0,00	0,00	0,00	0,00	0,00	0,00	0,00
P	0,00	0,01	0,00	0,00	0,00	0,00	0,00	0,00	0,00	0,01	0,00	0,00	0,00	0,01	0,00
F	0,00	0,00	0,00	0,00	0,00	0,00	0,00	0,00	0,00	0,00	0,00	0,00	0,00	0,00	0,00
Cl	0,00	0,00	0,00	0,00	0,00	0,00	0,00	0,00	0,00	0,00	0,00	0,00	0,00	0,00	0,00
Fo	72	53	76	69	75	80	82	79	80	65	74	82	70	64	77
[a] T °C	1217	1302	1203	1224	1200	1226	1217	1231	1225	1288	1255	1223	1266	1295	1198
$K_{D\ (Fe\text{-}Mg)}$	0,44	1,00	0,35	0,49	0,36	0,33	0,29	0,36	0,33	0,72	0,48	0,29	0,57	0,77	0,34

Table 1: Continued

Suite	T2	T2	T2	T2	T2	T2	T2	T2	T2	T2	T2	T2	T2	T2	T2
Analysis	150416 83_47	150416 83_51	150416 87_68	150416 87_69	150416 88_72	150416 88_73	150416 88_74	150416 88_81	150416 88_83	150416 88_84	150416 88_85	131016 102_50	150420 103_24	150420 103_29	150420 104_33
Type	*rim*	*matrix*	*micropheno.*	*micropheno.*	*centre*	*rim*	*centre*	*matrix*	*matrix*	*matrix*	*centre*	*included in Cpx*	*centre*	*micropheno.*	*icropheno. centr*
SiO_2	36,17	33,46	35,81	36,72	35,73	36,19	35,83	35,19	32,08	34,78	34,73	29,06	37,00	37,23	37,24
Al_2O_3	0,04	0,09	0,11	0,04	0,04	0,08	0,07	0,08	0,06	0,43	0,06	1,09	0,05	0,19	0,04
FeO	28,97	37,05	30,10	30,58	33,88	31,37	32,56	35,69	35,79	35,33	38,02	36,56	30,52	31,35	26,45
MnO	0,52	0,72	0,77	0,72	0,80	0,61	0,58	0,87	0,79	0,74	0,89	0,40	0,51	0,43	0,34
MgO	32,13	25,54	32,04	32,72	28,59	31,28	30,50	26,67	26,11	26,46	25,41	11,32	31,00	30,23	35,73
CaO	0,24	0,29	0,36	0,24	0,17	0,21	0,16	0,28	0,44	0,50	0,23	5,72	0,17	0,23	0,12
Na_2O	0,02	0,01	0,02	0,01	0,02	0,03	0,04	0,02	0,05	0,18	0,00	0,10	0,00	0,01	0,02
K_2O	0,00	0,00	0,00	0,00	0,00	0,00	0,02	0,03	0,00	0,03	0,01	0,09	0,01	0,00	0,00
TiO_2	0,05	0,12	0,06	0,04	0,06	0,05	0,02	0,13	0,10	0,06	0,03	0,13	0,03	0,13	0,02
NiO	0,04	0,01	0,01	0,00	0,00	0,02	0,00	0,06	0,10	0,02	0,03	0,01	0,09	0,00	0,00
Cr_2O_3	0,00	0,00	0,00	0,00	0,01	0,00	0,00	0,01	0,00	0,00	0,00	0,01	0,03	0,03	0,00
P_2O_5	0,11	0,11	0,08	0,12	0,04	0,11	0,02	0,28	0,22	0,26	0,08	0,20	0,08	0,30	0,11
F	0,04	0,00	0,01	0,00	0,00	0,01	0,00	0,00	0,00	0,00	0,03	0,02	0,00	0,00	0,00
Cl	0,00	0,00	0,01	0,01	0,00	0,00	0,00	0,00	0,00	0,00	0,00	0,03	0,01	0,00	0,02
Total	98,33	97,39	99,36	101,21	99,35	99,95	99,80	99,31	95,74	98,79	99,52	84,74	99,50	100,14	100,09
Si	0,99	0,97	0,98	0,99	1,00	0,99	0,99	0,99	0,95	0,98	0,99	1,01	1,01	1,01	0,99
Al	0,00	0,00	0,00	0,00	0,00	0,00	0,00	0,00	0,00	0,01	0,00	0,04	0,00	0,01	0,00
Fe	0,67	0,90	0,69	0,69	0,79	0,72	0,75	0,84	0,89	0,84	0,91	1,07	0,70	0,71	0,59
Mn	0,01	0,02	0,02	0,02	0,02	0,01	0,01	0,02	0,02	0,02	0,02	0,01	0,01	0,01	0,01
Mg	1,32	1,11	1,31	1,31	1,19	1,27	1,25	1,12	1,15	1,12	1,08	0,59	1,26	1,22	1,41
Ca	0,01	0,01	0,01	0,01	0,01	0,01	0,00	0,01	0,01	0,02	0,01	0,21	0,00	0,01	0,00
Na	0,00	0,00	0,00	0,00	0,00	0,00	0,00	0,00	0,00	0,01	0,00	0,01	0,00	0,00	0,00
K	0,00	0,00	0,00	0,00	0,00	0,00	0,00	0,00	0,00	0,00	0,00	0,00	0,00	0,00	0,00
Ti	0,00	0,00	0,00	0,00	0,00	0,00	0,00	0,00	0,00	0,00	0,00	0,00	0,00	0,00	0,00
Ni	0,00	0,00	0,00	0,00	0,00	0,00	0,00	0,00	0,00	0,00	0,00	0,00	0,00	0,00	0,00
Cr	0,00	0,00	0,00	0,00	0,00	0,00	0,00	0,00	0,00	0,00	0,00	0,00	0,00	0,00	0,00
P	0,00	0,00	0,00	0,00	0,00	0,00	0,00	0,01	0,01	0,01	0,00	0,01	0,00	0,01	0,00
F	0,00	0,00	0,00	0,00	0,00	0,00	0,00	0,00	0,00	0,00	0,00	0,00	0,00	0,00	0,00
Cl	0,00	0,00	0,00	0,00	0,00	0,00	0,00	0,00	0,00	0,00	0,00	0,00	0,00	0,00	0,00
Fo	66	55	65	66	60	64	63	57	57	57	54	36	64	63	71
[a] T °C	1235	1281	1209	1208	1226	1209	1214	1240	1236	1241	1250	1310	1228	1234	1202
$K_{D\ (Fe\text{-}Mg)}$	0,56	0,91	0,51	0,50	0,62	0,53	0,56	0,70	0,72	0,70	0,78	1,26	0,56	0,59	0,47

Table 1: Continued

Suite	T2	T2	T2	T2	T2	T2	T2	T2	T2	T2	T2	T2	T2	T2	T2
Analysis	150420 104_37	150420 104_39	150420 104_44	131016 109_56	131016 109_57	131016 109_58	131016 109_63	131016 109_64	131016 109_65	131016 109_66	150420 131_51	150420 131_52	150420 131_56	150420 131_57	150420 131_68
Type	*centre*	*microphenо. centre*	*microphenо. centre*	*centre*	*rim*	*matrix*	*included in Pl*	*included in Pl*	*centre*	*rim*	*centre*	*rim*	*centre*	*rim*	*centre*
SiO_2	38,63	37,66	37,04	38,57	37,90	36,23	35,18	37,73	37,73	37,57	39,11	38,41	39,75	40,54	39,93
Al_2O_3	0,05	0,05	0,06	0,00	0,03	0,00	0,05	0,02	0,06	0,00	0,04	0,92	0,03	0,06	0,02
FeO	21,36	25,29	23,81	21,61	21,75	29,81	37,46	21,43	21,73	25,82	14,55	23,71	15,25	15,44	15,89
MnO	0,27	0,40	0,35	0,30	0,43	0,58	0,72	0,28	0,23	0,36	0,17	0,34	0,13	0,16	0,14
MgO	38,24	36,30	36,97	40,59	39,59	32,61	25,42	39,37	39,57	35,66	46,39	30,96	44,24	44,23	43,85
CaO	0,12	0,18	0,13	0,24	0,23	0,23	0,31	0,30	0,24	0,24	0,15	0,53	0,18	0,16	0,16
Na_2O	0,01	0,02	0,04	0,00	0,02	0,02	0,01	0,02	0,00	0,00	0,00	0,06	0,00	0,03	0,03
K_2O	0,00	0,00	0,00	0,00	0,01	0,01	0,01	0,02	0,01	0,00	0,00	0,07	0,00	0,01	0,01
TiO_2	0,00	0,04	0,05	0,03	0,03	0,00	0,05	0,06	0,01	0,03	0,00	0,00	0,00	0,03	0,03
NiO	0,11	0,03	0,13	0,00	0,05	0,02	0,01	0,06	0,14	0,00	0,21	0,14	0,18	0,27	0,25
Cr_2O_3	0,01	0,05	0,05	0,02	0,02	0,02	0,01	0,03	0,00	0,00	0,01	0,00	0,01	0,00	0,04
P_2O_5	0,01	0,09	0,16	0,06	0,07	0,07	0,04	0,06	0,05	0,08	0,03	0,06	0,02	0,06	0,02
F	0,00	0,00	0,00	0,00	0,00	0,00	0,00	0,00	0,00	0,00	0,02	0,01	0,00	0,03	0,04
Cl	0,01	0,00	0,01	0,00	0,01	0,02	0,00	0,00	0,00	0,00	0,00	0,03	0,01	0,00	0,00
Total	98,83	100,09	98,79	101,43	100,13	99,60	99,27	99,36	99,77	99,76	100,68	95,23	99,80	101,02	100,40
Si	1,01	0,99	0,99	0,99	0,98	0,99	1,00	0,99	0,98	1,00	0,98	1,06	1,00	1,01	1,00
Al	0,00	0,00	0,00	0,00	0,00	0,00	0,00	0,00	0,00	0,00	0,00	0,03	0,00	0,00	0,00
Fe	0,47	0,56	0,53	0,46	0,47	0,68	0,89	0,47	0,47	0,57	0,30	0,54	0,32	0,32	0,33
Mn	0,01	0,01	0,01	0,01	0,01	0,01	0,02	0,01	0,01	0,01	0,00	0,01	0,00	0,00	0,00
Mg	1,49	1,43	1,47	1,55	1,53	1,32	1,08	1,53	1,54	1,41	1,73	1,27	1,66	1,64	1,64
Ca	0,00	0,01	0,00	0,01	0,01	0,01	0,01	0,01	0,01	0,01	0,00	0,02	0,00	0,00	0,00
Na	0,00	0,00	0,00	0,00	0,00	0,00	0,00	0,00	0,00	0,00	0,00	0,00	0,00	0,00	0,00
K	0,00	0,00	0,00	0,00	0,00	0,00	0,00	0,00	0,00	0,00	0,00	0,00	0,00	0,00	0,00
Ti	0,00	0,00	0,00	0,00	0,00	0,00	0,00	0,00	0,00	0,00	0,00	0,00	0,00	0,00	0,00
Ni	0,00	0,00	0,00	0,00	0,00	0,00	0,00	0,00	0,00	0,00	0,00	0,00	0,00	0,01	0,01
Cr	0,00	0,00	0,00	0,00	0,00	0,00	0,00	0,00	0,00	0,00	0,00	0,00	0,00	0,00	0,00
P	0,00	0,00	0,00	0,00	0,00	0,00	0,00	0,00	0,00	0,00	0,00	0,00	0,00	0,00	0,00
F	0,00	0,00	0,00	0,00	0,00	0,00	0,00	0,00	0,00	0,00	0,00	0,00	0,00	0,00	0,00
Cl	0,00	0,00	0,00	0,00	0,00	0,00	0,00	0,00	0,00	0,00	0,00	0,00	0,00	0,00	0,00
Fo	76	72	73	77	76	66	55	77	76	71	85	70	84	84	83
[a] T °C	1188	1199	1193	1204	1206	1242	1295	1206	1205	1225	1232	1305	1240	1242	1243
$K_{D\ (Fe\text{-}Mg)}$	0,35	0,44	0,41	0,33	0,35	0,58	0,93	0,34	0,35	0,46	0,31	0,76	0,34	0,35	0,36

Table 1: Continued

Suite	T2	T2	T2	T2	T2	T2	T2	T2	T2	T2	CA	CA	CA	CA	CA
Analysis	150420 131_69	150420 135_73	150420 135_74	150420 135_75	150420 135_76	150420 135_77	150420 135_78	150420 135_81	150420 135_82	150420 135_84	130218 03_14	130218 03_23	130218 03_26	130218 03_27	130218 03_29
Type	*rim*	*centre*	*middle*	*rim*	*centre*	*middle*	*rim*	*centre*	*rim*	*matrix*	*included in Pl*	*included in Pl rim.*	*pheno. centre*	*pheno. centre*	*micropheno. centre*
SiO_2	38,92	40,11	39,29	36,59	39,00	36,66	35,58	38,08	36,85	36,84	38,22	37,78	39,37	39,74	39,35
Al_2O_3	0,22	0,01	0,56	0,40	0,03	0,43	0,42	0,03	0,20	0,29	0,01	0,01	0,03	0,00	0,00
FeO	17,23	18,64	24,25	27,03	18,86	26,77	32,25	19,50	29,54	30,81	19,42	22,33	14,20	13,87	14,96
MnO	0,15	0,29	0,16	0,33	0,21	0,29	0,36	0,23	0,42	0,59	0,40	0,27	0,27	0,21	0,16
MgO	42,50	40,48	32,79	27,87	41,06	29,18	25,72	40,48	26,54	31,35	41,51	38,62	45,41	44,59	44,78
CaO	0,17	0,17	0,52	0,51	0,19	0,50	0,50	0,15	0,39	0,39	0,23	0,34	0,16	0,16	0,14
Na_2O	0,00	0,02	0,07	0,00	0,01	0,02	0,01	0,00	0,00	0,03	0,00	0,02	0,01	0,02	0,00
K_2O	0,01	0,00	0,01	0,01	0,01	0,01	0,02	0,01	0,01	0,03	0,00	0,00	0,00	0,00	0,02
TiO_2	0,02	0,06	0,11	0,08	0,03	0,03	0,11	0,00	0,04	0,10	0,00	0,01	0,00	0,00	0,06
NiO	0,22	0,09	0,12	0,08	0,18	0,10	0,03	0,19	0,00	0,00	0,08	0,09	0,29	0,28	0,24
Cr_2O_3	0,05	0,03	0,00	0,05	0,00	0,00	0,00	0,00	0,03	0,00	0,00	0,01	0,03	0,03	0,00
P_2O_5	0,04	0,05	0,13	0,17	0,06	0,20	0,20	0,05	0,12	0,20	0,14	0,16	0,01	0,05	0,03
F	0,02	0,01	0,02	0,00	0,00	0,00	0,00	0,00	0,00	0,00	0,07	0,01	0,03	0,01	0,00
Cl	0,00	0,01	0,02	0,02	0,01	0,00	0,01	0,01	0,00	0,01	0,00	0,01	0,00	0,01	0,00
Total	99,55	99,96	98,04	93,15	99,65	94,17	95,20	98,72	94,15	100,62	100,08	99,65	99,81	98,98	99,75
Si	0,99	1,02	1,05	1,05	1,00	1,04	1,03	0,99	1,06	0,99	0,98	0,99	0,99	1,00	0,99
Al	0,01	0,00	0,02	0,01	0,00	0,01	0,01	0,00	0,01	0,01	0,00	0,00	0,00	0,00	0,00
Fe	0,37	0,40	0,54	0,65	0,41	0,63	0,78	0,43	0,71	0,70	0,42	0,49	0,30	0,29	0,32
Mn	0,00	0,01	0,00	0,01	0,00	0,01	0,01	0,01	0,01	0,01	0,01	0,01	0,01	0,00	0,00
Mg	1,62	1,54	1,30	1,19	1,57	1,23	1,11	1,57	1,13	1,26	1,59	1,51	1,70	1,68	1,68
Ca	0,00	0,00	0,01	0,02	0,01	0,02	0,02	0,00	0,01	0,01	0,01	0,01	0,00	0,00	0,00
Na	0,00	0,00	0,00	0,00	0,00	0,00	0,00	0,00	0,00	0,00	0,00	0,00	0,00	0,00	0,00
K	0,00	0,00	0,00	0,00	0,00	0,00	0,00	0,00	0,00	0,00	0,00	0,00	0,00	0,00	0,00
Ti	0,00	0,00	0,00	0,00	0,00	0,00	0,00	0,00	0,00	0,00	0,00	0,00	0,00	0,00	0,00
Ni	0,00	0,00	0,00	0,00	0,00	0,00	0,00	0,00	0,00	0,00	0,00	0,00	0,01	0,01	0,00
Cr	0,00	0,00	0,00	0,00	0,00	0,00	0,00	0,00	0,00	0,00	0,00	0,00	0,00	0,00	0,00
P	0,00	0,00	0,00	0,00	0,00	0,00	0,00	0,00	0,00	0,00	0,00	0,00	0,00	0,00	0,00
F	0,00	0,00	0,00	0,00	0,00	0,00	0,00	0,00	0,00	0,00	0,01	0,00	0,00	0,00	0,00
Cl	0,00	0,00	0,00	0,00	0,00	0,00	0,00	0,00	0,00	0,00	0,00	0,00	0,00	0,00	0,00
Fo	81	79	71	65	80	66	59	79	62	64	79	76	85	85	84
[a] T °C	1247	1242	1282	1306	1238	1298	1329	1239	1320	1296	1241	1255	1224	1226	1227
$K_{D\ (Fe\text{-}Mg)}$	0,40	0,36	0,58	0,76	0,36	0,72	0,98	0,38	0,87	0,77	0,37	0,45	0,25	0,24	0,26

Table 1: Continued

Suite	CA	CA	CA	CA	CA	CA	CA	CA	CA	CA	CA	CA	CA	CA	CA
Analysis	130726 57_01	130726 57_04	130726 57_07	130726 57_08	130726 57_09	130726 57_10	130726 57_11	131002 57_50	131002 57_51	131002 57_52	131002 57_53	131002 57_55	140527 57_27	140527 57_28	140527 57_29
Type	*pheno. rim*	*pheno. centre*	*micropheno. rim*	*pheno. centre*	*pheno. rim*	*centre*	*rim*	*pheno. centre*	*pheno. rim*	*pheno. rim*	*pheno. centre*	*pheno. rim*	*pheno. centre*	*rim*	*centre*
SiO_2	38,96	40,02	38,92	39,58	39,07	40,28	39,94	39,11	38,00	36,84	39,68	37,89	38,97	37,87	39,34
Al_2O_3	0,00	0,00	0,00	0,01	0,00	0,01	0,01	0,05	0,04	0,22	0,01	0,02	0,03	0,03	0,01
FeO	19,68	14,69	21,14	13,45	20,79	12,82	15,99	15,10	21,37	23,45	13,76	23,64	14,26	18,99	13,82
MnO	0,18	0,19	0,24	0,18	0,26	0,15	0,22	0,16	0,25	0,42	0,16	0,26	0,23	0,35	0,17
MgO	41,28	45,43	40,78	45,90	40,15	45,98	44,89	44,27	39,00	36,29	45,71	37,17	45,31	41,23	45,84
CaO	0,16	0,12	0,23	0,11	0,18	0,11	0,14	0,15	0,21	0,21	0,15	0,22	0,08	0,12	0,11
Na_2O	0,01	0,00	0,00	0,01	0,00	0,01	0,01	0,02	0,00	0,01	0,00	0,04	0,01	0,00	0,00
K_2O	0,00	0,01	0,00	0,00	0,01	0,00	0,01	0,00	0,00	0,01	0,01	0,01	0,00	0,02	0,01
TiO_2	0,03	0,02	0,04	0,00	0,03	0,01	0,00	0,01	0,03	0,04	0,00	0,00	0,01	0,00	0,01
NiO	0,08	0,28	0,07	0,35	0,20	0,39	0,27	0,25	0,13	0,07	0,42	0,07	0,37	0,22	0,48
Cr_2O_3	0,02	0,01	0,00	0,04	0,00	0,05	0,00	0,03	0,03	0,00	0,06	0,04	0,04	0,00	0,00
P_2O_5	0,05	0,00	0,09	0,02	0,05	0,01	0,04	0,03	0,00	0,00	0,03	0,06	0,06	0,00	0,04
F	0,00	0,04	0,01	0,02	0,00	0,00	0,00	0,00	0,00	0,00	0,00	0,00	0,00	0,03	0,02
Cl	0,00	0,01	0,01	0,01	0,00	0,00	0,00	0,00	0,00	0,03	0,02	0,02	0,00	0,00	0,00
Total	100,44	100,83	101,52	99,67	100,73	99,83	101,51	99,17	99,05	97,57	99,99	99,42	99,38	98,86	99,85
Si	1,00	1,00	0,99	0,99	1,00	1,00	0,99	0,99	1,00	0,99	0,99	1,00	0,98	0,99	0,99
Al	0,00	0,00	0,00	0,00	0,00	0,00	0,00	0,00	0,00	0,01	0,00	0,00	0,00	0,00	0,00
Fe	0,42	0,31	0,45	0,28	0,45	0,27	0,33	0,32	0,47	0,53	0,29	0,52	0,30	0,41	0,29
Mn	0,00	0,00	0,01	0,00	0,01	0,00	0,00	0,00	0,01	0,01	0,00	0,01	0,00	0,01	0,00
Mg	1,57	1,69	1,55	1,72	1,53	1,71	1,66	1,68	1,52	1,46	1,71	1,46	1,71	1,60	1,72
Ca	0,00	0,00	0,01	0,00	0,01	0,00	0,00	0,00	0,01	0,01	0,00	0,01	0,00	0,00	0,00
Na	0,00	0,00	0,00	0,00	0,00	0,00	0,00	0,00	0,00	0,00	0,00	0,00	0,00	0,00	0,00
K	0,00	0,00	0,00	0,00	0,00	0,00	0,00	0,00	0,00	0,00	0,00	0,00	0,00	0,00	0,00
Ti	0,00	0,00	0,00	0,00	0,00	0,00	0,00	0,00	0,00	0,00	0,00	0,00	0,00	0,00	0,00
Ni	0,00	0,01	0,00	0,01	0,00	0,01	0,01	0,01	0,00	0,00	0,01	0,00	0,01	0,00	0,01
Cr	0,00	0,00	0,00	0,00	0,00	0,00	0,00	0,00	0,00	0,00	0,00	0,00	0,00	0,00	0,00
P	0,00	0,00	0,00	0,00	0,00	0,00	0,00	0,00	0,00	0,00	0,00	0,00	0,00	0,00	0,00
F	0,00	0,00	0,00	0,00	0,00	0,00	0,00	0,00	0,00	0,00	0,00	0,00	0,00	0,00	0,00
Cl	0,00	0,00	0,00	0,00	0,00	0,00	0,00	0,00	0,00	0,00	0,00	0,00	0,00	0,00	0,00
Fo	79	85	77	86	77	86	83	84	76	73	86	74	85	79	86
[a] T °C	1243	1225	1247	1221	1249	1221	1229	1227	1251	1263	1222	1261	1223	1240	1221
$K_{D\ (Fe\text{-}Mg)}$	0,51	0,35	0,55	0,31	0,55	0,30	0,38	0,36	0,59	0,69	0,32	0,68	0,34	0,49	0,32

Table 1: Continued

Suite	CA	CA	CA	CA	CA	CA	CA	CA	CA	CA	CA	CA	CA	CA	CA
Analysis	140527 57_30	140527 57_31	140527 63_56	140527 63_57	140527 63_58	140527 63_62	130726 65_11	130726 65_13	130726 65_16	140527 65_42	140527 65_43	130726 70_18	130726 70_20	140527 70_49	140527 70_50
Type	*centre*	*rim*	*centre*	*rim*	*rim*	*centre*	*pheno. centre*	*rim*	*pheno.centre*	*centre*	*rim*	*pheno. centre*	*pheno. centre*	*centre*	*rim*
SiO_2	37,94	38,40	39,58	38,14	38,43	39,41	39,71	37,42	39,02	39,55	38,16	39,62	39,91	39,57	38,81
Al_2O_3	0,02	0,02	0,00	0,00	0,00	0,00	0,00	0,00	0,02	0,01	0,00	0,00	0,00	0,00	0,03
FeO	19,51	23,07	17,28	19,65	23,28	16,90	15,40	25,24	18,36	17,22	23,91	15,27	15,14	16,02	19,49
MnO	0,38	0,57	0,37	0,45	0,59	0,37	0,16	0,30	0,19	0,32	0,58	0,16	0,19	0,34	0,44
MgO	41,47	38,00	43,61	41,22	37,59	43,71	45,03	36,24	41,63	43,78	38,07	45,85	45,72	44,41	41,63
CaO	0,09	0,20	0,11	0,07	0,18	0,13	0,14	0,19	0,12	0,12	0,20	0,11	0,11	0,13	0,10
Na_2O	0,02	0,00	0,00	0,01	0,03	0,04	0,00	0,03	0,00	0,01	0,01	0,00	0,01	0,01	0,00
K_2O	0,00	0,00	0,00	0,01	0,02	0,01	0,00	0,02	0,01	0,01	0,00	0,01	0,01	0,00	0,00
TiO_2	0,00	0,04	0,02	0,02	0,00	0,01	0,00	0,01	0,03	0,00	0,00	0,03	0,00	0,02	0,00
NiO	0,13	0,18	0,16	0,29	0,15	0,25	0,34	0,12	0,08	0,29	0,14	0,12	0,25	0,25	0,20
Cr_2O_3	0,00	0,01	0,00	0,02	0,00	0,00	0,02	0,02	0,00	0,00	0,00	0,00	0,00	0,00	0,00
P_2O_5	0,03	0,00	0,00	0,00	0,00	0,01	0,06	0,04	0,00	0,04	0,04	0,00	0,01	0,03	0,01
F	0,00	0,00	0,00	0,00	0,00	0,00	0,00	0,00	0,00	0,00	0,00	0,00	0,00	0,00	0,00
Cl	0,00	0,00	0,00	0,00	0,00	0,00	0,02	0,00	0,01	0,02	0,00	0,00	0,01	0,00	0,00
Total	99,57	100,48	101,13	99,86	100,25	100,82	100,87	99,62	99,45	101,36	101,10	101,17	101,35	100,78	100,70
Si	0,98	1,00	0,99	0,98	1,00	0,99	0,99	0,99	1,00	0,99	0,99	0,99	0,99	0,99	0,99
Al	0,00	0,00	0,00	0,00	0,00	0,00	0,00	0,00	0,00	0,00	0,00	0,00	0,00	0,00	0,00
Fe	0,42	0,50	0,36	0,42	0,51	0,36	0,32	0,56	0,39	0,36	0,52	0,32	0,31	0,34	0,42
Mn	0,01	0,01	0,01	0,01	0,01	0,01	0,00	0,01	0,00	0,01	0,01	0,00	0,00	0,01	0,01
Mg	1,60	1,47	1,63	1,59	1,46	1,64	1,68	1,43	1,59	1,64	1,47	1,70	1,69	1,66	1,58
Ca	0,00	0,01	0,00	0,00	0,01	0,00	0,00	0,01	0,00	0,00	0,01	0,00	0,00	0,00	0,00
Na	0,00	0,00	0,00	0,00	0,00	0,00	0,00	0,00	0,00	0,00	0,00	0,00	0,00	0,00	0,00
K	0,00	0,00	0,00	0,00	0,00	0,00	0,00	0,00	0,00	0,00	0,00	0,00	0,00	0,00	0,00
Ti	0,00	0,00	0,00	0,00	0,00	0,00	0,00	0,00	0,00	0,00	0,00	0,00	0,00	0,00	0,00
Ni	0,00	0,00	0,00	0,01	0,00	0,00	0,01	0,00	0,00	0,01	0,00	0,00	0,00	0,00	0,00
Cr	0,00	0,00	0,00	0,00	0,00	0,00	0,00	0,00	0,00	0,00	0,00	0,00	0,00	0,00	0,00
P	0,00	0,00	0,00	0,00	0,00	0,00	0,00	0,00	0,00	0,00	0,00	0,00	0,00	0,00	0,00
F	0,00	0,00	0,00	0,00	0,00	0,00	0,00	0,00	0,00	0,00	0,00	0,00	0,00	0,00	0,00
Cl	0,00	0,00	0,00	0,00	0,00	0,00	0,00	0,00	0,00	0,00	0,00	0,00	0,00	0,00	0,00
Fo	79	75	82	79	74	82	84	72	80	82	74	84	84	83	79
[a] T °C	1240	1259	1182	1189	1207	1181	1216	1255	1229	1222	1248	1195	1196	1200	1211
$K_{D\ (Fe\text{-}Mg)}$	0,50	0,65	0,36	0,43	0,56	0,35	0,33	0,68	0,43	0,38	0,61	0,33	0,33	0,35	0,46

Table 1: Continued

Suite	CA	CA	CA	CA	CA	CA	CA	CA	CA	CA	CA	CA	CA	CA	CA
Analysis	140527 70_52	140527 70_55	151214 92_01	151214 92_06	151214 92_07	151214 92_08	151214 93_11	151214 93_12	151214 93_17	140527 94_91	140527 94_98	151214 96_31	151214 96_32	151214 96_37	151214 96_38
Type	*centre*	*centre*	*pheno.*	*matrix*	*micropheno.*	*pheno.*	*pheno. centre*	*pheno. rim*	*pheno. centre*	*pheno.*	*micropheno. centre*	*pheno. centre*	*pheno. rim*	*micropheno.*	*matrix*
SiO_2	40,20	40,38	37,47	37,14	37,08	37,32	38,75	37,19	38,07	38,79	38,90	39,27	36,82	38,43	34,64
Al_2O_3	0,00	0,00	0,02	0,03	0,00	0,01	0,05	0,03	0,00	0,00	0,00	0,04	0,05	0,00	0,02
FeO	14,56	14,77	28,37	28,37	29,48	27,39	19,85	28,48	24,39	19,26	20,04	19,34	27,77	19,59	40,57
MnO	0,30	0,25	0,35	0,37	0,42	0,40	0,27	0,39	0,33	0,39	0,34	0,20	0,43	0,23	0,58
MgO	45,78	44,96	33,84	32,36	33,23	33,73	40,72	33,18	37,56	41,86	40,20	41,38	33,11	39,55	23,51
CaO	0,10	0,10	0,23	0,30	0,28	0,22	0,17	0,17	0,22	0,20	0,21	0,13	0,18	0,21	0,28
Na_2O	0,01	0,00	0,00	0,01	0,00	0,00	0,00	0,02	0,00	0,02	0,02	0,02	0,06	0,00	0,02
K_2O	0,00	0,01	0,00	0,00	0,00	0,00	0,00	0,00	0,00	0,02	0,01	0,00	0,00	0,01	0,01
TiO_2	0,00	0,01	0,03	0,10	0,02	0,00	0,00	0,02	0,05	0,01	0,00	0,02	0,04	0,00	0,06
NiO	0,16	0,20	0,07	0,08	0,07	0,00	0,17	0,04	0,00	0,04	0,04	0,10	0,10	0,10	0,00
Cr_2O_3	0,02	0,00	0,00	0,03	0,00	0,00	0,00	0,00	0,03	0,03	0,00	0,01	0,01	0,00	0,00
P_2O_5	0,02	0,00	0,03	0,17	0,04	0,00	0,04	0,07	0,07	0,05	0,03	0,07	0,00	0,01	0,08
F	0,01	0,00	0,01	0,00	0,00	0,00	0,02	0,10	0,00	0,03	0,00	0,05	0,03	0,00	0,00
Cl	0,00	0,00	0,00	0,00	0,01	0,01	0,01	0,00	0,00	0,00	0,01	0,00	0,01	0,01	0,01
Total	101,14	100,68	100,41	98,95	100,62	99,08	100,04	99,68	100,72	100,69	99,78	100,61	98,61	98,14	99,76
Si	1,00	1,01	1,00	1,01	0,99	1,01	1,00	1,00	0,99	0,99	1,00	1,00	1,00	1,01	0,99
Al	0,00	0,00	0,00	0,00	0,00	0,00	0,00	0,00	0,00	0,00	0,00	0,00	0,00	0,00	0,00
Fe	0,30	0,31	0,63	0,64	0,66	0,62	0,43	0,64	0,53	0,41	0,43	0,41	0,63	0,43	0,97
Mn	0,01	0,01	0,01	0,01	0,01	0,01	0,01	0,01	0,01	0,01	0,01	0,00	0,01	0,01	0,01
Mg	1,69	1,67	1,35	1,31	1,33	1,36	1,56	1,33	1,46	1,59	1,55	1,57	1,34	1,54	1,01
Ca	0,00	0,00	0,01	0,01	0,01	0,01	0,00	0,00	0,01	0,01	0,01	0,00	0,01	0,01	0,01
Na	0,00	0,00	0,00	0,00	0,00	0,00	0,00	0,00	0,00	0,00	0,00	0,00	0,00	0,00	0,00
K	0,00	0,00	0,00	0,00	0,00	0,00	0,00	0,00	0,00	0,00	0,00	0,00	0,00	0,00	0,00
Ti	0,00	0,00	0,00	0,00	0,00	0,00	0,00	0,00	0,00	0,00	0,00	0,00	0,00	0,00	0,00
Ni	0,00	0,00	0,00	0,00	0,00	0,00	0,00	0,00	0,00	0,00	0,00	0,00	0,00	0,00	0,00
Cr	0,00	0,00	0,00	0,00	0,00	0,00	0,00	0,00	0,00	0,00	0,00	0,00	0,00	0,00	0,00
P	0,00	0,00	0,00	0,00	0,00	0,00	0,00	0,00	0,00	0,00	0,00	0,00	0,00	0,00	0,00
F	0,00	0,00	0,00	0,00	0,00	0,00	0,00	0,01	0,00	0,00	0,00	0,00	0,00	0,00	0,00
Cl	0,00	0,00	0,00	0,00	0,00	0,00	0,00	0,00	0,00	0,00	0,00	0,00	0,00	0,00	0,00
Fo	85	84	68	67	67	69	79	67	73	79	78	79	68	78	51
[a] T °C	1196	1198	1278	1284	1282	1276	1183	1220	1198	1198	1204	1189	1227	1193	1302
$K_{D\ (Fe\text{-}Mg)}$	0,31	0,32	0,74	0,78	0,79	0,72	0,33	0,59	0,44	0,32	0,35	0,33	0,60	0,35	1,23

Table 1: Continued

Suite	CA	CA	CA	CA	CA	CA	CA	CA	CA	CA
Analysis	151214 96_40	151214 96_41	151214 96_43	150420 107_87	150420 107_88	150420 107_90	150420 107_92	150420 107_94	150420 107_96	150420 107_97
Type	*micropheno. centre*	*micropheno. rim*	*matrix*	*micropheno.*	*micropheno.*	*micropheno.*	*centre*	*centre*	*centre*	*rim*
SiO_2	38,13	35,37	33,94	38,13	38,50	36,51	38,24	38,54	38,39	37,18
Al_2O_3	0,07	0,02	0,02	0,03	0,05	0,04	0,05	0,06	0,04	0,05
FeO	25,11	36,93	45,33	22,32	21,11	28,65	20,37	19,71	21,53	26,70
MnO	0,32	0,42	0,56	0,31	0,24	0,57	0,31	0,29	0,30	0,55
MgO	35,94	26,64	19,62	37,86	39,31	33,82	39,84	39,63	40,66	35,08
CaO	0,29	0,28	0,31	0,23	0,17	0,30	0,13	0,11	0,17	0,23
Na_2O	0,00	0,02	0,01	0,02	0,02	0,03	0,01	0,00	0,01	0,01
K_2O	0,01	0,00	0,02	0,02	0,00	0,01	0,00	0,00	0,00	0,01
TiO_2	0,00	0,08	0,15	0,04	0,03	0,07	0,00	0,03	0,03	0,01
NiO	0,08	0,06	0,02	0,04	0,12	0,10	0,12	0,13	0,08	0,04
Cr_2O_3	0,02	0,00	0,00	0,00	0,00	0,00	0,00	0,00	0,01	0,02
P_2O_5	0,08	0,19	0,07	0,05	0,20	0,31	0,07	0,02	0,06	0,08
F	0,02	0,00	0,02	0,03	0,02	0,04	0,00	0,01	0,00	0,00
Cl	0,02	0,00	0,00	0,00	0,00	0,01	0,00	0,01	0,00	0,01
Total	100,09	100,01	100,07	99,10	99,75	100,46	99,13	98,54	101,28	99,97
Si	1,00	0,99	1,00	1,00	1,00	0,98	1,00	1,01	0,98	0,99
Al	0,00	0,00	0,00	0,00	0,00	0,00	0,00	0,00	0,00	0,00
Fe	0,55	0,87	1,11	0,49	0,46	0,64	0,44	0,43	0,46	0,60
Mn	0,01	0,01	0,01	0,01	0,01	0,01	0,01	0,01	0,01	0,01
Mg	1,41	1,11	0,86	1,48	1,52	1,35	1,55	1,54	1,55	1,39
Ca	0,01	0,01	0,01	0,01	0,00	0,01	0,00	0,00	0,00	0,01
Na	0,00	0,00	0,00	0,00	0,00	0,00	0,00	0,00	0,00	0,00
K	0,00	0,00	0,00	0,00	0,00	0,00	0,00	0,00	0,00	0,00
Ti	0,00	0,00	0,00	0,00	0,00	0,00	0,00	0,00	0,00	0,00
Ni	0,00	0,00	0,00	0,00	0,00	0,00	0,00	0,00	0,00	0,00
Cr	0,00	0,00	0,00	0,00	0,00	0,00	0,00	0,00	0,00	0,00
P	0,00	0,00	0,00	0,00	0,00	0,01	0,00	0,00	0,00	0,00
F	0,00	0,00	0,00	0,00	0,00	0,00	0,00	0,00	0,00	0,00
Cl	0,00	0,00	0,00	0,00	0,00	0,00	0,00	0,00	0,00	0,00
Fo	72	56	44	75	77	68	78	78	77	70
[a] T °C	1214	1274	1347	1198	1192	1221	1189	1189	1189	1214
$K_{D\ (Fe\text{-}Mg)}$	0,50	0,99	1,65	0,39	0,35	0,55	0,33	0,32	0,35	0,50

Table 2: Plagioclase major element composition (as wt%), structural formulas* and calculated temperatures[a], pressures[b] and water content in the melt[c].

Suite	T1	T1	T1	T1	T1	T1	T1	T1	T1	T1	T1	T1	T1	T1	T1	T1
Analysis	140527 85_77	140527 85_78	140527 85_82	140527 85_83	140527 85_86	140527 85_88	150416 86_54	150416 86_55	150416 86_58	150416 86_59	150416 86_61	150416 86_62	150416 89_86	150416 89_88	131016 95_12	131016 95_13
Type	*centre*	*rim*	*matrix*	*pheno.*	*pheno.*	*matrix*	*type 3 centre*	*type 3 rim*	*centre*	*micropheno.*	*centre*	*rim*	*pheno. centre*	*pheno. centre*	*centre*	*middle*
SiO_2	52,79	53,81	54,71	53,65	52,79	56,05	55,53	53,11	52,54	53,72	59,28	53,12	54,07	52,52	52,73	52,50
Al_2O_3	29,24	28,17	27,41	28,77	29,07	27,07	27,61	29,93	30,14	28,72	25,04	28,97	28,75	29,87	28,33	28,98
FeO	0,28	0,64	0,45	0,36	0,38	0,52	0,26	0,31	0,42	0,53	0,18	0,44	0,42	0,62	0,34	0,34
MnO	0,00	0,00	0,04	0,00	0,05	0,06	0,05	0,00	0,01	0,00	0,00	0,01	0,01	0,00	0,03	0,00
MgO	0,09	0,05	0,06	0,09	0,07	0,03	0,04	0,06	0,08	0,10	0,01	0,05	0,07	0,07	0,07	0,05
CaO	12,62	11,73	10,59	11,52	12,20	9,69	9,30	11,81	12,12	10,99	6,03	11,03	11,14	11,93	12,53	12,47
Na_2O	4,46	5,03	5,57	5,12	4,81	6,08	6,10	4,77	4,74	5,46	7,83	5,06	5,16	4,84	4,53	4,60
K_2O	0,27	0,39	0,40	0,48	0,36	0,45	0,69	0,36	0,35	0,35	1,12	0,44	0,48	0,40	0,37	0,32
TiO_2	0,07	0,17	0,20	0,10	0,10	0,20	0,04	0,07	0,07	0,12	0,06	0,16	0,15	0,14	0,08	0,05
NiO	0,00	0,00	0,00	0,00	0,00	0,01	0,00	0,00	0,00	0,05	0,00	0,03	0,00	0,01	0,11	0,00
Cr_2O_3	0,00	0,00	0,01	0,01	0,00	0,03	0,01	0,00	0,01	0,00	0,00	0,06	0,00	0,01	0,00	0,04
P_2O_5	0,01	0,02	0,08	0,02	0,02	0,00	0,06	0,04	0,03	0,03	0,01	0,04	0,16	0,02	0,04	0,04
F	0,02	0,06	0,01	0,01	0,00	0,00	0,02	0,01	0,00	0,01	0,05	0,06	0,00	0,00	0,02	0,03
Cl	0,00	0,00	0,00	0,01	0,00	0,00	0,01	0,00	0,01	0,02	0,00	0,00	0,00	0,00	0,00	0,00
Total	99,84	100,06	99,53	100,12	99,86	100,20	99,71	100,49	100,51	100,09	99,60	99,47	100,41	100,43	99,16	99,41
Si	2,40	2,45	2,49	2,43	2,40	2,53	2,51	2,40	2,38	2,44	2,67	2,42	2,44	2,38	2,42	2,40
Al	1,57	1,51	1,47	1,54	1,56	1,44	1,47	1,59	1,61	1,54	1,33	1,56	1,53	1,60	1,53	1,56
Fe^{3+}	0,01	0,02	0,02	0,01	0,01	0,02	0,01	0,01	0,02	0,02	0,01	0,02	0,02	0,02	0,01	0,01
Mn	0,00	0,00	0,00	0,00	0,00	0,00	0,00	0,00	0,00	0,00	0,00	0,00	0,00	0,00	0,00	0,00
Mg	0,01	0,00	0,00	0,01	0,00	0,00	0,00	0,00	0,01	0,01	0,00	0,00	0,00	0,00	0,00	0,00
Ca	0,62	0,57	0,52	0,56	0,60	0,47	0,45	0,57	0,59	0,53	0,29	0,54	0,54	0,58	0,62	0,61
Na	0,39	0,44	0,49	0,45	0,42	0,53	0,54	0,42	0,42	0,48	0,68	0,45	0,45	0,43	0,40	0,41
K	0,02	0,02	0,02	0,03	0,02	0,03	0,04	0,02	0,02	0,02	0,06	0,03	0,03	0,02	0,02	0,02
Ti	0,00	0,01	0,01	0,00	0,00	0,01	0,00	0,00	0,00	0,00	0,00	0,01	0,00	0,00	0,00	0,00
Ni	0,00	0,00	0,00	0,00	0,00	0,00	0,00	0,00	0,00	0,00	0,00	0,00	0,00	0,00	0,00	0,00
Cr	0,00	0,00	0,00	0,00	0,00	0,00	0,00	0,00	0,00	0,00	0,00	0,00	0,00	0,00	0,00	0,00
P	0,00	0,00	0,00	0,00	0,00	0,00	0,00	0,00	0,00	0,00	0,00	0,00	0,01	0,00	0,00	0,00
Fe	0,00	0,01	0,00	0,00	0,00	0,00	0,00	0,00	0,00	0,00	0,01	0,01	0,00	0,00	0,00	0,00
Cl	0,00	0,00	0,00	0,00	0,00	0,00	0,00	0,00	0,00	0,00	0,00	0,00	0,00	0,00	0,00	0,00
An	60	55	50	54	57	46	44	57	57	52	28	53	53	56	59	59
[a] T (^oC)	1229	1234	1237	1237	1232	1242	1242	1226	1225	1227	1291	1229	1185	1182	1256	1255
[b] P (Kbar)	13,6	15,0	16,6	15,5	14,4	18,2	18,2	13,7	13,5	15,1	27,5	14,7	10,6	9,6	14,8	14,8
[c] H2O (wt%)	0,77	0,71	0,53	0,72	0,75	0,33	0,37	0,03	0,05	0,14	1,57	0,03	0,08	0,15	0,46	0,43
$K_{D\ (Ab\text{-}An)}$	0,29	0,36	0,44	0,37	0,33	0,52	0,56	0,34	0,33	0,42	1,11	0,39	0,35	0,30	0,32	0,33

* Structural formulas calculated to 8 oxygens per formula unit and all the iron as ferric iron on tetrahedral position.

An: anorthite content in % calculated on basis of the relative proportions of anorthite (Ca ($Al_2Si_2O_8$)), albite (Na ($AlSi_3O_8$)) and orthose ((K, Na) ($AlSi_3O_8$)) after Deer et al. (1992).

[a] Temperatures calculated following the equation 24a of Putirka 2008. K_D: Ab - An Plg/liquid distribution coefficient (0,27 ± 0,11)

[b] Pressures calculated following the equation 25a of Putirka 2008.

[c] Water content calculated following the equation 25b of Putirka 2008.

Table 2: Continued.

Suite	T1	T1	T1	T1	T1	T1	T1	T1	T1	T1	T1	T1	T1	T1	T1	T1
Analysis	131016 95_14	131016 95_17	131016 95_18	131016 95_19	131016 95_20	131016 95_21	131016 95_22	131016 95_27	131016 97_43	131016 97_44	150416 98_93	150416 98_95	150416 98_96	150416 98_101	150420 99_04	150420 99_06
Type	*type 2 rim*	*matrix*	*centre*	*centre middle*	*middle*	*middle rim*	*type 2 rim*	*microphenо.*	*pheno. centre*	*centre*	*matrix*	*centre*	*rim*	*matrix*	*microphenо.*	*type 3 centre*
SiO_2	52,85	52,01	52,21	52,00	52,38	52,07	52,72	52,77	53,93	54,35	61,09	55,24	54,89	55,94	54,03	58,21
Al_2O_3	29,38	28,50	29,02	29,63	28,87	29,13	29,18	28,73	27,16	26,94	23,02	27,53	28,38	26,35	29,31	26,47
FeO	0,31	0,49	0,35	0,48	0,45	0,45	0,56	0,63	0,40	0,30	0,66	0,45	0,42	0,73	0,44	0,22
MnO	0,00	0,00	0,00	0,01	0,00	0,09	0,03	0,03	0,01	0,00	0,00	0,00	0,02	0,00	0,01	0,02
MgO	0,06	0,02	0,09	0,09	0,07	0,07	0,06	0,07	0,02	0,05	0,03	0,05	0,03	0,04	0,04	0,01
CaO	11,88	12,62	12,47	13,03	12,68	12,78	12,90	12,29	10,28	9,95	4,42	9,39	10,19	8,04	11,30	7,79
Na_2O	4,63	4,65	4,66	4,27	4,49	4,41	4,54	4,79	5,23	5,52	6,34	5,82	5,67	6,76	5,07	6,87
K_2O	0,37	0,34	0,34	0,29	0,30	0,30	0,26	0,32	0,62	0,64	4,12	0,77	0,66	1,14	0,46	1,21
TiO_2	0,07	0,11	0,04	0,09	0,09	0,09	0,10	0,11	0,05	0,11	0,19	0,11	0,13	0,15	0,08	0,01
NiO	0,03	0,00	0,00	0,00	0,06	0,00	0,00	0,01	0,00	0,00	0,02	0,02	0,01	0,00	0,03	0,01
Cr_2O_3	0,00	0,00	0,00	0,03	0,00	0,00	0,00	0,02	0,03	0,00	0,00	0,00	0,00	0,00	0,00	0,01
P_2O_5	0,01	0,08	0,04	0,04	0,06	0,03	0,04	0,00	0,01	0,05	0,03	0,04	0,04	0,06	0,03	0,02
F	0,05	0,00	0,01	0,00	0,00	0,01	0,00	0,05	0,00	0,00	0,00	0,02	0,07	0,02	0,00	0,00
Cl	0,00	0,01	0,02	0,00	0,02	0,01	0,00	0,00	0,01	0,01	0,00	0,00	0,00	0,02	0,00	0,00
Total	99,63	98,83	99,24	99,96	99,45	99,44	100,39	99,82	97,75	97,92	99,91	99,45	100,51	99,24	100,81	100,84
Si	2,41	2,40	2,40	2,37	2,40	2,39	2,39	2,41	2,50	2,51	2,76	2,51	2,47	2,55	2,43	2,60
Al	1,58	1,55	1,57	1,59	1,56	1,57	1,56	1,55	1,48	1,47	1,22	1,47	1,51	1,42	1,55	1,39
Fe^{3+}	0,01	0,02	0,01	0,02	0,02	0,02	0,02	0,02	0,02	0,01	0,02	0,02	0,02	0,03	0,02	0,01
Mn	0,00	0,00	0,00	0,00	0,00	0,00	0,00	0,00	0,00	0,00	0,00	0,00	0,00	0,00	0,00	0,00
Mg	0,00	0,00	0,01	0,01	0,00	0,00	0,00	0,00	0,00	0,00	0,00	0,00	0,00	0,00	0,00	0,00
Ca	0,58	0,62	0,61	0,64	0,62	0,63	0,63	0,60	0,51	0,49	0,21	0,46	0,49	0,39	0,54	0,37
Na	0,41	0,42	0,41	0,38	0,40	0,39	0,40	0,42	0,47	0,49	0,55	0,51	0,50	0,60	0,44	0,59
K	0,02	0,02	0,02	0,02	0,02	0,02	0,02	0,02	0,04	0,04	0,24	0,04	0,04	0,07	0,03	0,07
Ti	0,00	0,00	0,00	0,00	0,00	0,00	0,00	0,00	0,00	0,00	0,01	0,00	0,00	0,01	0,00	0,00
Ni	0,00	0,00	0,00	0,00	0,00	0,00	0,00	0,00	0,00	0,00	0,00	0,00	0,00	0,00	0,00	0,00
Cr	0,00	0,00	0,00	0,00	0,00	0,00	0,00	0,00	0,00	0,00	0,00	0,00	0,00	0,00	0,00	0,00
P	0,00	0,00	0,00	0,00	0,00	0,00	0,00	0,00	0,00	0,00	0,00	0,00	0,00	0,00	0,00	0,00
Fe	0,01	0,00	0,00	0,00	0,00	0,00	0,00	0,01	0,00	0,00	0,00	0,00	0,01	0,00	0,00	0,00
Cl	0,00	0,00	0,00	0,00	0,00	0,00	0,00	0,00	0,00	0,00	0,00	0,00	0,00	0,00	0,00	0,00
An	57	59	59	62	60	61	60	58	50	48	21	45	48	37	54	36
[a] T (^oC)	1257	1256	1256	1253	1254	1254	1253	1256	1173	1175	1402	1201	1196	1218	1194	1227
[b] P (Kbar)	15,3	14,9	15,0	14,1	14,5	14,4	14,4	15,2	11,1	11,8	33,8	14,3	13,1	17,8	11,4	18,6
[c] H2O (wt%)	0,42	0,44	0,43	0,46	0,44	0,45	0,43	0,40	0,43	0,35	0,21	0,03	0,12	0,36	0,46	0,24
$K_{D\ (Ab\text{-}An)}$	0,35	0,33	0,33	0,29	0,31	0,31	0,31	0,35	0,26	0,28	0,76	0,33	0,29	0,44	0,28	0,55

Table 2: Continued.

Suite	T1	T1	T1	T1	T1	T1	T1	T1	T1	T1	T1	T2	T2	T2	T2	T2
Analysis	150420 99_07	150420 101_10	150420 101_12	150420 101_19	131016 105_38	150420 106_100	150420 106_104	150420 106_111	131016 110_29	131016 110_30	131016 110_31	150416 11_26	150416 11_27	150416 11_31	150416 11_34	150416 11_35
Type	*microphenо.*	*centre*	*matrix*	*matrix*	*centre*	*centre*	*matrix*	*matrix*	*centre*	*rim*	*matrix*	*centre*	*rim*	*matrix*	*centre*	*rim*
SiO_2	54,07	52,94	54,66	62,22	55,23	55,31	54,28	56,91	52,29	51,96	51,05	49,89	48,58	55,25	49,03	53,61
Al_2O_3	28,66	30,04	28,25	21,88	27,92	28,17	28,82	27,29	29,11	28,76	29,31	31,72	32,52	27,78	32,55	28,24
FeO	0,44	0,39	0,60	0,43	0,24	0,36	0,51	0,64	0,32	0,36	0,57	0,30	0,46	0,88	0,59	0,86
MnO	0,00	0,00	0,00	0,04	0,00	0,03	0,00	0,00	0,07	0,02	0,04	0,04	0,00	0,04	0,00	0,00
MgO	0,07	0,07	0,05	0,04	0,04	0,08	0,07	0,09	0,07	0,10	0,09	0,10	0,08	0,09	0,12	0,21
CaO	10,82	12,31	10,25	2,58	10,48	10,26	11,24	9,36	12,26	12,09	13,27	14,28	15,39	9,66	15,17	10,71
Na_2O	5,24	4,64	5,52	7,31	5,66	5,90	5,36	6,46	4,75	4,76	4,02	3,40	2,98	5,94	2,89	5,41
K_2O	0,47	0,29	0,86	4,90	0,49	0,47	0,43	0,54	0,47	0,42	0,30	0,18	0,14	0,60	0,15	0,45
TiO_2	0,12	0,08	0,13	0,17	0,09	0,05	0,11	0,10	0,10	0,12	0,10	0,05	0,05	0,15	0,02	0,21
NiO	0,00	0,00	0,00	0,03	0,00	0,03	0,00	0,00	0,00	0,01	0,01	0,02	0,06	0,01	0,01	0,00
Cr_2O_3	0,04	0,00	0,00	0,02	0,02	0,01	0,02	0,02	0,00	0,02	0,00	0,02	0,01	0,00	0,00	0,02
P_2O_5	0,03	0,01	0,03	0,08	0,03	0,05	0,02	0,02	0,01	0,00	0,03	0,03	0,02	0,03	0,05	0,03
F	0,00	0,00	0,00	0,00	0,00	0,00	0,00	0,00	0,00	0,06	0,02	0,00	0,03	0,03	0,03	0,00
Cl	0,01	0,00	0,02	0,01	0,01	0,01	0,00	0,00	0,02	0,00	0,01	0,00	0,00	0,01	0,00	0,00
Total	99,96	100,79	100,37	99,69	100,19	100,71	100,88	101,43	99,48	98,65	98,80	100,02	100,34	100,46	100,60	99,73
Si	2,45	2,39	2,47	2,81	2,49	2,48	2,44	2,54	2,39	2,40	2,36	2,28	2,22	2,49	2,23	2,44
Al	1,53	1,60	1,50	1,17	1,48	1,49	1,53	1,43	1,57	1,56	1,60	1,71	1,75	1,48	1,75	1,52
Fe^{3+}	0,02	0,01	0,02	0,02	0,01	0,01	0,02	0,02	0,01	0,01	0,02	0,01	0,02	0,03	0,02	0,03
Mn	0,00	0,00	0,00	0,00	0,00	0,00	0,00	0,00	0,00	0,00	0,00	0,00	0,00	0,00	0,00	0,00
Mg	0,00	0,00	0,00	0,00	0,00	0,01	0,00	0,01	0,00	0,01	0,01	0,01	0,01	0,01	0,01	0,01
Ca	0,53	0,59	0,50	0,12	0,51	0,49	0,54	0,45	0,60	0,60	0,66	0,70	0,75	0,47	0,74	0,52
Na	0,46	0,41	0,48	0,64	0,50	0,51	0,47	0,56	0,42	0,43	0,36	0,30	0,26	0,52	0,26	0,48
K	0,03	0,02	0,05	0,28	0,03	0,03	0,02	0,03	0,03	0,02	0,02	0,01	0,01	0,03	0,01	0,03
Ti	0,00	0,00	0,00	0,01	0,00	0,00	0,00	0,00	0,00	0,00	0,00	0,00	0,00	0,01	0,00	0,01
Ni	0,00	0,00	0,00	0,00	0,00	0,00	0,00	0,00	0,00	0,00	0,00	0,00	0,00	0,00	0,00	0,00
Cr	0,00	0,00	0,00	0,00	0,00	0,00	0,00	0,00	0,00	0,00	0,00	0,00	0,00	0,00	0,00	0,00
P	0,00	0,00	0,00	0,00	0,00	0,00	0,00	0,00	0,00	0,00	0,00	0,00	0,00	0,00	0,00	0,00
Fe	0,00	0,00	0,00	0,00	0,00	0,00	0,00	0,00	0,00	0,01	0,00	0,00	0,00	0,00	0,00	0,00
Cl	0,00	0,00	0,00	0,00	0,00	0,00	0,00	0,00	0,00	0,00	0,00	0,00	0,00	0,00	0,00	0,00
An	52	58	48	12	49	48	52	43	57	57	63	69	73	46	74	51
[a] T (°C)	1195	1191	1208	1667	1194	1227	1224	1232	1249	1248	1242	1249	1246	1275	1246	1266
[b] P (Kbar)	11,9	11,2	14,5	56,3	13,3	14,7	13,2	16,4	15,7	15,7	13,9	10,1	9,2	17,3	9,2	15,3
[c] H2O (wt%)	0,39	0,47	0,59	1,69	0,28	0,21	0,01	0,45	0,67	0,65	0,69	0,19	0,11	0,18	0,11	0,01
$K_{D\ (Ab\text{-}An)}$	0,30	0,25	0,36	1,89	0,25	0,36	0,30	0,44	0,36	0,36	0,28	0,23	0,18	0,59	0,18	0,48

Table 2: Continued.

Suite	T2	T2	T2	T2	T2	T2	T2	T2	T2	T2	T2	T2	T2	T2	T2	T2
Analysis	150416 11_36	150416 11_37	150416 80_01	150416 80_05	150416 80_06	150416 81_15	150416 81_21	150416 83_48	150416 83_49	150416 83_50	150416 83_52	150416 87_64	150416 87_66	150416 87_71	150416 88_80	150416 88_82
Type	*centre*	*rim*	*centre*	*centre*	*matrix*	*centre*	*matrix*	*type 3 rim*	*rim*	*centre*	*matrix*	*centre*	*micropheno.*	*matrix*	*matrix*	*pheno.*
SiO_2	49,26	54,51	50,67	49,94	51,89	50,56	52,17	51,06	51,98	52,58	54,23	53,12	50,61	57,93	58,52	56,85
Al_2O_3	31,85	28,12	30,71	31,91	28,83	31,33	30,44	30,84	30,63	29,53	28,38	29,25	30,80	25,49	20,59	26,76
FeO	0,32	0,59	0,40	0,41	0,89	0,40	0,65	0,70	0,51	0,53	1,01	0,42	0,59	0,78	2,36	0,33
MnO	0,03	0,01	0,05	0,03	0,00	0,03	0,00	0,00	0,04	0,00	0,07	0,00	0,07	0,03	0,06	0,00
MgO	0,11	0,10	0,08	0,12	0,13	0,09	0,10	0,09	0,10	0,07	0,06	0,05	0,08	0,07	1,38	0,04
CaO	14,52	10,43	12,85	13,85	10,99	14,07	12,23	13,17	12,78	11,97	10,57	11,36	13,64	7,51	7,25	8,45
Na_2O	3,56	5,58	4,32	3,89	5,09	3,75	4,52	4,11	4,40	4,76	5,35	5,04	3,86	6,53	6,26	6,38
K_2O	0,17	0,51	0,23	0,18	0,46	0,17	0,24	0,23	0,24	0,27	0,49	0,45	0,21	1,08	2,06	0,83
TiO_2	0,08	0,09	0,06	0,05	0,25	0,10	0,13	0,08	0,11	0,07	0,16	0,03	0,07	0,19	0,59	0,07
NiO	0,05	0,04	0,00	0,00	0,00	0,00	0,06	0,00	0,00	0,00	0,00	0,03	0,03	0,00	0,03	0,00
Cr_2O_3	0,01	0,00	0,00	0,02	0,00	0,02	0,01	0,00	0,00	0,00	0,00	0,00	0,00	0,00	0,00	0,00
P_2O_5	0,02	0,04	0,00	0,00	0,09	0,03	0,01	0,05	0,02	0,00	0,03	0,03	0,06	0,01	0,88	0,06
F	0,02	0,00	0,00	0,00	0,00	0,00	0,00	0,00	0,00	0,00	0,00	0,00	0,00	0,00	0,01	0,00
Cl	0,00	0,00	0,00	0,01	0,00	0,00	0,00	0,00	0,00	0,01	0,00	0,00	0,01	0,01	0,06	0,01
Total	99,99	100,02	99,38	100,41	98,60	100,57	100,56	100,33	100,83	99,80	100,35	99,79	100,02	99,62	100,04	99,77
Si	2,26	2,47	2,33	2,27	2,40	2,30	2,36	2,32	2,35	2,39	2,45	2,42	2,31	2,62	2,67	2,56
Al	1,72	1,50	1,66	1,71	1,57	1,68	1,62	1,65	1,63	1,59	1,51	1,57	1,66	1,36	1,11	1,42
Fe^{3+}	0,01	0,02	0,02	0,02	0,03	0,02	0,02	0,03	0,02	0,02	0,04	0,02	0,02	0,03	0,09	0,01
Mn	0,00	0,00	0,00	0,00	0,00	0,00	0,00	0,00	0,00	0,00	0,00	0,00	0,00	0,00	0,00	0,00
Mg	0,01	0,01	0,01	0,01	0,01	0,01	0,01	0,01	0,01	0,01	0,00	0,00	0,01	0,00	0,09	0,00
Ca	0,71	0,51	0,63	0,68	0,54	0,69	0,59	0,64	0,62	0,58	0,51	0,55	0,67	0,36	0,35	0,41
Na	0,32	0,49	0,38	0,34	0,46	0,33	0,40	0,36	0,39	0,42	0,47	0,44	0,34	0,57	0,55	0,56
K	0,01	0,03	0,01	0,01	0,03	0,01	0,01	0,01	0,01	0,02	0,03	0,03	0,01	0,06	0,12	0,05
Ti	0,00	0,00	0,00	0,00	0,01	0,00	0,00	0,00	0,00	0,00	0,01	0,00	0,00	0,01	0,02	0,00
Ni	0,00	0,00	0,00	0,00	0,00	0,00	0,00	0,00	0,00	0,00	0,00	0,00	0,00	0,00	0,00	0,00
Cr	0,00	0,00	0,00	0,00	0,00	0,00	0,00	0,00	0,00	0,00	0,00	0,00	0,00	0,00	0,00	0,00
P	0,00	0,00	0,00	0,00	0,00	0,00	0,00	0,00	0,00	0,00	0,00	0,00	0,00	0,00	0,03	0,00
Fe	0,00	0,00	0,00	0,00	0,00	0,00	0,00	0,00	0,00	0,00	0,00	0,00	0,00	0,00	0,00	0,00
Cl	0,00	0,00	0,00	0,00	0,00	0,00	0,00	0,00	0,00	0,00	0,00	0,00	0,00	0,00	0,00	0,00
An	69	49	61	66	53	67	59	63	61	57	51	54	65	36	34	40
[a] T (°C)	1249	1268	1198	1197	1205	1232	1236	1227	1228	1230	1238	1227	1217	1262	1305	1252
[b] P (Kbar)	10,2	15,8	8,0	7,1	10,2	10,5	12,3	9,8	10,3	11,2	13,3	12,7	9,7	20,1	22,4	17,9
[c] H2O (wt%)	0,19	0,04	0,27	0,26	0,38	0,06	0,09	0,25	0,28	0,33	0,46	0,27	0,18	1,00	0,73	0,91
$K_{D\ (Ab\text{-}An)}$	0,23	0,51	0,22	0,18	0,30	0,19	0,27	0,23	0,26	0,29	0,38	0,28	0,18	0,56	0,55	0,48

Table 2: Continued.

Suite	T2	T2	T2	T2	T2	T2	T2	T2	T2	T2	T2	T2	T2	T2	T2	T2
Analysis	131016 102_51	131016 102_53	131016 102_54	150420 103_23	150420 103_27	150420 103_23	150420 103_27	150420 104_30	150420 104_31	150420 104_35	150420 104_40	150420 104_41	150420 104_47	150420 104_49	131016 109_59	131016 109_60
Type	*centre*	*matrix*	*micropheno. centre*	*centre*	*micropheno.*	*micropheno.*	*matrix*	*centre*	*rim*	*matrix*	*centre*	*rim*	*type 3 centre*	*Cpx reemplament*	*type 3 centre*	*type 3 rim*
SiO_2	52,29	52,86	51,53	46,85	55,53	51,21	51,86	57,80	52,50	53,01	48,35	52,92	60,34	54,61	59,59	51,91
Al_2O_3	29,43	28,70	28,98	34,24	27,90	31,47	30,47	27,27	30,01	30,02	33,31	30,29	24,00	28,35	24,73	29,54
FeO	0,41	0,60	0,50	0,52	0,25	0,66	0,79	0,12	0,63	0,91	0,58	0,63	0,76	0,72	0,19	0,47
MnO	0,01	0,00	0,02	0,00	0,00	0,00	0,04	0,00	0,04	0,00	0,00	0,00	0,01	0,00	0,00	0,00
MgO	0,06	0,04	0,06	0,04	0,02	0,05	0,05	0,01	0,03	0,03	0,06	0,03	0,05	0,05	0,01	0,07
CaO	13,12	12,45	12,76	16,09	10,24	13,23	12,46	8,85	12,60	12,14	16,12	12,95	5,79	9,84	6,72	12,94
Na_2O	4,08	4,36	4,22	2,02	5,60	3,98	4,48	6,57	4,10	4,71	2,42	4,37	6,35	5,68	6,51	4,08
K_2O	0,26	0,28	0,25	0,11	0,55	0,28	0,31	0,50	0,31	0,32	0,13	0,32	2,84	0,38	1,35	0,26
TiO_2	0,04	0,05	0,08	0,06	0,06	0,10	0,08	0,00	0,05	0,15	0,00	0,08	0,21	0,09	0,00	0,06
NiO	0,00	0,03	0,03	0,00	0,04	0,00	0,00	0,00	0,00	0,00	0,00	0,00	0,00	0,00	0,03	0,03
Cr_2O_3	0,00	0,00	0,00	0,00	0,00	0,02	0,00	0,03	0,01	0,00	0,00	0,00	0,00	0,00	0,00	0,01
P_2O_5	0,03	0,06	0,03	0,03	0,03	0,00	0,04	0,01	0,03	0,04	0,02	0,02	0,04	0,02	0,02	0,05
F	0,00	0,00	0,05	0,04	0,00	0,01	0,01	0,03	0,02	0,01	0,08	0,03	0,00	0,00	0,00	0,03
Cl	0,01	0,00	0,00	0,00	0,00	0,01	0,01	0,00	0,01	0,01	0,00	0,00	0,01	0,00	0,00	0,01
Total	99,73	99,42	98,52	100,00	100,21	101,03	100,60	101,19	100,34	101,34	101,06	101,64	100,38	99,74	99,16	99,46
Si	2,39	2,42	2,38	2,15	2,50	2,31	2,35	2,57	2,38	2,38	2,20	2,37	2,71	2,48	2,69	2,38
Al	1,58	1,55	1,58	1,85	1,48	1,68	1,63	1,43	1,60	1,59	1,79	1,60	1,27	1,51	1,31	1,59
Fe^{3+}	0,02	0,02	0,02	0,02	0,01	0,03	0,03	0,00	0,02	0,03	0,02	0,02	0,03	0,03	0,01	0,02
Mn	0,00	0,00	0,00	0,00	0,00	0,00	0,00	0,00	0,00	0,00	0,00	0,00	0,00	0,00	0,00	0,00
Mg	0,00	0,00	0,00	0,00	0,00	0,00	0,00	0,00	0,00	0,00	0,00	0,00	0,00	0,00	0,00	0,00
Ca	0,64	0,61	0,63	0,79	0,49	0,64	0,61	0,42	0,61	0,58	0,79	0,62	0,28	0,48	0,32	0,63
Na	0,36	0,39	0,38	0,18	0,49	0,35	0,39	0,57	0,36	0,41	0,21	0,38	0,55	0,50	0,57	0,36
K	0,01	0,02	0,01	0,01	0,03	0,02	0,02	0,03	0,02	0,02	0,01	0,02	0,16	0,02	0,08	0,02
Ti	0,00	0,00	0,00	0,00	0,00	0,00	0,00	0,00	0,00	0,01	0,00	0,00	0,01	0,00	0,00	0,00
Ni	0,00	0,00	0,00	0,00	0,00	0,00	0,00	0,00	0,00	0,00	0,00	0,00	0,00	0,00	0,00	0,00
Cr	0,00	0,00	0,00	0,00	0,00	0,00	0,00	0,00	0,00	0,00	0,00	0,00	0,00	0,00	0,00	0,00
P	0,00	0,00	0,00	0,00	0,00	0,00	0,00	0,00	0,00	0,00	0,00	0,00	0,00	0,00	0,00	0,00
Fe	0,00	0,00	0,01	0,01	0,00	0,00	0,00	0,00	0,00	0,00	0,01	0,00	0,00	0,00	0,00	0,00
Cl	0,00	0,00	0,00	0,00	0,00	0,00	0,00	0,00	0,00	0,00	0,00	0,00	0,00	0,00	0,00	0,00
An	63	60	62	81	49	64	59	41	62	58	78	61	28	48	33	63
[a] T (°C)	1177	1177	1177	1214	1236	1223	1225	1213	1200	1201	1193	1201	1327	1206	1223	1174
[b] P (Kbar)	8,0	8,6	8,3	6,6	13,9	9,6	10,6	14,7	8,5	9,4	5,7	8,7	25,3	12,3	17,8	7,0
[c] H2O (wt%)	0,39	0,41	0,40	0,60	0,52	0,23	0,26	1,14	0,40	0,47	0,65	0,41	1,08	0,80	1,08	0,16
$K_{D\ (Ab\text{-}An)}$	0,15	0,17	0,16	0,09	0,38	0,21	0,25	0,46	0,20	0,24	0,09	0,21	0,69	0,36	0,58	0,19

Table 2: Continued.

Suite	T2	T2	T2	T2	T2	T2	T2	CA	CA	CA	CA	CA	CA	CA	CA	CA
Analysis	131016 109_61	131016 109_62	150420 131_60	150420 131_65	150420 135_79	150420 135_80	150420 135_83	130218 03_15	130218 03_16	130218 03_17	130218 03_18	130218 03_19	130218 03_20	130218 03_24	130306 20_03	130306 20_04
Type	*matrix*	*centre*	*matrix*	*centre*	*centre*	*rim*	*matrix*	*centre*	*centre middle*	*middle*	*middle*	*middle rim*	*rim*	*matrix*	*pheno. centre*	*pheno. centre*
SiO_2	51,62	53,42	53,89	51,45	52,74	53,91	54,20	49,67	51,30	53,12	51,32	52,28	54,15	49,67	49,44	50,27
Al_2O_3	29,41	28,55	28,95	30,42	30,16	28,33	29,11	31,08	30,04	29,04	28,82	28,74	27,35	30,81	32,15	30,80
FeO	0,55	0,65	0,99	0,79	0,48	0,75	0,57	0,52	0,75	0,57	0,63	0,62	0,88	0,70	0,56	0,57
MnO	0,00	0,03	0,04	0,01	0,07	0,02	0,00	0,00	0,07	0,00	0,03	0,01	0,00	0,02	0,03	0,00
MgO	0,06	0,05	0,11	0,12	0,11	0,10	0,14	0,13	0,20	0,20	0,17	0,21	0,16	0,14	0,06	0,03
CaO	12,81	11,29	11,81	13,33	13,10	10,42	11,31	14,75	13,82	12,63	13,12	12,86	11,50	14,73	16,08	14,39
Na_2O	4,16	4,56	4,80	4,11	4,27	5,79	5,31	3,45	3,73	4,51	4,15	4,48	5,10	3,39	2,62	3,48
K_2O	0,29	0,95	0,47	0,24	0,16	0,45	0,27	0,08	0,17	0,18	0,15	0,20	0,31	0,13	0,07	0,10
TiO_2	0,08	0,11	0,07	0,05	0,07	0,11	0,15	0,04	0,00	0,04	0,06	0,12	0,11	0,07	0,04	0,05
NiO	0,05	0,00	0,00	0,02	0,04	0,01	0,02	0,05	0,02	0,03	0,02	0,02	0,05	0,01	0,00	0,01
Cr_2O_3	0,00	0,00	0,00	0,00	0,00	0,00	0,00	0,00	0,00	0,00	0,00	0,02	0,00	0,02	0,02	0,00
P_2O_5	0,01	0,05	0,05	0,03	0,06	0,08	0,07	0,02	0,01	0,01	0,05	0,03	0,00	0,03	0,02	0,02
F	0,00	0,00	0,02	0,03	0,02	0,03	0,04	0,05	0,00	0,00	0,03	0,01	0,00	0,00	0,00	0,00
Cl	0,02	0,01	0,01	0,00	0,01	0,01	0,02	0,02	0,00	0,00	0,01	0,02	0,00	0,00	0,04	0,00
Total	99,07	99,66	101,21	100,59	101,29	100,01	101,20	99,85	100,10	100,32	98,53	99,62	99,61	99,69	101,13	99,72
Si	2,37	2,44	2,42	2,34	2,37	2,45	2,43	2,28	2,34	2,41	2,38	2,39	2,47	2,28	2,24	2,30
Al	1,59	1,54	1,53	1,63	1,60	1,52	1,54	1,68	1,62	1,55	1,57	1,55	1,47	1,67	1,72	1,66
Fe^{3+}	0,02	0,02	0,04	0,03	0,02	0,03	0,02	0,02	0,03	0,02	0,02	0,02	0,03	0,03	0,02	0,02
Mn	0,00	0,00	0,00	0,00	0,00	0,00	0,00	0,00	0,00	0,00	0,00	0,00	0,00	0,00	0,00	0,00
Mg	0,00	0,00	0,01	0,01	0,01	0,01	0,01	0,01	0,01	0,01	0,01	0,01	0,01	0,01	0,00	0,00
Ca	0,63	0,55	0,57	0,65	0,63	0,51	0,54	0,73	0,68	0,61	0,65	0,63	0,56	0,73	0,78	0,71
Na	0,37	0,40	0,42	0,36	0,37	0,51	0,46	0,31	0,33	0,40	0,37	0,40	0,45	0,30	0,23	0,31
K	0,02	0,06	0,03	0,01	0,01	0,03	0,02	0,00	0,01	0,01	0,01	0,01	0,02	0,01	0,00	0,01
Ti	0,00	0,00	0,00	0,00	0,00	0,00	0,01	0,00	0,00	0,00	0,00	0,00	0,00	0,00	0,00	0,00
Ni	0,00	0,00	0,00	0,00	0,00	0,00	0,00	0,00	0,00	0,00	0,00	0,00	0,00	0,00	0,00	0,00
Cr	0,00	0,00	0,00	0,00	0,00	0,00	0,00	0,00	0,00	0,00	0,00	0,00	0,00	0,00	0,00	0,00
P	0,00	0,00	0,00	0,00	0,00	0,00	0,00	0,00	0,00	0,00	0,00	0,00	0,00	0,00	0,00	0,00
Fe	0,00	0,00	0,00	0,00	0,00	0,00	0,01	0,01	0,00	0,00	0,00	0,00	0,00	0,00	0,00	0,00
Cl	0,00	0,00	0,00	0,00	0,00	0,00	0,00	0,00	0,00	0,00	0,00	0,00	0,00	0,00	0,00	0,00
An	62	55	56	63	62	49	53	70	67	60	63	61	54	70		69
[a] T (°C)	1175	1190	1214	1207	1209	1220	1214	1178	1180	1181	1180	1181	1184	1179	1174	1185
[b] P (Kbar)	7,2	9,4	10,3	8,4	8,3	12,2	10,6	3,4	4,0	5,3	4,6	5,1	6,6	3,4	4,6	10,4
[c] H2O (wt%)	0,16	0,05	0,24	0,21	0,28	0,57	0,45	0,78	0,73	0,77	0,75	0,76	0,86	0,77	1,49	1,92
$K_{D\ (Ab\text{-}An)}$	0,20	0,24	0,29	0,22	0,23	0,39	0,33	0,19	0,21	0,28	0,25	0,28	0,35	0,18	0,14	0,36

Table 2: Continued.

Suite	CA	CA	CA	CA	CA	CA	CA	CA	CA	CA	CA	CA	CA	CA	CA	CA
Analysis	130306 20_11	130306 20_12	130726 57_02	130726 57_05	130726 57_06	140527 57_33	130306 60_17	130306 60_18	130306 60_19	130306 60_24	130306 61_31	130306 61_34	130306 61_35	130306 61_36	130306 61_37	140527 61_37
Type	*pheno. centre*	*pheno. Rim*	*matrix*	*micropheno.*	*micropheno. centre*	*matrix*	*Type 2 pheno. centre*	*Type 2 pheno. middle*	*Type 2 pheno. rim*	*micropheno.*	*Amp corona*	*pheno. centre*	*pheno. centre/ middle*	*pheno. middle/ rim*	*pheno. rim*	*reemplacement*
SiO_2	52,97	53,03	54,05	53,58	48,22	52,86	48,19	51,52	52,51	68,08	48,38	50,11	51,36	50,52	52,90	52,95
Al_2O_3	29,31	28,22	28,42	29,05	33,07	28,11	32,50	30,45	29,01	16,00	27,53	30,92	30,45	30,84	28,35	28,86
FeO	0,80	0,68	0,90	0,76	0,57	0,60	0,71	0,61	0,66	2,38	0,91	0,53	0,51	0,62	0,93	0,75
MnO	0,00	0,00	0,00	0,00	0,01	0,03	0,04	0,00	0,02	0,08	0,00	0,01	0,00	0,04	0,00	0,00
MgO	0,11	0,10	0,11	0,17	0,12	0,17	0,06	0,09	0,06	0,80	0,04	0,07	0,03	0,08	0,05	0,07
CaO	12,70	12,17	11,88	12,21	16,37	12,25	16,20	13,25	12,60	4,08	12,20	14,28	13,60	14,35	11,42	12,16
Na_2O	4,30	4,49	4,55	3,88	2,06	4,74	2,38	3,93	4,70	4,00	4,06	3,51	4,15	3,52	4,93	4,62
K_2O	0,14	0,15	0,22	0,17	0,06	0,19	0,10	0,13	0,18	2,86	0,22	0,09	0,11	0,07	0,07	0,19
TiO_2	0,01	0,01	0,02	0,01	0,00	0,08	0,05	0,00	0,01	0,68	0,07	0,06	0,03	0,03	0,06	0,10
NiO	0,02	0,08	0,00	0,00	0,07	0,00	0,02	0,05	0,05	0,00	0,00	0,00	0,01	0,00	0,02	0,02
Cr_2O_3	0,00	0,01	0,00	0,00	0,00	0,02	0,01	0,01	0,00	0,00	0,04	0,00	0,01	0,00	0,00	0,01
P_2O_5	0,02	0,08	0,01	0,02	0,01	0,04	0,03	0,04	0,02	0,15	0,03	0,03	0,05	0,01	0,07	0,00
F	0,02	0,03	0,00	0,00	0,00	0,02	0,08	0,05	0,05	0,10	0,02	0,05	0,03	0,01	0,01	0,00
Cl	0,01	0,01	0,01	0,00	0,01	0,00	0,01	0,00	0,00	0,17	0,04	0,00	0,00	0,00	0,03	0,00
Total	100,40	99,05	100,18	99,84	100,57	99,12	100,36	100,14	99,87	99,36	93,53	99,66	100,35	100,09	98,83	99,74
Si	2,40	2,43	2,45	2,43	2,20	2,43	2,21	2,35	2,40	3,04	2,37	2,30	2,34	2,31	2,43	2,41
Al	1,57	1,53	1,52	1,55	1,78	1,52	1,76	1,63	1,56	0,84	1,59	1,67	1,63	1,66	1,54	1,55
Fe^{3+}	0,03	0,03	0,03	0,03	0,02	0,02	0,03	0,02	0,03	0,09	0,04	0,02	0,02	0,02	0,04	0,03
Mn	0,00	0,00	0,00	0,00	0,00	0,00	0,00	0,00	0,00	0,00	0,00	0,00	0,00	0,00	0,00	0,00
Mg	0,01	0,01	0,01	0,01	0,01	0,01	0,00	0,01	0,00	0,05	0,00	0,00	0,00	0,01	0,00	0,00
Ca	0,62	0,60	0,58	0,59	0,80	0,60	0,80	0,65	0,62	0,20	0,64	0,70	0,66	0,70	0,56	0,59
Na	0,38	0,40	0,40	0,34	0,18	0,42	0,21	0,35	0,42	0,35	0,38	0,31	0,37	0,31	0,44	0,41
K	0,01	0,01	0,01	0,01	0,00	0,01	0,01	0,01	0,01	0,16	0,01	0,01	0,01	0,00	0,00	0,01
Ti	0,00	0,00	0,00	0,00	0,00	0,00	0,00	0,00	0,00	0,02	0,00	0,00	0,00	0,00	0,00	0,00
Ni	0,00	0,00	0,00	0,00	0,00	0,00	0,00	0,00	0,00	0,00	0,00	0,00	0,00	0,00	0,00	0,00
Cr	0,00	0,00	0,00	0,00	0,00	0,00	0,00	0,00	0,00	0,00	0,00	0,00	0,00	0,00	0,00	0,00
P	0,00	0,00	0,00	0,00	0,00	0,00	0,00	0,00	0,00	0,01	0,00	0,00	0,00	0,00	0,00	0,00
Fe	0,00	0,00	0,00	0,00	0,00	0,00	0,01	0,01	0,01	0,01	0,00	0,01	0,00	0,00	0,00	0,00
Cl	0,00	0,00	0,00	0,00	0,00	0,00	0,00	0,00	0,00	0,01	0,00	0,00	0,00	0,00	0,00	0,00
An	61	59	58	63	81	58	79	65	59	28		69	64	69	56	59
[a] T (°C)	1174	1175	1186	1184	1180	1184	1201	1204	1206	1383	1201	1197	1199	1197	1203	1214
[b] P (Kbar)	5,9	6,4	6,7	5,7	3,1	6,6	5,3	7,4	8,7	27,0	7,1	5,6	6,5	5,5	8,6	8,1
[c] H2O (wt%)	1,49	1,51	1,34	1,29	1,63	1,36	1,35	1,13	1,18	1,26	1,12	1,15	1,14	1,16	1,24	0,96
$K_{D\ (Ab\text{-}An)}$	0,19	0,21	0,31	0,26	0,10	0,32	0,10	0,20	0,25	0,66	0,19	0,14	0,18	0,14	0,25	0,22

Table 2: Continued.

Suite	CA	CA	CA	CA	CA	CA	CA	CA	CA	CA	CA	CA	CA	CA	CA	CA
Analysis	140527 61_38	130306 63_55	140527 63_61	130306 64_41	130306 64_42	130306 64_43	131002 64_44	131002 64_49	130726 65_15	140527 65_45	130306 66_48	130306 66_49	131002 66_56	131002 66_57	131002 66_61	140527 73_69
Type	*matrix*	*matrix*	*micropheno.*	*Type 2 pheno. centre*	*Type 2 pheno. middle*	*Type 2 pheno. rim*	*Incluida in Cpx*	*matrix*	*matrix*	*matrix*	*pheno. centre*	*Type 2 pheno. rim*	*pheno. centre*	*pheno. rim*	*micropheno.*	*Amp corona*
SiO_2	52,61	49,91	50,44	52,48	50,20	54,71	54,63	52,18	50,54	53,65	45,09	51,87	45,94	52,87	52,45	53,95
Al_2O_3	29,19	30,59	29,71	28,77	30,24	27,84	26,85	28,42	30,72	27,77	32,75	28,96	32,91	28,02	28,62	27,66
FeO	0,82	0,71	0,71	0,73	0,53	0,86	0,92	0,93	0,61	0,76	0,54	0,75	0,48	0,85	0,57	0,82
MnO	0,02	0,03	0,05	0,02	0,00	0,00	0,00	0,05	0,03	0,00	0,03	0,04	0,00	0,09	0,00	0,02
MgO	0,06	0,06	0,09	0,08	0,02	0,05	0,02	0,00	0,09	0,11	0,02	0,12	0,05	0,08	0,08	0,12
CaO	12,30	14,90	14,42	12,18	14,30	11,19	10,51	12,78	14,54	12,07	17,38	12,84	17,72	12,34	12,87	11,73
Na_2O	4,62	3,43	3,40	4,90	3,60	5,17	5,71	4,53	3,31	4,93	1,84	4,37	1,92	4,81	4,65	4,94
K_2O	0,22	0,15	0,16	0,22	0,15	0,36	0,44	0,30	0,15	0,27	0,02	0,13	0,04	0,11	0,11	0,22
TiO_2	0,06	0,02	0,06	0,04	0,03	0,01	0,11	0,07	0,01	0,07	0,02	0,01	0,00	0,01	0,00	0,06
NiO	0,03	0,03	0,00	0,03	0,00	0,00	0,04	0,00	0,02	0,00	0,03	0,02	0,04	0,00	0,03	0,02
Cr_2O_3	0,04	0,00	0,04	0,01	0,01	0,03	0,00	0,00	0,00	0,00	0,00	0,00	0,00	0,00	0,00	0,01
P_2O_5	0,02	0,00	0,02	0,07	0,01	0,00	0,02	0,04	0,00	0,00	0,06	0,00	0,00	0,03	0,07	0,02
F	0,06	0,06	0,05	0,00	0,06	0,06	0,03	0,00	0,03	0,02	0,00	0,00	0,00	0,00	0,00	0,00
Cl	0,00	0,00	0,00	0,00	0,00	0,02	0,01	0,01	0,00	0,00	0,01	0,03	0,01	0,00	0,00	0,00
Total	100,05	99,87	99,14	99,52	99,12	100,29	99,28	99,30	100,06	99,65	97,76	99,12	99,10	99,21	99,46	99,55
Si	2,40	2,29	2,33	2,40	2,32	2,48	2,50	2,40	2,31	2,45	2,13	2,39	2,14	2,43	2,40	2,46
Al	1,57	1,66	1,62	1,55	1,65	1,49	1,45	1,54	1,66	1,49	1,83	1,57	1,81	1,52	1,55	1,49
Fe^{3+}	0,03	0,03	0,03	0,03	0,02	0,03	0,04	0,04	0,02	0,03	0,02	0,03	0,02	0,03	0,02	0,03
Mn	0,00	0,00	0,00	0,00	0,00	0,00	0,00	0,00	0,00	0,00	0,00	0,00	0,00	0,00	0,00	0,00
Mg	0,00	0,00	0,01	0,01	0,00	0,00	0,00	0,00	0,01	0,01	0,00	0,01	0,00	0,01	0,01	0,01
Ca	0,60	0,73	0,71	0,60	0,71	0,54	0,52	0,63	0,71	0,59	0,88	0,63	0,89	0,61	0,63	0,57
Na	0,41	0,31	0,30	0,43	0,32	0,45	0,51	0,40	0,29	0,44	0,17	0,39	0,17	0,43	0,41	0,44
K	0,01	0,01	0,01	0,01	0,01	0,02	0,03	0,02	0,01	0,02	0,00	0,01	0,00	0,01	0,01	0,01
Ti	0,00	0,00	0,00	0,00	0,00	0,00	0,00	0,00	0,00	0,00	0,00	0,00	0,00	0,00	0,00	0,00
Ni	0,00	0,00	0,00	0,00	0,00	0,00	0,00	0,00	0,00	0,00	0,00	0,00	0,00	0,00	0,00	0,00
Cr	0,00	0,00	0,00	0,00	0,00	0,00	0,00	0,00	0,00	0,00	0,00	0,00	0,00	0,00	0,00	0,00
P	0,00	0,00	0,00	0,00	0,00	0,00	0,00	0,00	0,00	0,00	0,00	0,00	0,00	0,00	0,00	0,00
Fe	0,01	0,01	0,01	0,00	0,01	0,01	0,00	0,00	0,00	0,00	0,00	0,00	0,00	0,00	0,00	0,00
Cl	0,00	0,00	0,00	0,00	0,00	0,00	0,00	0,00	0,00	0,00	0,00	0,00	0,00	0,00	0,00	0,00
An	59	70	69	57	68	53	49	60	70	57	84	61	83	58	60	56
[a] T (°C)	1214	1171	1168	1170	1168	1173	1176	1171	1189	1195	1187	1191	1187	1191	1191	1207
[b] P (Kbar)	8,1	4,2	4,0	6,6	4,5	7,7	8,9	6,1	4,2	7,0	3,9	6,9	3,9	7,6	7,2	9,6
[c] H2O (wt%)	0,94	1,35	1,27	1,48	1,42	1,54	1,68	1,40	0,98	1,00	1,79	1,36	1,77	1,42	1,38	1,21
$K_{D\ (Ab\text{-}An)}$	0,22	0,14	0,14	0,22	0,14	0,26	0,30	0,20	0,15	0,27	0,06	0,21	0,07	0,23	0,22	0,26

Table 2: Continued.

Suite	CA	CA	CA	CA	CA	CA	CA	CA	CA	CA	CA	CA	CA	CA	CA	CA
Analysis	140527 73_73	140527 73_76	140527 76_01	140527 76_02	140527 76_03	140527 76_04	140527 76_07	130726 77_30	131016 77_08	131016 77_11	140527 77_12	140527 77_17	140527 77_18	140527 77_20	140527 78_22	140527 78_24
Type	*microphenо.*	*microphenо.*	*matrix*	*Amp corona*	*centre*	*rim*	*Amp corona*	*matrix*	*Intersticial in Cpx*	*Amp corona*	*Amp corona*	*Amp corona*	*microphenо.*	*Amp corona*	*Amp corona*	*matrix*
SiO_2	52,42	54,09	55,04	54,09	52,40	50,97	54,93	54,14	55,80	53,43	53,57	52,96	51,62	54,21	53,37	50,94
Al_2O_3	27,83	28,13	27,81	28,35	29,54	29,85	27,88	28,98	26,19	27,72	28,50	28,47	29,24	28,13	27,93	30,07
FeO	0,81	0,66	0,67	1,02	0,57	0,52	1,12	0,69	0,70	1,01	0,82	0,97	0,59	0,96	0,93	0,54
MnO	0,09	0,00	0,03	0,00	0,00	0,00	0,01	0,00	0,01	0,01	0,00	0,05	0,07	0,05	0,03	0,01
MgO	0,08	0,10	0,09	0,08	0,10	0,08	0,04	0,08	0,07	0,24	0,10	0,12	0,09	0,14	0,11	0,08
CaO	12,23	11,36	10,73	11,37	13,10	14,16	11,04	12,02	9,60	12,07	12,28	12,00	13,05	11,70	11,27	13,56
Na_2O	4,59	4,93	5,34	5,19	3,99	3,85	5,30	4,56	6,20	4,95	4,87	4,87	4,35	4,90	5,12	3,96
K_2O	0,25	0,19	0,21	0,30	0,12	0,10	0,24	0,13	0,27	0,19	0,20	0,21	0,12	0,16	0,21	0,11
TiO_2	0,01	0,00	0,07	0,11	0,00	0,04	0,10	0,07	0,04	0,03	0,05	0,13	0,00	0,07	0,08	0,00
NiO	0,03	0,03	0,04	0,04	0,03	0,06	0,00	0,00	0,01	0,02	0,00	0,01	0,02	0,00	0,03	0,00
Cr_2O_3	0,00	0,04	0,00	0,01	0,00	0,01	0,00	0,00	0,00	0,03	0,00	0,02	0,00	0,01	0,00	0,00
P_2O_5	0,10	0,06	0,03	0,02	0,00	0,02	0,02	0,01	0,00	0,00	0,01	0,03	0,02	0,00	0,00	0,00
F	0,00	0,00	0,00	0,00	0,00	0,00	0,02	0,02	0,00	0,00	0,00	0,04	0,00	0,02	0,03	0,01
Cl	0,01	0,00	0,00	0,00	0,00	0,00	0,00	0,00	0,00	0,01	0,00	0,00	0,00	0,01	0,00	0,00
Total	98,46	99,60	100,04	100,59	99,85	99,66	100,71	100,70	98,89	99,70	100,38	99,87	0,00	100,37	99,12	99,27
Si	2,43	2,46	2,49	2,45	2,39	2,34	2,48	2,44	2,55	2,44	2,43	2,42	2,37	2,45	2,45	2,34
Al	1,52	1,51	1,48	1,51	1,59	1,61	1,48	1,54	1,41	1,49	1,52	1,53	1,58	1,50	1,51	1,63
Fe^{3+}	0,03	0,03	0,03	0,04	0,02	0,02	0,04	0,03	0,03	0,04	0,03	0,04	0,02	0,04	0,04	0,02
Mn	0,00	0,00	0,00	0,00	0,00	0,00	0,00	0,00	0,00	0,00	0,00	0,00	0,00	0,00	0,00	0,00
Mg	0,01	0,01	0,01	0,01	0,01	0,01	0,00	0,01	0,00	0,02	0,01	0,01	0,01	0,01	0,01	0,01
Ca	0,61	0,55	0,52	0,55	0,64	0,70	0,53	0,58	0,47	0,59	0,60	0,59	0,64	0,57	0,55	0,67
Na	0,41	0,43	0,47	0,46	0,35	0,34	0,46	0,40	0,55	0,44	0,43	0,43	0,39	0,43	0,46	0,35
K	0,01	0,01	0,01	0,02	0,01	0,01	0,01	0,01	0,02	0,01	0,01	0,01	0,01	0,01	0,01	0,01
Ti	0,00	0,00	0,00	0,00	0,00	0,00	0,00	0,00	0,00	0,00	0,00	0,00	0,00	0,00	0,00	0,00
Ni	0,00	0,00	0,00	0,00	0,00	0,00	0,00	0,00	0,00	0,00	0,00	0,00	0,00	0,00	0,00	0,00
Cr	0,00	0,00	0,00	0,00	0,00	0,00	0,00	0,00	0,00	0,00	0,00	0,00	0,00	0,00	0,00	0,00
P	0,00	0,00	0,00	0,00	0,00	0,00	0,00	0,00	0,00	0,00	0,00	0,00	0,00	0,00	0,00	0,00
Fe	0,00	0,00	0,00	0,00	0,00	0,00	0,00	0,00	0,00	0,00	0,00	0,01	0,00	0,00	0,00	0,00
Cl	0,00	0,00	0,00	0,00	0,00	0,00	0,00	0,00	0,00	0,00	0,00	0,00	0,00	0,00	0,00	0,00
An	59	55	52	54	64	67	53	59	45	57	58	57	62	56	54	65
[a] T (°C)	1207	1206	1172	1174	1170	1169	1172	1166	1170	1167	1167	1168	1166	1167	1156	1155
[b] P (Kbar)	9,0	9,7	7,9	7,5	5,2	4,7	7,7	6,1	9,7	6,6	6,4	6,6	5,5	6,7	6,7	4,5
[c] H2O (wt%)	1,13	1,24	1,82	1,72	1,59	1,59	1,78	1,87	2,34	1,89	1,87	1,88	1,82	1,91	1,95	1,80
$K_{D\ (Ab\text{-}An)}$	0,24	0,27	0,25	0,23	0,15	0,14	0,24	0,20	0,35	0,22	0,21	0,22	0,18	0,23	0,22	0,14

Table 2: Continued.

Suite	CA	CA	CA	CA	CA	CA	CA	CA	CA	CA	CA	CA	CA	CA	CA	CA
Analysis	151214 82_24	151214 82_25	151214 82_28	151214 82_29	151214 92_03	151214 92_05	151214 93_10	151214 93_13	151214 93_14	151214 93_16	151214 93_19	140527 94_92	140527 94_94	140527 94_95	140527 94_96	140527 94_99
Type	*matrix*	*matrix*	*pheno. centre*	*matrix*	*pheno. rim*	*matrix*	*Type 3 rim*	*micropheno. centre*	*micropheno. rim*	*matrix*	*pheno.*	*pheno.*	*micropheno.*	*micropheno.*	*pheno.*	*micropheno.*
SiO_2	50,54	67,00	50,95	68,63	53,50	54,84	48,05	49,29	54,52	55,68	54,87	52,01	49,30	51,47	50,81	50,74
Al_2O_3	30,41	15,96	30,66	15,51	28,72	28,30	32,44	31,75	28,41	27,35	27,65	30,00	30,12	29,93	30,92	30,83
FeO	0,86	1,52	0,60	1,36	0,72	0,86	0,48	0,50	0,67	0,91	0,55	0,51	0,60	0,64	0,57	0,58
MnO	0,19	0,03	0,05	0,01	0,04	0,03	0,00	0,00	0,00	0,01	0,02	0,00	0,07	0,00	0,00	0,00
MgO	0,10	0,08	0,11	0,02	0,07	0,08	0,08	0,06	0,09	0,10	0,14	0,13	0,08	0,13	0,09	0,15
CaO	13,96	3,56	13,99	2,74	11,98	11,47	16,28	14,76	10,96	10,16	11,09	13,73	14,23	13,82	14,57	14,17
Na_2O	3,75	4,64	3,81	3,86	4,86	5,28	2,43	3,07	5,40	5,98	5,42	3,95	3,45	3,86	3,48	3,76
K_2O	0,14	2,78	0,12	3,66	0,27	0,31	0,06	0,14	0,37	0,42	0,32	0,16	0,17	0,15	0,17	0,15
TiO_2	0,05	0,93	0,10	0,98	0,13	0,15	0,06	0,04	0,15	0,16	0,11	0,08	0,11	0,09	0,05	0,05
NiO	0,00	0,00	0,01	0,00	0,00	0,00	0,00	0,07	0,00	0,05	0,00	0,00	0,04	0,00	0,00	0,00
Cr_2O_3	0,00	0,00	0,00	0,00	0,00	0,00	0,00	0,02	0,00	0,00	0,00	0,00	0,01	0,00	0,00	0,01
P_2O_5	0,07	0,11	0,00	0,09	0,07	0,07	0,04	0,02	0,02	0,02	0,01	0,00	0,01	0,01	0,02	0,04
F	0,01	0,06	0,00	0,04	0,00	0,03	0,03	0,00	0,00	0,02	0,02	0,00	0,03	0,00	0,01	0,01
Cl	0,00	0,09	0,00	0,11	0,01	0,00	0,00	0,00	0,01	0,00	0,00	0,00	0,01	0,01	0,01	0,00
Total	100,08	96,74	100,41	97,00	100,35	101,41	99,96	99,71	100,60	100,86	100,20	100,56	98,22	100,10	100,69	100,50
Si	2,31	3,06	2,32	3,11	2,42	2,46	2,21	2,26	2,46	2,50	2,48	2,36	2,30	2,35	2,31	2,31
Al	1,64	0,86	1,65	0,83	1,53	1,49	1,76	1,72	1,51	1,45	1,47	1,60	1,66	1,61	1,66	1,65
Fe^{3+}	0,03	0,06	0,02	0,05	0,03	0,03	0,02	0,02	0,03	0,03	0,02	0,02	0,02	0,02	0,02	0,02
Mn	0,01	0,00	0,00	0,00	0,00	0,00	0,00	0,00	0,00	0,00	0,00	0,00	0,00	0,00	0,00	0,00
Mg	0,01	0,01	0,01	0,00	0,00	0,01	0,01	0,00	0,01	0,01	0,01	0,01	0,01	0,01	0,01	0,01
Ca	0,68	0,17	0,68	0,13	0,58	0,55	0,80	0,73	0,53	0,49	0,54	0,67	0,71	0,68	0,71	0,69
Na	0,33	0,41	0,34	0,34	0,43	0,46	0,22	0,27	0,47	0,52	0,48	0,35	0,31	0,34	0,31	0,33
K	0,01	0,16	0,01	0,21	0,02	0,02	0,00	0,01	0,02	0,02	0,02	0,01	0,01	0,01	0,01	0,01
Ti	0,00	0,03	0,00	0,03	0,00	0,01	0,00	0,00	0,01	0,01	0,00	0,00	0,00	0,00	0,00	0,00
Ni	0,00	0,00	0,00	0,00	0,00	0,00	0,00	0,00	0,00	0,00	0,00	0,00	0,00	0,00	0,00	0,00
Cr	0,00	0,00	0,00	0,00	0,00	0,00	0,00	0,00	0,00	0,00	0,00	0,00	0,00	0,00	0,00	0,00
P	0,00	0,00	0,00	0,00	0,00	0,00	0,00	0,00	0,00	0,00	0,00	0,00	0,00	0,00	0,00	0,00
Fe	0,00	0,01	0,00	0,01	0,00	0,00	0,00	0,00	0,00	0,00	0,00	0,00	0,00	0,00	0,00	0,00
Cl	0,00	0,01	0,00	0,01	0,00	0,00	0,00	0,00	0,00	0,00	0,00	0,00	0,00	0,00	0,00	0,00
An	67	23	67	19	57	54	78	72	52	47	52	65	69	66	69	67
[a] T (^oC)	1148	1315	1148	1413	1218	1220	1213	1217	1227	1231	1226	1189	1189	1189	1189	1188
[b] P (Kbar)	4,9	26,2	4,9	32,9	8,8	9,7	5,1	6,1	10,8	12,3	10,7	7,1	6,5	7,0	6,4	6,7
[c] H2O (wt%)	1,84	2,73	1,85	2,37	0,83	0,91	0,77	0,58	0,72	0,91	0,73	0,42	0,43	0,42	0,43	0,43
$K_{D\ (Ab\text{-}An)}$	0,15	0,71	0,15	0,77	0,33	0,38	0,12	0,16	0,39	0,46	0,38	0,23	0,19	0,22	0,19	0,21

Table 2: Continued.

Suite	CA	CA	CA	CA	CA	CA	CA	CA	CA	CA	CA	CA	CA	CA	CA	CA
Analysis	151214 96_33	151214 96_34	151214 96_36	151214 96_42	150420 107_85	150420 107_86	150420 107_91	150420 107_95	150420 107_98	151214 108_46	151214 108_50	151214 108_51	151214 108_53	151214 108_56	151214 108_57	151214 108_59
Type	*pheno. centre*	*pheno. rim*	*matrix*	*micropheno. centre*	*centre*	*rim*	*micropheno.*	*micropheno.*	*micropheno.*	*matrix*	*micropheno. centre*	*micropheno. rim*	*matrix*	*pheno. centre*	*pheno. rim*	*matrix*
SiO_2	54,17	50,07	53,78	54,15	51,17	50,70	54,70	52,85	51,87	52,35	53,64	54,28	66,82	53,11	55,37	54,28
Al_2O_3	28,11	30,46	28,00	27,96	30,84	30,87	28,26	30,35	30,45	28,99	28,31	27,50	18,90	29,28	27,82	28,23
FeO	0,37	0,60	0,75	0,69	0,59	0,60	0,75	0,60	0,74	0,67	0,56	0,65	0,74	0,35	0,72	0,82
MnO	0,05	0,00	0,00	0,00	0,00	0,00	0,02	0,04	0,05	0,04	0,09	0,02	0,00	0,02	0,01	0,01
MgO	0,12	0,06	0,08	0,13	0,11	0,11	0,14	0,12	0,10	0,01	0,02	0,01	0,04	0,05	0,16	0,04
CaO	11,01	13,81	11,57	11,21	13,87	13,86	10,85	13,09	13,17	12,02	11,04	10,74	3,62	12,23	10,36	10,74
Na_2O	5,01	3,58	5,22	5,36	3,98	4,08	5,51	4,49	4,38	4,97	5,27	5,74	6,62	4,93	5,71	5,73
K_2O	0,20	0,17	0,36	0,32	0,13	0,14	0,32	0,19	0,16	0,30	0,32	0,34	2,46	0,24	0,29	0,28
TiO_2	0,00	0,09	0,13	0,19	0,07	0,02	0,13	0,05	0,12	0,08	0,05	0,05	0,30	0,01	0,12	0,08
NiO	0,04	0,08	0,00	0,00	0,00	0,00	0,00	0,00	0,00	0,01	0,03	0,06	0,00	0,00	0,00	0,02
Cr_2O_3	0,00	0,00	0,00	0,00	0,00	0,00	0,00	0,00	0,07	0,02	0,00	0,00	0,00	0,01	0,00	0,00
P_2O_5	0,00	0,01	0,02	0,00	0,00	0,00	0,00	0,01	0,00	0,02	0,06	0,00	0,03	0,04	0,04	0,08
F	0,01	0,02	0,00	0,04	0,00	0,00	0,01	0,01	0,04	0,00	0,02	0,00	0,00	0,00	0,02	0,06
Cl	0,01	0,00	0,00	0,00	0,00	0,00	0,00	0,00	0,00	0,00	0,01	0,00	0,00	0,00	0,00	0,02
Total	99,08	98,94	99,91	100,04	100,75	100,39	100,69	101,79	101,15	99,48	99,40	99,36	99,52	100,27	100,60	100,39
Si	2,47	2,31	2,45	2,46	2,32	2,31	2,46	2,37	2,34	2,40	2,45	2,48	2,97	2,41	2,49	2,46
Al	1,51	1,66	1,50	1,50	1,65	1,66	1,50	1,60	1,62	1,57	1,52	1,48	0,99	1,56	1,48	1,51
Fe^{3+}	0,01	0,02	0,03	0,03	0,02	0,02	0,03	0,02	0,03	0,03	0,02	0,02	0,03	0,01	0,03	0,03
Mn	0,00	0,00	0,00	0,00	0,00	0,00	0,00	0,00	0,00	0,00	0,00	0,00	0,00	0,00	0,00	0,00
Mg	0,01	0,00	0,01	0,01	0,01	0,01	0,01	0,01	0,01	0,00	0,00	0,00	0,00	0,00	0,01	0,00
Ca	0,54	0,68	0,56	0,55	0,67	0,68	0,52	0,63	0,64	0,59	0,54	0,53	0,17	0,59	0,50	0,52
Na	0,44	0,32	0,46	0,47	0,35	0,36	0,48	0,39	0,38	0,44	0,47	0,51	0,57	0,43	0,50	0,50
K	0,01	0,01	0,02	0,02	0,01	0,01	0,02	0,01	0,01	0,02	0,02	0,02	0,14	0,01	0,02	0,02
Ti	0,00	0,00	0,00	0,01	0,00	0,00	0,00	0,00	0,00	0,00	0,00	0,00	0,01	0,00	0,00	0,00
Ni	0,00	0,00	0,00	0,00	0,00	0,00	0,00	0,00	0,00	0,00	0,00	0,00	0,00	0,00	0,00	0,00
Cr	0,00	0,00	0,00	0,00	0,00	0,00	0,00	0,00	0,00	0,00	0,00	0,00	0,00	0,00	0,00	0,00
P	0,00	0,00	0,00	0,00	0,00	0,00	0,00	0,00	0,00	0,00	0,00	0,00	0,00	0,00	0,00	0,00
Fe	0,00	0,00	0,00	0,01	0,00	0,00	0,00	0,00	0,01	0,00	0,00	0,00	0,00	0,00	0,00	0,01
Cl	0,00	0,00	0,00	0,00	0,00	0,00	0,00	0,00	0,00	0,00	0,00	0,00	0,00	0,00	0,00	0,00
An	54	67	54	53	65	65	51	61	62	56	53	50	20	57	49	50
[a] T (^oC)	1197	1194	1200	1201	1184	1184	1190	1185	1185	1171	1172	1172	1335	1169	1172	1171
[b] P (Kbar)	9,3	6,4	9,5	9,9	6,7	6,8	10,1	7,6	7,4	7,7	8,6	9,3	30,0	7,4	9,5	9,2
[c] H2O (wt%)	0,97	0,80	0,92	0,98	0,99	0,98	1,21	1,00	1,00	1,12	1,22	1,33	2,93	1,12	1,37	1,35
$K_{D\ (Ab\text{-}An)}$	0,35	0,20	0,35	0,37	0,21	0,21	0,36	0,25	0,24	0,21	0,24	0,27	0,91	0,20	0,27	0,27

Table 3: clinopyroxene major element composition (as wt%), structural formulas*, and calculated temperatures[a] and pressures[b].

Suite	T1	T1	T1	T1	T1	T1	T1	T1	T2	T2	T2	T2	T2	T2	T2	T2	T2	T2	T2
Analysis	140527 85_79	140527 85_87	150416 86_56	150416 98_97	150420 101_15	150420 101_18	150420 106_108	150420 106_110	150416 11_30	150416 11_38	150416 11_39	150416 11_40	150416 11_42	150416 11_43	150416 80_13	150416 81_22	150416 83_53	150416 87_65	150416 87_70
Type	*included Pl*	*micropheno.*	*included in Pl*	*matrix*	*ofitic*	*ofitic*	*matrix*	*matrix*	*matrix*	*matrix*	*matrix*	*matrix*	*matrix*	*matrix*	*matrix*	*matrix*	*matrix.*	*included in Pl*	*matrix*
SiO_2	48,19	49,08	46,91	50,11	48,29	49,62	34,95	49,30	48,82	49,61	50,78	50,53	49,74	50,68	50,48	50,33	49,68	50,83	50,23
Al_2O_3	3,72	3,43	4,84	1,22	3,63	2,70	11,61	2,93	3,34	3,24	2,31	1,90	2,58	2,00	2,61	3,81	2,31	1,73	2,11
FeO total	8,78	8,86	8,69	13,14	10,30	10,86	6,71	10,90	9,25	7,87	7,58	9,37	8,92	7,72	10,44	8,84	11,01	9,18	9,67
MnO	0,35	0,27	0,31	0,57	0,19	0,31	0,11	0,36	0,22	0,23	0,17	0,30	0,27	0,31	0,26	0,26	0,38	0,35	0,41
MgO	12,57	12,98	12,16	12,23	12,93	13,15	6,02	12,20	14,22	14,91	15,74	15,61	15,60	15,59	14,14	13,48	12,76	15,17	14,87
CaO	22,73	22,16	21,59	20,14	20,69	20,97	12,61	21,83	21,05	21,24	21,33	19,66	20,12	21,34	19,83	18,76	18,26	20,52	20,59
Na_2O	0,60	0,58	0,71	0,52	0,53	0,53	4,33	0,57	0,49	0,39	0,39	0,38	0,41	0,37	0,44	0,63	0,54	0,46	0,47
K_2O	0,00	0,02	0,06	0,04	0,00	0,00	0,68	0,00	0,00	0,00	0,00	0,01	0,00	0,00	0,00	0,22	0,44	0,00	0,02
TiO_2	2,70	2,45	3,12	1,08	2,04	1,51	1,27	2,16	1,65	1,48	1,08	1,19	1,28	1,07	1,98	2,41	1,17	1,16	1,34
NiO	0,04	0,00	0,00	0,00	0,00	0,02	0,02	0,01	0,01	0,07	0,02	0,02	0,00	0,00	0,00	0,01	0,03	0,00	0,00
Cr_2O_3	0,00	0,01	0,00	0,00	0,01	0,01	0,02	0,00	0,06	0,15	0,11	0,05	0,07	0,12	0,02	0,02	0,02	0,03	0,02
P_2O_5	0,03	0,07	0,21	0,04	0,09	0,04	0,13	0,08	0,05	0,04	0,04	0,04	0,04	0,01	0,08	0,16	0,78	0,03	0,10
F	0,00	0,00	0,04	0,00	0,00	0,02	0,03	0,00	0,00	0,00	0,00	0,03	0,02	0,00	0,00	0,02	0,10	0,00	0,02
Cl	0,00	0,01	0,01	0,00	0,00	0,00	0,00	0,00	0,00	0,02	0,01	0,00	0,00	0,01	0,00	0,00	0,03	0,02	0,00
Total	99,71	99,91	98,64	99,08	98,69	99,73	78,50	100,32	99,17	99,26	99,56	99,07	99,03	99,21	100,27	98,96	97,49	99,47	99,84
Si	1,81	1,84	1,78	1,91	1,83	1,86	–	1,85	1,83	1,85	1,88	1,89	1,86	1,89	1,88	1,90	1,91	1,90	1,87
Al total	0,16	0,15	0,22	0,06	0,16	0,12	–	0,13	0,15	0,14	0,10	0,08	0,11	0,09	0,11	0,17	0,10	0,08	0,09
Al^{T}	0,16	0,15	0,22	0,06	0,16	0,12	–	0,13	0,15	0,14	0,10	0,08	0,11	0,09	0,11	0,10	0,09	0,08	0,09
Al^{M1}	0,00	0,00	0,00	0,00	0,01	0,00	–	0,00	0,00	0,00	0,00	0,00	0,00	0,00	0,00	0,07	0,02	0,00	0,00
Fe total	0,28	0,28	0,28	0,42	0,33	0,34	–	0,34	0,29	0,25	0,23	0,29	0,28	0,24	0,33	0,28	0,35	0,29	0,30
Fe^{+3}	0,11	0,07	0,09	0,09	0,09	0,11	–	0,08	0,13	0,10	0,10	0,10	0,13	0,10	0,03	0,00	0,02	0,10	0,12
Fe^{+3T}	0,03	0,01	0,01	0,03	0,00	0,02	–	0,02	0,02	0,01	0,02	0,03	0,03	0,03	0,00	0,00	0,00	0,03	0,04
Fe^{+3M1}	0,08	0,06	0,09	0,06	0,09	0,09	–	0,06	0,11	0,09	0,08	0,08	0,10	0,08	0,03	0,00	0,02	0,07	0,09
Fe^{+2M1}	0,14	0,15	0,14	0,21	0,12	0,13	–	0,19	0,05	0,04	0,02	0,02	0,00	0,02	0,13	0,11	0,20	0,14	0,05
Fe^{+2M2}	0,03	0,06	0,05	0,12	0,12	0,11	–	0,07	0,11	0,11	0,12	0,17	0,15	0,11	0,17	0,17	0,14	0,05	0,13
Mn	0,01	0,01	0,01	0,02	0,01	0,01	–	0,01	0,01	0,01	0,01	0,01	0,01	0,01	0,01	0,01	0,01	0,01	0,01
Mg total	0,70	0,72	0,69	0,70	0,73	0,74	–	0,68	0,79	0,83	0,87	0,87	0,87	0,86	0,79	0,76	0,73	0,84	0,82
Mg^{M1}	0,70	0,72	0,69	0,70	0,73	0,74	–	0,68	0,80	0,83	0,87	0,87	0,86	0,87	0,79	0,76	0,73	0,69	0,83
Mg^{M2}	0,00	0,00	0,00	0,00	0,00	0,00	–	0,00	0,00	0,00	0,00	0,00	0,00	0,00	0,00	0,00	0,00	0,00	0,00
Ca	0,91	0,89	0,88	0,82	0,84	0,84	–	0,88	0,85	0,85	0,85	0,79	0,80	0,85	0,79	0,76	0,75	0,82	0,82
Na	0,04	0,04	0,05	0,04	0,04	0,04	–	0,04	0,04	0,03	0,03	0,03	0,03	0,03	0,03	0,05	0,04	0,03	0,03
K	0,00	0,00	0,00	0,00	0,00	0,00	–	0,00	0,00	0,00	0,00	0,00	0,00	0,00	0,00	0,01	0,02	0,00	0,00
Ti	0,08	0,07	0,09	0,03	0,06	0,04	–	0,06	0,05	0,04	0,03	0,03	0,04	0,03	0,06	0,07	0,03	0,03	0,04
Ni	0,00	0,00	0,00	0,00	0,00	0,00	–	0,00	0,00	0,00	0,00	0,00	0,00	0,00	0,00	0,00	0,00	0,00	0,00
Cr	0,00	0,00	0,00	0,00	0,00	0,00	–	0,00	0,00	0,00	0,00	0,00	0,00	0,00	0,00	0,00	0,00	0,00	0,00
En	36,94	38,15	37,16	35,54	38,39	38,12	–	35,66	41,03	42,93	44,43	44,38	44,29	43,99	41,12	42,04	39,54	43	42
Q	1,79	1,81	1,75	1,85	1,81	1,81	–	1,82	1,80	1,82	1,85	1,85	1,82	1,85	1,87	1,79	0,89	1,85	1,82
J	0,09	0,08	0,10	0,08	0,08	0,08	–	0,08	0,07	0,06	0,06	0,06	0,06	0,05	0,06	0,09	0,00	0,07	0,07
[a] T (°C)	–	974	1075	–	1044	967	1303	–	939	1101	–	–	–	–	1029	1190	1159	–	–
[b] P (kbar)	–	0,3	7,9	–	4,4	0,7	34,4	–	2,7	4,7	–	–	–	–	2,5	10,8	7,7	–	–
$K_{D\ (Fe\text{-}Mg)}$	–	0,24	0,26	–	0,25	0,23	0,31	–	0,22	0,26	–	–	–	–	0,25	0,29	0,28	–	–

* Structural formulas calculated to 6 oxygens per formula unit and normalized to 4 cations where Fe^{3+} content is estimated through the charge balance method described by Droop (1987). Classification parameters and mineral names according to Morimoto (1988).

[a] Temperatures calculated following the equation 33 of Putirka 2008. K_D: Fe - Mg Cpx/liquid distribution coefficient (0,28 ± 0,08)

[b] Pressures calculated following the equation 32c of Putirka 2008.

The obvious abundance of analysis without calculated temperature and pressure values here is due to a frecuent error yielded by the clinopyroxene thermobarometers calibrated by Putirka (2008). This error is caused by the way the thermobarometers are calculated. The temperature and pressure values depend ultimatedly on the logarithm of clinopyroxene components ratios which in turn depend on the Jadeite component in the clinopyroxene. When jadeite component is cero the thermobarometer yields an error for the logarithm of cero is not defined (i.e. it does not exist). The jadeite coponent, on the other hand, is often cero because of the following procedure stablished by Putirka: If the Na content in an analysis (cations on 6 oxygen base) is inferior than the Al content in octahedric position, then the input for

Table 3: Continued.

Suite	T2	T2	T2	T2	T2	T2	T2	T2	T2	T2	T2	T2	T2	T2	T2	T2	T2	T2	T2
Analysis	150416 88_77	150416 88_78	131016 102_48	131016 102_52	150420 103_25	150420 104_32	150420 104_36	150420 104_48	150420 131_50	150420 131_53	150420 131_54	150420 131_55	150420 131_58	150420 131_59	150420 131_61	150420 131_62	150420 131_63	150420 131_64	150420 131_66
Type	*centre*	*rim*	*pheno. centre*	*matrix*	*microphenо.*	*microphenо.*	*matrix*	*pheno. centre*	*pheno. centre*	*pheno. centre*	*pheno. centre*	*pheno. centre*	*microphenо.*	*matrix*	*centre*	*middle*	*rim*	*centre*	*matrix*
SiO_2	48,87	49,65	50,62	51,09	53,18	49,13	51,59	48,63	52,01	52,93	50,02	52,59	50,37	48,52	49,66	47,86	50,40	49,54	51,47
Al_2O_3	4,17	3,78	3,03	0,34	0,39	5,30	2,89	3,38	3,21	2,20	5,45	2,16	4,47	3,20	4,57	5,88	3,63	5,64	2,43
FeO total	9,81	10,57	8,04	25,35	19,78	7,66	9,52	11,16	5,89	6,84	5,83	6,21	6,90	9,66	6,09	7,93	5,78	6,94	8,53
MnO	0,31	0,34	0,17	0,84	0,45	0,16	0,23	0,21	0,11	0,14	0,08	0,14	0,10	0,23	0,12	0,07	0,08	0,10	0,20
MgO	12,90	12,69	14,14	13,34	21,59	14,91	14,16	14,45	16,24	17,26	15,98	18,50	16,15	17,62	15,24	14,60	15,95	15,73	17,38
CaO	20,83	20,49	20,95	7,50	3,63	20,46	19,16	19,28	20,99	20,13	20,42	19,51	21,35	18,44	22,16	21,59	22,16	20,85	19,23
Na_2O	0,73	0,73	0,40	0,22	0,08	0,49	0,56	0,47	0,41	0,38	0,51	0,30	0,45	0,47	0,39	0,42	0,36	0,48	0,35
K_2O	0,00	0,00	0,00	0,02	0,01	0,00	0,17	0,05	0,00	0,00	0,00	0,01	0,00	0,00	0,00	0,00	0,00	0,01	0,04
TiO_2	1,26	1,18	0,90	0,38	0,29	1,36	1,03	1,27	0,35	0,32	0,78	0,34	0,65	0,86	0,72	1,14	0,55	0,93	0,63
NiO	0,10	0,02	0,02	0,00	0,02	0,00	0,03	0,02	0,08	0,03	0,00	0,00	0,00	0,07	0,03	0,01	0,00	0,00	0,00
Cr_2O_3	0,02	0,00	0,03	0,00	0,00	0,12	0,03	0,09	0,10	0,12	0,46	0,14	0,08	0,02	0,29	0,05	0,18	0,06	0,04
P_2O_5	0,03	0,00	0,01	0,00	0,00	0,02	0,11	0,08	0,06	0,07	0,04	0,03	0,03	0,12	0,03	0,02	0,01	0,02	0,08
F	0,00	0,05	0,03	0,01	0,04	0,05	0,01	0,08	0,01	0,00	0,00	0,00	0,02	0,02	0,05	0,00	0,00	0,00	0,01
Cl	0,00	0,00	0,00	0,02	0,00	0,00	0,02	0,00	0,01	0,01	0,00	0,00	0,00	0,00	0,02	0,00	0,01	0,01	0,01
Total	99,02	99,49	98,34	99,09	99,46	99,66	99,51	99,16	99,48	100,44	99,57	99,92	100,59	99,22	99,36	99,57	99,10	100,28	100,39
Si	1,84	1,86	1,91	2,00	1,99	1,81	1,93	1,82	1,91	1,93	1,83	1,91	1,83	1,79	1,83	1,77	1,86	1,81	1,88
Al total	0,19	0,17	0,13	0,02	0,02	0,23	0,13	0,15	0,14	0,09	0,24	0,09	0,19	0,14	0,20	0,26	0,16	0,24	0,10
Al^{T}	0,16	0,14	0,01	0,00	0,02	0,19	0,07	0,15	0,09	0,07	0,17	0,09	0,17	0,14	0,17	0,23	0,14	0,19	0,11
Al^{M1}	0,02	0,03	0,00	0,02	0,00	0,05	0,06	0,00	0,05	0,02	0,07	0,01	0,02	0,00	0,03	0,03	0,02	0,05	0,00
Fe total	0,31	0,33	0,25	0,83	0,62	0,24	0,30	0,35	0,18	0,21	0,18	0,19	0,21	0,30	0,19	0,25	0,18	0,21	0,26
Fe^{+3}	0,12	0,11	0,04	0,00	0,01	0,11	0,00	0,18	0,04	0,05	0,07	0,08	0,14	0,26	0,13	0,17	0,11	0,12	0,12
Fe^{+3T}	0,00	0,00	0,03	0,00	0,00	0,00	0,00	0,03	0,00	0,00	0,00	0,00	0,00	0,07	0,00	0,00	0,00	0,00	0,01
Fe^{+3M1}	0,12	0,11	0,04	0,00	0,01	0,11	0,00	0,15	0,04	0,05	0,07	0,08	0,14	0,19	0,13	0,17	0,11	0,12	0,11
Fe^{+2M1}	0,10	0,12	0,03	0,19	–	0,13	0,13	0,00	0,01	0,00	0,00	0,00	0,00	0,00	0,00	0,00	0,00	0,00	0,00
Fe^{+2M2}	0,09	0,11	0,13	0,64	0,61	0,13	0,17	0,17	0,13	0,16	0,11	0,11	0,07	0,04	0,06	0,08	0,07	0,09	0,14
Mn	0,01	0,01	0,01	0,03	0,01	0,00	0,01	0,01	0,00	0,00	0,00	0,00	0,00	0,01	0,00	0,00	0,00	0,00	0,01
Mg total	0,72	0,71	0,79	0,78	1,20	0,82	0,79	0,81	0,89	0,94	0,87	1,00	0,88	0,97	0,84	0,81	0,88	0,86	0,95
Mg^{M1}	0,72	0,71	0,93	0,78	0,98	0,81	0,79	0,81	0,89	0,92	0,82	0,90	0,82	0,79	0,81	0,77	0,85	0,80	0,88
Mg^{M2}	0,00	0,00	0,00	0,00	0,22	0,01	0,00	0,00	0,00	0,02	0,01	0,10	0,06	0,18	0,03	0,03	0,03	0,06	0,07
Ca	0,84	0,82	0,85	0,31	0,15	0,81	0,77	0,77	0,83	0,79	0,80	0,76	0,83	0,73	0,88	0,86	0,88	0,82	0,75
Na	0,05	0,05	0,03	0,02	0,01	0,04	0,04	0,03	0,03	0,03	0,04	0,02	0,03	0,03	0,03	0,03	0,03	0,03	0,02
K	0,00	0,00	0,00	0,00	0,00	0,00	0,01	0,00	0,00	0,00	0,00	0,00	0,00	0,00	0,00	0,00	0,00	0,00	0,00
Ti	0,04	0,03	0,03	0,01	0,01	0,04	0,03	0,04	0,01	0,01	0,02	0,01	0,02	0,02	0,02	0,03	0,02	0,03	0,02
Ni	0,00	0,00	0,00	0,00	0,00	0,00	0,00	0,00	0,00	0,00	0,00	0,00	0,00	0,00	0,00	0,00	0,00	0,00	0,00
Cr	0,00	0,00	0,00	0,00	0,00	0,00	0,00	0,00	0,00	0,00	0,01	0,00	0,00	0,00	0,01	0,00	0,01	0,00	0,00
En	38	38	42	40	61	44	42	42	47	48	47	51	46	48	44	42	45	45	48
Q	1,76	1,76	1,80	1,92	1,95	1,89	1,85	1,75	1,86	1,88	1,78	1,88	1,78	1,74	1,77	1,74	1,82	1,76	1,84
J	0,11	0,11	0,06	0,03	0,01	0,07	0,08	0,07	0,06	0,05	0,07	0,04	0,06	0,07	0,06	0,06	0,05	0,07	0,05
[a] T (°C)	1129	1135	1060	1099	1115	1139	1149	1033	1169	1176	1196	1162	1182	–	1158	1175	1152	1190	1100
[b] P (kbar)	10,2	9,8	5,2	1,5	0,8	11,0	8,2	4,1	8,2	7,6	12,1	7,0	11,4	–	10,7	13,2	9,4	12,5	4,5
$K_{D\ (Fe\text{-}Mg)}$	0,28	0,28	0,26	0,26	0,26	0,28	0,28	0,25	0,28	0,28	0,29	0,28	0,28	–	0,28	0,28	0,28	0,28	0,26

Table 3: Continued.

Suite	T2	T2	T2	CA	CA	CA	CA	CA	CA	CA	CA	CA	CA	CA	CA	CA	CA	CA
Analysis	150420 131_70	150420 131_71	150420 131_72	130218 03_21	130218 03_22	130218 03_25	130306 20_05	130218 28_03	130218 55_05	130218 55_06	130218 55_07	130218 55_08	130218 55_09	130218 55_10	130218 55_11	130218 55_12	130218 55_13	140527 57_32	130726 57_03
Type	*centre*			*included in Pl*	*matrix*	*matrix*	*Corona Amp*	*included in Pl*	*matrix*	*matrix*	*centre*	*pheno. rim*	*pheno. centre*	*pheno. centre*	*pheno. centre*	*pheno. rim*	*micropheno.*	*Ol corona*	*Ol corona*
SiO_2	49,86	50,61	53,43	51,49	53,55	53,345	52,59	53,11	51,24	51,41	51,14	46,21	50,70	50,04	51,86	50,67	51,59	54,11	51,30
Al_2O_3	5,02	4,68	2,40	1,73	0,49	0,629	2,71	0,41	2,08	1,16	2,62	5,86	2,87	3,77	2,42	2,64	3,09	0,85	0,75
FeO total	5,75	6,13	5,81	14,87	15,11	14,603	10,65	20,94	11,83	18,68	4,94	8,19	8,35	9,05	5,78	8,63	6,64	13,85	10,93
MnO	0,14	0,01	0,11	0,47	0,42	0,408	0,35	0,62	0,32	0,28	0,09	0,08	0,13	0,17	0,04	0,19	0,12	0,52	0,30
MgO	15,53	14,85	17,50	21,04	25,20	24,008	20,97	20,06	14,99	23,17	16,16	13,56	15,11	14,12	16,70	14,91	16,64	24,88	18,09
CaO	21,36	22,15	20,03	7,18	4,00	4,458	12,91	3,76	18,68	2,82	22,27	17,93	21,68	21,10	22,37	21,98	20,78	4,23	15,12
Na_2O	0,48	0,52	0,38	0,13	0,11	0,09	0,25	0,08	0,33	0,06	0,25	0,28	0,38	0,34	0,28	0,44	0,27	0,09	0,30
K_2O	0,00	0,00	0,01	0,01	0,01	0,012	0,02	0,02	0,03	0,02	0,00	0,03	0,01	0,00	0,00	0,00	0,01	0,01	0,01
TiO_2	0,85	0,95	0,45	0,65	0,34	0,349	0,74	0,32	0,81	0,47	0,50	0,77	0,54	0,66	0,41	0,55	0,56	0,39	0,62
NiO	0,06	0,00	0,02	0,04	0,00	0,018	0,02	0,01	0,00	0,06	0,07	0,00	0,05	0,02	0,05	0,00	0,03	0,05	0,01
Cr_2O_3	0,21	0,19	0,14	0,06	0,05	0,062	0,03	0,00	0,00	0,03	0,43	0,12	0,02	0,06	0,26	0,10	0,38	0,04	0,08
P_2O_5	0,04	0,03	0,05	0,05	0,03	0,035	0,03	0,00	0,02	0,27	0,02	0,01	0,02	0,00	0,04	0,01	0,00	0,03	0,06
F	0,05	0,00	0,04	0,00	0,02	0,001	0,06	0,02	0,00	0,00	0,04	0,00	0,00	0,00	0,02	0,00	0,05	0,00	0,04
Cl	0,00	0,00	0,00	0,01	0,00	0	0,00	0,00	0,00	0,01	0,01	0,00	0,00	0,00	0,01	0,00	0,00	0,00	0,00
Total	99,35	100,11	100,36	97,72	99,32	98,02	101,31	99,35	100,31	98,45	98,53	93,02	99,84	99,33	100,24	100,12	100,14	99,04	97,60
Si	1,83	1,86	1,94	1,94	1,95	1,98	1,89	2,00	1,91	1,92	1,90	1,84	1,88	1,87	1,89	1,87	1,89	1,98	1,93
Al total	0,22	0,20	0,10	0,08	0,02	0,03	0,11	0,02	0,09	0,05	0,11	0,27	0,13	0,17	0,10	0,12	0,13	0,04	0,03
Al^{T}	0,17	0,14	0,06	0,06	0,02	0,02	0,11	0,00	0,09	0,05	0,11	0,17	0,13	0,13	0,10	0,12	0,11	0,02	0,03
Al^{M1}	0,05	0,06	0,04	0,02	0,00	0,03	0,00	0,02	0,00	0,00	0,01	0,11	0,00	0,04	0,00	0,00	0,02	0,02	0,00
Fe total	0,18	0,19	0,18	0,47	0,46	0,45	0,32	0,66	0,37	0,58	0,15	0,27	0,26	0,28	0,18	0,27	0,20	0,42	0,34
Fe^{+3}	0,10	0,06	0,02	0,02	0,06	0,000	0,10	0,00	0,07	0,06	0,08	0,03	0,12	0,08	0,11	0,14	0,08	0,00	0,09
Fe^{+3T}	0,00	0,00	0,00	0,00	0,02	0,00	0,00	0,00	0,00	0,03	0,00	0,00	0,00	0,00	0,00	0,01	0,00	0,00	0,03
Fe^{+3M1}	0,10	0,06	0,02	0,02	0,04	0,00	0,10	0,00	0,10	0,03	0,08	0,03	0,12	0,08	0,10	0,13	0,08	0,00	0,06
Fe^{+2M1}	0,00	0,04	0,00	0,00	–	0,00	0,00	–	0,05	–	0,00	0,03	0,03	0,08	0,00	0,04	0,00	–	0,00
Fe^{+2M2}	0,07	0,09	0,16	0,45	0,40	0,45	0,22	0,66	0,22	0,53	0,08	0,21	0,11	0,13	0,07	0,09	0,12	0,42	0,26
Mn	0,00	0,00	0,00	0,01	0,01	0,01	0,01	0,02	0,01	0,01	0,00	0,00	0,00	0,01	0,00	0,01	0,00	0,02	0,01
Mg total	0,85	0,81	0,95	1,18	1,37	1,33	1,12	1,13	0,83	1,29	0,89	0,80	0,83	0,79	0,91	0,82	0,91	1,36	1,02
Mg^{M1}	0,82	0,81	0,92	0,95	0,96	0,96	0,88	0,97	0,83	0,95	0,89	0,80	0,83	0,79	0,88	0,82	0,87	0,97	0,93
Mg^{M2}	0,04	0,00	0,03	0,23	0,42	0,37	0,24	0,16	0,00	0,34	0,01	0,00	0,00	0,00	0,03	0,00	0,04	0,39	0,09
Ca	0,84	0,87	0,78	0,29	0,16	0,18	0,50	0,15	0,74	0,11	0,89	0,76	0,86	0,84	0,87	0,87	0,81	0,17	0,61
Na	0,03	0,04	0,03	0,01	0,01	0,01	0,02	0,01	0,02	0,00	0,02	0,02	0,03	0,02	0,02	0,03	0,02	0,01	0,02
K	0,00	0,00	0,00	0,00	0,00	0,00	0,00	0,00	0,00	0,00	0,00	0,00	0,00	0,00	0,00	0,00	0,00	0,00	0,00
Ti	0,02	0,03	0,01	0,02	0,01	0,01	0,02	0,01	0,02	0,01	0,01	0,02	0,01	0,02	0,01	0,02	0,02	0,01	0,02
Ni	0,00	0,00	0,00	0,00	0,00	0,00	0,00	0,00	0,00	0,00	0,00	0,00	0,00	0,00	0,00	0,00	0,00	0,00	0,00
Cr	0,01	0,01	0,00	0,00	0,00	0,00	0,00	0,00	0,00	0,00	0,01	0,00	0,00	0,00	0,01	0,00	0,01	0,00	0,00
En	45	43	50	60	69	67	58	58	43	65	46	44	43	41	46	42	47	69	51
Q	1,77	1,81	1,88	1,20	1,93	1,96	1,84	1,94	1,85	1,93	1,86	0,86	1,83	1,83	1,85	1,82	1,84	1,95	1,14
J	0,07	0,07	0,05	1,90	0,02	0,01	0,03	0,01	0,05	0,01	0,04	1,61	0,05	0,05	0,04	0,06	0,04	0,01	1,85
[a] T (°C)	1181	1174	1174	1116	–	1151	1122	1078	1054	–	1055	1097	1074	1086	1049	1033	1078	1160	–
[b] P (kbar)	11,6	11,3	7,2	4,2	–	3,3	7,3	1,7	3,6	–	5,4	8,2	6,7	7,6	4,9	4,0	6,2	4,4	–
$K_{D\ (Fe\text{-}Mg)}$	0,28	0,29	0,28	0,27	–	0,27	0,27	0,26	0,26	–	0,27	0,27	0,27	0,27	0,26	0,26	0,27	0,27	–

Table 3: Continued.

Suite	CA	CA	CA	CA	CA	CA	CA	CA	CA	CA	CA	CA	CA	CA	CA	CA	CA	CA
Analysis	130306 60_20	131016 60_02	131016 60_03	130306 61_27	130306 61_28	130306 61_33	131002 61_29	140527 61_35	140527 61_41	130306 63_54	140527 63_63	130306 64_39	130306 64_46	131002 64_33	131002 64_35	131002 64_37	131002 64_38	131002 64_39	131002 64_40
Type	*centre*		*matrix/ micropheno.*	*pheno. centre*	*pheno. rim*	*pheno. centre*	*included in Amp*	*reemplacement*		*pheno. centre*	*micropheno.*	*micropheno.*	*pheno. centre*		*micropheno.*	*middle*	*rim*	*micropheno. centre*	*micropheno. rim*
SiO_2	51,02	51,36	49,18	49,99	51,12	52,14	51,05	48,93	51,84	49,80	51,28	53,47	50,48	51,59	52,83	51,55	50,31	51,29	51,94
Al_2O_3	2,47	2,85	3,89	2,76	3,32	3,02	3,94	3,78	2,25	3,50	3,12	0,12	3,01	1,44	0,23	2,35	2,71	3,28	2,30
FeO total	7,74	7,61	8,15	10,72	6,36	6,08	5,67	7,06	6,02	8,23	6,13	6,78	6,70	8,34	6,88	6,71	9,05	7,00	6,59
MnO	0,24	0,34	0,28	0,21	0,20	0,09	0,05	0,27	0,25	0,20	0,15	0,22	0,08	0,23	0,10	0,17	0,14	0,08	0,12
MgO	17,52	16,44	15,13	12,36	16,42	16,73	14,70	15,53	17,19	15,14	16,46	16,55	16,52	15,91	15,71	16,34	15,47	15,91	16,60
CaO	20,46	20,84	21,77	22,08	22,62	22,64	22,15	21,81	20,85	21,13	22,24	22,94	21,78	21,24	23,23	20,99	20,59	22,17	22,03
Na_2O	0,34	0,36	0,45	0,55	0,36	0,48	0,00	0,33	0,56	0,35	0,29	0,20	0,31	0,30	0,20	0,30	0,34	0,33	0,26
K_2O	0,00	0,06	0,00	0,00	0,01	0,01	0,01	0,00	0,02	0,03	0,02	0,00	0,00	0,03	0,00	0,01	0,00	0,00	0,01
TiO_2	0,61	0,55	1,00	0,27	0,41	0,30	0,41	1,60	1,07	0,74	0,47	0,13	0,50	0,47	0,11	0,44	0,67	0,53	0,34
NiO	0,00	0,00	0,05	0,01	0,05	0,02	0,03	0,02	0,06	0,10	0,00	0,06	0,02	0,06	0,00	0,02	0,03	0,04	0,03
Cr_2O_3	0,01	0,00	0,07	0,06	0,06	0,11	0,15	0,00	0,00	0,07	0,26	0,01	0,29	0,00	0,01	0,32	0,00	0,16	0,09
P_2O_5	0,04	0,00	0,29	0,03	0,03	0,02	0,00	0,02	0,04	0,01	0,02	0,07	0,04	0,03	0,01	0,05	0,00	0,02	0,02
F	0,01	0,00	0,05	0,00	0,05	0,00	0,00	0,00	0,03	0,00	0,00	0,04	0,07	0,00	0,01	0,01	0,00	0,00	0,02
Cl	0,00	0,02	0,01	0,00	0,00	0,00	0,01	0,00	0,00	0,03	0,00	0,02	0,00	0,00	0,00	0,00	0,00	0,00	0,00
Total	100,47	100,43	100,31	99,03	101,00	101,63	98,17	99,36	100,16	99,33	100,45	100,61	99,79	99,63	99,33	99,23	99,31	100,82	100,35
Si	1,86	1,88	1,81	1,89	1,85	1,87	1,92	1,81	1,89	1,85	1,87	1,95	1,85	1,91	1,96	1,91	1,87	1,87	1,90
Al total	0,11	0,12	0,17	0,12	0,14	0,13	0,17	0,17	0,10	0,15	0,13	0,01	0,13	0,06	0,01	0,10	0,12	0,14	0,10
Al^{T}	0,11	0,12	0,17	0,11	0,14	0,13	0,09	0,17	0,10	0,15	0,13	0,01	0,13	0,06	0,01	0,09	0,12	0,13	0,10
Al^{M1}	0,00	0,00	0,00	0,01	0,00	0,00	0,09	0,02	0,00	0,00	0,00	0,00	0,00	0,00	0,00	0,01	0,00	0,01	0,00
Fe total	0,24	0,23	0,25	0,34	0,19	0,18	0,18	0,22	0,18	0,26	0,19	0,21	0,21	0,26	0,21	0,21	0,28	0,21	0,20
Fe^{+3}	0,17	0,12	0,18	0,12	0,17	0,14	0,00	0,14	0,11	0,13	0,11	0,10	0,17	0,11	0,08	0,07	0,12	0,11	0,11
Fe^{+3T}	0,04	0,00	0,02	0,00	0,01	0,00	0,00	0,00	0,02	0,00	0,00	0,04	0,02	0,03	0,03	0,00	0,01	0,00	0,01
Fe^{+3M1}	0,13	0,12	0,15	0,12	0,16	0,06	0,00	0,14	0,10	0,13	0,11	0,06	0,15	0,08	0,05	0,07	0,12	0,11	0,11
Fe^{+2M1}	0,00	0,00	0,00	0,16	0,00	0,00	0,07	0,00	0,00	0,00	0,00	0,07	0,00	0,03	0,08	0,00	0,01	0,00	0,00
Fe^{+2M2}	0,07	0,11	0,07	0,06	0,03	0,04	0,10	0,08	0,07	0,12	0,07	0,04	0,04	0,12	0,06	0,14	0,15	0,11	0,09
Mn	0,01	0,01	0,01	0,01	0,01	0,00	0,00	0,01	0,01	0,01	0,00	0,01	0,00	0,01	0,00	0,01	0,00	0,00	0,00
Mg total	0,95	0,90	0,83	0,70	0,89	0,90	0,82	0,86	0,93	0,84	0,89	0,90	0,90	0,88	0,87	0,90	0,86	0,86	0,90
Mg^{M1}	0,85	0,86	0,82	0,70	0,83	0,85	0,82	0,80	0,88	0,84	0,86	0,90	0,83	0,88	0,87	0,89	0,85	0,86	0,88
Mg^{M2}	0,10	0,03	0,01	0,00	0,06	0,05	0,00	0,06	0,06	0,00	0,03	0,00	0,07	0,00	0,00	0,00	0,00	0,00	0,02
Ca	0,80	0,82	0,86	0,89	0,88	0,87	0,89	0,87	0,81	0,84	0,87	0,90	0,86	0,84	0,92	0,83	0,82	0,87	0,86
Na	0,02	0,03	0,03	0,04	0,03	0,03	0,00	0,02	0,04	0,02	0,02	0,01	0,02	0,02	0,01	0,02	0,02	0,02	0,02
K	0,00	0,00	0,00	0,00	0,00	0,00	0,00	0,00	0,00	0,00	0,00	0,00	0,00	0,00	0,00	0,00	0,00	0,00	0,00
Ti	0,02	0,02	0,03	0,01	0,01	0,01	0,01	0,04	0,03	0,02	0,01	0,00	0,01	0,01	0,00	0,01	0,02	0,01	0,01
Ni	0,00	0,00	0,00	0,00	0,00	0,00	0,00	0,00	0,00	0,00	0,00	0,00	0,00	0,00	0,00	0,00	0,00	0,00	0,00
Cr	0,00	0,00	0,00	0,00	0,00	0,00	0,00	0,00	0,00	0,00	0,01	0,00	0,01	0,00	0,00	0,01	0,00	0,00	0,00
En	48	46	43	36	45	46	43	44	48	43	46	45	46	44	43	46	44	44	46
Q	1,82	1,82	1,76	1,81	1,79	1,81	1,89	1,80	1,82	1,80	1,84	1,91	1,80	1,87	1,93	1,87	1,84	1,83	1,86
J	0,05	0,05	0,06	0,08	0,05	0,07	0,00	0,05	0,08	0,05	0,04	0,03	0,04	0,04	0,03	0,04	0,05	0,05	0,04
[a] T (°C)	–	1096	1064	1091	1076	1085	–	977	1014	1105	1085	–	1031	–	–	1079	1049	1077	1050
[b] P (kbar)	–	6,7	7,1	8,3	7,6	7,6	–	3,1	2,3	9,9	8,4	–	5,8	–	–	7,2	6,1	8,5	5,8
$K_{D\ (Fe\text{-}Mg)}$	–	0,27	0,26	0,27	0,27	0,27	–	0,24	0,25	0,28	0,27	–	0,26	–	–	0,27	0,26	0,27	0,26

Table 3: Continued.

Suite	CA	CA	CA	CA	CA	CA	CA	CA	CA	CA	CA	CA	CA	CA	CA	CA	CA	CA
Analysis	131002 64_43	131002 64_45	131002 64_46	131002 64_48	130726 65_14	140527 65_47	130306 66_50	131002 66_60	130726 70_19	131002 70_01	131002 70_02	131002 70_03	131002 70_04	131002 70_05	131002 70_07	140527 70_53	140527 70_54	140527 73_67	140527 73_70
Type		*pheno. centre*	*pheno. centre*	*patchy zonation*	*Ol corona*		*pheno. rim*	*micropheno.*	*micropheno.*	*pheno. centre*	*pheno. rim*	*pheno. Centre*	*pheno. middle*	*pheno. rim*	*micropheno.*	*Ol rim*	*Ol rim*	*Amp corona*	*pheno. centre*
SiO_2	53,66	50,10	50,21	51,29	52,60	51,26	50,64	55,62	50,81	50,93	50,20	50,41	50,26	50,79	53,07	51,40	53,39	51,06	52,72
Al_2O_3	0,15	4,20	3,41	2,75	0,31	2,07	2,81	26,27	0,96	3,40	3,66	4,24	3,42	2,98	0,63	3,38	2,38	2,94	2,15
FeO total	6,71	8,90	8,70	5,79	13,64	10,07	9,31	1,08	5,78	5,53	8,01	6,39	8,21	8,89	6,66	5,52	4,71	7,94	5,78
MnO	0,07	0,16	0,23	0,09	0,28	0,11	0,26	0,00	0,09	0,09	0,15	0,11	0,13	0,12	0,08	0,11	0,22	0,44	0,14
MgO	16,10	13,07	13,16	15,82	24,68	16,55	18,42	0,01	16,52	15,77	14,75	15,54	15,35	16,14	16,38	16,39	17,46	17,75	16,58
CaO	22,39	21,75	21,80	22,56	4,94	18,57	17,39	9,74	21,90	22,91	21,09	22,06	20,28	18,65	21,74	22,03	22,05	19,23	22,05
Na_2O	0,27	0,49	0,49	0,34	0,09	0,31	0,31	6,39	0,27	0,27	0,36	0,29	0,33	0,33	0,23	0,29	0,32	0,35	0,35
K_2O	0,04	0,00	0,02	0,02	0,03	0,01	0,00	0,31	0,00	0,02	0,00	0,00	0,02	0,03	0,00	0,00	0,00	0,00	0,00
TiO_2	0,10	0,56	0,35	0,37	0,23	0,91	0,72	0,06	0,31	0,48	0,74	0,77	0,67	0,79	0,38	0,55	0,27	0,79	0,32
NiO	0,02	0,01	0,03	0,01	0,04	0,00	0,00	0,00	0,01	0,01	0,04	0,00	0,03	0,00	0,03	0,06	0,06	0,03	0,06
Cr_2O_3	0,00	0,15	0,12	0,43	0,05	0,04	0,03	0,01	0,56	0,40	0,07	0,51	0,08	0,00	0,00	0,46	0,62	0,08	0,12
P_2O_5	0,00	0,04	0,02	0,00	0,00	0,14	0,00	0,04	0,02	0,02	0,08	0,04	0,02	0,01	0,05	0,04	0,02	0,00	0,05
F	0,00	0,00	0,01	0,01	0,00	0,00	0,00	0,00	0,01	0,00	0,02	0,00	0,03	0,00	0,00	0,00	0,05	0,05	0,02
Cl	0,02	0,00	0,00	0,01	0,00	0,00	0,02	0,00	0,00	0,00	0,01	0,00	0,00	0,00	0,01	0,00	0,02	0,00	0,01
Total	99,51	99,42	98,54	99,47	96,89	100,02	99,90	99,52	97,23	99,81	99,16	100,37	98,79	98,71	99,27	100,23	101,56	100,66	100,35
Si	1,98	1,87	1,89	1,89	1,96	1,89	1,85	2,01	1,91	1,87	1,87	1,85	1,88	1,90	1,97	1,88	1,91	1,85	1,92
Al total	0,01	0,18	0,15	0,12	0,01	0,09	0,12	1,12	0,04	0,15	0,16	0,18	0,15	0,13	0,03	0,15	0,10	0,13	0,09
Al^{T}	0,01	0,13	0,11	0,11	0,01	0,09	0,12	0,00	0,04	0,13	0,13	0,15	0,13	0,10	0,03	0,12	0,09	0,13	0,08
Al^{M1}	0,00	0,06	0,05	0,01	0,00	0,00	0,00	0,99	0,00	0,02	0,03	0,03	0,03	0,03	0,00	0,02	0,02	0,00	0,01
Fe total	0,21	0,28	0,27	0,18	0,43	0,31	0,29	0,03	0,18	0,17	0,25	0,20	0,26	0,28	0,21	0,17	0,14	0,24	0,18
Fe^{+3}	0,04	0,06	0,07	0,10	0,05	0,08	0,16	0,00	0,12	0,09	0,08	0,09	0,09	0,06	0,03	0,08	0,07	0,16	0,07
Fe^{+3T}	0,01	0,00	0,00	0,00	0,02	0,02	0,03	0,00	0,04	0,00	0,00	0,00	0,00	0,00	0,01	0,00	0,00	0,02	0,00
Fe^{+3M1}	0,03	0,06	0,08	0,10	0,03	0,06	0,13	0,00	0,07	0,09	0,08	0,09	0,09	0,06	0,03	0,08	0,07	0,14	0,07
Fe^{+2M1}	0,08	0,13	0,13	0,00	–	0,00	0,00	0,00	0,00	0,00	0,05	0,00	0,01	0,00	0,06	0,00	0,00	0,00	0,00
Fe^{+2M2}	0,09	0,09	0,07	0,08	0,37	0,23	0,13	0,03	0,07	0,07	0,12	0,11	0,16	0,22	0,11	0,09	0,07	0,09	0,19
Mn	0,00	0,00	0,01	0,00	0,01	0,00	0,01	0,00	0,00	0,00	0,00	0,00	0,00	0,00	0,00	0,00	0,01	0,01	0,00
Mg total	0,89	0,73	0,74	0,87	1,37	0,91	1,01	0,00	0,93	0,86	0,82	0,85	0,85	0,90	0,90	0,89	0,93	0,96	0,90
Mg^{M1}	0,89	0,73	0,74	0,87	0,96	0,91	0,85	0,00	0,90	0,86	0,82	0,85	0,85	0,90	0,90	0,88	0,89	0,84	0,90
Mg^{M2}	0,00	0,00	0,00	0,00	0,42	0,00	0,16	0,00	0,03	0,00	0,00	0,00	0,00	0,00	0,00	0,02	0,05	0,12	0,00
Ca	0,89	0,87	0,88	0,89	0,20	0,74	0,68	0,38	0,88	0,90	0,84	0,87	0,81	0,75	0,86	0,86	0,85	0,75	0,86
Na	0,02	0,04	0,04	0,02	0,01	0,02	0,02	0,45	0,02	0,02	0,03	0,02	0,02	0,02	0,02	0,02	0,02	0,02	0,02
K	0,00	0,00	0,00	0,00	0,00	0,00	0,00	0,01	0,00	0,00	0,00	0,00	0,00	0,00	0,00	0,00	0,00	0,00	0,00
Ti	0,00	0,02	0,01	0,01	0,01	0,03	0,02	0,00	0,01	0,01	0,02	0,02	0,02	0,02	0,01	0,02	0,01	0,02	0,01
Ni	0,00	0,00	0,00	0,00	0,00	0,00	0,00	0,00	0,00	0,00	0,00	0,00	0,00	0,00	0,00	0,00	0,00	0,00	0,00
Cr	0,00	0,00	0,00	0,01	0,00	0,00	0,00	0,00	0,02	0,01	0,00	0,01	0,00	0,00	0,00	0,01	0,02	0,00	0,00
En	45	39	39	45	68	46	51	0	46	45	43	44	44	47	46	46	48	49	46
Q	1,94	1,82	1,82	1,84	1,45	1,88	1,82	0,41	1,09	1,84	1,83	1,82	1,83	1,87	1,94	1,85	1,85	1,79	1,95
J	0,04	0,07	0,07	0,05	1,92	0,04	0,04	0,89	1,80	0,04	0,05	0,04	0,05	0,05	0,03	0,04	0,04	0,05	0,05
[a] T (°C)	–	1096	1093	1071	–	991	959	–	–	1083	1119	1101	1122	1134	906	1100	1106	1040	1086
[b] P (kbar)	–	10,0	9,4	8,0	–	0,5	0,0	–	–	8,1	9,4	9,3	9,0	8,6	4,8	8,3	7,4	4,1	6,0
$K_{D\ (Fe\text{-}Mg)}$	–	0,28	0,28	0,27	–	0,24	0,23	–	–	0,27	0,28	0,27	0,28	0,28	0,23	0,27	0,28	0,25	0,27

Table 3: Continued.

Suite	CA	CA	CA	CA	CA	CA	CA	CA	CA	CA	CA	CA	CA	CA	CA	CA	CA	CA	CA
Analysis	140527 73_71	140527 73_72	140527 73_74	130726 74_33	130726 74_35	130726 74_36	130726 74_37	130726 74_38	131002 74_12	140527 76_08	140527 76_10	131002 77_18	131002 77_19	131016 77_05	131016 77_06	131016 77_09	131016 77_10	140527 77_11	140527 77_16
Type	*pheno. middle*	*micropheno.*	*micropheno.*	*pseudomorph*	*pheno. centre*	*pheno. centre/ middle*	*pheno. middle/ rim*	*pheno. rim*	*pseudomorph*	*Amp corona*	*Amp corona*	*pheno. centre*	*pheno. rim*	*pheno.centre*	*pheno.rim*	*Amp corona.*	*Amp corona.*	*Amp corona*	*Amp corona*
SiO_2	50,57	53,15	52,36	53,69	51,09	50,60	51,70	49,91	53,36	51,02	50,72	51,00	52,06	51,29	50,90	51,07	50,80	50,32	51,65
Al_2O_3	3,85	0,25	0,18	0,50	4,06	4,66	3,08	3,45	0,43	2,46	2,48	2,98	2,04	2,60	2,69	2,25	2,07	2,49	1,52
FeO total	7,03	7,72	7,70	6,31	8,10	8,72	5,85	8,05	6,77	8,31	7,97	6,28	7,15	7,33	7,91	8,32	8,95	8,14	8,11
MnO	0,20	0,34	0,29	0,19	0,11	0,24	0,06	0,20	0,14	0,25	0,26	0,04	0,13	0,16	0,22	0,29	0,33	0,29	0,23
MgO	15,02	15,28	15,29	17,02	15,26	14,54	16,32	15,55	16,58	15,40	16,07	15,69	16,10	15,62	15,51	15,17	15,02	15,49	16,41
CaO	22,83	23,00	22,82	21,41	20,21	19,96	21,65	21,47	22,21	21,01	21,71	23,02	22,65	22,59	21,71	21,89	20,64	21,37	20,64
Na_2O	0,37	0,34	0,33	0,27	0,46	0,48	0,36	0,40	0,29	0,32	0,34	0,00	0,00	0,36	0,27	0,32	0,41	0,35	0,30
K_2O	0,00	0,00	0,00	0,00	0,00	0,00	0,02	0,00	0,00	0,03	0,01	0,00	0,00	0,00	0,00	0,00	0,00	0,02	0,01
TiO_2	0,69	0,23	0,10	0,14	0,49	0,50	0,22	0,50	0,10	0,68	0,67	0,44	0,35	0,45	0,45	0,56	0,68	0,67	0,42
NiO	0,02	0,00	0,03	0,00	0,02	0,00	0,06	0,02	0,01	0,00	0,00	0,02	0,04	0,05	0,03	0,00	0,00	0,00	0,06
Cr_2O_3	0,00	0,00	0,02	0,00	0,02	0,07	0,52	0,03	0,00	0,01	0,01	0,18	0,01	0,09	0,00	0,04	0,21	0,02	0,00
P_2O_5	0,07	0,04	0,02	0,06	0,02	0,02	0,02	0,05	0,03	0,02	0,00	0,02	0,02	0,00	0,03	0,09	0,16	0,05	0,03
F	0,00	0,01	0,00	0,00	0,00	0,05	0,01	0,01	0,00	0,00	0,02	0,03	0,00	0,00	0,06	0,05	0,00	0,03	0,01
Cl	0,00	0,00	0,00	0,00	0,00	0,02	0,00	0,00	0,00	0,01	0,01	0,00	0,00	0,00	0,00	0,00	0,00	0,00	0,01
Total	100,65	100,34	99,14	99,60	99,84	99,84	99,86	99,61	99,91	99,50	100,26	99,70	100,52	100,55	99,76	100,05	99,26	99,22	99,41
Si	1,85	1,96	1,95	1,98	1,88	1,87	1,89	1,84	1,96	1,89	1,86	1,88	1,91	1,88	1,88	1,89	1,90	1,87	1,91
Al total	0,17	0,01	0,01	0,02	0,18	0,20	0,13	0,15	0,02	0,11	0,11	0,13	0,09	0,11	0,12	0,10	0,09	0,11	0,07
Al^{T}	0,15	0,01	0,01	0,02	0,12	0,13	0,11	0,15	0,02	0,11	0,11	0,12	0,09	0,11	0,12	0,10	0,09	0,11	0,07
Al^{M1}	0,02	0,00	0,00	0,00	0,06	0,07	0,03	0,00	0,00	0,00	0,00	0,01	0,00	0,01	0,00	0,00	0,01	0,00	0,00
Fe total	0,22	0,24	0,24	0,19	0,25	0,27	0,18	0,25	0,21	0,26	0,24	0,19	0,22	0,22	0,24	0,26	0,28	0,25	0,25
Fe^{+3}	0,12	0,08	0,10	0,03	0,06	0,07	0,08	0,16	0,07	0,09	0,16	0,08	0,07	0,13	0,13	0,12	0,09	0,14	0,11
Fe^{+3T}	0,00	0,03	0,04	0,00	0,00	0,00	0,00	0,01	0,02	0,00	0,03	0,00	0,00	0,00	0,00	0,02	0,00	0,02	0,02
Fe^{+3M1}	0,12	0,05	0,06	0,03	0,06	0,07	0,08	0,15	0,05	0,09	0,13	0,09	0,07	0,13	0,13	0,11	0,09	0,12	0,09
Fe^{+2M1}	0,00	0,11	0,09	0,03	0,03	0,04	0,00	0,00	0,04	0,04	0,00	0,03	0,04	0,00	0,01	0,00	0,00	0,00	0,00
Fe^{+2M2}	0,10	0,06	0,05	0,13	0,16	0,16	0,10	0,09	0,10	0,13	0,03	0,08	0,11	0,09	0,11	0,13	0,19	0,11	0,14
Mn	0,01	0,01	0,01	0,01	0,00	0,01	0,00	0,01	0,00	0,01	0,01	0,00	0,00	0,00	0,01	0,01	0,01	0,01	0,01
Mg total	0,82	0,84	0,85	0,93	0,84	0,80	0,89	0,86	0,91	0,85	0,88	0,86	0,88	0,85	0,85	0,84	0,84	0,86	0,91
Mg^{M1}	0,85	0,84	0,85	0,93	0,84	0,80	0,87	0,83	0,91	0,85	0,85	0,86	0,88	0,84	0,85	0,84	0,84	0,86	0,90
Mg^{M2}	0,00	0,00	0,00	0,00	0,00	0,00	0,02	0,02	0,00	0,00	0,03	0,00	0,00	0,01	0,00	0,04	0,04	0,00	0,01
Ca	0,89	0,91	0,91	0,84	0,80	0,79	0,85	0,85	0,87	0,84	0,85	0,91	0,89	0,89	0,86	0,87	0,83	0,85	0,82
Na	0,03	0,02	0,02	0,02	0,03	0,03	0,03	0,03	0,02	0,02	0,02	0,00	0,00	0,03	0,02	0,02	0,03	0,02	0,02
K	0,00	0,00	0,00	0,00	0,00	0,00	0,00	0,00	0,00	0,00	0,00	0,00	0,00	0,00	0,00	0,00	0,00	0,00	0,00
Ti	0,02	0,01	0,00	0,00	0,01	0,01	0,01	0,01	0,00	0,02	0,02	0,01	0,01	0,01	0,01	0,02	0,02	0,02	0,01
Ni	0,00	0,00	0,00	0,00	0,00	0,00	0,00	0,00	0,00	0,00	0,00	0,00	0,00	0,00	0,00	0,00	0,00	0,00	0,00
Cr	0,00	0,00	0,00	0,00	0,00	0,00	0,02	0,00	0,00	0,00	0,00	0,01	0,00	0,00	0,00	0,00	0,01	0,00	0,00
En	42	42	42	47	44	43	46	44	46	44	44	44	44	43	43	42	43	44	46
Q	1,81	1,91	1,90	1,94	1,83	1,79	1,84	1,79	1,92	1,85	1,76	1,88	1,91	1,83	1,83	1,83	1,86	1,82	1,87
J	0,05	0,05	0,05	0,04	0,07	0,07	0,05	0,06	0,04	0,05	0,05	0,00	0,00	0,05	0,04	0,05	0,06	0,05	0,04
[a] T (°C)	1084	–	–	1081	1233	1158	1185	1216	–	1048	–	–	–	1020	1050	996	999	969	–
[b] P (kbar)	8,4	–	–	1,3	10,3	7,9	8,2	11,2	–	6,3	–	–	–	5,8	7,3	4,0	3,6	2,8	–
$K_{D\ (Fe\text{-}Mg)}$	0,27	–	–	0,26	0,29	0,28	0,29	0,29	–	0,26	–	–	–	0,26	0,27	0,25	0,25	0,25	–

Table 3: Continued.

Suite	CA	CA	CA	CA	CA	CA	CA	CA	CA	CA	CA	CA	CA	CA
Analysis	140527 77_19	140527 78_23	140527 78_25	151214 92_02	151214 92_04	151214 93_15	151214 93_20	140527 94_97	151214 96_39	150420 107_89	150420 107_99	151214 108_58	151214 108_63	151214 108_66
Type	*Amp corona*	*Amp corona*	*matrix*	*Ol corona*	*matrix*	*matrix*	*matrix*	*pheno.*	*matrix*	*centre*	*matrix*	*matrix*	*micropheno.*	*matrix*
SiO_2	50,56	50,34	51,93	50,24	52,81	52,43	50,87	50,58	50,64	51,18	54,65	50,92	49,17	50,49
Al_2O_3	2,64	2,73	1,51	0,59	0,88	2,49	1,14	2,39	2,16	3,20	7,39	0,81	4,29	0,55
FeO total	8,02	8,40	7,47	20,37	17,42	18,21	18,73	6,84	12,92	7,55	10,04	23,32	9,05	23,65
MnO	0,26	0,38	0,31	0,37	0,38	0,38	0,43	0,21	0,30	0,21	0,18	0,55	0,25	0,56
MgO	15,58	16,03	17,03	25,41	22,65	18,94	19,79	16,72	16,51	16,99	9,66	15,86	13,53	16,82
CaO	21,45	20,82	20,45	3,12	3,96	6,52	6,08	21,23	14,85	20,06	9,93	6,89	20,87	4,58
Na_2O	0,33	0,33	0,22	0,06	0,11	0,63	0,29	0,34	0,25	0,43	1,73	0,14	0,50	0,13
K_2O	0,01	0,00	0,01	0,01	0,00	0,14	0,12	0,01	0,00	0,01	1,88	0,07	0,01	0,03
TiO_2	0,77	0,85	0,28	0,45	0,61	0,57	0,61	0,82	1,15	0,70	1,47	0,39	1,13	0,43
NiO	0,06	0,00	0,06	0,02	0,04	0,00	0,00	0,02	0,00	0,00	0,06	0,00	0,05	0,01
Cr_2O_3	0,14	0,12	0,02	0,02	0,05	0,02	0,03	0,21	0,26	0,18	0,00	0,02	0,02	0,01
P_2O_5	0,00	0,02	0,00	0,01	0,05	0,30	0,05	0,02	0,06	0,03	0,64	0,20	0,02	0,00
F	0,06	0,05	0,03	0,03	0,00	0,11	0,02	0,02	0,07	0,00	0,07	0,04	0,00	0,03
Cl	0,00	0,00	0,00	0,01	0,01	0,02	0,01	0,01	0,01	0,00	0,07	0,00	0,02	0,02
Total	99,89	100,05	99,31	100,72	98,96	100,76	98,17	99,39	99,19	100,54	97,76	99,20	98,90	97,29
Si	1,87	1,85	1,92	1,82	1,96	1,93	1,93	1,86	1,90	1,86	2,09	1,96	1,85	1,98
Al total	0,11	0,12	0,07	0,03	0,04	0,11	0,05	0,10	0,10	0,14	0,33	0,04	0,19	0,03
Al^{T}	0,12	0,12	0,07	–	–	–	–	0,10	–	0,14	0,00	–	–	–
Al^{M1}	0,00	0,00	0,00	–	–	–	–	0,00	–	0,00	0,33	–	–	–
Fe total	0,25	0,26	0,23	0,62	0,54	0,56	0,59	0,21	0,41	0,23	0,32	0,75	0,28	0,77
Fe^{+3}	0,15	0,16	0,10	–	–	–	–	0,14	–	0,12	0,00	–	–	–
Fe^{+3T}	0,02	0,03	0,02	–	–	–	–	0,03	–	0,00	0,00	–	–	–
Fe^{+3M1}	0,13	0,13	0,09	–	–	–	–	0,11	–	0,12	0,00	–	–	–
Fe^{+2M1}	0,00	0,00	0,00	–	–	–	–	0,00	–	0,00	0,08	–	–	–
Fe^{+2M2}	0,10	0,10	0,13	–	–	–	–	0,07	–	0,11	0,25	–	–	–
Mn	0,01	0,01	0,01	0,01	0,01	0,01	0,01	0,01	0,01	0,01	0,01	0,02	0,01	0,02
Mg total	0,86	0,88	0,94	1,38	1,26	1,04	1,12	0,92	0,92	0,92	0,55	0,91	0,76	0,98
Mg^{M1}	0,85	0,85	0,90	–	–	–	–	0,86	–	0,86	0,55	–	–	–
Mg^{M2}	0,00	0,04	0,04	–	–	–	–	0,06	–	0,07	0,00	–	–	–
Ca	0,85	0,82	0,81	0,12	0,16	0,26	0,25	0,84	0,60	0,78	0,41	0,28	0,84	0,19
Na	0,02	0,02	0,02	0,00	0,01	0,05	0,02	0,02	0,02	0,03	0,13	0,01	0,04	0,01
K	0,00	0,00	0,00	0,00	0,00	0,01	0,01	0,00	0,00	0,00	0,09	0,00	0,00	0,00
Ti	0,02	0,02	0,01	0,01	0,02	0,02	0,02	0,02	0,03	0,02	0,04	0,01	0,03	0,01
Ni	0,00	0,00	0,00	0,00	0,00	0,00	0,00	0,00	0,00	0,00	0,00	0,00	0,00	0,00
Cr	0,00	0,00	0,00	0,00	0,00	0,00	0,00	0,01	0,01	0,01	0,00	0,00	0,00	0,00
En	44	45	47	65	64	54	56	47	48	48	43	46	40	50
Q	1,81	1,80	1,87	1,50	1,41	1,30	1,36	1,82	1,52	1,82	0,62	1,20	1,60	0,98
J	0,05	0,05	0,03	0,01	0,02	0,09	0,04	0,05	0,04	0,06	1,10	0,02	0,07	0,00
[a] T (°C)	987	–	932	–	1145	1272	–	–	1088	1114	1335	1070	1081	1073
[b] P (kbar)	3,9	–	0,8	–	3,6	10,3	–	–	3,5	7,7	12,5	2,0	9,3	1,6
$K_{D\,(Fe\text{-}Mg)}$	0,25	–	0,23	–	0,27	0,29	–	–	0,26	0,27	0,31	0,26	0,27	0,26

Table 4: Orthopyroxene major element composition (as wt%), structural formulas* and calculated temperatures[a] and pressures[b].

Suite	T2	T2	T2	T2	T2	CA	CA	CA	CA	CA	CA	CA	CA	CA	CA	CA
Analysis	150416 88_75	150420 103_28	150420 104_34	150420 104_38	150420 104_42	130306 20_08	140527 57_34	130306 60_13	130306 60_15	131016 60_04	130306 61_30	140527 61_36	140527 61_40	140527 63_59	140527 63_60	130306 64_44
Type	*Ol corona*	*reemplacement*	*Ol corona*	*included in Ol*	*included in Pl*	*micropheno. centre*	*micropheno. centre*	*pseudomorph*	*micropheno.*	*micropheno.*	*Amp corona*	*reemplacement in Amp*	*matrix*	*Ol rim*	*micropheno. centre*	*pheno. centre*
SiO_2	50,28	49,47	52,05	54,78	54,52	56,99	54,24	53,59	55,30	55,11	54,28	53,84	54,93	53,76	53,63	54,04
Al_2O_3	3,52	0,71	0,64	1,02	1,92	2,85	0,85	1,91	1,22	0,93	1,82	1,49	2,42	1,37	2,00	2,17
FeO total	19,10	23,03	18,95	13,12	14,07	12,39	13,65	12,20	12,33	12,59	12,57	12,40	11,14	13,14	14,01	11,48
MnO	0,52	0,45	0,38	0,17	0,26	0,36	0,56	0,32	0,36	0,38	0,45	0,48	0,42	0,57	0,49	0,24
MgO	23,20	22,15	25,41	27,86	29,70	23,75	27,41	30,03	28,40	28,93	29,32	29,38	29,22	26,18	27,31	30,12
CaO	1,54	2,33	1,19	1,53	0,65	1,59	2,40	1,83	1,42	1,55	1,53	1,39	1,54	1,93	2,34	1,20
Na_2O	0,06	0,09	0,01	0,04	0,02	0,41	0,03	0,03	0,05	0,05	0,03	0,04	0,23	0,00	0,00	0,04
K_2O	0,00	0,01	0,01	0,00	0,01	0,60	0,01	0,02	0,01	0,00	0,01	0,00	0,21	0,00	0,02	0,00
TiO_2	0,36	0,32	0,53	0,53	0,25	0,26	0,30	0,37	0,28	0,30	0,37	0,61	0,50	0,36	0,33	0,16
NiO	0,00	0,00	0,00	0,04	0,04	0,01	0,01	0,00	0,02	0,01	0,02	0,02	0,03	0,08	0,00	0,05
Cr_2O_3	0,00	0,02	0,04	0,00	0,00	0,00	0,02	0,22	0,00	0,00	0,07	0,01	0,02	0,03	0,02	0,50
P_2O_5	0,02	0,06	0,01	0,01	0,01	0,04	0,02	0,01	0,01	0,07	0,00	0,01	0,01	0,00	0,01	0,02
F	0,00	0,00	0,00	0,04	0,00	0,02	0,02	0,03	0,04	0,00	0,00	0,01	0,02	0,01	0,05	0,00
Cl	0,00	0,00	0,01	0,00	0,01	0,05	0,00	0,00	0,01	0,02	0,00	0,01	0,02	0,00	0,00	0,01
Total	98,60	98,64	99,22	99,14	101,46	99,31	99,51	100,58	99,42	99,92	100,47	99,69	100,70	97,43	100,21	100,02
Si	1,87	1,87	1,92	1,98	1,91	2,03	1,96	1,89	1,98	1,96	1,92	1,92	1,93	1,98	1,92	1,91
Al total	0,15	0,03	0,03	0,04	0,08	0,12	0,04	0,08	0,05	0,04	0,08	0,06	0,10	0,06	0,08	0,09
Al^{T}	0,13	0,03	0,03	0,02	0,08	0,12	0,04	0,08	0,02	0,04	0,08	0,06	0,07	0,02	0,08	0,09
Al^{M1}	0,03	0,00	0,00	0,02	0,00	0,00	0,01	0,00	0,03	0,00	0,00	0,02	0,03	0,04	0,00	0,00
Fe total	0,59	0,73	0,58	0,40	0,41	0,38	0,41	0,36	0,37	0,38	0,37	0,37	0,33	0,41	0,42	0,34
Fe^{+3}	0,09	0,22	0,11	0,00	0,08	0,00	0,04	0,13	0,00	0,00	0,06	0,07	0,05	0,00	0,07	0,07
Fe^{+3T}	0,00	0,10	0,06	0,00	0,01	0,00	0,00	0,13	0,00	0,00	0,00	0,00	0,00	0,00	0,00	0,00
Fe^{+3M1}	0,09	0,12	0,05	0,00	0,08	0,00	0,04	0,10	0,00	0,03	0,06	0,07	0,05	0,00	0,07	0,07
Fe^{+2M2}	0,00	0,51	0,48	0,40	0,33	0,38	0,37	0,23	0,37	0,00	0,00	0,30	0,28	0,41	0,35	0,00
Mn	0,02	0,01	0,01	0,01	0,01	0,01	0,02	0,01	0,01	0,01	0,01	0,01	0,01	0,02	0,01	0,01
Mg total	1,29	1,25	1,39	1,50	1,55	1,29	1,47	1,58	1,52	1,54	1,55	1,56	1,53	1,44	1,46	1,59
Mg^{M1}	0,78	0,88	0,93	0,97	0,92	0,84	0,94	0,89	0,96	0,96	0,93	0,89	0,91	0,95	0,92	0,91
Mg^{M2}	0,50	0,38	0,47	0,53	0,64	0,43	0,53	0,69	0,56	0,58	0,62	0,67	0,62	0,50	0,54	0,68
Ca	0,06	0,09	0,05	0,06	0,02	0,06	0,09	0,07	0,05	0,06	0,06	0,05	0,06	0,08	0,09	0,05
Na	0,00	0,01	0,00	0,00	0,00	0,03	0,00	0,00	0,00	0,00	0,00	0,00	0,02	0,00	0,00	0,00
K	0,00	0,00	0,00	0,00	0,00	0,03	0,00	0,00	0,00	0,00	0,00	0,00	0,01	0,00	0,00	0,00
Ti	0,01	0,01	0,01	0,01	0,01	0,01	0,01	0,01	0,01	0,01	0,01	0,02	0,01	0,01	0,01	0,00
Ni	0,00	0,00	0,00	0,00	0,00	0,00	0,00	0,00	0,00	0,00	0,00	0,00	0,00	0,00	0,00	0,00
Cr	0,00	0,00	0,00	0,00	0,00	0,00	0,00	0,01	0,00	0,00	0,00	0,00	0,00	0,00	0,00	0,01
En	66	60	68	77	78	74	74	78	78	78	78	78	79	74	74	80
Q	1,35	1,85	1,92	1,95	1,91	1,73	1,94	1,87	1,94	1,60	1,60	1,91	1,87	1,92	1,89	1,63
J	0,01	0,01	0,00	0,01	0,00	0,06	0,00	0,00	0,01	0,01	0,00	0,01	0,03	0,00	0,00	0,00
[a] T (°C)	1078	1036	1050	1125	1105	1095	1105	1070	1078	1074	1059	1064	1094	–	–	1078
[b] P (kbar)	6,4	6,0	1,1	3,9	2,1	7,1	2,8	0,34	2,1	1,1	0,8	0,4	3,2	–	–	0,1
$K_{D\ (Fe\text{-}Mg)}$	0,43	0,59	0,47	0,30	0,30	0,42	0,53	0,32	0,34	0,34	0,34	0,34	0,30	0,46	0,47	0,31

* Structural formulas calculated to 6 oxygens per formula unit and normalized to 4 cations where Fe^{3+} content is estimated through the charge balance method described by Droop (1987). Classification parameters and mineral names according to Morimoto (1988).

[a] Temperatures calculated following the equation 28a of Putirka 2008. KD: Fe - Mg Opx/liquid distribution coefficient (0,29± 0,06)

[b] Pressures calculated following the equation 29a of Putirka 2008.

Table 4: Continued.

Suite	CA	CA	CA	CA	CA	CA	CA	CA	CA	CA	CA	CA	CA	CA	CA	CA
Analysis	130306 64_45	130306 64_47	131002 64_32	131002 64_36	131002 64_47	130726 65_17	140527 65_44	140527 65_48	130306 66_52	131002 66_59	131002 66_62	131002 70_06	140527 70_51	140527 73_68	140527 73_75	130726 74_41
Type	*pheno. rim*	*matrix*		*centre*	*patchy zonation*	*matrix*	*Ol corona*	*matrix*	*matrix*	*micropheno.*	*microphen.*	*micropheno. centre*	*Ol corona*	*Amp corona*	*micropheno.*	*micropheno. centre*
SiO_2	52,95	52,65	53,85	52,78	53,65	54,22	53,84	53,92	53,69	53,13	54,49	53,07	53,85	53,99	54,80	55,74
Al_2O_3	0,80	1,96	2,18	2,58	2,17	0,24	1,14	1,51	1,58	2,19	0,92	1,85	1,60	1,80	0,81	0,83
FeO total	16,92	15,50	11,72	11,86	11,62	14,89	14,55	13,48	13,39	13,73	12,70	15,51	13,94	12,02	11,70	12,95
MnO	0,45	0,35	0,20	0,28	0,18	0,28	0,43	0,14	0,38	0,23	0,28	0,25	0,50	0,57	0,48	0,23
MgO	26,44	27,10	29,49	28,16	28,63	27,06	27,25	27,25	28,40	27,98	28,61	26,29	27,75	28,69	30,38	29,36
CaO	1,68	1,76	1,20	1,50	1,33	2,18	2,29	2,24	2,14	1,62	1,60	1,96	2,06	2,01	1,56	1,59
Na_2O	0,02	0,03	0,03	0,04	0,02	0,05	0,05	0,05	0,05	0,02	0,04	0,04	0,02	0,06	0,03	0,04
K_2O	0,00	0,01	0,01	0,00	0,00	0,01	0,02	0,01	0,03	0,00	0,00	0,01	0,01	0,03	0,00	0,00
TiO_2	0,21	0,35	0,19	0,21	0,18	0,19	0,40	0,37	0,32	0,31	0,16	0,34	0,35	0,41	0,20	0,07
NiO	0,03	0,00	0,07	0,09	0,08	0,00	0,01	0,06	0,02	0,01	0,06	0,00	0,02	0,01	0,04	0,00
Cr_2O_3	0,00	0,03	0,34	0,19	0,22	0,01	0,05	0,11	0,01	0,02	0,00	0,00	0,01	0,02	0,03	0,02
P_2O_5	0,00	0,00	0,00	0,05	0,01	0,00	0,00	0,02	0,06	0,02	0,01	0,04	0,01	0,06	0,00	0,00
F	0,00	0,02	0,00	0,00	0,01	0,02	0,01	0,00	0,00	0,00	0,00	0,03	0,00	0,00	0,02	0,00
Cl	0,00	0,02	0,03	0,00	0,00	0,00	0,00	0,01	0,00	0,02	0,00	0,04	0,01	0,00	0,00	0,01
Total	99,50	99,77	99,28	97,73	98,08	99,15	100,05	99,16	100,08	99,24	98,86	99,35	100,13	99,65	100,06	100,85
Si	1,93	1,90	1,92	1,92	1,94	1,97	1,94	1,95	1,91	1,91	1,96	1,93	1,93	1,93	1,94	1,97
Al total	0,03	0,08	0,09	0,11	0,09	0,01	0,05	0,06	0,07	0,09	0,04	0,08	0,07	0,08	0,03	0,03
Al^{T}	0,03	0,08	0,08	0,08	0,06	0,01	0,05	0,05	0,07	0,09	0,04	0,08	0,07	0,07	0,03	0,03
Al^{M1}	0,00	0,00	0,01	0,03	0,03	0,00	0,00	0,01	0,00	0,01	0,00	0,00	0,00	0,00	0,00	0,00
Fe total	0,52	0,47	0,35	0,36	0,35	0,45	0,44	0,41	0,40	0,41	0,38	0,47	0,42	0,36	0,35	0,38
Fe^{+3}	0,10	0,11	0,06	0,04	0,02	0,05	0,06	0,02	0,09	0,07	0,03	0,06	0,06	0,05	0,09	0,03
Fe^{+3T}	0,04	0,02	0,00	0,00	0,00	0,02	0,02	0,00	0,02	0,00	0,00	0,00	0,01	0,00	0,03	0,00
Fe^{+3M1}	0,06	0,09	0,06	0,04	0,02	0,03	0,05	0,02	0,07	0,07	0,03	0,06	0,06	0,05	0,06	0,03
Fe^{+2M2}	0,42	0,36	0,29	0,33	0,34	0,40	0,37	0,39	0,31	0,35	0,35	0,41	0,36	0,31	0,26	0,35
Mn	0,01	0,01	0,01	0,01	0,01	0,01	0,01	0,00	0,01	0,01	0,01	0,01	0,02	0,02	0,01	0,01
Mg total	1,44	1,46	1,57	1,53	1,54	1,46	1,46	1,47	1,51	1,50	1,54	1,42	1,48	1,53	1,60	1,54
Mg^{M1}	0,93	0,90	0,92	0,93	0,90	0,97	0,94	0,96	0,92	0,92	0,97	0,93	0,94	0,94	0,94	0,97
Mg^{M2}	0,50	0,56	0,65	0,60	0,65	0,50	0,52	0,51	0,59	0,58	0,57	0,50	0,55	0,59	0,67	0,58
Ca	0,07	0,07	0,05	0,06	0,05	0,08	0,09	0,09	0,08	0,06	0,06	0,08	0,08	0,08	0,06	0,06
Na	0,00	0,00	0,00	0,00	0,00	0,00	0,00	0,00	0,00	0,00	0,00	0,00	0,00	0,00	0,00	0,00
K	0,00	0,00	0,00	0,00	0,00	0,00	0,00	0,00	0,00	0,00	0,00	0,00	0,00	0,00	0,00	0,00
Ti	0,01	0,01	0,01	0,01	0,00	0,01	0,01	0,01	0,01	0,01	0,00	0,01	0,01	0,01	0,01	0,00
Ni	0,00	0,00	0,00	0,00	0,00	0,00	0,00	0,00	0,00	0,00	0,00	0,00	0,00	0,00	0,00	0,00
Cr	0,00	0,00	0,01	0,01	0,01	0,00	0,00	0,00	0,00	0,00	0,00	0,00	0,00	0,00	0,00	0,00
En	71	73	80	78	79	73	73	75	75	76	77	72	74	77	79	77
Q	1,92	1,88	1,91	1,91	1,93	1,95	1,92	1,94	1,90	1,91	1,95	1,91	1,92	1,91	1,92	1,95
J	0,00	0,00	0,00	0,01	0,00	0,01	0,01	0,01	0,01	0,00	0,01	0,01	0,00	0,01	0,00	0,01
[a] T (°C)	1027	1042	1077	1081	1079	1092	1098	1110	1053	1045	1057	1071	1080	1079	1074	1066
[b] P (kbar)	0,1	0,2	0,2	1,4	0,4	2,8	2,7	3,0	0,6	0,5	0,4	2,7	1,1	1,9	0,5	0,7
$K_{D\ (Fe-Mg)}$	0,52	0,47	0,32	0,34	0,33	0,54	0,52	0,48	0,37	0,39	0,35	0,58	0,49	0,32	0,29	0,36

Table 4: Continued.

Suite	CA	CA	CA	CA	CA	CA	CA	CA	CA	CA	CA	CA	CA	CA	CA
Analysis	140527 78_21	151214 82_21	151214 82_22	151214 82_23	151214 82_26	151214 82_27	151214 82_30	151214 92_09	150420 107_93	151214 108_44	151214 108_45	151214 108_48	151214_ 108_52	151214 108_54	151214 108_55
Type	*Amp. corona*	*pheno. centre*	*pheno. rim*	*pheno. centre*	*matrix*	*pheno. rim*	*matrix*	*Ol corona*	*matrix*	*pheno. centre*	*pheno. rim*	*micropheno. centre*	*micropheno. centre*	*pheno. rim*	*pheno. centre*
SiO_2	52,33	54,04	53,80	54,27	54,00	54,82	53,69	53,73	44,65	51,77	54,04	52,82	52,13	51,51	52,28
Al_2O_3	2,19	1,98	1,97	2,32	1,50	1,47	1,12	1,03	5,43	3,51	0,84	0,79	1,80	1,54	2,67
FeO total	13,77	12,54	12,52	12,37	15,22	12,49	16,08	17,10	22,14	13,41	18,33	18,69	19,68	24,13	17,26
MnO	0,58	0,26	0,29	0,20	0,35	0,23	0,31	0,35	0,49	0,20	0,41	0,47	0,35	0,33	0,23
MgO	26,38	29,51	28,91	28,22	27,33	28,64	25,37	24,37	19,55	26,08	24,67	24,08	23,31	20,58	25,09
CaO	2,05	1,34	1,11	1,29	1,65	1,27	1,86	2,27	0,69	1,46	1,61	1,76	1,47	0,69	1,43
Na_2O	0,02	0,03	0,03	0,07	0,04	0,02	0,05	0,06	0,89	0,04	0,05	0,04	0,03	0,02	0,01
K_2O	0,00	0,00	0,02	0,00	0,00	0,01	0,00	0,02	1,48	0,00	0,01	0,02	0,01	0,00	0,00
TiO_2	0,45	0,29	0,22	0,26	0,28	0,22	0,29	0,64	0,82	0,43	0,29	0,28	0,35	0,35	0,37
NiO	0,00	0,05	0,04	0,04	0,05	0,01	0,06	0,00	0,02	0,04	0,00	0,03	0,01	0,00	0,06
Cr_2O_3	0,24	0,35	0,27	0,46	0,00	0,19	0,04	0,03	0,00	0,06	0,01	0,00	0,01	0,11	0,04
P_2O_5	0,06	0,02	0,02	0,02	0,00	0,00	0,01	0,02	0,40	0,00	0,00	0,00	0,03	0,01	0,02
F	0,00	0,01	0,08	0,05	0,00	0,05	0,00	0,00	0,00	0,00	0,02	0,00	0,02	0,00	0,00
Cl	0,00	0,00	0,00	0,01	0,00	0,02	0,00	0,00	0,06	0,00	0,01	0,00	0,00	0,00	0,00
Total	98,07	100,41	99,26	99,56	100,41	99,45	98,86	99,61	96,60	97,01	100,28	98,98	99,20	99,27	99,47
Si	1,92	1,91	1,92	1,94	1,94	1,96	1,97	1,97	1,71	1,91	1,97	1,96	1,94	1,95	1,91
Al total	0,09	0,08	0,08	0,10	0,06	0,06	0,05	0,04	0,24	0,15	0,04	0,03	0,08	0,07	0,12
Al^{T}	0,08	–	–	–	–	–	–	–	0,25	–	–	–	–	–	–
Al^{M1}	0,01	–	–	–	–	–	–	–	0,00	–	–	–	–	–	–
Fe total	0,42	0,37	0,37	0,37	0,46	0,37	0,49	0,53	0,71	0,41	0,56	0,58	0,61	0,76	0,53
Fe^{+3}	0,03	–	–	–	–	–	–	–	0,40	–	–	–	–	–	–
Fe^{+3T}	0,00	–	–	–	–	–	–	–	0,05	–	–	–	–	–	–
Fe^{+3M1}	0,03	–	–	–	–	–	–	–	0,35	–	–	–	–	–	–
Fe^{+2M2}	0,39	–	–	–	–	–	–	–	0,31	–	–	–	–	–	–
Mn	0,02	0,01	0,01	0,01	0,01	0,01	0,01	0,01	0,02	0,01	0,01	0,01	0,01	0,01	0,01
Mg total	1,44	1,56	1,54	1,50	1,46	1,53	1,39	1,33	1,12	1,44	1,34	1,33	1,29	1,16	1,37
Mg^{M1}	0,93	–	–	–	–	–	–	–	0,63	–	–	–	–	–	–
Mg^{M2}	0,50	–	–	–	–	–	–	–	0,49	–	–	–	–	–	–
Ca	0,08	0,05	0,04	0,05	0,06	0,05	0,07	0,09	0,03	0,06	0,06	0,07	0,06	0,03	0,06
Na	0,00	0,00	0,00	0,00	0,00	0,00	0,00	0,00	0,07	0,00	0,00	0,00	0,00	0,00	0,00
K	0,00	0,00	0,00	0,00	0,00	0,00	0,00	0,00	0,07	0,00	0,00	0,00	0,00	0,00	0,00
Ti	0,01	0,01	0,01	0,01	0,01	0,01	0,01	0,02	0,02	0,01	0,01	0,01	0,01	0,01	0,01
Ni	0,00	0,00	0,00	0,00	0,00	0,00	0,00	0,00	0,00	0,00	0,00	0,00	0,00	0,00	0,00
Cr	0,01	0,01	0,01	0,01	0,00	0,01	0,00	0,00	0,00	0,00	0,00	0,00	0,00	0,00	0,00
En	73	78	78	78	73	78	71	68	60	75	68	67	65	59	70
Q	1,91	1,61	1,58	1,55	1,52	1,58	1,46	1,42	1,45	1,49	1,40	1,40	1,35	1,19	1,42
J	0,00	0,00	0,00	0,01	0,01	0,00	0,01	0,01	0,13	0,01	0,01	0,01	0,00	0,00	0,00
[a] T (°C)	1036	1051	1053	1063	1032	1054	1028	1094	1035	1100	1048	1040	1033	992	1053
[b] P (kbar)	0,1	0,7	0,0	1,6	0,4	0,2	1,3	4,6	9,2	4,1	2,7	2,2	2,6	2,7	1,4
$K_{D\ (Fe\text{-}Mg)}$	0,41	0,29	0,29	0,30	0,38	0,30	0,43	0,62	0,74	0,25	0,36	0,38	0,41	0,57	0,34

Table 5: Amphibole major element composition (as wt%), structural formulas* and calculated temperatures, pressures and water contents [a].

Suite	CA	CA	CA	CA	CA	CA	CA	CA	CA	CA	CA	CA	CA	CA	CA	CA	CA	CA	CA	CA
Analysis	130306 20_01	130306 20_02	130306 20_06	140527 20_64	130306 60_21	130306 60_22	130306 60_23	130306 61_29	140527 61_39	130306 66_51	131002 66_58	140527 73_65	140527 73_66	130726 74_39	130726 74_40	140527 76_05	140527 76_06	130726 77_25	140527 77_13	140527 77_14	140527 78_26
Name	–	Mg-Hst	Tsch-Prg	Tsch-Prg	Mg-Hst	Mg-Hst	Mg-Hst	Mg-Hst	Tsch-Prg	Mg-Hst	Mg-Hst	Mg-Hst	Mg-Hst	Mg-Hst	Mg-Hst	Tsch-Prg	Mg-Hst	Tsch-Prg	Tsch-Prg	Mg-Hst	Mg-Hst
Type	*centre*	*middle*	*Anf*	*pheno.*	*centre*	*middle*	*rim*	*centre*	*centre*	*centre*	*centre*	*centre*	*centre*	*centre*	*rim*	*centre*	*rim*	*centre*	*centre*	*rim*	*centre*
SiO_2	44,38	45,04	45,13	43,50	42,96	41,72	42,57	43,69	44,86	42,58	43,68	43,00	42,19	43,54	44,23	42,15	43,14	44,84	42,44	43,75	43,15
Al_2O_3	11,31	11,38	11,19	11,56	12,51	12,90	12,66	12,72	11,00	11,97	10,74	11,86	12,49	12,19	11,25	12,85	12,18	11,00	12,28	11,35	12,58
FeO	10,59	8,69	8,16	10,00	8,37	10,73	9,64	9,41	7,55	10,14	10,33	9,04	10,16	11,11	8,53	12,64	9,02	8,35	12,44	8,92	10,20
MnO	0,06	0,08	0,11	0,23	0,04	0,09	0,09	0,12	0,00	0,14	0,14	0,14	0,22	0,12	0,08	0,13	0,13	0,16	0,29	0,14	0,07
MgO	16,43	16,45	17,57	15,13	16,74	14,99	16,37	15,47	17,15	15,88	15,64	16,06	14,96	15,02	16,57	13,68	16,09	16,70	13,94	16,64	15,28
CaO	11,26	12,17	11,99	11,74	12,28	11,54	11,74	11,68	11,73	11,95	11,79	12,15	11,71	11,82	11,85	11,69	11,90	11,16	11,59	11,97	11,82
Na_2O	1,09	2,18	2,09	1,63	2,40	2,36	2,55	2,35	2,27	2,38	2,39	2,30	2,55	2,25	2,23	2,08	2,20	2,15	2,23	2,29	2,34
K_2O	0,32	0,38	0,37	0,32	0,54	0,51	0,51	0,49	0,40	0,39	0,37	0,56	0,44	0,52	0,61	0,42	0,36	0,38	0,35	0,34	0,37
TiO_2	1,71	1,94	1,55	1,80	2,08	2,35	1,97	1,50	1,78	2,13	2,30	2,15	2,16	1,38	1,38	2,13	1,95	1,20	1,92	1,95	1,97
NiO	0,03	0,00	0,10	0,03	0,05	0,00	0,13	0,00	0,11	0,12	0,00	0,04	0,00	0,04	0,03	0,00	0,03	0,01	0,00	0,00	0,07
Cr_2O_3	0,00	0,07	0,34	0,00	0,29	0,01	0,02	0,00	0,24	0,01	0,03	0,07	0,06	0,04	0,13	0,00	0,03	0,10	0,00	0,10	0,00
P_2O_5	0,03	0,00	0,00	0,05	0,02	0,00	0,02	0,03	0,02	0,03	0,02	0,02	0,00	0,02	0,03	0,00	0,05	0,04	0,03	0,05	0,02
F	0,16	0,11	0,02	0,10	0,12	0,09	0,15	0,06	0,08	0,11	0,02	0,07	0,12	0,06	0,08	0,00	0,10	0,05	0,08	0,15	0,08
Cl	0,03	0,04	0,04	0,05	0,03	0,04	0,04	0,04	0,02	0,10	0,02	0,02	0,04	0,04	0,03	0,02	0,03	0,01	0,03	0,01	0,02
Total	97,34	98,47	98,62	96,10	98,36	97,27	98,37	97,50	97,18	97,86	97,46	97,44	97,04	98,10	96,99	97,78	97,15	96,13	97,59	97,60	97,94
Si	6,24	6,38	6,32	6,31	6,10	6,02	6,05	6,25	6,39	6,11	6,30	6,19	6,12	6,24	6,35	6,09	6,19	6,42	6,14	6,25	6,18
Al^T	1,76	1,62	1,68	1,69	1,90	1,98	1,95	1,75	1,61	1,89	1,70	1,81	1,88	1,76	1,65	1,91	1,81	1,58	1,86	1,75	1,82
Ti^T	0,00	0,00	0,00	0,00	0,00	0,00	0,00	0,00	0,00	0,00	0,00	0,00	0,00	0,00	0,00	0,00	0,00	0,00	0,00	0,00	0,00
Al^C	0,12	0,27	0,16	0,29	0,20	0,21	0,17	0,40	0,24	0,14	0,12	0,21	0,26	0,30	0,26	0,28	0,25	0,28	0,24	0,16	0,30
Ti^C	0,18	0,21	0,16	0,20	0,22	0,26	0,21	0,16	0,19	0,23	0,25	0,23	0,24	0,15	0,15	0,23	0,21	0,13	0,21	0,21	0,21
Cr^C	0,00	0,01	0,04	0,00	0,03	0,00	0,00	0,00	0,03	0,00	0,00	0,01	0,01	0,00	0,01	0,00	0,00	0,01	0,00	0,01	0,00
Fe^{3+C}	1,53	0,57	0,92	0,84	0,72	0,93	1,00	0,71	0,68	0,88	0,70	0,64	0,70	0,82	0,70	0,89	0,80	0,94	0,91	0,81	0,76
Mg^C	3,45	3,47	3,67	3,27	3,55	3,23	3,47	3,30	3,64	3,40	3,36	3,45	3,24	3,21	3,55	2,95	3,44	3,56	3,01	3,54	3,26
Fe^{2+C}	0,28	0,46	0,03	0,37	0,27	0,36	0,15	0,42	0,22	0,34	0,54	0,45	0,54	0,51	0,32	0,64	0,28	0,06	0,59	0,25	0,46
Mn^C	0,01	0,01	0,01	0,03	0,00	0,01	0,01	0,01	0,00	0,02	0,02	0,02	0,03	0,01	0,01	0,02	0,02	0,02	0,04	0,02	0,01
Fe^{2+B}	0,00	0,00	0,00	0,00	0,00	0,00	0,00	0,00	0,00	0,00	0,00	0,00	0,00	0,00	0,00	0,00	0,00	0,00	0,00	0,00	0,00
Ca^B	1,70	1,85	1,80	1,82	1,87	1,78	1,79	1,79	1,79	1,84	1,82	1,87	1,82	1,81	1,82	1,81	1,83	1,71	1,80	1,83	1,81
Na^B	0,30	0,15	0,20	0,18	0,13	0,22	0,21	0,21	0,21	0,16	0,18	0,13	0,18	0,19	0,18	0,19	0,17	0,29	0,20	0,17	0,19
Na^A	0,00	0,44	0,36	0,28	0,53	0,44	0,49	0,44	0,42	0,50	0,49	0,52	0,54	0,44	0,44	0,39	0,44	0,31	0,42	0,46	0,46
K^A	0,06	0,07	0,07	0,06	0,10	0,09	0,09	0,09	0,07	0,07	0,07	0,10	0,08	0,09	0,11	0,08	0,07	0,07	0,06	0,06	0,07
[a] T (°C)	–	944	943	940	995	990	990	964	940	978	943	977	983	954	946	970	972	922	960	959	971
[a] P (kbar)	–	2,9	2,7	3,3	3,9	4,5	4,0	4,2	2,7	3,5	2,7	3,5	4,1	3,7	3,0	4,5	3,7	2,8	3,9	3,0	4,1
[a] H_2O_{melt}	–	6,04	5,52	7,18	5,54	6,26	5,54	6,89	5,44	5,70	5,21	5,48	6,28	6,50	5,31	7,36	6,39	5,95	7,02	5,55	6,76

* Structural formulas calculated to 23 oxygens per formula unit and normalized to 13-CKN cations as described by Leake et al. (1997).

[a] Temperature, pressure and watter content (wt%) calculatet with the exel spread sheet by Ridolfi (2010).

Table 6: Oxides major element composition (as wt%) and structural formulas*.

Suite	CA	T1	T1	T1	T1	T1	T2	T2	T2	T1	T1	CA	CA	CA	CA	CA	CA
Analysis	130218 03_28	131016 95_15	131016 95_24	131016 95_25	131016 105_34	131016 105_41	131016 102_49	131016 102_55	150416 87_67	150416 98_90	150420 99_09	151214 93_18	151214 96_34	151214 108_47	151214 108_49	151214 108_60	151214 108_64
Species	Cromita	Espinela	Magnetita / Ulvoespinela	Magnetita / Ulvoespinela	Magnetita / Ulvoespinela	Magnetita / Ulvoespinela	Magnetita / Ulvoespinela	Magnetita / Ulvoespinela	Magnetita / Ulvoespinela	Magnetita / Ulvoespinela	Magnetita / Ulvoespinela	Cromita	Cromita	Magnetita / Ulvoespinela	Ilmenite	Ilmenite	Ilmenite
Type	*Included in Ol*	*included in Pl*	*included in Pl*		*pheno.*	*pheno.*	*included in Cpx*		*included in Ol*	*pheno.*	*pheno.*	*included in Ol*	*matrix*	*matrix*	*micropheno.*	*pheno.*	
SiO_2	0,08	0,06	0,09	0,05	0,12	0,07	0,02	0,07	0,35	0,09	0,08	5,75	0,05	0,07	0,00	0,00	6,96
Al_2O_3	19,09	58,85	5,31	2,65	3,80	3,23	4,65	3,74	2,95	4,08	3,11	8,49	20,72	1,22	0,12	0,22	0,97
Fe_2O_3	0,00	0,00	0,00	0,00	0,00	0,00	0,00	0,00	0,00	0,00	0,00	0,00	0,00	0,00	0,00	0,00	0,00
FeO t	35,33	24,41	66,41	65,81	67,90	68,95	70,77	71,36	63,25	66,24	59,05	42,31	33,03	73,19	47,86	47,66	42,21
MnO	0,36	0,15	0,56	0,57	0,67	0,78	0,46	0,53	0,63	0,68	0,44	0,27	0,27	0,43	0,44	0,40	0,21
MgO	9,77	16,66	4,19	2,75	2,23	2,02	4,23	2,97	3,78	2,78	3,11	10,10	9,38	1,24	1,55	2,48	5,86
CaO	0,04	0,02	0,04	0,00	0,03	0,00	0,04	0,00	0,39	0,02	0,02	0,20	0,04	0,19	0,09	0,00	2,70
Na_2O	0,02	0,03	0,03	0,04	0,07	0,02	0,00	0,03	0,04	0,00	0,02	0,00	0,01	0,03	0,00	0,00	0,10
K_2O	0,01	0,00	0,01	0,00	0,01	0,01	0,00	0,00	0,01	0,00	0,00	0,02	0,01	0,00	0,00	0,00	0,00
TiO_2	1,64	0,51	19,09	24,21	22,70	22,84	14,96	16,84	23,78	22,06	29,71	7,85	2,79	21,70	48,37	48,95	39,64
NiO	0,11	0,13	0,06	0,04	0,02	0,00	0,02	0,05	0,06	0,13	0,00	0,05	0,11	0,02	0,00	0,06	0,00
Cr_2O_3	33,06	0,23	0,09	0,09	0,08	0,14	0,56	0,20	0,13	0,07	0,00	21,47	30,74	0,05	0,05	0,01	0,19
Total	99,50	101,05	95,86	96,21	97,62	98,05	95,70	95,79	95,37	96,16	95,54	96,52	97,14	98,13	98,47	99,78	98,84
Si	0,02	0,01	0,03	0,02	0,04	0,02	0,01	0,02	0,11	0,03	0,02	1,60	0,01	0,02	0,00	0,00	0,34
Al	5,99	14,72	1,99	0,99	1,41	1,20	1,80	1,46	1,10	1,53	1,12	2,79	6,55	0,47	0,01	0,01	0,06
Fe^{+3}	3,00	1,38	5,86	4,29	4,73	4,84	7,79	7,22	4,22	4,78	1,55	2,53	2,31	5,93	0,32	0,35	0,50
Fe^{+2}	4,50	2,86	10,17	11,98	11,77	11,92	9,30	10,25	11,36	11,47	13,16	6,94	4,83	12,08	1,69	1,62	1,15
Mn	0,08	0,03	0,15	0,15	0,18	0,21	0,13	0,15	0,17	0,18	0,11	0,06	0,06	0,12	0,02	0,02	0,01
Mg	3,88	5,27	1,98	1,30	1,04	0,95	2,07	1,46	1,78	1,32	1,42	4,20	3,75	0,60	0,12	0,19	0,43
Ca	0,01	0,00	0,01	0,00	0,01	0,00	0,01	0,00	0,13	0,01	0,01	0,06	0,01	0,07	0,00	0,00	0,14
Na	0,01	0,01	0,02	0,03	0,04	0,01	0,00	0,02	0,03	0,00	0,01	0,00	0,00	0,02	0,00	0,00	0,01
K	0,00	0,00	0,00	0,00	0,00	0,00	0,00	0,00	0,01	0,00	0,00	0,01	0,00	0,00	0,00	0,00	0,00
Ti	0,33	0,08	4,56	5,77	5,36	5,40	3,70	4,18	5,64	5,26	6,83	1,65	0,56	5,29	1,88	1,87	1,46
Ni	0,02	0,02	0,01	0,01	0,00	0,00	0,01	0,01	0,01	0,03	0,00	0,01	0,02	0,00	0,00	0,00	0,00
Cr	6,96	0,04	0,02	0,02	0,02	0,04	0,15	0,05	0,03	0,02	0,00	4,73	6,52	0,01	0,00	0,00	0,01
Total	24,81	24,44	24,80	24,56	24,60	24,59	24,96	24,83	24,59	24,63	24,23	24,60	24,63	24,61	4,05	4,06	4,10

* Structural formulas calculated to 32 oxygens per formula unit in the case of spinel and 6 for ilmenite. Fe^{3+} content calculated following the procedure described by Droop (1987).

Table 7: Apatite major element composition (as wt%) and structural formulas*.

Suite	T1	T1	T1	T1	T2	T1	T1	T2
Analysis	131016 105_33	131016 105_35	131016 105_37	131016 97_45	150416 88_79	150416 98_100	150420 99_02	150420 104_46
Type		*included in Mt*	*pheno.*	*included in Pl*	*included in Cpx*	*matrix*	*included in Ol*	*included in Mt*
SiO_2	0,09	0,06	0,05	0,19	0,39	0,27	0,23	3,65
Al_2O_3	0,00	0,00	0,00	0,01	0,05	0,00	0,00	1,47
FeO total	0,78	0,95	0,43	0,72	0,74	0,43	0,71	1,57
MnO	0,12	0,03	0,00	0,06	0,06	0,02	0,08	0,10
MgO	0,24	0,34	0,37	0,23	0,36	0,34	0,18	0,28
CaO	55,65	53,75	54,53	55,54	54,84	53,76	54,75	48,47
Na_2O	0,12	0,05	0,09	0,01	0,09	0,00	0,05	0,44
K_2O	0,03	0,00	0,00	0,04	0,00	0,03	0,03	0,09
TiO_2	0,00	0,07	0,00	0,01	0,00	0,04	0,00	0,94
P_2O_5	42,09	41,19	43,58	42,36	41,96	41,79	42,17	39,15
F	2,18	3,00	2,61	3,01	2,23	3,32	3,12	3,07
Cl	0,20	0,14	0,15	0,24	0,35	0,18	0,23	0,41
Total	101,48	99,56	101,80	102,43	101,06	100,16	101,55	99,64
Si	0,01	0,01	0,01	0,03	0,06	0,04	0,04	0,60
Al	0,00	0,00	0,00	0,00	0,01	0,00	0,00	0,28
Fe	0,11	0,13	0,06	0,10	0,10	0,06	0,10	0,21
Mn	0,02	0,00	0,00	0,01	0,01	0,00	0,01	0,01
Mg	0,06	0,08	0,09	0,05	0,09	0,08	0,04	0,07
Ca	9,85	9,59	9,48	9,64	9,71	9,46	9,55	8,50
Na	0,04	0,01	0,03	0,00	0,03	0,00	0,02	0,14
K	0,01	0,00	0,00	0,01	0,00	0,01	0,01	0,02
Ti	0,00	0,01	0,00	0,00	0,00	0,00	0,00	0,12
P	5,89	5,81	5,99	5,81	5,87	5,81	5,81	5,43
F	1,14	1,58	1,34	1,54	1,16	1,72	1,61	1,59
Cl	0,06	0,04	0,04	0,07	0,10	0,05	0,06	0,11

* Structural formulas calculated to 26 oxygens per formula unit.

Table 8: Major (wt%) and trace element (ppm) composition and Sr-Nd-Pb-O isotopic ratios of sampled rocks in the MGVF.

Sample	M1	M2	M3	M4	M5	M6	M7	M8	M9	M10	M11	M12
Volcano	*Paracho Viejo*	*Paracho Viejo*	*Paracho Viejo*	*Paracho Viejo*	*Cumbuan*	*Cumbuan*	*Janamo*	*Los Amoles*	*Los Amoles*	*San Miguel*	*Cicapien*	*Cupatacuiro*
Lat.	19.61909	19.63764	19.64212	19.61994	19.64772	19.64794	19.51554	19.58582	19.58165	19.61809	19.59363	19.60947
Long.	-102.07224	-102.07529	-102.08479	-102.07237	-102.06189	-102.07511	-102.11589	-102.12574	-102.12312	-102.10201	-102.09616	-102.08404
SiO_2	52.72	54.84	55.53	55.00	51.90	52.21	59.50	53.21	53.07	51.52	51.20	52.58
TiO_2	0.83	0.95	0.93	0.96	1.09	1.10	0.68	0.81	0.80	0.84	1.74	0.85
Al_2O_3	16.85	16.82	16.82	16.83	18.16	18.06	17.26	17.50	17.38	16.48	17.73	17.38
Fe_2O_3t	8.17	7.72	7.49	7.67	8.59	8.54	6.04	7.96	7.97	8.42	9.73	7.99
MnO	0.14	0.13	0.13	0.13	0.14	0.14	0.10	0.13	0.13	0.13	0.15	0.13
MgO	7.46	6.31	5.89	6.27	5.85	5.97	4.26	7.28	7.34	7.98	5.51	6.71
CaO	9.51	8.09	7.64	7.75	9.75	9.37	6.55	8.71	8.69	9.49	9.29	8.90
Na_2O	3.18	3.28	3.43	3.43	3.47	3.61	4.02	3.84	3.81	3.38	3.97	3.73
K_2O	0.66	1.25	1.28	1.27	0.77	0.87	1.47	0.85	0.86	1.11	1.37	0.84
P_2O_5	0.16	0.24	0.26	0.27	0.25	0.27	0.22	0.20	0.20	0.29	0.47	0.21
l.o.i.	0.00	0.00	0.17	0.15	0.00	0.00	0.00	0.40	0.00	0.02	0.00	0.00
Total	99.51	99.63	99.56	99.73	99.85	99.88	99.96	100.87	100.17	99.66	100.66	99.19
Mg#	69.66	67.25	66.42	67.26	63.13	63.72	63.95	69.70	69.84	70.44	58.77	67.87
Rb	6.20	19.48	20.55	18.91	9.29	10.67	26.28	10.35	10.24	18.05	18.67	10.61
Ba	209	376	419	401	247	285	532	257	253	327	363	273
Sr	481	442	465	444	468	486	534	497	489	889	523	518
Cs	0.258	0.457	0.451	0.420	0.222	0.247	0.760	0.308	0.311	0.530	0.349	0.394
La	7.37	14.98	16.48	16.04	11.46	12.88	16.73	9.73	9.60	18.44	23.18	10.16
Ce	16.38	31.04	33.79	33.04	24.78	27.63	33.07	21.04	20.64	41.50	48.23	21.96
Pr	2.36	4.11	4.42	4.32	3.43	3.78	4.18	2.94	2.85	5.64	6.26	3.07
Nd	10.58	16.76	17.95	17.73	14.96	16.15	16.71	12.55	12.48	23.31	26.01	13.39
Sm	2.60	3.72	3.87	3.83	3.54	3.75	3.36	2.91	2.85	4.55	5.50	3.12
Eu	0.921	1.179	1.195	1.213	1.193	1.285	1.040	0.961	0.939	1.410	1.773	1.034
Gd	2.59	3.58	3.63	3.54	3.48	3.69	2.95	2.75	2.72	3.64	5.05	2.99
Tb	0.415	0.571	0.565	0.555	0.547	0.577	0.446	0.436	0.424	0.533	0.786	0.463
Dy	2.57	3.39	3.43	3.29	3.41	3.51	2.61	2.64	2.64	3.02	4.64	2.77
Ho	0.517	0.686	0.678	0.649	0.690	0.696	0.500	0.530	0.525	0.588	0.915	0.550
Er	1.49	1.95	1.91	1.82	1.95	1.98	1.42	1.52	1.49	1.66	2.57	1.58
Tm	0.225	0.293	0.285	0.279	0.294	0.298	0.213	0.229	0.222	0.248	0.373	0.232
Yb	1.51	1.98	1.95	1.85	1.95	2.00	1.46	1.54	1.52	1.70	2.53	1.60
Lu	0.235	0.318	0.307	0.290	0.310	0.320	0.225	0.249	0.240	0.268	0.395	0.244
Y	14.54	19.83	19.50	18.26	19.74	19.94	14.70	15.12	15.01	16.41	25.27	15.56
Zr	65.48	132.80	141.50	135.30	99.70	107.30	127.20	85.64	83.70	111.70	171.90	86.24
Hf	1.94	3.38	3.65	3.46	2.53	2.75	3.36	2.38	2.33	3.12	4.24	2.37
Nb	2.24	6.54	7.32	7.71	6.24	7.34	4.74	2.88	2.87	4.48	20.62	3.07
Ta	0.171	0.514	0.573	0.603	0.452	0.539	0.400	0.226	0.214	0.345	1.586	0.235
Pb	3.44	5.56	6.02	5.78	3.46	4.04	8.11	4.25	4.18	4.26	3.91	4.28
Th	0.585	1.600	1.696	1.574	0.871	1.018	1.976	0.847	0.827	1.620	2.211	0.937
U	0.224	0.503	0.564	0.531	0.298	0.337	0.625	0.305	0.302	0.607	0.700	0.309
Sc	—	—	—	—	—	—	—	—	—	—	—	—
V	201	159	149	140	208	199	116	176	170	169	209	183
Cr	323	233	215	228	104	145	121	290	297	325	93	248
Co	33.00	31.17	28.76	28.21	29.85	29.30	19.50	29.98	30.31	33.39	30.28	29.11
Ni	93.44	120.70	112.30	117.80	50.09	61.93	73.90	101.80	105.20	138.40	51.24	81.01
Cu	53.35	37.88	39.28	40.85	51.63	39.22	27.68	47.05	44.54	51.80	56.08	47.25
Zn	90.28	80.61	82.55	78.10	85.76	84.94	77.31	79.43	77.30	81.09	87.13	81.38
Li	—	—	—	—	—	—	—	—	—	—	—	—
Be	—	—	—	—	—	—	—	—	—	—	—	—
B	—	—	—	—	—	—	—	—	—	—	—	—
Ga	—	—	—	—	—	—	—	—	—	—	—	—
Mo	—	—	—	—	—	—	—	—	—	—	—	—
Sn	—	—	—	—	—	—	—	—	—	—	—	—
Sb	—	—	—	—	—	—	—	—	—	—	—	—
W	—	—	—	—	—	—	—	—	—	—	—	—
Tl	—	—	—	—	—	—	—	—	—	—	—	—
$^{18}O/^{16}O$	5.83	—	—	—	—	—	—	—	—	—	—	—
Std error	0.42	—	—	—	—	—	—	—	—	—	—	—
$^{87}Sr/^{86}Sr$	0.70381	0.70391	0.70472	0.70449	—	0.70379	—	0.70462	—	0.70326	0.70351	—
± 1SD %	0.002	0.002	0.002	0.002	—	0.002	—	0.002	—	0.002	0.002	—
$^{143}Nd/^{144}Nd$	0.51285	0.51282	0.51275	0.51278	—	0.51281	—	0.51279	—	0.51295	0.51287	—
± 1SD %	0.002	0.002	0.004	0.003	—	0.002	—	0.002	—	0.002	0.002	—
$^{206}Pb/^{204}Pb$	18.604	18.695	18.698	—	—	18.698	—	18.637	—	18.613	18.717	—
± 1SD %	0.014	0.046	0.048	—	—	0.032	—	0.037	—	0.022	0.018	—
$^{207}Pb/^{204}Pb$	15.572	15.592	15.597	—	—	15.607	—	15.579	—	15.564	15.576	—
± 1SD %	0.015	0.055	0.044	—	—	0.037	—	0.039	—	0.025	0.020	—
$^{208}Pb/^{204}Pb$	38.327	38.473	38.488	—	—	38.501	—	38.383	—	38.299	38.398	—
± 1SD %	0.015	0.073	0.046	—	—	0.047	—	0.036	—	0.028	0.022	—

Table 8: Continued.

Sample	M13	M14	M15	M16	M17	M18	M19	M20	M21	M27	M28	M29
Volcano	*Cupatacuiro*	*Parícutin*	*Parícutin*	*Parícutin*	*Parícutin*	*El Jabali*	*El Juanyan*	*El Metate*	*El Metate*	*La Calabaza*	*Cuate*	*Las Cabras*
Lat.	19.60072	19.49462	19.4988	19.53547	19.50717	19.4409	19.683	19.5582	19.5710	19.751	19.795	19.83066
Long.	-102.08476	-102.25587	-102.25767	-102.24743	-102.26365	-102.0782	-101.991	-102.0376	-102.0147	-101.684	-101.968	-101.89577
SiO_2	52.46	59.08	59.65	55.09	57.10	54.23	55.44	61.29	59.52	56.36	60.78	54.73
TiO_2	0.85	0.80	0.82	1.09	0.88	0.93	0.99	0.67	0.73	0.99	0.80	1.04
Al_2O_3	17.33	17.30	17.13	17.49	17.19	17.71	16.88	17.69	17.78	17.41	16.79	17.43
Fe_2O_3t	7.93	6.36	6.50	8.08	7.12	7.56	7.63	5.38	5.90	7.32	6.16	7.95
MnO	0.13	0.10	0.09	0.12	0.10	0.12	0.13	0.09	0.10	0.12	0.10	0.13
MgO	6.67	3.82	3.59	5.46	5.39	6.61	6.25	3.09	3.36	4.92	3.15	6.30
CaO	8.92	6.17	6.28	7.00	6.93	8.08	7.60	6.59	6.88	7.39	5.81	7.54
Na_2O	3.68	4.04	4.09	4.09	4.01	3.84	3.67	3.91	4.13	3.82	3.85	3.61
K_2O	0.83	1.64	1.64	1.24	1.30	0.89	1.20	1.45	1.79	1.46	2.06	1.23
P_2O_5	0.20	0.29	0.29	0.36	0.30	0.21	0.27	0.21	0.32	0.27	0.30	0.06
l.o.i.	0.00	0.00	0.00	0.00	0.00	0.00	0.00	0.34	0.44	0.00	0.49	0.00
Total	98.77	99.57	99.99	100.47	100.25	100.04	99.95	100.70	100.96	99.96	100.29	99.91
Mg#	67.91	60.15	58.13	62.95	65.55	68.76	67.34	59.08	58.90	62.82	56.28	66.59
Rb	10.37	28.63	26.57	16.54	19.42	10.16	17.56	21.76	30.87	25.36	38.44	15.73
Ba	268	577	556	388	426	286	383	430	534	433	595	367
Sr	517	544	517	583	556	588	505	1111	1388	507	457	498
Cs	0.364	0.879	0.786	0.540	0.596	0.493	0.530	0.740	1.033	0.686	0.925	0.497
La	9.98	20.99	20.27	18.62	16.51	10.46	15.91	16.89	23.12	15.92	21.75	15.99
Ce	21.58	41.83	40.64	38.93	33.88	22.89	32.49	35.25	48.70	33.56	45.22	31.57
Pr	3.01	5.34	5.22	5.11	4.48	3.21	4.21	4.55	6.37	4.31	5.66	4.12
Nd	13.16	21.06	20.85	20.96	18.62	14.12	17.39	18.01	25.24	17.51	22.03	16.73
Sm	3.09	4.29	4.34	4.52	4.01	3.25	3.77	3.44	4.72	3.71	4.46	3.78
Eu	1.020	1.167	1.170	1.387	1.234	1.075	1.190	1.088	1.408	1.166	1.203	1.216
Gd	2.95	4.10	4.06	4.57	3.47	2.92	3.51	2.76	3.52	3.50	3.85	3.59
Tb	0.463	0.645	0.629	0.712	0.523	0.459	0.533	0.385	0.474	0.531	0.579	0.589
Dy	2.75	3.41	3.44	3.98	3.08	2.72	3.14	2.17	2.63	3.04	3.28	3.42
Ho	0.547	0.640	0.648	0.785	0.586	0.539	0.615	0.403	0.472	0.600	0.623	0.648
Er	1.56	1.92	1.96	2.27	1.67	1.49	1.73	1.12	1.31	1.67	1.80	1.83
Tm	0.236	0.269	0.273	0.329	0.242	0.219	0.257	0.165	0.187	0.248	0.264	0.277
Yb	1.58	1.79	1.84	2.23	1.64	1.50	1.73	1.11	1.24	1.66	1.84	1.73
Lu	0.244	0.269	0.270	0.336	0.254	0.235	0.275	0.172	0.193	0.263	0.294	0.271
Y	15.39	19.43	19.45	21.90	17.20	14.94	18.04	11.74	13.55	17.00	18.89	16.61
Zr	83.91	177.70	174.22	167.54	138.90	90.68	133.40	121.90	155.30	146.20	183.50	131.44
Hf	2.38	4.42	4.45	4.19	3.51	2.45	3.27	3.35	4.10	3.45	4.39	3.43
Nb	3.05	8.61	7.86	9.95	6.60	3.35	6.83	3.76	4.35	7.94	10.13	6.90
Ta	0.236	0.586	0.528	0.691	0.506	0.249	0.511	0.307	0.344	0.637	0.845	0.523
Pb	4.15	8.61	8.40	6.50	6.52	4.79	5.42	7.03	7.23	6.52	8.89	5.52
Th	0.876	2.151	2.184	1.798	1.669	1.021	1.415	2.195	3.230	1.989	3.057	1.390
U	0.294	0.600	0.637	0.560	0.539	0.336	0.488	0.688	1.061	0.627	1.012	0.459
Sc	—	14.36	15.42	16.80	—	—	—	—	—	—	—	16.43
V	186	115	112	131	131	172	162	108	122	138	105	145
Cr	250	98	84	193	183	207	263	36	54	115	56	231
Co	28.89	18.78	17.76	24.97	24.17	29.50	29.26	15.80	18.32	23.08	16.17	29.94
Ni	78.18	54.51	43.20	96.83	112.60	110.80	118.10	26.06	31.29	55.08	30.51	125.65
Cu	42.24	26.25	24.25	29.94	32.01	40.81	38.61	23.98	28.06	29.62	21.82	38.51
Zn	79.71	81.02	80.28	85.12	87.65	83.44	85.82	76.02	86.22	76.10	80.14	77.64
Li	—	—	—	—	—	—	—	—	—	—	—	—
Be	—	—	—	—	—	—	—	—	—	—	—	—
B	—	—	—	—	—	—	—	—	—	—	—	—
Ga	—	—	—	—	—	—	—	—	—	—	—	—
Mo	—	—	—	—	—	—	—	—	—	—	—	—
Sn	—	—	—	—	—	—	—	—	—	—	—	—
Sb	—	—	—	—	—	—	—	—	—	—	—	—
W	—	—	—	—	—	—	—	—	—	—	—	—
Tl	—	—	—	—	—	—	—	—	—	—	—	—
$^{18}O/^{16}O$	—	—	7.13	—	—	—	—	6.51	—	—	—	6.74
Std error	—	—	0.30	—	—	—	—	0.04	—	—	—	0.04
$^{87}Sr/^{86}Sr$	0.70396	0.70414	0.70416	0.70387	0.70399	0.70344	0.70391	0.70335	0.70322	0.70403	0.70413	—
± 1SD %	0.002	0.002	0.003	0.001	0.003	0.003	0.003	0.003	0.003	0.002	0.002	—
$^{143}Nd/^{144}Nd$	0.51277	0.51276	0.51272	0.51282	0.51278	0.51280	0.51280	0.51282	0.51289	0.51277	0.51274	—
± 1SD %	0.003	0.002	0.002	0.003	0.002	0.002	0.002	0.002	0.002	0.002	0.002	—
$^{206}Pb/^{204}Pb$	18.643	—	18.673	18.665	18.675	18.635	18.709	18.595	18.585	—	18.718	—
± 1SD %	0.049	—	0.029	0.021	0.036	0.037	0.021	0.026	0.020	—	0.019	—
$^{207}Pb/^{204}Pb$	15.582	—	15.577	15.582	15.592	15.578	15.624	15.567	15.567	—	15.605	—
± 1SD %	0.040	—	0.029	0.022	0.035	0.037	0.029	0.026	0.021	—	0.022	—
$^{208}Pb/^{204}Pb$	38.393	—	38.419	38.411	38.452	38.388	38.568	38.302	38.288	—	38.537	—
± 1SD %	0.041	—	0.030	0.023	0.036	0.041	0.039	0.026	0.024	—	0.025	—

Table 8: Continued.

Sample	M30	M31	M33	M34	M35	M36	M37	M38	M39	M40	M41	M42
Volcano	*Las Cabras*	*Las Cabras*	*Capaxtiro*	*Capaxtiro*	*Capaxtiro*	*La Pinerita*	*Cheranguarán*	*Zacán*	*Sta. Catarina*	*El Metate*	*Parícutin*	*Parícutin*
Lat.	19.82636	19.84452	19.84369	19.82256	19.83874	19.3833	19.4627	19.56965	19.61814	19.4534	19.5298	19.52586
Long.	-101.89825	-101.84349	-101.84494	-101.81454	-101.78463	-102.09164	-102.08602	-102.29634	-102.15557	-101.9709	-102.27645	-102.27468
SiO_2	55.43	58.03	62.49	64.34	61.36	51.72	59.11	58.17	59.84	58.20	56.41	56.46
TiO_2	1.09	0.88	0.65	0.54	0.63	1.14	0.77	0.88	0.72	0.70	0.94	0.94
Al_2O_3	17.31	16.06	16.44	16.05	16.24	17.93	17.08	17.86	16.68	18.23	17.59	17.33
Fe_2O_3t	7.86	6.82	5.47	4.60	5.33	9.04	6.23	6.83	5.84	5.89	7.30	7.34
MnO	0.13	0.12	0.10	0.08	0.09	0.15	0.10	0.11	0.09	0.10	0.11	0.11
MgO	5.66	5.25	3.14	2.40	3.01	7.25	4.22	3.85	3.50	3.30	5.37	5.47
CaO	7.40	6.54	5.56	4.74	5.61	8.39	6.46	6.39	6.18	7.20	6.95	6.97
Na_2O	3.60	3.73	3.90	3.85	3.76	3.52	3.78	3.59	3.73	4.19	3.98	4.00
K_2O	1.44	1.68	1.96	2.27	1.92	0.78	1.64	1.65	1.85	1.32	1.29	1.28
P_2O_5	0.11	0.28	0.22	0.18	0.21	0.04	0.23	0.05	0.26	0.24	0.31	0.32
l.o.i.	0.00	0.00	0.08	0.15	0.53	0.00	0.05	0.76	0.42	0.40	0.00	0.00
Total	99.86	99.24	100.00	99.21	98.69	99.76	99.67	100.14	99.11	99.77	100.13	100.00
Mg#	64.42	65.95	59.06	56.69	58.64	66.85	62.99	58.66	60.11	58.47	64.93	65.18
Rb	22.42	32.86	36.54	49.73	37.41	6.07	28.46	26.47	34.72	17.52	19.25	18.97
Ba	401	430	603	703	637	260	563	594	588	376	434	428
Sr	463	397	443	403	472	558	480	566	508	1398	604	590
Cs	0.653	0.860	0.953	1.467	0.976	0.215	0.604	0.766	1.107	0.454	0.648	0.634
La	18.14	16.21	18.08	21.88	20.15	12.63	18.83	22.11	21.02	17.89	18.46	18.02
Ce	37.15	34.82	37.97	41.75	39.26	25.37	37.36	43.83	41.52	38.47	37.90	37.15
Pr	4.83	4.49	4.77	5.05	4.92	3.55	4.72	5.56	5.18	5.10	4.95	4.91
Nd	19.61	18.07	18.53	19.15	19.03	14.81	18.74	22.16	20.27	19.91	20.17	19.96
Sm	4.59	3.92	3.78	3.75	3.84	3.59	3.83	4.85	4.06	3.75	4.32	4.26
Eu	1.405	1.162	1.059	0.970	1.077	1.240	1.111	1.394	1.153	1.176	1.274	1.247
Gd	4.32	3.60	3.26	3.20	3.33	3.48	3.42	4.55	3.59	3.25	4.12	4.13
Tb	0.696	0.558	0.494	0.480	0.501	0.595	0.513	0.723	0.538	0.465	0.662	0.648
Dy	4.18	3.31	2.86	2.78	2.88	3.56	2.94	4.17	3.04	2.34	3.54	3.60
Ho	0.793	0.653	0.541	0.530	0.563	0.690	0.573	0.772	0.591	0.436	0.681	0.670
Er	2.20	1.88	1.59	1.56	1.62	1.90	1.63	2.12	1.64	1.21	1.99	1.99
Tm	0.348	0.285	0.232	0.230	0.239	0.290	0.237	0.325	0.243	0.174	0.289	0.280
Yb	2.13	1.98	1.66	1.62	1.64	1.87	1.59	2.06	1.65	1.15	1.88	1.85
Lu	0.337	0.316	0.261	0.252	0.255	0.285	0.251	0.325	0.257	0.171	0.289	0.283
Y	20.85	19.62	16.39	16.28	16.52	17.76	15.95	21.17	16.09	12.55	20.62	20.29
Zr	156.21	138.90	144.30	165.80	152.10	101.19	148.10	186.03	162.80	119.84	161.31	159.74
Hf	3.87	3.44	3.72	4.15	3.91	2.80	3.87	4.55	4.21	3.29	3.93	3.93
Nb	10.55	9.17	6.28	6.58	6.18	5.64	6.07	7.26	7.22	4.27	8.29	8.20
Ta	0.807	0.828	0.590	0.641	0.573	0.420	0.547	0.541	0.649	0.319	0.525	0.530
Pb	5.98	7.18	9.07	11.18	10.08	4.23	8.47	8.60	9.27	5.46	6.71	6.71
Th	2.114	2.764	3.002	3.740	3.068	0.975	2.246	2.462	2.859	2.006	1.772	1.772
U	0.784	1.166	1.045	1.371	0.995	0.275	0.689	0.615	0.903	0.603	0.502	0.499
Sc	20.30	—	—	—	—	20.59	—	15.74	—	13.14	17.66	17.03
V	143	127	101	80	103	176	121	142	106	118	137	135
Cr	181	196	57	56	53	253	79	77	64	37	208	200
Co	29.35	24.66	15.07	11.76	14.61	38.62	18.87	25.06	15.73	16.74	25.23	24.59
Ni	104.69	96.36	37.35	27.35	34.74	159.17	80.15	56.20	43.00	23.75	107.87	101.10
Cu	38.56	32.22	20.03	20.15	19.34	62.95	28.37	34.43	22.99	21.50	33.02	31.92
Zn	77.60	74.03	73.24	67.87	78.68	84.16	76.96	90.53	74.68	66.17	87.53	85.37
Li	—	—	—	—	—	—	—	—	—	—	—	—
Be	—	—	—	—	—	—	—	—	—	—	—	—
B	—	—	—	—	—	—	—	—	—	—	—	—
Ga	—	—	—	—	—	—	—	—	—	—	—	—
Mo	—	—	—	—	—	—	—	—	—	—	—	—
Sn	—	—	—	—	—	—	—	—	—	—	—	—
Sb	—	—	—	—	—	—	—	—	—	—	—	—
W	—	—	—	—	—	—	—	—	—	—	—	—
Tl	—	—	—	—	—	—	—	—	—	—	—	—
$^{18}O/^{16}O$	—	—	6.82	8.96	—	—	—	—	—	—	—	6.66
Std error	—	—	0.04	0.04	—	—	—	—	—	—	—	0.40
$^{87}Sr/^{86}Sr$	0.70384	—	0.70413	0.70426	0.70411	0.70383	0.70410	0.70410	0.70396	0.70318	0.70397	0.70395
± 1SD %	0.004	—	0.003	0.003	0.003	0.003	0.003	0.003	0.003	0.003	0.002	0.002
$^{143}Nd/^{144}Nd$	0.51288	—	0.51271	0.51273	0.51272	0.51288	0.51273	0.51274	0.51273	0.51288	0.51283	0.51281
± 1SD %	0.002	—	0.002	0.002	0.002	0.002	0.002	0.002	0.002	0.002	0.002	0.002
$^{206}Pb/^{204}Pb$	18.690	—	18.705	18.708	18.728	—	18.690	—	18.706	18.547	18.660	—
± 1SD %	0.027	—	0.027	0.018	0.025	—	0.020	—	0.019	0.039	0.037	—
$^{207}Pb/^{204}Pb$	15.573	—	15.598	15.594	15.628	—	15.590	—	15.611	15.544	15.575	—
± 1SD %	0.029	—	0.026	0.019	0.025	—	0.020	—	0.019	0.038	0.038	—
$^{208}Pb/^{204}Pb$	38.416	—	38.501	38.503	38.602	—	38.471	—	38.538	38.199	38.391	—
± 1SD %	0.03	—	0.027	0.017	0.025	—	0.02	—	0.019	0.037	0.041	—

Table 8: Continued.

Sample	M43	M44	M45	M46	M47	M48	M49	M50	M51	M52	M53	M54
Volcano	*Parícutin*	*Parícutin*	*Parícutin*	*Parícutin*	*Parícutin*	*Parícutin*	*Angahuan*	*Angahuan*	*S.Lorenzo*	*Cherán*	*El Pilón*	*La Mojonera*
Lat.	19.52278	19.52591	19.52302	19.49489	19.48726	19.48193	19.52804	19.52934	19.51415	19.70961	19.7084	19.70272
Long.	-102.24556	-102.23636	-102.22915	-102.22321	-102.23306	-102.24023	-102.18925	-102.1932	-102.11633	-101.89489	-101.8809	-101.84027
SiO_2	56.70	59.67	57.18	56.43	57.43	57.56	55.65	56.84	55.32	61.12	56.90	56.90
TiO_2	0.86	0.80	0.89	1.03	0.82	0.85	1.02	1.10	1.10	0.66	0.80	0.80
Al_2O_3	17.70	17.14	17.50	17.89	17.89	17.77	17.88	17.02	17.36	17.37	18.06	18.06
Fe_2O_3t	6.94	6.41	7.18	7.52	6.80	6.88	7.34	7.35	7.83	5.39	6.86	6.86
MnO	0.10	0.09	0.10	0.11	0.11	0.10	0.12	0.12	0.12	0.07	0.10	0.11
MgO	4.74	3.57	5.29	5.34	4.08	4.15	4.58	4.42	5.14	2.77	3.68	3.88
CaO	6.96	6.20	6.89	7.15	6.58	6.72	7.45	6.61	7.29	6.04	6.70	6.99
Na_2O	4.01	4.04	4.03	4.11	3.98	4.10	3.80	3.97	3.76	3.70	3.85	3.83
K_2O	1.31	1.66	1.29	1.31	1.42	1.38	1.36	1.69	1.45	2.10	1.36	1.36
P_2O_5	0.29	0.29	0.30	0.35	0.29	0.29	0.29	0.51	0.34	0.18	0.21	0.23
l.o.i.	0.00	0.00	0.00	0.00	0.00	0.00	0.00	0.00	0.08	0.42	0.91	0.69
Total	99.58	99.78	100.66	101.00	99.48	99.58	99.44	99.54	99.78	99.83	99.43	99.71
Mg#	63.20	58.35	64.96	64.11	60.16	60.28	61.05	60.16	62.26	56.42	57.40	58.69
Rb	20.38	25.23	21.34	18.40	23.81	23.52	21.54	23.90	22.24	36.53	19.93	23.60
Ba	451	519	476	422	515	519	496	498	465	588	508	397
Sr	581	460	652	596	586	638	513	749	485	536	600	759
Cs	0.691	0.786	0.713	0.598	0.767	0.777	0.527	0.473	0.459	1.191	0.685	0.570
La	17.70	18.82	19.18	19.27	19.75	19.85	18.70	24.71	19.29	19.36	15.79	18.74
Ce	36.32	37.42	39.54	39.70	40.02	40.23	38.84	50.38	39.93	33.92	31.58	32.82
Pr	4.72	4.75	5.21	5.16	5.16	5.24	5.19	6.61	5.30	4.50	4.22	4.81
Nd	19.16	18.91	21.25	21.06	20.80	21.19	20.97	26.28	21.45	17.15	17.23	19.46
Sm	4.04	3.95	4.56	4.46	4.36	4.50	4.84	5.41	4.73	3.43	3.82	4.05
Eu	1.205	1.041	1.358	1.337	1.250	1.276	1.466	1.616	1.420	0.993	1.136	1.277
Gd	3.89	3.83	4.40	4.49	4.28	4.33	4.67	4.96	4.45	3.16	3.45	3.83
Tb	0.604	0.582	0.696	0.697	0.660	0.657	0.752	0.740	0.720	0.479	0.536	0.576
Dy	3.38	3.17	3.77	3.81	3.67	3.72	4.17	3.88	3.86	2.45	2.88	3.10
Ho	0.651	0.586	0.714	0.728	0.673	0.697	0.811	0.738	0.762	0.475	0.545	0.600
Er	1.88	1.80	2.13	2.19	2.02	2.09	2.38	2.04	2.18	1.34	1.55	1.68
Tm	0.266	0.250	0.282	0.297	0.282	0.285	0.340	0.293	0.300	0.188	0.224	0.228
Yb	1.73	1.69	1.95	1.98	1.88	1.89	2.36	1.99	2.05	1.31	1.50	1.50
Lu	0.268	0.255	0.303	0.313	0.290	0.287	0.345	0.296	0.315	0.185	0.223	0.225
Y	19.13	17.59	21.39	21.42	20.57	21.61	24.01	20.79	21.45	13.87	16.03	18.91
Zr	153.57	159.65	170.08	167.41	173.83	176.03	173.25	212.81	175.60	135.81	117.81	123.85
Hf	3.89	4.17	4.26	4.16	4.28	4.19	4.05	4.67	4.11	3.40	3.17	3.28
Nb	7.74	7.16	8.13	9.67	7.88	8.25	9.45	17.38	10.88	5.39	4.41	6.51
Ta	0.504	0.499	0.521	0.630	0.512	0.530	0.614	1.101	0.728	0.441	0.354	0.485
Pb	7.18	7.95	7.27	6.66	7.89	7.60	6.84	7.54	6.48	8.94	7.57	5.60
Th	1.621	2.068	1.877	1.972	1.902	1.823	1.662	2.603	1.771	2.577	1.759	2.026
U	0.466	0.578	0.533	0.541	0.534	0.542	0.492	0.798	0.548	0.794	0.521	0.634
Sc	16.84	12.51	18.33	17.63	15.44	17.11	21.72	15.42	19.72	12.10	16.32	16.24
V	131	101	145	136	124	137	174	126	155	116	162	152
Cr	169	75	227	181	102	119	106	88	151	11	26	54
Co	22.86	16.37	26.13	24.00	20.69	22.90	22.92	20.72	25.09	15.08	20.40	21.70
Ni	83.76	41.07	107.80	88.20	59.71	64.14	52.69	65.89	79.81	23.01	26.00	29.60
Cu	31.03	22.35	33.70	30.90	28.93	31.48	34.94	29.46	33.28	24.38	27.14	26.42
Zn	81.78	72.31	93.30	84.75	87.64	93.85	75.95	73.80	71.32	60.06	78.24	61.49
Li	—	—	—	—	—	—	—	—	—	—	—	—
Be	—	—	—	—	—	—	—	—	—	—	—	—
B	—	—	—	—	—	—	—	—	—	—	—	—
Ga	—	—	—	—	—	—	—	—	—	—	—	—
Mo	—	—	—	—	—	—	—	—	—	—	—	—
Sn	—	—	—	—	—	—	—	—	—	—	—	—
Sb	—	—	—	—	—	—	—	—	—	—	—	—
W	—	—	—	—	—	—	—	—	—	—	—	—
Tl	—	—	—	—	—	—	—	—	—	—	—	—
$^{18}O/^{16}O$	7.05	7.37	—	6.63	—	7.37	—	—	—	—	—	—
Std error	0.40	0.40	—	0.40	—	0.40	—	—	—	—	—	—
$^{87}Sr/^{86}Sr$	0.70403	0.70422	0.70399	0.70389	0.70408	0.70409	0.70396	0.70356	—	0.70413	0.70414	0.70334
± 1SD %	0.002	0.002	0.002	0.002	0.002	0.002	0.003	0.002	—	0.003	0.004	0.004
$^{143}Nd/^{144}Nd$	0.51280	0.51276	0.51273	0.51283	0.51278	0.51277	0.51281	0.51277	—	0.51275	0.51275	0.51282
± 1SD %	0.002	0.002	0.003	0.002	0.002	0.004	0.002	0.002	—	0.004	0.002	0.002
$^{206}Pb/^{204}Pb$	18.679	18.691	—	—	—	18.692	18.688	18.663	—	18.674	18.668	—
± 1SD %	0.020	0.032	—	—	—	0.059	0.043	0.032	—	0.026	0.031	—
$^{207}Pb/^{204}Pb$	15.595	15.597	—	—	—	15.606	15.586	15.568	—	15.578	15.583	—
± 1SD %	0.020	0.036	—	—	—	0.064	0.045	0.035	—	0.031	0.034	—
$^{208}Pb/^{204}Pb$	38.467	38.482	—	—	—	38.497	38.456	38.381	—	38.427	38.429	—
± 1SD %	0.022	0.042	—	—	—	0.068	0.049	0.035	—	0.039	0.038	—

Table 8: Continued.

Sample	M55	M56	M57	M58	M59	M60	M61	M62	M63	M64	M65	M66
Volcano	*La Caja*	*La Mojonera*	*El Metate*	*El Metate*	*El Metate*	*El Metate*	*El Metate*	*El Metate*	*El Metate*	*El Metate*	*El Metate*	*El Metate*
Lat.	19.71491	19.67441	19.5073	19.4903	19.4895	19.4902	19.5575	19.5580	19.5782	19.5764	19.4757	19.4552
Long.	-101.82122	-101.83172	-102.0399	-102.0320	-102.0103	-102.0106	-102.0246	-102.0220	-101.9701	-101.9846	-101.9481	-101.9580
SiO_2	57.78	58.04	55.02	59.96	52.11	57.90	60.07	60.49	59.40	60.09	57.02	59.26
TiO_2	0.81	0.88	0.92	0.71	1.02	0.80	0.69	0.67	0.70	0.68	0.90	0.68
Al_2O_3	17.18	17.75	17.48	17.26	17.79	18.27	18.00	17.26	17.36	17.42	17.29	18.08
Fe_2O_3t	6.69	6.80	7.63	5.93	8.59	6.11	5.66	5.77	6.21	5.89	7.30	5.71
MnO	0.10	0.11	0.13	0.10	0.14	0.11	0.09	0.10	0.11	0.10	0.13	0.10
MgO	3.98	3.51	5.78	3.14	7.18	3.36	3.19	3.36	4.01	3.40	5.05	3.17
CaO	6.95	6.18	7.56	5.77	8.32	7.10	6.58	5.95	6.43	6.11	6.84	6.75
Na_2O	3.63	4.01	3.44	3.86	3.41	3.94	3.98	3.74	3.68	3.78	3.63	4.03
K_2O	1.59	1.66	1.18	2.19	0.93	1.61	1.48	1.92	1.80	1.76	1.49	1.41
P_2O_5	0.24	0.30	0.05	0.10	0.03	0.11	0.00	0.05	0.02	0.01	0.05	0.04
l.o.i.	0.49	0.27	0.50	0.50	0.00	0.26	0.00	0.14	0.24	0.25	0.00	0.30
Total	99.43	99.52	99.68	99.52	99.45	99.56	99.48	99.45	99.95	99.47	99.66	99.53
Mg#	59.95	56.48	65.59	57.14	67.77	58.07	58.66	59.41	61.85	59.20	63.50	58.31
Rb	30.29	25.12	14.49	36.09	11.33	23.36	18.55	33.11	30.66	25.32	21.14	18.58
Ba	518	560	365	702	258	449	402	620	576	497	436	396
Sr	777	503	496	705	532	1586	1120	723	802	606	462	1259
Cs	0.826	0.693	0.424	1.171	0.484	0.710	0.407	1.082	1.091	0.892	0.663	0.589
La	19.41	20.67	15.92	29.61	10.97	24.82	16.99	22.75	20.96	17.41	16.15	19.57
Ce	39.93	41.65	31.36	59.25	22.38	54.32	34.30	44.08	41.32	33.21	31.71	39.22
Pr	5.26	5.52	4.17	7.08	3.20	6.74	4.41	5.52	5.31	4.17	4.08	4.90
Nd	20.83	21.89	16.94	27.62	13.42	26.60	17.05	21.54	21.07	16.31	16.46	19.06
Sm	4.57	4.63	3.94	5.53	3.36	4.97	3.38	4.52	4.52	3.55	3.75	3.67
Eu	1.341	1.335	1.259	1.460	1.184	1.495	1.073	1.233	1.279	1.014	1.127	1.135
Gd	4.23	4.36	3.60	4.51	3.15	3.65	2.79	3.60	3.72	3.04	3.51	2.89
Tb	0.660	0.671	0.616	0.656	0.547	0.538	0.435	0.560	0.567	0.483	0.574	0.447
Dy	3.48	3.58	3.53	3.41	3.22	2.79	2.22	2.91	2.99	2.69	3.27	2.35
Ho	0.665	0.688	0.666	0.607	0.626	0.492	0.421	0.555	0.566	0.504	0.624	0.438
Er	1.91	1.98	1.80	1.65	1.72	1.33	1.19	1.51	1.54	1.40	1.75	1.21
Tm	0.278	0.283	0.271	0.243	0.261	0.188	0.167	0.222	0.226	0.202	0.268	0.171
Yb	1.88	1.93	1.74	1.54	1.70	1.26	1.11	1.46	1.45	1.32	1.74	1.15
Lu	0.271	0.283	0.265	0.238	0.256	0.191	0.162	0.221	0.225	0.205	0.266	0.172
Y	20.24	20.07	17.20	15.87	16.06	13.25	11.38	15.06	15.46	12.79	16.01	11.49
Zr	173.42	182.54	132.25	177.89	93.74	154.35	119.35	158.04	154.09	124.86	131.31	115.21
Hf	3.99	4.28	3.45	4.67	2.58	4.25	3.29	4.06	3.84	3.49	3.52	3.32
Nb	8.46	8.20	8.87	6.94	4.27	4.61	3.98	5.97	4.96	4.89	6.61	4.04
Ta	0.548	0.555	0.765	0.547	0.319	0.345	0.304	0.472	0.370	0.416	0.548	0.311
Pb	7.51	8.07	5.72	9.98	4.18	6.46	5.46	8.93	7.90	7.80	6.60	5.86
Th	2.305	1.813	1.471	3.431	1.041	2.857	2.033	2.956	2.935	2.483	1.804	6.683
U	0.711	0.523	0.450	1.104	0.353	0.904	0.627	0.889	0.915	0.751	0.551	0.642
Sc	19.13	13.69	16.45	10.76	18.52	11.76	10.88	11.48	13.48	11.37	13.51	9.33
V	170	121	131	98	168	116	101	108	128	97	121	97
Cr	76	50	146	48	242	39	29	62	89	53	125	29
Co	23.82	18.56	29.76	16.36	35.68	19.09	16.96	18.68	23.89	16.38	24.46	16.36
Ni	47.79	34.36	132.00	30.35	150.21	24.21	22.81	41.46	55.95	30.13	95.67	19.25
Cu	32.27	24.64	38.17	23.19	39.56	22.75	11.58	25.63	29.80	20.51	27.30	22.63
Zn	80.54	72.62	77.15	77.49	79.74	77.14	66.78	76.16	79.52	63.70	68.91	69.19
Li	—	—	—	—	—	—	—	—	—	—	—	—
Be	—	—	—	—	—	—	—	—	—	—	—	—
B	—	—	—	—	—	—	—	—	—	—	—	—
Ga	—	—	—	—	—	—	—	—	—	—	—	—
Mo	—	—	—	—	—	—	—	—	—	—	—	—
Sn	—	—	—	—	—	—	—	—	—	—	—	—
Sb	—	—	—	—	—	—	—	—	—	—	—	—
W	—	—	—	—	—	—	—	—	—	—	—	—
Tl	—	—	—	—	—	—	—	—	—	—	—	—
$^{18}O/^{16}O$	—	—	6.69	7.25	7.17		6.42	6.67	6.65	—	6.96	—
Std error	—	—	0.17	0.04	0.16	—	0.16	0.16	0.16	—	0.16	—
$^{87}Sr/^{86}Sr$	—	0.70420	0.70396	0.70406	—	0.70310	0.70330	0.70388	0.70375	0.70382	0.70402	0.70324
± 1SD %	—	0.002	0.003	0.002	—	0.002	0.003	0.003	0.002	0.002	0.002	0.003
$^{143}Nd/^{144}Nd$	—	0.51274	0.51281	0.51282	—	0.51295	0.51286	0.51276	0.51285	0.51276	0.51283	0.51288
± 1SD %	—	0.002	0.002	0.002	—	0.002	0.002	0.002	0.003	0.002	0.002	0.002
$^{206}Pb/^{204}Pb$	—	—	18.675	18.661	—	18.537	18.587	18.652	18.634	18.654	18.675	18.572
± 1SD %	—	—	0.035	0.037	—	0.031	0.034	0.024	0.030	0.027	0.025	0.029
$^{207}Pb/^{204}Pb$	—	—	15.580	15.575	—	15.544	15.559	15.577	15.574	15.582	15.575	15.559
± 1SD %	—	—	0.035	0.036	—	0.031	0.034	0.024	0.032	0.027	0.027	0.030
$^{208}Pb/^{204}Pb$	—	—	38.425	38.398	—	38.174	38.274	38.395	38.368	38.407	38.415	38.259
± 1SD %	—	—	0.036	0.036	—	0.03	0.034	0.024	0.031	0.027	0.028	0.029

Table 8: Continued.

Sample	M67	M68	M69	M70	M71	M72	M73	M74	M75	M76	M77	M78
Volcano	*El Metate*	*El Metate*	*El Metate*	*El Metate*	*El Metate*	*El Metate*	*El Metate*	*El Metate*	*El Metate*	*El Metate*	*El Metate*	*El Metate*
Lat.	19.4353	19.5012	19.4924	19.5519	19.5515	19.5471	19.5435	19.5415	19.5396	19.5380	19.5381	19.5387
Long.	-101.8049	-101.6371	-101.9893	-101.9635	-101.9632	-101.9690	-101.9738	-101.9771	-101.9855	-101.9890	-101.9885	-101.9908
SiO_2	53.40	59.36	58.28	58.11	60.85	58.07	57.29	60.23	60.62	60.99	60.69	61.04
TiO_2	0.86	0.71	0.76	0.73	0.60	0.79	0.78	0.69	0.60	0.59	0.60	0.58
Al_2O_3	16.35	17.64	18.21	17.53	17.19	18.53	18.37	17.83	17.77	18.26	18.60	18.01
Fe_2O_3t	7.98	6.10	6.23	6.67	5.53	6.01	6.08	5.81	5.47	5.45	5.45	5.38
MnO	0.11	0.10	0.10	0.10	0.08	0.10	0.10	0.09	0.08	0.08	0.08	0.08
MgO	7.09	4.03	3.45	4.65	3.22	3.37	3.30	3.39	2.88	2.97	3.13	2.98
CaO	7.19	6.44	7.04	6.94	5.99	6.89	6.80	6.06	5.99	5.95	5.94	5.90
Na_2O	3.68	3.83	4.03	3.73	3.78	4.21	4.09	3.93	4.09	4.22	3.99	4.20
K_2O	1.56	1.56	1.22	1.52	1.82	1.73	1.69	1.89	1.38	1.44	1.43	1.45
P_2O_5	0.33	0.00	0.24	0.21	0.21	0.34	0.35	0.27	0.17	0.17	0.17	0.17
l.o.i.	1.18	0.22	0.31	0.22	0.28	0.45	0.25	0.25	0.52	0.36	0.52	0.61
Total	99.73	99.99	99.86	100.42	99.56	100.49	99.09	100.45	99.56	100.47	100.61	100.41
Mg#	69.08	62.43	58.19	63.65	59.46	58.54	57.70	59.48	57.02	57.82	59.11	58.21
Rb	14.53	23.04	17.88	26.87	32.83	—	30.33	33.01	—	22.67	—	—
Ba	685	492	371	487	574	—	505	609	—	462	—	—
Sr	1082	659	1581	695	711	—	1618	921	—	775	—	—
Cs	0.500	0.892	0.419	0.787	1.001	—	0.713	1.126	—	0.680	—	—
La	41.59	16.42	19.52	17.27	19.53	—	25.60	23.16	—	13.76	—	—
Ce	75.61	30.81	43.20	36.09	39.18	—	57.02	48.06	—	27.68	—	—
Pr	8.90	3.96	5.56	4.75	4.98	—	7.46	6.15	—	3.52	—	—
Nd	32.58	15.68	21.53	19.31	19.52	—	28.96	23.90	—	14.20	—	—
Sm	5.28	3.50	3.90	4.02	3.90	—	5.26	4.58	—	2.89	—	—
Eu	1.496	1.054	1.181	1.141	1.069	—	1.464	1.239	—	0.898	—	—
Gd	3.92	3.09	3.16	3.48	3.26	—	3.97	3.57	—	2.48	—	—
Tb	0.565	0.481	0.438	0.502	0.462	—	0.531	0.487	—	0.350	—	—
Dy	2.90	2.64	2.42	2.86	2.62	—	2.76	2.61	—	1.95	—	—
Ho	0.539	0.508	0.475	0.564	0.515	—	0.517	0.501	—	0.388	—	—
Er	1.43	1.41	1.27	1.54	1.39	—	1.36	1.32	—	1.02	—	—
Tm	0.213	0.207	—	—	—	—	—	—	—	—	—	—
Yb	1.31	1.34	1.20	1.46	1.33	—	1.24	1.23	—	0.96	—	—
Lu	0.200	0.206	0.181	0.223	0.200	—	0.184	0.187	—	0.147	—	—
Y	13.84	13.14	13.19	15.89	14.59	—	14.49	14.04	—	10.82	—	—
Zr	115.96	110.29	127.23	137.45	145.47	—	170.04	155.16	—	104.16	—	—
Hf	3.38	3.15	3.29	3.30	3.53	—	4.31	3.84	—	2.63	—	—
Nb	8.24	4.30	5.01	4.82	5.84	—	5.43	5.95	—	3.81	—	—
Ta	0.549	0.358	0.309	0.312	0.395	—	0.331	0.377	—	0.264	—	—
Pb	25.32	7.75	4.84	6.76	8.33	—	6.87	8.10	—	6.67	—	—
Th	2.942	2.068	2.207	2.506	3.092	—	3.067	3.774	—	1.923	—	—
U	0.657	0.649	0.681	0.826	0.979	—	1.072	1.150	—	0.618	—	—
Sc	19.76	13.65	14.68	18.26	13.99	—	14.21	13.71	—	12.46	—	—
V	143	121	120	141	113	—	124	116	—	104	—	—
Cr	435	85	36	88	56	—	37	47	—	27	—	—
Co	35.86	19.91	17.33	22.30	16.21	—	17.66	16.85	—	15.40	—	—
Ni	208.38	44.81	22.12	50.30	28.98	—	23.66	29.16	—	24.36	—	—
Cu	36.45	14.72	29.86	35.43	31.39	—	31.63	33.16	—	28.60	—	—
Zn	103.39	70.09	67.95	68.18	65.71	—	71.38	72.15	—	67.54	—	—
Li	—	—	10.65	12.94	16.62	—	11.91	15.17	—	16.33	—	—
Be	—	—	1.21	1.28	1.40	—	1.48	1.60	—	1.14	—	—
B	—	—	—	—	—	—	—	—	—	—	—	—
Ga	—	—	21.64	19.35	19.57	—	21.73	20.67	—	20.17	—	—
Mo	—	—	0.52	0.98	1.19	—	0.69	1.02	—	0.77	—	—
Sn	—	—	0.99	0.87	0.91	—	1.05	0.94	—	0.80	—	—
Sb	—	—	0.04	0.08	0.10	—	0.06	0.09	—	0.12	—	—
W	—	—	0.16	0.23	0.33	—	0.19	0.28	—	0.23	—	—
Tl	—	—	0.06	0.11	0.13	—	0.10	0.15	—	0.07	—	—
$^{18}O/^{16}O$	—	—	—	—	—	6.48	5.84	6.65	—	—	—	—
Std error	—	—	—	—	—	0.16	0.11	0.16	—	—	—	—
$^{87}Sr/^{86}Sr$	0.70432	0.70402	0.70307	0.70375	0.70371	—	0.70315	0.70368	—	0.70378	—	—
± 1SD %	0.002	0.002	0.003	0.003	0.002	—	0.002	0.002	—	0.002	—	—
$^{143}Nd/^{144}Nd$	0.51271	0.51281	0.51296	0.51274	0.51281	—	0.51298	0.51289	—	0.51283	—	—
± 1SD %	0.002	0.003	0.002	0.002	0.002	—	0.002	0.002	—	0.002	—	—
$^{206}Pb/^{204}Pb$	18.689	18.665	18.550	18.625	18.652	—	18.555	18.625	—	18.636	—	—
± 1SD %	0.030	0.023	0.03	0.02	0.03	—	0.03	0.02	—	0.03	—	—
$^{207}Pb/^{204}Pb$	15.585	15.576	15.569	15.571	15.586	—	15.561	15.579	—	15.582	—	—
± 1SD %	0.030	0.024	0.04	0.02	0.03	—	0.03	0.03	—	0.03	—	—
$^{208}Pb/^{204}Pb$	38.460	38.406	38.257	38.350	38.417	—	38.239	38.366	—	38.392	—	—
± 1SD %	0.03	0.024	0.04	0.02	0.03	—	0.03	0.02	—	0.03	—	—

Table 8: Continued.

Sample	M79	M80	M81	M82	M83	M84	M85	M86	M87	M88	M89	M90
Volcano	*El Metate*	*Cerro El Melón*	*La Soledad*	*Cerro Prieto*	*Cerro Colorado*	*Loma Pitahayera*	*Huitzatarito*	*Cerros Lobería*	*Cerro Colorado*	*El Cerrito Colorado*	*La Loma*	*Cerro El Guilote*
Lat.	19.5389	20.0606	20.0960	20.1387	20.2370	20.2872	20.4860	20.3831	20.4003	20.4102	20.5672	20.6765
Long.	-101.9783	-101.1775	-101.2141	-101.2020	-101.2044	-101.6463	-101.5733	-101.4469	-101.3133	-101.1905	-101.4544	-101.4668
SiO_2	60.77	53.43	50.48	61.05	51.96	54.79	46.89	47.60	53.26	53.25	49.33	50.94
TiO_2	0.58	1.91	1.88	0.82	1.97	1.25	3.23	2.72	1.82	1.89	3.07	1.40
Al_2O_3	18.12	17.02	17.85	17.97	17.95	17.89	17.17	17.11	18.05	18.49	15.53	18.27
Fe_2O_3t	5.29	9.93	9.77	5.63	9.77	8.47	13.51	12.79	9.55	9.65	13.86	9.04
MnO	0.08	0.16	0.15	0.10	0.16	0.14	0.20	0.20	0.16	0.16	0.19	0.17
MgO	2.94	4.36	5.22	2.70	4.32	4.42	5.06	4.49	3.65	3.58	3.51	6.02
CaO	5.83	6.97	7.57	5.80	7.35	7.75	7.98	7.76	6.89	6.73	7.00	9.15
Na_2O	4.08	3.98	4.33	3.69	4.04	3.55	4.15	3.85	4.30	4.33	3.46	3.57
K_2O	1.45	2.00	1.78	2.05	1.64	1.41	1.67	1.94	2.31	2.08	2.46	1.09
P_2O_5	0.18	0.66	0.67	0.22	0.57	0.36	0.74	0.89	0.75	0.77	0.99	0.37
l.o.i.	0.43	0.00	0.00	0.69	0.04	0.72	0.00	0.33	0.00	0.00	0.23	0.06
Total	99.76	100.41	99.70	100.71	99.78	100.74	100.59	99.67	100.72	100.93	99.64	100.08
Mg#	58.29	52.45	57.36	54.71	52.67	56.75	48.50	46.89	48.99	48.27	38.90	62.64
Rb	22.81	69.49	26.14	41.49	38.16	—	27.11	27.60	—	29.95	38.71	15.21
Ba	462	1647	505	576	805	—	486	476	—	570	805	1097
Sr	824	1327	745	558	1096	—	706	627	—	657	451	511
Cs	0.610	1.036	0.233	1.533	0.556	—	0.911	0.301	—	0.489	0.340	0.445
La	14.17	79.71	33.03	20.96	46.50	—	32.59	38.27	—	37.12	48.46	19.68
Ce	28.91	160.38	68.99	40.06	95.37	—	67.04	78.89	—	73.84	101.73	38.76
Pr	3.65	20.06	8.81	5.16	12.33	—	8.53	9.96	—	9.13	13.22	5.47
Nd	14.68	78.61	34.75	20.14	49.93	—	34.81	40.08	—	35.97	53.85	23.51
Sm	2.97	16.61	7.14	4.18	10.76	—	7.60	8.63	—	7.43	11.98	5.33
Eu	0.909	4.625	2.064	1.141	3.157	—	2.371	2.592	—	2.122	3.027	1.715
Gd	2.49	14.99	6.31	3.77	10.29	—	7.05	7.88	—	6.58	11.11	5.30
Tb	0.351	2.220	0.917	0.563	1.516	—	1.027	1.145	—	0.951	1.648	0.789
Dy	1.95	12.92	5.27	3.32	8.97	—	5.81	6.51	—	5.43	9.63	4.79
Ho	0.385	2.469	1.005	0.653	1.753	—	1.076	1.211	—	1.039	1.832	0.963
Er	1.01	6.72	2.70	1.79	4.83	—	2.82	3.19	—	2.77	4.89	2.66
Tm	—	—	—	—	—	—	—	—	—	—	—	—
Yb	0.96	6.14	2.45	1.70	4.31	—	2.39	2.75	—	2.49	4.38	2.45
Lu	0.146	0.897	0.364	0.257	0.640	—	0.348	0.400	—	0.365	0.632	0.368
Y	10.68	69.12	28.03	18.82	52.83	—	29.76	33.23	—	28.59	50.54	28.03
Zr	106.63	662.89	261.71	171.94	377.43	—	241.73	268.01	—	261.28	425.22	140.97
Hf	2.72	13.41	5.39	3.94	8.05	—	5.09	5.61	—	5.47	9.06	3.14
Nb	3.90	78.61	34.75	20.14	49.93	—	34.81	40.08	—	35.97	53.85	23.51
Ta	0.269	5.320	1.905	0.560	2.865	—	2.909	3.344	—	2.705	3.596	0.544
Pb	6.59	14.43	5.39	8.48	8.75	—	3.10	3.64	—	6.48	7.87	3.77
Th	2.082	7.782	2.820	3.080	4.357	—	2.881	3.561	—	3.882	4.214	2.232
U	0.641	2.452	0.900	0.961	1.299	—	0.967	1.064	—	1.249	1.199	0.642
Sc	12.33	43.33	19.75	14.05	33.47	—	20.78	19.15	—	17.11	22.11	28.93
V	103	346	165	112	311	—	215	173	—	161	192	207
Cr	28	155	109	45	126	—	31	30	—	16	9	151
Co	15.17	56.66	30.97	15.46	51.02	—	35.29	32.73	—	23.64	31.90	29.71
Ni	23.44	83.60	72.07	20.18	81.78	—	27.24	23.38	—	14.53	13.91	51.78
Cu	32.07	59.56	40.19	16.61	51.56	—	32.58	32.89	—	29.12	35.77	33.60
Zn	64.16	214.40	91.20	65.72	153.37	—	100.22	110.57	—	99.52	161.57	71.56
Li	15.38	30.01	12.31	11.88	16.96	—	9.01	13.03	—	13.77	11.37	8.91
Be	1.21	4.95	2.26	1.54	3.16	—	2.04	2.50	—	2.41	3.25	1.30
B	—	—	—	—	—	—	—	—	—	—	—	—
Ga	20.33	48.40	20.27	19.24	34.99	—	21.94	22.47	—	22.34	26.67	18.54
Mo	0.78	6.43	2.17	1.45	3.57	—	2.41	3.09	—	3.85	4.40	0.81
Sn	1.62	3.63	1.65	1.16	2.37	—	1.73	1.96	—	1.81	2.55	0.83
Sb	0.10	0.18	0.05	0.12	0.08	—	0.06	0.06	—	0.09	0.07	0.05
W	0.46	1.07	0.31	0.36	0.51	—	0.32	0.46	—	0.78	0.68	0.15
Tl	0.07	0.17	0.06	0.20	0.13	—	0.06	0.03	—	0.05	0.15	0.07
$^{18}O/^{16}O$	6.19	—	5.68	—	—	—	5.34	—	6.40	—	—	6.83
Std error	0.11	—	0.11	—	—	—	0.11	—	0.11	—	—	0.26
$^{87}Sr/^{86}Sr$	0.70386	0.70389	0.70356	0.70403	0.70377	—	0.70338	—	—	0.70378	0.70426	0.70378
± 1SD %	0.003	0.00330	0.003	0.002	0.004	—	0.002	—	—	0.002	0.002	0.004
$^{143}Nd/^{144}Nd$	0.51277	0.51280	0.51293	0.51279	0.51283	—	0.51286	—	—	0.51282	0.51276	0.51284
± 1SD %	0.002	0.00140	0.002	0.002	0.002	—	0.003	—	—	0.002	0.002	0.004
$^{206}Pb/^{204}Pb$	18.637	18.741	18.727	18.703	18.758	—	18.881	—	—	18.766	18.831	18.627
± 1SD %	0.03	0.020	0.023	0.021	0.015	—	0.046	—	—	0.023	0.016	0.019
$^{207}Pb/^{204}Pb$	15.593	15.584	15.579	15.604	15.594	—	15.591	—	—	15.607	15.607	15.578
± 1SD %	0.03	0.020	0.025	0.022	0.014	—	0.045	—	—	0.026	0.018	0.019
$^{208}Pb/^{204}Pb$	38.417	38.489	38.441	38.502	38.523	—	38.629	—	—	38.543	38.668	38.358
± 1SD %	0.03	0.020	0.023	0.022	0.015	—	0.044	—	—	0.030	0.019	0.020

Table 8: Continued.

Sample	M91	M92	M93	M94	M95	M96	M97	M98	M99	M100	M101	M102
Volcano	*La Sanabria*	*La Minilla*	*Cerro Gordo*	*Cerro Sotelo*	*Cerro de La Cruz*	*Cerro Sotelo*	*Cerro de la Cal*	*Palo Blanco*	*Peña Colorada*	*Cerro Guantecillos*	*San Nicolás*	*Rincón de Parangueo*
Lat.	20.6253	20.4389	20.4250	20.4645	20.5354	20.5020	20.5417	20.5083	20.4939	20.4638	20.3867	20.4219
Long.	-101.3256	-100.9070	-100.9878	-101.0812	-101.1942	-101.1344	-101.2138	-101.2053	-101.2122	-101.2067	-101.2502	-101.2579
SiO_2	58.16	53.61	55.03	52.27	48.14	54.71	50.87	50.61	48.40	50.60	50.72	56.86
TiO_2	0.95	1.60	1.53	1.90	2.48	1.61	2.21	2.21	2.80	2.38	2.00	1.44
Al_2O_3	18.02	18.12	17.77	17.46	18.55	17.64	16.33	16.18	15.66	16.24	17.17	17.88
Fe_2O_3t	5.99	8.88	8.50	9.64	12.22	8.75	13.47	13.21	15.14	13.70	10.86	7.89
MnO	0.10	0.14	0.14	0.16	0.18	0.14	0.22	0.21	0.21	0.21	0.19	0.13
MgO	3.81	5.58	4.11	4.77	4.44	4.42	2.65	2.61	3.17	2.46	3.19	2.18
CaO	6.86	7.40	7.58	7.84	7.79	7.53	5.89	6.11	6.54	6.23	7.45	5.99
Na_2O	3.74	3.62	3.69	3.84	3.97	3.71	4.38	4.35	4.01	3.65	4.45	4.52
K_2O	1.62	1.06	1.39	1.50	1.60	1.64	2.95	2.87	2.49	2.23	2.21	2.94
P_2O_5	0.25	0.40	0.43	0.60	0.54	0.47	1.51	1.59	1.29	1.48	0.89	0.48
l.o.i.	0.36	0.08	0.00	0.45	0.00	0.36	0.00	0.00	0.00	0.56	0.77	0.18
Total	99.87	100.49	100.18	100.41	99.91	100.98	100.47	99.93	99.71	99.73	99.89	100.49
Mg#	61.57	61.25	54.89	55.42	47.77	55.98	33.09	33.18	34.49	31.07	42.52	41.00
Rb	22.76	—	—	—	26.88	29.21	51.46	—	38.78	—	30.71	47.62
Ba	467	—	—	—	446	558	921	—	813	—	827	688
Sr	623	—	—	—	685	482	456	—	478	—	554	537
Cs	0.414	—	—	—	0.193	0.830	0.483	—	0.199	—	0.119	0.584
La	15.51	—	—	—	30.20	26.37	66.90	—	55.09	—	42.35	53.21
Ce	34.03	—	—	—	62.36	56.63	137.77	—	115.94	—	90.77	103.47
Pr	4.57	—	—	—	7.83	7.44	17.57	—	15.01	—	11.88	12.49
Nd	19.28	—	—	—	31.72	30.38	70.12	—	61.18	—	48.17	46.62
Sm	4.30	—	—	—	7.01	6.75	15.04	—	13.43	—	10.48	9.08
Eu	1.356	—	—	—	2.130	1.748	3.839	—	3.521	—	3.089	2.086
Gd	3.89	—	—	—	6.52	6.39	13.56	—	12.33	—	9.47	7.76
Tb	0.560	—	—	—	0.962	0.961	1.986	—	1.811	—	1.399	1.146
Dy	3.22	—	—	—	5.57	5.76	11.43	—	10.44	—	8.02	6.66
Ho	0.620	—	—	—	1.056	1.128	2.152	—	1.963	—	1.518	1.292
Er	1.64	—	—	—	2.79	3.10	5.79	—	5.26	—	4.06	3.57
Tm	—	—	—	—	—	—	—	—	—	—	—	—
Yb	1.50	—	—	—	2.47	2.87	5.17	—	4.62	—	3.62	3.35
Lu	0.222	—	—	—	0.360	0.426	0.758	—	0.675	—	0.536	0.503
Y	17.26	—	—	—	28.98	31.63	59.69	—	54.59	—	41.85	34.82
Zr	147.85	—	—	—	222.81	267.90	525.06	—	430.32	—	361.81	367.69
Hf	3.58	—	—	—	4.80	5.69	10.81	—	8.96	—	7.44	7.70
Nb	19.28	—	—	—	31.72	30.38	70.12	—	61.18	—	52.22	37.28
Ta	0.399	—	—	—	2.648	1.028	4.773	—	3.926	—	2.725	2.004
Pb	6.43	—	—	—	3.40	7.03	6.83	—	6.20	—	5.53	6.95
Th	2.026	—	—	—	3.014	2.914	6.027	—	4.354	—	3.256	5.114
U	0.631	—	—	—	0.835	0.923	1.756	—	1.334	—	0.651	1.511
Sc	16.05	—	—	—	18.37	22.41	16.75	—	20.66	—	20.92	16.23
V	127	—	—	—	197	154	69	—	162	—	123	148
Cr	67	—	—	—	8	108	2	—	5	—	40	10
Co	17.76	—	—	—	35.24	24.56	20.93	—	29.25	—	21.04	16.26
Ni	33.08	—	—	—	21.90	36.54	1.60	—	7.48	—	18.15	8.81
Cu	18.99	—	—	—	27.13	29.47	20.44	—	35.48	—	27.10	20.27
Zn	68.56	—	—	—	106.25	90.07	154.25	—	173.28	—	113.05	90.10
Li	7.99	—	—	—	8.96	8.17	14.35	—	17.62	—	13.11	14.01
Be	1.36	—	—	—	2.14	2.03	4.26	—	3.39	—	2.91	2.66
B	—	—	—	—	—	—	—	—	—	—	—	—
Ga	19.82	—	—	—	22.45	20.52	26.56	—	27.68	—	23.26	23.90
Mo	0.90	—	—	—	2.71	1.76	5.97	—	4.66	—	3.13	3.02
Sn	0.85	—	—	—	1.70	1.60	2.68	—	2.16	—	1.83	1.74
Sb	0.05	—	—	—	0.05	0.06	0.08	—	0.06	—	0.03	0.08
W	0.15	—	—	—	0.51	0.41	0.83	—	0.72	—	0.48	0.57
Tl	0.12	—	—	—	0.04	0.15	0.04	—	0.02	—	0.03	0.16
$^{18}O/^{16}O$	—	6.64	7.13	7.21	6.30	—	—	5.76	—	—	—	7.38
Std error	—	0.11	0.11	0.26	0.26	—	—	0.26	—	—	—	0.36
$^{87}Sr/^{86}Sr$	0.70412	—	—	—	—	0.70414	0.70382	—	0.70414	—	—	0.70368
± 1SD %	0.003	—	—	—	—	0.002	0.003	—	0.003	—	—	0.004
$^{143}Nd/^{144}Nd$	0.51269	—	—	—	—	0.51275	0.51281	—	0.51278	—	—	0.51278
± 1SD %	0.002	—	—	—	—	0.003	0.002	—	0.002	—	—	0.002
$^{206}Pb/^{204}Pb$	18.650	—	—	—	—	18.745	18.771	—	18.810	—	—	18.748
± 1SD %	0.017	—	—	—	—	0.016	0.030	—	0.033	—	—	0.024
$^{207}Pb/^{204}Pb$	15.585	—	—	—	—	15.601	15.596	—	15.611	—	—	15.600
± 1SD %	0.019	—	—	—	—	0.019	0.031	—	0.041	—	—	0.026
$^{208}Pb/^{204}Pb$	38.403	—	—	—	—	38.527	38.603	—	38.656	—	—	38.544
± 1SD %	0.020	—	—	—	—	0.023	0.034	—	0.046	—	—	0.024

Table 8: Continued.

Sample	M103	M104	M105	M106	M107	M108	M109	M110	M111	M112	M113	M114
Volcano	*La Alberca*	*Hoya Blanca*	*Hoya Pequeña*	*Hoya de Cintora*	*Cerro La Batea*	*Hoya Álvarez*	*Cerro Colorado*	*San Vicente de Joyuelo*	*Pantaleón*	*Cerros de las Tetillas*	*Cerros de las Tetillas*	*Inchamácuaro*
Lat.	20.3866	20.3805	20.3684	20.3625	20.3396	20.3268	20.2362	20.2389	19.9969	20.0328	20.0350	20.0863
Long.	-101.2003	-101.2151	-101.2285	-101.2222	-101.1925	-101.1996	-101.2530	-101.2264	-100.8098	-100.8444	-100.8378	-100.8400
SiO_2	52.66	55.08	51.36	51.48	54.35	58.24	52.80	47.43	61.05	55.73	53.36	56.27
TiO_2	1.76	1.68	1.70	2.05	1.61	1.41	1.95	3.00	1.09	1.11	1.90	1.40
Al_2O_3	17.93	17.44	16.91	17.28	17.79	17.90	16.74	17.81	16.33	18.77	17.30	17.26
Fe_2O_3t	9.77	8.52	12.02	11.30	8.90	7.62	9.80	12.67	8.23	7.41	9.98	7.83
MnO	0.16	0.14	0.24	0.20	0.14	0.11	0.15	0.19	0.13	0.12	0.17	0.13
MgO	3.94	3.80	2.23	3.40	4.12	2.64	4.37	5.36	1.44	4.13	4.11	3.68
CaO	7.07	6.73	6.00	7.02	7.16	5.71	6.73	8.19	4.21	7.21	7.21	7.31
Na_2O	4.08	4.02	4.94	4.41	3.86	4.17	4.17	3.96	4.51	3.64	3.71	3.63
K_2O	1.92	2.37	2.86	2.22	1.74	2.25	2.24	1.78	2.93	1.61	1.76	1.84
P_2O_5	0.57	0.54	1.07	0.93	0.50	0.38	0.46	0.61	0.48	0.24	0.52	0.33
l.o.i.	0.00	0.01	0.00	0.00	0.54	0.26	0.19	0.00	0.00	0.01	0.03	0.40
Total	99.86	100.32	99.32	100.27	100.70	100.69	99.59	100.99	100.07	99.97	100.07	100.07
Mg#	50.33	52.88	31.82	43.09	53.79	46.53	52.85	51.52	30.63	58.37	50.89	54.16
Rb	26.15	80.96	42.17	32.68	—	46.27	44.49	25.84	66.83	29.77	28.95	34.58
Ba	567	988	1256	870	—	641	402	400	764	469	696	550
Sr	844	1332	536	585	—	528	516	679	384	610	561	500
Cs	0.166	0.778	0.321	0.064	—	0.779	0.368	0.364	2.052	0.843	0.831	1.127
La	31.73	59.78	56.52	46.03	—	24.26	30.34	31.51	40.72	18.29	27.12	22.14
Ce	66.83	123.58	119.30	97.97	—	49.06	61.43	63.86	85.48	36.59	57.90	47.58
Pr	8.51	15.45	15.55	12.81	—	6.13	7.38	7.79	11.89	4.93	7.80	6.15
Nd	33.83	60.46	63.07	52.12	—	24.41	28.77	31.05	44.31	20.15	32.26	25.04
Sm	6.80	12.37	13.61	11.29	—	5.24	6.22	6.58	9.58	4.40	7.27	5.56
Eu	1.962	3.359	4.246	3.335	—	1.466	1.756	2.147	2.111	1.396	2.003	1.586
Gd	5.75	10.70	12.22	10.26	—	4.81	5.79	6.15	8.91	4.28	7.04	5.33
Tb	0.822	1.560	1.792	1.503	—	0.712	0.870	0.904	1.355	0.641	1.061	0.803
Dy	4.59	8.93	10.35	8.65	—	4.12	5.07	5.20	8.01	3.78	6.29	4.76
Ho	0.875	1.701	1.952	1.612	—	0.803	0.970	0.981	1.474	0.715	1.161	0.892
Er	2.36	4.64	5.21	4.29	—	2.14	2.59	2.60	4.22	2.01	3.29	2.51
Tm	—	—	—	—	—	—	—	—	—	—	—	—
Yb	2.13	4.28	4.68	3.74	—	1.98	2.38	2.28	3.98	1.87	3.03	2.32
Lu	0.320	0.627	0.683	0.554	—	0.291	0.341	0.332	0.585	0.276	0.446	0.342
Y	24.33	47.60	53.39	44.17	—	22.17	26.73	26.64	45.83	21.04	36.12	26.59
Zr	219.21	400.00	451.62	380.33	—	195.24	233.98	223.72	430.37	145.13	275.05	214.91
Hf	4.87	9.17	9.23	7.96	—	4.44	5.26	4.75	8.58	3.22	5.47	4.52
Nb	28.66	63.31	76.30	55.27	—	21.64	44.77	51.88	27.61	9.61	19.16	11.58
Ta	1.698	4.165	4.062	2.951	—	1.363	2.937	3.099	1.497	0.641	1.121	0.720
Pb	5.84	12.80	7.38	6.40	—	7.96	5.65	2.62	13.63	3.46	5.09	7.52
Th	3.514	9.625	4.487	3.659	—	3.727	5.186	3.334	6.355	2.660	3.165	3.472
U	1.035	2.726	1.265	0.457	—	1.137	1.471	1.026	2.262	0.885	1.092	1.023
Sc	17.07	33.74	22.42	22.36	—	14.75	16.48	23.07	13.73	15.48	17.78	18.96
V	175	312	45	130	—	143	163	272	68	153	152	165
Cr	18	83	6	38	—	18	55	24	3	58	31	48
Co	24.74	43.18	13.40	21.93	—	18.02	27.49	36.89	11.36	22.98	28.45	21.20
Ni	18.09	43.59	4.09	17.82	—	10.84	33.61	22.60	1.04	29.89	23.19	13.29
Cu	26.93	46.61	17.02	26.22	—	22.02	27.15	31.85	15.94	22.00	26.78	27.58
Zn	92.52	146.63	141.19	121.57	—	80.26	86.00	105.77	105.42	76.23	103.41	79.17
Li	12.04	27.92	18.78	14.76	—	12.57	16.87	8.11	26.03	7.97	9.41	10.43
Be	1.94	4.36	3.55	2.00	—	1.94	2.67	1.96	3.11	1.53	2.07	1.57
B	—	—	—	—	—	—	—	—	—	—	—	—
Ga	21.86	39.42	26.72	24.65	—	20.90	21.14	23.24	24.18	19.82	21.50	20.37
Mo	2.02	4.39	5.54	2.59	—	1.74	2.60	2.96	2.78	1.29	1.95	1.65
Sn	1.12	3.57	2.58	2.06	—	1.47	2.38	1.54	3.29	0.76	1.58	1.47
Sb	0.05	0.13	0.06	0.01	—	0.10	0.08	0.06	0.11	0.08	0.07	0.10
W	0.34	0.98	0.73	0.35	—	0.82	0.66	0.47	0.47	0.30	0.32	0.30
Tl	0.04	0.13	0.05	0.04	—	0.16	0.10	0.03	0.40	0.06	0.09	0.22
$^{18}O/^{16}O$	—	—	6.44	6.23	—	—	—	—	7.81	7.29	7.88	7.21
Std error	—	—	0.36	0.36	—	—	—	—	0.36	0.36	0.36	0.36
$^{87}Sr/^{86}Sr$	—	0.70378	0.70375	0.70371	—	0.70398	—	0.70353	0.70417	0.70384	0.70400	0.70411
± 1SD %	—	0.003	0.004	0.002	—	0.002	—	0.002	0.002	0.003	0.001	0.002
$^{143}Nd/^{144}Nd$	—	0.51284	0.51284	0.51285	—	0.51278	—	0.51288	0.51282	0.51279	0.51279	0.51276
± 1SD %	—	0.003	0.002	0.002	—	0.002	—	0.002	0.003	0.005	0.002	0.002
$^{206}Pb/^{204}Pb$	—	18.731	18.754	18.748	—	18.749	—	18.783	18.785	18.725	18.753	18.757
± 1SD %	—	0.023	0.022	0.032	—	0.014	—	0.019	0.022	0.026	0.028	0.026
$^{207}Pb/^{204}Pb$	—	15.598	15.581	15.579	—	15.604	—	15.579	15.630	15.604	15.607	15.623
± 1SD %	—	0.022	0.028	0.033	—	0.015	—	0.020	15.630	15.604	15.607	15.623
$^{208}Pb/^{204}Pb$	—	38.510	38.545	38.502	—	38.561	—	38.552	38.636	38.513	38.536	38.594
± 1SD %	—	0.024	0.034	0.034	—	0.014	—	0.022	0.032	0.036	0.027	0.026

Table 8: Continued.

Sample	M115	M116	M117	M118	M119	M120	M121	M122	M123	M124	M125	M126
Volcano	*Obrajuelo*	*Estancia del Cármen*	*Estancia del Cármen*	*Salvatierra*	*Esancia del Cármen*	*Cerro de las Cruces*	*Cerro Ascañas*	*Maar de Yuriria*	*Cerro Poruyo*	*Cupareo*	*Panales Jamaica*	*Las Tetillas*
Lat.	20.0863	20.0861	20.0868	20.1834	20.1066	20.0945	20.0866	20.2012	20.1609	20.2295	20.3146	20.2015
Long.	-100.8735	-100.8869	-100.8827	-100.8926	-100.9144	-100.9802	-100.9864	-101.1308	-101.0838	-100.9931	-100.8267	-100.9133
SiO_2	57.12	57.69	56.93	55.13	57.93	56.77	53.43	57.52	56.62	51.94	54.11	55.25
TiO_2	1.29	1.44	1.36	1.43	1.29	1.44	1.74	1.10	1.41	1.81	1.04	1.44
Al_2O_3	18.34	16.94	17.24	16.87	16.92	17.42	16.49	17.33	17.06	16.93	18.63	16.87
Fe_2O_3t	7.01	7.85	7.81	8.54	7.42	7.86	9.81	7.34	8.27	10.40	7.80	8.56
MnO	0.11	0.13	0.11	0.14	0.12	0.13	0.16	0.12	0.13	0.17	0.13	0.14
MgO	2.89	2.98	3.19	4.83	3.51	3.33	5.23	3.61	3.81	5.35	4.97	4.69
CaO	7.34	6.59	7.17	6.95	6.07	6.02	7.76	6.87	6.53	8.28	8.33	7.06
Na_2O	3.76	4.01	3.90	3.56	3.88	3.96	3.48	3.43	3.71	3.39	3.37	3.58
K_2O	1.68	1.80	1.64	1.95	2.06	2.39	1.38	1.89	1.91	1.02	0.88	1.86
P_2O_5	0.29	0.34	0.32	0.47	0.48	0.58	0.46	0.28	0.39	0.55	0.23	0.47
l.o.i.	0.24	0.30	0.42	0.09	0.41	0.08	0.13	0.57	0.13	0.23	0.58	0.12
Total	100.07	100.07	100.10	99.96	100.07	99.97	100.07	100.06	99.97	100.07	100.07	100.05
Mg#	50.93	48.84	50.68	58.71	54.31	51.55	57.27	55.32	53.67	56.40	61.56	57.95
Rb	36.97	41.57	38.66	30.16	37.48	35.49	—	29.04	33.35	11.65	13.52	29.84
Ba	512	643	878	504	751	628	—	511	449	400	293	742
Sr	535	470	467	556	544	582	—	590	577	535	709	567
Cs	0.898	0.860	1.212	0.719	0.946	0.759	—	0.849	0.751	0.186	0.284	0.711
La	22.29	28.95	41.21	29.15	30.75	31.59	—	20.09	24.42	20.23	12.11	30.04
Ce	44.50	56.08	66.55	60.69	60.29	64.18	—	42.07	50.62	45.40	28.41	61.85
Pr	5.92	7.18	10.27	7.78	7.68	8.09	—	5.34	6.41	6.37	3.80	8.04
Nd	24.02	29.36	38.69	31.20	30.04	31.52	—	21.43	25.71	27.78	16.41	32.11
Sm	5.29	6.39	8.06	6.59	6.16	6.50	—	4.61	5.52	6.52	3.77	6.78
Eu	1.567	1.760	2.206	1.729	1.721	1.867	—	1.377	1.581	1.976	1.318	1.799
Gd	5.15	6.39	7.84	6.11	5.65	5.84	—	4.35	5.16	6.46	3.75	6.31
Tb	0.768	0.956	1.160	0.906	0.826	0.849	—	0.646	0.770	0.976	0.570	0.932
Dy	4.54	5.72	6.78	5.25	4.71	4.80	—	3.76	4.49	5.89	3.46	5.41
Ho	0.848	1.108	1.350	1.028	0.876	0.885	—	0.702	0.887	1.165	0.690	1.015
Er	2.37	3.12	3.67	2.87	2.47	2.46	—	1.98	2.47	3.22	1.94	2.86
Tm	—	—	—	—	—	—	—	—	—	—	—	—
Yb	2.15	2.86	3.25	2.64	2.26	2.26	—	1.85	2.31	2.95	1.82	2.65
Lu	0.317	0.425	0.470	0.395	0.342	0.328	—	0.276	0.346	0.436	0.271	0.394
Y	27.09	33.74	37.36	28.50	26.43	25.88	—	20.70	24.41	31.60	18.80	30.22
Zr	187.07	226.42	211.32	272.53	256.45	265.10	—	176.05	204.00	215.72	119.17	279.01
Hf	3.95	4.89	4.90	5.72	5.26	5.44	—	3.83	4.66	4.66	2.76	5.54
Nb	10.50	12.03	11.20	22.40	25.24	33.71	—	12.29	20.20	11.86	5.39	22.67
Ta	0.659	0.773	0.762	1.270	1.428	1.909	—	0.763	1.349	0.721	0.335	1.225
Pb	7.39	7.45	7.33	7.50	9.01	8.42	—	7.50	7.43	5.09	3.81	7.53
Th	3.602	3.964	3.581	3.063	3.306	3.394	—	2.306	3.387	1.165	1.334	3.055
U	1.039	1.106	1.032	0.960	1.105	1.211	—	0.761	1.025	0.384	0.328	1.000
Sc	17.01	18.45	19.27	16.89	13.92	13.65	—	15.23	15.14	22.91	17.77	17.63
V	142	161	162	150	124	124	—	155	158	207	172	154
Cr	32	24	57	117	58	45	—	44	54	88	91	122
Co	17.59	22.74	19.08	26.04	19.69	18.89	—	21.18	23.57	30.83	24.55	26.01
Ni	10.98	8.44	12.27	59.60	30.68	21.74	—	21.44	27.62	43.66	32.68	50.92
Cu	22.79	25.34	24.38	29.95	24.54	25.78	—	23.80	26.59	28.71	18.12	31.82
Zn	71.82	82.14	75.86	91.12	81.73	86.49	—	79.86	83.77	93.61	71.31	91.77
Li	10.37	10.43	12.03	9.42	11.14	11.07	—	10.02	13.81	9.18	9.24	10.93
Be	1.58	1.89	1.81	1.97	2.10	2.26	—	1.48	1.98	1.52	1.00	1.97
B	—	—	—	—	—	—	—	—	—	—	—	—
Ga	20.62	20.44	20.19	20.34	20.33	21.15	—	20.49	20.77	19.98	19.11	20.65
Mo	1.41	1.56	1.37	2.15	2.52	2.95	—	1.79	2.15	1.41	1.02	2.18
Sn	1.36	1.55	1.60	1.61	1.63	1.61	—	1.14	1.67	1.23	0.78	1.66
Sb	0.09	0.10	0.09	0.09	0.14	0.13	—	0.10	0.11	0.06	0.07	0.09
W	0.26	0.30	0.29	0.34	0.38	0.37	—	0.37	0.39	0.20	0.29	0.32
Tl	0.18	0.12	0.18	0.18	0.21	0.10	—	0.15	0.13	0.05	0.05	0.15
$^{18}O/^{16}O$	7.32	7.65	8.17	6.98	7.25	6.65	—	—	6.54	6.79	—	7.36
Std error	0.36	0.42	0.33	0.42	0.33	0.42	—	—	0.17	0.17	—	0.17
$^{87}Sr/^{86}Sr$	0.70407	0.70414	0.70414	0.70393	0.70392	0.70393	—	0.70404	0.70360	0.70405	0.70373	0.70402
± 1SD %	0.003	0.002	0.002	0.003	0.003	0.002	—	0.002	0.002	0.004	0.003	0.005
$^{143}Nd/^{144}Nd$	0.51273	0.51274	0.51273	0.51279	0.51279	0.51284	—	0.51280	0.51279	0.51275	0.51278	0.51280
± 1SD %	0.004	0.002	0.002	0.002	0.002	0.002	—	0.002	0.005	0.002	0.002	0.002
$^{206}Pb/^{204}Pb$	18.731	18.754	18.760	18.737	18.747	18.767	—	18.716	18.711	18.747	18.700	18.741
± 1SD %	0.026	0.021	0.024	0.023	0.023	0.025	—	0.025	0.022	0.026	0.024	0.044
$^{207}Pb/^{204}Pb$	15.599	15.619	15.628	15.606	15.611	15.616	—	15.609	15.601	15.616	15.605	15.613
± 1SD %	15.599	15.619	15.628	15.606	15.611	0.026	—	0.024	0.022	0.026	0.024	0.046
$^{208}Pb/^{204}Pb$	38.523	38.592	38.618	38.545	38.555	38.566	—	38.539	38.509	38.563	38.497	38.562
± 1SD %	0.026	0.021	0.028	0.032	0.025	0.027	—	0.026	0.023	0.028	0.027	0.048

Table 8: Continued.

Sample	M127	M128	M129	M130	M131	M132	M133	M134	M135	M136	M137	M138
Volcano	*Cerro Tetillas*	*Uriréo*	*Chamacuero*	*Chamacuero*	*El Pilar*	*Las Letras*	*Las Ranas*	*Janamuato*	*Janamuato*	*Alberca de Los Espinos*	*Caurio*	*Alberca de Guadalupe*
Lat.	20.2144	20.2040	19.3016	19.3016	20.2410	20.2273	20.2168	20.0990	20.1138	19.9039	19.8941	19.8018
Long.	-100.9203	-100.8121	-99.1830	-99.1838	-101.4092	-101.4449	-101.4587	-101.5794	-101.5956	-101.7725	-101.8142	-101.4525
SiO_2	55.48	58.52	54.63	54.99	53.18	56.99	54.54	55.75	51.81	59.08	60.68	58.26
TiO_2	1.45	0.95	1.09	1.07	1.19	1.18	1.46	1.26	1.83	0.92	0.70	0.90
Al_2O_3	16.82	17.27	17.61	17.62	16.74	17.61	17.28	17.42	17.17	17.16	17.17	17.45
Fe_2O_3t	8.62	6.73	8.12	7.81	8.11	7.34	8.60	7.96	9.73	6.73	5.64	6.74
MnO	0.14	0.11	0.13	0.12	0.12	0.10	0.13	0.13	0.15	0.11	0.10	0.11
MgO	4.78	3.94	5.31	4.99	5.68	3.68	4.50	4.03	5.40	3.56	3.59	3.81
CaO	7.05	6.47	7.81	7.57	8.07	6.61	7.41	6.94	7.49	6.15	6.08	6.76
Na_2O	3.62	3.49	3.79	3.68	4.19	4.06	4.19	3.92	4.22	4.11	4.03	3.91
K_2O	1.77	1.96	1.23	1.45	1.90	1.53	1.42	1.77	1.44	1.91	1.72	1.62
P_2O_5	0.48	0.28	0.27	0.28	0.55	0.33	0.44	0.39	0.59	0.34	0.22	0.25
l.o.i.	0.00	0.33	0.04	0.04	0.07	0.06	0.05	0.06	0.05	0.08	0.06	0.06
Total	100.06	100.05	100.03	99.61	99.79	99.49	100.02	99.62	99.88	100.15	99.96	99.87
Mg#	58.26	59.56	62.20	61.64	63.79	55.79	56.84	56.03	58.26	57.13	61.57	58.71
Rb	31.40	36.45	23.00	24.20	31.14	30.66	24.09	30.91	24.17	37.56	35.28	36.71
Ba	513	520	399	399	701	566	497	527	554	668	523	540
Sr	564	547	786	808	1005	606	650	585	589	536	673	578
Cs	0.710	1.052	0.210	0.371	0.781	0.800	0.658	0.669	0.507	0.737	0.845	1.307
La	29.16	23.05	19.93	19.01	37.99	35.87	48.61	24.68	30.49	26.62	17.69	19.76
Ce	61.68	47.96	42.22	42.58	79.36	48.82	57.42	52.54	65.14	55.30	37.02	39.89
Pr	7.92	6.12	5.40	5.39	9.40	8.17	9.48	6.62	8.35	6.97	4.75	5.14
Nd	31.66	24.35	21.77	21.59	36.78	32.45	43.00	26.38	33.45	26.83	18.43	19.93
Sm	6.72	5.14	4.60	4.57	6.92	6.67	8.49	5.64	7.20	5.53	3.79	4.17
Eu	1.753	1.343	1.367	1.348	1.856	1.868	2.348	1.550	2.031	1.461	1.070	1.223
Gd	6.22	4.74	4.39	4.26	5.68	6.74	8.62	5.19	6.79	4.99	3.39	3.82
Tb	0.923	0.704	0.656	0.632	0.772	0.965	1.219	0.768	1.012	0.736	0.496	0.561
Dy	5.35	4.10	3.89	3.73	4.07	5.63	7.06	4.49	5.96	4.29	2.85	3.23
Ho	0.989	0.801	0.780	0.746	0.768	1.127	1.399	0.879	1.162	0.851	0.571	0.617
Er	2.79	2.24	2.15	2.04	2.05	3.06	3.79	2.40	3.19	2.35	1.57	1.71
Tm	—	—	—	—	—	—	—	—	—	—	—	—
Yb	2.60	2.11	2.01	1.92	1.83	2.69	3.28	2.23	2.92	2.26	1.53	1.59
Lu	0.385	0.315	0.303	0.288	0.270	0.400	0.480	0.333	0.432	0.340	0.232	0.238
Y	29.61	22.71	22.17	20.37	20.96	33.80	42.75	24.40	32.37	23.30	16.34	17.46
Zr	274.52	210.86	168.09	170.43	193.03	189.68	200.81	218.65	279.88	229.26	147.43	146.74
Hf	5.41	4.63	3.77	3.89	4.47	4.31	4.50	4.73	5.71	5.23	3.61	3.40
Nb	22.46	10.10	9.54	9.11	15.05	12.11	15.32	16.40	25.84	14.05	6.72	8.99
Ta	1.204	0.641	0.584	0.567	0.843	0.728	0.888	0.961	1.557	0.855	0.568	0.572
Pb	7.45	8.28	5.21	5.64	8.73	7.83	6.66	7.55	5.92	9.51	7.66	7.96
Th	3.041	3.549	1.683	1.845	3.874	2.460	2.295	2.324	2.981	2.741	2.681	2.263
U	0.961	0.958	0.590	0.619	1.125	0.784	0.764	0.795	0.871	0.898	0.873	0.809
Sc	17.33	14.97	21.32	20.50	20.40	18.59	21.53	19.43	21.62	17.16	15.65	18.08
V	152	133	155	153	170	138	158	154	155	120	110	127
Cr	127	93	109	100	135	61	76	48	125	58	63	63
Co	26.20	20.31	28.38	25.77	28.07	20.55	24.80	22.33	29.40	18.69	17.75	20.55
Ni	52.38	34.51	63.75	50.79	86.11	30.17	34.32	36.83	75.48	35.69	39.56	38.68
Cu	29.68	25.49	37.38	36.10	53.71	31.00	31.36	37.73	39.37	33.35	29.16	33.81
Zn	92.26	75.81	80.56	77.46	98.95	85.06	91.88	84.99	91.33	77.83	65.87	71.98
Li	9.97	11.71	7.89	9.86	15.22	8.13	12.23	10.65	11.55	18.32	16.78	13.60
Be	2.01	1.57	1.27	1.28	1.90	1.56	1.80	1.61	1.96	1.65	1.26	1.30
B	—	—	5.41	6.64	7.04	8.56	7.66	12.93	5.44	13.37	10.54	15.41
Ga	20.65	19.64	19.99	20.05	21.45	20.35	21.46	20.82	20.73	19.98	19.62	19.72
Mo	2.15	1.66	0.68	0.83	1.12	1.01	1.20	1.38	1.56	1.63	0.93	0.83
Sn	1.61	1.42	1.08	1.12	1.28	1.21	1.31	1.35	1.71	1.42	0.91	1.10
Sb	0.09	0.11	0.06	0.06	0.09	0.08	0.08	0.09	0.08	0.12	0.11	0.15
W	0.30	0.36	0.21	0.20	0.22	0.25	0.28	0.28	0.29	0.35	0.27	0.28
Tl	0.13	0.21	0.06	0.11	0.19	0.13	0.11	0.11	0.15	0.10	0.06	0.14
$^{18}O/^{16}O$	7.51	7.91	—	—	—	—	—	—	—	—	—	—
Std error	0.17	0.17	—	—	—	—	—	—	—	—	—	—
$^{87}Sr/^{86}Sr$	0.70392	0.70406	0.70341	0.70342	0.70425	0.70410	0.70409	0.70407	0.70373	0.70393	0.79360	0.70402
± 1SD %	0.002	0.002	0.003	0.002	0.003	0.003	0.003	0.002	0.004	0.002	0.004	0.003
$^{143}Nd/^{144}Nd$	0.51281	0.51275	0.51286	0.51286	0.51284	0.51278	0.51282	0.51285	0.51285	0.51279	0.51277	0.51280
± 1SD %	0.003	0.002	0.001	0.002	0.002	0.002	0.002	0.004	0.002	0.002	0.002	0.003
$^{206}Pb/^{204}Pb$	18.745	18.722	18.671	18.663	18.716	18.715	18.712	18.716	18.749	18.712	—	—
± 1SD %	0.030	0.022	0.020	0.017	0.030	0.028	0.022	0.025	0.027	0.017	—	—
$^{207}Pb/^{204}Pb$	15.618	15.609	15.584	15.576	15.599	15.600	15.598	15.599	15.601	15.602	—	—
± 1SD %	0.037	0.023	0.018	0.016	0.029	0.029	0.022	0.026	0.032	0.020	—	—
$^{208}Pb/^{204}Pb$	38.578	38.540	38.419	38.391	38.490	38.503	38.484	38.497	38.517	38.512	—	—
± 1SD %	0.043	0.022	0.020	0.017	0.030	0.030	0.023	0.026	0.038	0.021	—	—

Table 8: Continued.

Sample	M139	M140	M141	M142	M143	M144
Volcano	*La Alberca*	*Tzintzimacato Chico*	*San Bernabé*	*Las Trojes*	*La Noria*	*Iratzio*
Lat.	19.7991	19.7872	19.7290	19.7526	19.6226	19.6584
Long.	-101.4464	-101.4358	-101.3957	-101.3768	-101.4638	-101.4040
SiO_2	58.71	58.66	59.66	53.62	59.28	59.65
TiO_2	1.01	0.78	0.84	1.60	0.96	0.87
Al_2O_3	17.59	18.66	16.89	17.28	17.37	16.79
Fe_2O_3t	6.32	5.98	6.00	9.09	6.39	6.08
MnO	0.11	0.10	0.10	0.13	0.10	0.10
MgO	3.30	3.22	3.72	4.26	3.51	3.86
CaO	5.90	6.61	6.19	7.69	6.14	6.05
Na_2O	4.07	4.03	3.82	3.88	4.07	3.63
K_2O	2.12	1.52	1.87	1.31	1.90	2.21
P_2O_5	0.30	0.20	0.24	0.47	0.28	0.21
l.o.i.	0.06	0.05	0.06	0.05	0.07	0.07
Total	99.48	99.81	99.37	99.36	100.06	99.49
Mg#	56.78	57.55	60.93	54.13	58.03	61.48
Rb	39.84	28.04	35.15	21.39	39.85	50.51
Ba	505	420	536	472	608	587
Sr	638	776	676	604	549	450
Cs	1.724	0.762	0.853	0.666	1.005	2.045
La	20.49	14.04	20.16	23.61	22.30	21.49
Ce	39.97	29.42	41.90	47.14	44.95	43.50
Pr	5.29	3.89	5.39	6.55	5.70	5.60
Nd	20.62	15.53	20.90	27.09	21.77	21.52
Sm	4.31	3.28	4.31	6.09	4.57	4.56
Eu	1.284	1.041	1.204	1.768	1.268	1.178
Gd	3.95	3.02	3.88	5.92	4.15	4.19
Tb	0.578	0.440	0.565	0.878	0.615	0.626
Dy	3.34	2.54	3.27	5.20	3.59	3.66
Ho	0.663	0.507	0.650	1.031	0.713	0.733
Er	1.80	1.37	1.78	2.81	1.96	2.00
Tm	—	—	—	—	—	—
Yb	1.71	1.29	1.70	2.56	1.87	1.90
Lu	0.257	0.196	0.257	0.378	0.281	0.284
Y	17.82	15.02	17.50	29.83	19.46	19.91
Zr	159.15	111.23	167.67	203.69	185.78	181.93
Hf	3.70	2.80	3.98	4.47	4.33	4.37
Nb	13.69	5.63	8.43	16.72	13.40	9.41
Ta	0.892	0.381	0.540	0.936	0.839	0.638
Pb	7.86	6.41	8.14	6.12	8.63	9.21
Th	3.429	1.850	2.520	1.829	3.050	4.302
U	1.121	0.627	0.770	0.672	0.931	1.163
Sc	14.69	14.71	15.59	21.36	16.16	16.43
V	107	115	121	172	119	115
Cr	46	20	68	69	53	79
Co	17.65	17.05	18.31	24.04	18.44	18.75
Ni	25.31	13.83	43.28	28.86	33.31	35.02
Cu	17.24	22.06	34.46	28.01	31.20	30.44
Zn	70.94	80.84	71.22	94.51	72.24	69.09
Li	13.11	11.48	14.47	8.67	18.41	18.40
Be	1.55	1.09	1.32	1.62	1.47	1.43
B	16.69	9.46	11.39	9.47	13.50	15.01
Ga	19.55	19.98	19.61	20.99	19.34	18.93
Mo	1.08	0.56	1.00	1.05	1.34	1.11
Sn	1.16	0.81	1.15	1.28	1.31	1.47
Sb	0.14	0.11	0.13	0.09	0.13	0.13
W	0.29	0.19	0.30	0.27	0.39	0.39
Tl	0.35	0.10	0.13	0.10	0.14	0.23
$^{18}O/^{16}O$	—	—	—	—	—	—
Std error	—	—	—	—	—	—
$^{87}Sr/^{86}Sr$	0.70373	0.70367	0.70377	0.70398	0.70395	0.70418
± 1SD %	0.003	0.003	0.002	0.004	0.003	0.004
$^{143}Nd/^{144}Nd$	0.51286	0.51280	0.51280	0.51282	0.51273	0.51278
± 1SD %	0.004	0.002	0.003	0.003	0.002	0.003
$^{206}Pb/^{204}Pb$	18.686	18.655	18.696	18.711	—	18.710
± 1SD %	0.018	0.016	0.016	0.017	—	0.014
$^{207}Pb/^{204}Pb$	15.588	15.585	15.597	15.594	—	15.601
± 1SD %	0.019	0.016	0.016	0.020	—	0.014
$^{208}Pb/^{204}Pb$	38.441	38.405	38.482	38.475	—	38.506
± 1SD %	0.020	0.016	0.017	0.024	—	0.015

Table 9: Composition of basement rocks and possible contaminants considered for modeling.

Contaminant	Granulite VS1	Granulite VS2	Granite 96MR088	Granite MG-05-21	Granite MG-05-51	Granite Z625	Granite LHG	CT1	CT2	CSN	CL
Cs	0.006	0.005	–	2.090	6.250	17.150	–	2.090	2.090	2.090	2.090
Rb	0.640	0.310	–	84.0	117.0	210.1	204.0	84.0	84.0	84.0	84.0
Ba	149	56	–	435	507	569	537	435	435	569	569
Sr	570	554	–	237	249	175	135	135	237	237	350
Pb	1.40	0.90	–	4.90	8.80	22.79	8.80	8.80	4.90	4.90	22.79
Th	0.087	0.055	–	9.930	9.830	13.100	–	9.930	9.930	9.830	9.830
U	0.032	0.019	–	1.260	2.620	7.930	–	1.260	1.260	2.620	2.620
Zr	17.8	13.6	–	13.8	9.8	134	251	13.8	13.8	251.0	251
Hf	0.481	0.379	–	0.547	0.432	4.000	–	0.547	0.547	0.547	0.547
Ta	0.480	0.050	–	0.750	0.590	1.780	–	1.780	0.750	0.590	0.750
Y	7.32	3.93	–	47.20	23.10	15.93	32.00	47.20	47.20	47.20	15.93
Nb	7.54	0.55	–	9.42	6.69	11.09	14.00	9.42	9.42	14.00	11.09
Sc	21.00	19.40	–	29.90	19.50	6.10	–	29.90	29.90	29.90	29.90
Cr	56.60	433.90	–	41.30	70.30	9.00	10.00	41.30	41.30	41.30	41.30
Ni	21.40	60.80	–	16.70	27.40	2.00	2.00	16.70	16.70	16.70	16.70
Co	37.8	28.6	–	23.7	19.6	–	–	23.7	23.7	23.7	23.7
V	119	96	–	157	154	22	107	157	157	157	157
Ga	20	15.3	–	18.2	17.1	–	14	18.2	18.2	18.2	18.2
Zn	126	39	–	60	70	–	59	60	60	60	60
Cu	9.4	26	–	109	62	–	43	109	109	109	109
La	7.61	1.93	–	23.00	16.50	25.40	28.00	23.00	23.00	28.00	25.40
Ce	15.50	4.16	–	52.40	36.90	48.69	52.00	52.40	52.40	48.69	48.69
Pr	1.960	0.607	–	7.370	4.880	5.350	–	7.370	7.370	7.370	4.880
Nd	8.41	2.72	–	31.00	19.50	20.30	25.25	31.00	31.00	31.00	19.50
Sm	1.690	0.690	–	7.670	4.470	4.720	–	7.670	7.670	7.670	4.720
Eu	0.933	0.439	–	1.510	0.877	0.850	–	1.510	1.510	1.510	0.877
Gd	1.590	0.705	–	7.880	4.350	3.760	–	7.880	7.880	7.880	3.760
Tb	0.236	0.114	–	1.250	0.684	0.570	–	1.250	1.250	1.250	0.684
Dy	1.320	0.703	–	7.940	4.160	3.060	–	7.940	7.940	7.940	3.060
Ho	0.265	0.139	–	1.620	0.834	0.540	–	1.620	1.620	1.620	0.540
Er	0.717	0.379	–	4.490	2.260	1.410	–	4.490	4.490	4.490	1.410
Tm	–	–	–	–	–	0.210	–	–	–	–	–
Yb	0.697	0.377	–	4.220	2.120	1.330	–	4.220	4.220	4.220	1.330
Lu	0.119	0.064	–	0.621	0.310	0.200	–	0.621	0.621	0.621	0.200
$^{87}Sr/^{86}Sr$	0.7043	0.7046	0.7088	0.7045	0.7045	0.7092	0.7064	0.7092	0.7092	0.7092	0.7092
$^{143}Nd/^{144}Nd$	0.5128	0.5128	0.5126	0.5128	0.5128	0.5125	0.5120	0.5125	0.5125	0.5125	0.5125
$^{206}Pb/^{204}Pb$	18.787	18.730	18.879	18.798	18.729	19.000	18.862	19.100	19.000	19.000	18.798
$^{207}Pb/^{204}Pb$	15.602	15.597	15.659	15.603	15.599	15.653	15.599	15.653	15.653	15.653	15.653
$^{208}Pb/^{204}Pb$	38.599	38.511	38.862	38.641	38.544	38.825	38.699	38.825	38.825	38.825	38.825
$\delta^{18}O‰$	–	–	–	19.00	9.96	–	–	9.96	–	9.96	9.96

VS1, VS2, MG-05-21 and MG-05-51 from Ortega-Gutierrez et al. (2014); LHG from Luhr & Carmichael (1985) and Luhr (1997); Z625 from Blatter et al. (2007); CT1, CT2, CSN and CL, adapted compositions finally adopted for the models.

Table 10: Calculated compositions obtained in AFC models.

Trend	**T1**			**T2**		**CA SN**	**CAL**
Sample + Contaminat	M110 + CT1	M85 + CT1	M106 + CT1	M81 + CT2	M81 + LHG	M130 + CSN	M1 + CL
*** F**	66.8%	66.8%	66.8%	61.0%	61.0%	71.2%	62.8%
Cs	0.86	1.60	0.45	0.90	-	0.79	0.83
Rb	40.00	41.69	49.12	47.25	92.00	43.11	27.58
Ba	684.33	809.50	1368.89	928.09	955.72	637.18	416.74
Sr	533.58	554.12	461.76	726.87	706.23	646.81	430.38
Pb	5.19	5.85	10.44	9.60	10.63	8.21	9.49
Th	5.37	4.72	5.83	5.36	-	3.98	3.05
U	1.73	1.65	0.90	1.78	-	1.25	0.92
Zr	327.25	353.39	554.58	416.53	480.19	270.37	154.71
Hf	5.14	5.50	8.56	6.92	-	4.94	2.72
Ta	4.56	4.30	4.36	3.13	-	0.85	0.41
Y	46.56	51.02	71.63	54.55	50.58	34.16	25.01
Nb	73.57	70.32	78.26	52.63	53.85	14.45	5.77
Sc	-	-	-	24.13	-	25.80	-
Cr	0.37	0.37	0.37	0.57	0.14	1.00	0.82
Ni	0.54	0.56	0.52	0.42	0.06	4.11	2.55
Co	-	-	-	10.58	-	19.50	20.87
V	-	-	-	46.78	41.65	100.45	103.02
W	-	-	-	-	-	-	-
Ga	-	-	-	-	-	30.82	-
Zn	-	-	-	-	-	116.19	153.76
Cu	-	-	-	-	-	66.79	108.29
La	40.50	41.76	57.45	50.55	51.78	27.62	15.13
Ce	86.47	90.35	128.05	109.53	109.43	61.22	32.89
Pr	12.29	13.33	19.36	15.47	-	8.24	4.53
Nd	44.96	49.78	71.91	57.69	56.22	32.55	19.25
Sm	9.68	10.98	15.68	12.02	-	7.04	4.70
Eu	3.07	3.36	4.63	3.33	-	1.96	1.49
Gd	10.32	11.64	16.28	11.77	-	6.93	4.73
Tb	1.39	1.55	2.18	1.63	-	1.01	0.75
Dy	8.99	9.88	14.00	10.18	-	6.22	4.55
Ho	1.72	1.86	2.64	1.97	-	1.25	0.90
Er	4.61	4.93	7.08	5.36	-	3.44	2.58
Tm	-	-	-	-	-	-	-
Yb	3.77	3.91	5.72	4.67	-	3.17	2.51
Lu	0.60	0.63	0.93	0.74	-	0.49	0.40
$^{87}Sr/^{86}Sr$	0.703712	0.703565	0.703920	0.703934	0.703674	0.703655	0.704475
$^{143}Nd/^{144}Nd$	0.512827	0.512814	0.512825	0.512865	0.512821	0.512804	0.512767
$^{206}Pb/^{204}Pb$	18.878	18.939	18.800	18.764	18.757	18.692	18.699
$^{207}Pb/^{204}Pb$	15.601	15.607	15.590	15.589	15.583	15.583	15.612
$^{208}Pb/^{204}Pb$	38.634	38.681	38.550	38.493	38.498	38.429	38.572
$\delta^{18}O‰$	8.17	7.41	-	-	-	-	7.06

* F (residual melt %)

Table 11: Mineral-melt distribution coefficients for trace elements considered for modelling

	Olivine	Opx	Cpx	Plg	Ap	Magnetite	Ilmenite
Cs	0.000	0.010	0.130	0.130		0.500	
Rb	0.002	0.003	0.005	0.3; 0.1		0.150	
K	0.013	0.009	0.007	0.2; 0.156		0.045	
Ba	0; 0.002	0.002	0.001	0.03; 0.3		0.180	0.000
Sr	0.002	0.007	0.096	2.000	8.000	0.110	
Pb	0.000	0.001	0.006	0.18; 0.36		0.150	
Th	0.040	0.130	0.030	0.010		0.420	0.001
U	0.045	0.035	0.040	0.010		0.120	0.008
Zr	0.005	0.030	0.121	0.048		0.100	0.290
Hf	0.004	0.055	0.263	0.051		3.000	0.380
Ti	0.011	0.024	0.100	0.040		7.500	
Ta	0.000	0.150	0.013	0.040		0.7; 0.4	1.70
Y	0.004	0.200	0.438	0.030		0.200	0.005
Nb	0.002	0.150	0.003	0.010		0.7; 0.4	2.00
Sc	0.680	1.20	3.20	0.040			0.580
Cr	0.700	10.0	34.0	0.080		153	6.00
Ni	29.0	5.00	14.0	0.040		29.0	3.80
Co	5.90	3.00	2.00	0.070		7.40	1.90
V	0.800	0.600	1.350	0.022		26.0	11.0
W							
Ga							0.400
P							
Zn							3.00
Cu							0.790
La	0.001	0.002	0.044	0.270		1.500	0.000
Ce	0.001	0.003	0.084	0.200		1.300	0.001
Pr	0.001	0.005	0.124	0.170			0.000
Nd	0.001	0.005	0.173	0.140		1.000	0.001
Sm	0.001	0.010	0.283	0.110		1.100	0.001
Eu	0.002	0.013	0.312	0.180		0.600	0.001
Gd	0.002	0.016	0.336	0.066			0.003
Tb	0.002	0.019	0.364	0.060		1.000	0.007
Dy	0.002	0.022	0.363	0.055			0.010
Ho	0.002	0.026	0.378	0.048			0.011
Er	0.002	0.030	0.351	0.041			
Tm	0.002	0.040	0.297	0.036		1.000	0.100
Yb	0.002	0.049	0.313	0.031		0.900	0.170
Lu	0.002	0.060	0.265	0.025			0.084

Data selected from values for basalt and basaltic andesite compositions in GERM database (Nielsen, 2016).

Appendix 3: Publications

Losantos, E., Cebriá, J. M., Morán-Zenteno, D. J., Martiny, B. M. & López Ruiz, José (2015). Composición isotópica de oxígeno de las lavas del volcán Parícutin (Campo volcánico de Michoacán-Guanajuato, México). GEOS. Reunión Anual de la Unión Geofísica Mexicana. Puerto Vallarta, México, 98–99.

Losantos, E., Cebriá, J. M., Morán-Zenteno, D. J., Martiny, B. M. & López-Ruiz, J. (2014). Condiciones de cristalización y diferenciación de las lavas del volcán El Metate (Campo Volcánico de Michoacán-Guanajuato, México). Estudios Geológicos 70, 020.

COMPOSICIÓN ISOTÓPICA DE OXÍGENO DE LAS LAVAS DEL VOLCÁN PARICUTÍN (CAMPO VOLCÁNICO DE MICHOACÁN-GUANAJUATO, MÉXICO)

Emma Losantos [a], José-María Cebriá [a], Dante Jaime Morán-Zenteno [b], Barbara Mary Martiny [b], José López Ruiz [a]

a Instituto de Geociencias (CSIC-UCM)
b Instituto de Geología (UNAM)

Ref. beca FPI: BES-2012-052390

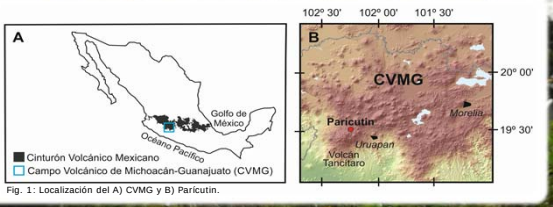

Fig. 1: Localización del A) CVMG y B) Parícutin.

El Parícutin es un volcán monogenético situado en el sector sur del Campo Volcánico de Michoacán-Guanajuato (CVMG) (Fig. 1), uno de los campos volcánicos más grandes del Cinturón Volcánico Mexicano, y representa su actividad eruptiva más reciente (1943-1952).

El Parícutin es tradicionalmente considerado como una referencia mundial para las series calcoalcalinas originadas por un proceso AFC (asimilación y cristalización fraccionada simultáneas) desde que Ray E. Wilcox (1954) concluyera que ninguno de esos mecanismos por separado podría dar lugar a la serie de lavas del Parícutin.

Autor	Hipótesis y Conclusiones	Basado en:
Wilcox 1954 **Fig. 2**	• La suite de lavas del Parícutin es producto de un proceso AFC. • Las condiciones térmicas son las necesarias para la asimilación? • La asimilación de corteza continental fanerozoica ocurrió antes de la erupción en un reservorio magmático único composicionalmente zonado.	Observaciones petrográficas y variaciones en elementos mayores.
Miesch 1979	• Divide el proceso evolutivo en tres etapas.	Tres tendencias lineales distintas en elementos mayores.
McBirney et al. 1987 **Fig. 3**	• Explica las tres etapas: 1ª fraccionación (FC simple) de Ol y Plg; 2ª y 3ª AFC de un componente rico en Sr radiogénico con fraccionación de Opx y Plg • Cámara magmática única y zonada. • El nuevo aporte de calor podría haber llegado desde el magma en convección que permanece en la cámara.	Balance de masas de elementos traza e isótopos El calculo del calor de cristalización de Ol y Plg demuestra que no es suficiente para la asimilación.
Luhr 2001	• Redefine las tres etapas como: 1) Febrero-Julio 1943 2) Desde Agosto de 1943-1946 3) Desde finales de 1946 hasta 1952 • Erupción de varios batch de magma antes del cambio composicional de 1947, interpretado por McBirney como un aumento de la contaminación cortical.	 K_2O<1 (wt%); Tendencia volumen/K_2O esencialmente plana. K_2O ~ 1.2 (wt%); tendencia volumen/K_2O ligeramente positiva. K_2O de 1.2 a 1.7 (wt%); tendencia volumen/K_2O con pendiente pronunciada. Gap composicional entre las etapas 1 y 2, y amplia variación de K_2O para un mismo SiO_2 con dependencia temporal.
Erlund et al. 2010 **Fig. 4**	• Dos batch distintos entre la fase 1 y la 2 y 3. • La fase 3 se corresponde con la extrusión del magma más evolucionado alojado en un complejo de diques y sills. • Modelo alternativo a la gran cámara estratificada: Los magmas de la primera etapa ascendieron desde un reservorio profundo. Las siguientes desde un complejo somero de diques y sills donde el magma se contamina al estar en estrecho contacto con la roca de caja.	Diferencia composicional y estilo eruptivo entre las dos primeras. Datos de profundidades de cristalización de Ol extraídos de inclusiones fundidas: 14 km para la fase 1 y mucho más someras para las 2 y 3.
Cebriá et al. 2011 **Fig. 5**	• Las variaciones geoquímicas se explican por cambios en la mineralogía que está fraccionando: primero dominada por Plg + Ol y después por Opx. • El proceso AFC estuvo activo desde el principio • Contaminante granítico heterogéneo. • Proponen un contaminante parcialmente fundido antes de la asimilación.	Modelización cuantitativa con MELTS software. Las líneas de descenso calculadas en su modelo no encajan con un escenario de cristalización fraccionada simple. Gran dispersión en los diagramas isótopo-elemento. Termodinámicamente no pueden justificar las altas tasas de asimilación.
Rowe et al. 2011	• Varios cuerpos magmáticos pequeños con evoluciones independientes.	Variación composicional abrupta en elementos incompatibles.

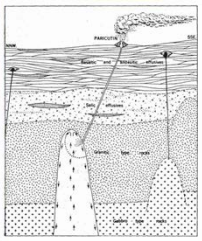

Fig. 2: Wilcox 1954

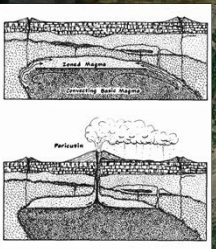

Fig. 3: McBirney 1979

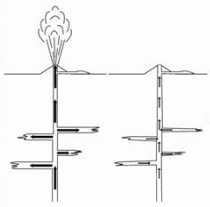

Fig. 4: Erlund 2010

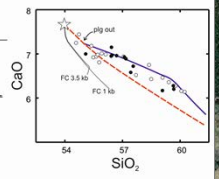

Fig. 5: Cebriá 2011

Para complementar la información geoquímica y perfilar el modelo petrogenético cuantitativo establecido para dicha serie, se han analizado los valores isotópicos de oxígeno de un grupo de lavas representativas de dicha serie, sin evidencias significativas de alteración secundaria. Los análisis isotópicos se realizaron en muestras de roca total, que fueron preparadas siguiendo el método de fluorinización laser descrito por Kusakabe et al. (2004), y se analizaron con un espectrómetro de masas SIRA VG Isotech dual inlet con triple colector en los laboratorios NERC del SUERC, Glasgow, UK.

Discusión

El comportamiento de los isótopos de oxígeno durante un proceso AFC depende de los parámetros $\delta^{18}O_0$ (líquido inicial), $\delta^{18}O_A$ (material asimilado), m (relación entre el material asimilado y el cristalizado) y F (porcentaje de líquido residual, en este caso establecido a partir del modelo de Cebriá et al. 2011).

- Como datos de partida para $\delta^{18}O_0$ tomamos 6.3 ($^0/_{00}$) (Straub et al. 2014, dato más bajo para el cinturón volcánico) y 6.99 $^0/_{00}$ (Johnson et al. 2009, calculado a partir de un dato de $\delta^{18}O_{Ol}$ en Parícutin). El rango que mejor reproduce los datos (Figs. 6 y 7) es más restringido (6.5-6.99 $^0/_{00}$).
- Como $\delta^{18}O_A$ se ha utilizado inicialmente el valor 9,94 $^0/_{00}$ (xenolito 51-W-1; McBirney 1987). El cálculo con ese valor (o inferior) no permite reproducir la pendiente observada en los datos, siendo necesario adoptar un valor de $\delta^{18}O$ = 11 $^0/_{00}$, correspondiente a los valores más altos observados en rocas graníticas (ver Bindeman , 2008).
- Como dato de partida de m se tomó el obtenido en Cebriá et al. 2011 (m=2). Como se puede observar, este valor no permite reproducir la pendiente observada en los datos, siendo necesario un valor de m = 1.7 o inferior.

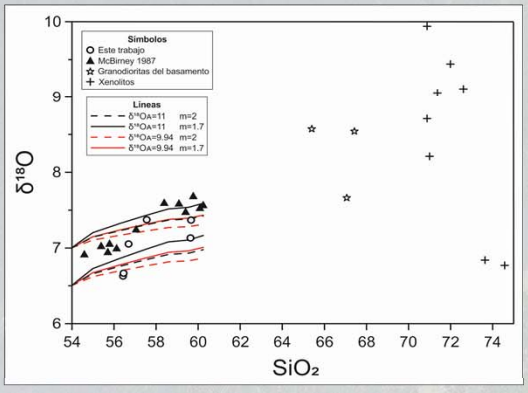

Fig. 6: Diagrama de variación de la relación $\delta^{18}O$ ($^0/_{00}$) vs SiO_2 (Wt%), datos de McBirney 1987 y de este trabajo.

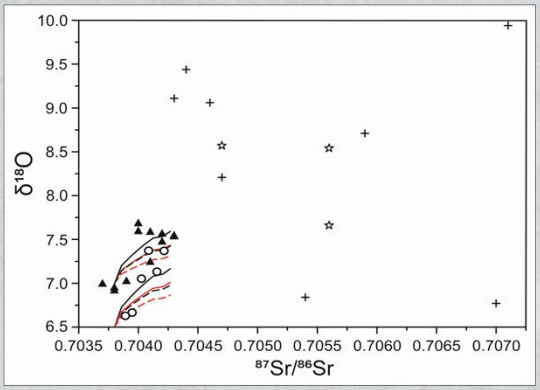

Fig. 7: Diagrama $\delta^{18}O$ ($^0/_{00}$) vs. $^{87}Sr/^{86}Sr$. La forma sigmoidal de la curva de mezcla sería indicativa de un proceso AFC (asimilación con cristalización fraccionada), según James (1981). Leyenda como en Fig. 6.

Conclusiones

- La curva que mejor se ajusta a los datos es la que tiene como parámetros: $\delta 18O_0$ = 6.5-7 $^0/_{00}$; $\delta 18O_A$ = 11 $^0/_{00}$ y m = 1.7
- Se ha comprobado que, para un mismo m, el aumento de $\delta^{18}O_A$ incrementa ligeramente la pendiente pero que afecta mucho más la variación de m para un mismo $\delta^{18}O_A$.
- Es necesario un $\delta^{18}O_A \geq 11$ $^0/_{00}$. Esto descarta como posibles contaminantes los xenolitos y las rocas graníticas hasta ahora analizadas.
- El valor $\delta^{18}O_0 \approx 6.5$ $^0/_{00}$ implica una fuente mantélica enriquecida por fluidos procedentes de la subducción.
- m ≤ 1.7 implica una proporción de material asimilado muy alta que por tanto requeriría un material asimilado parcialmente fundido para que sea termodinámicamente viable.
- Este modelo concuerda con los establecidos por Erlund et al. 2010 y Cebriá et al. 2011 en tanto que apuesta por un proceso AFC continuado de la fase 2 en adelante y requiere un mecanismo que permita una alta tasa de asimilación.

A. R. McBirney; H. P. Taylor; and R. L. Armstrong (1987). Paricutin re-examined: a classic example of crustal assimilation in calc-alkaline magma. Contributions to Mineralogy and Petrology, 95: 4-20.
A. T. Miesch (1979). Vector analysis of chemical variation in the lavas of Paricutin volcano, Mexico. Mathematical Geology, Vol. 11, Nº 4.
E. J. Erlund; K. V. Cashman; P. J. Wallace; L. Pioli; M. Rosi; E. Johnson; H. Delgado Granados (2010). Compositional evolution of magma from Parícutin volcano, Mexico: The tephra record. Journal of Volcanology and Geothermal Research, 197: 167-187.
Ilya Bindeman (2008). Oxygen isotopes in mantle and crustal magmas as revealed by single crystal analysis. Reviews in Mineralogy and Geochemistry, Vol. 69, 445-478.
James F. Luhr (2001). Glass inclusions and melt volatile contents at Parícutin volcano, Mexico. Contributions to Mineralogy and Petrology, 142: 261-283.
James D. E. (1981). The combined use of oxygen and radiogenic isotops as indicators of crustal contamination. Annual Review of Earth and Planetary Sciences, 9: 311-344.
J. M. Cebriá; B. M. Martiny; J. López-Ruiz; D. J. Morán-Zenteno (2011). The Paricutin calc-alkaline lavas: New geochemical and petrogenetic modelling constrains on the crustal assimilation process. Journal of Volcanology and Geochemical Research, 201: 113-125.
Minoru Kusakabe; Seiji Maruyama; Tomoki Nakamura; and Toru Yada (2004). CO_2 Laser-BrF_5 fluorination technique for analysis of oxigen three isotopes of rocks and minerals. Journal of the Mass Spectrometry Society of Japan, Vol. 52, Nº 4.
Michael C. Rowe; David W. Peate and Ingrid Ukstins Peate (2010). An investigation into the nature of the magmatic plumbing system at Paricutin volcano, Mexico. Journal of Petrology, Vol. 52, Nº 11, 2187-2220.
Ray E. Wilcox (1954). Petrology at Paricutin volcano Mexico. Geological Survey Bulletin, 965-c.

Estudios Geológicos
julio-diciembre 2014, 70(2), e020
ISSN-L: 0367-0449
doi: http://dx.doi.org/10.3989/egeol.41806.349

Condiciones de cristalización y diferenciación de las lavas del volcán El Metate (Campo Volcánico de Michoacán-Guanajuato, México)

Crystallization conditions during the differentiation of the El Metate volcano lavas (Michoacán-Guanajuato Volcanic Field, México)

E. Losantos[1], J.M. Cebriá[1], D.J. Morán-Zenteno[2], B.M. Martiny[2], J. López-Ruiz[1]

[1] Instituto de Geociencias (CSIC, UCM). José Gutiérrez Abascal, 2. 28006 Madrid. España. Email: e.losantos@csic.es
[2] Instituto de Geología (UNAM). Ciudad Universitaria. 04510 México, D.F. México

RESUMEN

El Metate es un volcán en escudo situado en el sector sur del Campo Volcánico de Michoacán-Guanajuato, uno de los dos campos volcánicos más grandes del Cinturón Volcánico Transmexicano. Su actividad tuvo lugar aproximadamente 4.700 ± 200 a B.P y produjo más de quince coladas de afinidad calcoalcalina que muestran diferente grado de diferenciación.

Las temperaturas calculadas mediante geotermómetros mineral-líquido para olivino, plagioclasa, y piroxenos muestran que la fase más temprana en cristalizar fue el olivino (1232–1198 °C), seguido de plagioclasa (1162–1126 °C), ortopiroxeno (1147–1027 °C) y clinopiroxeno (1147–1018 °C). Las estimaciones de presión sugieren que la cristalización comenzó a ~7 kbar y continuó hasta niveles superficiales. El contenido en agua del fundido durante la cristalización de la plagioclasa fue de ~1.6% en peso.

Las temperaturas calculadas a partir del contenido en Al de los anfíboles, indican que cristalizaron entre 995 y 922 °C, a una presión media de 3.5 kbar y con un contenido en H_2O del fundido de entre 5.2% y 6.9%. Aunque estos valores estarían de acuerdo con que el anfíbol representa una fase tardía en el proceso de cristalización, el que estos cristales presenten siempre texturas de desequilibrio, que se observan también de forma ocasional en otras fases, sugiere que pueden representar xenocristales y/o que la cristalización de estas lavas ha tenido lugar en sistema abierto.

Palabras clave: Geotermobarometría; cristalización fraccionada; química mineral; diferenciación magmática.

ABSTRACT

El Metate is a shield volcano located in the southern sector of the Michoacan-Guanajuato Volcanic Field, one of two largest monogenetic volcanic fields of the Transmexican Volcanic Belt. It was active *c.* 4.700 ± 200 years B.P and emitted about fifteen calcalkaline lava flows showing variable differentiation degrees.

Temperatures calculated from mineral-liquid geothermobarometers for olivine, plagioclase and pyroxene, suggest that olivine was the earliest fractionating phase (1232–1198 °C), followed by plagioclase (1162–1126 °C),

Recibido el 16 de junio de 2014 / Aceptado el 10 de noviembre de 2014 / Publicado online el 17 de diciembre de 2014

Citation / Cómo citar este artículo: E. Losantos et al. (2014). Condiciones de cristalización y diferenciación de las lavas del volcán El Metate (Campo Volcánico de Michoacán-Guanajuato, México). Estudios Geológicos 70(2): e020. http://dx.doi.org/10.3989/egeol.41589.349.

orthopyroxene (1147–1027 °C) and clinopyroxene (1147–1018 °C). Pressure estimations indicate that crystallization started at ~7 kbar and progressed up to surface levels. Water contents in the melts during crystalliztion of plagioclase is estimated at ~1.6%.

Temperatures calculated on the basis of Al content in amphibole, provide a crystallization range between 995 and 922 °C, at an average pressure of 3.5 kbar and water contents between 5.2% and 6.9%. Although these values could agree with a scenario where amphibole represents a late crystallization phase along the previous fractionating sequence, the systematic presence of disequilibrium textures, which are also observed occasionally in other phases, suggest that other possibilities such as open-system crystallization cannot be discarded.

Keywords: Geothermobarometry; fractional crystallization; mineral chemistry; magmatic differentiation.

Introducción

Para establecer la evolución de los fundidos desde su acumulación en la cámara magmática hasta su ascenso y extrusión, es necesario conocer la temperatura y la presión a la que se formaron las diferentes fases que han cristalizado en el magma. Una de las aproximaciones más frecuentes consiste en estimar dichos parámetros a partir de la composición de las fases minerales, mediante la aplicación de geotermobarómetros basados en equilibrios químicos mineral-mineral y mineral-líquido. En la actualidad la aplicación de esta metodología se ha facilitado mucho al contarse con un completo arsenal de calibraciones para las fases más comunes en sistemas ígneos y adaptadas a un amplio rango de condiciones de presión, temperatura y composición (ver Putirka, 2008).

En efecto, estudios recientes sobre geotermobarometría en magmas basálticos (ver p.ej. Costa *et al.*, 2013; Dahren *et al.*, 2012; Keiding & Sigmarsson, 2012) han confirmado que este tipo de cálculos permite obtener información detallada sobre la evolución y funcionamiento del sistema magmático durante la diferenciación, incluidos aquellos que tienen lugar en sistema abierto, como la asimilación o la mezcla de magmas, y que son esenciales para perfilar cualquier modelo petrogenético. De hecho, como han demostrado otro tipo de estudios, contar con información sobre la evolución de la paragénesis mineral permite cuantificar con mayor precisión los procesos de diferenciación (ver p.ej. Cebriá *et al.*, 2011).

Por estas razones, y en el contexto de una investigación más amplia sobre la petrogénesis del volcanismo en el Campo Volcánico de Michoacán-Guanajuato (México) se ha realizado un estudio geotermobarométrico (P-T-H_2O) a partir de la paragénesis mineral observada en un primer conjunto de 11 muestras representativas de las lavas emitidas por el volcán El Metate, como paso previo para establecer un modelo petrogenético cuantitativo que pueda ser aplicable a volcanes similares de la región. Las muestras fueron seleccionadas de modo que cubrieran la secuencia de lavas emitidas por el volcán. En este trabajo se detallan los resultados preliminares de dicha aproximación.

Contexto geológico

El Cinturón Volcánico Transmexicano (CVTM), es considerado el mayor arco volcánico Neógeno de Norteamérica, extendiéndose por la parte central del país en una franja entre las latitudes 18° 30′ N y 21° 30′ N sobre el extremo sur de la placa norteamericana (Fig. 1). Está constituido por campos monogenéticos, estratovolcanes y mesetas volcánicas cuya distribución está controlada por la tectónica regional (Ferrari *et al.*, 1999; Ferrari *et al.*, 2012; Johnson & Harrison, 1989; Suter *et al.*, 1999). La composición de las lavas muestra una gran variabilidad composicional, si bien predominan los términos calcoalcalinos (ver Ferrari *et al.*, 2012; Gómez-Tuena *et al.*, 2007 y referencias incluidas).

El Campo Volcánico de Michoacán-Guanajuato (CVMG) es uno de los dos campos monogenéticos más grandes del CVTM (Hasenaka, 1994; Hasenaka & Carmichael, 1985). Se sitúa en la parte centro-occidental del mismo y comprende cerca de 400 volcanes de tamaño medio (2–12 km de diámetro basal y 100–1000 m de altura; Hasenaka, 1994) y alrededor de 1000 afloramientos de menor entidad producidos por actividad monogenética, incluyendo maares, domos y conos de ceniza (Hasenaka & Carmichael, 1987), entre los cuales pueden encontrarse ~377 pequeños volcanes en escudo andesíticos (Hasenaka, 1994) y más raramente estratovolcanes (e.g. Tancítaro, Patamban), distribuidos en una

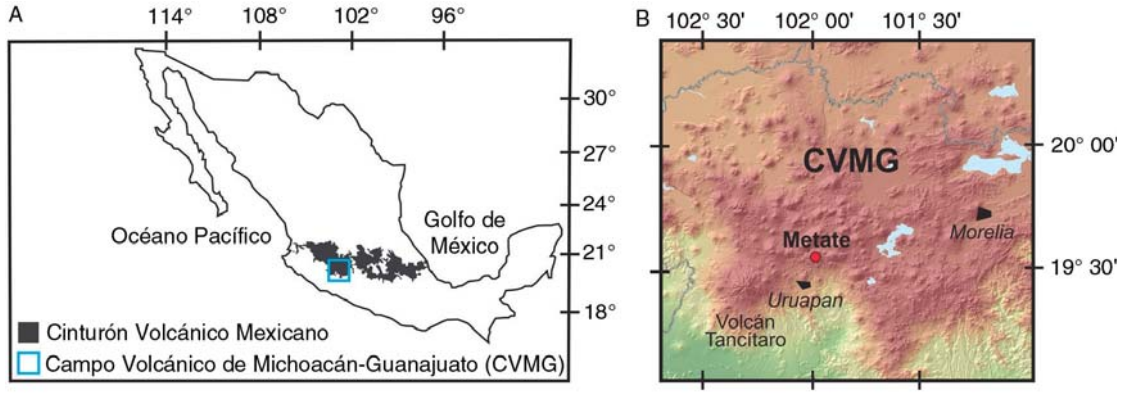

Fig. 1.—A) Situación del Cinturón Volcánico Mexicano (CVM) y del Campo Volcánico de Michoacán-Guanajuato (CVMG). B) Localización del volcán El Metate en el CVMG.

superficie de unos 40000 km^2. Se considera que el volcanismo monogenético en esta zona empezó hace ~3 Ma (Hasenaka & Carmichael, 1985), con una clara tendencia del frente volcánico a migrar hacia el suroeste. Predominan los términos calcoalcalinos, aunque también existen alcalinos y más raramente adakíticos (ver Ferrari *et al.*, 2012; Gómez-Tuena *et al.*, 2007 y referencias incluidas).

El Metate es un volcán en escudo que ocupa un área de algo más de 101 km^2 en el sector sur del CVMG (Fig. 1). Produjo en torno a quince coladas de lavas de las que apenas existe información petrológica ni geoquímica (una única muestra de afinidad calcoalcalina descrita en Hasenaka & Carmichael, 1987). La edad de este volcán tampoco está bien definida, ya que solo existe una determinación radiométrica, basada en ^{14}C, de 4700 ± 200 años (Hasenaka & Carmichael, 1985).

Métodos analíticos

Los análisis de elementos mayores en roca total se realizaron con un espectrómetro secuencial de rayos X Siemens SRS 3000 siguiendo el procedimiento descrito en Lozano-Santa Cruz & Bernal (2005) en el Laboratorio Universitario de Geoquímica Isotópica (LUGIS) del Instituto de Geología, Universidad Nacional Autónoma de México (UNAM).

La química mineral fue determinada mediante microsonda electrónica. Se utilizó una microsonda JEOL® "Superprobe JXA-8900 M" con cuatro analizadores WDS, del Centro Nacional de Microscopía Electrónica de la Universidad Complutense de Madrid. Los análisis se realizaron sobre láminas pulidas metalizadas con una película de grafito y las condiciones de medida fueron de 15 kV de diferencia de potencial y un haz de electrones de 20 nA de intensidad de corriente y 5 μm de diámetro. Los tiempos de medida fueron de 10 segundos en la posición del pico y 5 en la de cada fondo, con unos límites de detección de 0.5–6% en peso para óxidos con concentraciones >1.5% en peso y <10% para óxidos con concentraciones <1.5% en peso. Los patrones usados fueron: sillimanita, albita, almandino, kaersutita, microclina, ilmenita, fluorapatito, escapolita, aleación de Ni, cromita, gahnita, bentonita y estroncianita que proceden del Smithsonian Institute (Washington DC, EEUU) y de la Universidad de Harvard (Boston, EEUU). Se analizaron Si, Al, Fe, Mn, Mg, Ca, Na, K, Ti, Ni, Cr y P en olivino, plagioclasa, clinopiroxeno, ortopiroxeno y anfíbol. Excepto en el caso del anfíbol, los análisis se realizaron exclusivamente en aquellos cristales o zonas de los cristales que no mostraban evidencias de desequilibrio respecto a la matriz que los engloba.

Petrología y geoquímica

En la Tabla 1 se recoge la composición en elementos mayores de las rocas objeto de estudio y en las Tablas 2 a 6, se resume la composición de las fases consideradas en cada una de dichas muestras.

Todas las rocas consideradas presentan textura hipocristalina, inequigranular, porfídica y vacuolar (Fig. 2). La matriz es microcristalina y está compuesta por plagioclasa (Pl), ortopiroxeno (Opx), clinopiroxeno (Cpx), óxidos, olivino (Ol),

Tabla 1**—Análisis químicos de roca total (% en peso) de lavas del volcán El Metate**

	M20	M57	M60	M61	M63	M64	M65	M66	M70	M74	M77
SiO_2	61.29	55.02	57.90	60.07	59.40	60.09	57.02	59.26	58.11	60.23	60.69
TiO_2	0.67	0.92	0.80	0.69	0.70	0.68	0.90	0.68	0.73	0.69	0.60
Al_2O_3	17.69	17.48	18.27	18.00	17.36	17.42	17.29	18.08	17.53	17.83	18.60
$Fe_2O_3^t$	5.38	7.63	6.11	5.66	6.21	5.89	7.30	5.71	6.67	5.81	5.45
MnO	0.09	0.13	0.11	0.09	0.11	0.10	0.13	0.10	0.10	0.09	0.08
MgO	3.09	5.78	3.36	3.19	4.01	3.40	5.05	3.17	4.65	3.39	3.13
CaO	6.59	7.56	7.10	6.58	6.43	6.11	6.84	6.75	6.94	6.06	5.94
Na_2O	3.91	3.44	3.94	3.98	3.68	3.78	3.63	4.03	3.73	3.93	3.99
K_2O	1.45	1.18	1.61	1.48	1.80	1.76	1.49	1.41	1.52	1.89	1.43
P_2O_5	0.21	0.05	0.11	0.00	0.02	0.01	0.05	0.04	0.21	0.27	0.17
LOI	0.34	0.50	0.26	0.00	0.24	0.25	0.00	0.30	0.22	0.25	0.52
Total	100.70	99.68	99.56	99.73	99.95	99.47	99.70	99.53	100.42	100.45	100.61

*LOI: pérdida por calcinación.

Tabla 2**—Análisis químicos, porcentaje de componente forsterita y temperatura calculada de fenocristales y microfenocristales de olivinos en lavas del volcán El Metate**

	M57						M65
	1	2	3	4	5	6	1
	Feno.	Microfeno.	Feno.	Microfeno.	Feno.	Feno.	Feno.
SiO_2	38.96	38.92	39.07	39.94	36.84	37.99	37.42
Al_2O_3	—	—	—	0.01	0.22	0.04	—
FeO^T	19.68	21.14	20.79	15.99	23.45	22.68	25.24
MnO	0.18	0.24	0.26	0.22	0.42	0.26	0.30
MgO	41.28	40.78	40.15	44.89	36.29	38.16	36.24
CaO	0.16	0.23	0.18	0.14	0.21	0.14	0.19
Na_2O	0.01	—	—	0.01	0.01	0.03	0.03
K_2O	—	0.00	0.01	0.01	0.01	0.01	0.02
TiO_2	0.03	0.04	0.03	0.00	0.04	—	0.01
NiO	0.08	0.07	0.20	0.27	0.07	0.09	0.12
Cr_2O_3	0.02	—	—	—	—	—	0.02
P_2O_5	0.05	0.09	0.05	0.04	—	0.03	0.04
F	—	0.01	—	—	—	—	—
Cl	—	0.01	—	0.00	0.03	—	—
Total	100.44	101.52	100.73	101.51	97.55	99.42	99.62
% Fo	79	77	77	83	73	75	72
T(°C)	1212	1216	1218	1198	1232	1225	1225

Análisis químicos expresados en % en peso del óxido.
Todos los análisis en fenocristales han sido realizados en los bordes.

y ocasionalmente vidrio. A excepción de los óxidos, las fases que componen la matriz aparecen asimismo como feno y microfenocristales, siendo Pl y piroxenos comunes a todas las muestras, mientras que el Ol aparece solo ocasionalmente. El anfíbol (Amp) también aparece como fenocristal en algunas de las muestras estudiadas. Por lo que respecta a su composición química (Tabla 1), las lavas de El Metate presentan un rango de variación en SiO_2 relativamente reducido por lo que

Tabla 3—**Análisis químicos, porcentaje de los componentes An y Ab, y valores de temperatura (T), presión (P) y contenido en agua (H_2O%) calculados para cristales de plagioclasa en lavas del volcán El Metate**

	M20	M57	M60	M61	M63	M64		M65	M66			M77
	1	1	1	1	1	1	2	1	1	2	3	1
	Feno.	Microfeno.	Feno.	Feno.	Matriz	Feno.	Matriz	Matriz	Feno.	Feno.	Microfeno.	Matriz.
SiO_2	53.03	53.58	52.51	52.90	49.91	54.71	52.18	50.54	51.87	52.87	52.45	54.14
Al_2O_3	28.22	29.05	29.01	28.35	30.59	27.84	28.42	30.72	28.96	28.02	28.62	28.98
FeO^T	0.68	0.76	0.66	0.93	0.71	0.86	0.93	0.61	0.75	0.85	0.57	0.69
MnO	—	—	0.02	—	0.03	—	0.05	0.03	0.04	0.09	—	—
MgO	0.10	0.17	0.06	0.05	0.06	0.05	—	0.09	0.12	0.08	0.08	0.08
CaO	12.17	12.21	12.60	11.42	14.90	11.19	12.78	14.54	12.84	12.34	12.87	12.02
Na_2O	4.49	3.88	4.70	4.93	3.43	5.17	4.53	3.31	4.37	4.81	4.65	4.56
K_2O	0.15	0.17	0.18	0.07	0.15	0.36	0.30	0.15	0.13	0.11	0.11	0.13
TiO_2	0.01	0.01	0.01	0.06	0.02	0.01	0.07	0.01	0.01	0.01	—	0.07
NiO	0.08	—	0.05	0.02	0.03	—	—	0.02	0.02	—	0.03	—
Cr_2O_3	0.01	—	0.00	0.00	—	0.03	—	—	0.00	—	—	—
P_2O_5	0.08	0.02	0.02	0.07	0.00	—	0.04	—	0.00	0.03	0.07	0.01
F	0.03	—	0.05	0.01	0.06	0.06	—	0.03	0.00	—	—	0.02
Cl	0.01	0.00	0.00	0.03	0.00	0.02	0.01	0.00	0.03	0.00	—	0.00
Total	99.05	99.84	99.87	98.83	99.87	100.29	99.30	100.06	99.12	99.21	99.46	100.70
% An	60.0	63.5	59.7	56.1	70.6	54.5	60.9	70.8	61.9	58.6	60.5	59.3
% Ab	40.0	36.5	40.3	43.9	29.4	45.5	39.1	29.2	38.1	41.4	39.5	40.7
T (°C)	1135	1148	1150	1148	1144	1126	1133	1162	1147	1143	1145	1128
H_2O %	1.7	1.5	1.5	1.5	1.5	1.8	1.6	1.2	1.6	1.7	1.6	2.1
P (Kbar)	5.4	4.7	7.3	7.2	3.7	6.5	5.3	3.6	5.9	6.5	6.1	5.2

Análisis químicos expresados en % en peso del óxido. Todos los análisis en fenocristales han sido realizados en los bordes.
T calculada según ecuación 3; H2O calculada según ecuación 4; P calculada según ecuación 5.

están representadas casi exclusivamente por términos andesíticos (Fig. 3), con bajas relaciones FeO^T/MgO. Los relativamente altos contenidos de SiO_2 (61–55%) y bajos de MgO (5.8−3%) y del índice #Mg (66–58) indican que en todos los casos se trata de rocas evolucionadas.

En general las concentraciones de MgO, Fe_2O_3, y CaO, disminuyen respecto a SiO_2 (Fig. 4), mientras que K_2O, Na_2O, P_2O_5 y en cierta medida Al_2O_3, tienden a aumentar. Sin embargo, la distribución de estas rocas en los diagramas SiO_2-elemento revela la existencia de dos tendencias contrastadas. Como se puede observar sobre todo en el diagrama SiO_2-MgO, un grupo de muestras (M-20, M-60, M-61 y M-66), se distribuyen a lo largo de una pauta de menor pendiente respecto a la trayectoria representada por el resto. Asimismo las pautas generales de enriquecimiento/empobrecimiento no son siempre coincidentes. Así el primer grupo de muestras exhibe un empobrecimiento en K_2O, Na_2O y Al_2O_3 al aumentar el contenido de SiO_2, mientras que el resto muestra un enriquecimiento.

Fases minerales

Olivino

Los olivinos son en su mayoría feno y microfenocristales (Fig. 2A), aunque también aparecen como microcristales formando la matriz. En general son subidiomorfos, de bordes rotos o con golfos de corrosión, así como con zonas internas huecas. Si bien al microscopio es difícil de distinguir, en la microsonda se ha podido detectar que los fenocristales pueden presentar bordes de recrecimiento y en algún caso, una fina corona de Opx. El olivino aparece exclusivamente en las muestras con mayor

Tabla 4—**Análisis químicos, número de magnesio y valores de temperatura (T) y presión (P) calculados para cristales de ortopiroxeno en lavas del volcán El Metate**

	M60		M64		M65	M66			M70	M74
	1	2	1	2	1	1	2	3	1	1
	Microfeno.	Microfeno.	Feno.	Microfeno.	Matriz	Matriz	Microfeno.	Microfeno.	Microfeno.	Microfeno.
SiO_2	55.30	55.11	52.95	52.65	54.22	53.69	53.13	54.49	53.91	55.74
Al_2O_3	1.22	0.93	0.80	1.96	0.24	1.58	2.19	0.92	0.46	0.83
FeO^T	12.33	12.59	16.92	15.50	14.89	13.39	13.73	12.70	15.00	12.95
MnO	0.36	0.38	0.45	0.35	0.28	0.38	0.23	0.28	0.32	0.23
MgO	28.40	28.93	26.44	27.10	27.06	28.40	27.98	28.61	27.38	29.36
CaO	1.42	1.55	1.68	1.76	2.18	2.14	1.62	1.60	2.05	1.59
Na_2O	0.05	0.05	0.02	0.03	0.05	0.05	0.02	0.04	0.04	0.04
K_2O	0.01	0.00	0.00	0.01	0.01	0.03	—	—	0.00	0.00
TiO_2	0.28	0.30	0.21	0.35	0.19	0.32	0.31	0.16	0.21	0.07
NiO	0.02	0.01	0.03	0.00	0.00	0.02	0.01	0.06	0.00	0.00
Cr_2O_3	0.00	0.00	0.00	0.03	0.01	0.01	0.02	—	0.00	0.02
P_2O_5	0.01	0.07	0.00	0.00	0.00	0.06	0.02	0.01	0.03	0.00
F	0.04	0.00	0.00	0.02	0.02	0.00	—	—	0.00	0.00
Cl	0.01	0.02	0.00	0.02	0.00	0.00	0.02	—	0.00	0.01
Total	99.42	99.92	99.50	99.77	99.15	100.08	99.24	98.86	99.39	100.85
#Mg	80	81	78	80	79	74	81	81	79	73
T (°C)	1078	1147	1027	1042	1092	1053	1104	1113	1071	1066
P (Kbar)	2.1	2.2	0.0	0.2	2.8	0.6	0.1	1.1	2.0	0.7

Análisis químicos expresados en % en peso del óxido. Todos los análisis en fenocristales han sido realizados en los bordes
T calculada según ecuación 6; P calculada según ecuación 7.

contenido en MgO (>4.5%) y muestran un rango composicional relativamente estrecho entre Fo83 y Fo72 (Tabla 2).

Plagioclasa

La plagioclasa se encuentra presente en todas las rocas estudiadas como fenocristales, microfenocristales, formando parte de la matriz y como inclusiones microcristalinas en fenocristales de otras fases. Es posible distinguir cuatro poblaciones principales de cristales de Pl (Fig. 2B, C y D):

Tipo 1: Cristales idio-subidiomorfos que pueden ser tanto feno como microfenocristales o cristales de la matriz y que presentan macla de Carlsbad o polisintética. Esporádicamente algunos fenocristales pueden tener extinción ondulante o presentar un núcleo alterado.

Tipo 2: Feno y microfenocristales con zonación oscilatoria muy marcada, en ocasiones con extinción ondulante sobreimpuesta, que pueden tener bordes corroídos y recrecimientos y/o núcleos alterados y con inclusiones. Con frecuencia en estas plagioclasas se encuentra gran cantidad de microcristales de apatito incluidos en los bordes recrecidos (que también se observan en la matriz en algunas muestras), siendo las inclusiones del núcleo indistinguibles.

Tipo 3: Fenocristales totalmente alterados y de bordes corroídos, en los que se sigue apreciando el maclado, y con un borde de recrecimiento también corroído (textura de reabsorción generalizada tipo "*spongy cellular, sieved*" (ver Streck, 2008).

Tipo 4: Microcristales que se encuentran en coronas que rodean a los cristales de anfíbol o como inclusiones en algunos piroxenos (Fig. 2D).

El rango composicional observado en las plagioclasas analizadas es relativamente amplio, entre An71 y An54, y corresponden en su mayor parte a labradoritas (Fig. 5), excepto dos ejemplares de bitownita identificados en la matriz microcristalina. A pesar de la existencia de cuatro poblaciones principales de plagioclasas, el rango

Tabla 5—**Análisis químicos, número de magnesio y valores de temperatura (T) y presión (P) calculados para cristales de clinopiroxeno en lavas del volcán El Metate**

	M60		M61	M63	M64			M66	M70		M74	M77
	1	2	1	1	1	2	3	1	1	2	1	1
	Matriz	Microfeno.	Feno.	Feno.	Feno.	Microfeno.	Microfeno.	Feno.	Feno.	Feno.	Feno.	Feno.
SiO_2	51.36	49.18	51.12	49.80	50.48	50.313	51.941	50.64	50.20	50.79	49.91	50.90
Al_2O_3	2.85	3.89	3.32	3.50	3.01	2.706	2.302	2.81	3.66	2.98	3.45	2.69
FeO^T	7.61	8.15	6.36	8.23	6.70	9.051	6.587	9.31	8.01	8.89	8.05	7.91
MnO	0.34	0.28	0.20	0.20	0.08	0.14	0.124	0.26	0.15	0.12	0.20	0.22
MgO	16.44	15.13	16.42	15.14	16.52	15.465	16.599	18.42	14.75	16.14	15.55	15.51
CaO	20.84	21.77	22.62	21.13	21.78	20.594	22.026	17.39	21.09	18.65	21.47	21.71
Na_2O	0.36	0.45	0.36	0.35	0.31	0.337	0.261	0.31	0.36	0.33	0.40	0.27
K_2O	0.06	—	0.01	0.03	0.00	—	0.012	0.00	0.00	0.03	—	0.00
TiO_2	0.55	1.00	0.41	0.74	0.50	0.674	0.342	0.72	0.74	0.79	0.50	0.45
NiO	—	0.05	0.05	0.10	0.02	0.034	0.034	—	0.04	—	0.02	0.03
Cr_2O_3	—	0.07	0.06	0.07	0.29	—	0.094	0.03	0.07	—	0.03	—
P_2O_5	0.00	0.29	0.03	0.01	0.04	—	0.016	—	0.08	0.01	0.05	0.03
F	—	0.05	0.05	—	0.07	—	0.023	0.00	0.02	—	0.01	0.06
Cl	0.02	0.01	—	0.03	0.00	—	—	0.02	0.01	—	0.00	—
Total	100.43	100.31	101.00	99.33	99.79	99.31	100.36	99.90	99.17	98.71	99.62	99.76
#Mg	89	92	97	87	96	84	91	89	83	80	91	88
T (°C)	1111	1098	1069	1097	1045	1080	1069	1018	1128	1147	1099	1064
P (Kbar)	4.9	5.9	3.6	5.5	2.5	4.1	2.9	0.4	6.3	6.5	6.3	3.6

Análisis químicos expresados en % en peso del óxido. Todos los análisis en fenocristales han sido realizados en los bordes.
T calculada según ecuación 9; P calculada según ecuación 8.

composicional observado en los análisis de feno- y microfenocristales y microcristales (ver la sección de geotermometría) muestran un rango equivalente al del conjunto de plagioclasas, con cierta tendencia de los cristales de la matriz a proyectarse en el extremo más anortítico del espectro (labradorita-bitownita), mientras que los bordes de microfenocristales se proyectan en la región de tendencia albítica.

Las plagioclasas de Tipo 3 (de textura de reabsorción generalizada tipo "*spongy cellular sieved*") no han podido ser caracterizadas geoquímicamente dado el alto grado de alteración que presentan. Tampoco se han caracterizado las plagioclasas presentes en las coronas de los anfíboles, ya que pueden representar productos de reacciones de desequilibrio.

Ortopiroxeno

El ortopiroxeno raramente se encuentra como fenocristal, pero es frecuente como microfenocristal, asi como en la matriz o formando parte del núcleo de un cristal con recrecimiento de clinopiroxeno.

Los cristales analizados se clasifican como enstatitas (Fig. 5) y tienen un rango composicional que oscila entre valores de #Mg (#Mg = Mg/(Mg+Fe^{+2}) × 100) desde 81% a 73% (Tabla 4) para los microfenocristales, mientras que los cristales de la matriz se proyectan en un rango composicional algo más estrecho (79–74%).

Clinopiroxeno

El clinopiroxeno aparece como fenocristales, microfenocristales así como en la matriz. La mayor parte de los microfeno y microcristales tienen inclusiones de opacos, mientras que los fenocristales muestran zonas isótropas, principalmente en el núcleo, y se caracterizan por tener un estrecho borde de recrecimiento (Fig. 2A). Algunos cristales exhiben además características particulares: pueden encontrarse en continuidad óptica con Opx formando un zonado en parches, o bien hallarse en forma de agregados de cristales con zonación concéntrica, donde el núcleo está formado por Opx y las zonas externas por Cpx.

El valor #Mg de los Cpx analizados varía entre 97–80% (Tabla 5) y se proyectan como augitas en

Tabla 6—**Análisis químicos, clasificación y valores de temperatura (T), presión (P) y contenido en agua del fundico (H_2O) calculados para cristales de anfíbol en lavas del volcán El Metate**

	M20		M60			M61	M66		M74		M77
	1	2	1			1	1	2	1		1
	Medio	Centro	a Centro	b Medio	c Borde	Centro	Centro	Centro	a Centro	b Borde	Centro
SiO_2	45.04	45.13	42.96	41.72	42.57	43.69	42.58	43.68	43.54	44.23	44.839
Al_2O_3	11.38	11.19	12.51	12.90	12.66	12.72	11.97	10.74	12.19	11.25	11.001
FeO^T	8.69	8.16	8.37	10.73	9.64	9.41	10.14	10.33	11.11	8.53	8.349
MnO	0.08	0.11	0.04	0.09	0.09	0.12	0.14	0.14	0.12	0.08	0.161
MgO	16.45	17.57	16.74	14.99	16.37	15.47	15.88	15.64	15.02	16.57	16.697
CaO	12.17	11.99	12.28	11.54	11.74	11.68	11.95	11.79	11.82	11.85	11.159
Na_2O	2.18	2.09	2.40	2.36	2.55	2.35	2.38	2.39	2.25	2.23	2.152
K_2O	0.38	0.37	0.54	0.51	0.51	0.49	0.39	0.37	0.52	0.61	0.382
TiO_2	1.94	1.55	2.08	2.35	1.97	1.50	2.13	2.30	1.38	1.38	1.204
NiO	—	0.10	0.05	—	0.13	—	0.12	—	0.04	0.03	0.008
Cr_2O_3	0.07	0.34	0.29	0.01	0.02	—	0.01	0.03	0.04	0.13	0.095
P_2O_5	—	—	0.02	—	0.02	0.03	0.03	0.02	0.02	0.03	0.044
F	0.11	0.02	0.12	0.09	0.15	0.06	0.11	0.02	0.06	0.08	0.051
Cl	0.04	0.04	0.03	0.04	0.04	0.04	0.10	0.02	0.04	0.03	0.01
Total	98.52	98.64	98.41	97.32	98.44	97.54	97.93	97.47	98.14	97.03	96.15
Clasificación	magnesio-Hastingsita	magnesio-Hastingsita	magnesio-Hastingsita	magnesio-Hastingsita	magnesio-Hastingsita	Pargasita	magnesio-Hastingsita	magnesio-Hastingsita	magnesio-Hastingsita	magnesio-Hastingsita	magnesio-Hastingsita
T (°C)	944	943	995	990	990	964	978	922	954	946	943
P (Kbar)	2.9	2.7	3.9	4.5	4.0	4.2	3.5	2.8	3.7	3.0	2.7
H_2O (%)	6.0	5.5	5.5	6.3	5.5	6.9	5.7	5.2	6.5	5.3	5.9

Análisis químicos expresados en % en peso del óxido.
T calculada según ecuación 10; P calculada según ecuación 11; H_2O calculada según ecuación 12.

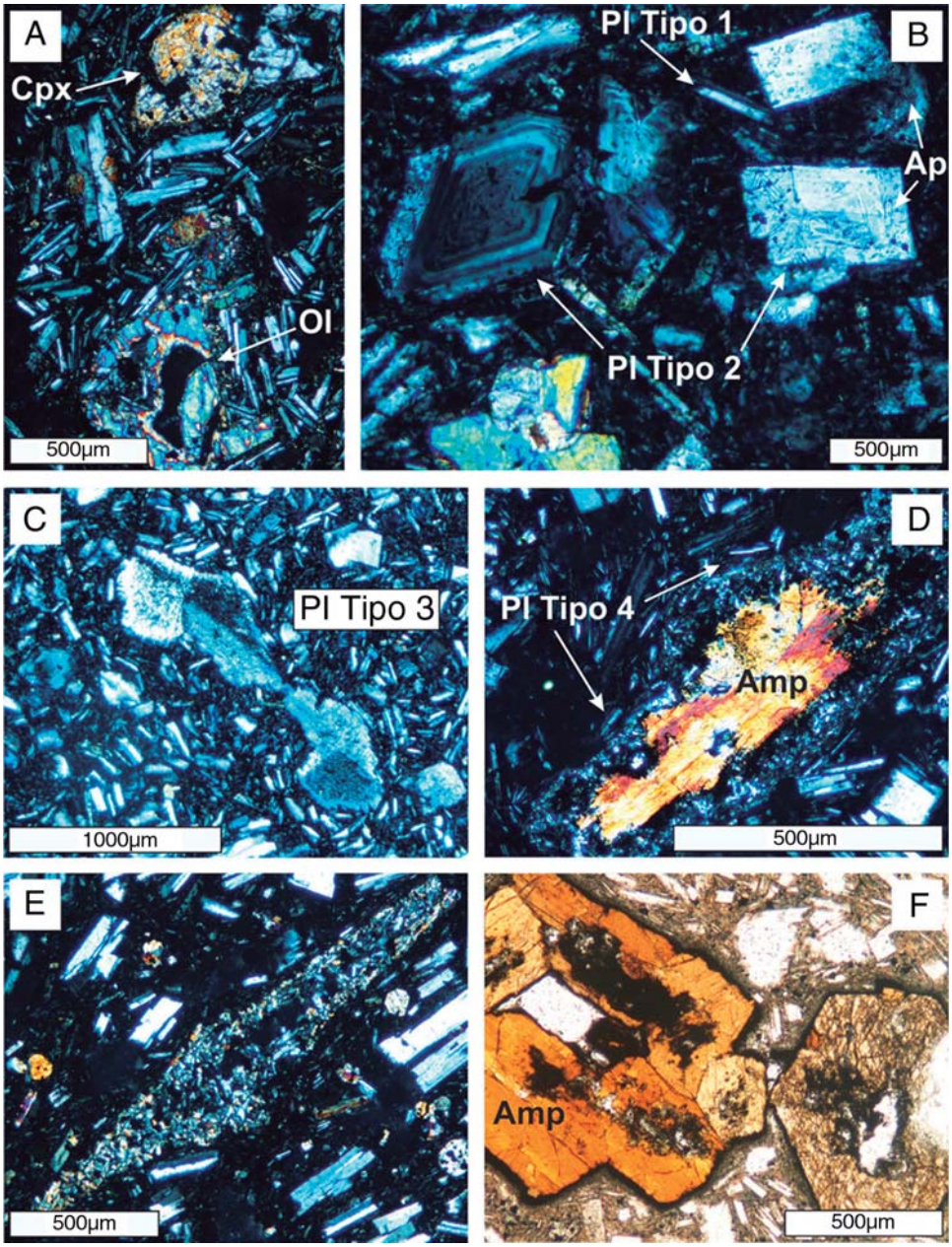

Fig. 2.—A) Fenocristales de olivino y clinopiroxeno en una matriz de plagioclasas de Tipo 4 (muestra M-57, nícoles cruzados). B–C) Ejemplos de plagioclasas de los tipos 1, 2 y 3 e inclusiones de apatito (muestra M-64, nícoles cruzados); D) Anfíbol con corona de opacita granular compuesta por Plg+Cpx+óxidos (muestra M-20, nícoles cruzados); E) pseudomorfo de anfíbol completamente reemplazado (muestra M-60, nícoles cruzados); F) Anfíboles con corona de opacita simplectítica (muestra M-57, nícoles paralelos).

el diagrama de clasificación Mg-Ca-Fe (Fig. 5). Los cristales de la matriz y los microfenocristales presentan las composiciones más magnésicas, con rangos de #Mg entre 84-92%. En cambio, los bordes de los fenocristales analizados abarcan un amplio abanico de composiciones (#Mg = 80–97%).

Anfíbol

El Amp aparece como fenocristal y también como microfenocristal y muestra una compleja historia de alteración que incluye dos tipos de opacitización (*sensu* Plechov *et al.*, 2008). Por un lado,

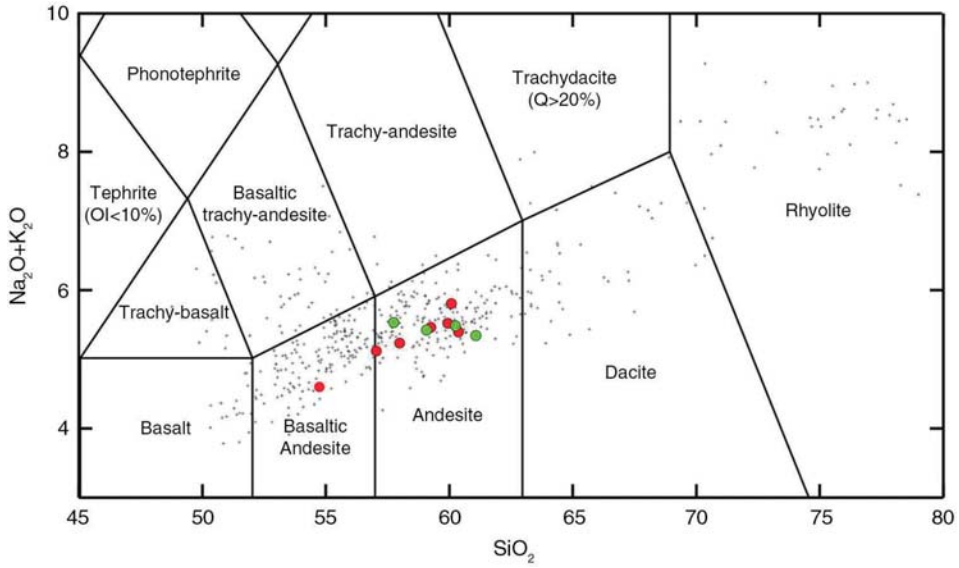

Fig. 3.—Proyección de las lavas de El Metate (círculos rojos y verdes) y rocas del Campo Volcánico de Michoacán–Guanajuato (cruces, según datos en Gómez-Tuena *et al.*, 2007 y referencias incluidas) en el diagrama TAS (Le Bas *et al.*, 1992). Datos en porcentaje en peso.

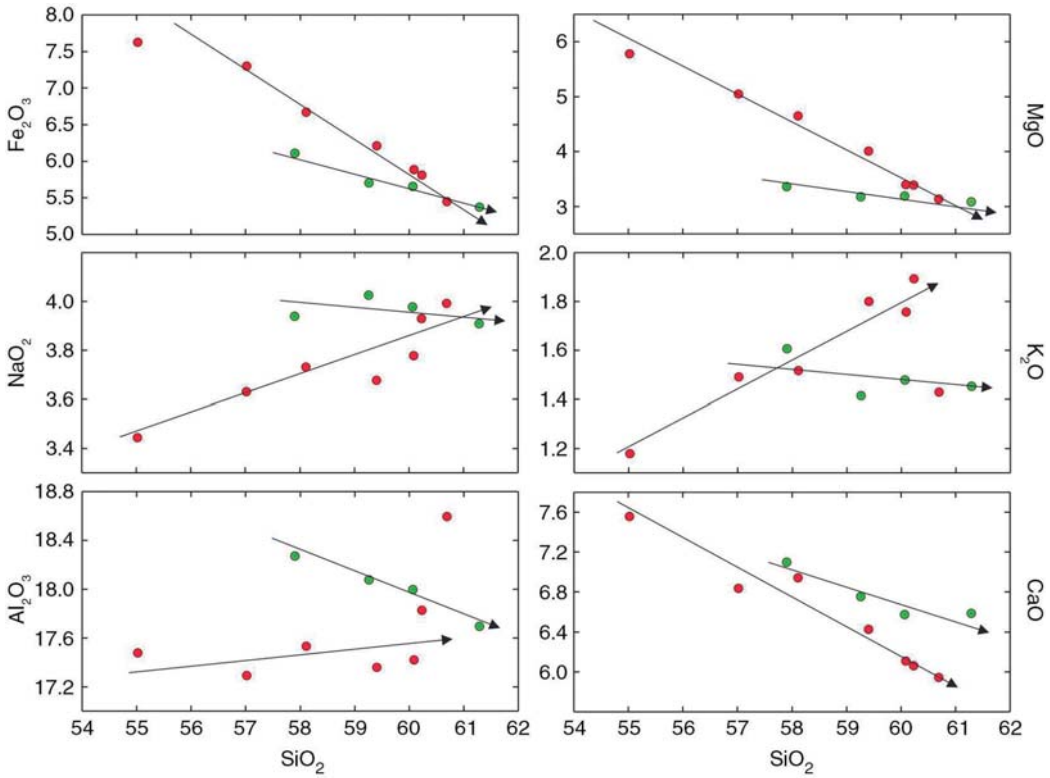

Fig. 4.—Diagramas SiO_2-óxidos (en % en peso) para las lavas de El Metate. Se indican las dos pautas de diferenciación observadas.

se puede observar opacitización en coronas, que a su vez están compuestas por dos zonas: una parte interna que se desarrolla directamente en contacto con el anfíbol (opacita granular) y compuesta por Pl, Cpx y óxidos de entre 3 y 10 μm; y una parte externa de opacita simplectítica, que en ocasiones

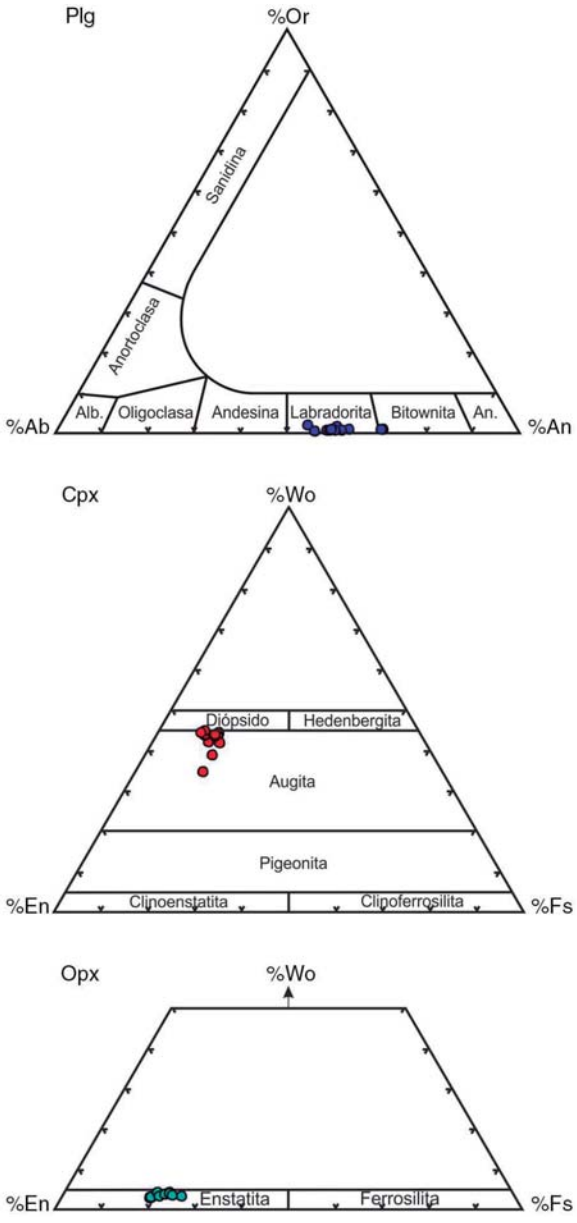

Fig. 5.—Diagramas de clasificación de plagioclasas (Ab-An-Or) y de piroxenos (Wo-En-Fe).

es la única que se desarrolla, compuesta por un agregado isótropo de minerales de grano fino cuya composición no pudo ser determinada. Por otro lado, también se observa opacitización en forma de áreas de descomposición volumétrica. Se denomina de este modo a zonas de reemplazamiento en el interior del cristal que han sido alteradas a través de planos de debilidad y que en este caso están compuestas mayoritariamente por cristales de clinopiroxeno que heredan la orientación estructural del anfibol al que reemplazan.

Atendiendo al tipo de corona de opacita que presentan, se pueden distinguir dos tipos de cristales: a) los casi euhedrales con tamaños que pueden ir desde fenocristales hasta microfenocristales, que no suelen presentar alteración en áreas de descomposición volumétrica y muestran únicamente coronas de opacita simplectítica (isótropa) (Fig. 2F), y b) los que presentan corona de opacita granular de Pl, Cpx y opacos muy desarrollada (Fig. 2D), que en ocasiones llega a reemplazar todo el mineral (pseudomorfos) (Fig. 2E). Estos cristales no suelen presentar opacita isótropa y son de tamaño inferior a los primeros. Todas las muestras con anfíbol incluyen ambos tipos, si bien los primeros son los más frecuentes.

En todos los casos se corresponden a anfíboles cálcicos y se clasifican como Mg-hastingsitas, a excepción de una pargasita (mayor contenido en Na respecto a Ca). No se han observado diferencias composicionales entre los diferentes tipos de cristales identificados petrográficamente.

Geotermobarometría

A partir de las diferentes formulaciones de geotermómetros y geobarómetros disponibles en la literatura (ver Putirka, 2008) se seleccionaron aquellos que mejor se adaptan en cada caso al rango composicional de las rocas objeto de estudio, así como a la paragénesis representada por Pl, Cpx, Opx, Ol y Amp.

La mayoría de estos geotermobarómetros estiman las condiciones P-T a partir de equilibrios químicos mineral-mineral o mineral-líquido. En consecuencia, para aplicarlos de forma estricta, solo se pueden considerar aquellos cristales o zonas de los mismos, que no presenten evidencias de desestabilización y se encuentren en contacto con la fase (sea mineral o líquido) con la que se encuentra en equilibrio. En consecuencia, los cálculos basados en equilibrios mineral-líquido se han limitado a las composiciones obtenidas en aquellas zonas de los minerales sin texturas de desequilibrio y que se encuentran en contacto con la matriz, asumiendo que la composición de la roca total representa de forma aproximada la composición del magma en equilibrio con las fases que contiene. Este es el caso de los termobarómetros

para Ol, Cpx, Opx y Pl, que se basan en relaciones de intercambio entre el mineral y el fundido en equilibrio. Sin embargo, para el Amp las consideraciones anteriores no son aplicables debido a que el termobarómetro disponible utiliza únicamente la composición del mineral, por lo que se pueden utilizar tanto las composiciones obtenidas en el centro como en el borde del cristal.

Olivino

En el caso del olivino hemos adoptado la ecuación 22 de Putirka (2008), basada en el equilibrio olivino-líquido:

$$\begin{aligned} T(^{\circ}C) = &\left\{15294.6 + 1318.8P(GPa) + 2.4834[P(GPa)]^2\right\} / \\ &\left\{8.048 + 2.8352 \ln D_{Mg}^{Ol/liq} + 2.097 \ln\left[1.5\left(C_{NM}^{L}\right)\right]\right. \\ &+ 2.575 \ln\left[3\left(C_{SiO_2}^{liq}\right)\right] - 1.41NM + 0.222H_2O^{liq} \\ &\left. + 0.5P(GPa)\right\} \end{aligned} \quad [1]$$

donde:

$$D_{Mg}^{Ol/liq} = X_{Mg}^{Ol} / X_{Mg}^{liq}$$

$$C_{NM}^{L} = X_{FeO}^{liq} + X_{MnO}^{liq} + X_{MgO}^{liq} + X_{CaO}^{liq} + X_{CoO}^{liq} + X_{NiO}^{liq}$$

$$C_{SiO_2}^{liq} = X_{SiO_2}^{liq}$$

$$NF = \frac{7}{2}\ln\left(1 - X_{AlO_{1.5}}^{liq}\right) + 7\ln\left(1 - X_{TiO_2}^{liq}\right)$$

Esta ecuación es esencialmente una modificación del modelo de Beattie (1993), basado en el reparto de Mg entre olivino y líquido, pero que evita las sobreestimaciones en el cálculo de T en condiciones hidratadas.

Para testar la existencia de equilibrio entre olivino y el líquido, se utiliza el coeficiente de distribución Fe-Mg de la reacción:

$$MgO^{Ol} + FeO^{liq} = MgO^{liq} + FeO^{Ol}$$

cuya expresión es:

$$K_D\left(Fe - Mg\right)^{Ol-liq} = \left(X_{Fe}^{Ol} * X_{Mg}^{liq}\right) / \left(X_{Mg}^{Ol} * X_{Fe}^{liq}\right) \quad [2]$$

Como demostraron Roeder & Emslie (1970), este parámetro varía muy poco con la T o la composición del par olivino-líquido y tiene un valor prácticamente constante de 0.30 ± 0.03 en sistemas basálticos a P<2–3 GPa.

Plagioclasa

En el caso de la plagioclasa, teniendo en cuenta la habitual presencia de agua en rocas calcoalcalinas (típicamente entre 1% y 4% en volcanes del CVMG; Johnson *et al.* 2010), hemos adoptado la ecuación 24a de Putirka (2008), que considera la posible presencia de agua en el líquido y reduce los errores respecto a calibraciones anteriores (p.ej. Ghiorso *et al.*, 2002; Mathez, 1973; Putirka, 2005).

$$\begin{aligned} \frac{10^4}{T(K)} = &6.4706 + 0.3128 \ln\left\{\frac{X_{An}^{Pl}}{X_{CaO}^{liq}(X_{AlO_{1.5}}^{liq})^2(X_{SiO_2}^{liq})^2}\right\} \\ &- 8.103\left(X_{SiO_2}^{liq}\right) + 4.87\left(X_{KO_{0.5}}^{liq}\right) + 1.5346\left(X_{Ab}^{Pl}\right)^2 \\ &+ 8.661\left(X_{SiO_2}^{liq}\right) - 3.341 * 10^{-2}\left(P(kbar)\right) \\ &+ 0.18047(H_2O^{liq}) \end{aligned} \quad [3]$$

Para los cálculos de presión hemos utilizado la ecuación. 25a de Putirka (2008), originaria de Putirka (2005), por coherencia con el termómetro.

$$\begin{aligned} P(kbar) = &\\ &-42.2 + 4.94 \times 10^{-2} T(K) + 1.16 \times 10^{-2} T(K) \\ &\ln\left\{\frac{X_{Ab}^{Pl} X_{AlO_{1.5}}^{liq} X_{CaO}^{liq}}{X_{An}^{Pl} X_{NaO_{0.5}}^{liq} X_{SiO_2}^{liq}}\right\} - 382.3\left(X_{SiO_2}^{liq}\right)^2 \\ &+514.2\left(X_{SiO_2}^{liq}\right)^3 - 19.6\ln\left(X_{Ab}^{Pl}\right) - 139.8\left(X_{CaO}^{liq}\right) \\ &+287.2\left(X_{NaO_{0.5}}^{liq}\right) + 163.9\left(X_{KO_{0.5}}^{liq}\right) \end{aligned} \quad [4]$$

Como prueba de equilibrio del par Pl-liq se ha utilizado la constante de equilibrio $K_D(An\text{-}Ab)^{Pl\text{-}liq}$. Aunque este parámetro varía respecto a P, T y H_2O, al ser dividido en dos intervalos de T se obtienen

valores relativamente constantes de K_D(An-Ab)$^{Pl\text{-}liq} = 0{,}10 \pm 0{,}05$ para T<1050 °C y K_D(An-Ab)$^{Pl\text{-}liq} = 0{,}27 \pm 0{,}11$ para T >1050°C.

También se ha empleado la expresión 25b de (Putirka, 2008) ya que el equilibrio Pl-líquido proporciona un buen higrómetro cuando T es conocida:

$$H_2O(Wt) = 25.95 - 0.0032T(°C)$$

$$\ln\left\{\frac{X^{Pl}_{An}}{X^{liq}_{CaO}\left(X^{liq}_{AlO_{1.5}}\right)^2\left(X^{liq}_{SiO_2}\right)^2}\right\} - 18.9\left(X^{liq}_{KO_{0.5}}\right) + 14.5\left(X^{liq}_{MgO}\right)$$

$$-40.3\left(X^{liq}_{CaO}\right) + 5.7\left(X^{pl}_{An}\right) + 0.108P(Kbar) \quad [5]$$

Puesto que estas expresiones requieren conocer previamente algunos parámetros de las otras, la resolución se ha efectuado mediante cálculo iterativo.

Ortopiroxeno

Para estimar las temperaturas de cristalización del ortopiroxeno hemos adoptado el termómetro calibrado por Putirka (2008) en su ecuación 28a. Esta expresión rectifica algunos problemas de sobreestimación de T asociados con el anterior termómetro de Beattie (1993), que hasta entonces era el único disponible, basado en el equilibrio Opx-líquido. La nueva calibración es aplicable en un amplio rango de P y entre 750–1600 °C, SiO_2 = 33–77% y H_2O = 0–14.2%, con un error de ± 39 °C (n = 793).

$$\frac{10^4}{T(°C)} = 4.07 - 0.329\left[P(GPa)\right] + 0.12\left[H_2O^{liq}\right]$$

$$+0.567\ln\left[\frac{X^{Opx}_{Fm_2Sio_2O_6}}{\left(X^{liq}_{SiO_2}\right)^2\left(X^{liq}_{FeO} + X^{liq}_{MnO} + X^{liq}_{MgO}\right)^2}\right]$$

$$-3.06\left[X^{liq}_{MgO}\right] - 6.17\left[X^{liq}_{KO_{0.5}}\right] + \left(Mg\#^{liq}\right) + 2.57\left[X^{Opx}_{Fe}\right] \quad [6]$$

donde Fm = Fe + Mn + Mg

Para los cálculos de P hemos seleccionado la ecuación 29a de Putirka (2008), que utiliza la correlación positiva de $FmAl_2SiO_6$ respecto a P (entre 0.001 y 0.05 kbar) y proporciona estimaciones con un error de ± 2.6 kbar.

$$P(kbar) =$$

$$-13.97 + 0.0129T(°C) + 0.001416T(°C)$$

$$\ln\left[\frac{X^{Opx}_{NaAlSiO_2O_6}}{X^{liq}_{NaO_{0.5}}X^{liq}_{AlO_{1.5}}\left(X^{liq}_{SiO_2}\right)^2}\right] - 19.64\left(X^{liq}_{SiO_2}\right)$$

$$+47.49\left(X^{liq}_{MgO}\right) + 6.99\left(X^{Opx}_{Fe}\right) + 37.37\left(X^{Opx}_{FmAl_2SiO_6}\right)$$

$$+0.748\left(H_2O^{liq}\right) + 79.67\left(X^{liq}_{NaO_{0.5}} + X^{liq}_{KO_{0.5}}\right) \quad [7]$$

Como test de equilibrio del par Opx-líquido nos basamos en el diagrama de Rhodes (Rhodes *et al.*, 1979) y el valor K_D (Fe-Mg)$^{Opx\text{-}liq} = 0.29 \pm 0.06$ (para n = 785). Este valor no depende de P y T, pero disminuye ligeramente con el aumento en contenido en sílice de modo que K_D (Fe-Mg)$^{Opx\text{-}liq}$ = $0{,}4805 - 0{,}3733 * X_{Si}^{liq}$.

Clinopiroxeno

Los barómetros para clinopiroxenos se basan en la reacción $NaO_{0.5}^{liq} + AlO_{1.5}^{liq} + 2SiO_2^{liq} = NaAlSi_2O_6^{cpx}$, si bien los modelos más recientes han sido calibrados usando H_2O^{liq} (en % en peso) como variable para describir mejor las muestras hidratadas (Grove & Juster, 1989; Kinzler & Grove, 1992; Patiño Douce, 2005; Putirka *et al.*, 1996; Putirka, 2008; Scaillet & MacDonald, 2003; Sisson & Grove, 1993a; Sisson & Grove, 1993b; Walter & Presnall, 1994). De estas, hemos seleccionado para el cálculo de P la expresión 32c de Putirka (2008), por su buen ajuste respecto a valores experimentales (error estimado de ± 1.5 kbar para n = 99).

$$P(kbar) = -57.9 + 0.0475T(K) - 40.6\left(X^{liq}_{FeO}\right) - 47.7\left(X^{Cpx}_{CaTs}\right)$$

$$+0.676\left(H_2O^{liq}\right) - 153\left(X^{liq}_{CaO_{0.5}}X^{liq}_{SiO_2}\right) + 6.89\left[\frac{X^{Cpx}_{Al}}{X^{lq}_{AlO_{1.5}}}\right] \quad [8]$$

Análogamente, para los cálculos de temperatura se ha utilizado la ecuación 33 de (Putirka, 2008), con errores estimados de ± 42 °C (para n = 320 hidratado) y ± 46 °C (para n = 854 anhidro).

$$\frac{10^4}{T(K)} = 7.53 - 0.14 \ln\left(\frac{X_{Id}^{Cpx} X_{CaO}^{liq} X_{Fm}^{liq}}{X_{DiHd}^{Cpx} X_{Na}^{liq} X_{Al}^{liq}}\right) + 0.07(H_2O^{liq}) - 14.9\left(X_{CaO}^{liq} X_{SiO_2}^{liq}\right) - 0.08 \ln\left(X_{TiO_2}^{liq}\right) - 3.62\left(X_{NaO_{0.5}}^{liq} + X_{KO_{0.5}}^{liq}\right) - 1.1\left(Mg\#^{liq}\right) - 0.18 \ln\left(X_{EnFs}^{Cpx}\right) - 0.027P(kbar) \quad [9]$$

Como test de equilibrio se ha calculado el valor de $K_D(Fe\text{-}Mg)^{Cpx\text{-}liq}$, que adopta un valor de 0,28 ± 0,08 mostrando poca variación respecto a la temperatura (Putirka, 2008).

Anfíbol

Para calcular los valores de P y T de cristalización de los anfíboles hemos adoptado el reciente termobarómetro de Ridolfi *et al.* (2010), que no se basa en el equilibrio con el líquido y representa el único modelo actualmente disponible para anfíboles en magmas calcoalcalinos. Esta expresión permite asimismo calcular el porcentaje de H_2O del magma a partir del cual cristalizaría el anfíbol analizado.

$$T = -151.487 Si^* + 2{,}041 \quad [10]$$

donde:

$$Si^* = Si + \frac{^{[4]}Al}{15} - 2^{[4]}Ti - \frac{^{[6]}Al}{2} - \frac{^{[6]}Al}{1.8} + \frac{Fe^{3+}}{9} + \frac{Fe^{2+}}{3.3} + \frac{Mg}{26} + \frac{^{B}Ca}{5} + \frac{^{B}Na}{1.3} - \frac{^{A}Na}{15} + \frac{^{A}[\ ]}{2.3}$$

$$T = 19.209e^{(1.438 Al_T)} \quad [11]$$

donde Al_T es aluminio total.

$$H_2O_{melt} = 5.215^{[6]}Al^* + 12.28 \quad [12]$$

donde:

$$^{[6]}Al^* = {}^{[6]}Al + \frac{^{[6]}Al}{13.9} - \frac{Si + {}^{[6]}Ti}{5} - \frac{^{c}Fe^{2+}}{3} - \frac{mg}{1.7} + \frac{Ca + {}^{A}[\ ]}{1.2} + \frac{^{A}Na}{2.7} - 1.56K - \frac{Fe\#}{1.6}$$

Resultados

Como se ha indicado anteriormente, la aplicación de geotermómetros basados en equilibrios mineral-líquido plantea ciertas limitaciones ya que requiere contar con pares que no muestren signos de desequilibrio (p.ej. bordes corroídos o coronas de reacción). Además, si se acepta que la composición del líquido está representada por la roca total, es necesario asumir que el equilibrio se verifica únicamente con el borde de los minerales presentes en la roca. En consecuencia, las temperaturas obtenidas se limitan a la etapa final de cristalización de dichas fases. Para obtener las temperaturas a las que se produjo la cristalización de zonas internas de los minerales, sería necesario conocer la composición del líquido en equilibrio en el momento de la cristalización de dichas zonas.

De acuerdo con lo expuesto, en este trabajo los cálculos basados en geotermómetros mineral-líquido se han restringido a aquellos análisis obtenidos en minerales que no muestran evidencias texturales de desequilibrio respecto a la matriz y limitados bien a minerales que no muestran zonación (usualmente microcristales), o bien a bordes de fenocristales o microfenocristales. Asimismo, como se ha indicado más arriba, se han considerado únicamente aquellos pares mineral-líquido que proporcionan valores K_D dentro de los rangos considerados de equilibrio en cada caso. En las Tablas 2 a 6 y en la fig. 6 se recogen los resultados obtenidos de esta aproximación.

En el caso del Ol (Tabla 2), las temperaturas obtenidas oscilan entre 1232−1198°C, con una tendencia general a disminuir la temperatura de cristalización a medida que progresa la diferenciación (Fig.6A).

Los cálculos para equilibrios Pl-liq proporcionan unas temperaturas y presiones de 1162–1126 °C, y 7.3−3.6 kbar respectivamente (Tabla 3). No se han observado diferencias significativas en los valores de T respecto al contenido en SiO_2 entre los distintos tipos de plagioclasas ni entre fenocristales y microcristales. Por otro lado, la variación de P respecto a T sugiere un rango de presiones bastante más amplio que el que se observa en las temperaturas calculadas.

Por su parte, la cristalización de los ortopiroxenos abarca un rango de temperaturas entre 1147 °C y 1027 °C (Tabla 4), con una tendencia general a la

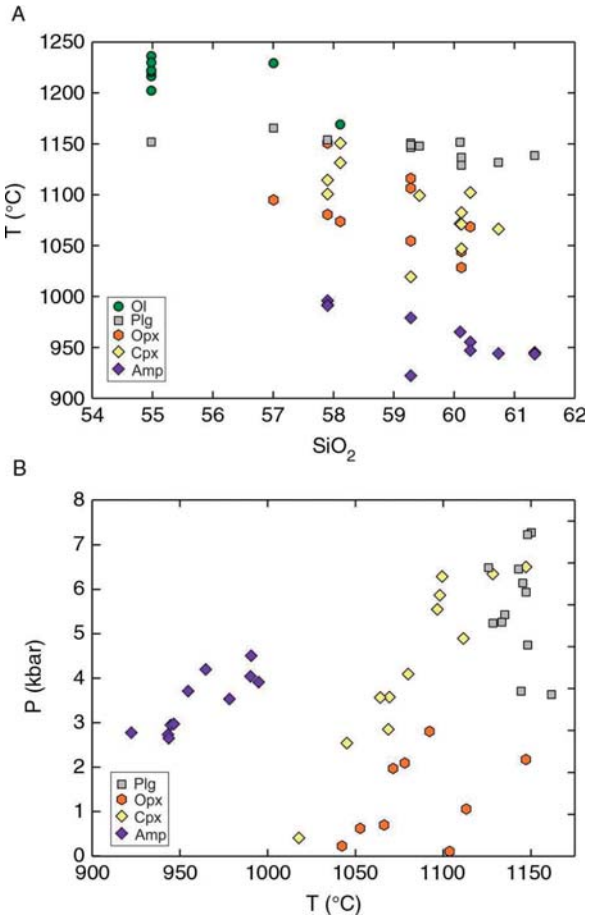

Fig. 6.—A) Diagrama de temperatura vs. SiO2 (% en peso) en roca total; y B) Diagrama de presión vs temperatura obtenidos para olivino, plagioclasa, ortopiroxeno, clinopiroxeno y anfíbol en las lavas de El Metate.

T al aumentar el contenido de SiO_2 (Fig. 6A). En el gráfico P-T los resultados se disponen con pocas excepciones en una relación directa de disminución de P con respecto a T (Fig. 6B). Como en el caso de las plagioclasas, no se observan diferencias entre las dos trayectorias de evolución o los tipos de Opx identificados.

El clinopiroxeno presenta el rango más amplio de temperaturas, desde los 1147 °C a los 1018 °C (Tabla 5), con cierta tendencia a disminuir el valor de T con el aumento de SiO_2 (Fig. 6A). La variación de P con respecto a la T sigue, como en el resto de fases analizadas, la relación directa habitual. Al igual que en el caso de Pl y Opx, tampoco se observan diferencias significativas en función de las diferentes tipologías de cristales analizados o de las pautas de evolución identificadas a partir de elementos mayores en roca total.

Los anfíboles analizados indican un rango de variación de T para la cristalización de esta fase entre 995 y 922 °C (Tabla 6), disponiéndose en una pauta de pendiente negativa respecto al aumento del contenido en SiO_2 de la roca correspondiente (Fig. 6A). Tanto los núcleos como los bordes analizados se proyectan en todo el rango de variación de T-SiO_2, aunque en este caso se aprecia cierta disminución de T de centro a borde en los cristales zonados. Por otro lado, las muestras con menor SiO_2 presentan los valores de P más altos, siguiendo una tendencia P-T análoga al resto de fases minerales (Fig. 6B).

Discusión y conclusiones

Como se desprende de las variaciones composicionales basadas en elementos mayores, puestas de manifiesto en los diagramas SiO_2-elemento (Fig. 4), las lavas de El Metate se han fraccionado a partir de dos pautas de diferenciación constrastadas. Sin embargo, por lo que respecta a sus características petrográficas, apenas se observan diferencias significativas entre ambas tendencias. Así, la presencia de olivino, que está limitada a una de las pautas de evolución, coincide con los términos de menor grado de diferenciación (es decir, con mayor MgO y #Mg, y menor SiO_2), que están ausentes en la otra línea de diferenciación. Asimismo, si bien la presencia de anfíbol es característica de la serie con menor abundancia de MgO, dicha fase también se encuentra en las rocas con mayor grado de diferenciación del otro grupo (y por ende, con menor contenido relativo en MgO y K_2O). A pesar de estas diferencias, en todos los casos Pl, Opx y Cpx, aparecen como fenocristales y por tanto deben haber participado en el proceso de diferenciación de ambas series, sin que tampoco se hayan detectado diferencias significativas en lo que se refiere a la composición o la textura de ninguna de las fases estudiadas entre ambos grupos de rocas.

Por lo que respecta a las características del proceso de diferenciación, la frecuente presencia de texturas de desequilibrio en muchas de las fases (p.ej. zonaciones complejas, bordes corroídos y recrecimientos en plagioclasas, bordes de opacita y coronas de reacción en anfíboles), sugieren una evolución relativamente compleja. La posibilidad

más razonable, siendo además el escenario más habitualmente observado en el volcanismo monogenético de Michoacán (ver p.ej. Cebriá *et al.*, 2011; Corona-Chávez *et al.*, 2006; Chesley *et al.*, 2002; Luhr & Carmichael, 1985; Urrutia-Fucugauchi & Uribe-Cifuentes, 1999), sugiere a una evolución en sistema abierto, que podría implicar tanto la asimilación de material xenolítico como inyecciones de nuevos aportes de magma en el sistema. Por este motivo resulta especialmente adecuada la aproximación adoptada aquí, considerando exclusivamente aquellos minerales que representan fases en equilibrio con el magma que los engloba y cuya composición se asume respresentada por la composición de la roca total. Obviamente, esto implica que los resultados termobarométricos obtenidos se refieren al momento final de la cristalización de cada fase y por tanto es posible que no aporten información sobre las etapas previas de cristalización, cuyo estudio requeriría establecer la composición de los respectivos líquidos en equilibrio.

En la fig. 6A se presentan las temperaturas obtenidas para cada una de las fases respecto al contenido en SiO_2 de la roca, que se puede asumir como indicador del grado de diferenciación. Como se puede observar, la secuencia de cristalización se verifica en un relativamente estrecho margen de temperatura, comenzando con la aparición de Ol (1232−1198 °C), seguido de Pl (1162–1126 °C), Opx (1147−1027 °C) y Cpx (1147–1018 °C). En esta secuencia, el Ol deja de cristalizar con la aparición del Opx y los fenocristales de Pl con la del Cpx. Por su parte, el Amp cristalizaría en una última etapa, entre los 995°C y 922°C.

Los datos de P obtenidos (Fig. 6B) por los diferentes geobarómetros, indican que la cristalización se verifica entre los ~7 y 0 kbar, con una correspondencia directa entre P y T lo que sugiere que el proceso de diferenciación tuvo lugar desde ~25 km de profundidad hasta niveles superficiales.

Es de destacar que, como se ha descrito, los cristales de anfíbol presentan en todos los casos evidencias de desequilibrio, a pesar de lo cual se han podido calcular valores de T, P y contenido en agua gracias a la aplicación de un geotermobarómetro basado únicamente en la composición del mineral, por lo que estos datos solo aportan las condiciones de cristalización de los Amp, independientemente de que se encuentren o no en equilibrio con la roca huesped. En consecuencia, cabe la posibilidad de que los cristales de anfíbol representen xenocristales y que por tanto no se encuentren en equilibrio con el magma que los engloba. La procedencia de estos xenocristales podría resultar bien de la asimilación de las rocas atravesadas por el magma durante su ascenso a la superficie o bien de la mezcla con un pulso de magma más silíceo y de menor temperatura. Por otro lado, las condiciones geotermobarométricas calculadas y las variaciones en elementos mayores, también podrían explicarse si el Amp se genera en la última etapa en la secuencia de cristalización de estos magmas. Este supuesto se vería apoyado por la existencia de Amp en las dos tendencias de diferenciación identificadas, apareciendo siempre en los términos más evolucionados (con menor contenido en MgO) y en relación directa con un característico empobrecimiento en K_2O (que sería consecuencia del fraccionamiento de esta fase). Asimismo, esta hipotesis se vería reforzada ya que la cristalización de Amp está limitada a presiones entre 5 y 2.5 kbar. Esto podría explicar su desequilibrio al alcanzar niveles superficiales, donde se produce la desgasificación del magma y una reducción drástica del contenido en H_2O.

Al igual que en el caso del Amp, las evidencias de desequilibrio de otras fases pueden explicarse por desestabilización de dichas fases tras su cristalización durante etapas previas de la diferenciación, al variar las condiciones fisicoquímicas del magma en etapas posteriores de su evolución. Por ejemplo, en el caso de la Pl la desestabilización puede ser debida al incremento en el contenido de agua durante la cristalización, que como hemos visto se sitúa en torno al 1.6 % durante su cristalización y alcanzaría hasta el 6.9% durante la cristalización de Amp. Esta es una situación relativamente frecuente en magmas calcoalcalinos y se ha observado también en volcanes cercanos como el Paricutin (Cebriá *et al.*, 2011), donde su desaparición como fenocristal coincidiendo con la aparición de Opx, se interpretó como consecuencia del aumento en H_2O, en este caso debido a la entrada de agua en el sistema por asimilación de un componente cortical.

En resumen, los datos preliminares obtenidos en este estudio permiten establecer las condiciones

P-T-H_2O bajo las que ha tenido lugar el proceso de diferenciación de las lavas de El Metate. Así, la secuencia de cristalización Ol ± Pl-Opx-Cpx(±Amp?) parece iniciarse a unos 25 km de profundidad y temperaturas en torno a 1230 °C. El aumento del contenido en H_2O que se produce en el sistema al progresar la cristalización pudo haber provocado en primer lugar que la Pl deje de ser una fase estable en el sistema y que cuando en torno a los 990°C se alcanza un porcentaje de agua de ~7% se inicie la cristalización del Amp, que dejará de ser estable a niveles superficiales. No obstante las texturas de desequilibrio que presentan estas dos fases minerales sugieren que algunos cristales de Pl y los de Amp pueden tener un origen xenolítico.

Estos datos preliminares constituyen la base necesaria para perfilar un modelo petrogenético, que permita definir con precisión los parámetros del proceso, pero requieren resolver previamente algunas de las incógnas planteadas y que se encuentran actualmente en estudio. Así por ejemplo, es necesario establecer precisiones sobre las variaciones composicionales y termobarométricas a nivel de cristal en aquellos casos donde se observan zonaciones, lo que requiere además establecer la composición de sus correspondientes líquidos en equilibrio. Esto permitiría confirmar o descartar si en algún caso se trata de xenocristales y si se ha producido o no la entrada de nuevos aportes de magma en el sistema. Esta situación también podrá verificarse a partir del estudio de los microcristales presentes en coronas de reacción, como las observadas en Amp. Finalmente, contar con un mayor número de datos permitirá confirmar que realmente no existen diferencias termobarométricas entre las dos pautas de diferenciación observadas a partir de los elementos mayores de las rocas, como parecen indicar los primeros datos aquí expuestos.

AGRADECIMIENTOS

Este trabajo ha sido financiado mediante el proyecto CGL2011-23422 del Ministerio de Economía y Competitividad de España. Asimismo se agradece la concesión a E. Losantos de una beca FPI (BES-2012-052390) asignada a dicho proyecto.

Agradecemos a Rufino Lozano-Santa Cruz y Laura Luna González, del Instituto de Geología (UNAM) por los análisis de FRX y por el apoyo en los trabajos de campo respectivamente, y a Alfredo Fernández Larios del Centro Nacional de Microscopía Electrónica (UCM) por su asistencia en los análisis por microsonda electrónica. Gracias especiales a Francisco Pérez Torrado (Universidad de Las Palmas de Gran Canaria) y a José Luis Arce (Instituto de Geología, UNAM) por la revisión del manuscrito original, que han mejorado el trabajo y han aportado nuevas ideas para futuras investigaciones.

Referencias

Beattie, P. (1993). Olivine-melt and orthopyroxene-melt equilibria. Contributions to Mineralogy and Petrology, 115(1): 103–111. http://dx.doi.org/10.1007/BF00712982.

Cebriá, J.M.; Martiny, B.M.; López-Ruiz, J. & Morán-Zenteno, D.J. (2011). The Parícutin calc-alkaline lavas: New geochemical and petrogenetic modelling constraints on the crustal assimilation process. Journal of Volcanology and Geothermal Research, 201(1–4): 113–125. http://dx.doi.org/10.1016/j.jvolgeores.2010.11.011.

Corona-Chávez, P.; Reyes-Salas, M.; Gardu-o-Monroy, V.H.; Israde-Alcántara, I.; Lozano-Santa Cruz, R.; Morton-Bermea, O. & Hernández-Álvarez, E. (2006). Assimilation of granitic xenoliths in the Michoacán-Guanajuato volcanic field: The case of Arócutin, Michoacán, Mexico. Revista Mexicana de Ciencias Geológicas, 23(2): 233–245.

Costa, F.; Andreastuti, S.; Bouvet de Maisonneuve, C. & Pallister, J.S. (2013). Petrological insights into the storage conditions, and magmatic processes that yielded the centennial 2010 Merapi explosive eruption. Journal of Volcanology and Geothermal Research, 261: 209–235. http://dx.doi.org/10.1016/j.jvolgeores.2012.12.025.

Chesley, J.; Ruiz, J.; Righter, K.; Ferrari, L. & Gómez-Tuena, A. (2002). Source contamination versus assimilation: An example from the Trans-Mexican volcanic arc. Earth and Planetary Science Letters, 195(3–4): 211–221. http://dx.doi.org/10.1016/S0012-821X(01)00580-5.

Dahren, B.; Troll, V.; Andersson, U.; Chadwick, J.; Gardner, M.; Jaxybulatov, K. & Koulakov, I. (2012). Magma plumbing beneath Anak Krakatau volcano, Indonesia: evidence for multiple magma storage regions. Contributions to Mineralogy and Petrology, 163(4): 631–651. http://dx.doi.org/10.1007/s00410-011-0690-8.

Ferrari, L.; López-Martínez, M.; Aguirre-Díaz, G. & Carrasco-Núñez, G. (1999). Space-time patterns of Cenozoic arc volcanism in central Mexico: From the Sierra Madre Occidental to the Mexican Volcanic Belt. Geology, 27(4): 303–306. http://dx.doi.org/10.1130/0091-7613(1999)027<0303:STPOCA>2.3.CO;2.

Ferrari, L.; Orozco-Esquivel, T.; Manea, V. & Manea, M. (2012). The dynamic history of the Trans-Mexican

Volcanic Belt and the Mexico subduction zone. Tectonophysics, 522–523(0): 122–149. http://dx.doi.org/10.1016/j.tecto.2011.09.018.

Ghiorso, M.S.; Hirschmann, M.M.; Reiners, P.W. & Kress, V.C. (2002). The pMELTS: A revision of MELTS for improved calculation of phase relations and major element partitioning related to partial melting of the mantle to 3 GPa. Geochemistry, Geophysics, Geosystems, 3(5): 1–35. http://dx.doi.org/10.1029/2001GC000217.

Gómez-Tuena, A.; Orozco-Esquivel, M.T. & Ferrari, L. (2007). Igneous petrogenesis of the Trans-Mexican Volcanic Belt. In: Geology of México: Celebrating the Centenary of the Geological Society of México. (Alaniz-Álvarez, S.A. & Nieto-Samaniego, A.F., eds.) Geological Society of America Special Paper 422, 129–181. http://dx.doi.org/10.1130/2007.2422(05).

Grove, T.L. & Juster, T.C. (1989). Experimental investigations of low-Ca pyroxene stability and olivine-pyroxene-liquid equilibria at 1-atm in natural basaltic and andesitic liquids. Contributions to Mineralogy and Petrology, 103(3): 287–305. http://dx.doi.org/10.1007/BF00402916.

Hasenaka, T. (1994). Size, distribution, and magma output rate for shield volcanoes of the Michoacán-Guanajuato volcanic field, Central Mexico. Journal of Volcanology and Geothermal Research, 63(1–2): 13–31. http://dx.doi.org/10.1016/0377-0273(94)90016-7.

Hasenaka, T. & Carmichael, I.S.E. (1985). The cinder cones of Michoacán-Guanajuato, central Mexico: their age, volume and distribution, and magma discharge rate. Journal of Volcanology and Geothermal Research, 25(1–2): 105–124. http://dx.doi.org/10.1016/0377-0273(85)90007-1.

Hasenaka, T. & Carmichael, I.S.E. (1987). The Cinder Cones of Michoacán-Guanajuato, Central Mexico: Petrology and Chemistry. Journal of Petrology, 28(2): 241–269. http://dx.doi.org/10.1093/petrology/28.2.241.

Johnson, C.A. & Harrison, C.G.A. (1989). Tectonics and volcanism in Central Mexico: A landsat thematic mapper perspective. Remote Sensing of Environment, 28(0): 273–286. http://dx.doi.org/10.1016/0034-4257(89)90119-3.

Johnson, E.R.; Wallace, P.J.; Cashman, K.V. & Delgado Granados, H. (2010). Degassing of volatiles (H_2O, CO_2, S, Cl) during ascent, crystallization, and eruption at mafic monogenetic volcanoes in central Mexico. Journal of Volcanology and Geothermal Research, 197(1–4): 225–238. http://dx.doi.org/10.1016/j.jvolgeores.2010.02.017.

Keiding, J.K. & Sigmarsson, O. (2012). Geothermobarometry of the 2010 Eyjafjallajökull eruption: New constraints on Icelandic magma plumbing systems. Journal of Geophysical Research: Solid Earth, 117 (B9): B00C09.

Kinzler, R.J. & Grove, T.L. (1992). Primary magmas of mid-ocean ridge basalts 1. Experiments and methods. Journal of Geophysical Research, 97(B5): 6885–6906. http://dx.doi.org/10.1029/91JB02840.

Le Bas, M.J.; Le Maitre, R.W. & Woolley, A.R. (1992). The construction of the Total Alkali-Silica chemical classification of volcanic rocks. Mineralogy and Petrology, 46(1): 1–22. http://dx.doi.org/10.1007/BF01160698.

Lozano-Santa Cruz, R. & Bernal, J.P. (2005). Characterization of a new set of eight geochemical reference materials for XRF major and trace element analysis. Revista Mexicana de Ciencias Geológicas, 22(3): 329–344.

Luhr, J.F. & Carmichael, I. (1985). Jorullo Volcano, Michoacán, Mexico (1759–1774): The earliest stages of fractionation in calc-alkaline magmas. Contributions to Mineralogy and Petrology, 90(2): 142–161. http://dx.doi.org/10.1007/BF00378256.

Mathez, E. (1973). Refinement of the Kudo-Weill plagioclase thermometer and its application to basaltic rocks. Contributions to Mineralogy and Petrology, 41(1): 61–72. http://dx.doi.org/10.1007/BF00377654.

Patiño Douce, A.E. (2005). Vapor-absent melting of tonalite at 15–32 kbar. Journal of Petrology, 46(2): 275–290. http://dx.doi.org/10.1093/petrology/egh071.

Plechov, P.Y.; Tsai, A.E.; Shcherbakov, V.D. & Dirksen, O.V. (2008). Opacitization conditions of hornblende in Bezymyannyi volcano andesites (March 30, 1956 eruption). Petrology, 16(1): 19–35. http://dx.doi.org/10.1134/S0869591108010025.

Putirka, K.; Johnson, M.; Kinzler, R.; Longhi, J. & Walker, D. (1996). Thermobarometry of mafic igneous rocks based on clinopyroxene-liquid equilibria, 0–30 kbar. Contributions to Mineralogy and Petrology, 123(1): 92–108. http://dx.doi.org/10.1007/s004100050145.

Putirka, K.D. (2005). Igneous thermometers and barometers based on plagioclase + liquid equilibria: Tests of some existing models and new calibrations. American Mineralogist, 90(2–3): 336–346. http://dx.doi.org/10.2138/am.2005.1449.

Putirka, K.D. (2008). Thermometers and Barometers for Volcanic Systems. Reviews in Mineralogy and Geochemistry, 69(1): 61–120. http://dx.doi.org/10.2138/rmg.2008.69.3.

Rhodes, J.M.; Dungan, M.A.; Blanchard, D.P. & Long, P.E. (1979). Magma mixing at mid-ocean ridges: Evidence from basalts drilled near 22°N on the mid-Atlantic Ridge. Tectonophysics, 55(1–2): 35–61. http://dx.doi.org/10.1016/0040-1951(79)90334-2.

Ridolfi, F.; Renzulli, A. & Puerini, M. (2010). Stability and chemical equilibrium of amphibole in calc-alkaline magmas: an overview, new thermobarometric formulations and application to subduction-related volcanoes. Contributions to Mineralogy and Petrology, 160(1): 45–66. http://dx.doi.org/10.1007/s00410-009-0465-7.

Roeder, P.L. & Emslie, R.F. (1970). Olivine-liquid equilibrium. Contributions to Mineralogy and Petrology, 29: 275–289. http://dx.doi.org/10.1007/BF00371276.

Scaillet, B. & MacDonald, R. (2003). Experimental constraints on the relationships between peralkaline rhyolites of the Kenya Rift Valley. Journal of Petrology, 44(10): 1867–1894. http://dx.doi.org/10.1093/petrology/egg062.

Sisson, T.W. & Grove, T.L. (1993a). Experimental investigations of the role of H_2O in calc-alkaline differentiation and subduction zone magmatism. Contributions to Mineralogy and Petrology, 113(2): 143–166. http://dx.doi.org/10.1007/BF00283225.

Sisson, T.W. & Grove, T.L. (1993b). Temperatures and H2O contents of low-MgO high-alumina basalts. Contributions to Mineralogy and Petrology, 113(2): 167–184. http://dx.doi.org/10.1007/BF00283226.

Streck, M.J. (2008). Mineral Textures and Zoning as Evidence for Open System Processes. Reviews in Mineralogy and Geochemistry, 69(1): 595–622. http://dx.doi.org/10.2138/rmg.2008.69.15.

Suter, M.; Contreras, J.; Gómez-Tuena, A.; Siebe, C.; Quintero-Legorreta, O.; García-Palomo, A.; Macías, J.L.; Alaniz-Álvarez, S.A.; Nieto-Samaniego, A.F. & Ferrari, L. (1999). Effect of strain rate in the distribution of monogenetic and polygenetic volcanism in the Transmexican volcanic belt: Comments and Reply. Geology, 27(6): 571–575. http://dx.doi.org/10.1130/0091-7613(1999)027<0571:EOSRIT>2.3.CO;2.

Urrutia-Fucugauchi, J. & Uribe-Cifuentes, R.M. (1999). Lower-crustal xenoliths from the Valle de Santiago maar field, Michoacan-Guanajuato volcanic field, central Mexico. International Geology Review, 41(12): 1067–1081. http://dx.doi.org/10.1080/00206819909465192.

Walter, M.J. & Presnall, D.C. (1994). Melting behavior of simplified lherzolite in the system CaO-MgO-Al_2O_3-SiO_2-Na_2O from 7 to 35 kbar. Journal of Petrology, 35(2): 329–359. http://dx.doi.org/10.1093/petrology/35.2.329.

Front cover: Top Parícutin lava field and Pico de Tancítaro National Park; Bottom, Pirámide de la Luna in Teotihuacán.

Back cover: The research team on the field.

UNIVERSIDAD
COMPLUTENSE
MADRID